

Advances in Polymer Science 277

Finizia Auriemma
Giovanni Carlo Alfonso
Claudio De Rosa *Editors*

Polymer Crystallization II

From Chain Microstructure to Processing

 Springer

Editorial Board:

- A. Abe, Yokohama, Kanagawa, Japan
- A.-C. Albertsson, Stockholm, Sweden
- G.W. Coates, Ithaca, NY, USA
- J. Genzer, Raleigh, NC, USA
- S. Kobayashi, Kyoto, Japan
- K.-S. Lee, Daejeon, South Korea
- L. Leibler, Paris, France
- T.E. Long, Blacksburg, VA, USA
- M. Möller, Aachen, Germany
- O. Okay, Istanbul, Turkey
- V. Percec, Philadelphia, PA, USA
- B.Z. Tang, Hong Kong, China
- E.M. Terentjev, Cambridge, UK
- P. Theato, Hamburg, Germany
- M.J. Vicent, Valencia, Spain
- B. Voit, Dresden, Germany
- U. Wiesner, Ithaca, NY, USA
- X. Zhang, Beijing, China

Aims and Scope

The series *Advances in Polymer Science* presents critical reviews of the present and future trends in polymer and biopolymer science. It covers all areas of research in polymer and biopolymer science including chemistry, physical chemistry, physics, material science.

The thematic volumes are addressed to scientists, whether at universities or in industry, who wish to keep abreast of the important advances in the covered topics.

Advances in Polymer Science enjoys a longstanding tradition and good reputation in its community. Each volume is dedicated to a current topic, and each review critically surveys one aspect of that topic, to place it within the context of the volume. The volumes typically summarize the significant developments of the last 5 to 10 years and discuss them critically, presenting selected examples, explaining and illustrating the important principles, and bringing together many important references of primary literature. On that basis, future research directions in the area can be discussed. *Advances in Polymer Science* volumes thus are important references for every polymer scientist, as well as for other scientists interested in polymer science - as an introduction to a neighboring field, or as a compilation of detailed information for the specialist.

Review articles for the individual volumes are invited by the volume editors. Single contributions can be specially commissioned.

Readership: Polymer scientists, or scientists in related fields interested in polymer and biopolymer science, at universities or in industry, graduate students.

Special offer:

For all clients with a standing order we offer the electronic form of *Advances in Polymer Science* free of charge.

More information about this series at <http://www.springer.com/series/12>

Finizia Auriemma • Giovanni Carlo Alfonso •
Claudio De Rosa

Editors

Polymer Crystallization II

From Chain Microstructure to Processing

With contributions by

P.-A. Albouy • G.C. Alfonso • W. Bras • D. Cavallo •
M. van Drongelen • D.A. Ivanov • H. Li •
G.W.M. Peters • G. Portale • Z. Qiu • P.C. Roozmond •
M. Rosenthal • P. Sotta • X. Sun • E.M. Troisi • R. Xin •
S. Yan • J. Zhang

 Springer

Editors

Finizia Auriemma
Department of Chemical Sciences
University of Naples Federico II
Napoli, Italy

Giovanni Carlo Alfonso
Department of Chemistry and Industrial
Chemistry
University of Genova
Genova, Italy

Claudio De Rosa
Department of Chemical Sciences
University of Naples Federico II
Napoli, Italy

ISSN 0065-3195

Advances in Polymer Science

ISBN 978-3-319-50683-8

DOI 10.1007/978-3-319-50684-5

ISSN 1436-5030 (electronic)

ISBN 978-3-319-50684-5 (eBook)

Library of Congress Control Number: 2002045271

© Springer International Publishing AG 2017

This work is subject to copyright. All rights are reserved by the Publisher, whether the whole or part of the material is concerned, specifically the rights of translation, reprinting, reuse of illustrations, recitation, broadcasting, reproduction on microfilms or in any other physical way, and transmission or information storage and retrieval, electronic adaptation, computer software, or by similar or dissimilar methodology now known or hereafter developed.

The use of general descriptive names, registered names, trademarks, service marks, etc. in this publication does not imply, even in the absence of a specific statement, that such names are exempt from the relevant protective laws and regulations and therefore free for general use.

The publisher, the authors and the editors are safe to assume that the advice and information in this book are believed to be true and accurate at the date of publication. Neither the publisher nor the authors or the editors give a warranty, express or implied, with respect to the material contained herein or for any errors or omissions that may have been made.

Printed on acid-free paper

This Springer imprint is published by Springer Nature

The registered company is Springer International Publishing AG

The registered company address is: Gewerbestrasse 11, 6330 Cham, Switzerland

Preface

The APS volumes “Polymer Crystallization: From Chain Microstructure to Processing” appear about 10 years after the three APS volumes (180, 181, and 191) “Interphases and Mesophases in Polymer Crystallization” edited by Giuseppe Allegra. The volumes follow a series of workshops on polymer crystallization held in Genova in 2010, 2012, and 2014, which were triggered by the need to stimulate debate and share new ideas among leading scientists from academia and industry on emerging topics related to the crystallization of polymers. We decided to collect some of these contributions into two APS volumes, eventually including the contributions of additional authors to fix the new concepts, ideas, and findings into a unified project reflecting the state of art.

With the development of new theoretical and experimental tools for investigating matter at the atomic level, significant advances in the understanding of phenomena associated with polymer crystallization have been achieved. However, elucidating the fundamental physical and chemical issues that govern the crystallization process in a polymer, by which chain molecules move from the melt state to a semicrystalline state with formation of lamellar crystals, is still a challenge.

The volumes include a wide range of different topics. The first section of Volume I is related to molecular aspects of polymer crystallization, with chapters on polymorphism (“Crystallization of Statistical Copolymers”), properties of statistical copolymers (“Molecular View of Properties of Random Copolymers of Isotactic Polypropylene”), the crystallization of cyclic polymers (“Crystallization of Cyclic Polymers”), and precision ethylene copolymers (“Crystallization of Precision Ethylene Copolymers”). This section ends with a chapter devoted to the crystallization of giant molecules (“Supramolecular Crystals and Crystallization with Nanosized Motifs of Giant Molecules”). The second section of Volume I deals with two different basic aspects of the nucleation process that are also important in industrial processes: self-nucleation (“Self-nucleation of Crystalline Phases Within Homopolymers, Polymer Blends, Copolymers and Nanocomposites”) and nucleation at high supercooling (“Crystal Nucleation of Polymers at High Supercooling of the Melt”).

Volume II begins with a section concerning aspects of polymer crystallization that have often been overlooked in the literature and are related to concomitant crystallization and cross-nucleation (“Concomitant Crystallization and Cross-Nucleation in Polymorphic Polymers”), surface-induced epitaxial crystallization (“Epitaxial Effects on Polymer Crystallization”), and study of the origin of banded spherulites with nanofocus X-ray diffraction (“Microstructure of Banded Polymer Spherulites: New Insights from Synchrotron Nanofocus X-Ray Scattering”). The two latter chapters are illustrative examples of modern investigation of crystal morphology at the molecular level. The second section of Volume II collects important issues in industrial application and processing. Topics includes the use of synchrotron light for studying phase transformation during processing or deformation in real time (“Real-Time Fast Structuring of Polymers Using Synchrotron WAXD/SAXS Techniques”), the role of amorphous phase in stress-induced crystallization of natural rubber (“Strain-Induced Crystallization in Natural Rubber”), the influence of cooling rate and pressure on polymer crystallization (“Non-isothermal Crystallization of Semicrystalline Polymers: The Influence of Cooling Rate and Pressure”), and the modeling of flow-induced crystallization (“Modeling Flow-Induced Crystallization”).

We are thankful to all contributors to the project for their high quality work.

These two volumes cover only a few aspects of polymer crystallization, and final solutions to the big problems in the field have not been assessed. Several topics covered in the volumes are still under development and need additional in-depth analyses, checks, and improvements. Nonetheless we hope that the selected topics will stimulate new discussions, inspire new theories and experiments, intrigue new followers, and initiate new research in this fascinating world.

Napoli, Italy

Genova, Italy
04 July 2016

Finizia Auriemma
Claudio De Rosa
Giovanni Carlo Alfonso

Contents

Concomitant Crystallization and Cross-Nucleation in Polymorphic Polymers	1
Dario Cavallo and Giovanni C. Alfonso	
Epitaxial Effects on Polymer Crystallization	55
Rui Xin, Jie Zhang, Xiaoli Sun, Huihui Li, Zhaobin Qiu, and Shouke Yan	
Microstructure of Banded Polymer Spherulites: New Insights from Synchrotron Nanofocus X-Ray Scattering	95
Dimitri A. Ivanov and Martin Rosenthal	
Real-Time Fast Structuring of Polymers Using Synchrotron WAXD/SAXS Techniques	127
Giuseppe Portale, Enrico M. Troisi, Gerrit W.M. Peters, and Wim Bras	
Strain-Induced Crystallization in Natural Rubber	167
Pierre-Antoine Albouy and Paul Sotta	
Non-isothermal Crystallization of Semi-Crystalline Polymers: The Influence of Cooling Rate and Pressure	207
M. van Drongelen, P.C. Roozmond, and G.W.M. Peters	
Modeling Flow-Induced Crystallization	243
Peter C. Roozmond, Martin van Drongelen, and Gerrit W.M. Peters	
Index	295

Concomitant Crystallization and Cross-Nucleation in Polymorphic Polymers

Dario Cavallo and Giovanni C. Alfonso

Abstract Crystallization of polymorphic polymers can lead to different structures, starting from the same melt or solution. Comprehensive understanding of crystallization modalities in such systems is of primary technological and scientific relevance, because it can enable prediction – and possible control – of the polymorphic composition of a material and, in turn, of its properties. Several structuring pathways are possible. A given structure can develop either directly or through successive metastable states. The latter case obeys the so-called Ostwald’s rule of stages. Under particular thermodynamic and kinetic conditions, two or more polymorphs can nucleate and grow concomitantly. Moreover, cross-nucleation is observed when a faster growing polymorph nucleates on a previously existing polymorph. This chapter is focused on concomitant crystallization and cross-nucleation between polymer polymorphs, two topics that have seldom been considered in the past and lack critical review. First, the scattered pieces of information in the polymer literature are collected and discussed. Within this framework, we present two relevant examples taken from our own work, concerning concomitant crystallization of poly(pivalolactone) polymorphs and cross-nucleation in seeded crystallization of isotactic poly(1-butene).

Keywords concomitant crystallization • cross-nucleation • nucleation • polymorphic polymers • polymorphism

Contents

1	Introduction	2
2	Crystallization Pathways in Polymorphic Systems	3
2.1	Ostwald’s Rule of Stages	3

D. Cavallo (✉) and G.C. Alfonso
Department of Chemistry and Industrial Chemistry, University of Genoa, Via Dodecaneso 31,
16146 Genoa, Italy
e-mail: dario.cavallo@unige.it

2.2	Concomitant Crystallization of Polymorphs	7
2.3	Cross-Nucleation Between Polymorphs	22
3	Case Study I: Concomitant Crystallization of Poly(pivalolactone)	35
4	Case Study II: Cross-Nucleation in Seeded Crystallization of Isotactic Poly (1-butene)	42
5	Conclusions	49
	References	50

1 Introduction

Polymorphism, which is the ability of a given substance to acquire different ordered arrangements in the solid state (i.e., to crystallize into different structures) is an ubiquitous phenomenon in nature and material science. Basically, all types of crystallizable compounds can exhibit polymorphism: it is found in complex organic molecules [1], in simple molecules such as water [2], and even in single chemical elements (e.g., sulfur and phosphorus).

Clearly, the different structures of the same substance (i.e., the polymorphs) can display remarkably different physical properties, including melting point, solubility, and electrical properties. Striking examples are the polymorphs (also referred to as allotropes) of carbon: diamond and graphite. The differences in their mechanical properties such as hardness and electrical conductivity are self-evident.

In the field of pharmaceuticals, the polymorphism of a certain drug is of great concern. Crystallization of the same molecule into different structures can result in largely different dissolution rates and bioavailability [1]. Given the importance of this issue, it is not surprising that the production of different crystalline modifications of a given drug has been the object of patent litigations between pharmaceutical industries.

Crystallizable macromolecules (i.e., semicrystalline polymers) are no exception and frequently show polymorphism [3–5]. To give some examples, both isotactic poly(4-methyl-1-pentene) (i-P4M1P) and poly(vinylidene fluoride) (PVDF) present five known structures [6, 7]. Polymer crystals are characterized by the ordered packing of chain segments, which acquire a regular and low energy conformation, into a unit cell. Therefore, two basic types of polymorphs can be found in semicrystalline polymers. Polymorphism can arise from different packing modes of sequences of repeating units possessing identical regular conformation, or from the possible existence of several low-energy conformations for a given polymer. An example of the first type is isotactic polypropylene (i-PP), in which the same threefold helical conformation is packed in a monoclinic, trigonal, or orthorhombic lattice in the α -, β - and γ -forms, respectively [8, 9]. The chains of syndiotactic polypropylene (s-PP), on the other hand, adopt a helical conformation in Form I crystals and a more extended *trans* planar conformation in Form III [10].

Also in the case of macromolecules, polymorphs of the same polymer can exhibit largely different properties. For instance, the β -phase of PVDF exhibits piezoelectric properties, whereas the α -phase does not [11]. In addition, the mechanical response

can also vary substantially between different crystalline modifications of the same polymer. In the case of i-PP, the trigonal β -phase displays enhanced toughness compared with the monoclinic α -phase of the same material [12, 13].

The ability to “steer” the crystallization process by controlling which structure develops (when multiple choices involving both packing mode and conformation exist) represents the holy grail of material scientists and crystallization engineers. What drives the system towards the formation of a particular polymorph is an issue of fundamental scientific and technological relevance. Hence, an understanding of the intimate mechanisms of polymorphic crystallization is of paramount importance. Although we are fairly able to describe the crystallization process by taking into account thermodynamic and kinetic aspects, control of the phenomenon is far less straightforward. In this respect, a striking example is that of “disappearing polymorphs” [14]. The term refers to cases of organic molecules in which a given polymorph, which has previously been routinely obtained, suddenly becomes very difficult to prepare. This behavior, which challenges the notion of reproducibility of a scientific experiment, is attributed to unintentional contamination with “seeds” (i.e., small crystallites or foreign bodies) that promote formation of the unwanted polymorph.

Different crystallization pathways can be recognized when dealing with polymorphic substances. A common observation is the so-called Ostwald’s rule of stages [15], according to which a phase transition occurs through steps of increasing thermodynamic stability (i.e., from the least to the most stable polymorph in successive stages). If suitable thermodynamic and kinetic conditions are met, two (or more) polymorphs can also form concomitantly, that is, they nucleate independently and grow simultaneously in the same melt or supersaturated solution [16]. A fast growing polymorph can also nucleate heterogeneously on the surface of another polymorph, without requiring any phase transition between them. This latter scheme has recently been referred to as cross-nucleation [17].

In this chapter we present an overview of the different crystallization pathways encountered in polymorphic polymers. First, a comprehensive review of the examples of concomitant polymorphism and cross-nucleation in polymer literature are provided. In this framework, we discuss some relevant case studies from our own work, namely, the concomitant crystallization of α - and γ -forms of poly (pivalolactone) (PPVL) and Form II-on-Form I cross-nucleation in isotactic poly (1-butene) (i-PBu).

2 Crystallization Pathways in Polymorphic Systems

2.1 *Ostwald’s Rule of Stages*

At the end of the nineteenth century, Ostwald proposed his famous rule, which states that “when leaving a metastable state, a given chemical system does not seek out the most stable state, rather the nearest metastable state that can be reached

without loss of free energy.” Although Ostwald’s statement is sometime indicated as a “law,” it must be remembered that it is an empirical observation, void of solid theoretical foundation.

Nevertheless, Ostwald’s rule is widely observed in a variety of systems, such as organic molecules [1], inorganic compounds [18], proteins [19–21], and colloids [22, 23]. On the other hand, a number of exceptions to Ostwald’s rule of stages have been observed [1, 24–26].

Several attempts to rationalize the empirical Ostwald’s rule have been carried out. Possible explanations rely on analysis of nucleation kinetics of the stable and metastable phases [27–29], or are based on irreversible thermodynamics, which show that Ostwald’s rule of stages minimizes entropy production [30, 31].

In the field of polymer crystallization, the occurrence of Ostwald’s rule of stages and the role of metastable states have been reviewed and discussed in detail by Keller and Cheng [32–35]. It is not the purpose of this chapter to provide examples additional to their work, but rather to focus on crystallization pathways that have been substantially disregarded in the polymer literature, namely, concomitant polymorphism and cross-nucleation. Therefore, we only briefly describe the proposed interpretation of Ostwald’s rule of stages in polymer crystallization, focusing on the peculiarity of polymer molecules with respect to other materials. A more detailed discussion and review of relevant cases can be found elsewhere [32–35].

Conformation to Ostwald’s rule of the phase transition in polymeric systems rests on both kinetics and thermodynamics. Similar to the case of crystals of small molecules [27–29], a kinetic justification of the phenomenon has been proposed, in which the rates of formation of the competing stable and metastable phases are considered. The overall rate of phase transition can be controlled either by the primary nucleation rate or by the growth rate. For the range of undercoolings (i.e., the difference between the equilibrium melting temperature and the actual temperature) in which the growth rate is determined by the secondary nucleation process, a general expression for the overall transition rate, R , is:

$$R = \alpha \cdot \exp\left(\frac{\beta}{T\Delta T^n}\right) \quad (1)$$

where α contains transport and frequency terms; β is the free energy barrier, which relates to the work required to form a nucleus (primary or secondary) of critical size; n is an integer dependent on the type of nucleation; and $\Delta T = T_m^0 - T$ is the undercooling, where (T_m^0) is the equilibrium melting temperature and T is the actual temperature. The barrier term is proportional to the ratio between the surface free energy and the melting enthalpy of the particular phase considered ($\sigma/\Delta H$). Equation (1) holds for each polymorph. All other factors being equal, the smaller the free energy barrier, the faster the transformation rate.

The validity of Ostwald’s rule indicates that $R_{\text{metastable}} > R_{\text{stable}}$, but this relation only holds if:

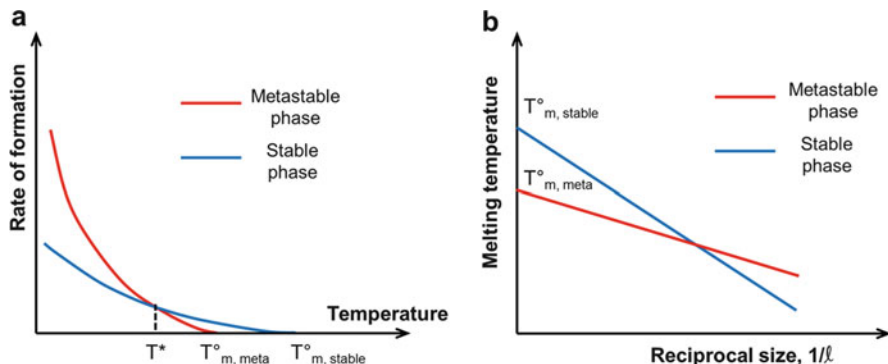


Fig. 1 (a) Formation rate as a function of temperature for polymers exhibiting polymorphism. (b) Melting temperature as a function of lamellar thickness for two different structures of the same polymer

$$\left(\frac{\sigma}{\Delta H}\right)_{\text{meta}} < \left(\frac{\sigma}{\Delta H}\right)_{\text{stable}} \quad (2)$$

Given that the transition rates are equal to zero at the equilibrium melting point of the specific structure ($T_{m,meta}^0$ and $T_{m,stable}^0$) and that $T_{m,meta}^0 < T_{m,stable}^0$, in the most probable situation the two formation rates cross over below a certain temperature [32]. The result is schematically depicted in Fig. 1a. It can be deduced that Ostwald's rule of stages has some intrinsic limits of validity. Indeed, three different temperature regions, characterized by distinct crystallization behaviors, are found. For temperatures between the equilibrium melting point of the stable and metastable phases, structuring can only occur directly to the stable phase (i.e., the behavior predicted by Ostwald's rule cannot be observed). However, below a certain temperature, T^* , an inversion of the formation rate of the two structures occurs, with the metastable phase developing faster than the stable phase, in agreement with Ostwald's rule of stages. Finally, in the temperature region between T^* and $T_{m,meta}^0$ the formation rates of the two structures are comparable, and the outcome of the crystallization process can be the concomitant crystallization of the two polymorphs.

Inversion of the formation rate of the different phases with temperature, which provides a kinetic justification for Ostwald's principle, has been observed experimentally for a number of polymers possessing crystalline and liquid crystalline (metastable) phases [36–38]. The same situation has also been reported for the more pertinent cases of true crystalline polymorphs, such as for the trigonal β -phase and monoclinic α -phase of i-PP [39, 40] and for the α - and β -phases of poly(butylene adipate) (PBA) [41] and s-PS [42].

As mentioned above, Ostwald's rule of stages in polymer crystallization is not only based on kinetic issues, but it also involves thermodynamics. In order to appreciate the link between kinetics and thermodynamics, the peculiar shape of polymer crystals must be accounted for. In fact, chain-folded lamellar crystals,

whose thickness is typically in the range 5–50 nm, are the basic morphological entities of semicrystalline polymers. The reduced crystal size in one direction results in a destabilizing effect of the high-energy fold surfaces, which needs to be taken into account because surface effects on crystal stability are typically negligible only for phase sizes well beyond the micrometer level. The melting point depression associated with the reduced size of polymer crystals can be quantified by the Gibbs–Thomson relation:

$$T_m = T_m^0 \left(1 - \frac{2\sigma_e}{l\Delta H} \right) \quad (3)$$

where T_m is the actual melting temperature of a crystal of thickness l , T_m^0 is the equilibrium melting temperature (of an ideal crystal of infinite size), ΔH is the melting enthalpy of the crystal, and σ_e is the fold surface free energy. The effect of the lateral surfaces of the lamella on crystal stability can usually be neglected. As shown in Fig. 1b for a polymorphic polymer, the actual melting temperature of the lamellar crystals is linearly dependent on the reciprocal of their thickness. It becomes clear that phase (or polymorph) stability is dependent on size. The terms “stable” or “metastable” polymorph must be referred to phases of macroscopic (i.e., “infinite”) size. In this context, the “classical” stability is determined by the equilibrium melting point: $T_{m,\text{stable}}^0 > T_{m,\text{meta}}^0$. If more than one polymorph is present, each has its own, different size dependence of the melting point according to Eq. (3) (see Fig. 1b). The slope of the linear relationship between T_m and l^{-1} is equal to $T_m^0(\sigma_e/\Delta H)$. If the inequality $(\sigma_e/\Delta H)_{\text{meta}} < (\sigma_e/\Delta H)_{\text{stable}}$ holds, the two lines of Fig. 1b cross over at a particular value of reciprocal lamellar thickness. This means that the stability of the two polymorphs can invert with size. In other words, a macroscopically metastable phase can become the more stable phase when its dimensions are small enough, and vice versa. The conventionally stable phase becomes metastable when its size is sufficiently small. The stability inversion of polymorphs with size has been experimentally observed, for example, in polyethylene crystallizing under pressure (hexagonal and orthorhombic phases) [32–34], in monoclinic and orthorhombic PBA [41], and in α - and β -polymorphs of s-PS [42].

We notice that the condition for the inversion of polymorph stability with size is the same as that of Eq. (2), which pertains to inversion in the order of transformation rates between stable and metastable polymorphs. Thus, the link between thermodynamics and kinetic factors behind Ostwald’s rule of stages in polymers is provided. Indeed, the stability diagram of Fig. 1b indicates the minimum phase size required to attain stability at a given temperature. From the kinetics point of view, this smallest stable size is related to the size of the critical nucleus, which determines the energetic barrier for crystal growth: the smaller the critical size, the faster the transformation. Therefore, the concepts of higher stability of the “macroscopically” metastable polymorph in the limits of small size and faster formation rate are interlinked.

Consequently, Ostwald's rule of stages is often obeyed in polymers because, at the beginning of the crystallization process, the metastable phase is the stable phase (as a result of its small size) and, at the same time (again thanks to the small size) is the phase that develops faster.

2.2 Concomitant Crystallization of Polymorphs

Before describing examples of concomitant crystallization of polymorphs, the thermodynamic and kinetic requirements for its occurrence are briefly introduced. Considering for simplicity a dimorphic system, two different situations can be distinguished from the thermodynamic point of view (see Fig. 2). By plotting the Gibbs free energy of the various phases (liquid, polymorph 1, and polymorph 2) as a function of temperature, monotropic or enantiotropic behavior can be identified as shown in Fig. 2a, b, respectively.

In a monotropic polymorphic system, one of the polymorphs (polymorph 1 in Fig. 2a) is metastable throughout the entire temperature range with respect to the second polymorph. In this system, only polymorph 2 and the liquid are ultimately stable, below and above $T_{m,2}$, respectively. Enantiotropic behavior is instead observed when each of the three phases is stable in a certain temperature range. Inversion of the stability of the two polymorphs occurs with increasing temperature above the $T_{2 \gg 1}$ indicated in Fig. 2b. Eventually, the liquid become the most stable phase above the melting point of polymorph 1, $T_{m,1}$.

Obviously, a necessary (but not sufficient) condition for concomitant crystallization in a monotropic system is that the crystallizing liquid should be undercooled with respect to both polymorphs (i.e., the temperature should be lower than $T_{m,1}$ of Fig. 2a). This strictly thermodynamic requirement implicitly contains a kinetic constraint. In order to reach such a low temperature, the stable polymorph has to possess slow crystallization kinetics, otherwise it would consume all the crystallizable liquid. This is often the case for semicrystalline polymers, which can typically

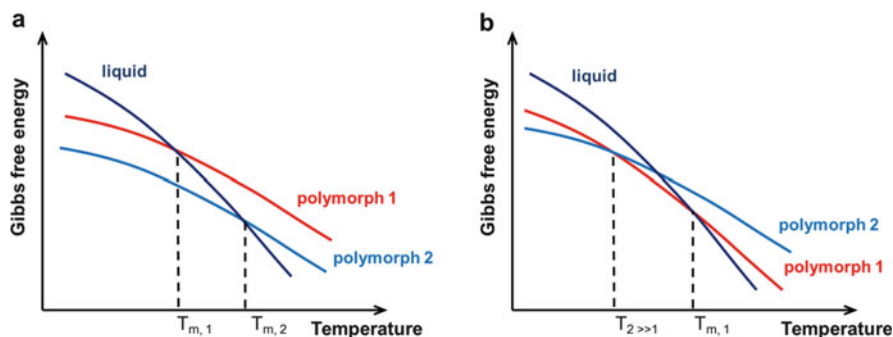


Fig. 2 Gibbs free energy versus temperature at constant pressure for (a) monotropic and (b) enantiotropic systems

attain very large undercooling before being able to crystallize at a measurable rate. Analogously, in the enantiotropic system described in Fig. 2b, concomitant crystallization of polymorphs 1 and 2 can be observed only if the crystallization temperature is lower than the melting point of polymorph 2 ($T_{m,2}$, not shown in the figure).

As indicated by Fig. 2, as a consequence of thermodynamics, at a given temperature (and pressure) only one of the polymorphs is stable, all others being metastable. Therefore, the simultaneous crystallization of two polymorphs is an out-of-equilibrium situation and the metastable polymorph tends to transform into the stable polymorph. Clearly, the lifetime of the metastable structure is determined by the kinetics of transition. As a matter of fact, transient polymorphs can disappear almost instantaneously, can last for a long time (e.g., weeks) as in the case of Form II of *i*-PBu [43, 44]), or even survive practically indefinitely (e.g., the β -phase of *i*-PP). The non-equilibrium nature of concomitant crystallization of polymorphs holds both for monotropic and enantiotropic systems, at any temperature, with the exception of the polymorph 2-to-polymorph 1 transition temperature ($T_{2\gg 1}$ in Fig. 2b). At that temperature, both structures are equally stable and co-exist in an equilibrium mixture. For lower temperatures, polymorph 1 tends to transform into polymorph 2, and vice versa at higher temperatures.

We now examine the kinetic aspects underlying polymorphic crystallization. A nucleation event is assumed to be the rate-determining step of the crystallization process. This can be either primary or secondary nucleation, that is, the formation of a new nucleus in the bulk of the undercooled melt or at the growth front of the crystal. Under this condition, the kinetics of polymorph crystallization can be understood by considering diagrams of the system free energy as a function of an appropriate reaction coordinate (see Fig. 3). The reaction coordinate is an abstract coordinate that represents the progress along the transformation pathway, from liquid to crystalline state. In this case, it can be identified with the size or the “order parameter” of a crystalline cluster.

The formation rate of a nucleus of the new phase is associated with a free energy penalty, caused by the creation of new interfaces. On the other hand, this loss of free

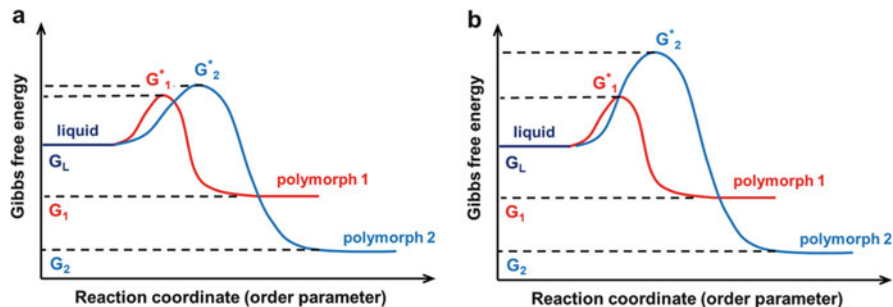


Fig. 3 Gibbs free energy versus reaction coordinate for systems in which concomitant crystallization is (a) likely or (b) unlikely to occur

energy is counterbalanced by a gain in stability that is proportional to the volume of the nascent phase. As a result, an activation energy barrier for the nucleation process is originated, the height of which depends on the nucleus size and, in turn, on the undercooling. In order to observe spontaneous growth of the nucleus, this activation energy barrier has to be overcome. The frequency of nucleation events (i.e., the crystallization rate in a wider sense) is inversely related to the magnitude of this activation barrier. It is important to note that crystallization kinetics in a polymorphic system has nothing to do with the relative stability of the two forms. This is schematized in Fig. 3. Polymorph 2 is more stable than polymorph 1; nevertheless, its crystallization is slower given the higher energy barrier associated with the formation of a nucleus of critical size ($G_2^* > G_1^*$).

From a kinetics perspective, it is clear that, in order to observe concomitant crystallization of polymorphs, the activation free energy landscape should resemble the scheme shown in Fig. 3a. In this case, the energy barriers for nucleation of the two polymorphs are very similar and concomitant crystallization can occur.

Figure 3b represents a situation in which concomitant crystallization of polymorphs 1 and 2 is unlikely. The less stable polymorph 1 is kinetically favored ($G_1^* < G_2^*$) over polymorph 2 and should be the main crystallization product. However, the resulting system would be in a metastable state and could evolve towards the thermodynamic “target” product (polymorph 2). A paradigmatic example of the scheme in Fig. 3b for polymorphic polymers is crystallization of i-PBu. The stable trigonal Form I grows about 100 times slower than the metastable tetragonal Form II, as a result of an energetic barrier for secondary nucleation that is more than four times larger for Form I than for Form II [45, 46]. By contrast, concomitant observation of Forms II and I is possible in the crystallization of 1-butene/propene copolymers. Copolymerization both lowers the energy barrier for direct evolution of Form I from the molten state (thus following the scheme of Fig. 3a) and accelerates the thermodynamically driven Form II-to-Form I transformation [47, 48].

Next we give some examples of concomitant crystallization of polymorphs. Many cases of concomitant polymorphism in small organic molecules have been neatly summarized and discussed in the review by Bernstein, Davey, and Henck [16]. The interested reader can also find there some extraordinary cases of trimorphic concomitant crystallization. However, a similar review is lacking for polymers. To highlight the extent and importance of the phenomenon in the realm of polymers, we report and attempt to rationalize all examples that, to the best of our knowledge, can be found in the literature.

The various examples, collected in a schematic form in Table 1, are discussed in detail. These concomitantly crystallizing polymorphs can also show cross-nucleation between them; we consider this aspect in a later Section 2.3.

Table 1 Examples of polymorphic polymers showing concomitant crystallization of different structures

Polymer	Polymorphs (name, structure)	Crystallization conditions	References
i-PP	α (monoclinic), β (trigonal)	<ul style="list-style-type: none"> • Melt crystallization between approximately 110 and 140°C • Presence of selective (β-phase) nucleants • Crystallization in temperature gradients • Application of shear flow fields 	[39, 40, 49–55]
i-PP	α (monoclinic), γ (orthorhombic)	<ul style="list-style-type: none"> • Melt crystallization at high pressures and temperature (e.g., $P > 75$ MPa, $T > 140^\circ\text{C}$) • Crystallization of defective, metallocene synthesized i-PP 	[56–59]
i-PBu	Form II (tetragonal), Form III (orthorhombic)	• Melt crystallization in the presence of traces of amyl acetate	[60]
i-P4M1P	Form I (tetragonal), Form III (tetragonal)	• Crystallization from slowly cooled diluted xylene and semidiluted <i>n</i> -octane solutions	[61]
i-P4M1P	Form II (monoclinic), Form III (tetragonal)	• Crystallization from semidiluted solutions of carbon disulfide, cyclooctane, cycloheptane, tetraethyltin, and tetramethyltin	[62]
s-PS	α (trigonal), β (orthorhombic)	• Isothermal crystallization between 230 and 260°C (or cooling at rates $>10^{-2}$ and $<30^\circ\text{C/s}$) after mild heat treatment of the melt	[63–66]
PVDF	α (pseudo-orthorhombic), γ (monoclinic)	• Melt crystallization at high temperatures (≈ 155 to 175°C)	[67–69]
PVDF	α (pseudo-orthorhombic), β (orthorhombic)	• Solution casting at intermediate evaporation temperatures/solvent evaporation rates.	[70–72]
PHP	β (orthorhombic), γ (orthorhombic)	• Melt crystallization at temperatures between 30 and 65°C	[73]
PHP	β (orthorhombic), γ (orthorhombic), δ (not given)	• Melt crystallization at intermediate undercoolings ($T = 65\text{--}60^\circ\text{C}$) after annealing in the melt at low temperatures	[74]
PBA	α (monoclinic), β (orthorhombic)	• Melt crystallization at intermediate undercoolings ($30^\circ\text{C} > T > 27^\circ\text{C}$)	[41, 75–82]
PBN	α (triclinic), β (triclinic)	<ul style="list-style-type: none"> • Non-isothermal melt crystallization at rates between 0.2 and 10°C/min • Isothermal melt crystallization between 210 and 225°C 	[83, 84]
PHexT	α (monoclinic), β (triclinic)	• Isothermal melt crystallization between 90 and 135°C	[85, 86]

(continued)

Table 1 (continued)

Polymer	Polymorphs (name, structure)	Crystallization conditions	References
PHepT	α (orthorhombic), β (not given)	• Melt crystallization between 55 and 80°C after annealing in the melt at low temperatures ($T = 110^\circ\text{C}$)	[87]
PE15Cl	Form I (triclinic), Form II (not given)	• Melt crystallization in a very narrow temperature range (53–54°C)	[88]

i-PP isotactic polypropylene, *i*PBu isotactic poly(1-butene), *i*-P4M1P isotactic poly(4-methyl-1-pentene), *s*-PS syndiotactic polystyrene, PVDF poly(vinylidene fluoride), PHP poly(3-hydroxypropionate), PBA poly(butylene adipate), PBN poly(butylene-2,6-naphthalate), PHexT poly(hexamethylene terephthalate), PHepT poly(heptamethylene terephthalate), PE15Cl polyethylene with a chlorine atom on every 15th backbone carbon atom

2.2.1 Isotactic Polypropylene

One of the most studied cases of concomitant polymorphism is that of the trigonal β -phase and monoclinic α -phase of *i*-PP [39, 40, 49–55]. The β -form is metastable with respect to the α -structure over the whole temperature range [55]; upon heating it melts and re-crystallizes in the monoclinic structure. The two structural modifications can be distinguished by polarized optical microscopy (POM), given that the spherulites of the β -polymorph are much more birefringent than those of the α -phase, and they can also show banding associated with twisting of lamellae along the radial direction (see Fig. 4a) [50, 53, 89]. The trigonal modification grows slightly faster (20–30%) than monoclinic polymorphs at temperatures between about 133–141 and 90–105°C, as shown in Fig. 4b [39, 40, 54].

Notwithstanding its faster growth, the probability of β -phase spontaneous nucleation is much lower than that of the α -modification. Therefore, concomitant crystallization of the two polymorphs is quite rare in the neat polymer [89].

However, there are very efficient and selective nucleating agents for trigonal modification (e.g., calcium pimelate) [90]. Concomitant crystallization of the α - and β -polymorphs is thus observed in *i*-PP loaded with a small amount (0.01–0.5 wt %) of β -phase nucleants [39, 40, 50, 53, 54]. Alternatively, concomitant crystallization of the two polymorphs in neat polymer can occur if the crystallization is carried out using a temperature gradient [49] or in the presence of a shear flow field [51, 52].

Isotactic polypropylene provides another example of concomitant crystallization of polymorphs, that of α - and γ - (orthorhombic) phases. In common Ziegler–Natta *i*-PP, formation of the γ -polymorph is promoted when crystallizing under elevated pressures: its content starts to increase at a few hundred bar, and eventually prevails over the α -phase at pressures around 1.5 kbar [56, 91]. The stability of the two structures is very close; the α -phase is thought to be slightly more stable at ambient conditions, but the situation can change with increasing pressure [56]. Concomitant crystallization of the two polymorphs occurs in a wide range of temperature and pressures; typically, for a given pressure, the α - and γ -phases coexist for

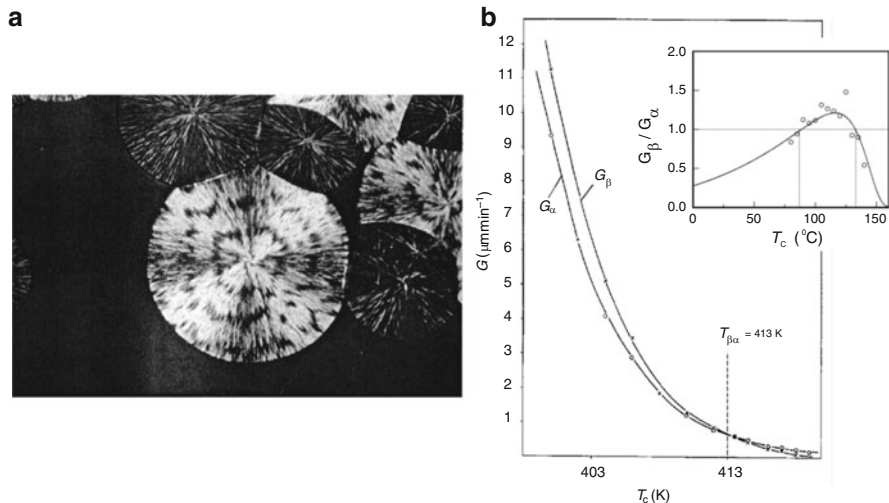


Fig. 4 (a) Optical micrograph showing β - (brighter, banded) and α - (darker) spherulites in i-PP. (b) Temperature dependence of the linear growth rate of α - and β -modifications. *Inset*: Ratio of the β - over α -growth rate as a function of crystallization temperature. Adapted with permission from [50, 53, 54]

crystallizations below a critical temperature. For example, a mixture of the two structures is found in samples crystallized under a pressure of 1.25 kbar at temperatures between 145 and 155°C. Higher temperatures result in the development of the γ -phase only [56].

It is important to note that, in contrast to what happens in i-PP β -phase, concomitantly crystallizing α - and γ -polymorphs do not form different spherulites. Instead, the two structures are intermixed inside the same spherulitic superstructure, with γ -phase lamellae nucleating epitaxially on α -phase lamellae [91, 92]. As a consequence, wide-angle X-ray diffraction (WAXD) is needed to distinguish the monoclinic and orthorhombic structures.

A high content of γ -form develops in metallocene synthesized i-PPs containing stereo- or regiodefects along the chains. The amount of γ -phase increases with increasing total defect content [57–59]. A mixture of monoclinic (α -) and orthorhombic (γ -) modifications is obtained over a large range of crystallization temperature, with the relative content of the two forms depending on the undercooling and chain regularity. Kinetic studies have revealed that both polymorphs start to grow at the same time and develop at the same rate [57].

It is worth mentioning that the γ -polymorph can also crystallize concomitantly with the β -structure if proper β -selective nucleating agents are present. This happens, for instance, in the crystallization under pressure of nucleated Ziegler–Natta i-PP [93]. Crystallization of a defective metallocenic i-PP gives rise to a more complex picture. If a high load of β -phase nucleants is added, concomitant

crystallization of the three polymorphs (α -, β -, and γ -) was found, both in isothermal and non-isothermal conditions [94].

2.2.2 Isotactic Poly(1-Butene)

Isotactic poly(1-butene) (i-PBu) exhibits an intriguing polymorphic behavior. Three structures, characterized by different chain conformations and packing modes, have been identified [43, 95–97]. The chain segments in the crystals adopt a 3/1, 11/3, and 4/1 helical conformation in Forms I, II, and III, respectively. Crystallization of the orthorhombic Form III is typically observed in dilute or semidilute solutions, whereas melt crystallization invariably leads to the formation of the tetragonal structure, Form II. However, Form II is metastable and evolves toward the ultimately stable trigonal Form I during storage at room temperature.

The concomitant formation of Form III with either Form I or Form II from i-PBu solutions has been reported [98, 99]. However, the results have not been rationalized; indeed, the outcome of solution crystallization, in terms of polymorphic composition, is not straightforward. It has been shown that it critically depends on several experimental parameters, such as the crystalline structure prior to dissolution, the dissolution temperature and time, and the crystallization/solvent evaporation conditions [98, 99]. More interestingly, Forms III and II have been crystallized concomitantly from the melt in the presence of traces of amyl acetate [60]. The two structures can be recognized by their different spherulitic morphologies (see Fig. 5). In addition to the typical highly birefringent Form II spherulites, weakly birefringent teardrop-shaped spherulites are also observed. These latter Form III spherulites display concentric extinction rings, indicating lamellar twisting (Fig. 5). A very small quantity of Form I is also obtained along with the two other major components.

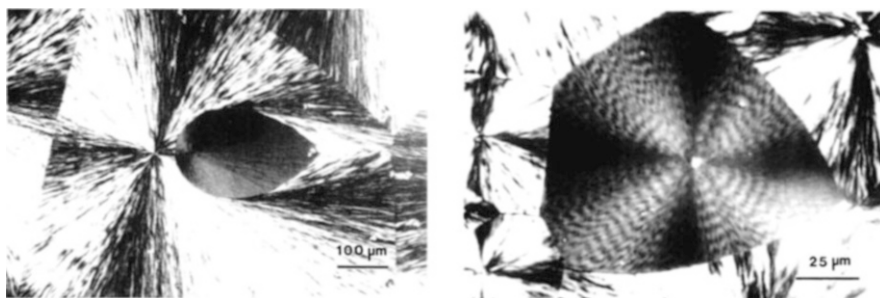


Fig. 5 Optical micrographs showing concomitant crystallization in i-PBu: bright Form II and weakly birefringent Form III spherulites. Reproduced with permission from [60]

2.2.3 Isotactic Poly(4-methyl-1-pentene)

Isotactic poly(4-methyl-1-pentene) (i-P4M1P) shows a very rich polymorphic behavior. Up to five structures have been identified [6, 61, 62, 100]. Form I is the most stable structure, and is the polymorph that develops in melt-crystallization. The chains possess a $7/2$ helical conformation and are packed in a tetragonal unit cell. The other polymorphs crystallize from solutions of the polymer in various solvents [61, 62]. Form II has a $4/1$ helical conformation of the chains, and a monoclinic unit cell. The same chain conformation is shared by Form III, with a tetragonal packing. Form IV has a more extended $3/1$ helix, arranged in a hexagonal structure. Form V, which has been found in concentrated cyclohexane gels, is suggested to be a polymer–solvent compound, but no structural details have been given [101, 102].

A systematic investigation of i-P4MP1 crystallization forms in various solvents, and under different cooling rates, has been carried out by Charlet et al. [61, 62]. Several conditions led to the simultaneous crystallization of more than one structure. A mixture of Forms I and III was obtained from slowly cooled dilute xylene solutions. The same two polymorphs also developed in semidilute (0.02–0.08 vol%) *n*-octane solutions. The use carbon disulfide, some cycloalkanes, and tetraalkyltins as solvent resulted in concomitant formation of Forms II and III [62].

2.2.4 Syndiotactic Polystyrene

Syndiotactic polystyrene (s-PS) displays a complex polymorphic behavior: four different crystalline forms, two mesomorphic structures, and several clathrates have been reported [63, 103]. Two of the crystalline polymorphs (α - and β -phases) are able to crystallize concurrently from the melt if appropriate conditions are adopted. Both structures present all-*trans* planar zig-zag conformation of the chains, packed in a trigonal or orthorhombic lattice for the α - and β -forms, respectively [103]. The thermal stability of the two polymorphs is similar, with the β -phase exhibiting a slightly higher equilibrium melting point than the α -form [64]. However, a stability inversion with crystallite size has been suggested [42]. s-PS belongs to the family of polymers whose crystallization outcome, in terms of polymorphic composition, is greatly affected by the melt annealing treatment (melt memory) [63, 65]. In particular, the fraction of α -phase obtained under a given crystallization condition decreases with increasing melt annealing temperature and time (i.e., with the progressive destruction of temperature-sensitive nuclei of the α -form).

If the melting conditions are mild enough to leave some residual α -nuclei, concomitant crystallization of α - and β -phases is found over a wide range of cooling rates or isothermal crystallization temperatures [63–66]. As an example, Fig. 6a shows WAXD patterns obtained for an s-PS sample cooled at about $10^\circ\text{C}/\text{min}$ from

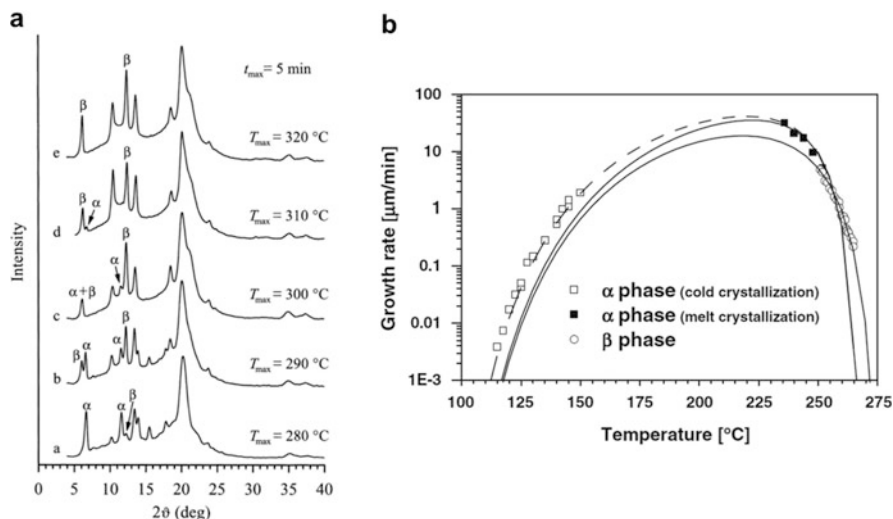


Fig. 6 (a) Wide angle X-ray diffraction patterns of s-PS crystallized on cooling at $10^{\circ}\text{C}/\text{min}$ after 5 min annealing in the melt at the indicated temperatures. (b) Measured and extrapolated growth rate of the α - and β -polymorphs of s-PS. Adapted with permission from [63, 64]

various maximum melt temperatures. Concomitant presence of the two polymorphs is observed for melt annealing temperatures lower than $300\text{--}310^{\circ}\text{C}$ [63].

The α - and β -polymorphs are concomitantly produced in melt crystallization upon cooling at rates between 10^{-2} and $30^{\circ}\text{C}/\text{s}$, with their relative amount being a function of the cooling rate [104]. At higher and lower cooling rates, only α - or β -phase is formed, respectively. Equivalently, a mixture of the two structures develops at crystallization temperatures between 230 and 260°C . High temperature favors formation of the β -phase, whereas the α -phase prevails at low temperatures [66]. This is in agreement with the measured growth rates of the two polymorphs, which intersect at around 260°C (see Fig. 6b). The orthorhombic β -structure grows increasingly faster than α -crystals at temperatures higher than 260°C . Both structures reach their maximum growth rate around 225°C , but at this low temperature the α -phase grows about two–three times faster than the β -form [64].

2.2.5 Poly(vinylidene fluoride)

Poly(vinylidene fluoride) (PVDF) exhibits five different crystalline modifications [7], three of which are of interest regarding concomitant polymorphism. The α -form is the polymorph commonly obtained by melt crystallization. The unit cell comprises two chains with TGTG' conformation packed in a pseudo-orthorhombic cell. In the piezoelectric β -form, *trans*-planar chains pack in an orthorhombic lattice. The γ -polymorph exhibits a monoclinic unit cell, with *a*- and *b*-axis repeat distances

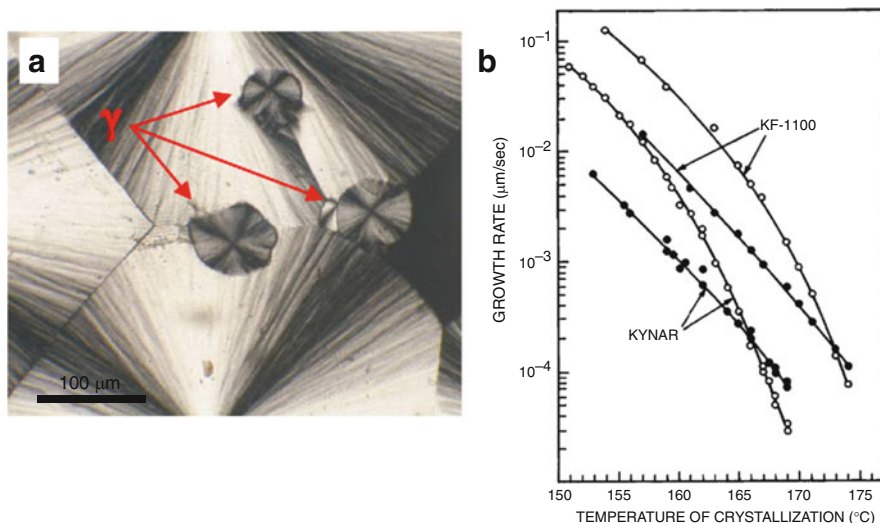


Fig. 7 (a) γ -phase spherulites surrounded by highly birefringent α -phase spherulites in PVDF crystallized at 160°C. (b) Growth rates of α - (open circles) and γ - (black circles) spherulites as a function of crystallization temperature for two different PVDF samples. Adapted with permission from [67, 69]

identical to the α -form but double the c -axis periodicity, compatible with a T_3GT_3G' conformation of the chain segments [67].

Crystallization from the melt at relatively high temperatures leads to the concurrent formation of α - and γ -phase spherulites (see Fig. 7a) [67–69]. The γ -form spherulites, recognizable by the weak birefringence and sometimes irregular shape, are typically more limited in number and size than their α -counterparts. The temperature region for concomitant α - and γ -crystallization varies with the molecular features of the particular PVDF sample; it roughly spans 20°C, ranging from 155 to 175°C [67, 68]. In a large part of this temperature range, α -form spherulites grow much faster than those of the γ -form; therefore, the latter are typically engulfed by the former. However, the ratio of the growth rates of the two polymorphs is not constant with temperature. With decreasing undercooling the ratio approaches unity and, at temperatures close to the melting point of the less stable α -form, the growth rates invert their order, that is, the γ -phase grows faster than the α -polymorph (see Fig. 7b) [67].

Crystallization of PVDF from cast solutions in various solvents often leads to concomitant formation of α - and β -phases. Systematic studies were conducted by Gregorio et al. [70–72]. A 20 wt% PVDF solution in dimethylacetamide was allowed to evaporate at various temperatures, and the phase content of the recovered polymer film was determined by infrared spectroscopy. Co-existence of α - and β -forms was found for evaporation temperatures between about 70 and 110°C; lower temperatures favored formation of only the β -phase, whereas at higher temperatures PVDF crystallized completely in the α -form [70]. Further studies

varying the type of solvent and polymer concentration revealed that the polymorphic outcome basically depends on the evaporation rate. At low rates the β -phase prevails, whereas high rates of solvent removal result in predominant formation of the α -polymorph. A mixture of the two structures is obtained at intermediate evaporation rates, which have been quantitatively evaluated to be between 1×10^{-4} and $3.5 \times 10^{-4} \text{ g s}^{-1} \text{ cm}^{-2}$ [72]. These values of evaporation rates are reached at different evaporation temperatures for the various solvents, depending on the relative boiling point. For example, β -phase forms together with α -phase at evaporation temperatures between 80 and 120°C for *N,N*-dimethylformamide (boiling point of 153°C) and between 100 and 140°C in *N*-methyl-2-pyrrolidone (boiling point 202°C) [71].

2.2.6 Poly(3-hydroxypropionate)

Poly(3-hydroxypropionate) (PHP) belongs to the family of biodegradable polymers, which are receiving increased attention because of their low environmental impact. This polyester can crystallize from the melt in two orthorhombic structures, β - and γ -forms, which share the same all-*trans* chain conformation [5, 73, 74]. Moreover, an additional form, adopting a helical conformation, develops in low molecular weight samples [74]. The γ - and β -phases crystallize concomitantly upon melt crystallization between approximately 30 and 65°C, with the relative content of the two depending on crystallization temperature. The γ -polymorph prevails at high temperatures, suggesting that it is the more thermodynamically stable form, whereas the β -phase is kinetically favored [73]. In low molecular weight PHP, an additional polymorph, the δ -phase, is found. Its nucleation is critically dependent on the temperature of melt annealing. Provided that a sufficiently low melting temperature is chosen, δ -phase can crystallize concurrently with γ - and β -forms [73, 74]. Spherulites of the δ -polymorph nucleate and grow first, followed by the formation of mixed γ/β spherulitic morphologies.

2.2.7 Poly(butylene adipate)

The monoclinic (α -) and orthorhombic (β -) structures of poly(butylene adipate) (PBA) share the same planar zig-zag chain conformation, which is slightly compressed in the case of the α -polymorph [5]. The monoclinic structure is the most stable, with an equilibrium melting point of 64°C, compared with 54°C for the β -form. However, this polymer provides an example of polymorph stability inversion with size, therefore the α -phase is the stable structure only when macroscopic crystals are considered (see Sect. 2.1) [41].

Generally speaking, the kinetically favored β -phase crystallizes at large undercoolings, whereas the α -phase prevails at higher temperatures. Concomitant crystallization of the two polymorphs is observed in an intermediate range of undercoolings [41, 75–77]. Only α -phase develops above approximately 30°C,

whereas the β -phase largely prevails at crystallization temperatures below 27°C. In contrast to other polymers, in which the concomitant crystallization of polymorphs can take place in a wide range of conditions (e.g., i-PP), the temperature window for the simultaneous formation of the α - and β -phases of PBA is extremely narrow, about 3–4°C, at most [41, 75].

The temperature range for concomitant crystallization can, however, be widened by blending miscible amorphous [78] or semicrystalline [79, 80] polymers with PBA, or by adding to the polymer suitable nanoparticles that enhance α -form nucleation [81]. In these cases, the minimum temperature for the occurrence of α -phase is lowered, thus extending the temperature range of concomitant crystallization up to 12–15°C [78, 81]. On the other hand, copolymerization of butylene adipate with hexamethylenedipate (HA), a co-unit that is easily hosted in the lattice of PBA β -phase, progressively hinders the concomitant crystallization of the two forms [82]. Indeed, the temperature range of coexistence of the two structures becomes narrower with increasing HA concentration in the copolymer. Crystallization of only the β -phase in the whole temperature range is observed for HA contents above 30 mol% [82].

2.2.8 Poly(butylene-2,6-naphthalate)

The aromatic polyester poly(butylene-2,6-naphthalate) (PBN) is an engineering plastic that can crystallize in two crystal forms [105]. Both α - and β -structures pack in a triclinic unit cell, with the β -form having a slightly higher crystalline density with respect to the α -structure [106]. The chain conformations of the two polymorphs also differ in the extension of the methylene residues and in the co-planarity of the ester groups and the naphthalene rings [107].

Polymorphic crystallization of PBN has been investigated by means of WAXD in non-isothermal and isothermal conditions [83, 84]. Reflections of both structures are found in the diffraction patterns of samples crystallized non-isothermally, by cooling at rates between 0.2 and 10°C/min. Concomitant crystallization of the two forms is also observed for isothermal crystallization temperatures in the range 210–225°C [84]. The relative content of α - and β -polymorphs varies with crystallization temperature: the α -phase content increases with increasing undercooling and exclusive formation of this polymorph is obtained below 205°C.

2.2.9 Other Examples

Two aromatic polyesters with a relatively long methylene sequence, poly(hexamethylene terephthalate) (PHexT) and poly(heptamethylene terephthalate) (PHepT), have been reported by Woo et al. to exhibit concomitantly crystallizing polymorphs [85–87, 108]. PHexT develops α - and β -forms in different relative amounts when crystallized between 90 and 135°C. Two different spherulitic morphologies exist for the two polymorphs: spherulites with a well-developed Maltese

cross with α -monoclinic structure and dendritic-type spherulites with β -triclinic phase [85, 86]. PHepT shows a much more complex crystalline morphology, with up to six different types of spherulites for α - and β -polymorphs [87]. Starting from a sample crystallized in the β -phase, mild melting treatment at low annealing temperature leads to concomitant crystallization of the α - and β -polymorphs in a wide temperature range (55–80°C).

The crystallization of a precisely substituted polyethylene, containing a chlorine atom along the polymer chain on each and every 15th backbone carbon (PE15Cl), provides a further example of concomitant crystallization of polymorphs [88]. Form I is proposed to be triclinic, with chains in all-*trans* conformation, and melts around 60°C. Form II has a non-planar, herringbone-like packing of the chains, and its crystals are stable up to about 70°C. Surprisingly, the system changes from crystallizing in the pure Form I to developing only Form II within 1°C of undercooling [88]. The two polymorphs crystallize concurrently only between 53 and 54°C. In this extremely narrow temperature range, the formation rates of the two structures invert their order.

Poly(ethylene oxide) (PEO) is known to form molecular complexes with several guest small organic molecules [109–111]. In these systems, PEO and the small-molecule guest crystallize in the same crystalline lattice, with a specific stoichiometric ratio between polymer repeating units and guest compound. The formation of these molecular complexes does not generally rely on selective interactions between the molecule and the polymer chain; instead, it is the result of a more general physical association based on steric complementarity. Some of these compounds are found to be polymorphic and also display concomitant crystallization of the different forms. PEO/resorcinol molecular complex (with 2:1 stoichiometry) crystallizes into α - and β -polymorphs, which exhibit melting points around 90 and 70°C, respectively [112]. Unbanded α -form and banded β -form spherulites crystallize together from the melt at room temperature. Also PEO/*para*-nitrophenol molecular complex (with 2:3 stoichiometry) show two polymorphs: a stable α -phase and a metastable β -phase [113]. The two forms grow simultaneously from the melt over a wide temperature range. The α -phase grows significantly faster than the β -form for all the explored temperatures. The difference in growth rate can be as large as an order of magnitude in the proximity of the β -phase melting point.

Recent examples of concomitant crystallization of polymorphs have also been reported for poly(1,3-dioxolan) (PDOL) [114] and polyethylene with precisely spaced ethyl branches on every 21st carbon (EB21) [115]. However, the focus of these studies was on the occurrence of cross-nucleation between polymorphs. Therefore, they are discussed in the next section.

A description of concomitant crystallization of PPVL, based on experimental work of our group [116], is presented in Sect. 3. This polymer crystallizes concurrently in two different structures: the monoclinic α -form and the orthorhombic γ -polymorph. The γ -phase is elusive to study, because it is the minor component and develops very slowly. The γ -spherulites are quickly engulfed by the fast-growing α -phase, which often nucleates at their periphery (a case of cross-nucleation; see Sect. 2.3). Therefore, the reduced size of γ -spherulites is not

adequate for determining their growth rate using direct methods. Section 3 includes the description of a method to quantitatively derive the growth rate of the slow polymorph, by means of analysis of the interspherulitic boundary profiles [116].

2.2.10 Polymorphic Self-Poisoning?

In the framework of concomitant crystallization of polymorphs, we briefly mention the occurrence of a peculiar effect on the structuring kinetics that arises from the competitive crystallization of two forms. An unusual temperature dependence of the overall crystallization rate/growth rate on temperature has been sometimes reported, both for melt [73, 77] and solution [117, 118] crystallization. The observations are summarized in Fig. 8; the temperature dependence of growth (or crystallization) rate displays two maxima separated by a sharp minimum at intermediate temperatures.

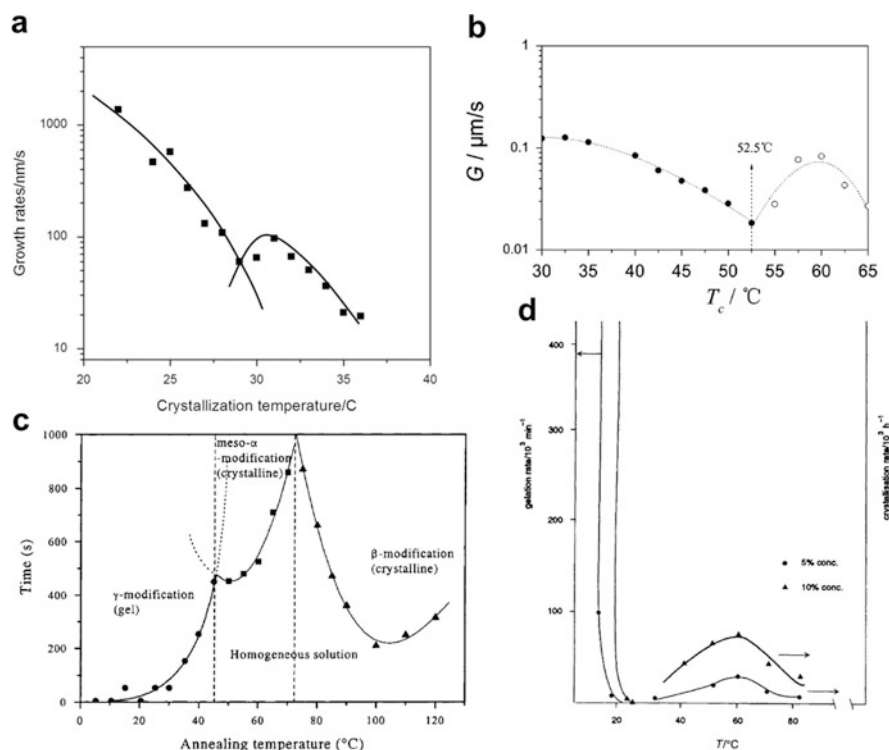


Fig. 8 Growth rates as a function of crystallization temperature for (a) PBA and (b) PHP. (c) Onset time for crystallization in a 10 wt% solution of s-PS in *cis*-decalin at different temperatures. (d) Rates of crystallization/gelation as a function of temperature for a solution i-PS in *trans*-decalin. Adapted with permission from [73, 77, 117, 118]

In low molecular weight PBA (Fig. 8a), the α -phase develops above 30°C and the β -form below 26°C. A small decrease in the spherulitic growth rate is measured at around 28°C, where both polymorphs develop from the melt [77]. An even clearer situation is encountered in PHP (Fig. 8b). Here, the minimum between the two bell-shaped curves is more evident: the growth rate decreases by almost one order of magnitude in the vicinity of 53°C. Away from the temperature of such a minimum, pure β - or γ -phases develop, at high and low temperatures, respectively. Again, a mixture of the two forms is obtained at temperatures close to the minimum in the growth rate [73].

A similar situation is found in solution crystallization of *s*-PS and *i*-PS. In *cis*-decalin, *s*-PS forms a crystalline β -phase at around 100°C and an α -mesophase at lower temperatures (about 50°C). In the temperature range in which the two structures compete (i.e., between 65 and 75°C), a large decrease in the transformation time can be seen. At 70°C the crystallization time is more than four times longer than the minimum time of the β -phase at 100°C (Fig. 8c) [117]. Also, *i*-PS displays an unusual temperature dependence of the crystallization rate (Fig. 8d), with a very deep minimum around room temperature. Crystals with different 3/1 helical and *trans*-planar chain conformation are obtained above and below this temperature, respectively [118].

A further example (not shown in Fig. 8) is that of poly(L-lactic acid) (PLLA), where the temperature dependence of spherulitic growth rate is described by a double bell-shaped curve [119–121]. The first maximum, occurring around 125°C, is ascribed to formation of the orthorhombic α -form, whereas the acceleration at lower temperatures is attributed to the development of a conformationally disordered pseudo-hexagonal modification, denoted as α' [122].

It should be stressed that, in these systems, the decrease in growth/crystallization rate with decreasing temperature is not a consequence of decreased mobility, as usually observed in melt crystallization. Indeed, both for PBA and PHP the minimum growth rate is found at temperatures much higher than the relative glass transition temperature [73, 77]. The same is true for solution crystallization of isotactic and syndiotactic polystyrenes [117, 118], because the increase in solution viscosity with decreasing temperature is minimal. Moreover, changes in molecular mobility would not explain the inversion of temperature dependence of crystallization rate following a further decrease in temperature. Clearly, a different explanation is needed.

Keller discussed in detail this phenomenon for *i*-PS [118]. He pointed out that this effect resembles known examples of “self-poisoning” of growing crystals of long linear alkanes [123–125]. These systems crystallize in chain-extended or chain-folded conformation depending on the temperature. With decreasing crystallization temperature, the growth rate of the extended-chain crystals first increases (as expected), passes through a maximum, and then decreases to a sharp minimum. Upon further decrease in temperature, the growth rate rises again when once-folded crystals predominantly develop. Such a minimum in the plot of growth rate versus temperature is thought to result from competition between different conformations of segments attaching at the crystal growth front. Folded-chain nuclei form on the

growth face of extended-chain crystals, hindering the deposition of chain stems in the extended conformation.

In analogy with the above case of self-poisoning, Keller also described the anomalous crystallization behavior of i-PS solutions as a mutual blocking effect of the two competing chain conformations in their respective crystal formation. This obviously occurs only in the temperature range where the two conformations can co-exist [118]. This hindering effect of the same chain on polymorph crystallization rate can be described as “polymorphic self-poisoning.” Although in the case of i-PS, the poisoning originates from the different chain conformations of the different developing crystals, this is not true for the other mentioned cases. For PBA, PHP, and s-PS the two developing polymorphs share the same chain conformation [73, 77, 117]. Thus, the hindering effect is probably of crystallographic origin, with the geometry of the secondary nucleus at the crystal growth front being different for the two forms.

It is worth mentioning that polymorphic self-poisoning has been already invoked for small organic molecules. In particular, in a polar steroid, a group of crystal faces exhibits retarded growth as a consequence of the formation of an ultrathin layer of metastable polymorph covering the surface [126].

2.3 Cross-Nucleation Between Polymorphs

Cross-nucleation refers to the heterogeneous nucleation of a polymorph on a different, pre-existing polymorph, and it does not involve any kind of direct phase transformation between the two [17]. Although the occurrence of cross-nucleation was observed in polymers [49] before being seen in small organic molecules [127], the phenomenon did not receive much attention in polymer literature. By contrast, several examples on the topic exist for molecular crystals, including some systematic experimental and simulation work. In order to grasp the basic phenomenological features of cross-nucleation, these latter works are reviewed in the next section. Then, recent evidence of cross-nucleation in the field of polymer crystallization, together with older observations and a few overlooked examples, is discussed.

2.3.1 Cross-Nucleation in Small Organic Molecules

Yu was the first to discuss the nucleation of one polymorph by another for small organic molecules [127]. He reported the examples of two hexitols, D-mannitol and D-sorbitol. Melt crystallization of D-mannitol proceeds via the nucleation of a metastable δ -polymorph, followed by nucleation of a more stable α -polymorph on the surface of δ -spherulites (see Fig. 9a). In his experiments, the new α -polymorph grows faster than the δ -polymorph. For what concerns D-sorbitol, the melt was seeded with crystals of the stable γ -form. Crystallization around the

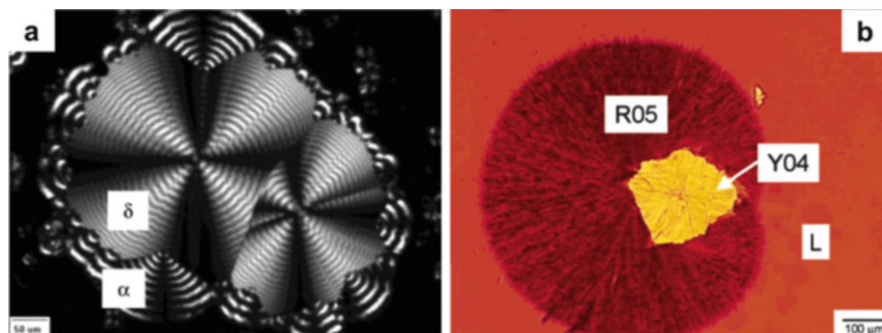


Fig. 9 (a) Cross-nucleation in D-mannitol: α -phase nucleating on δ -polymorph. (b) Cross-nucleation between ROY polymorphs: R05 nucleating on Y04. Adapted with permission from [77, 127, 128]

seed occurred in the metastable E-polymorph [127]. Already from these first examples, it is clear that seeds of one polymorph can nucleate another crystal structure of either higher or lower thermodynamic stability, provided it grows faster than the original polymorph.

The new phenomenon, termed cross-nucleation, was further investigated in spontaneous and seeded crystallization of 5-methyl-2-[(2-nitrophenyl)amino]-3-thiophenecarbonitrile [128], named ROY for the red, orange, and yellow crystals of its ten polymorphs [129]. Extensive, and sometimes selective, cross-nucleation between ROY polymorphs was found. An example is provided in Fig. 9b, showing a seed of the Y04 polymorph, which cross-nucleates the fast-growing R05 phase and is then engulfed by the newborn spherulite.

The study of ROY polymorphs confirms that thermodynamic stability is not the governing factor for cross-nucleation (i.e., the “daughter” phase can either be of higher or lower stability than the “parent” phase). On the other hand, the new cross-nucleating polymorph always grows faster than (or at least as fast as) the initial polymorph. This is a necessary, but not sufficient, condition for observing cross-nucleation. For instance, Y04 grows the slowest of all polymorphs at room temperature, but only R and R05 phases were observed to nucleate on it. This selectivity of the cross-nucleation process is apparently not related to epitaxy, because no evident lattice matching is found for any pair of cross-nucleating polymorphs. On the other hand, solution crystallization of a steroid provides evidence that epitaxy can play a role in cross-nucleation between polymorphs, both for the case of metastable-on-stable [130] and vice-versa [131]. However, changing the composition of the solvent mixture leads to cross-nucleation of the metastable polymorph on the stable polymorph without any preferred orientation (i.e., lacking epitaxial relationship between the two phases) [130]. It can thus be concluded that epitaxy is not a fundamental requirement for cross-nucleation to occur.

The group of Yu also focused on the effect of crystallization temperature on cross-nucleation in D-mannitol containing 10 wt% of melt-miscible poly(vinylpyrrolidone) [132]. The number of α -phase nuclei formed per surface unit of

δ -polymorph in the unit time was found to greatly increase with undercooling and with the presence of the polymeric additive. The α -on- δ cross-nucleation rate increases by about one order of magnitude with decreasing the crystallization temperature from 110 to 105°C [132]. The fast-growing α -polymorph of D-mannitol was also able to cross-nucleate on seeds of the most stable β -polymorph, below a certain crystallization temperature [133].

Nucleation of a crystal polymorph on the surface of another has also been reported during the solution-mediated transformation of an initial metastable structure into the stable structure (e.g., in 2,6-dihydroxybenzoic acid and L-glutamic acid) [105, 134–136]. In these cases, because the phase transformation proceeds towards increasingly stable phases, according to Ostwald's rule of stages, the cross-nucleating polymorph should always be more stable than the parent.

The issue of cross-nucleation was also addressed by means of molecular dynamics simulation [137–143]. The advantage of computer simulation techniques is that molecular details of the polymorphic nucleation and growth steps, which are experimentally inaccessible, can be inferred. All the main phenomenological features of cross-nucleation are captured in the simulated crystallization of a liquid composed of spherical particles, governed by Lennard–Jones potential [137–141]. During the growth stage, the stable face-centered cubic (fcc) polymorph cross-nucleates the metastable and faster growing hexagonal close-packed (hcp) structure [137, 138]. Given the activated nature of the cross-nucleation process, it can become unlikely if the undercooling is reduced, leading to the formation of pure fcc phase [139]. When the crystallization conditions are such that the fcc and hcp growth rates are comparable, both hcp-on-fcc and fcc-on-hcp (i.e., metastable-on-stable and stable-on-metastable) cross-nucleation events are observed [140, 141]. Molecular dynamics of more complex systems, such as polymorphic clathrate hydrates, also reveals cross-nucleation [142, 143]. These studies underline the importance of the formation of an interfacial transition layer between polymorphs that do not share a common crystal plane.

2.3.2 Recent Examples of Cross-Nucleation in Semicrystalline Polymers

The term “cross-nucleation” appeared in the polymer literature only very recently, in two studies of polymorphic crystallization in poly(1,3-dioxolan) (PDOL) and in polyethylene with precisely spaced ethyl branches on every 21st backbone carbon [114, 115].

PDOL exhibits very complex polymorphic behavior, with the existence of at least three modifications. Two forms are found to grow concomitantly and undergo a fast solid-state phase transformation [144–146]. Prud'homme et al. nucleated a spherulite of Phase I at subambient temperature, and subsequently brought the system to room temperature. A second phase, IIa, grows radially from Phase I, and then suddenly transforms to the highly birefringent Phase IIb. Once the transformation is complete a third phase (Phase III) cross-nucleates on Phase IIb

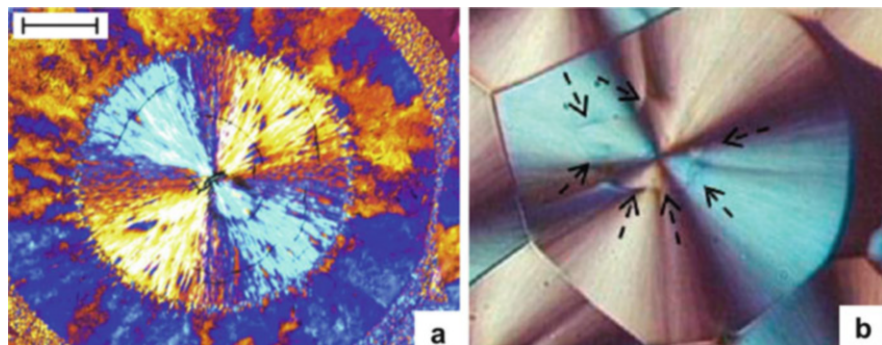


Fig. 10 (a) Morphology of PDOL crystallized at 23°C, showing three optically distinguishable phases: Phase I, Phase IIb, and Phase III, from the core to the exterior of the crystals. *Scale bar*: 200 μm. (b) Cross-nucleation between Form I and Form II of EB21 crystallized at 25°C. *Arrows* show the zig-zag shaped boundary between the two polymorphs. Adapted with permission from [74, 77, 114, 115]

(see Fig. 10a) [114]. Phase III nucleates selectively only on Phase IIb. Its spontaneous nucleation has never been observed, in analogy with the selective cross-nucleation of R05 polymorph on the Y04 structure in ROY [128]. The cross-nucleating Phase III is metastable with respect to Phase IIb, which, in turn, is more stable than Phase I. Concerning the growth rates, Phase III grows slower than Phase IIa; however, cross-nucleation (on Phase IIb) is possible, because the solid-state transformation of Phase IIa into Phase IIb stops the growth of modification II.

Polyethylene with precisely spaced ethyl branches on every 21st carbon (EB21) crystallizes in two forms, featuring different WAXD patterns. At a crystallization temperature of 25°C, the two structures develop concomitantly: Form I nucleates and grows first, followed by the growth of Form II [115]. POM revealed that the second spherulite stems from the growth front of an initially formed spherulite. The interface between the two spherulites is zig-zag shaped (see Fig. 10b). Although the two morphologies are difficult to distinguish with optical microscopy, selected area microbeam X-ray diffraction studies confirmed that they actually pertain to the two structures, with Form II cross-nucleating on Form I. Accordingly, the measured growth rate of Form II is about 30% faster than that of Form I. It has been suggested that the presence of ethyl branches, included in the lattice with a well-defined crystallographic orientation, disturbs the lateral growth of a secondary nucleated stem of Form I. On the other hand, the more disordered packing of Form II results in lower hindrance to the growth process by the short chain branches; hence, the faster growth of Form II and its cross-nucleation on Form I [115].

These new experiments were honestly claimed to be the first to confirm the existence of cross-nucleation in polymers; however, an extensive literature search disclosed several other examples, which are discussed in the following sections.

2.3.3 Older Examples of Cross-Nucleation in Semicrystalline Polymers: The Case of α/β “Growth Transition” in Isotactic Polypropylene

To the best of our knowledge, the first observation of cross-nucleation in polymers dates back to 1977, when Lovinger et al. described the peculiar “growth transformation” occurring in an i-PP sample solidified in a temperature gradient or isothermally (see Fig. 11a) [49]. The authors described the initiation of a spherulite of the trigonal β -phase (more birefringent than the α -phase) at the growth front of the monoclinic α -phase, and named the process “growth transformation.” The sudden change in the growing structure was interpreted as an “accidental discrepancy” at the tip of the growing lamella, causing the chains to pack in a different mode, which can eventually be preserved and overtake the original structure because of its faster growth rate.

It was speculated that assemblies of molecular helices similar to the packing of the β -polymorph can exist in the melt. When they are reached by the α -phase growth front, they induce the formation of a nucleus of the β -modification [49]. Because the α -polymorph is more stable than the β -polymorph, a question was raised about the possibility of observing the reverse transformation (i.e., β -to- α). Lovinger et al. concluded that such transformation would not be possible, because the growth rate of the β -phase is faster than that of the α -form, eventually causing engulfment of monoclinic nuclei by the growing β -crystals. It can be noticed that the well-established [127, 128, 137, 138] constraint on the growth rate of cross-nucleating polymorphs was already understood. However, because inversion in the order of the growth rates of i-PP α - and β -polymorphs with temperature (see Fig. 4) was not yet known [39], Lovinger’s deduction about the possible occurrence of β -to- α growth transformation was necessarily biased.

The phenomenon of nucleation of one polymorph by another in i-PP has been described with different terms such as “growth transformation” [49], “bifurcation of growth” [39], and “growth transition” [40]. We stress that all these names refer to the very same phenomenon, which, in more recent years, has been defined as cross-

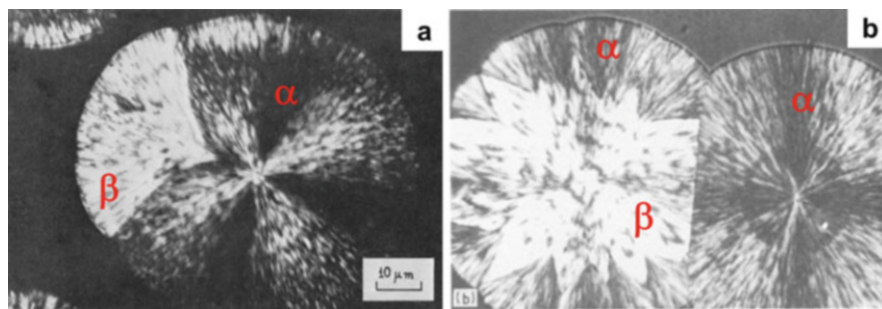


Fig. 11 (a) α -to- β and (b) β -to- α growth transition (or cross-nucleation) in i-PP. Adapted with permission from [49, 50]

nucleation [128]. Hereafter, we use the term “growth transition,” which has become the most popular in polymer literature. This is in order not to generate confusion by introducing a new term (cross-nucleation) that, although probably more correct, is foreign to the referred works.

Because of the high industrial and scientific relevance of i-PP, many reports on α -to- β growth transition followed the original work of Lovinger et al. [39, 40, 50, 147–150].

Extensive work on the topic was carried out by the group of Varga. With the aim of extending the temperature range for the determination of the relative growth rates of α - and β -phases, stepwise crystallization temperature profiles were imposed on non-nucleated i-PP [39, 147]. The β -spherulites were produced in a low temperature step, followed by measurement of the rate of their continued growth at different higher temperatures. These measurements revealed the existence of a crossover temperature ($T_{\beta\alpha}$), around 140°C, above which the growth rate of the α -phase exceeds that of the β -polymorph (see Fig. 4b). When the second temperature step was higher than $T_{\beta\alpha}$, pinpoint α -nuclei develop and grow, starting from the periphery of the β -spherulite and resulting in characteristic β/α twin morphology, as shown in Fig. 11b.

Given the difference in melting point between the two structures [55] (see Fig. 12), a clearer picture of the spatial distribution of the two polymorphs was obtained upon heating. The sample was first crystallized stepwise at $T_{C1} = 135^\circ\text{C}$ and $T_{C2} = 141.5^\circ\text{C}$ for a certain time, and subsequently heated to 167°C. At T_{C1} , concomitant crystallization of β - and α -spherulites occurs. Figure 12a shows the morphology developed at T_{C2} . The cores of the two spherulites, indicated in red in the image, are the α - and β -crystals grown at T_{C1} . The parts highlighted with green symbols are those formed at T_{C2} .

Because T_{C2} lies above $T_{\beta\alpha}$, the growth of the β -spherulite (Fig. 12a, left side) is frequently interrupted by β -to- α growth transitions. On the other hand, the α -phase spherulite (Fig. 12a, right side) continues growth in the monoclinic (α -) modification. When the temperature is raised to 167°C, the β -phase melts, revealing the

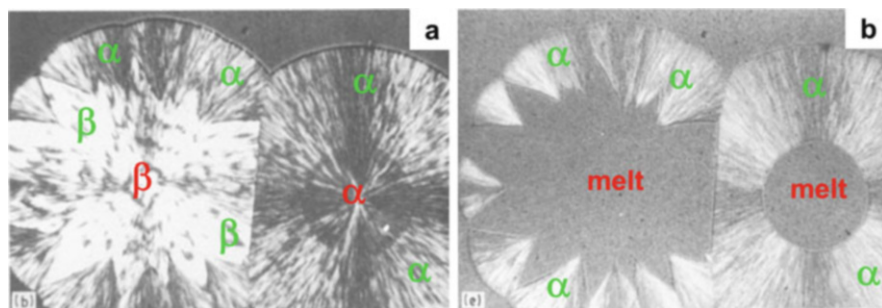


Fig. 12 α -phase and β -phase spherulites, with β -to- α growth transitions on the latter, at (a) 141.5°C and (b) 167°C. Red indicates the α - and β -crystals grown at 135°C; green indicates those formed at 141.5°C. Adapted with permission from [50]

α -phase overgrowth nucleated on its surface (see Fig. 12b). The characteristic shape of the α -phase regions demonstrate a point-like nucleation on the β -spherulite, and allows us to exclude the possibility that they might be α -spherulite inclusions formed separately in the melt. Incidentally, at 167°C, the α -core of the spherulite shown on the right of Fig. 12a is also molten, because it contains thinner α -lamellae formed at a lower crystallization temperature.

Therefore, both α -to- β [49, 147] and β -to- α [39, 147] growth transitions have been observed; the “direction” of the transition can be reversed simply by crossing $T_{\beta\alpha}$ (i.e., by passing from faster growth of the β -polymorph compared with the α -polymorph to the opposite situation). However, α -to- β growth transition is reported to be rare or sporadic in quiescently crystallized i-PP [39]. This indicates that the faster growth rate of one polymorph is a necessary condition for observation of cross-nucleation, but, as pointed out by Yu in the study of ROY polymorphs [128], it is not sufficient. The α -to- β growth transition is always observed, obviously below $T_{\beta\alpha}$, from oriented row-nucleated α -phase morphologies produced by the application of a shear flow to the polymer melt [51]. It is worth mentioning that in a random propene/ethylene copolymer containing a β -nucleating agent, the β -to- α growth transition is seen over the whole explored temperature range because the growth rate of the α -form is always greater than that of the β -modification (i.e., a $T_{\beta\alpha}$ does not exist for this material) [148].

Varga discussed the observation of β -to- α growth transition at the light of the Hoffman–Lauritzen secondary nucleation theory of polymer crystal growth [151]. He showed that the free energy barriers for the nucleation of α - and β -surface nuclei on the growth front of β -crystals are comparable above a certain temperature, leading to similar probabilities for the two nucleating events [39]. This theoretical explanation also justifies a peculiar observation: in contrast to other reports on the temperature dependence of cross-nucleation kinetics in small organic molecules [132], β -to- α growth transition seems to become more frequent with increasing crystallization temperature [39].

We recall from Fig. 4b that the growth rates of α - and β -polymorphs intersect at two different temperatures, with the α -phase growing faster than the β -phase above about 140°C and below 105°C [39, 40, 54]. Accordingly, a low temperature β -to- α growth transition should be expected. In fact, experiments in which a β -nucleated i-PP is first grown at high temperature and subsequently quenched to room temperature confirm this expectation [40, 150]. This behavior was described as “growth kinetics phase reentrancy.”

Lotz investigated the structural basis of the β -to- α growth transition [40]. By inducing the transition at the edge of a β -form single crystal, the mutual orientation of the two phases could be established through careful morphological examination (see Fig. 13, left). Small elongated α -crystals grow with orientation parallel or at 60° with respect to the (110) growth faces of the β -phase single crystal.

The structural details of the growth transition between the two polymorphs are highlighted in Fig. 13 (right) [40]. The contact face corresponds to the most densely packed planes of the two phases, with very close interhelix distances. Both planes are made of isochiral helices and differ only by the azimuthal setting of one helix

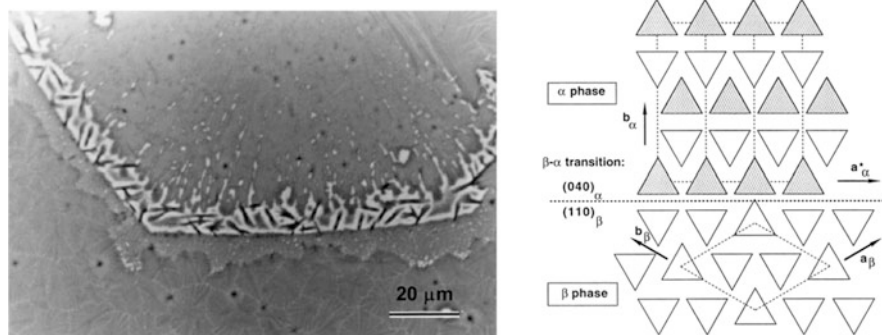


Fig. 13 *Left*: Phase contrast optical micrograph of a hexagonal β -phase single crystal of i-PP, with small α -phase crystals developed at the edge. *Right*: Structural relationship between β - and α -phases at the point of growth transition. *Triangles* represent helical i-PP stems comprising three monomers per turn. Adapted with permission from [40]

out of three. Therefore, reorientation of this helix would be sufficient to generate a small patch of the other, faster growing, phase [40].

2.3.4 Other Cases of “Growth Transition” in Polymorphic Polymers

Two other examples of growth transition exist in the polymer literature, but these cases are much less studied than that of α -to- β growth transition in i-PP.

Lovinger reported γ -to- α growth transition in PVDF. As seen in Sect. 2.2.5, α - and γ -phase PVDF spherulites grow concomitantly in an intermediate range of undercoolings [67–69, 117]. Spherulites of the metastable α -phase grow about seven times faster than those of the γ -polymorph at around 155°C (see Fig. 7b). As a consequence of the faster growth of the α -polymorph, γ -to- α growth transition occurs at the growing tips of the lamellae in γ -spherulites, causing rapid envelopment of the parent spherulite by the daughter α -phase (as shown in Fig. 14a). The structural details at the γ -to- α transition points were further investigated by means of electron microscopy. No discontinuity between the two morphologies was observed, thus suggesting that the α -growth is not initiated by external factors such as temperature fluctuations [67].

Lovinger reported that, at intermediate temperatures, many γ -spherulites were seen to have undergone such growth transition “at two, three, or more points of their peripheries.” He also considered that “the statistical probability for initiation of α -growth” (by γ -spherulites) “depends strongly on the difference in growth rate between the two.” These observations clearly indicate a temperature dependence of growth transition kinetics. Although not explicitly discussed by Lovinger, it can be deduced that growth transition events become more frequent with decreasing crystallization temperature, a feature in agreement with data on cross-nucleation kinetics of D-mannitol [132].

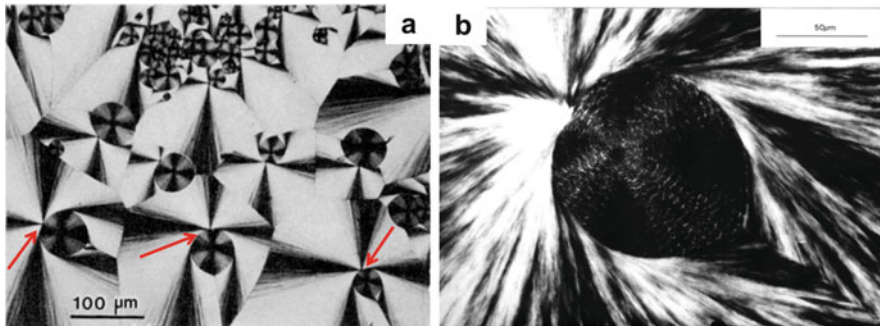


Fig. 14 (a) α -phase spherulites nucleating at the edge of γ -form spherulites in PVDF. (b) Banded and weakly birefringent γ -phase PPVL spherulite engulfed by an α -form spherulite nucleated by growth transition at its periphery. Adapted with permission from [67]

Interestingly, although at high temperatures (i.e., close to the melting point of the α -form) an inversion of the growth rates of the two polymorphs is observed (see Fig. 7b), no α -to- γ growth transition could be found. Again, this is consistent with the fact that a faster growth rate of one polymorph is a necessary, but not sufficient, condition for cross-nucleation to occur.

A last example of growth transition was reported by our group for polymorphic PPVL [116]. A detailed description of the concomitant crystallization of α - and γ -polymorphs of this polymer, including its effect on the morphology of the samples, is given in Sect. 3. Here, we briefly mention observations related to the growth transition of PPVL.

The morphology of isothermally crystallized PPVL often shows small and weakly birefringent spherulites of the orthorhombic γ -form engulfed by large and highly birefringent spherulites of the monoclinic α -phase nucleated by a growth transition mechanism. An example is provided in Fig. 14b. The growth transition phenomenon in PPVL was associated by Alfonso et al. with the existence of subcritical clusters of the α -phase in the undercooled melt. These clusters are not big enough to act as primary (three-dimensional) nuclei, but their dimensions could be sufficient for the formation of stable surface nuclei [116]. Therefore, when the apex of the growing γ -form lamella reaches one of these clusters, their arrangement is preserved in the crystal, causing polymer molecules to alter their packing mode from the orthorhombic to the monoclinic lattice. It was also shown that propagation of the newly formed crystal lattice depends on the relative growth rates of the two polymorphs: the dominant structure at late stages being that of the faster growing phase. The occurrence of the opposite α -to- γ growth transition is also considered possible; however, given the higher growth rate of the α -form in the entire explored temperature range, γ -on- α nuclei could only spread over a very short distance before being halted by a faster growing α -lamella.

Concerning the temperature dependence of the growth transition process, an increased number of γ -spherulites exhibiting multiple α -nuclei at their periphery

were observed on increasing undercoolings. Below a certain temperature, growth transition events became so frequent that the boundaries between the two types of spherulites were no longer discernible. Both PVDF and PPVL growth transitions seem to be in general agreement with measurement of cross-nucleation kinetics in small organic molecules, because they show an increase in frequency with decreasing temperature. On the other hand, the case of α -to- β growth transition in *i*-PP displays the opposite trend [39]. This peculiar temperature dependence in *i*-PP deserves further experimental investigation.

2.3.5 Overlooked Examples of Cross-Nucleation in Semicrystalline Polymers

Although not necessarily discussed in these terms, the peculiar spherulitic morphology arising from cross-nucleation/growth transition has been observed in a few other polymers, namely in low molecular weight PHP and PBA [74, 77].

Short chains of PHP are able to arrange themselves in the δ -phase, with helical conformation, or in the all-*trans* β - and γ -polymorphs (see Sect. 2.2.6) [74]. When low melt annealing temperatures are adopted, the sample crystallizes concomitantly in a mixture of δ - and γ -phases at 70°C. The δ -form spherulites nucleate heterogeneously in the first stage of crystallization, forming a compact morphology with Maltese cross. A more coarse and open spherulitic morphology, typical of the γ -phase, develops in a later stage. Often, but not always, this new morphology nucleates at the edges of δ -form spherulites (see Fig. 15a). At this specific crystallization temperature, the growth rate of the γ -phase spherulites is about 65% greater than that of the faster nucleating δ -phase.

PBA is known to show a crystallization temperature-dependent polymorphism (see Sect. 2.2.7). Monoclinic (α -) and orthorhombic (β -) crystals can grow simultaneously from the melt in a limited temperature window [77]. When concomitant crystallization occurs, primary nuclei of the α -phase develop first, and ring-less spherulites grow to some extent. After a certain time, several nuclei of banded, β -phase spherulites appear at the edges of the unbanded α -form (see Fig. 15b). The ring-banded spherulites of the β -form grow at a rate that is about twice that of the α -phase [77]. Interestingly, two transitions of the spherulitic morphology are sometimes observed along the radial growth direction: α -to- β followed by β -to- α . Molecular dynamics simulation of cross-nucleation has shown this behavior to be feasible when the polymorphs grow at similar rates [140, 141]. Nevertheless, in the case of PBA, the onset of reverse cross-nucleation events (β -to- α) towards the end of the crystallization is attributed to a variation in the melt composition. Indeed, as a consequence of molecular segregation, PBA melt becomes progressively enriched in low molecular weight species as the crystallization proceeds.

In the cases above, the occurrence of cross-nucleation can be appreciated by analyzing the microscale morphology of polymer spherulites. However, given the hierarchical organization of polymer crystals (i.e., from nanoscale lamellae to

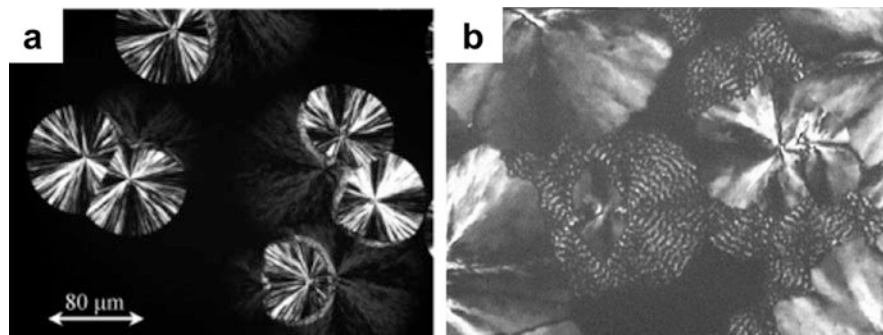


Fig. 15 (a) γ -form spherulites (weak birefringence) nucleated on the surface of pre-existing δ -phase morphologies in PHP. (b) Ring-banded β -spherulites of PBA nucleating on ring-less α -phase. Adapted with permission from [74, 77]

microscale spherulites), cross-nucleation can also manifest itself at different length scales.

One renowned case is the mentioned (Sect. 2.2.1) α/γ crystallization in *i*-PP [91, 92]. In this situation, the nucleation of one polymorph on the other (γ -on- α) takes place at the lamellar level, by an epitaxial mechanism. The γ -crystals nucleate on the lateral (010) faces of the α -crystals, the b -axes of the two structures are parallel, and the chain axis of the orthorhombic phase forms an angle of about 50° with the (α -) lamellar surface [92]. Noticeably, the reverse case of α -on- γ nucleation is not observed. Another example of polymorphic polymer crystals that nucleate epitaxially one over the other is found in poly(hexamethylene terephthalate) [152]. Chain-folded triclinic (β -) crystals nucleate on chain-extended fibrillar α -phase crystals with a specific orientation, which is determined by the epitaxial relationship between the two polymorphs.

These two polymers demonstrate that epitaxy can exist between cross-nucleating structures; however, as observed in small organic molecules [128, 130, 131], it is not a strict requirement. Clearly, the efficiency of cross-nucleation in the two cases (i.e., at the spherulitic or lamellar scale) is largely different. When nucleation of one polymorph on the other takes place at the length scale of the crystalline lamellae, an extremely high cross-nucleation density (i.e., number of cross-nuclei per unit of available surface) can be realized. Despite the huge difference in the frequency of nucleation events, the two cases of nucleation at the lamellar or spherulitic level should be both considered as limiting examples of cross-nucleation between polymer polymorphs.

Several examples of cross-nucleation or growth transition in polymorphic polymers have been presented in previous sections. It can be seen that this phenomenon is quite widespread or, at least, not rare. In particular, it cannot be excluded that, if suitable crystallization conditions are met, cross-nucleation could also occur in other concomitantly crystallizing polymers (see Sect. 2.2) in which it has not yet been observed. In this respect, a novel example of cross-nucleation in *i*-PBu, as highlighted in our own recent research [153, 154], is presented in Sect. 4. Although

i-PBu crystallization and polymorphism have been studied for the last 50 years, the existence of cross-nucleation was never previously reported.

2.3.6 Blends of Poly(lactic acid) Enantiomers: Cross-Nucleation Between Racemate and Conglomerate Crystals

A peculiar situation from the nucleation perspective, which can fall into a broader definition of cross-nucleation, arises in the crystallization of mixtures of enantiomeric molecules [17, 155]. There are several crystallization possibilities for a racemic liquid of a chiral molecule. A racemate is produced when the crystal contains both enantiomers in the unit cell, in a one-to-one ratio; a conglomerate is instead a physical mixture of the two enantiomerically pure crystals; and a solid solution contains the two oppositely configured molecules in a random arrangement in the crystal.

Yu et al. studied the crystallization of the chiral drug tazofelone (TZF) [155]. The racemic TZF liquid crystallizes spontaneously as a racemate, which is more stable than the conglomerate at any temperature. However, when the system is seeded with crystals of the pure enantiomers, a rare solid solution (with racemic composition) is formed. Although the solid solution is metastable compared with the racemic crystal, it can prevail in the crystallization process because it nucleates on the pure enantiomorph seeds and grows much faster than the competing racemate. Yu describes this crystallization scheme as cross-nucleation between phases whose compositions are partially the same, that is, TZF solid solution (composed of *R* and *S* enantiomers) on TZF enantiopure crystal (*R* or *S* configured molecules) [155].

Polymerization of an optically pure chiral molecule leads to the production of an enantiopure polymer. A mixture of polymer enantiomers can crystallize either as a conglomerate or as a racemate. In the latter case, crystals composed of enantiomers with a 50/50 composition are more frequently described as “stereocomplex” in the polymer literature. The most studied case is that of poly(lactic acid) (PLA) [156]. Lactic acid monomer can be synthesized in two enantiomeric forms, *L*- and *D*-lactic acid, resulting in two enantiomeric polymers, poly(*L*-lactic acid) and poly(*D*-lactic acid) (PLLA and PDLA, respectively). When either of the pure enantiomers is crystallized alone, distorted orthorhombic crystals (α -phase), hereafter called “homocrystals,” with melting point of around 170°C, are obtained. On the other hand, the crystallization of a racemic blend of PLLA and PDLA proceeds with the development of stereocomplex crystals, where an equal amount of PLLA and PDLA chains are packed in a trigonal cell. Notably, the melting temperature of stereocomplex PLA exceeds that of the homocrystal by around 50°C [5, 156].

In blends of enantiomeric PLA, stereocomplex crystals can form at temperatures above the melting point of the homocrystals. In the temperature range in which both structures develop, stereocomplex spherulites show shorter induction times (i.e., nucleation times) and growth rates up to an order of magnitude larger than those of PLLA or PDLA α -structures [157]. Despite the large kinetic advantage of the

stereocomplex crystals with respect to homocrystals, PLLA/PDLA blends often crystallize as a mixture of the two structures. The ratio of stereocomplex to homocrystal fractions decreases with the deviation of blend composition from the equimolar value (50/50% PLLA/PDLA) and with increasing the molecular weight of the polymers [158].

When both stereocomplex and homocrystals co-exist in the same sample, kinetic studies reveal a clear nucleating effect of the racemate crystals on the enantiopure species [159–163]. Indeed, relatively small amounts of PDLA (in the range 0.1–15 wt%) have been used as nucleating agents for PLLA homocrystals [159–161]. Investigation of the mechanism of crystallization rate enhancement with respect to the pure enantiomer has shown that PLLA homocrystallization is preceded by stereocomplex formation, which provides a high number of heterogeneous nuclei on which enantiopure crystals can grow. The efficiency of stereocomplex crystals as nucleating agents for homocrystals is far superior to that of talc, a commonly adopted PLLA nucleant [159].

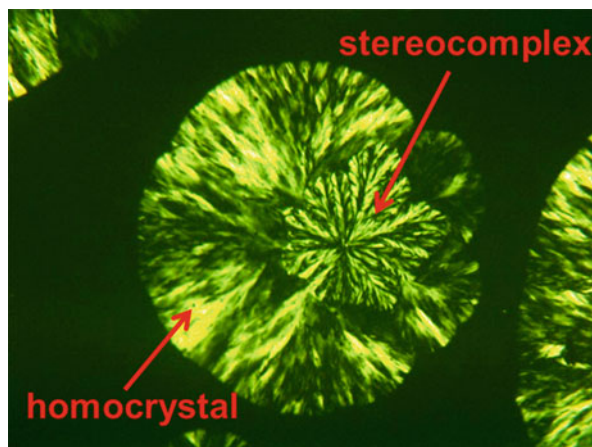
The heterogeneous nucleation of PLA homocrystals by the stereocomplex is easily highlighted by stepwise crystallization experiments. In a 90/10 wt% PLLA/PDLA blend stereocomplex spherulites are first grown at 180°C, above the homocrystal melting point. Then, the sample is quenched to a low crystallization temperature (100°C), whereby a transcrystalline homocrystal layer develops at the edges of the stereocomplex spherulite [162]. We stress that the kinetic requirement for the occurrence of cross-nucleation is fulfilled. Indeed, in a 90/10 wt% PLLA/PDLA blend, the growth rate of the homocrystal at low temperatures is greater than that of the stereocomplex, because the latter is difficult to form in compositionally unbalanced blends of PLA enantiomers [164]. Also, in the case of 50/50 wt% PLLA/PDLA blends, recent results are consistent with a homocrystal-on-stereocomplex cross-nucleation mechanism [165]. In fact, *in situ* WAXD during crystallization of racemic PLA blends revealed that stereocomplexation and homocrystallization are successive rather than simultaneous, with the former preceding the latter in isothermal conditions [165].

A further example of PLA homocrystal cross-nucleation on a stereocomplex, is shown in Fig. 16 [166]. The micrograph was taken during the crystallization at 130°C of a 50/50 blend of star-shaped PDLA oligomers with high molecular weight PLLA. Stereocomplex crystals start to grow first from the melt, and form an open, dendritic-like morphology. At the growth front of the stereocomplex, several homocrystal spherulites (characterized by a more compact appearance) nucleate and grow. The boundary between the two structures is zig-zag shaped, because the growth of stereocomplex spherulites is interrupted, at several different times, by the cross-nucleation of the homocrystal.

At this stage, the analogy of the PLA stereocomplex/homocrystal case with the crystallization of TZF racemic liquid discussed by Yu [155] is evident. Both situations represent a particular case of cross-nucleation between phases having partially the same composition [17, 155].

Incidentally, the nucleation of PLA homocrystals on a stereocomplex was suggested to follow an epitaxial mechanism [167]. However, selected area electron

Fig. 16 PLA homocrystal nucleated on stereocomplex spherulite in a 50/50 star-shaped PDLA/linear PLLA blend



diffraction studies of PLA α -crystals grown on oriented stereocomplex films recently demonstrated that epitaxy does not play any role in PLA homocrystal-on-stereocomplex nucleation [163]. This is a result of the crystallographic mismatching between the 10/3 and 3/1 helical conformations of PLA chains in the α -crystal and in the stereocomplex, respectively.

3 Case Study I: Concomitant Crystallization of Poly (pivalolactone)

Poly(pivalolactone) (PPVL) is a highly crystalline polyester that displays three crystalline modifications (α -, β -, and γ -) [168–170]. Whereas the β -phase, formed only by stretching α -PPVL, has a planar zig-zag chain conformation, the α - and γ -polymorphs both possess a 2/1 helix, which is packed either in a monoclinic (α -crystals) or orthorhombic (γ -crystals) lattice. The monoclinic α -phase is the most stable structure, with a melting point around 230–240°C, compared with the 210–220°C of the γ -phase. As mentioned in Sect. 2.2.9, α - and γ -phases can crystallize concomitantly in a wide temperature range, the relative content of the two phases being strongly dependent on both crystallization and melt-annealing conditions [171].

Melt-memory effects on the polymorphism of PPVL were investigated in detail by Meille [171]. Starting from a sample containing exclusively the α -phase, the same polymorph was predominantly obtained upon re-crystallization if the melt annealing temperature was lower than 240°C or higher than 280°C. A mixture of α - and γ -structures was instead obtained for melt temperatures between these two limits when the re-crystallization occurred at moderate undercoolings (i.e., between 120 and 160°C). Crystallization temperatures higher than 180°C led to pure α -phase, independently of the melt treatment. These results can be explained by

considering that α -phase self-nuclei survive in the melt to different extents, depending on the annealing temperature. Upon increasing melt annealing temperature, the α -nuclei gradually disappear, and a meaningful fraction of γ -phase is also obtained. At temperatures above 280°C, thermal degradation of the polymer occurs and can affect γ -phase crystallizability.

A careful analysis of the growth kinetics of α -form spherulites has been performed, including the determination of growth regimes, fold surface free energy, and equilibrium melting temperature [172, 173]. The α - and γ -spherulites present different morphologies, with the γ -phase spherulites displaying weak birefringence and irregular banding, in contrast to the highly birefringent and non-banded α -spherulites [174]. Attempts to directly measure γ -phase growth rate have been unsuccessful. The reason is that the γ -phase is typically the minor component in a temperature range where the high nucleation density and fast growth of the α -phase prevent γ -spherulites from attaining dimensions suitable for accurate growth rate evaluation. To bypass this problem, an indirect method to obtain the linear growth rate of the γ -form of PPVL has been developed. The method is based on analysis of the profile of the α/γ interspherulitic boundary in the special case in which the slow growing γ -spherulites are engulfed by the fast growing α -spherulites nucleated at the γ -form growth front via cross-nucleation.

The geometric shape of interspherulitic boundaries, in the case of growth of different modifications, was quantitatively described by Varga [175] and Lednický [176]. By considering pseudo-two-dimensional crystallization, as occurs in films with thickness smaller than the spherulite diameter, Varga derived an equation describing the boundary lines between adjacent spherulites as a function of the relative growth rates of the polymorphs, the time lag between nucleation events, and the distance between nuclei. Depending on the values of these parameters, straight lines, circles, hyperbolas, and fourth-order polynomial curves were obtained and, to some extent, observed in the crystallization of α - and β -i-PP [175].

In the most general case, a primary nucleus of a spherulite, growing at a constant linear rate G_B and appearing at $t=0$ at the origin of the Cartesian axes, is considered. A second spherulite, with growth rate G_A , begins to grow from a point along the x -axis at a distance R_0 from the origin, at time $t=t_0 \geq 0$. The ratio of the two growth rates, G_A/G_B , is defined as Z . Initially, the two bodies grow independently as expanding circles; their contour is given by the following relationships [175]:

$$x^2 + y^2 = r_B^2 = G_B^2 t^2 \quad (4)$$

$$(x - R_0)^2 + y^2 = r_A^2 = G_A^2 (t - t_0)^2 \quad (5)$$

The equation describing the boundary line between the two spherulites is obtained by solving simultaneously Eqs. (4) and (5), because all points on the boundary line should satisfy both equations. With a simple substitution, the general interspherulitic boundary shape is given by the fourth-order equation:

$$(Z^2 - 1)(x^2 + y^2) - 2ZG_A t_0 (x^2 + y^2)^{1/2} + 2R_0 x + G_A^2 t_0^2 - R_0^2 = 0 \quad (6)$$

When spherulites of the same type are considered (i.e., $Z = 1$), Eq. (6) reduces to the hyperbola:

$$\{[2(x - R_0/2)]/(G t_0)\}^2 - 4y^2/(R_0^2 - G^2 t_0^2) = 1 \quad (7)$$

Moreover, for homologous spherulites nucleated at the same time ($Z = 1$, $t_0 = 0$), a straight boundary line is obtained that corresponds to the axis of the segment that connects the growth centers. In the special case of cross-nucleation of a fast growing polymorph on the advancing front of another polymorph, the foreseen boundary between the two spherulites has the shape of a Pascal limaçon.

Varga's analysis disregarded the possibility that, for two spherulites growing at different rates, in certain directions the slower spherulite acts as a shield for the development of the other spherulite. This shielding effect was later taken into account by Lednicky [176], who realized that a description of the complete interspherulitic boundary requires two different equations. Equation (6) holds only up to the "shielding point", i.e., the point where the boundary starts bending off from the direction of the tangent to the slow growing spherulite passing through the center of the fast growing one. Thereafter, each point of the boundary becomes the center of a new virtual growing body whose lamellae run, at most, tangentially to the instantaneous interspherulitic profile. This mechanism was supported by optical microscopy observations of the growth of α - and γ -spherulites in PVDF [176].

The analysis of interspherulitic boundary profiles was next applied to the concomitant crystallization of α - and γ -phases in PPVL [116]. Figure 17 summarizes several types of α/α and α/γ interspherulitic profiles. Spherulites of the monoclinic α -form can either nucleate at the same time or with a given time lag, as shown in Fig. 17a and b, respectively. In the first case, straight lines separate adjacent spherulites. When the two nucleation events are not simultaneous, according to Eq. (7), the spherulites form a hyperbolic boundary upon impingement.

Given the slower growth rate of γ -crystals, spherulites of the orthorhombic modification are typically engulfed by the fast growing α -phase. Two examples are shown in Fig. 17c, d. The weakly birefringent γ -spherulite of Fig. 17c is engulfed by the brighter α -spherulite, which nucleated far away from the γ -growth front. The interspherulitic profile formed upon impingement initially obeys Eq. (6). However, the profile changes after the shielding point (i.e., the point identified by the tangent to the γ -spherulite passing from the center of the α -spherulite). After the shielding points, the α -fibrils begin to bend off from the radial direction, and each point of the γ -spherulite surface becomes a growth center from which the α -fibrils propagate tangentially to the interspherulitic boundary. Figure 17d shows a γ -spherulite engulfed by an α -spherulite cross-nucleated at its periphery. In this last case, the shielding effect is active from the very beginning of

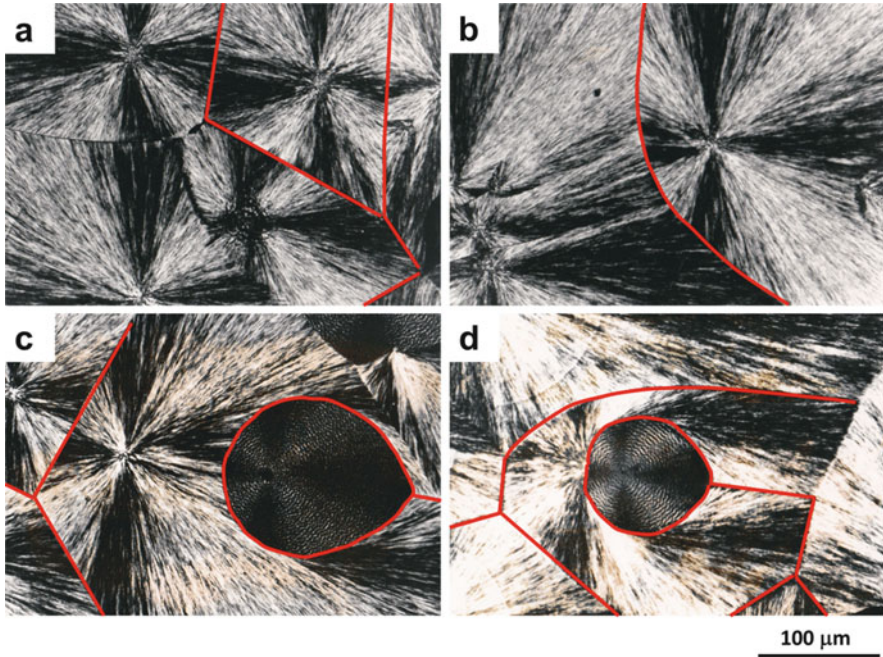


Fig. 17 Examples of interspherulitic boundary profiles for isothermally crystallized PPVL. Some of the profiles are highlighted in *red* for the sake of clarity. (a, b) α/α boundary profiles and (c, d) γ -spherulites engulfed by α -spherulites

boundary profile formation. Thus, the interspherulitic boundary conforms to a different equation, which is derived in the following section. We can notice that a straight α/α boundary is obtained by the impingement of the two branches of the α -spherulite surrounding the γ -spherulite. This is expected because the two branches grow at the same rate and from the same instant. On the other hand, a curved α/α interspherulitic profile is also observed in the top part of the micrograph, as a result of differences in the nucleation times between the top α -spherulite and the α -on- γ cross-nucleated spherulite.

In order to derive an equation describing the interspherulitic boundary profiles between a γ -spherulite and the α -spherulite that cross-nucleates at its periphery, this situation (shown in Figs. 14b and 17d) is schematized in Fig. 18.

The γ -spherulite nucleates at $t = 0$ at the point $C_\gamma(0,0)$, taken as the origin of the axes, and grows at constant rate, G_γ . At time $t = t_0$ the growth front along the x -axis reaches the point $C_\alpha(R_0,0)$, where a nucleus of the α -form develops, and the daughter α -spherulite begins to grow at a linear rate G_α , with $G_\alpha > G_\gamma$. A given point $P(t)$ on the curved interspherulitic profile has a distance from the origin equal to $r_\gamma = G_\gamma t$ and the vector r makes an angle φ with the x -direction. After a short time interval, dt , the interspherulitic boundary reaches a point whose distance from C_γ is increased by:

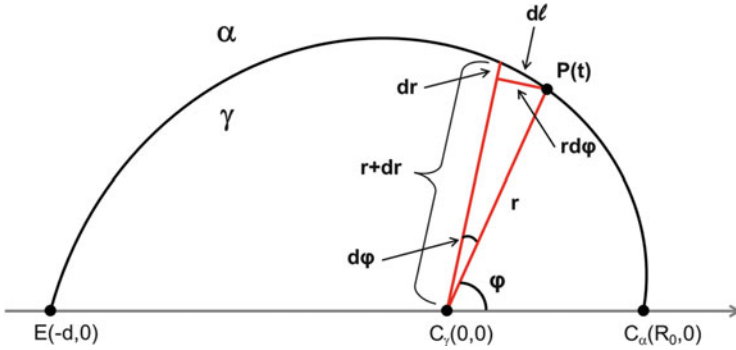


Fig. 18 Scheme of α/γ interspherulitic profile for the particular case in which the α -spherulite cross-nucleates on the γ -spherulite. See text for details

$$dr_\gamma = G_\gamma dt \tag{8}$$

while the angle is increased by $d\varphi$. Because α -growth proceeds tangentially to the curve, the corresponding length of the arc is:

$$dl = G_\alpha dt \tag{9}$$

The arc defined above is the hypotenuse of a right-angled triangle, therefore:

$$(dl)^2 = (dr)^2 + (rd\varphi)^2 \tag{10}$$

By substitution of Eqs. (8) and (9) into Eq. (10), and by recalling that $Z = G_\alpha/G_\gamma$, we obtain the following differential equation:

$$d\varphi = \left[(Z^2 - 1)^{\frac{1}{2}}/t \right] dt \tag{11}$$

This equation is readily integrated, by considering the initial condition $\varphi = 0$ at $t = t_0$, to give:

$$\varphi(t) = (Z^2 - 1)^{1/2} \ln(t/t_0) \tag{12}$$

If we consider that t is related to the distance of the curve from point C_γ , $t = r(t)/G_\gamma$ and $t_0 = R_0/G_\gamma$, the ratio of the two growth rates is related to angular position and distance from the origin by:

$$Z = \left(1 + \{ \varphi(t)/\ln[r(t)/R_0] \}^2 \right)^{1/2} \tag{13}$$

Incidentally, the mathematical expression that describes the interspherulitic

boundary profile is that of a logarithmic spiral. Equation (13) can be used to evaluate Z given the coordinates of the interspherulitic profile [116]. However, the relative growth rate of the two polymorphs can be readily obtained from the shape of the engulfed γ -spherulite. Indeed, we can consider that the two symmetrical branches of the curve meet, other than in $C_\alpha(R_0,0)$, at point E $(-d,0)$ (see Fig. 18), where the growth of the γ -spherulite is arrested. Point E is reached when $\varphi = \pi$, at time $t = d/G_\gamma$, with d being the distance of the point from the origin C_γ . Thus, from Eq. (13), it follows that:

$$Z = \left(1 + \{\pi/\ln[d/R_0]\}^2\right)^{1/2} \quad (14)$$

The ratio between α - and γ -growth rates is therefore simply related to a shape factor of the engulfed spherulite, d/R_0 , corresponding to the ratio of long and short semi-axes of the γ -spherulite along the x -direction. In particular, the shape factor decreases with increasing ratio of the growth rates of the two polymorphs, Z . The parameter d/R_0 (i.e., the ratio between the length of the segments EC_γ and $C_\gamma C_\alpha$) can be measured from a micrograph taken at the end of the isothermal crystallization. In this way, knowing the value of α -spherulite growth rate, it is possible to determine G_γ , which is not otherwise accessible.

Figure 19 shows two examples of morphologies obtained by crystallizing PPVL at different temperatures. It is possible to appreciate that the engulfed γ -spherulite is clearly less elongated at the higher crystallization temperature.

The change of shape is the result of a variation in the relative growth rate, Z . For $G_\alpha \gg G_\gamma$, growth of the γ -spherulite is soon interrupted by lamellae of the α -phase growing along its periphery. The shape therefore tends to be circular. In contrast, when the two growth rates have similar values, the γ -spherulite can grow over a long distance before being engulfed, resulting in a characteristic tear-drop shape. Figure 19 thus suggests that the value of Z increases with decreasing undercooling.

The dependence of the shape factor of engulfed γ -spherulite on crystallization temperature is summarized in Fig. 20a. The value of d/R_0 varies from about 5 at the

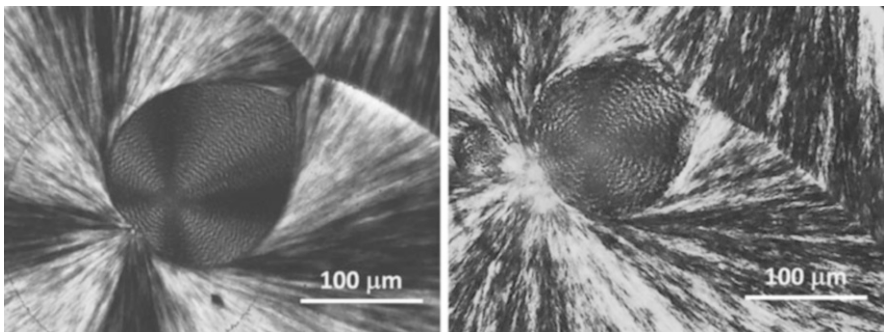


Fig. 19 Shape of γ -spherulites engulfed by α -spherulites after crystallization at 150°C (*left*) and 175°C (*right*)

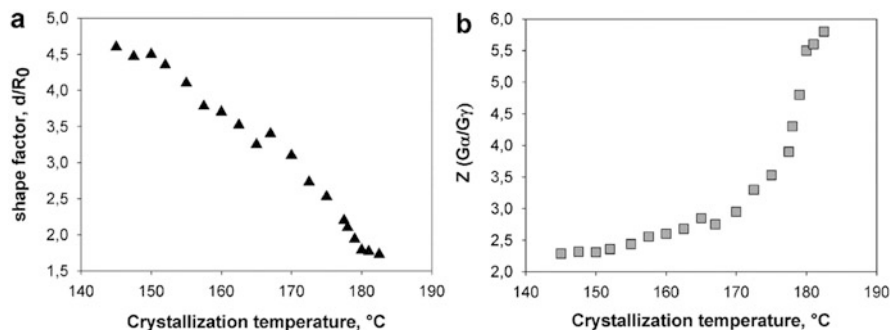


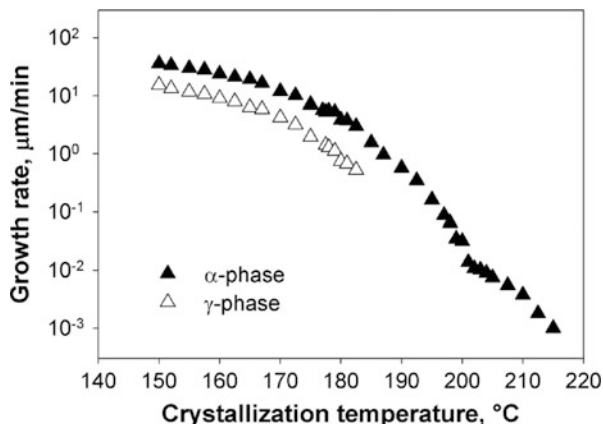
Fig. 20 (a) Shape factor d/R_0 and (b) relative growth rate Z as functions of crystallization temperature

highest undercooling to less than 2 at around 180 °C. The morphological variation, from an elongated tear-drop to an almost circular shape, is associated with an increase in Z (i.e., the ratio G_α/G_γ). The Z values obtained from Eq. (14) at the different crystallization temperatures are reported in Fig. 20b. At around 180 °C, α -spherulites grow about six times faster than γ -spherulites, whereas with increasing undercooling the difference is reduced: ratios slightly higher than 2 are obtained below 150 °C. Clearly the growth rates of the two polymorphs possess different temperature dependences. In addition, the growth rate of the γ -form vanishes upon approaching the γ -phase equilibrium melting point, which is lower than that of the α -phase.

The measured growth rate of the α -phase and that of the γ -phase, calculated from the value of Z , are plotted as a function of temperature in Fig. 21. The growth rate of the metastable γ -polymorph is always lower than that of the α -phase, and, as judged from the trend of the curves, this holds true over the whole crystallizability window of PPVL. As anticipated, the growth rate of the γ -phase extrapolated at temperatures close to its melting point (e.g., above ca. 190 °C) is orders of magnitude slower than that of the monoclinic α -structure. At the lowest accessible isothermal crystallization temperatures, this spread is greatly reduced and α -spherulites grow only twice as fast as γ -spherulites.

These growth rate data for PPVL polymorphs are helpful in explaining the observations of Meille [171] concerning the fractional content of the two structures as a function of crystallization temperature. According to Meille, γ -form can be obtained only in a range of crystallization temperatures going from 100 to 170 °C, whereas samples crystallized outside this temperature range contain essentially the α -form. Our growth rate data are consistent with these results. Indeed, at high crystallization temperatures, the γ -nuclei grow so slowly that they are unable to produce an appreciable amount of crystallinity before α -nuclei appear and rapidly fill the volume. In fact, we note that the ratio between α - and γ -crystallinity in a bulk sample roughly scales with the third power of Z . At low temperatures, the growth rate of the two polymorphs becomes comparable. However, as mentioned in

Fig. 21 Temperature dependence of the growth rates of α - and γ -polymorphs of PPVL



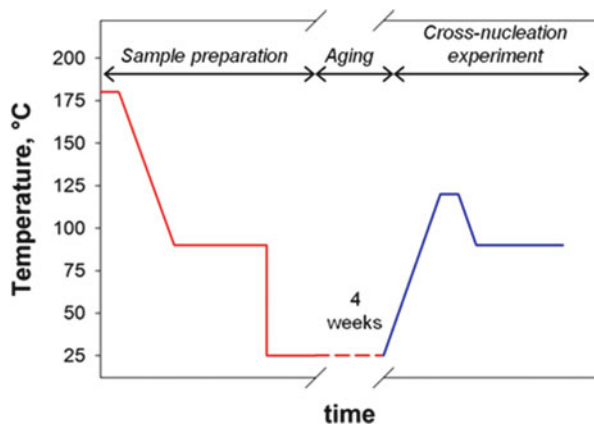
Sect. 2.3.3, and in agreement with the temperature dependence of cross-nucleation kinetics in small molecules [132], an enhanced frequency of α -on- γ nucleation events is expected with decreasing crystallization temperature. The formation of multiple α -nuclei on the surface of the same γ -spherulite forbids appreciable development of the slow-growing modification, even if the value of Z is low or close to unity.

4 Case Study II: Cross-Nucleation in Seeded Crystallization of Isotactic Poly(1-butene)

The main features of *i*-PBu polymorphism were briefly outlined in Sect. 2.2. We recall here the essential notions to help explain the in situ seeding procedure and cross-nucleation experiments.

Crystallization from the melt at any temperature always results in the formation of the metastable tetragonal Form II. However, upon storage at room temperature, this modification evolves to the most stable trigonal Form I polymorph, according to Ostwald's rule of stages. The completion of this phase transition requires several days or a few weeks at ambient temperature and pressure; faster conversion was observed in samples first crystallized at higher temperatures [43, 44]. Direct growth of the trigonal Form I has been observed in ultrathin films (<100 nm) seeded by solution-grown Form I single crystals [45, 46]. Kinetic measurements revealed that the growth rate of Form I is about two orders of magnitude slower than that of Form II at all the experimentally accessible crystallization temperatures. As a consequence, it is apparent that only Form II-on-Form I cross-nucleation can be observed. Moreover, because the two polymorphs do not crystallize concomitantly under any conditions in bulk samples, seeding a *i*-PBu melt with crystals of the trigonal form is required in order to induce cross-nucleation.

Fig. 22 Applied thermal history for in situ seeding and cross-nucleation experiments in i-PBu. Adapted with permission from [154]



We developed a straightforward in situ seeding method for melt crystallized i-PBu samples. The detailed thermal history is schematized in Fig. 22.

In the first step, a dual crystalline morphology is created, by allowing a melt-relaxed sample to isothermally crystallize at 90°C for a short time and subsequently quenching it in a room-temperature water bath. The sample crystallizes partly in the high temperature isothermal treatment and partly during the quenching step or when the bath temperature is reached. As a consequence of this thermal treatment, the sample morphology consists of a small number of large spherulites crystallized at low undercooling, surrounded by fine-grained crystals [153, 154]. Afterwards, the sample is aged at room temperature for 4 weeks, to permit the complete solid-state polymorphic transformation from the original tetragonal Form II to the stable trigonal Form I [43, 44].

After this, the cross-nucleation experiment is performed. The aged sample is first heated to 120°C. At this temperature, the transformed crystals (originally formed at low temperature) melt while the large spherulites (grown at higher temperature), which also have undergone full Form II-to-Form I transformation, appear intact. We emphasize that the annealing temperature at this stage must be high enough to destroy any possible residual Form II nuclei (i.e., to avoid self-nucleation) [153], but low enough to prevent the melting of Form I seeds. After annealing to relax the partially molten polymer, the sample is finally brought to the chosen crystallization temperature and the development of morphology is followed by polarized optical microscopy (POM).

In order to prove the effectiveness of the procedure, thermal and structural characterization of the in situ seeded samples is carried out at two stages of the sample preparation: after the dual-step crystallization and before the cross-nucleation experiment (i.e., after Form II-to-Form I transformation has occurred). Wide Angle X-ray diffraction (WAXD) patterns and differential scanning calorimetry (DSC) melting traces are presented in Fig. 23.

WAXD patterns are shown in Fig. 23a, both after the dual crystallization steps and after ageing at room temperature for a period of 4 weeks. The diffraction profile of the as-prepared i-PBu films confirms the exclusive formation of tetragonal

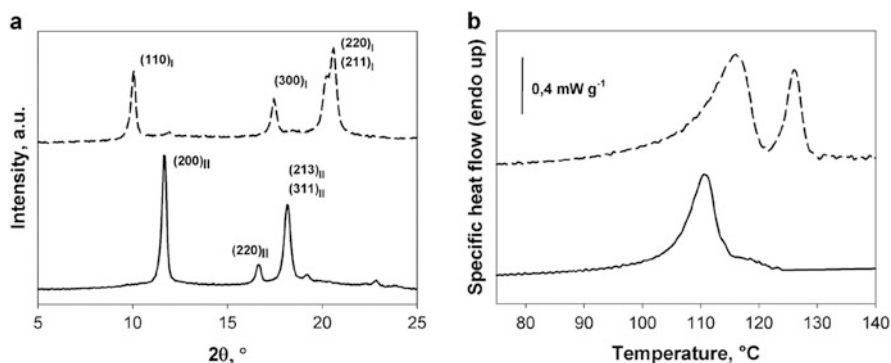


Fig. 23 (a) WAXD profiles (b) and melting endotherms for i-PBu films after crystallization and aging according to protocol shown in Fig. 22. Quenched and aged samples are shown with *solid* and *dashed* lines, respectively. Adapted with permission from [153]

Form II, as revealed by the presence of the indicated diagnostic $(200)_{II}$, $(220)_{II}$ and $(213)_{II} + (311)_{II}$ reflections [95, 177]. On the other hand, the solid-state transformation to the trigonal Form I is practically completed after 1 month of storage at room temperature, as evidenced by the characteristic diffraction peaks of the $(110)_I$, $(300)_I$ and $(220)_I + (211)_I$ planes of Form I. A faint trace of the $(200)_{II}$ reflection can still be observed, indicating a minimal residual content of Form II, which might be assigned to the slowly transforming less perfect crystals [44].

The DSC heating scans reported in Fig. 23b integrate the structural information and serve as a guide for the following cross-nucleation experiments. The un-aged film shows a melting peak temperature slightly above 110°C , characteristic of Form II [44]. The particular thermal history applied results in a bimodal population of lamellae. The thicker lamellae, produced in the isothermal step at 90°C , appear as a high temperature shoulder around 118°C in the melting endotherm. Form II–I transition is accompanied by an increase in the melting enthalpy and by an upward shift of $10\text{--}15^{\circ}\text{C}$ in the melting temperature [44]. Accordingly, the transformed sample exhibits two melting peaks, centered around 116 and 126°C . The high temperature peak corresponds to the melting of Form I crystals resulting from the thickest Form II lamellae, originally grown at 90°C . From the thinner lamellae produced in the quenching step, Form I crystals with low melting point, but still appreciably higher than that of the parent structure, are originated. It is important to notice that, as deduced from the melting curve of the aged sample, the thermal treatment at 120°C before the cross-nucleation step allows complete melting of the thinner crystals, while keeping intact the thicker lamellae in the spherulites grown isothermally at 90°C .

The outcome of a typical cross-nucleation experiment is illustrated in Fig. 24. The first micrograph shows the initial sample morphology, at room temperature. The dual morphology, consisting of large spherulites and microcrystalline material, is clearly observed. Figure 24b shows the morphology after partial crystallization of i-PBu melt at 85°C in the presence of a Form I spherulite. Together with the expected growth of heterogeneously nucleated spherulites in the bulk molten

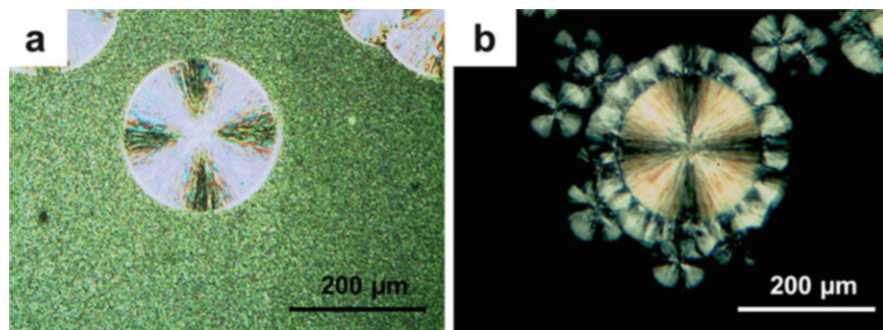


Fig. 24 (a) Example of the dual morphology of i-PBu samples before cross-nucleation experiments. (b) POM image of Form II-on-Form I cross-nucleation after 3 min at 85°C. Adapted with permission from [153]

material, the development of a transcrystalline “corona” around the pre-existing Form I spherulite is observed. Both cross- and bulk-nucleated new crystals belong to the Form II polymorph, as revealed by their melting point, their linear growth rate, and by WAXD characterization of cross-nucleated samples [153, 154].

At this low temperature, the cross-nucleation density along the circumference of the Form I spherulite is rather high, giving rise to a nicely symmetrical shape of the growth front in the new Form II morphology. Moreover, there is no apparent time lag between the onset of growth in the bulk of the amorphous phase and in the cross-nucleated region. This can be deduced by considering that the radius of bulk-nucleated spherulites and the thickness of cross-nucleated corona have comparable sizes, while an identical growth rate is measured. The effect of cross-nucleation temperature on the process kinetics is discussed later in this section.

At this stage, it is worth comparing our results with previous seeding experiments on i-PBu. An early attempt to form the trigonal structure in bulk samples, using self-nuclei derived from the partial melting of Form I was unsuccessful [178]. Under these conditions, the authors reported the invariant crystallization of the tetragonal modification, and deduced the “exceedingly” slow growth rate of Form I compared with Form II.

Our cross-nucleation experiments are in agreement and explain the old self-nucleation results, showing that the presence of Form I seeds does not necessarily induce the growth of trigonal crystals, but can speed up the crystallization of Form II by providing heterogeneous nucleation sites. An apparent disagreement exists between the present cross-nucleation results and those of Yamashita et al., who showed growth of Form I crystals from seeds of trigonal form produced in solution [45, 46]. The observed difference can be attributed to sample size and/or sample preparation effects [153]. Indeed, direct melt crystallization of Form I under the confined conditions of ultrathin films has been reported [179].

On the basis of knowledge about the structural details of the Form II-to-Form I transformation [180], some considerations on the cross-nucleation mechanism can

be put forward. Clearly, the unraveling of possible epitaxial relationships requires the study of samples crystallized as single crystals, as in the case of *i*-PP β -to- α growth transition [40]. If epitaxial crystallization plays a role in cross-nucleation of *i*-PBu Form II on Form I, we deem that the planes involved would be (110) of the tetragonal modification and (110) of the trigonal structure. Indeed, along these two planes the helices are isochiral and the interhelical distance is known to be essentially preserved upon the occurrence of the Form II-to-Form I solid-state transformation [180]. However, we stress once more that epitaxy is not a necessary requisite for the occurrence of cross-nucleation, nor for heterogeneous nucleation. As a matter of fact, heterogeneous nucleation of semicrystalline polymers at the interface with various amorphous substrates, such as rubber particles or glassy polymers, has been experimentally observed [181–183].

The conformation of crystalline chain stems, in addition to chain packing, is also of importance for polymer polymorphism [3–5]. Therefore, its role on polymer cross-nucleation should be discussed. Recall that the cross-nucleation of *i*-PBu occurs between two structures possessing different minimal energy chain conformations, namely 3/1 and 11/3 helices for Form I and Form II, respectively [43, 95, 177]. Comparing this case with previous literature data in which cross-nucleation was either neglected or addressed as “growth transition,” it is clear that this behavior is not restricted to *i*-PBu. The monoclinic α -phase of PVDF, whose chains possess a TGTG' conformation, can cross-nucleate on the γ -structure, characterized by a more extended T3GT3G' chain arrangement [67]. In PHP, at high temperature, the all-*trans* γ -phase nucleates on δ -crystals with 2/1 helical conformation [74]. A difference in chain conformation also exists for α - and β -forms of PBA [77]. On the other hand, the *i*-PP and PPVL polymorphs that nucleate on the pre-existing polymorphs share the same chain conformations, 3/1 helical and (TTGG)₂, respectively [39, 40, 49, 116, 147]. Therefore, conformational analogy between the chain segments in the different polymorphs, although possible, does not seem to be the controlling factor in polymer cross-nucleation.

Concerning the thermodynamic stability of cross-nucleating polymer polymorphs, analogously to observations in small organic molecules [128], nucleation of both metastable-on-stable and the opposite are found. For instance, *i*-PBu Form II and PVDF α -phase are metastable with respect to the polymorph on which they nucleate, that is, Form I and γ -phase, respectively [67, 153, 154]. Nevertheless, *i*-PP β -to- α and PPVL α -on- γ growth transitions are examples of stable forms cross-nucleating on metastable polymorphs [39, 40, 116, 147].

By following the time evolution of cross-nucleation experiments, kinetic information on the phenomenon can be gained [154]. An example of a time-resolved POM study is shown in Fig. 25. Red circles highlight cross-nucleation sites, and the increase in the number of cross-nuclei with crystallization time can be easily appreciated. Moreover, provided their number is not too high, a straightforward quantification is possible, as shown later in this section.

The adopted seeding procedure enabled us to probe the effect of temperature on cross-nucleation. Figure 26 shows selected micrographs from cross-nucleation experiments carried out at different undercoolings. The resulting morphology

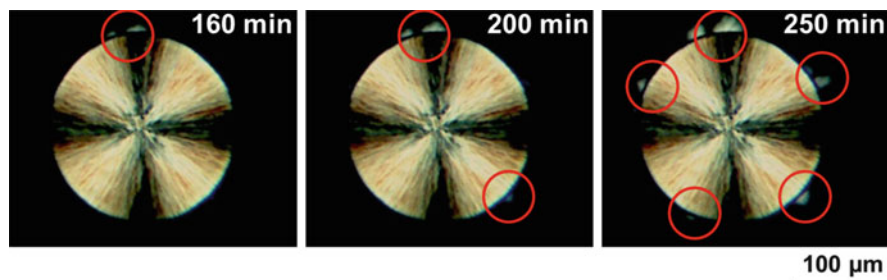


Fig. 25 POM micrographs showing example of cross-nucleation kinetics at a crystallization temperature of 105°C. Large Form I spherulites serve as nucleation sites for small Form II crystals, which are indicated by *red circles*. Adapted with permission from [154]

surrounding Form I spherulites is irregular. The observed uneven growth front of cross-nucleated Form II originates from a difference in the “onset time” between different locations on the surface of Form I crystals. For a given crystallization temperature, an increase in the number of Form II growing sites with holding time can be appreciated (see Figs. 25 and 26).

Clearly, cross-nucleation events become progressively rarer with increasing temperature (consider the different number of growing sites at a given crystallization time). It is deduced that, as a consequence of the energetic barrier for nucleation, at lower undercoolings more “attempts” are needed to successfully create a surface cross-nucleus that is able to grow. In other words, the frequency of efficient cross-nucleation events is lower at higher temperatures. In the experimental time-window, nucleation on other heterogeneities present in the melt does not occur, in contrast to the situation at higher undercooling (see Fig. 24b). Apparently, Form I seeds are able to nucleate Form II more efficiently than commonly available sources of heterogeneous nuclei in the polymer melt.

A quantitative evaluation of cross-nucleation rate can be attempted by counting the number of nucleation sites as a function of time, from micrographs such as those shown in Fig. 25, and dividing it by the exposed surface area of Form I spherulites. This area can be estimated by multiplying the spherulite circumference by the measured thickness of the sample.

Figure 27a shows the trend of cross-nucleation density as a function of time for different crystallization temperatures. For all the investigated temperatures, the number of Form II cross-nuclei per unit of Form I exposed surface increases linearly with time. Therefore, it is possible to define the cross-nucleation rate as the slope of the lines in Fig. 27a. This slope decreases with increasing crystallization temperature.

These data on kinetics of cross-nucleation in *i*-PBU as a function of temperature are in agreement with the behavior of small organic molecules, in particular with that observed for *D*-mannitol by Yu et al. [132]. Moreover, the data are also consistent with previous qualitative reports on the temperature dependence of growth transition frequency in PVDF and PPVL (see Sect. 2.3.3)

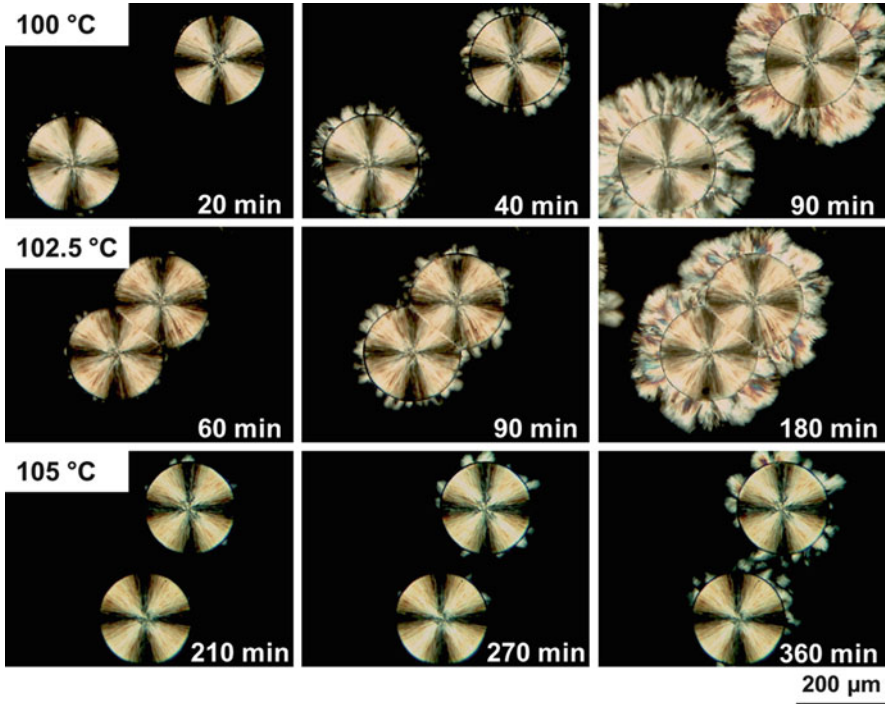


Fig. 26 Effect of temperature on cross-nucleation kinetics and morphology. Adapted with permission from [154]

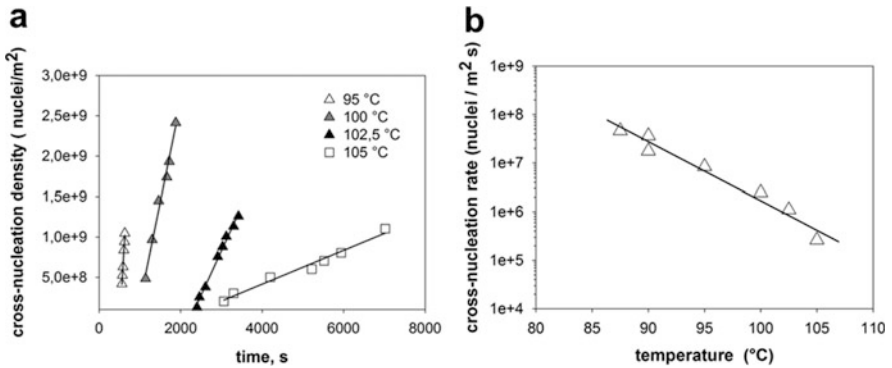


Fig. 27 (a) Cross-nucleation density as a function of time for samples crystallized at the indicated temperatures. (b) Cross-nucleation rate as a function of temperature. The lines are drawn to guide the eye. Adapted with permission from [154]

[67, 116]. However, a discrepancy exists with respect to the behavior of β -to- α growth transition in i-PP, which is seen to become more frequent with decreased undercooling [39].

Cross-nucleation rates are plotted against temperature in Fig. 27b. The semi-logarithmic plot shows the exponential dependence of the rate of cross-nuclei formation on temperature. The frequency of cross-nucleation events decreases by about two orders of magnitude in response to a decrease in undercooling of 15°C.

Applying classical nucleation theory [184] to data on cross-nucleation kinetics, it is possible to calculate the free energy barrier for the formation of a nucleus of critical size, ΔG^* . A value of around 43 kJ/mol is obtained for the formation of Form II nuclei on Form I crystals' surface. This value, which represents the energy barrier for a process of heterogeneous nucleation, is about one half of that reported for the homogeneous nucleation of i-PBu Form II [185]. Also, it is smaller than typical values for the critical energy barrier derived from droplet experiments (homogeneous nucleation) for other polymers (e.g., polyethylene, i-PP) [186].

5 Conclusions

Crystallization of polymorphic polymers can follow different pathways. In general, the different polymorphs can undergo a series of phase transitions from the least to the most stable; they can nucleate and grow independently at the same time; or they can heterogeneously nucleate on each other. Observations of the latter two cases, defined as concomitant crystallization and cross-nucleation, respectively, are rather scattered in the polymer literature. In this chapter we provide a comprehensive critical review of examples known to us.

Concomitant crystallization of different polymorphs is observed in at least 16 different polymers, for which thermodynamic and kinetic requirements for its occurrence are met under certain conditions, both in melt or solution crystallization. The interesting case of PPVL is described in detail. In this polymer, the α - and γ -polymorphs develop concomitantly at high undercooling. However, the growth of γ -phase spherulites cannot be followed in real-time, because they are quickly engulfed by the fast growing α -spherulites that cross-nucleate at their periphery, and never attain suitable size. A way to circumvent this problem through analysis of the interspherulitic boundary profiles was suggested. The method allows indirect measurement of γ -phase growth rates, which are not otherwise accessible, by measuring the experimentally accessible α -form spherulitic growth rates and a suitable shape factor that characterizes the engulfed γ -spherulites

Among the cases of polymers exhibiting concomitant crystallization, several examples of cross-nucleation between polymorphs can be found. The novel case of Form II-on-Form I cross-nucleation in i-PBu was discovered by a seeding procedure. We suspect that more examples might exist. Indeed, given the strong dependence of the phenomenon on crystallization conditions, if a given pair of polymorphs does not exhibit cross-nucleation it could be that, in the examined experimental conditions, cross-nucleation is unlikely to occur for kinetic reasons. In particular, it is even conceivable that cross-nuclei of another structure always form at the growth front of a growing polymorph. However, even if these events occur

with an acceptable frequency, cross-nucleation would become visible only in the cases in which the growth rate of the daughter phase overtakes that of the parent phase.

The critical literature review, along with novel examples of concomitant polymorphism and cross-nucleation presented in this chapter, is aimed at providing a rational picture of the phenomena and their relevance in the crystallization of polymorphic polymers. We hope that this manuscript promotes further studies on the topic, aimed at obtaining a better understanding of polymer polymorphic crystallization. This new level of insight is required to gain control of the formation of desired polymorphs – the ultimate goal of material scientists and crystallization engineers.

References

1. Bernstein J (2002) *Polymorphism in molecular crystals*. Oxford University Press, New York
2. Salzmann CG, Radaelli PG, Slater B, Finney JL (2011) *Phys Chem Chem Phys* 13:18468
3. Danusso F (1967) *Polymer* 8:281
4. Corradini P, Guerra G (1992) *Polymorphism in polymers*. In: Armistead KA (ed) *Macromolecules: synthesis, order and advanced properties*, vol 100/1, *Advances in polymer science*. Springer, Berlin, p 183
5. Pan P, Inoue Y (2009) *Prog Polym Sci* 34:605
6. De Rosa C (2003) *Macromolecules* 36:6087
7. Lovinger AJ (1982) *Macromolecules* 15:40
8. Brückner S, Meille SV, Petraccone V, Pirozzi B (1991) *Prog Polym Sci* 16:361
9. Lotz B, Wittmann JC, Lovinger AJ (1996) *Polymer* 37:4979
10. De Rosa C, Auremma F (2006) *Prog Polym Sci* 31:145
11. McKinney JE, Davis GT, Broadhurst MG (1980) *J Appl Phys* 51:1676
12. Karger-Kocsis J (1996) *Polym Eng Sci* 36:203
13. Karger-Kocsis J (1996) *Polym Bull* 36:119
14. Dunitz JD, Bernstein J (1995) *Acc Chem Res* 28:193
15. Ostwald W (1897) *Z Phys Chem* 22:289
16. Bernstein J, Davey RJ, Henck J-O (1999) *Angew Chem Int Ed* 38:3440
17. Yu L (2007) *CrystEngComm* 9:847
18. Chung S-Y, Kim Y-M, Kim J-G, Kim Y-J (2009) *Nat Phys* 5:68
19. Gliko O, Neumaier N, Pan W, Haase I, Fischer M, Bacher A, Weinkauff S, Vekilov PG (2005) *J Am Chem Soc* 127:3433
20. Chung S, Shin S-H, Bertozzi CR, De Yoreo JJ (2010) *Proc Natl Acad Sci USA* 107:16536
21. Sauter A, Roosen-Runge F, Zhang F, Lotze G, Jacobs RMJ, Schreiber F (2015) *J Am Chem Soc* 137:1485
22. Auer S, Frenkel D (2001) *Nature* 409:1020
23. Zhang TH, Liu XY (2009) *Angew Chem Int Ed* 48:1308
24. Leyssale J-M, Delhommelle J, Millot C (2005) *J Chem Phys* 122:184518
25. Kitamura M (2009) *CrystEngComm* 11:949
26. Chen C, Cook O, Nicholson CE, Cooper SJ (2011) *Cryst Growth Des* 11:2228
27. Stranski IT, Totomanow D (1933) *Z Phys Chem* 163:399
28. Cardew PT, Davey RJ (1982) *Symposium on the tailoring of crystal growth*. Institution of Chemical Engineers, London, p 1.1
29. Davey RJ (1993) *Faraday Discuss* 95:160

30. Van Santen RA (1984) *J Phys Chem* 88:5768
31. Threlfall T (2003) *Org Process Res Dev* 7:1017
32. Keller A, Hikosaka M, Rastogi S, Toda A, Barham PJ, Goldbeck-Wood G (1994) *J Mater Sci* 29:2579
33. Keller A, Cheng SZD (1998) *Polymer* 39:4461
34. Cheng SZD, Zhu L, Li CY, Honigfort PS, Keller A (1999) *Thermochim Acta* 332:105
35. Cheng SZD (2008) *Phase transitions in polymers: the role of metastable states*. Elsevier, Amsterdam
36. Pardey R, Wu SS, Chen J, Harris FW, Cheng SZD, Keller A, Aducci J, Facinelli JV, Lenz RW (1994) *Macromolecules* 27:5794
37. Heberer D, Keller A, Percec V (1995) *J Polym Sci B Polym Phys* 33:1877
38. Cavallo D, Mileva D, Portale G, Zhang L, Balzano L, Alfonso GC, Androsch R (2012) *ACS Macro Lett* 1:1051
39. Varga J, Ille A, Fujiwara Y (1990) *Period Polytech Chem Eng* 34:255
40. Lotz B (1998) *Polymer* 39:4561
41. Gan Z, Kuwabara K, Abe H, Iwata T, Doi Y (2004) *Biomacromolecules* 5:371
42. Ho R-M, Lin C-P, Tsai H-Y, Woo E-M (2000) *Macromolecules* 33:6517
43. Luciani L, Seppälä J, Löfgren B (1988) *Prog Polym Sci* 13:37
44. Danusso F, Gianotti G (1965) *Die Makromol Chem* 88:149
45. Yamashita M, Hoshino A, Kato M (2007) *J Polym Sci B Polym Phys* 45:684
46. Yamashita M (2009) *J Cryst Growth* 311:560
47. Androsch R, Hohlfeld R, Frank W, Nase M, Cavallo D (2013) *Polymer* 54:2528
48. Stolte I, Cavallo D, Alfonso GC, Portale G, Drongelen MV, Androsch R (2014) *Eur Polym J* 60:22
49. Lovinger AJ, Chua JO, Gryte CC (1977) *J Polym Sci* 15:641
50. Varga J (1992) *J Mater Sci* 27:2557
51. Varga J, Karger-Kocsis J (1996) *J Polym Sci B Polym Phys* 34:657
52. Somani RH, Hsiao BS, Nogales A, Fruitwala H, Srinivas S, Tsou AH (2001) *Macromolecules* 34:5902
53. Varga J (2002) *J Macromol Sci B* 41:1121
54. Nakamura K, Shimizu S, Umemoto S, Thierry A, Lotz B, Okui N (2008) *Polym J* 40:915
55. Sajkiewicz P, Grady A, Ziabicki A, Misztal-Faraj B (2010) *ePolymers* 10:1398
56. Mezghani K, Phillips PJ (1998) *Polymer* 39:3735
57. Alamo RG, Kim M-H, Galante MJ, Isasi JR, Mandelkern L (1999) *Macromolecules* 32:4050
58. Thomann R, Semke H, Maier RD, Thomann Y, Scherble J, Mülhaupt R, Kressler J (2001) *Polymer* 42:4597
59. De Rosa C, Auriemma F, Circelli T, Waymouth RM (2002) *Macromolecules* 35:3622
60. Lotz B, Thierry A (2002) *Macromolecules* 36:286
61. Charlet G, Delmas G, Revol JF, Manley RSJ (1984) *Polymer* 25:1613
62. Charlet G, Delmas G (1984) *Polymer* 25:1619
63. De Rosa C, Ruiz de Ballesteros O, Di Gennaro M, Auriemma F (2003) *Polymer* 44:1861
64. Sorrentino A, Pantani R, Titomanlio G (2008) *Colloid Polym Sci* 286:983
65. Sorrentino A, Pantani R, Titomanlio G (2007) *J Polym Sci B Polym Phys* 45:196
66. Sun YS, Woo EM (1999) *Macromolecules* 32:7836
67. Lovinger AJ (1980) *J Polym Sci* 18:793
68. Prest WM, Luca DJ (1975) *J Appl Phys* 46:4136
69. Silva MP, Sencadas V, Botelho G, Machado AV, Rolo AG, Rocha JG, Lanceros-Mendez S (2010) *Mater Chem Phys* 122:87
70. Gregorio JR, Cestari M (1994) *J Polym Sci B Polym Phys* 32:859
71. Gregorio R Jr, Borges DS (2008) *Polymer* 49:4009
72. Chinaglia DL, Gregorio R, Stefanello JC, Pisani Altafim RA, Wirges W, Wang F, Gerhard R (2010) *J Appl Polym Sci* 116:785
73. Zhu B, He Y, Asakawa N, Yoshie N, Nishida H, Inoue Y (2005) *Macromolecules* 38:6455

74. Zhu B, He Y, Asakawa N, Nishida H, Inoue Y (2005) *Macromolecules* 39:194
75. Gan Z, Abe H, Doi Y (2002) *Macromol Chem Phys* 203:2369
76. Woo EM, Wu MC (2005) *J Polym Sci B Polym Phys* 43:1662
77. Liu J, Ye H-M, Xu J, Guo B-H (2011) *Polymer* 52:4619
78. Lugito G, Woo EM (2012) *Macromol Chem Phys* 213:2228
79. Yang J, Pan P, Hua L, Zhu B, Dong T, Inoue Y (2010) *Macromolecules* 43:8610
80. Yang J, Pan P, Hua L, Xie Y, Dong T, Zhu B, Inoue Y, Feng X (2011) *Polymer* 52:3460
81. Tang Y-R, Xu J, Guo B-H (2015) *Ind Eng Chem Res* 54:1832
82. Liang Z, Pan P, Zhu B, Inoue Y (2010) *Macromolecules* 43:6429
83. Chiba T, Asai S, Xu W, Sumita M (1999) *J Polym Sci B Polym Phys* 37:561
84. Ju M-Y, Huang J-M, Chang F-C (2002) *Polymer* 43:2065
85. Woo E, Wu P-L, Chiang C-P, Liu H-L (2004) *Macromol Rapid Commun* 25:942
86. Ghosh AK, Woo EM, Sun Y-S, Lee L-T, Wu M-C (2005) *Macromolecules* 38:4780
87. Yen KC, Woo EM, Tashiro K (2010) *Polymer* 51:5592
88. Kaner P, Ruiz-Orta C, Boz E, Wagener KB, Tasaki M, Tashiro K, Alamo RG (2014) *Macromolecules* 47:236
89. Padden FJ, Keith HD (1959) *J Appl Phys* 30:1479
90. Mathieu C, Thierry A, Wittmann JC, Lotz B (2002) *J Polym Sci B Polym Phys* 40:2504
91. Campbell RA, Phillips PJ, Lin JS (1993) *Polymer* 34:4809
92. Lotz B, Graff S, Wittmann JC (1986) *J Polym Sci B Polym Phys* 24:2017
93. Yang G, Li X, Chen J, Yang J, Huang T, Liu X, Wang Y (2012) *Colloid Polym Sci* 290:531
94. Krache R, Benavente R, López-Majada JM, Pereña JM, Cerrada ML, Pérez E (2007) *Macromolecules* 40:6871
95. Natta VG, Corradini P, Bassi IW (1956) *Die Makromol Chem* 21:240
96. Danusso F, Gianotti G (1963) *Die Makromol Chem* 61:139
97. Holland VF, Miller RL (1964) *J Appl Phys* 35:3241
98. Chau KW, Geil PH (1984) *J Macromol Sci B* 23:115
99. Kaszonyiova M, Rybnikar F, Geil PH (2005) *J Macromol Sci B* 44:377
100. De Rosa C, Borriello A, Venditto V, Corradini P (1994) *Macromolecules* 27:3864
101. Aharoni SM, Charlet G, Delmas G (1981) *Macromolecules* 14:1390
102. Wegsteen K, Berghmans H (1998) *Macromol Chem Phys* 199:267
103. Woo EM, Sun YS, Yang CP (2001) *Prog Polym Sci* 26:945
104. Sorrentino A, Pantani R, Titomanlio G (2010) *J Polym Sci B Polym Phys* 48:1757
105. Watanabe H (1976) *Kobunshi Ronbunshu* 33:229
106. Koyano H, Yamamoto Y, Saito Y, Yamanobe T, Komoto T (1998) *Polymer* 39:4385
107. Milani A (2014) *Polymer* 55:3729
108. Yen KC, Woo EM (2009) *Polymer* 50:662
109. Point J-J, Damman P (1990) *Makromol Chem Macromol Symp* 39:301
110. Dosièrè M (1997) *Macromol Symp* 114:51
111. Tarallo O (2002) *Encyclopedia of polymer science and technology*. Wiley, New York
112. Delaite E, Point JJ, Damman P, Dosièrè M (1992) *Macromolecules* 25:4768
113. Damman P, Point JJ (1995) *Macromolecules* 28:2050
114. Frascini C, Jiménez L, Kalala B, Prud'Homme RE (2012) *Polymer* 53:188
115. Nozue Y, Seno S, Nagamatsu T, Hosoda S, Shinohara Y, Amemiya Y, Berda EB, Rojas G, Wagener KB (2012) *ACS Macro Lett* 1:772
116. Alfonso GC, Moretti P, Pallenzone P, Yin J (1995) *Opt Eng* 34:3385
117. De Rudder J, Bergé B, Berghmans H (2002) *Macromol Chem Phys* 203:2083
118. Keller A (1995) *Faraday Discuss* 101:1
119. Di Lorenzo ML (2005) *Eur Polym J* 41:569
120. Pan P, Kai W, Zhu B, Dong T, Inoue Y (2007) *Macromolecules* 40:6898
121. Pan P, Zhu B, Kai W, Dong T, Inoue Y (2008) *J Appl Polym Sci* 107:54
122. Cocca M, Androsch R, Righetti MC, Malinconico M, Di Lorenzo ML (2014) *J Mol Struct* 1078:114

123. Organ SJ, Ungar G, Keller A (1989) *Macromolecules* 22:1995
124. Organ SJ, Keller A, Hikosaka M, Ungar G (1996) *Polymer* 37:2517
125. Ungar G, Putra EGR, de Silva DSM, Shcherbina MA, Waddon AJ (2005) *Interphases and mesophases in polymer crystallization I*, vol 180. Springer, Berlin, p 45
126. Stoica C, Tinnemans P, Meekes H, van Enkevort WJP, Vlieg E (2006) *Cryst Growth Des* 6:1311
127. Yu L (2003) *J Am Chem Soc* 125:6380
128. Chen S, Xi H, Yu L (2005) *J Am Chem Soc* 127:17439
129. Yu L (2010) *Acc Chem Res* 43:1257
130. Stoica C, Tinnemans P, Meekes H, Vlieg E, van Hoof PJCM, Kaspersen FM (2005) *Cryst Growth Des* 5:975
131. Stoica C, Verwer P, Meekes H, Vlieg E, van Hoof PJCM, Kaspersen F (2005) *J Cryst Growth* 275:e1727
132. Tao J, Yu L (2006) *J Phys Chem B* 110:7098
133. Tao J, Jones KJ, Yu L (2007) *Cryst Growth Des* 7:2410
134. Davey RJ, Blagden N, Righini S, Alison H, Ferrari ES (2002) *J Phys Chem B* 106:1954
135. Ferrari ES, Davey RJ (2004) *Cryst Growth Des* 4:1061
136. Cashell C, Corcoran D, Hodnett BK (2003) *Chem Commun* 374
137. Desgranges C, Delhommelle J (2006) *J Am Chem Soc* 128:10368
138. Desgranges C, Delhommelle J (2006) *J Am Chem Soc* 128:15104
139. Desgranges C, Delhommelle J (2007) *Phys Rev Lett* 98:235502
140. Desgranges C, Delhommelle J (2007) *J Phys Chem B* 111:1465
141. Desgranges C, Delhommelle J (2007) *J Chem Phys* 126:054501
142. Nguyen AH, Jacobson LC, Molinero V (2012) *J Phys Chem C* 116:19828
143. Nguyen AH, Molinero V (2014) *J Chem Phys* 140:084506
144. Sasaki S, Takahashi Y, Tadokoro H (1972) *J Polym Sci Polym Phys Ed* 10:2363
145. Prud'Homme RE (1977) *J Polym Sci Polym Phys Ed* 15:1619
146. Archambault P, Prud'Homme RE (1980) *J Polym Sci Polym Phys Ed* 18:35
147. Varga J (1982) *Die Angew Makromol Chem* 104:79
148. Varga J, Schulek-Tóth F (1996) *J Therm Anal* 47:941
149. Varga J, Ehrenstein GW (1997) *Colloid Polym Sci* 275:511
150. Lotz B, Fillon B, Thierry A, Wittmann J-C (1991) *Polym Bull* 25:101
151. Lauritzen JJI, Hoffman JD (1959) *J Chem Phys* 31:1680
152. Hall IH, Ibrahim BA (1982) *Polymer* 23:805
153. Cavallo D, Gardella L, Portale G, Müller AJ, Alfonso GC (2013) *Polymer* 54:4637
154. Cavallo D, Gardella L, Portale G, Müller AJ, Alfonso GC (2014) *Macromolecules* 47:870
155. Huang J, Chen S, Guzei IA, Yu L (2006) *J Am Chem Soc* 128:11985
156. Tsuji H (2005) *Macromol Biosci* 5:569
157. Tsuji H, Tezuka Y (2004) *Biomacromolecules* 5:1181
158. Tsuji H, Ikada Y (1993) *Macromolecules* 26:6918
159. Schmidt SC, Hillmyer MA (2001) *J Polym Sci B Polym Phys* 39:300
160. Yamane H, Sasai K (2003) *Polymer* 44:2569
161. Tsuji H, Takai H, Saha SK (2006) *Polymer* 47:3826
162. Saeidlou S, Huneault MA, Li H, Sammut P, Park CB (2012) *Polymer* 53:5816
163. Wen T, Xiong Z, Liu G, Zhang X, de Vos S, Wang R, Joziassse CAP, Wang F, Wang D (2013) *Polymer* 54:1923
164. Bouapao L, Tsuji H (2009) *Macromol Chem Phys* 210:993
165. Pan P, Han L, Bao J, Xie Q, Shan G, Bao Y (2015) *J Phys Chem B* 119:6462
166. Gardella L, Basso A, Prato M, Monticelli O (2015) *RSC Adv* 5:46774
167. Brochu S, Prud'Homme RE, Barakat I, Jerome R (1995) *Macromolecules* 28:5230
168. Brückner S, Meille SV, Porzio W (1988) *Polymer* 29:1586
169. Meille SV, Brückner S, Lando JB (1989) *Polymer* 30:786
170. Prud'Homme RE, Marchessault RH (1974) *Die Makromol Chem* 175:2705

171. Meille SV (1994) *Polymer* 35:2607
172. Roitman DB, Marand H, Miller RL, Hoffman JD (1989) *J Phys Chem* 93:6919
173. Marand H, Hoffman JD (1990) *Macromolecules* 23:3682
174. Meille SV, Konishi T, Geil PH (1984) *Polymer* 25:773
175. Varga J (1983) *Die Angew Makromol Chem* 112:161
176. Lednický F (1987) *Die Makromol Chem* 188:619
177. Natta G, Corradini P, Bassi IW (1960) *Nuovo Cimeato* 15:52
178. Powers J, Hoffman JD, Weeks JJ, Quinn FA Jr (1965) *J Res Natl Bur Stand* 69A:335
179. Zhang B, Yang D, Yan S (2002) *J Polym Sci B Polym Phys* 40:2641
180. Kopp S, Wittmann JC, Lotz B (1994) *J Mater Sci* 29:6159
181. Bartczak Z, Argon AS, Cohen RE, Kowalewski T (1999) *Polymer* 40:2367
182. Carvalho JL, Dalnoki-Veress K (2011) *Eur Phys J E* 34:1
183. Langhe DS, Hiltner A, Baer E (2012) *J Appl Polym Sci* 125:2110
184. Turnbull D, Fisher JC (1949) *J Chem Phys* 17:71
185. Wolkowicz MD (1978) *J Polym Sci Polym Symp* 63:365
186. Koutsky JA, Walton AG, Baer E (1967) *J Appl Phys* 38:1832

Epitaxial Effects on Polymer Crystallization

Rui Xin, Jie Zhang, Xiaoli Sun, Huihui Li, Zhaobin Qiu, and Shouke Yan

Abstract The macroscopic properties of semicrystalline polymeric materials are remarkably dependent on their microstructure and morphology. This offers an effective way to tailor the properties of such materials through crystal engineering. For purposeful control of the crystal structure and crystalline morphology, many sophisticated techniques have been developed. For example, to obtain a particular crystal structure of a polymorphic polymer, proper choice of heterogeneous nucleation agent is frequently used, and highly oriented crystalline materials can be produced through crystallization under shear field. It should be pointed out that even though special crystallization pathways have been developed to control the individual structure of a semicrystalline polymer in a specific aspect, synchronous control of multiscale structures with several aspects still remains a challenge. In this connection, surface-induced epitaxial crystallization shows significant advantages over other methods. It is well documented in numerous research studies that epitaxial crystallization of polymers allows simultaneous control of the crystal structure, orientation, and spatial arrangement of the backbone chain. This review discusses how surface-induced epitaxy influences the crystallization behavior of semicrystalline polymers and what kinds of unique crystal structures and morphologies of the polymers can be obtained. We hope that this provides useful information for polymer processing in different application fields and promotes the technical development of new methods for preparation of high polymeric materials for advanced applications.

Keywords Crystallization • Epitaxy • Polymer • Property • Structure

R. Xin, J. Zhang, X. Sun (✉), H. Li, Z. Qiu, and S. Yan (✉)
State Key Laboratory of Chemical Resource Engineering, Beijing University of
Chemical Technology, Beijing 100029, China
e-mail: xiaolisun@mail.buct.edu.cn; skyan@mail.buct.edu.cn

Contents

1	Introduction	56
2	Epitaxial Crystallization of Polymers on Different Substrates and the Mechanisms Involved	58
2.1	Epitaxial Crystallization of Polymers on Inorganic Substrates	58
2.2	Epitaxial Crystallization of Polymers on Organic Substrates	59
2.3	Epitaxial Crystallization Between Polymers	62
3	Methods for Structural Characterization of Epitaxial Systems	68
3.1	Molecular Vibration Spectroscopy	68
3.2	X-Ray Diffraction	69
3.3	Microscopy	69
4	Influence of Epitaxy on Polymer Crystallization and Its Impact on Material Properties	73
4.1	Influence of Epitaxy on the Crystallization Kinetics of Polymers	73
4.2	Structure Regulation and Its Impact on Material Properties	74
5	Methods of Realizing Polymer Epitaxy	83
6	Conclusions and Outlook	86
	References	88

1 Introduction

Polymers offer many advantages for modern technologies, which has lead to a permanent place for polymeric materials in many sophisticated applications. This is related to the fact that the properties of polymeric materials can fulfill the requirements of specific applications and provide advantages that include low cost, easy fabrication (e.g., no need for a special clean room and/or high temperature processes), and low density (which is one of the most important factors when choosing polymeric materials for a specific application). It has been well documented that polymeric materials offer greater potential to meet market requirements than other materials, because the properties of the materials can be easily tailored by their structure at different scales. First, the chemical structure at molecular scale determines the essential properties and/or functionality of a polymer. Subtle manipulation of the chemical composition, functional groups, and chain architecture can give rise to completely new polymeric materials with completely different properties or functionalities. For example, polymers with π -conjugated backbone chains provide exceptional electrical properties for applications in organic field-effect transistors (OFETs) and sensors [1–5]. Second, multiscale structures in the condensed state of polymeric materials exhibit remarkable influence on their mechanical and physical properties. As examples, the stiffness and strength of polymer fibers with highly oriented molecular chains can exceed those of their isotropic counterparts by orders of magnitude [6, 7]. Furthermore, the electrical conductivity of doped and aligned conjugated macromolecules is more than 100-fold greater than that of their non-oriented counterparts [8–10]. For crystalline polymers, the crystal structure and orientation are very important factors that affect the properties and sometimes

even the functionality of a polymer. For this aspect, poly(vinylidene fluoride) (PVDF) provides an excellent example. Its α -form crystals (composed of helical chains) can be used only as ordinary thermoplastics, but its β -form crystals (composed of planar zigzag chains) exhibit exceptional piezo- and pyro-electric properties [11]. Among many others, the β -form of isotactic polypropylene (iPP), which has greater macroscopic toughness and ductility than its α -counterpart, provides another familiar example [12–14]. It is examples such as these that have resulted in the structural manipulation of semicrystalline polymeric materials becoming an extremely important issue in the field of polymer physics.

Similarly to small molecules, the crystallization of macromolecules takes place in two stages (i.e., formation of a crystal nucleus and subsequent crystal growth). Nucleation can occur either homogeneously or heterogeneously when it is induced by the presence of heterogeneities. Heterogeneous nucleation provides an efficient pathway for controlling the crystal structure of polymers. For example, iPP is a semicrystalline polymer with pronounced polymorphisms [15–20]. Although its α -form can be easily obtained through normal melt and solution crystallization, its metastable β -form is, in most cases, generated through crystallization in the presence of β -iPP nucleation agents [21–27]. Surface-induced epitaxial crystallization of polymers is a typical case of heterogeneous nucleation. It was found that epitaxial crystallization is effective in governing the crystallization process of polymers. It can control the crystal structure and its orientation. For instance, the use of a special nucleation agent can generally produce only spherulitic structures of β -iPP. The crystallization of iPP from the melt via epitaxy on γ -quinacridone and dicyclohexylterephthalamide substrates not only initiates β -iPP crystallization but also results in biaxial orientation of β -iPP (i.e., biaxially oriented thin β -iPP film is obtained) [19]. This is of great significance because oriented β -form iPP cannot be achieved from β -iPP spherulites via mechanical means because of the β - α transition on stretching. Taking this into account, study of epitaxial crystallization of polymers is of particular interest from both practical and scientific points of view.

The purpose of this review is to present the state-of-art concerning polymer epitaxy. It provides information on how epitaxy influences the crystallization behavior of polymers. Section 2 describes the epitaxial crystallization of polymers on different substrates and the mechanisms involved. In the third part, the methods used for structural characterization of epitaxial systems are introduced. Section 4 mainly focuses on the possible influence of epitaxy on polymer crystallization, including kinetics and structure. The impact of structure regulation on the macroscopic properties of the materials is illustrated with some selected examples. Then, several common and effective methods for conducting polymer epitaxy are described in Sect. 5. At the end of this review, a brief conclusion and further perspectives for this field are given.

2 Epitaxial Crystallization of Polymers on Different Substrates and the Mechanisms Involved

2.1 Epitaxial Crystallization of Polymers on Inorganic Substrates

The term “epitaxy” was introduced by Royer [28], who developed the early theory of epitaxial growth based on structural analogy between the substrate and overgrowth materials in the contact lattice planes [29]. Epitaxy is defined, most generally, as the process by which crystals of one phase (guest crystals) grow on the surface of a crystal of another phase (host crystal) in one or more strictly defined crystallographic orientations [30]. It was discovered in 1817 when mineralogists recognized that various natural minerals appear in unique shapes [31]. Laboratory-grown epitaxial single crystals of small molecules were obtained by Frankenheim in 1936 [32]. Epitaxial crystallization of polymers was first performed on inorganic substrates in the 1950s by Willems and Fischer [33–38]. These works have been well reviewed in detail by Mauritz et al. [39]. Following these early works, it was subsequently found that a variety of inorganic substrates, such as alkali halides, graphite and quartz, can force polymer crystals into an epitaxial oriented crystallization [40–45]. Of these, alkali halides are the most used substrates for epitaxial growth of polymers because of their good availability and the possibility of varying, more or less continuously, the crystallographic parameters of the unit cell. As an example, Fig. 1 shows the bright-field (BF) electron micrograph and the corresponding electron diffraction pattern of PVDF epitaxially crystallized on the (001) surface of potassium bromide. In this case, the PVDF crystallizes in its β -form with biaxial orientation. Through systematic analyses of these epitaxial systems, significant progress has been made towards a better understanding of polymer/

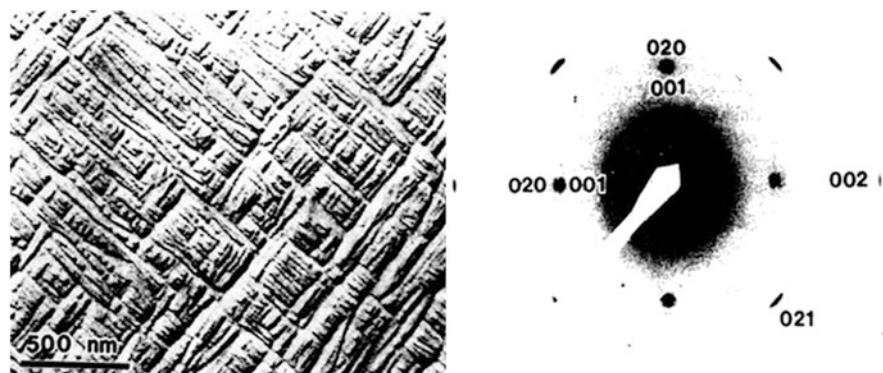


Fig. 1 Bright field electron micrograph (*left*) and corresponding electron diffraction pattern of PVDF epitaxially crystallized on the (001) surface of potassium bromide (*right*). Reproduced with permission from Lovinger [46], copyright © 1981, published by Elsevier Ltd

alkali halide epitaxy, from both experimental and theoretical points of view. In all polymer–alkali halide systems, it was found that the polymer chains aligned along the $\langle 110 \rangle$ directions on the (001) faces of the alkali halides. Considering that the overgrowths of polymer on the (001) alkali halide cleavage planes (having unit cell lengths ranging from 0.401 nm for LiF to 0.705 nm for KI) possess the same chain orientation, it was suggested that the special alignment of the polymers was caused by electrostatic interaction of ion rows of like charges with the polymer chains [39, 46–50].

2.2 *Epitaxial Crystallization of Polymers on Organic Substrates*

The epitaxial crystallization of polymers on crystals of organic compounds was discovered later. Walton et al. [51] published a noteworthy paper considering the possibility of epitaxy of polymers on crystals of organic compounds. Willems was the first to demonstrate oriented overgrowth of paraffins on aromatic hydrocarbons [33, 52]. Thereafter, a few scattered examples of organic substrate-induced epitaxial crystallization of polymers appeared in the literature up to the early 1970s [53, 54]. Excellent reviews regarding this aspect were given by Swei et al. [55] and Wittmann and Lotz [56]. In this field, after a few investigations devoted to epitaxial crystallization of polymers on organic substrates [57–59], the dominant substrates for epitaxial growth of polymers rapidly became aromatic substances such as linear polyphenyls (e.g., bi-, ter-, quater-phenyls), condensed aromatic hydrocarbons (naphthalene, anthracene, etc.), and aromatic carboxylic acids and their salts [60–62]. This is associated with their nearly endless possible variations in terms of chemical, physical, and crystallographic properties. It was found that polyolefins, aliphatic polyesters, and polyamides can crystallize epitaxially on organic substrates [60–63]. Figure 2 shows an electron diffraction pattern of polyethylene (PE) epitaxially grown on *p*-terphenyl and its schematic interpretation. The electron diffraction pattern presented in Fig. 2a shows sharp and well-defined reflections of the *p*-terphenyl crystal and somewhat arced reflections of the overgrowth PE. The presence of two sets of (002) PE reflections, more clearly displayed in the corresponding sketch in Fig. 2b, indicates that the polymer chain axes are lying in two different directions in the film plane. The PE chains are parallel to the [110] and $[\bar{1}\bar{1}0]$ directions of *p*-terphenyl crystal. In other words, the PE molecular chains are aligned parallel to the $\langle 110 \rangle$ directions of the *p*-terphenyl crystal. The appearance of (310) and (210) PE reflections on the equator tells us that the contact plane of PE with the (001) face of *p*-terphenyl is its (110) lattice plane because the (310) and (210) diffracting planes are nearly perpendicular to the (110) plane. According to experimental information, the epitaxial relationship between PE and *p*-terphenyl can be explained in terms of geometric matching. It was calculated that the intermolecular distance along the (110) direction of the *p*-terphenyl is 0.491 nm.

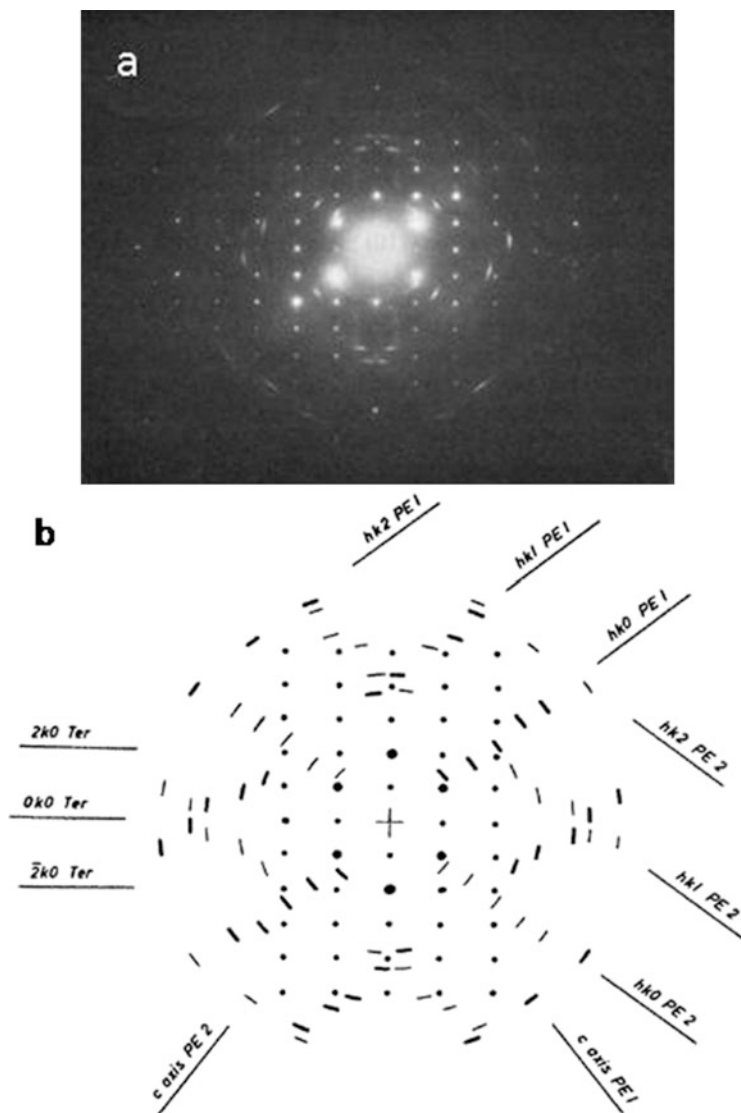


Fig. 2 (a) Electron diffraction pattern of PE film grown epitaxially on *p*-terphenyl crystal surface. (b) Sketch of the diffraction pattern with indexing of the reflections (only the various layer lines are indicated). Diffractions of *p*-terphenyl show as spots, whereas the arced reflections originate from PE. Reproduced with permission from Wittmann and Lotz [61], copyright © 1981, published by Wiley-VCH

This matches twice the *c*-axis repeat distance of PE (0.2534 nm), with a mismatch of ca. 3.5%, which is well within the normally accepted upper limit of 10–15% [56]. Another more pronounced lattice matching is achieved between the polymer

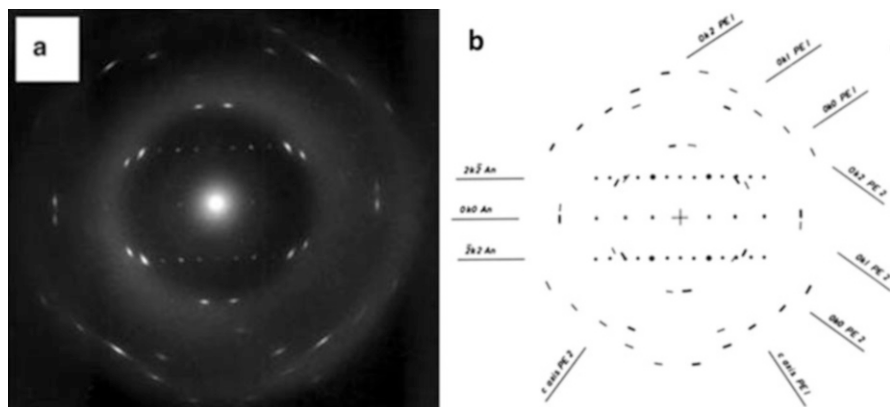
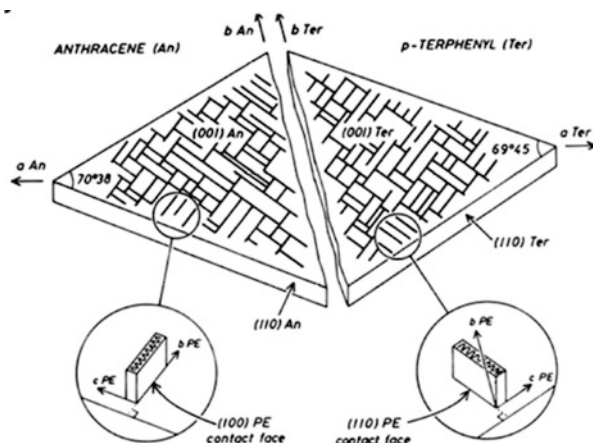


Fig. 3 (a) Electron diffraction pattern and (b) interpretation of the epitaxial crystallization of PE on the surface of an anthracene crystal. The diffractions of the substrate crystal show as spots, whereas the arced reflections originate from PE. Reproduced with permission from Wittmann and Lotz [61], copyright© 1981, published by Wiley-VCH

interchain distance of PE in the (110) lattice plane (0.448 nm) and the inter-row periodicity of *p*-terphenyl in the $\langle 110 \rangle$ (0.46 nm), with a mismatching of only 2.6%. On the basis of this analysis, it was concluded that two-dimensional matching between *p*-terphenyl and PE is the key factor for the occurrence of epitaxial crystallization.

The importance of two-dimensional matching in epitaxial crystallization of polymers on organic substrates has been illustrated by the different epitaxial behavior of PE on anthracene single crystals. As presented in Fig. 3, after melting and recrystallization of PE in contact with the (001) anthracene crystal surface, the selected-area electron diffraction (Fig. 3a) shows sharp diffraction spots for both materials. The slightly arced reflections associated with the PE overgrowth are all indexed as $(0kl)$, indicating a chain alignment of PE parallel to the substrate. As sketched in Fig. 3b, the two superimposed PE diffraction patterns are recognized to be rotated by an angle of ca. 70° and aligned symmetrically with respect to the b^* axis of the anthracene crystal. This inclination angle corresponds to the angle made by $[110]$ and $[\bar{1}\bar{1}0]$ directions of the anthracene crystal, similar to the case of epitaxy of PE on *p*-terphenyl. However, in this case, the contact plane of the PE is the (100) lattice plane. This is related to better two-dimensional matching. The matching between the intermolecular distance along the (110) direction of the anthracene (0.524 nm) and twice the PE chain axis repeat of 0.2534 nm is achieved with a mismatching of only $\sim 3\%$. A second quasiperfect lattice matching is found between the interchain distance of PE along the b -axis (0.494 nm) and the anthracene (110) inter-row distance of 0.493 nm. It is this excellent matching that results in the change of contact plane of PE from (110) on *p*-terphenyl to (100) on anthracene. A sketch displaying the relative orientations of PE lamellae and PE unit cells on anthracene and *p*-terphenyl is presented in Fig. 4.

Fig. 4 Relative orientations of PE lamellae and PE unit cells (*insets*) on anthracene (*left*) and *p*-terphenyl (*right*). Note the difference in polymer contact planes. Reproduced with permission from Wittmann and Lotz [61], copyright © 1981, published by Wiley-VCH



2.3 Epitaxial Crystallization Between Polymers

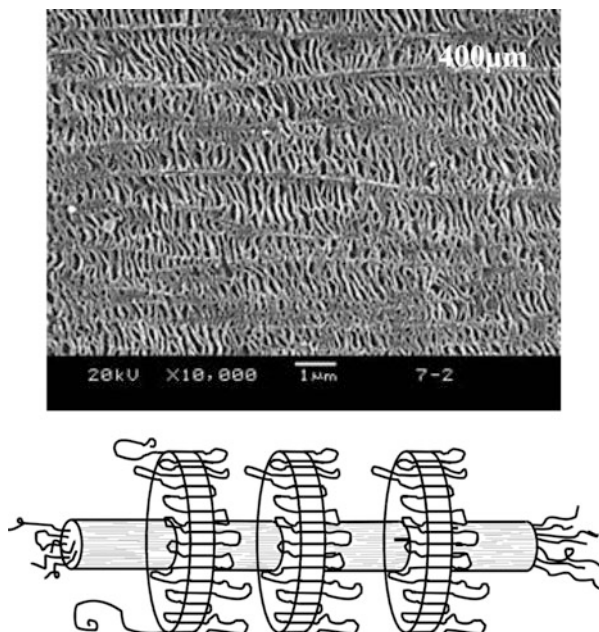
Generally, polymers crystallize to form spherulites made up of radially arranged lamellae (i.e., thin folded-chain lamellar crystals) [64]. Given their long chain character and peculiar morphology, polymers are not amenable to the numerous methods used for preparation of thin films of low molecular weight organic and inorganic materials. Because of this difficulty, investigation of epitaxial crystallization between polymers has been delayed. Most of the publications dealing with polymer–polymer epitaxy appeared only at the beginning of the 1980s. Nevertheless, since then, the study of polymer–polymer epitaxy has become an extremely active subject in the field of polymer science and significant progress has been made towards a better understanding of the problems specific to polymer–polymer epitaxy.

2.3.1 Homoepitaxy of Polymers

The well-known shish–kebab structure formed in sheared or elongated polymeric materials is a typical example of epitaxial growth of a polymer on its own polymer substrate. The folded-chain lamellar crystals (kebabs) grow epitaxially on the extended-chain crystals (shishes), with their molecular chains parallel to each other (see Fig. 5) [65–71]. This kind of epitaxy is generally defined as homoepitaxy, or less frequently as autoepitaxy [30]. In this case, the crystallographic orientations between the kebab and shish crystals are identical. It can, therefore, also be explained by two-dimensional matching.

Another representative example of homoepitaxy is the characteristic and unique lamellar branching of iPP in its α -form [72, 73]. It can be obtained from solution crystallization of cast films [74], crystallization from melt in the bulk [75, 76], and even during fiber spinning [77–79]. A number of investigations have been

Fig. 5 *Top:* Scanning electron microscopy (SEM) image shows the shish-kebab structure of high-density polyethylene obtained via dynamic packing injection molding. *Bottom:* Shish-kebab polymer structure frequently observed in sheared or stretched samples. Reproduced with permission from Cao et al. [65], copyright © 2006, published by Elsevier Ltd



conducted on the mechanism of formation of this intercrossing lamellar structure [80–87]. As presented in Fig. 6a, the characteristic texture of the branching is a result of the coexistence of two sets of lamellae (frequently referred to as mother and daughter lamellae) at an angle of ca. 100° to each other. Electron diffraction demonstrates that their crystallographic b -axes are in common, whereas the a - and c -axes of the mother lamellae are parallel to the c - and a -axes of the daughter lamellae (see Fig. 6b, c). Taking the monoclinic unit cell of α -iPP with lattice constants of $a = 0.666$ nm, $b = 2.078$ nm, $c = 0.650$ nm, and $\beta = 99.62^\circ$ into account, the wide angle lamellar branching was first interpreted on the basis of the rather similar interplane distances along the a - and c -axes. In other words, the unique lamellar branching of α -iPP was explained in terms of homoepitaxy based on a two-dimensional lattice matching between the a - and c -axes, with a rather small mismatching of 2.3% [82, 83, 86]. Lotz and Wittmann proposed a further explanation on the molecular scale [85]. It is well documented that, in the α -iPP crystal, helices of alternatively opposite handedness are required along the b -axis for favorable interaction of the methyl groups (Fig. 7a). During crystallization, if an iPP helix with the same handedness is deposited on a (010) face of α -iPP, favorable interaction of the methyl groups can only be achieved when the helix axis is inclined ca. 100° (Fig. 7b). Based on their elaborate analysis, Lotz and Wittmann associated the lamellar branching of iPP with the result of a crystal growth defect. In other words, the linear array of methyl side groups on the (010) plane of one set of the lamellae fits into the channels between similar arrays in the (010) plane of the

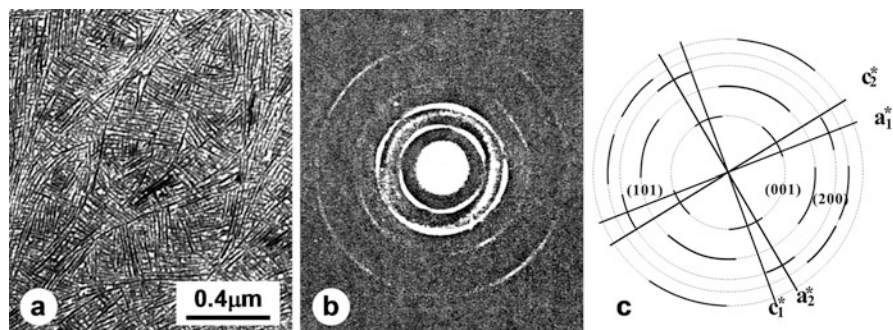


Fig. 6 (a) Phase-contrast bright field transmission electron micrograph of a solution-cast iPP thin film and (b) its corresponding diffraction pattern. (c) Sketch of the diffraction pattern shown in (b) with the main diffraction arcs indexed. Reproduced with permission from Wu et al. [86], copyright © 2013, published by Springer

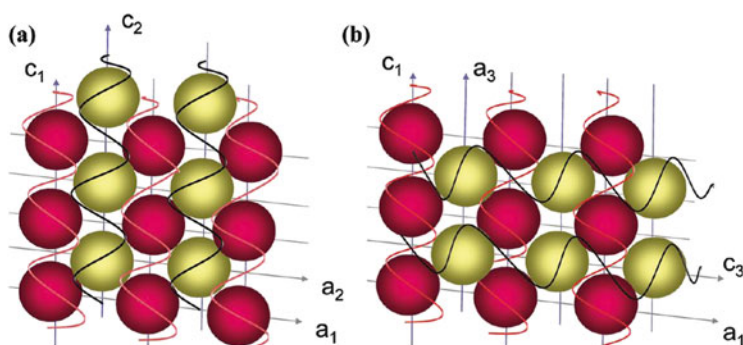


Fig. 7 Wide angle lamellar branching of α -iPP. (a) Parallel deposition of iPP helices on the ac -plane of the α -phase, giving rise to continuous α -phase growth. The methyl groups at the growth face are marked by *red circles* within the a_1c_1 -plane. The methyl groups marked by *yellow circles* represent the depositing antichiral stem in the a_2c_2 -plane, which are parallel to the stem orientation in the original α -phase crystal (a_1 is parallel to a_2 , and c_1 is parallel to c_2). (b) Molecular deposition of iPP helices on the ac -plane of the α -phase, leading to lamellar branching in iPP. The methyl groups at the growth face are marked by *red circles* within the a_1c_1 -plane. The methyl groups marked by *yellow circles* represent the depositing stem with the a_3c_3 -plane, which is either 80° or 100° from the stem orientation in the original α -phase crystal. Reproduced with permission from Lotz et al. [18], copyright © 1996, published by Elsevier Ltd

other set. This kind of “stacking fault” accounts for the experimental observation that rapid crystallization conditions favor lamellar branching of iPP.

2.3.2 Heteroepitaxy Between Polymers

Heteroepitaxy refers to the oriented overgrowth of one crystal on a substrate of another crystal. Excellent reviews have been presented on this subject by Wittmann

and Lotz as well as Petermann [56, 88]. In contrast to the cases of inorganic and organic substrate-induced epitaxial crystallization, no large specific crystallographic surfaces of polymer crystal are available because of chain folding. As a consequence, early attempts to study epitaxial crystallization between polymers were made using non-oriented polymer thin films as substrate [89–92]. Later, crystallization of polymers at highly oriented fiber surfaces were studied [93–100]. At the same time, attention was paid to cold-drawn and spun polymer blend systems. It was noticed that after certain thermal treatments, cold-drawn and spun polymer blends could develop a special mutual orientation. As an example, when cold-drawn blends of iPP and PE were heat treated at a temperature between the melting temperature of PE (135°C) and iPP (165°C) (e.g., 150°C) a cross-hatched lamellar structure of PE together with uniaxially oriented iPP crystals was found [101, 102]. The appearance of cross-hatched PE lamellae was at that time correlated with thermal shrinking stress or oriented spherulite growth. The possibility of epitaxial crystallization of PE on the surface of iPP matrix was, however, ruled out. With the development of skillful experimental techniques for preparing ultrathin oriented polymeric substrate films, heteroepitaxy between polymers was studied in detail.

The best illustrative model system is epitaxial crystallization between PE and iPP [103–105]. Figure 8 presents a BF electron micrograph and its corresponding diffraction pattern for PE crystallized on a highly oriented iPP ultrathin film. The BF micrograph (Fig. 8a) shows the cross-hatched lamellar structure of PE. Electron diffraction (Fig. 8b) confirms the existence of fixed mutual orientation between the PE and iPP. As sketched in Fig. 8c, the molecular chains of the polymers are at 50° to each other. The same mutual orientation relationship between PE and iPP systems was always observed in solution-cast films of their blend or by crystallizing one of the polymers from dilute solution on the other polymeric substrate

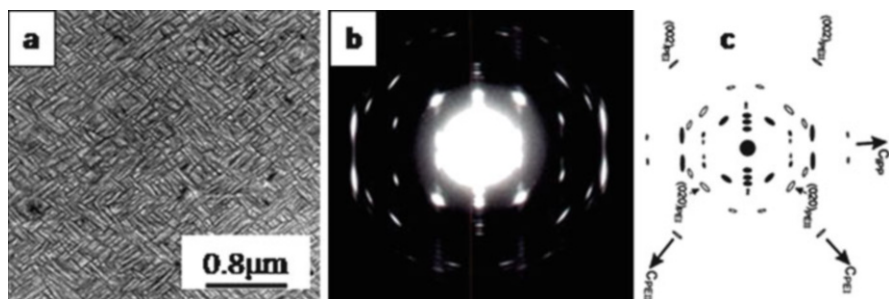


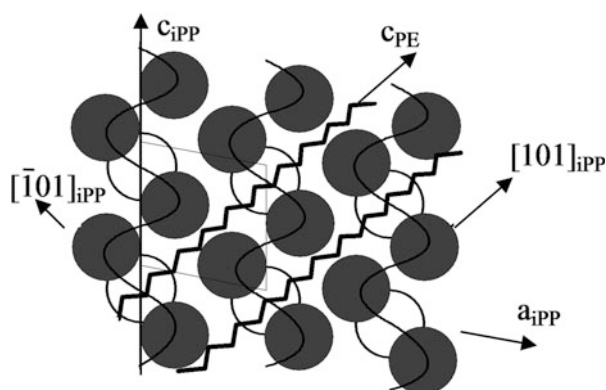
Fig. 8 (a) Bright field electron micrograph of PE crystallized on an oriented iPP substrate and (b) its corresponding diffraction pattern. The sample was obtained through annealing a PE/iPP double-layered film at 150°C for 10 min and subsequently quenched to room temperature in air. The molecular chain direction of the iPP substrate is horizontal, which is consistent with the electron diffraction. (c) Representation of the diffraction pattern, with *solid ellipses* indicating the reflection spots of the oriented iPP and the *open ellipses* indicating the reflection spots of the overgrowth PE crystals. Reproduced with permission from Li and Yan [106], copyright © 2011, American Chemical Society

[74, 107]. Careful analysis of the epitaxy between PE and iPP demonstrated that, except for a 50° chain inclination of both polymers, the planes of both polymers in contact are the (010) lattice plane for iPP and (100) lattice plane for PE [106]. It was also found that the (010) lattice plane of iPP is also the common contact plane for the polyamide/iPP and polyester/iPP epitaxial systems [103]. This is related to the structural features of the (010) lattice plane of the monoclinic iPP unit cell.

As schematically presented in Fig. 9, the characteristic geometry of this lattice plane is rows of methyl groups, which stick out of the lattice plane. It was calculated that the densest population of methyl groups is found in direction parallel to the [101] direction, with an average distance between adjacent methyl groups of about 0.425 nm. The rows parallel to the $[\bar{1}01]$ direction are next in density, with the methyl groups 0.505 nm apart from each other, followed by those in a - and c -axes directions. Therefore, it is easy to deduce that the distance between two adjacent methyl group rows in the [101] direction is 0.505 nm. This matches the distance between adjacent molecule chains of PE in the (100) planes (i.e., 0.494 nm). Furthermore, the angle between the methyl group rows along the [101] direction and the chain direction of iPP is exactly 50° , which also fits the chain inclination angle of PE with respect to iPP. Taking all these into account, Wittmann and Lotz explained the epitaxy of PE on iPP in terms of parallel alignment of PE chains along the methyl group rows in the [101] direction with chain-row matching [108]; the mismatch of ca. 2% is well within the normally accepted upper limit of 10–15%. For the epitaxial systems of iPP with polyamide/iPP and polyester/iPP, it was suggested that the aliphatic sequences in the polyamides and polyesters, which are ~ 0.48 nm apart from each other, play an important role in the epitaxial arrangement, based on one-dimensional chain-row matching.

It should be pointed out that the structural analogy, which leads to the matching between the substrate and overgrowth polymer, reveals a favorable interaction on the molecular scale [109–111]. This has been best demonstrated by the ordering process of polycaprolactone (PCL) in the melt on highly oriented PE substrate. It was confirmed that the epitaxial crystallization of PCL on highly oriented PE substrate results in a parallel chain alignment of both polymers, as a result of the

Fig. 9 Epitaxial alignment of a PE molecular chain on the (010) lattice plane of monoclinic iPP. Out-sticking methyl groups are indicated by *black circles*, and the *zigzag lines* represent PE molecular chains



almost identical orthorhombic unit cell parameters along the *a*- and *b*-axes of PCL ($a = 0.747$ and $b = 0.498$ nm) and PE ($a = 0.74$ and $b = 0.494$ nm) [109]. It is helpful to use Fourier transform infrared spectroscopy (FTIR) to check whether parallel chain alignment can be achieved in the melt of PCL. As shown in Fig. 10a, WAXD experiments confirm that PCL melt placed on highly oriented PE substrate does not crystallize at 59°C for 22 h [111]. The crystallization of PCL takes place during the cooling process at around 50°C (Fig. 10b). Polarized FTIR measurements illustrate, however, a gradual parallel alignment of the PCL chains along the chain direction of PE over time at 59°C (Fig. 10c, d), confirming the occurrence of soft epitaxy of PCL on the PE substrate. This indicates that the parallel alignment of PCL chains on oriented PE substrate originates from the favorable mutual interaction between PCL and PE, leading to the formation of a planar zigzag chain conformation, similar to that in its crystalline phase. During the cooling process, the ordered PCL chains act as crystallization precursors and initiate the parallel

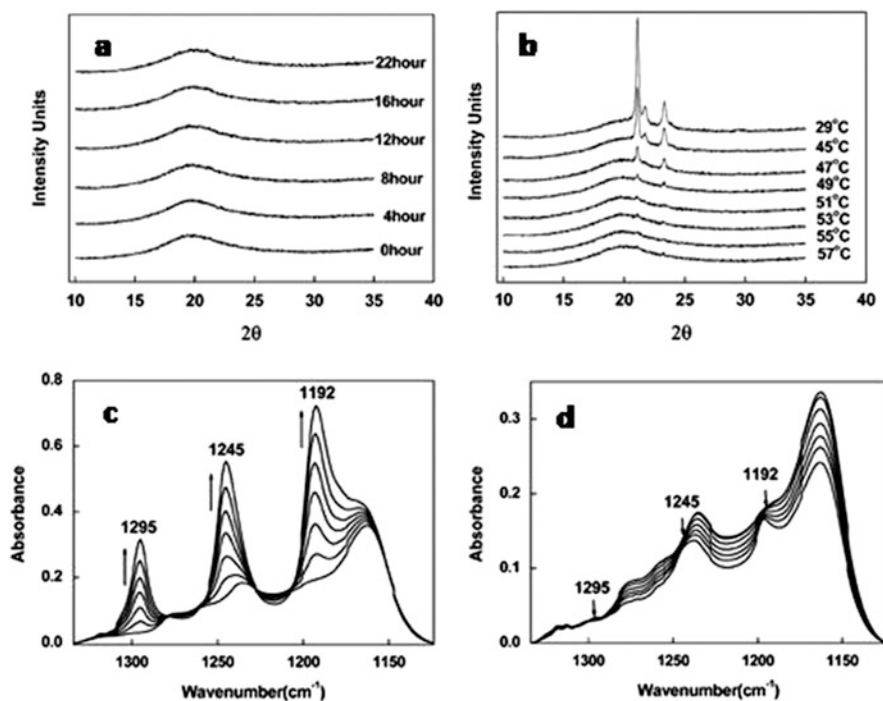


Fig. 10 (a, b) WAXD intensity profile of PCL melt on oriented PE substrate collected at 59°C (a) after different times and (b) during the subsequent cooling process. The sample was first heated to 85°C for 10 min to erase the possible thermal history, and then cooled direct to 59°C 22 h and finally cooled to room temperature. In the cooling process, the sample was stabilized at each temperature for 10 min. (c, d) Time-dependent polarized FTIR spectra of PCL melts kept on an oriented PE substrate at 59°C with polarized beam aligned (c) parallel or (d) perpendicular to the PE chain direction. Reproduced with permission from Yan et al. [110] and Chang et al. [111], copyright © 2006 and 2010, American Chemical Society

epitaxial crystallization of PCL on PE substrate. It is further suggested that the orientation of PCL molecular chains in the melt starts from a monolayer directly in contact with the PE substrate. The ordered thin layer becomes thicker while the ordered chain sequence length becomes longer with time. In sufficient time, all of the PCL chains within a layer of 5 μm in thickness can be organized into the ordered structure well above the melting point [111]. The pre-aligned polymer chains in the melt lower the nucleation barrier. Thus, when lowering the temperature below the melting point, these pre-aligned chains can easily form nuclei and crystals grow at a relatively higher temperature, leading to the epitaxial crystallization of PCL on the PE substrate with extremely broad lamellae. It should be pointed out that, even though the influence of partial melting of the fiber in the fiber/matrix single-polymer composites on epitaxial crystal growth has been studied through dynamic Monte Carlo simulations [112], an understanding of heteroepitaxy on the basis of interactions at the molecular or even atomic scales has still not been achieved, especially for polymer systems.

3 Methods for Structural Characterization of Epitaxial Systems

When Barker began an organized study on possible epitaxial combinations [113], the only available observational technique was optical microscopy, which provides information about the crystallographic accumulation on relative growth patterns. With the development of X-ray diffraction, analysis of the crystal structure become possible, and a molecular description of epitaxy has been realized through comparing the periodic arrangement of the atoms of the involved crystals. Many techniques have now been successfully used to characterize the epitaxial structure of polymer systems. Some frequently used techniques and their advantages are briefly introduced next.

3.1 Molecular Vibration Spectroscopy

Molecular vibration spectroscopy is very sensitive to both chain conformation and the local molecular environment of a polymer [114]. The method has proved to be a powerful tool for time-resolving the molecular structure and the conformational ordering of semicrystalline polymers [115–126]. As already mentioned in Sect. 2.3.2, FTIR has been successfully used to study the chain ordering of PCL in the melt on a PE substrate, which cannot be done by microscopic techniques. Also, the molecular chain orientation in the amorphous state can only be analyzed by FTIR in polarized mode [127]. Moreover, FTIR is helpful for the studying crystals exhibiting two very close crystallographic unit cell periods. As an example,

regioregular poly(3-hexylthiophene) (P3HT) has an orthorhombic unit cell with parameters $a = 1.663$, $b = 0.775$, and $c = 0.777$ nm [128]. In the ac -plane, the almost identical location of the (002) or (020) diffractions makes it difficult to determine the molecular chain orientation. In this case, polarized FTIR can help ascertain the crystal orientation [129]. Apart from FTIR, polarized Raman, UV–visible, and photoluminescence spectroscopies can also be used for studying the oriented structure of epitaxially grown polymers [130].

3.2 X-Ray Diffraction

It was the discovery of X-ray diffraction that made the analysis of epitaxial structure on a molecular scale possible. For epitaxy between polymers, the early works on characterization of mutual orientation of cold-drawn and spun polymer blends after suitable thermal treatment were carried out using X-ray diffraction, because the samples were usually too thick to characterize by other techniques [97, 131]. In addition, considering that only fiber orientation could be achieved in this kind of sample, it was necessary to make three-dimensional observations for a precise analysis of the system [132].

3.3 Microscopy

Initially, optical microscopy was used to study epitaxy by the accumulation of crystallonomic information on relative growth patterns. It is now often employed for a preliminary check on the existence of preferred orientation, especially for uniaxially oriented systems. This is simply conducted by rotating the sample about the light beam axis. As shown in Fig. 11e, f, preferred orientation of the crystals normally produces a light extinction phenomenon. Even though optical microscopy cannot provide the exact mutual crystallographic orientation of epitaxial pairs, it has important advantage of being able to follow the epitaxial crystallization process when equipped with a hot stage, which can supply information about when (during isothermal crystallization, see Fig. 11a–d) and at what temperature (during the cooling process) the epitaxy starts [109]. Moreover, it can provide a large area (e.g., square millimeters) of morphological information about the epitaxial system, such as the uniformity and surface smoothness.

Atomic force microscopy (AFM) is a very powerful method for illustrating the surface fine structure of polymers. Combination with a hot stage leads to the AFM being a wonderful technique for following the crystallization process of polymers at the lamellar scale, enabling measurement of growth velocity of individual lamella [133–137]. AFM has therefore frequently been used in studies of epitaxial crystallization to obtain structural information about the overgrowth polymer at the lamellar scale [138, 139]. The use of AFM has made it possible to disclose the

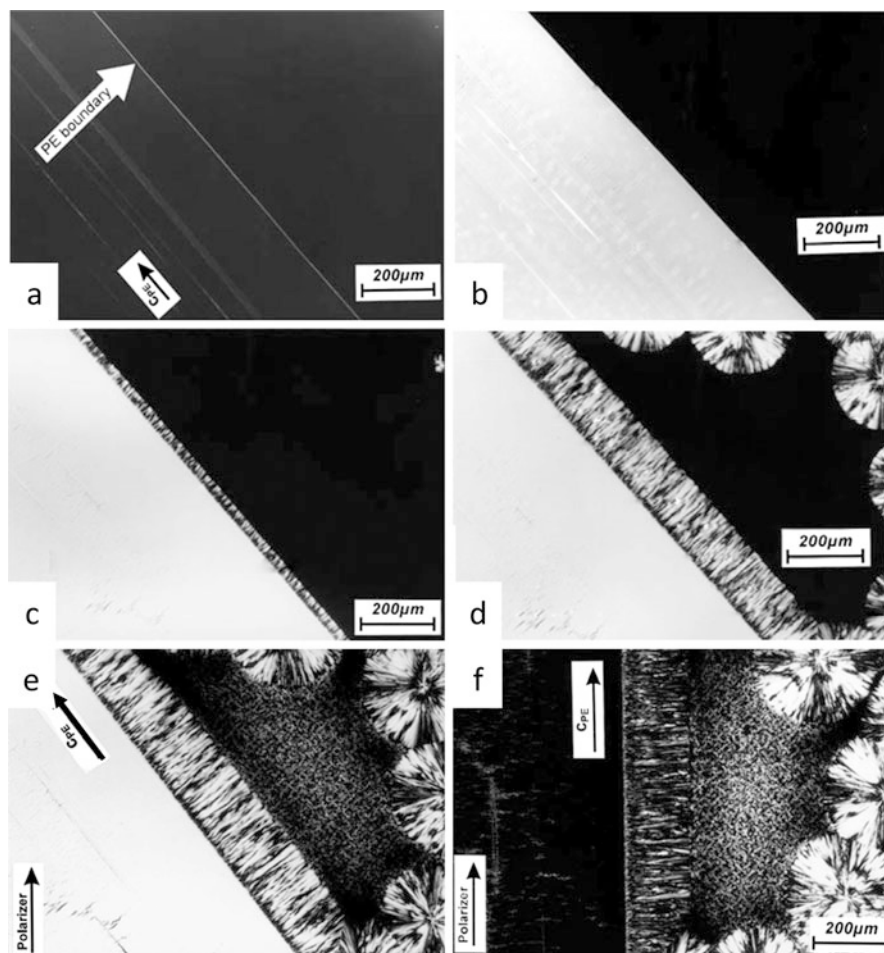


Fig. 11 Series of optical micrographs taken under cross-polarizers, showing the PCL crystallized at a boundary area of an oriented PE substrate. The PE substrate is located in the *lower left corner* of the picture. Its molecular chain direction is parallel to the boundary line, as indicated by arrows labeled C_{PE} . The sample was (a) heat-treated at 80°C for 10 min and subsequently cooled to 55°C for (b) 0, (c) 6, and (d) 50 h of isothermal crystallization. (e) Sample quenched to room temperature after 3 days of isothermal crystallization at 55°C . (f) Micrograph taken with the same sample and in the same area as for (e) but having different chain orientation of PE substrate with respect to the polarization direction. The polarization direction of the light is vertical. Reproduced with permission from Liu et al. [109], copyright © 2003, Springer

fine structure of the overgrowth polymer in the contact plane (i.e., the interacting plane of the polymer with the substrate) when detached from the substrate. As one example, Tracz et al. [140–142] studied the surface of PE crystallized in contact with atomically flat substrates, such as pyrolytic graphite, MoS_2 , and talc, and discovered very unusual morphology in the contact layer with respect to the bulk or

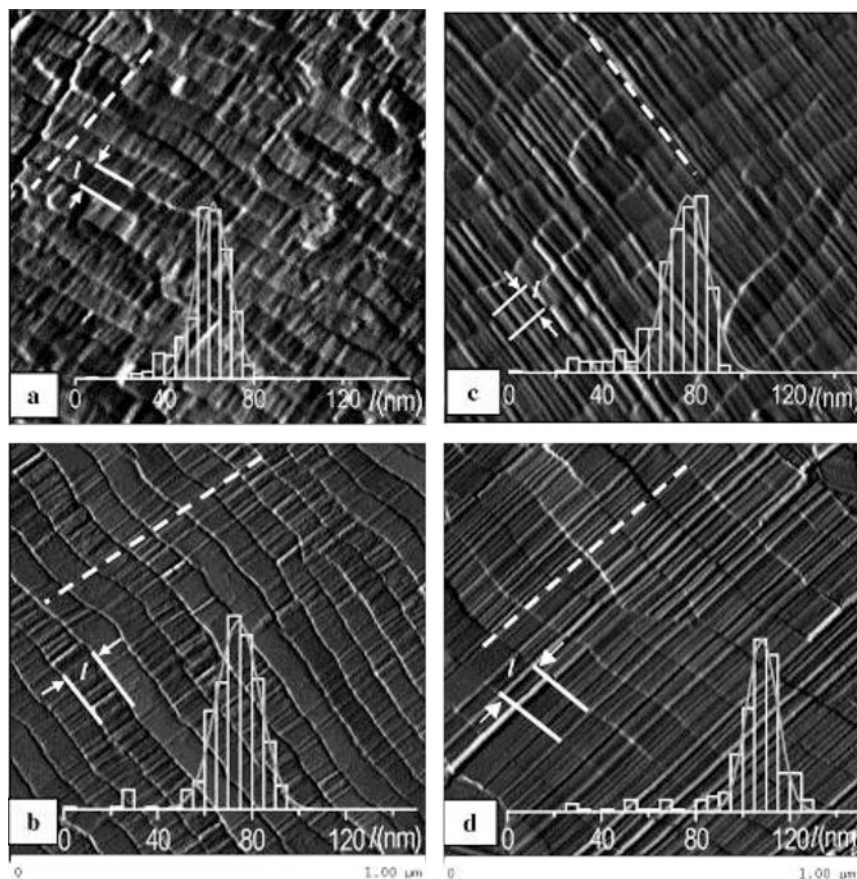


Fig. 12 AFM tapping mode, amplitude images of the contact layer of PE crystallized on (a, b) talc or (c, d) MoS₂. The cooling rate was 10°C/min for (a, c) and 0.2°C/min for (b, d). The lamellar thickness l is indicated by two *parallel solid lines*. The *dashed lines* show the chain direction labeled by blocks (striations). The *histograms* show the distributions of the lamellar thickness. Reproduced with permission from Tracz et al. [141], copyright © 2003, American Chemical Society

the free top surface. As presented in Fig. 12, the lamellae of PE in the contact layer are several times thicker than normal lamellae. This suggests the formation of extended-chain structures in the contact plane rather than folded-chain lamellae. It should be mentioned here that a high-resolution AFM image with fine structure in the contact plane at the molecular level is particularly important in understanding the origin of epitaxy. For this aspect, Lotz et al. have reported an excellent illustration [143]. They studied the epitaxial crystallization of syndiotactic polypropylene (sPP) on a series of linear oligophenyl substrates. As shown in Fig. 13, with the help of AFM they provided the first direct observation of arrays of both right-handed and left-handed individual sPP helices embedded in their

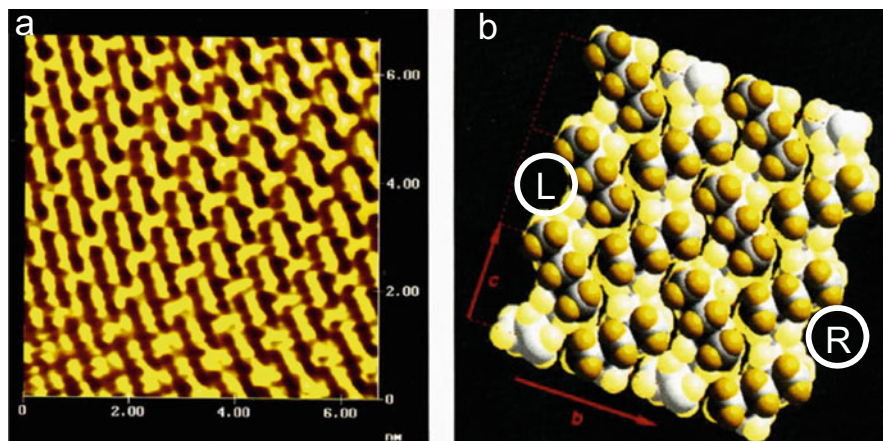


Fig. 13 (a) Fourier-filtered high-resolution AFM image of sPP epitaxially crystallized on the (001) face of a *p*-terphenyl crystal in the contact plane, recorded in the liquid cell (force imaging, constant height mode, scan rate 57 Hz or 8 s). (b) Representation of the AFM image using molecular modeling and shown in correct mutual orientation of the left- and right-handed sPP helices along the crystallographic *a*-axis in $(t_2g_2)_2$ conformation, as indicated by *L* and *R*. Reproduced with permission from Stocker et al. [143], copyright © 1994, American Chemical Society

crystallographic environments, especially the succession of CH_3 , CH_2 , and CH_3 groups tilted at 45° to the helical axes in the contact *bc*-plane. It is such results that enable the structure matching between epitaxial pairs to be more clearly and precisely determined.

Another important technique for fully understanding the mutual orientation relationship between epitaxial pairs is transmission electron microscopy (TEM), which can be operated in different but highly complementary modes (i.e., conventional bright field, electron diffraction, and dark field) [144–154]. The combined information in real and reciprocal spaces enables a precise understanding of structural issues at multiple length scales (e.g., polymorphism, mutual orientation, and contact planes) of polymer crystals and the dimensions of crystalline and amorphous domains. It is especially helpful in obtaining correct correlation of the molecular orientation to the observed morphology, which can sometimes help in understanding the chain packing habit of the overgrowth polymer. For example, Fig. 14a shows an AFM image of the lamellar structure of epitaxially crystallized poly(ethylene adipate) (PEA). The appearance of the cross-hatched lamellar structure, with PEA lamellae at ca. $\pm 66.5^\circ$ from the chain direction of the PE substrate crystals, could easily lead to the erroneous conclusion that the chain axes of PEA incline with an angle of $\pm 23.5^\circ$ to the chain direction of PE. The corresponding electron diffraction pattern (Fig. 14b) tells us that there is a parallel chain alignment of both polymer chains. This is caused by the folding of parallel oriented PEA chains in the $\{00l\}$ plane, as schematically presented in Fig. 14c [147].

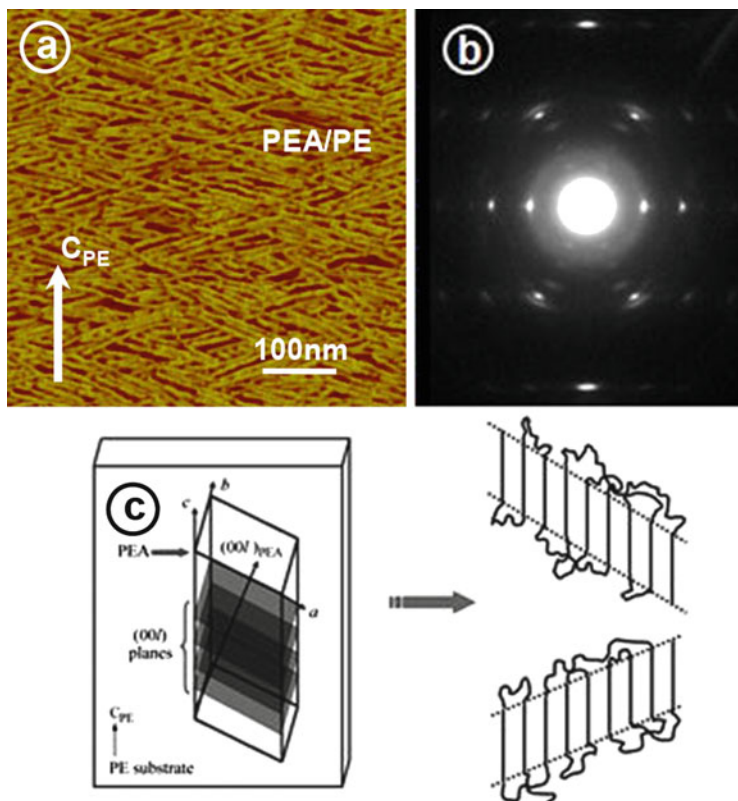


Fig. 14 (a) AFM phase image showing the fine structural features of PEA crystallized from solution on highly oriented PE substrate. The molecular chain direction of PE is indicated by an *arrow*. (b) The corresponding electron diffraction pattern of a PEA/PE double layer. (c) Crystal orientation of PEA with respect to the PE substrate (*left*) and the chain folding in lamellar crystals (*right*). Reproduced with permission from Yan et al. [147], copyright © 2013, Springer

4 Influence of Epitaxy on Polymer Crystallization and Its Impact on Material Properties

4.1 Influence of Epitaxy on the Crystallization Kinetics of Polymers

It is well known that the specific interaction between substrate and polymer can strongly affect the physical properties of polymers, including the glass transition temperature [155–162] and molecular mobility [163–166], which in turn influence the crystallization kinetics of the polymers [167–169]. Frank and coworkers have carried out systematic research on these issues [168–174]. The influence of foreign surfaces on crystallization kinetics is multifarious, depending on the polymer used,

film thickness, and interaction between substrate and polymer melt. Generally, a substantial decrease in the lateral diffusion coefficient of polymer films thinner than 150 nm unambiguously reduces the crystal growth rate and therefore slows down the overall crystallization rate [167, 169, 172, 175]. For some polymers in extreme cases, it is impossible to cultivate crystallinity in thin or ultrathin films. As an example, the crystallization of poly(di-*n*-hexylsilane) is prohibited in ultrathin films less than 15 nm in thickness [170]. Another example is the inhibition of crystallization in ultrathin films of poly(3-hydroxybutyrate) (PHB) [176], which provides a way to produce in vivo-like amorphous PHB [177]. For epitaxial systems, the overall crystallization rate increases remarkably as a result of the enhanced nucleation ability, especially in cases where homogeneous nucleation is difficult. For example, isotactic poly(methylmethacrylate) (PMMA) is a polymer with an extremely slow crystallization rate [178–180]. The temperature for its maximum crystallization rate has been reported to be 120°C, at which the bulk crystallization takes tens of days [181]. The crystallization of PMMA from the glassy state on oriented PE surfaces is, however, much faster, taking only tens of hours for complete crystallization [127].

4.2 Structure Regulation and Its Impact on Material Properties

The previous section briefly described the influence of epitaxy on the crystallization kinetics of polymeric materials, which can provide useful information for processing. The most important feature of surface-induced polymer epitaxy is the ability to regulate the structure of the overgrowth polymer, because it is the key factor in tailoring the macroscopic properties and even functionality of polymeric materials. Therefore, this section focuses on what structures of semicrystalline polymers can be controlled through epitaxial crystallization and its impact on property modification.

The existence of any kind of interface can affect the crystal structure or/and the crystal orientation of semicrystalline polymers. The influence depends remarkably on the film thickness, crystallization temperature, and interfacial interaction. Numerous excellent works on thin and ultrathin film crystallization of polymers have been conducted in the past few decades [182–189]. Generally, thin polymer films of nanometer thickness crystallized at relatively low supercooling encourage the formation of a specific orientation of typical single crystals such as thin lamellar crystals; in such thin films, the molecular chains lie normal to the substrate (i.e., the lamellae lie “flat-on” against the substrate) [190–206]. Figure 15 presents AFM height and amplitude images showing regular flat-on single crystals of sPP [106]. The electron diffraction pattern demonstrates an upright chain orientation. By contrast, when crystallizing a polymer thin film at higher supercooling, spherulites made up of radically arranged edge-on lamellae (chain axes oriented parallel to

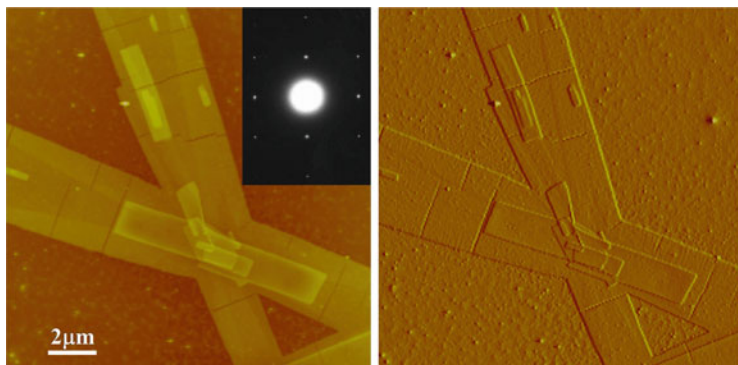


Fig. 15 AFM height (*left*) and amplitude (*right*) images of sPP crystallized on a mica surface at 125°C. The *inset* presents the electron diffraction pattern of the single crystal, which indicates an upright chain orientation. The single layer of crystal is about 15 nm in thickness. Reproduced with permission from Li and Yan [106], copyright © 2011, American Chemical Society

the substrate) are observed [207–211]. This is seen in Fig. 16, which shows the spherulitic structure of isotactic polystyrene composed of edge-on lamellae grown at 160°C [211]. The different crystal orientations are also related to interfacial interactions. Recent dynamic Monte Carlo simulations indicate that, at high crystallization temperatures, thin polymer films on a slippery wall predominantly exhibit edge-on lamellar crystals, whereas they show mainly flat-on lamellar crystals on a sticky wall [182].

For systems with epitaxial ability, control of the structure and morphology of overgrowth polymers is different and more prominent. As already demonstrated in Sect. 2.2, the prerequisite for the occurrence of polymer epitaxy on organic substrates (i.e., geometric matching) successfully regulates the molecular chain orientation and special arrangement of the PE. Even though the matching between polymer epitaxial pairs is less pronounced as compared with systems of polymer on low molecular weight organic substrates (one-dimensional versus two-dimensional lattice matching), it also shows obvious structure control capability in several aspects.

4.2.1 Control of Chain Orientation

The fixed mutual orientation of the overgrowth material with respect to the substrate provides an efficient way to control the chain orientation of the overgrowth polymer. It was found that the occurrence of polymer epitaxy always leads to an alignment of the polymer chains in the film plane, regardless of the film thickness and crystallization temperature. Also, chain orientation in the film can be precisely governed on the basis of the favorable interaction between polymers. The molecular chains of overgrowth polymer can be arranged either at fixed angles to the substrate molecular chains (as depicted in Fig. 8 for PE/iPP epitaxy) or parallel to the

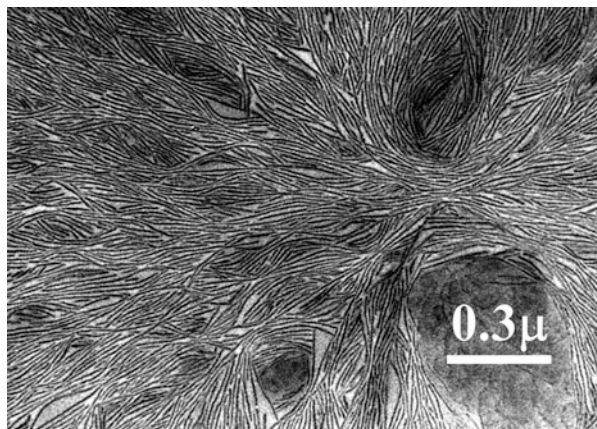


Fig. 16 Transmission electron micrograph showing the edge-on lamellar structure of isotactic polystyrene crystallized on a carbon surface at 160°C. The film thickness is about 50 nm. Reproduced with permission from Li and Yan [106], copyright © 2011, Springer

substrate molecular chain [56, 95, 97, 104, 108, 109, 151–154, 212–225] (as shown in Fig. 17 for epitaxy of PE on friction transfer highly oriented poly(tetrafluoroethylene) (PTFE) substrate). Tables 1 and 2 summarize the known parallel and non-parallel epitaxial polymer pairs reported in the literature to date. From Tables 1 and 2, we can see that different chain orientations of a single polymer can be achieved by epitaxial crystallization on different substrates, while the same substrate can induce diverse chain orientations of different polymers. Moreover, taking the interactivity of the substrate and the deposited polymer of the epitaxial polymer pairs into account, the substrate and deposited polymer of the different epitaxial systems listed in Tables 1 and 2 can be mutually exchanged. The epitaxial crystallization of iPP on PE substrate is a representative example. As presented in Fig. 18, when crystallizing iPP from the melt on a uniaxially oriented PE substrate, the same mutual orientation, but with iPP chains at $\pm 50^\circ$ from the chain direction of the PE substrate, is observed (compare Fig. 18 with Fig. 8) [226].

The strictly defined unique molecular chain orientations can be adopted within the field of macromolecular engineering for efficient modification of material properties. For example, in the cross-hatched lamellar structure, the mechanical soft amorphous interlamellar regions of one phase are bridged by the crystalline lamellae of the other phase (as schematically depicted in Fig. 19), which leads to a significant improvement in mechanical properties [227, 228]. It was further demonstrated that by dipping the iPP sheets in a PE solution before thermal bonding, the adhesion between laminas increases enormously [229, 230]. This can clearly be utilized in polymer blends and composites when stretched and thermally treated under appropriate conditions. On the other hand, parallel chain alignment can find applications in the fabrication of functional polymeric materials. For example, OFETs based on soluble conjugated polymers have attracted considerable attention.

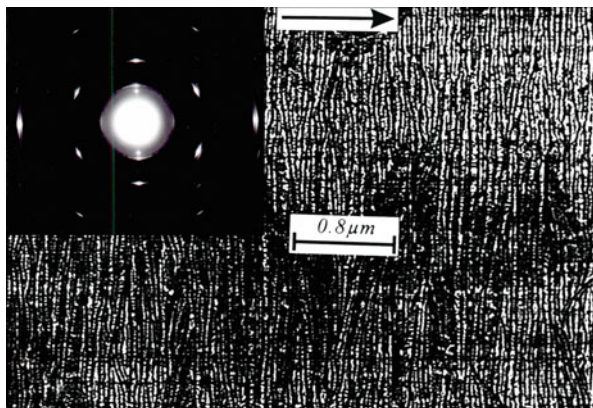


Fig. 17 Bright field electron micrograph and the corresponding electron diffraction pattern (*inset*) of PE epitaxially crystallized on a friction transfer highly oriented PTFE substrate. The sample was heat treated at 150°C for 10 min and subsequently cooled to room temperature. The *arrow* shows the chain direction of the corresponding PTFE substrate crystals. Reproduced with permission from Li and Yan [106], copyright © 2011, American Chemical Society

Table 1 Epitaxial crystallization polymer systems with parallel chain alignment

Deposited polymers	Substrate polymers	References
Wax, paraffin	PE	[82, 107]
	Poly(ethylene sebacate)	
	Polyoxymethylene	
PE	PTFE	[106–108]
	Polyoxymethylene	
PCL	PE	[106, 108, 109]
	PTFE	
	Polyoxymethylene	
PBA	PE	[110, 111]
PEA	PE	[98]

Table 2 Epitaxial crystallization polymer systems with non-parallel chain alignment

Deposited polymers	Substrate polymers	Chain cross-angle (°)	References
PE	iPP	50	[112]
iPP	Nylon-6, 6.6, 11, 12. ...	50	[112]
Polybutadiene	iPP	50	[109]
Poly(ϵ -caprolactone)	iPP	50	[113]
Polyoctenamer	iPP	50	[114]
PE	sPP	37	[115]
sPP	PE	37	[116]
sPP	Nylon-12	37	[117]
iPP	PTFE	57	[118]
Poly(L-lactide)	PE	90	[119]
PBA	iPP	50	[120]

Fig. 18 Electron micrograph and corresponding diffraction pattern (*inset*) of iPP epitaxially crystallized from the melt on uniaxially oriented PE substrate. The *arrow* represents the molecular chain direction of PE substrate film. Reproduced with permission from Li and Yan [106], copyright © 2011, American Chemical Society

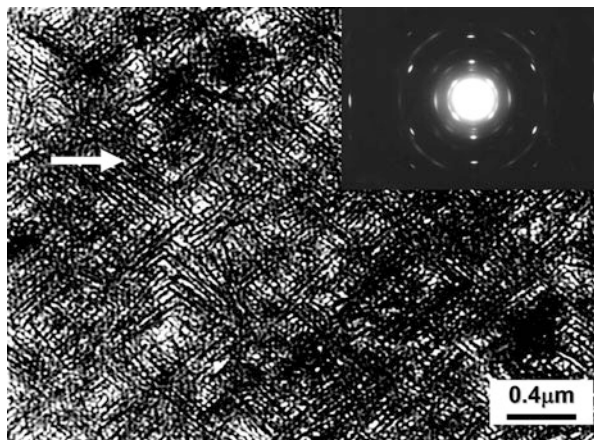
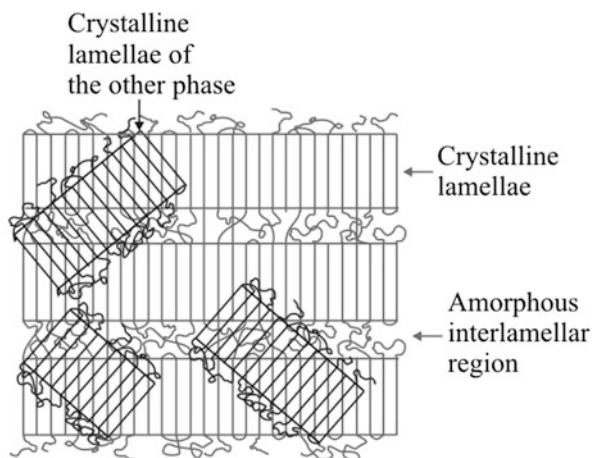


Fig. 19 Epitaxially oriented cross-hatched PE lamellar crystals on uniaxially oriented iPP substrate, in which the mechanically soft amorphous interlamellar regions of one phase are bridged by the crystalline lamellae of the other phase. Reproduced with permission from Li and Yan [106], copyright © 2011, American Chemical Society



Enormous effort has been devoted to improving the key performance parameters of OFETs, such as carrier mobility, on/off ratio, and threshold voltage. It was found that the performance of single crystal nanowires of semiconducting polymers is always excellent compared with thin films of random structure [231, 232]. Taking this into account, epitaxial crystallization provides a simple and very efficient way of fabricating thin films of semiconducting materials with unique crystal orientation to improve their performance [233–238]. Such films demonstrate significant improvement in properties, as illustrated in Fig. 20 [239].

4.2.2 Control of Crystal Modification

Many polymers display pronounced polymorphisms depending on their structure features, thermal treatments, and mechanical handling [240–248]. Polymers with

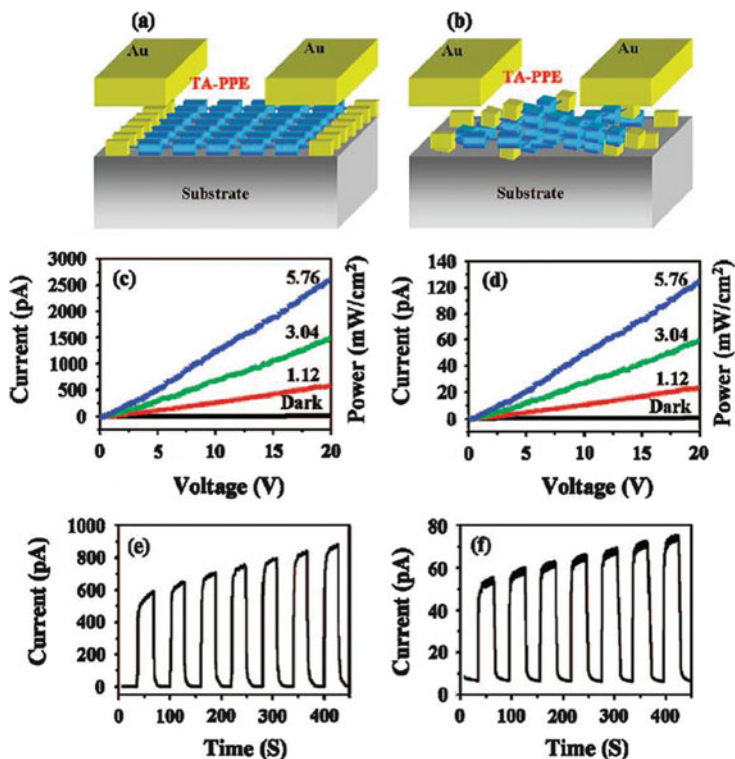


Fig. 20 Photoswitchers of poly(*para*-phenylene ethynylene)s with thioacetyl end groups (TA-PPE) film. (a) with and (b) without orientation. (c) Photoresponse and (e) photoswitch behavior of TA-PPE film with alignment. (d) Photoresponse and (f) photoswitch behavior of TA-PPE film without alignment. Reproduced with permission from Dong et al. [239], copyright © 2008, American Chemical Society

different crystal structures exhibit unambiguously distinct properties or even diverse functionality. Therefore, control of the crystal structure of polymeric materials is sometimes more important than control of chain orientation. It is quite familiar that a special nucleating agent is frequently used to control crystal modification (e.g., β -crystallization of iPP) [22–24]. In addition, special crystallization procedures, such as use of a thermal gradient [249], are frequently encountered during processing [250–254], and are sometimes also helpful in controlling the crystal modification of polymorphic polymers. For example, β -iPP crystals can be produced by melt crystallization under a temperature gradient through a kinetically favored α -to- β growth transition [217, 249, 255, 256]. Epitaxial crystallization provides another reliable way to control the crystal modification of semicrystalline polymers [46, 56, 62, 257–259]. As an example, Fig. 21 presents the controlled crystallization of poly(butylenes adipate) (PBA), an aliphatic biodegradable

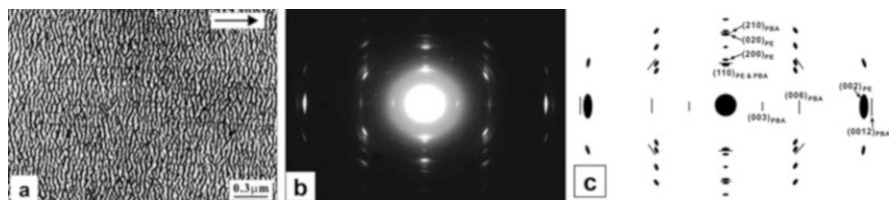


Fig. 21 (a) Bright field transmission electron micrograph, (b) the corresponding electron diffraction pattern, and (c) sketch illustrating the mutual chain orientation of PBA crystallized from the melt onto highly oriented PE substrate. Reproduced with permission from Sun et al. [217], copyright © 2005, American Chemical Society

polyester exhibiting two different modifications designated α and β [260–262]. It was reported that the polymorphisms of PBA are related to the crystallization temperature [263–266]. At temperatures above 32°C, PBA chains pack in the α -form, whereas its β -form crystals are formed at temperatures below 27°C. In the intermediate temperature window (27–32°C), coexistence of both α - and β -phases is seen. The crystal structure-dependent degradation rate of PBA (i.e., faster degradation of α -PBA than β -PBA) [267] illustrates the importance of the crystal structure. From Fig. 21a it can be seen that PBA film grown on PE substrate consists of highly oriented edge-on lamellae aligned perpendicularly to the chain direction of the PE substrate [217]. The corresponding electron diffraction pattern of the PBA/PE double layers, with sharp and well-defined reflection spots of both PBA and PE (see Fig. 21b), confirms that both PBA and PE layers are highly oriented. The appearance of (00l) PBA reflection spots in the direction of the (002) PE diffraction spots proves parallel chain alignment of PBA and PE. It has been further identified that all of the PBA reflection spots in Fig. 21b are accounted for by its orthorhombic unit cell in β -form.

It needs be emphasized here that the crystal structure of PBA crystallized on PE substrate is not temperature dependent. In other words, the epitaxial crystallization of PBA on PE substrate results in the formation of its β -form at any temperature. This is associated with a better matching between β -PBA and PE. Similar β -PBA crystallization behavior was also found on iPP substrate [268]. The chain orientation of PBA in the PBA/iPP system is, however, different from that in the PBA/PE system. Instead of a parallel chain alignment on the PE substrate, a cross-hatched lamellar structure of PBA with the molecular chains $\pm 50^\circ$ from the chain direction of iPP crystal is obtained, reflecting a similar matching situation as for PE/iPP epitaxy. From the above experimental evidence, it is clear that epitaxy can control not only the crystal structure, but also the chain orientation of polymers. This reveals the advantage of epitaxy over use of a nucleation agent in controlling the specific crystalline modification.

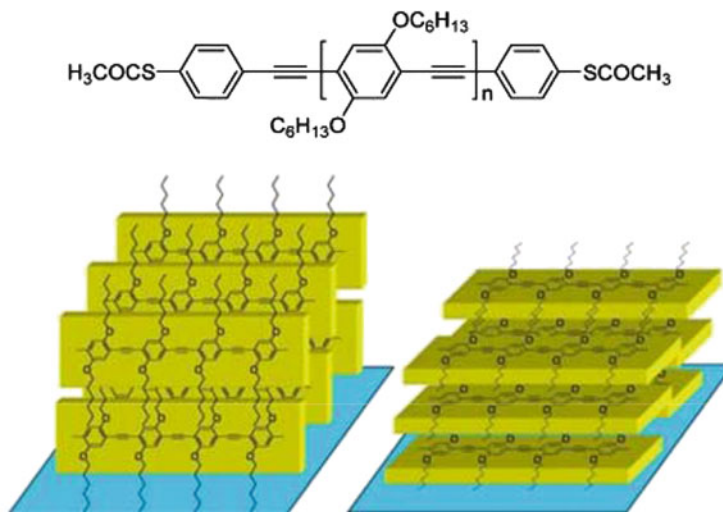


Fig. 22 Molecular structure of TA-PPE (*top*) and its two extreme spatial arrangements, side-on (*bottom left*) and face-on (*bottom right*). Reproduced with permission from Zhou and Yan [269], copyright © 2013, American Chemical Society

4.2.3 Control of the Spatial Arrangement of the Backbone Chain Plane

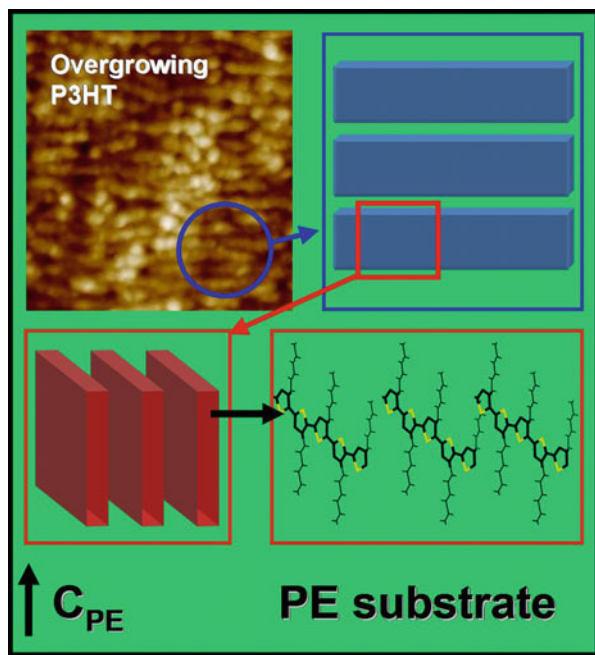
Another aspect of particular interest for obtaining high performance polymer thin films is the spatial arrangement of planar backbone chains. This has been well illustrated by the highly crystalline rigid rod conjugated TA-PPE, which possesses a planar backbone chain (see Fig. 22). For this kind of molecule, both the chain axis orientation and chain spatial arrangement of the π -conjugated skeleton are important factors that influence the performance of resulting materials [269]. Figure 22 presents the two extreme arrangements of planar TA-PPE molecules. In one case, the π -conjugated skeleton planes are perpendicular to the film plane (Fig. 22, bottom left), referred to as “side-on” to distinguish them from the edge-on oriented crystalline lamellae. In the other case, the π -conjugated skeleton planes lie parallel to the film plane (Fig. 22, bottom right), expressed as “face-on” to distinguish them from flat-on oriented crystalline lamellae. Property measurements reveal a prominent influence of chain orientation and spatial arrangement on the performance of devices incorporating these polymers [270, 271]. It was found that the switch on/off ratio of photoswitchers with TA-PPE molecules aligned along the carrier transport direction of the device can reach as high as 330–400, whereas for devices with randomly oriented molecules the ratio is only 8–12 [239]. Moreover, the charge carrier mobility of OFETs based on TA-PPE nanowires with side-on molecular chains aligned along the nanowire is confirmed to be three to four orders of magnitude higher than those based on randomly orientated thin films [232].

Section 4.2.2 described control of the crystal structure and chain orientation of deposited polymers through benign matching during epitaxy. Considering that the

favorable crystallographic interaction is generally related to a certain lattice plane of the deposited polymer, it should also be possible to achieve favorable matching through changing the contact plane of the polymers. In this case, the selected contact plane becomes the key factor for determining the spatial arrangement of planar backbone chains. A good illustrative example is the epitaxial crystallization of PE on iPP and sPP substrates. As mentioned in Sect. 2.3.2, when crystallizing PE on a highly oriented iPP substrate, the lattice plane of PE crystal in contact with the iPP substrate is its (100) lattice plane, as confirmed by the electron diffraction shown in Fig. 8b through the absence of (200) diffractions [151, 152, 215]. However, the favorable interaction between PE and sPP is realized in the (110) lattice plane of the PE crystal. As a result, when crystallizing PE on a highly oriented sPP substrate, the lattice plane of PE crystal in contact with the sPP substrate changes to its (110) lattice plane [154]. According to the crystal structure of PE, the setting angles of the two PE chains involved in one unit cell, defined as the angle between the *trans*-planar C–C chain skeleton and (0*k*0) lattice planes, are $\pm 42^\circ$ [272, 273]. This means that the alignment of PE molecular chains on iPP substrate leads to the *trans*-planar C–C chain skeleton of PE about $\pm 42^\circ$ from the normal of iPP film. In the case of PE/sPP epitaxy, it is either about 8.3° or about 81.7° from the normal of sPP film. Therefore, combining with the different mutual chain orientations described in Table 2, the arrangement of PE molecular chains including chain axis orientation and spatial *trans*-planar C–C chain skeleton alignment is well controlled.

This also works for conjugated rigid chain polymers. For example, P3HT can adopt different crystal structures and chain alignments depending on crystallization conditions. It has been well reported that different properties can be achieved with various molecular chain arrangements. This has stimulated many studies of the crystallization behavior of P3HT under different conditions. The results of previous studies indicate that uniaxially oriented P3HT thin films can be fabricated using the friction transfer technique or surface-induced epitaxy. Friction transferred P3HT thin films are generally composed of edge-on crystalline lamellae with molecular chains aligned in the film plane and along the sliding direction [274, 275]. Moreover, it has been confirmed that the molecular backbone planes in the friction transferred thin films are parallel to the film surface (i.e., a face-on molecular orientation as shown in Fig. 22, bottom right). On the other hand, the epitaxial crystallization of P3HT on different substrates also produces edge-on lamellae with molecular chains arranged in the film plane but oriented in a special manner depending on the substrate [233, 234, 236, 237]. The epitaxial crystallization of P3HT on highly oriented PE thin films results in the formation of a parallel aligned edge-on lamellar structure of P3HT (see Fig. 23, upper left), in which the P3HT molecular chain axis is aligned in the film plane and along the PE chain direction [130]. Meanwhile, it has been confirmed that the (100) lattice plane of P3HT is in contact with the PE substrate. This demonstrates that the epitaxy of P3HT on oriented PE thin film also provides a side-on molecular orientation, as sketched in Fig. 23, bottom left.

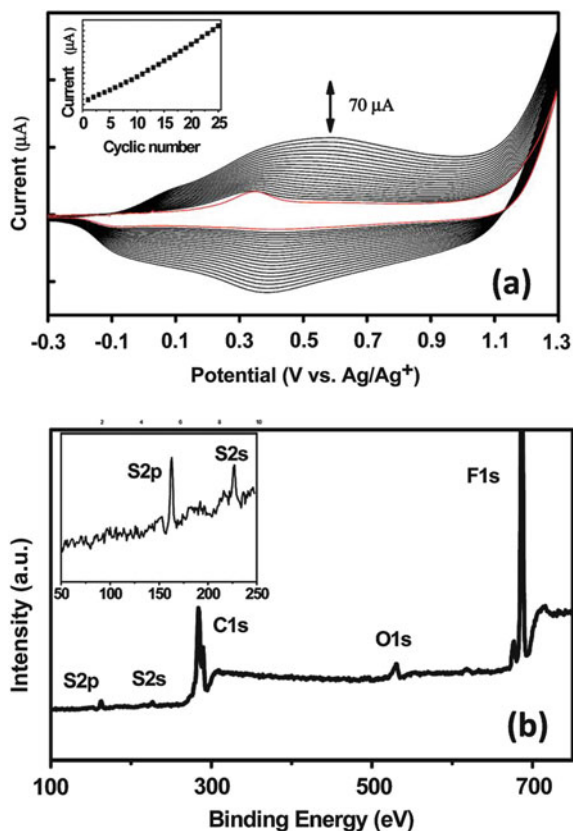
Fig. 23 *Top left:* AFM image of P3HT epitaxially crystallized on highly oriented PE substrate, showing the parallel aligned lamellar structure. *Top right and bottom:* Molecular alignment in the parallel oriented lamellae. Reproduced with permission from Zhou and Yan [269], copyright © 2013, American Chemical Society



5 Methods of Realizing Polymer Epitaxy

As mentioned above, the realization of epitaxial crystallization between polymers is somewhat difficult compared with the epitaxial crystallization of polymers on single crystals of small molecular weight compounds. A simple and effective way for obtaining a controlled microstructure and the desired macroscopic properties for the material is suitable post-thermal treatment of co-stretched polymer blends with epitaxial ability. It is, however, difficult to make a detailed study of the structure relationship, especially determination of the contact planes. Thin film epitaxy is generally conducted by superimposing the thin film on an appropriate oriented crystalline substrate, followed by melting and recrystallization of the overgrowth polymer. This can be easily realized for systems in which the substrate has a higher melting temperature than the overgrowth polymer. When the overgrowth polymer has a higher thermal stability (i.e., a higher melting temperature), its epitaxial crystallization on a substrate with lower melting point is mostly carried out by crystallization from the solution or glassy state [127]. In some cases, in situ epitaxial crystallization during synthesis provides another efficient pathway for obtaining a highly order structure of the final polymeric product, which is especially important for those polymers that are difficult to melt or dissolve in solvents. The epitaxial crystallization of poly(3-methylthiophene) (P3MT) on highly oriented PVDF substrate during electrochemical polymerization provides an example [276]. Figure 24 shows the cyclic voltammetry (CV) plot for the polymerization

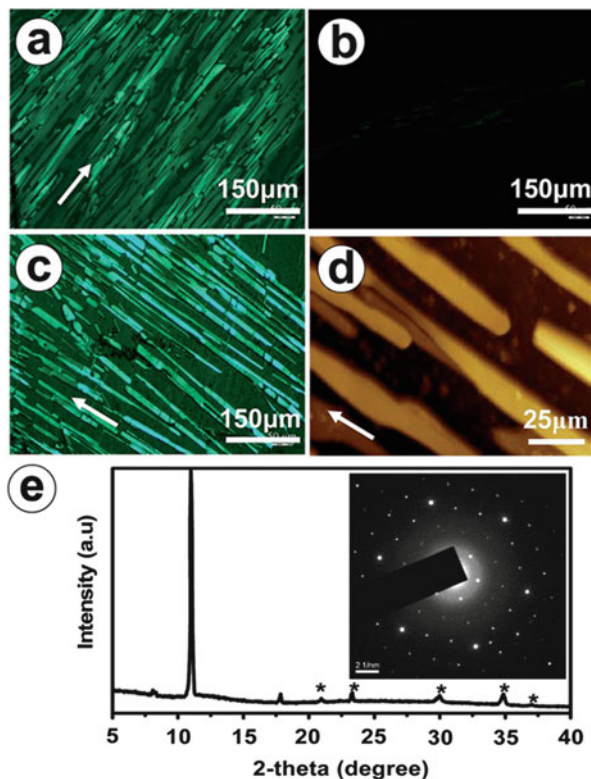
Fig. 24 (a) Cyclic voltammetry plot for the polymerization of 3-methylthiophene at a scan rate of 40 mV s^{-1} . The first scan is shown in red. (b) XPS spectrum of de-doped P3MT on PVDF film; the inset shows an expansion of the range from 50 to 250 eV. Reproduced with permission from Sun et al. [276], copyright © 2014, RSC



of 3-methylthiophene and the X-ray photoelectron spectrum (XPS) of the de-doped P3MT on PVDF film. From Fig. 24a, it can be seen that electron transfer can occur readily to the electrode to enable the P3MT film to grow on the PVDF substrate. Both the anodic and cathodic peak currents increase in successive cycles, indicating the coupling reaction of 3-methylthiophene units and growth of the polymer film on the electrode [13, 25, 44]. The inset of Fig. 24a shows the evolution of the oxidation peak current at ca. 0.6 V versus cycle number, illustrating a linear increase in the polymerization of 3-methylthiophene on the electrode. The XPS of de-doped P3MT on PVDF film (Fig. 24b) shows characteristic sulfur and fluorine peaks, with no detectable phosphorus or nitrogen, indicating the successful deposition and de-doping of P3MT.

Figure 25a–c shows optical micrographs of P3MT film electrochemically deposited onto oriented PVDF. Figure 25a shows a regular structure with lathlike P3MT crystals of microns in length with strong birefringence. Light extinction when the sample is rotated about the beam axis (see Fig. 25b) indicates high orientation of the P3MT crystals, that is, the occurrence of epitaxial crystallization of P3MT on the highly oriented PVDF during electropolymerization. AFM studies show that the

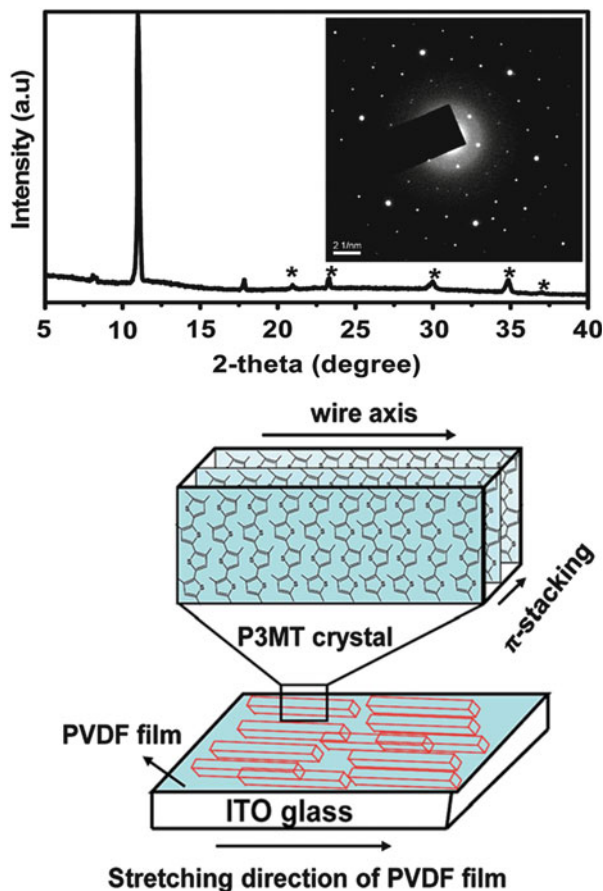
Fig. 25 (a–c) Polarized optical micrographs of P3MT films electrodeposited onto ITO glass covered with oriented PVDF film. The *arrows* indicate the PVDF molecular chain directions: (a) 45° , (b) 0° , and (c) -45° from the polarizer direction. The deposition conditions were (a, b) 40 mV s^{-1} , 50 cycles and (c) 10 mV s^{-1} , 10 cycles. (d) AFM image corresponding to (c). Reproduced with permission from Sun et al. [276], copyright © 2014, RSC



morphologies of P3MT are dependent on the conditions of electrochemical deposition. As shown in Fig. 25c, d, lathlike crystals with a width of 10–20 μm and thickness of 0.6 μm are obtained using a low scan rate and few scan cycles. With increasing numbers of cycles, a two-dimensional close-packed film composed of lathlike P3MT crystals can be obtained. X-ray and electron diffractions (Fig. 26, top), help to determine the exact molecular orientation of P3MT (as shown in Fig. 26, bottom). These P3MT films exhibit a remarkably high conductivity with anisotropic feature.

Another method that should be emphasized here is directional epitaxial crystallization, as used by Brinkmann and Lotz et al. [56, 61–63, 233]. In brief, the method achieves orientation of polymers by crystallization from solution in a crystallizable solvent, which first plays the role of solvent for the polymers and then the role of substrate for epitaxy of polymers after crystallization. As an example, Fig. 27 shows the AFM phase image of an oriented P3HT film grown by directional epitaxial crystallization in 1,3,5-trichlorobenzene (TCB) [234]. In this case, the TCB was used as a crystallizable solvent of P3HT. At temperatures above 63°C (melting point of TCB), the melting TCB acts as solvent for P3HT. By cooling to a temperature below 63°C , the first TCB crystals formed serve as substrate for epitaxial growth of P3HT, leading to formation of highly oriented P3HT thin

Fig. 26 *Top*: XRD profile and electron diffraction pattern (*inset*) of P3MT electrodeposited onto oriented PVDF film after detaching the PVDF layer. *Bottom*: Orientation of P3HT as deduced from the diffractions. Reproduced with permission from Sun et al. [276], copyright © 2014, RSC

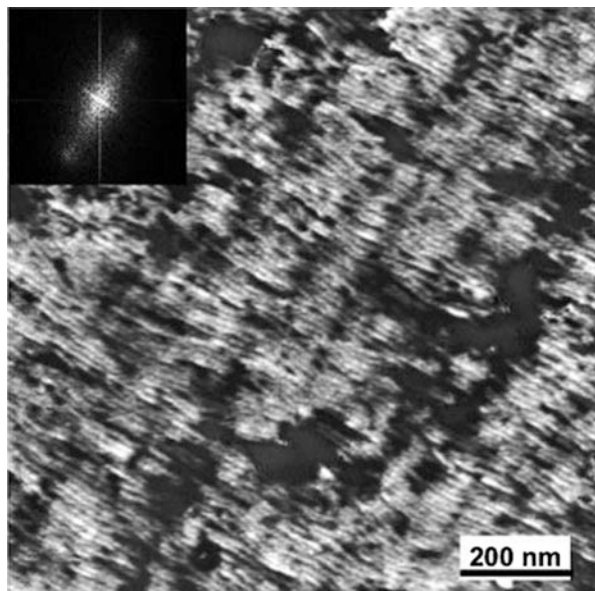


films (see Fig. 27). In this way, highly oriented P3HT films can be readily obtained by removing the crystalline TCB through sublimation under a primary vacuum. During the directional epitaxial crystallization of P3HT by TCB, long range in-plane orientation of P3HT can be achieved by using an oriented PTFE substrate to guide the oriented crystallization of TCB. This is of great importance for obtaining large areas of highly oriented thin films of functional materials [234].

6 Conclusions and Outlook

This review illustrates the effect of epitaxy on several aspects of the crystallization of polymers. First, epitaxial ability can accelerate the kinetics of polymer crystallization as a result of enhanced nucleation ability, especially for those crystallizations where homogeneous nucleation is difficult. The most important influence of

Fig. 27 AFM phase image of an oriented P3HT film grown by directional epitaxial crystallization in TCB. *Inset* shows the corresponding fast Fourier transform. Reproduced with permission from Brinkmann and Rannou [234], copyright © 2007, Wiley-VCH



epitaxy on polymer crystallization rests on its ability to generate highly crystalline thin polymer films with strictly defined orientation, which includes molecular chain orientation, the crystal structure of polymers with polymorphisms, and the spatial arrangement of the planar backbone molecular chains. It should be pointed out that control of these structures can be realized simultaneously by the proper choice of substrate for epitaxy. This synergistic multistructure regulation illustrates the supreme advantage of epitaxy over the nucleation agent-induced crystallization of polymers. Even though epitaxial crystallization provides a simple and efficient method for fabricating polymeric materials with special crystalline structures, and thus with improved properties or even new functionalities, its use to design and fabricate polymeric materials with properties matching specific product requirements has not yet been well developed. Therefore, further research in this field is needed to explore how to utilize the induced unusual crystallization behavior of polymers for preparing advanced polymeric materials.

Challenges in this field include the technical development of morphological manipulation of multiphase and multicomponent polymer systems, such as copolymers and polymer blends. For example, polymeric solar cells have emerged as attractive candidates for renewable energy devices. However, the efficiency of the best available polymer solar cells still lags behind that of conventional silicon devices. Based on the close relationship between the microstructure of such polymeric devices and their final properties, the optimal design and implementation of the structures of donor and acceptor materials in the devices, including phase structure and molecular chain orientation, offers an effective approach for fabrication of high efficiency photovoltaic devices. This could be regulated by one-component epitaxial crystallization with controlled interlamellar phase

separation of a blend or even by epitaxial crystallization of both polymer components. This kind of structural control of block copolymers has already been reported by the group of De Rosa, Lotz, and Thomas [277, 278].

Acknowledgment A portion of this material is based on research supported by the National Natural Science Foundation of China under grant numbers 50833006, and 50973008.

References

1. Brown RA, Pomp A, Hart CM, de Leeuw DM (1995) *Science* 270:972
2. Huitema HEA, Gelinck GH, van der Putten JBPH, Kuijk KE, Hart CM, Cantatore E, Herwig PT, van Breemen AJJM, de Leeuw DM (2001) *Nature* 414:599
3. Jang Y, Kim DH, Park YD, Cho JH, Hwang M, Cho K (2005) *Appl Phys Lett* 87:152105
4. Crone BK, Dodabalapur A, Sarpeshkar R, Gelperin A, Katz HE, Bao Z (2001) *J Appl Phys* 91:10140
5. Crone BK, Dodabalapur A, Lin YY, Filas RW, Bao Z, LaDuca A, Sarpeshkar R, Katz HE, Li W (2000) *Nature* 403:521
6. Ciferri A, Ward IM (1979) *Ultra-high modulus polymers*. Applied Science, London
7. Smith P, Lemstra PJ (1980) *Mater Sci* 15:505
8. Oh SY, Akagi K, Shirakawa H (1989) *Synth Met* 32:245
9. Gagnon DR, Karasz FE, Thomas EL, Lenz RW (1987) *Synth Met* 20:245
10. Andreatta A, Tokito S, Smith P, Heeger AJ (1990) *Mol Cryst Liq Cryst* 189:169
11. Wada Y (1982) *Electronic properties of polymers*. Wiley, New York
12. Meille SV, Ferro DR, Brückner S, Lovinger AJ, Padden FJ (1994) *Macromolecules* 27:2615
13. Karger-Kocsis J (1996) *Polym Eng Sci* 36:203
14. Karger-Kocsis J, Varga J, Ehrenstein GW (1997) *J Appl Polym Sci* 64:2057
15. Padden FJ, Keith HD (1959) *J Appl Phys* 30:1479
16. Keith HD, Padden FJ, Walter NM, Wyckoff HW (1959) *J Appl Phys* 30:1485
17. Jones AT, Aizlewood JM, Beckett DR (1964) *Makromol Chem* 75:134
18. Lotz B, Wittmann JC, Lovinger AJ (1996) *Polymer* 37:4979
19. Stocker W, Schumacher M, Graff S, Thierry A, Wittmann JC, Lotz B (1998) *Macromolecules* 31:807
20. Torre J, Cortázar M, Gomez MA, Marco C, Ellis G, Rickel C, Dumas P (2006) *Macromolecules* 39:5564
21. Varga J (2002) *J Macromol Sci B Phys* 41:1121
22. Varga J (1986) *J Therm Anal* 31:165
23. Varga J (1989) *J Therm Anal* 35:1891
24. Shi GY, Zhang XD, Qiu ZX (1992) *Makromol Chem* 193:583
25. Li JX, Cheung WL (1999) *Polymer* 40:2085
26. Yi QF, Wen XJ, Dong JY, Han CC (2008) *Polymer* 49:5053
27. Liu MX, Guo BC, Du ML, Chen F, Jia DM (2009) *Polymer* 50:3022
28. Royer L (1928) *Bull Soc Fr Mineral Cristallogr* 51:7
29. Royer L (1954) *Bull Soc Fr Mineral Cristallogr* 77:1004
30. Bonev I (1972) *Acta Crystallogr A* 28:508
31. Gomer R, Smith CS (1953) *Structure and properties of solid surfaces*. University of Chicago Press, Chicago
32. Frankenheim ML (1836) *Ann Phys* 37:516
33. Willems J (1955) *Naturwissenschaften* 42:176
34. Fischer EW (1958) *Kolloidn Zh* 159:108
35. Willems J (1957) *Experientia* 13:276

36. Willems J (1958) *Discuss Faraday Soc* 25:111
37. Willems J (1959) *Experientia* 15:175
38. Fischer EW (1958) *Discuss Faraday Soc* 25:204
39. Mauritz KA, Baer E, Hopfinger AJ (1978) *J Polym Sci Macromol Rev* 13:1
40. Tuinstra F, Baer E (1970) *J Polym Sci Polym Lett Ed* 8:861
41. Hobbs SY (1971) *Nature Phys Sci* 234:12
42. Boucher EA (1973) *J Mater Sci* 8:146
43. Seifert H, Müller-Buschbaum B (1965) *Naturwissenschaften* 52:155
44. Müller-Buschbaum B, Seifert H (1965) *Kolloidn Zh* 205:46
45. Willems J (1967) *Experientia* 23:409
46. Lovinger AJ (1981) *Polymer* 22:412
47. Koutsky JA, Waiton AG, Baer E (1966) *J Polym Sci A2* 4:611
48. Carr SH, Keller A, Baer E (1970) *J Polym Sci A2* 8:1467
49. Mauritz KA, Baer E, Hopfinger AJ (1973) *J Polym Sci Polym Phys Ed* 11:2185
50. Ihn KJ, Tsuji M, Isoda S, Kawagushi A, Katayama KI, Tanaka Y, Sato H (1989) *Makromol Chem* 190:837
51. Willems J (1950) *Angew Chem* 62:335
52. Macchi EM, Morosoff N, Morawetz H (1968) *J Polym Sci A1* 6:2033
53. Morosoff N, Lim D, Morawetz H (1964) *J Am Chem Soc* 87:3167
54. Walton AG, Carr SH, Baer E (1968) *Polym Prepr Am Chem Soc* 9:603
55. Swei GS, Lando JB, Rickert SE, Mauritz KA (1986) *Encycl Polym Sci Eng* 6:209
56. Wittmann JC, Lotz B (1990) *Prog Polym Sci* 15:909
57. Smith P, Pennings J (1974) *Polymer* 15:413
58. Smith P, Pennings J (1976) *J Mater Sci* 11:1450
59. Wittmann JC, John Manley RS (1977) *J Polym Sci Polym Phys Ed* 15:1089
60. Wittmann JC, John Manley RS (1978) *J Polym Sci Polym Phys Ed* 16:1891
61. Wittmann JC, Lotz B (1981) *J Polym Sci Polym Phys Ed* 19:1837
62. Wittmann JC, Lotz B (1981) *J Polym Sci Polym Phys Ed* 19:1853
63. Wittmann JC, Hodge AM, Lotz B (1983) *J Polym Sci Polym Phys* 21:2495
64. Wunderlich B (1973) *Macromolecular physics, vol 1*. Academic, New York
65. Cao W, Wang K, Zhang Q, Du R, Fu Q (2006) *Polymer* 47:6857
66. Wunderlich B, Melillo L (1966) *Science* 154:1329
67. Liang S, Yang H, Wang K, Zhang Q, Du R, Fu Q (2008) *Acta Mater* 56:506
68. Su R, Zhang Z, Gao X, Ge Y, Wang K, Fu Q (2010) *J Phys Chem B* 114:9994
69. Gao Y, Zong GY, Bai HW, Fu Q (2014) *Chin J Polym Sci* 32:245
70. Jiang Z, Wang Y, Fu L, Whiteside B, Wyborn J, Norris K, Wu Z, Coates P, Men Y (2013) *Macromolecules* 46:6981
71. Jiang X, Liao Q, Zhou J, Wang Z, Chan C, Li L (2013) *J Polym Sci B Polym Phys* 51:907
72. Khoury F (1966) *J Res Natl Bur Stand A* 70:29
73. Sauer JA, Morrow DR, Richardson GC (1965) *J Appl Phys* 36:3017
74. Shen Y, Yang D, Feng Z (1991) *J Mater Sci* 26:1941
75. Norton DR, Keller A (1985) *Polymer* 26:704
76. Binsbergen FL, de Lange BGM (1968) *Polymer* 9:23
77. Compostella M, Coen A, Bertinotti F (1962) *Angew Chem* 74:618
78. Katayama K, Amano T, Nakamura N (1968) *Kolloid Z Z Polym* 226:125
79. Andersen PG, Carr SH (1975) *J Mater Sci* 10:870
80. Selikhova VT, Zubov YA, Markova GS, Kargin VA (1965) *Polym Sci USSR* 7:232
81. Padden FJ, Keith HD (1966) *J Appl Phys* 37:4013
82. Padden FJ, Keith HD (1973) *J Appl Phys* 44:1217
83. Lovinger AJ (1983) *J Polym Sci Polym Phys Ed* 21:97
84. Bassett DC, Olley RH (1984) *Polymer* 25:935
85. Lotz B, Wittmann JC (1986) *J Polym Sci Polym Phys Ed* 24:1541
86. Wu J, Zhou HX, Liu Q, Yan S (2013) *Chin J Polym Sci* 31:841

87. Li H, Sun X, Wang J, Yan S, Schultz JM (2006) *J Polym Sci Polym Phys* 44:1114
88. Petermann J (1995) Epitaxial growth on and with polypropylene. In: Karger-Kocsis J (ed) *Polypropylene: structure, blends and composites*, vol 1. Chapman & Hall, London, p 140
89. Chatterjee AM, Price FP, Newmann S (1975) *J Polym Sci Polym Phys Ed* 13:2369
90. Chatterjee AM, Price FP, Newmann S (1975) *J Polym Sci Polym Phys Ed* 13:2385
91. Chatterjee AM, Price FP, Newmann S (1975) *J Polym Sci Polym Phys Ed* 13:2391
92. Seth KK, Kenpster CJE (1977) *J Polym Sci Symp* 58:297
93. Willems J (1963) *Naturwissenschaften* 50:92
94. Kobayashi K, Takahashi T (1964) *Mem Fac Eng Kyoto Univ* 26:247
95. Takahashi T, Inamura M, Tsujimoto I (1970) *J Polym Sci Polym Lett Ed* 8:651
96. Willems J (1973) *Kolloid Z Z Polym* 251:496
97. Takahashi T, Teraoka F, Tsujimoto I (1976) *J Macromol Sci Phys B*12:303
98. Buleon A, Chanzy H, Roche E (1976) *J Polym Sci Polym Phys Ed* 14:1913
99. Iguchi M, Murase I (1975) *J Polym Sci Polym Phys Ed* 13:1461
100. Campbell D, Quayyum MM (1980) *J Polym Sci Polym Phys Ed* 18:83
101. Nishio Y, Yamane T, Takahashi T (1984) *J Macromol Sci Phys B*23:17
102. Kojima M, Stake H (1984) *J Polym Sci Polym Phys Ed* 22:285
103. Lotz B, Wittmann JC (1986) *J Polym Sci Polym Phys Ed* 24:1559
104. Lotz B, Wittmann JC (1984) *Macromol Chem* 185:2043
105. Lotz B, Wittmann JC (1987) *J Polym Sci Polym Phys Ed* 25:1079
106. Li H, Yan S (2011) *Macromolecules* 44:417
107. Kawaguchi A, Okihara T, Murakami S, Ohara M, Katayama K, Petermann J (1991) *J Polym Sci Polym Phys Ed* 29:683
108. Wittmann JC, Lotz B (1985) *J Polym Sci Polym Phys Ed* 23:205
109. Liu J, Li H, Yan S, Xiao Q, Petermann J (2003) *Colloid Polym Sci* 281:601
110. Yan C, Li H, Zhang J, Ozaki Y, Shen D, Yan D, Shi AC, Yan S (2006) *Macromolecules* 39:8041
111. Chang H, Zhang J, Li L, Wang Z, Yang C, Takahashi I, Ozaki Y, Yan S (2010) *Macromolecules* 43:362
112. Cheng S, Hu W, Ma Y, Yan S (2007) *Polymer* 48:4264
113. Barker TV (1906) *J Chem Soc Trans* 89:1120
114. Esposito LD, Koenig JL (1976) *J Polym Sci Polym Phys Ed* 12:1731
115. Nakaoki T, Yamanaka T, Ohira Y, Horii F (2000) *Macromolecules* 33:2718
116. Tashiro K, Ueno Y, Yoshioka A, Kobayashi M (2001) *Macromolecules* 34:310
117. Wu HD, Tseng CR, Chang FC (2001) *Macromolecules* 34:2992
118. Matsuba G, Kaji K, Nishida K, Kanaya T, Imai M (1999) *Macromolecules* 32:8932
119. Jiang Y, Gu Q, Li L, Shen DY, Jin XG, Chan CM (2003) *Polymer* 44:3509
120. Zhang J, Duan Y, Shen D, Yan S, Noda I, Ozaki Y (2004) *Macromolecules* 37:3292
121. Song K, Rabolt JF (2001) *Macromolecules* 34:1650
122. Soto A, Voyiatzis GA (2002) *Macromolecules* 35:2095
123. Chae B, Lee SW, Ree M, Jung YM, Kim SB (2003) *Langmuir* 19:687
124. Giussani E, Brambilla L, Fazzi D, Sommer M, Kayunkid N, Brinkmann M, Castiglioni C (2015) *J Phys Chem B* 119:2062
125. Yan C, Zhang Y, Hu Y, Ozaki Y, Gan Z, Yan S, Takahashi I (2008) *J Phys Chem B* 112:3311
126. Liu J, Wang J, Li H, Shen D, Zhang J, Ozaki Y, Yan S (2006) *J Phys Chem B* 110:738
127. Tu C, Jiang S, Li H, Yan S (2013) *Macromolecules* 46:5215
128. Tashiro K, Kobayashi M (1997) *Polymer* 38:2867
129. Zhou H, Jiang S, Yan S (2011) *J Phys Chem B* 115:13449
130. Moggio I, Le Moigne J, Arias-Marin E, Issautier D, Thierry A, Comoretto D, Dellepiane G, Cuniberti C (2001) *Macromolecules* 34:7091
131. Na B, Zhang Q, Wang K, Li L, Fu Q (2005) *Polymer* 46:819
132. Asano T, Yan S, Petermann J, Yoshida S, Tohyama N, Imaizumi K, Sugiyama T (2003) *J Macromol Sci B*42:489

133. Wang Y, Chan CM, Jiang Y, Li L, Ng KM (2007) *Macromolecules* 40:4002
134. Xu J, Guo BH, Zhang ZM, Zhou JJ, Jiang Y, Yan S, Li L, Wu Q, Chen GQ, Schultz JM (2004) *Macromolecules* 37:4118
135. Jiang Y, Yan DD, Gao X, Han CC, Jin XG, Li L, Wang Y, Chan CM (2003) *Macromolecules* 36:3652
136. Lei YG, Chan CM, Li JX, Ng KM, Wang Y, Jiang Y, Li L (2002) *Macromolecules* 35:6751
137. Li L, Chan CM, Yeung KL, Li JX, Ng KM, Lei Y (2001) *Macromolecules* 34:316
138. Prokhorov VV, Klinov DV, Chinarev AA, Tuzikov AB, Gorokhova IV, Bovin NV (2011) *Langmuir* 27:5879
139. Wang Z, Chang H, Wang T, Wang H, Yan D (2014) *J Phys Chem B* 118:4212
140. Tracz A, Jeszka JK, Kucińska I, Chapel JP, Boiteux G, Kryszewski MJ (2002) *Appl Polym Sci* 86:1329
141. Tracz A, Kucińska I, Jeszka JK (2003) *Macromolecules* 36:10130
142. Takenaka Y, Miyaji H, Hoshino A, Tracz A, Jeszka JK, Kucinska I (2004) *Macromolecules* 37:9667
143. Stocker W, Schumacher M, Graff S, Lang J, Wittmann JC, Lovinger AJ, Lotz B (1994) *Macromolecules* 27:6948
144. Lotz B, Lovinger AJ, Cais RE (1988) *Macromolecules* 21:2375
145. Cartier L, Okihara T, Lotz B (1998) *Macromolecules* 31:3303
146. Puiggali J, Ikada Y, Tsuji H, Cartier L, Okihara T, Lotz B (2000) *Polymer* 41:8921
147. Yan C, Guo L, Chang H, Yan S (2013) *Chin J Polym Sci* 31:1173
148. Yan S, Lin J, Yang D, Petermann J (1994) *J Mater Sci* 29:1773
149. Yan S, Lin J, Yang D, Petermann J (1994) *Macromol Chem Phys* 195:195
150. Yan S, Petermann J, Yang D (1997) *J Polym Sci Polym Phys Ed* 35:1415
151. Yan S, Yang D, Petermann J (1998) *Polymer* 39:4569
152. Yan S, Petermann J (2000) *J Polym Sci Polym Phys Ed* 38:80
153. Yan S, Katzenberg F, Petermann J, Yang D, Shen Y, Straupe C, Wittmann JC, Lotz B (2000) *Polymer* 41:2613
154. Yan S, Bonnet M, Petermann J (2000) *Polymer* 41:1139
155. Keddie JL, Jones RAL, Cory RA (1994) *Europhys Lett* 27:59
156. Frank CW, Rao V, Despotopoulou MM, Rease RFW, Hinsberg WD, Miller RD, Rabolt JF (1996) *Science* 273:912
157. Forrest JA, Dalnoki-Veress K, Dutcher JR (1997) *Phys Rev E* 56:5705
158. De Maggio GB, Frieze WE, Gidley DW, Zhu M, Hristov HA, Yee AF (1997) *Phys Rev Lett* 78:1524
159. Forrest JA, Mattson J (2000) *Phys Rev E* 61:R53
160. Fryer DS, Nealey PF, de Pablo JJ (2000) *Macromolecules* 33:6439
161. Torres JA, Nealey PF, de Pablo JJ (2000) *Phys Rev Lett* 85:3221
162. Kim JH, Jang J, Zin WC (2001) *Langmuir* 17:2703
163. Zheng X, Sauer BB, van Alsten JG, Schwarz SA, Rafailovich MH, Sokolov J, Rubinstein M (1995) *Phys Rev Lett* 74:407
164. Zheng X, Rafailovic MH, Sokolov J, Strzhemechny Y, Schwarz SA, Sauer BB, Rubinstein M (1997) *Phys Rev Lett* 79:241
165. Russell TP, Kumar SK (1997) *Nature* 386:771
166. Lin EK, Kolb R, Satija SK, Wu WL (1999) *Macromolecules* 32:3753
167. Reiter G, Sommer JU (1998) *Phys Rev Lett* 80:3771
168. Despotopoulou MM, Frank CW, Miller RD, Rabolt JF (1996) *Macromolecules* 29:5797
169. Schönherr H, Frank CW (2003) *Macromolecules* 36:188
170. Despotopoulou MM, Frank CW, Miller RD, Rabolt JF (1995) *Macromolecules* 28:6687
171. Schönherr H, Frank CW (2003) *Macromolecules* 36:1188
172. Schönherr H, Frank CW (2003) *Macromolecules* 36:1199
173. Schönherr H, Waymouth RM, Frank CW (2003) *Macromolecules* 36:2412

174. Schönherr H, Wiyatno W, Pople J, Frank CW, Fuller GG, Gast AP, Waymouth RM (2002) *Macromolecules* 35:2654
175. Frank B, Gast AP, Russell TP, Brown HR, Hawker C (1996) *Macromolecules* 29:6531
176. Capitán MJ, Rueda DR, Ezquerro TA (2004) *Macromolecules* 37:5653
177. Calvert P (1992) *Nature* 360:535
178. Brinkhuis RHR, Schouten AJ (1992) *Macromolecules* 25:2717
179. De Boer A, Alberda van Ekenstein GOR, Challa G (1975) *Polymer* 16:930
180. Zhao D, Li L, Che B, Cao Q, Lu Y, Xue Q (2004) *Macromolecules* 37:4744
181. Schneider B, Štokr J, Spěváček J, Baldrian J (1987) *Macromol Chem* 188:2705
182. Ma Y, Hu W, Reiter G (2006) *Macromolecules* 39:5159
183. Reiter G, Sommer JU (2000) *J Chem Phys* 112:4376
184. Sommer JU, Reiter G (2000) *J Chem Phys* 112:4384
185. Vonau F, Aubel D, Bouteiller L, Reiter G, Simon L (2007) *Phys Rev Lett* 99:086103
186. Ma Y, Zha L, Hu W, Reiter G, Han CC (2008) *Phys Rev E* 77:061801
187. Grozeva N, Botizb I, Reiter G (2008) *Eur Phys J E* 27:63
188. Sommer JU, Reiter G (2001) *Europhys Lett* 56:755
189. Xu J, Ma Y, Hu W, Rehahn M, Reiter G (2009) *Nat Mater* 8:348
190. Keller A, O'Connor A (1957) *Nature* 180:1289
191. Bassett DC, Frank FC, Keller A (1959) *Nature* 184:810
192. Keller A (1962) *Polymer* 3:393
193. Lovinger AJ, Keith HD (1979) *Macromolecules* 12:919
194. Kovacs AJ, Straupe C (1979) *Faraday Discuss* 68:225
195. Keith HD, Padden FJ, Lotz B, Wittmann JC (1989) *Macromolecules* 22:2230
196. Bu Z, Yoon Y, Ho RM, Zhou W, Jangchud I, Eby RK, Cheng SZD, Hsieh ET, Johnson TW, Geerts RG, Palackal SJ, Hawley GR, Welch MB (1996) *Macromolecules* 29:6575
197. Sakai Y, Imai M, Kaji K, Tsuji M (1996) *Macromolecules* 29:8830
198. Sutton SJ, Izumi K, Miyaji H, Miyamoto Y, Miyatashi S (1997) *J Mater Sci* 32:5621
199. Abe H, Kikkawa Y, Iwata T, Aoki H, Akehata T, Doi Y (2000) *Polymer* 41:867
200. Taguchi K, Miyaji H, Izumi K, Hoshimo A, Miyamoto Y, Kokawa R (2001) *Polymer* 42:7443
201. Zhang B, Yang D, De Rosa C, Yan S, Petermann J (2001) *Macromolecules* 34:5221
202. Zhang B, Yang D, De Rosa C, Yan S (2002) *Macromolecules* 35:4646
203. Hu ZJ, Huang HY, Zhang FJ, Du BY, He TB (2004) *Langmuir* 20:3271
204. Duan Y, Jiang Y, Jiang S, Li L, Yan S, Schultz JM (2004) *Macromolecules* 37:9283
205. Mareau VH, Prud'homme RE (2005) *Macromolecules* 38:398
206. Jiang S, Li H, De Rosa C, Auriemma F, Yan S (2010) *Macromolecules* 43:1449
207. Theodorou DN (1989) *Macromolecules* 22:4578
208. Mansfield KF, Theodorou DN (1990) *Macromolecules* 23:4430
209. Mansfield KF, Theodorou DN (1991) *Macromolecules* 24:4295
210. Harmandaris VA, Kaoulas KC, Mavrantzas VG (2005) *Macromolecules* 38:5796
211. Liu T, Yan S, Bonnet M, Lieberwirth I, Rogausch KD, Petermann J (2000) *J Mater Sci* 35:5047
212. Fenwick D, Smith P, Wittmann JC (1996) *J Mater Sci* 31:128
213. Petermann J, Xu Y, Loos J, Yang D (1992) *Polym Commun* 33:1096
214. Schumacher M, Lovinger AJ, Agarwal P, Wittmann JC, Lotz B (1994) *Macromolecules* 27:6956
215. Yan S, Späth T, Petermann J (2000) *Polymer* 41:4863
216. Takahashi T, Ogata N (1971) *Polym Lett* 9:895
217. Sun Y, Li H, Huang Y, Chen E, Zhao L, Gan Z, Yan S (2005) *Macromolecules* 38:2739
218. Petermann J, Xu Y (1991) *J Mater Sci* 26:1211
219. Richards RB (1951) *J Polym Sci* 6:397
220. Horio M (1964) The theory of crimp of textile fibers. *Mem Fac Eng Kyoto Univ* 26:222
221. Petermann J, Xu Y, Loos J, Yang D (1992) *Macromol Chem* 193:611

222. Tao X, Yan S, Yang D (1993) *Chin Chem Lett* 4:1093
223. Xu Y, Asano T, Kawaguchi A, Rieck U, Petermann J (1989) *J Mater Sci Lett* 8:675
224. Yan S, Petermann J, Yang D (1996) *Polymer* 37:2681
225. An YK, Jiang SD, Yan SK, Sun JR, Chen XS (2011) *Chin J Polym Sci* 29:513
226. Yan S, Katzenberg F, Petermann JJ (1999) *Polym Sci Phys Ed* 37:1893
227. Laurens C, Ober R, Creton C, Léger L (2001) *Macromolecules* 34:2932
228. Jaballah A, Rieck U, Petermann JJ (1990) *Mater Sci* 25:3105
229. Lee I, Schultz JM (1986) *Polymer* 27:1219
230. Lee I, Schultz JM (1988) *J Mater Sci* 23:4237
231. Sun Y, Tan L, Jiang S, Qian HL, Wang ZH, Yan DW, Di CA, Wang Y, Wu WP, Yu G, Yan S, Wang CR, Hu WP, Liu YQ, Zhu DB (2007) *J Am Chem Soc* 129:1882
232. Dong H, Jiang S, Jiang L, Liu Y, Li H, Hu W, Wang E, Yan S, Wei Z, Xu W, Gong X (2009) *J Am Chem Soc* 131:17315
233. Brinkmann M, Wittmann JC (2006) *Adv Mater* 18:860
234. Brinkmann M, Rannou P (2007) *Adv Funct Mater* 17:101
235. Brinkmann M, Rannou P (2009) *Macromolecules* 42:1125
236. Brinkmann M, Contal C, Kayunkid N, Djuric T, Resel R (2010) *Macromolecules* 43:7604
237. Kayunkid N, Uttiya S, Brinkmann M (2010) *Macromolecules* 43:4961
238. Jiang S, Qian H, Liu W, Wang C, Wang Z, Yan S, Zhu D (2009) *Macromolecules* 42:9321
239. Dong H, Li H, Wang E, Wei Z, Xu W, Hu W, Yan S (2008) *Langmuir* 24:13241
240. Sun X, Li H, Lieberwirth I, Yan S (2007) *Macromolecules* 40:8244
241. Wang J, Li H, Liu J, Duan Y, Jiang S, Yan S (2003) *J Am Chem Soc* 125:1496
242. Orts WJ, Marchessault RH, Bluhm TL, Hamer GK (1990) *Macromolecules* 23:5368
243. Zhang J, Duan Y, Sato H, Tsuji H, Noda I, Yan S, Ozaki Y (2005) *Macromolecules* 38:8012
244. Hoogsteen W, Postema AR, Pennings AJ, ten Brinke G, Zugenmair P (1990) *Macromolecules* 23:634
245. Sasaki S, Asakura T (2003) *Macromolecules* 36:8385
246. Wang T, Li H, Yan S (2012) *Chin J Polym Sci* 30:269
247. Sun X, Pi F, Zhang J, Takahashi I, Ozaki Y, Wang F, Yan S (2011) *J Phys Chem B* 115:1950
248. Li H, Sun X, Yan S, Schultz JM (2008) *Macromolecules* 41:5062
249. Lovinger AJ, Chua JO, Gryte CC (1977) *J Polym Sci Polym Phys Ed* 15:641
250. Grubb DT, Odell JA, Keller A (1975) *J Mater Sci* 10:1510
251. Li H, Jiang S, Wang J, Wang D, Yan S (2003) *Macromolecules* 36:2802
252. Li H, Zhang X, Kuang X, Wang J, Wang D, Li L, Yan S (2004) *Macromolecules* 37:2847
253. Sun X, Li H, Zhang X, Wang J, Wang D, Yan S (2006) *Macromolecules* 39:1087
254. Sun X, Li H, Wang J, Yan S (2006) *Macromolecules* 39:8720
255. Crissman JM (1969) *J Polym Sci* 7:389
256. Fujiwara Y (1975) *Colloid Polym Sci* 253:273
257. Zhang J, Yang D, Thierry A, Wittmann JC, Lotz B (2001) *Macromolecules* 34:6261
258. Kopp S, Wittmann JC, Lotz B (1994) *Polymer* 35:908
259. Kopp S, Wittmann JC, Lotz B (1994) *Polymer* 35:916
260. Fuller CS, Erickson CL (1937) *J Am Chem Soc* 59:344
261. Fuller CS, Erickson CL (1939) *J Am Chem Soc* 61:2575
262. Fuller CS, Erickson CL (1939) *J Phys Chem* 43:323
263. Gan Z, Kuwabara K, Abe H, Iwata T, Doi Y (2004) *Biomacromolecules* 5:371
264. Pouget E, Almontassir A, Casas MT, Puiggali J (2003) *Macromolecules* 36:698
265. Gan Z, Abe H, Doi Y (2002) *Macromol Chem Phys* 203:2369
266. Woo EM, Wu MC (2005) *J Polym Sci Polym Phys Ed* 43:1662
267. Gan Z, Kuwabara K, Abe H, Iwata T, Doi Y (2005) *Polym Degrad Stab* 87:191
268. Sun Y, Li H, Huang Y, Chen E, Gan Z, Yan S (2006) *Polymer* 47:2455
269. Zhou H, Yan S (2013) *Macromol Chem Phys* 214:639
270. Lim JA, Liu F, Ferdous S, Muthukumar M, Briseno AL (2010) *Mater Today* 13:14
271. Brinkmann M (2011) *J Polym Sci B* 49:1218

272. Abbate S, Gussoni M, Zerbi G (1979) *J Phys Chem* 70:3577
273. Yan C, Zhang J, Yan S (2006) *Chin Sci Bull* 51:2844
274. Nagamatsu S, Takashima W, Kaneto K, Yoshida Y, Tanigaki N, Yase K (2003) *Macromolecules* 36:5252
275. Hartmann L, Tremel K, Uttiya S, Crossland E, Ludwigs S, Kayunkid N, Vergnat C, Brinkmann M (2011) *Adv Funct Mater* 21:4047
276. Sun D, Li Y, Ren Z, Bryce MR, Li H, Yan S (2014) *Chem Sci* 5:3240
277. Park C, De Rosa C, Fetters LJ, Lotz B, Thomas EL (2001) *Adv Mater* 13:724
278. De Rosa C, Park C, Lotz B, Wittmann JC, Fetters LJ, Thomas EL (2000) *Macromolecules* 33:4871

Microstructure of Banded Polymer Spherulites: New Insights from Synchrotron Nanofocus X-Ray Scattering

Dimitri A. Ivanov and Martin Rosenthal

Abstract We report on the banded polymer morphology of several semicrystalline commodity polymers such as high-density poly(ethylene), poly(trimethylene terephthalate), poly(vinylidene fluoride), and poly(3-hydroxybutyrate). The internal structural organization and 3D shape of the constitutive crystalline lamellae have been topics of interest in polymer physics for the last 50 years. However, conventional morphological characterization techniques (electron and/or optical microscopy) can be misleading in such analyses and have resulted in wrong interpretations of the twisted lamella growth mechanisms. We present nanofocus synchrotron X-ray scattering experiments and describe the analysis used to interpret the arrays of nanodiffractograms acquired along the spherulitic radii. It is shown that the crystal twist occurring during radial outward growth is regular and uniform. The 3D lamella shape is in most cases similar to the classic helicoid, whereas in other cases, such as the lamellae of poly(propylene adipate), it corresponds to a spiral structure. Access to comprehensive microstructural information about bulk samples makes it possible to better understand the twisted growth mechanisms and check the premises of the Keith and Padden model linking the direction of chain tilt and lamella twist hand. It is demonstrated that this model cannot explain the banding behavior

D.A. Ivanov (✉)

Institut de Sciences des Matériaux de Mulhouse - IS2M, CNRS UMR7361, 15 Jean Starcky, 68057 Mulhouse, France

Faculty of Fundamental Physical and Chemical Engineering, Lomonosov Moscow State University (MSU), GSP-1, Leninskie gory - 1, 119991 Moscow, Russia
e-mail: dimitri.ivanov@uha.fr

M. Rosenthal

Faculty of Fundamental Physical and Chemical Engineering, Lomonosov Moscow State University (MSU), GSP-1, Leninskie gory - 1, 119991 Moscow, Russia

European Synchrotron Radiation Facility (ESRF), 6 rue Jules Horowitz, 38043 Grenoble, France

in poly(trimethylene terephthalate) and therefore needs reconsideration. In-depth analysis of the microstructure allows more general conclusions to be drawn regarding correlation of chiralities pertinent to different spatial scales, ranging from that of the constitutive monomer to the supramolecular level of twisted lamellae.

Keywords Banded polymer spherulite • Chain tilt • High-density poly(ethylene) • Lamella chirality • Nanocalorimetry • Nanofocus X-ray scattering • Poly(3-hydroxybutyrate) • Poly(trimethylene terephthalate) • Synchrotron radiation

Contents

1	Introduction	96
2	Experimental Details	103
2.1	Experimental Setup	103
2.2	Methodology of Data Analysis	104
3	Results and Discussion	107
3.1	High-Density Poly(ethylene)	107
3.2	Poly(propylene adipate)	110
3.3	Poly(trimethylene terephthalate)	113
3.4	Poly(3-hydroxybutyrate)	120
3.5	Correlation of Chiralities at Different Spatial Scales	121
4	Conclusions	122
	References	123

1 Introduction

Formation of banded polymer spherulites, probably the most fascinating polymer morphology, has been attracting the interest of polymer physicists for more than 50 years. As nicely put by D.C. Bassett in his review on polymer spherulites, “no aspect of spherulitic growth has been more intriguing nor more challenging to interpret than the spectacular phenomenon of banding” [1]. Generally, spherulites are one of the most common crystal forms observed for a very wide variety of organic and inorganic compounds. The word “spherulite” (cf. Fig. 1) emphasizes the overall spherical symmetry of such crystal aggregates, which implies that crystal growth starts from a central nucleus and proceeds radially outwards. The spherical shape also implies that the crystal growth rate in the material is independent of the direction in space, meaning that the material properties in the amorphous state are isotropic. Observation of spherulites dates back to the works of Talbot [2], who studied crystallization of borax from phosphoric acid almost two centuries ago. In the years following this discovery, research on spherulites was significantly extended to molecular crystals by Lehmann [3], who found the use of a heating stage particularly well suited in combination with polarizing optical microscopy. Since that time, a great number of substances of different natures have been reported to exhibit spherulitic morphology (see, e.g., [4]).

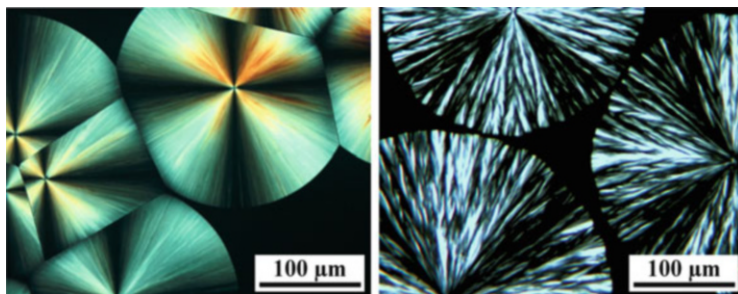


Fig. 1 Spherulites of poly(trimethylene terephthalate) (*left*) and poly(lactic acid) stereocomplex (*right*) visualized with the help of polarized optical microscopy

The banded, or ringed, polymer spherulite is a particular type of spherulitic aggregate in which zones of polarized light extinction form defined concentric circular or spiraling shapes. The reason for such extinction patterns were soon recognized as being a result of the optical indicatrix rotating about the fast crystal growth axis [5, 6]. This conclusion was also supported by one of the oldest microfocus X-ray measurements, dating back to 1960 [7]. Since then, there have been innumerable observations of spherulite banding in polymers, which necessarily make any review on this topic incomplete. To display some of these magnificent optical textures, we have selected examples of poly(ethylene adipate), poly(3-hydroxybutyrate) (PHB), poly(vinylidene fluoride) (PVDF), poly(trimethylene terephthalate) (PTT), poly(propylene adipate) (PPA) and high-density poly(ethylene) (HDPE) (cf. Fig. 2). It can be seen that the banded morphologies differ in terms of the bandwidth and band regularity, the presence or absence of colors, etc. Moreover, in some instances, one can notice an additional superstructure overlaid on the simple pattern of concentric extinction rings, as in the case of PPA. The microstructure of this polymer is discussed in more detail in Sect. 3.

It is probably instructive to consider in some detail the case of PVDF, a commodity fluorinated polymer that has been extensively investigated over the last 40 years because of its unique high performance properties, exploited in various technological applications [8, 9]. Apart from the nice optical textures, this polymer is renowned for its rich polymorphic behavior. In thin films crystallized from the melt, two types of PVDF spherulites can be identified by optical microscopy: large spherulites of the α -form [10, 11] and smaller γ -spherulites [12]. In cross-polarized light, the α -spherulites distinctly show high birefringence and regular concentric banding, whereas the birefringence is lower and banding does not appear at all for the γ -spherulites as a result of their distinctly different morphology, which can be perceived as morphological irregularity. The characteristic optical textures of PVDF crystallized from the melt at crystallization temperature (T_c) of 162.5°C are given in Fig. 3.

An alternative possibility for observation of PVDF structures at higher resolution is offered by atomic force microscopy (AFM). In the AFM micrographs in

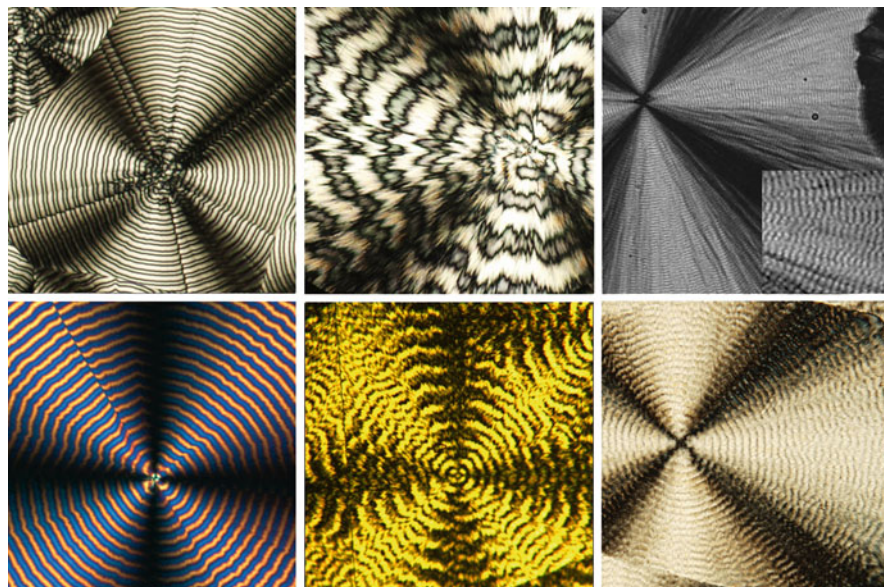


Fig. 2 Banded polymer spherulites of poly(ethylene adipate) (*top left*), poly(3-hydroxybutyrate) (*top center*), poly(vinylidene fluoride) (*top right*), poly(trimethylene terephthalate) (*bottom left*), poly(propylene adipate) (*bottom center*) and high-density poly(ethylene) (*bottom right*)

Fig. 3, one can clearly distinguish the lamellar morphology of PVDF, which is inaccessible using optical microscopy. In particular, regular ridges revealing individual lamellae can be easily inspected for the presence of banded α -spherulites. However, the microstructure of γ -spherulites, which seem more disordered in visible light, also reveals curvy lamellar shapes of very different appearance. Thus, it can be seen that the γ -crystals appear as spirals standing upright in the film. A close-up of the border region between the two types of spherulites is also presented in Fig. 3. The corresponding 3D shapes of the crystals of both polymorphs can be associated with classic helicoids and scrolls, respectively (cf. Fig. 4).

It is widely accepted today that the curving of crystals is a result of interfacial stresses operating along the crystal–amorphous interface. Very similar forms have also been documented for inorganic partially crystalline systems such as the so-called biomorphs, or silica–calcium carbonate composites [13]. In such systems, as well as in polymers, curving of the crystals is believed to be induced by the unbalanced stresses acting on each of the crystal surfaces. In the case of a crystalline sheet, or lamella, the unbalanced stresses present on the two basal planes result in simple rolling up of the crystal to form a two-dimensional (2D) spiral or scroll (cf. Fig. 4, right). To form a helicoid (i.e., a figure generated by simultaneous rotation and translation of a straight section), it is not enough for the stresses to be unbalanced on the two opposite surfaces. In addition, it requires the presence of at least a pair of crystals glued together along their long axis, whereby the stresses on

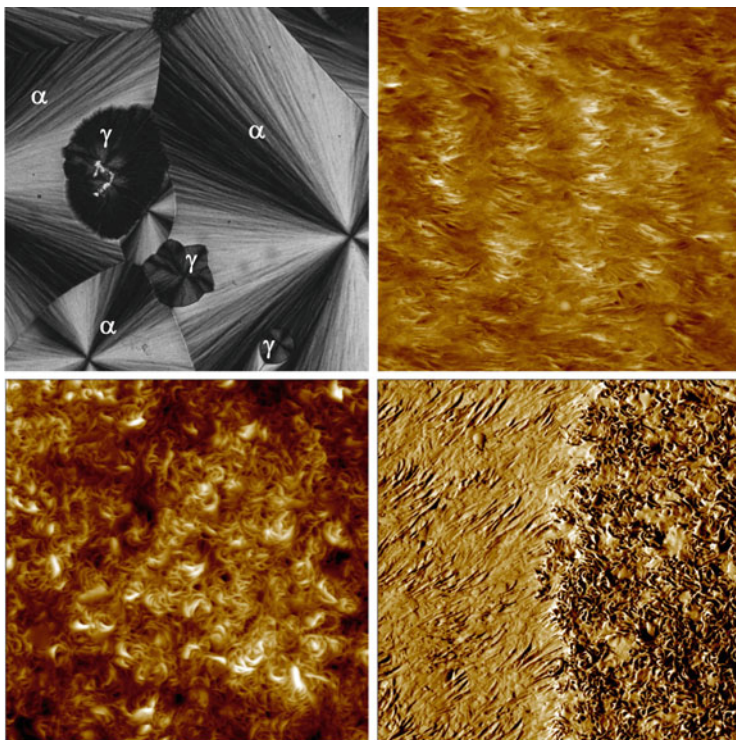


Fig. 3 Spherulites pertinent to the α - and γ -phases of poly(vinylidene fluoride) crystallized at 162.5°C. *Top left*: polarized optical micrograph. *Top right and bottom left*: AFM topography images of the α - and γ -phase spherulites, respectively. *Bottom right*: AFM phase image showing the interphase between the α - and γ -spherulites. The AFM image size is $10 \times 10 \mu\text{m}^2$

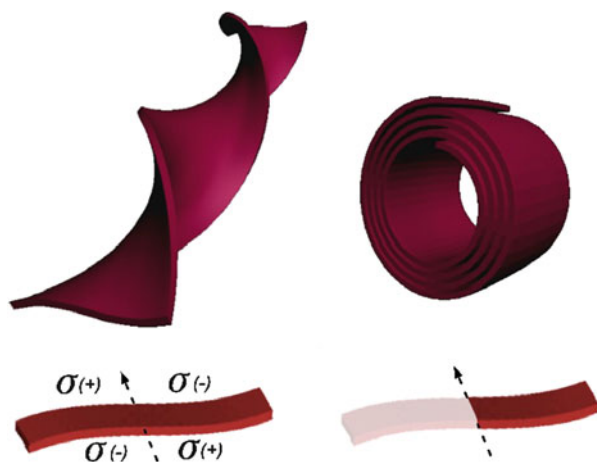


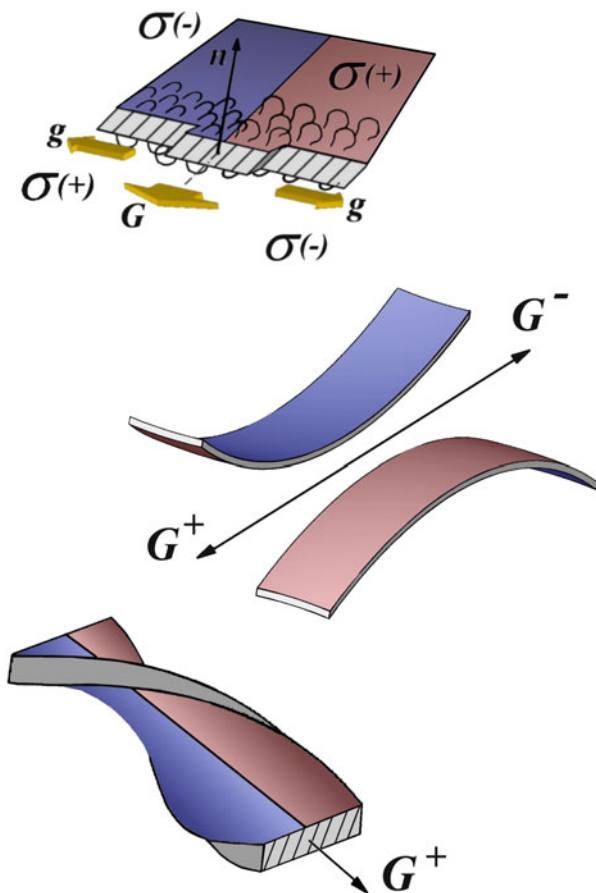
Fig. 4 Underlying surface stresses resulting in formation of different 3D shapes of twisted lamellae, such as helicoid (*left*) and scroll (*right*). Notations $\sigma(+)$ and $\sigma(-)$ indicate the positive and negative surface stresses, i.e., those that tend to increase and decrease the crystal surface, respectively

each of them are mutually inverted, as shown in Fig. 4 (left). One of the obvious reasons for stress generation in semicrystalline polymers is the density difference between the amorphous and crystalline regions, making the crystal–amorphous interphase topologically constrained.

One of the first models designed to explain the formation of twisted polymer crystals was the screw-dislocation model proposed by Basset and Hodge [14], which was based on observations of poly(ethylene) morphology. The model suggests that the twist originates from successive isochiral screw dislocations, leading to an isochiral splaying and twisting of the lamellar crystal. In this case, each screw dislocation contributes to the overall deviation by a certain defined increment. The isochirality of the screw dislocation is identified by the chain tilt of the crystalline stems within the lamellar crystal with respect to its normal [15]. From this model, the authors proposed a correlation between stem inclination and twisting of the lamellar crystal, which would be efficient in releasing the stresses at the fold surfaces [16]. Toda and co-authors further developed this model in an attempt to correlate the chain tilt in the lamellar crystal with the sense of the screw dislocation [17, 18].

However, the most widely cited model for twisting lamellar crystals was proposed in the seminal paper by Keith and Padden [19]. The model put forward, termed the “KP-model” in the rest of this chapter, was specifically developed for the case of poly(ethylene), and later extended [20] to other polymer systems, which makes it of a general nature. The underlying assumptions of the KP-model are schematically depicted in Fig. 5. The KP-model assumes the existence on the lamellar surface of chain folds of different conformation, which could reflect local environmental and spatial encumbrance during their formation (“reeling” of the chains from the quiescent melt). The main factor responsible for generation of chain folds of various configurations is thought to be the chain tilt with respect to the normal to the lamella basal plane, the feature that breaks the high symmetry of PE-based lamellae. Keith and Padden speculated [19] that the fold conformation consumes more space when the chain overhangs the growth front, or when it has to fold around an acute angle, leading to a positive pressure (red region of the lamellar surface in Fig. 5, top). By contrast, the fold is thought to be less space hindering when folding occurs around an obtuse angle (blue region in Fig. 5). The crystal growth mechanisms leading to the stress distribution proposed by Keith and Padden were based on the Lauritzen–Hofman theory, in the frame of which a secondary nucleus appears on a crystal surface and propagates laterally at a rate g to complete the outmost row of crystalline stems and give rise to the experimentally measurable propagation rate G . The part of the KP-model regarding chain folds is the most fragile to criticism (see, e.g., [21]) because the qualitative arguments of Keith and Padden do not seem sufficiently rigorous. Furthermore, Keith and Padden assume that the crystalline lamella is built of two equivalent laterally connected parts with opposite distributions of surface stresses, in such a way that, if cut along the growth axis with virtual scissors, the lamella parts (halves) would have a tendency to bend in the opposite directions (Fig. 5, middle). However, because the two parts are laterally connected to each other, the only way to reduce the free energy of such an

Fig. 5 Illustration of the Keith and Padden model. The sign of the surface stress generated by the differential chain fold congestion is rendered in *red* for positive and *blue* for negative



object would be to adopt a twisted shape (Fig. 5, bottom). Interestingly, the effect of the unbalanced surface stresses leading to a torque and thus to a twist were experimentally modeled by Keith and Padden using swollen rubber bands [19]. A straightforward consequence of the KP-model is the fact that if a lamella crystal grows radially outwards, the chiralities of the two lamella halves would be inverted (cf. Fig. 5, middle). This may, however, be in contradiction with what is known, for example, for banded spherulites of chiral polymers that typically form lamella helicoids of only one defined twisting hand.

Generally, it is clear that experimental verification of the KP-model was certainly problematic at the time when the model was put forward because of the absence of experimental techniques that could assess all the required microstructural parameters in bulk samples. Although examination of the chain fold conformation remains problematic even today, determination of the chain tilt in bulk isotropic samples was, in our opinion, totally unrealistic. Despite the inefficiency of conventional experimental techniques, the KP-model stimulated intense discussion

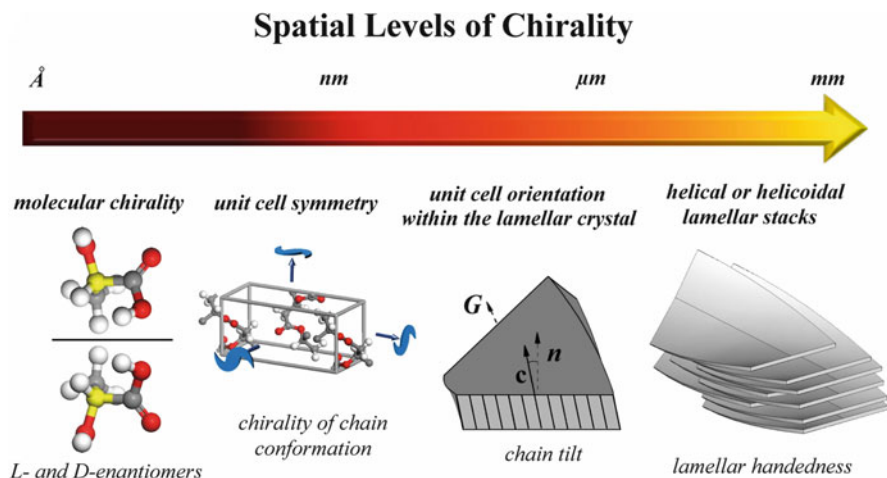


Fig. 6 Chirality parameters of a semicrystalline polymer pertinent to different spatial scales

in the literature on the possible correlations of chiralities present in polymer systems at different spatial scales (cf. Fig. 6), including monomer chirality, chirality of the unit cell, the chiral environment of crystalline lamellae, and the handedness of twisted lamella crystals.

With the advent of synchrotron-based X-ray scattering employing micro- and nanosized X-ray beams, the possibility of gaining deeper insights into the microstructure of bulk semicrystalline samples is becoming realistic. Micro- and nanofocus X-ray scattering techniques have already proved their power in identifying the crystal growth axis and local crystal orientation in banded and nonbanded spherulites of poly(L-lactic acid) [22], PHB [23, 24], isotactic polystyrene [25], isotactic poly(butene-1) [25], HDPE [26], PTT [27–29], and PPA [30]. The use of modern X-ray optics to focus the X-ray beam on a sample to a spot of less than a few microns can provide a wealth of structural information at the local scale, such as crystal orientation and chain tilt with respect to the lamella basal plane as well as lamella handedness. In most microfocus X-ray experiments, the supralamellar, or lamella bundle, structure is analyzed by scanning the banded spherulite along the fast crystal growth direction (i.e., the spherulite radius). However, in our opinion, detailed analysis of chain orientation within the lamellar crystal and its correlation to the twist sense is still lacking in the literature. Nozue and co-authors [31] employed this technique to identify the sense of crystal rotation while scanning along the radial axis of banded poly(caprolactone)/poly(vinyl butyrate) spherulites using the finite curvature of the Ewald sphere. This approach is discussed later in this chapter. Moreover, theoretical methods for analysis of the 3D lamella shapes based on microfocus X-ray patterns have recently been proposed [32–34].

The remainder of this chapter describes the methodology of nanofocus X-ray scattering experiments on banded polymer spherulites and the main analysis tools used to extract microstructural information (cf. section 2). The application of

nanofocused X-ray scattering is exemplified for several commodity polymers, demonstrating the power of the technique in analyzing the mechanisms of twisted lamella growth. The chiral parameters governing lamella formation and their correlation with the symmetry of the constitutive crystal lattices are discussed for several achiral and chiral polymers (cf. section 3).

2 Experimental Details

2.1 Experimental Setup

In a typical scanning nanodiffraction experiment, X-ray beams with footprints smaller than 200 nm are used to gather spatially resolved structural information on quasi-2D specimens. The experimental layout, as implemented at the nanodiffraction facility of the ID13 beamline at the European Synchrotron Radiation Facility (ESRF), is schematically presented in Fig. 7. The X-ray beam is generated by electron bunches accelerated to 6.3 GeV passing through the undulator inside the storage ring. The white X-ray beam is then prefocused over a distance of about 98 m using a set of white-beam beryllium lenses. X-ray photons with energy of 15 keV are selected using a Si₁₁₁ channel-cut monochromator. The final focusing of the beam close to the sample position is realized with silicon-based composite refractive lenses (CRL) allowing for beam sizes in the 40–150 nm range, depending on the beam prefocusing. However, this way of focusing the X-ray beam comes with a loss of about 90% of the initial X-ray beam intensity as a result of the low efficiency and low acceptance of the final focusing optics. A typical photon flux in the described focusing mode is about 10¹⁰ photons (ph) per second, giving a

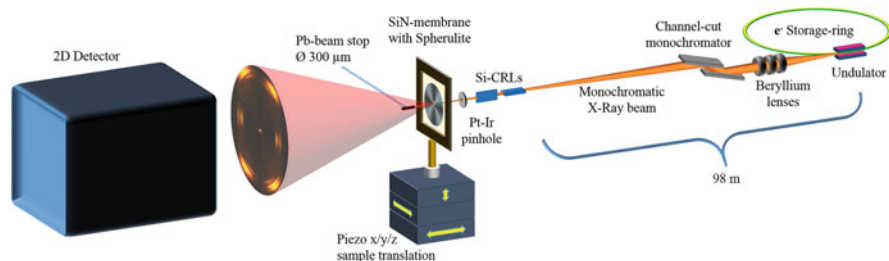


Fig. 7 Nanofocus X-ray scattering setup at the ID13 beamline of the ESRF. The X-ray beam generated by the undulators is focused over a distance of about 98 m. The final focusing of the beam close to the sample position is realized using composite refractive lenses, allowing beam sizes in the nanometer range. A typical experiment on a banded spherulite includes acquiring arrays of diffractograms along the spherulite radius. The small footprint of the X-ray beam on the sample can reveal the highly ordered local texture of the banded spherulite. The radial and azimuthal positions of the different diffraction peaks and their variation along the spherulite radius make it possible to address lamella chirality, lamella basal plane orientation, chain tilt and, generally, twisted growth mechanisms

typical flux density of about $2.8 \times 10^6 \text{ ph s}^{-1} \text{ nm}^{-2}$. A Pt–Ir pinhole placed directly upstream of the sample allows low background measurements, being a premise for high-resolution scanning experiments on weakly scattering samples. The developed approach for addressing the microstructure of banded spherulite in a scanning nanodiffraction experiment includes acquiring arrays of diffractograms along the spherulite radius with the help of large-area 2D detectors. The X-ray beam is first roughly positioned on a sample with the help of an on-axis optical microscope (not shown here). Further refinement of the beam location on the sample is performed by observing azimuthal positions of the known diffraction peaks of the sample. The main idea of the experiment is to realize radial scans across the whole spherulite. Precise motion of the sample along the x -, y - and z -directions is operated by combination of a so-called hexapod and a specially designed array of piezo-actuators. The use of a micron-sized beamstop of less than $300 \text{ }\mu\text{m}$ in diameter protects the sensitive 2D X-ray detector against saturation and overexposure from the direct beam, and allows recording wide- and small-angle scattering intensity at the same time. This dual angular-range detection is of high importance because data analysis requires correlation of information on the crystal morphology, such as lamella basal plane orientation assessed by SAXS, with that of the crystal lattice orientation measured with WAXS.

2.2 Methodology of Data Analysis

The methodology used for data analysis of all 1D scanning experiments is schematically illustrated in Fig. 8 for the case of melt-crystallized PTT. The recorded spatially resolved arrays of 2D diffraction patterns (Fig. 8, top left) are reduced and analyzed using appropriate integration algorithms. In our case, data correction, reduction, and integration were conducted using home-built routines designed in the IgorPro[®] software package (WaveMetrics Ltd). As mentioned, the X-ray beam position on the sample was refined using the azimuthal angles of some reference diffraction peaks of the studied polymer to make a radial scan across the spherulite. For PTT, Fig. 8 exemplifies the case when the radial scan is vertical. This means that, because the crystal growth direction in PTT is parallel to the \mathbf{a} -vector of the unit cell, the 00l, 0k0, and 0kl peaks populate the horizontal, or equatorial, direction of the patterns. By continuously monitoring the peak positions during fine lateral displacement of the specimen using the piezo-motors, it is straightforward to identify a location on the vertical line passing through the spherulite center. When a location characterized by vertical orientation of the \mathbf{a} -vector is found, it is convenient to search for the spherulite center. The latter can be found on the radial scan thanks to local disordering of the crystal texture, which is expressed by significantly increased azimuthal width of the peaks.

In the first analysis step, the scattered intensity $I(q,r)$ corresponding to the array of 2D diffraction patterns successively recorded along the spherulite radius is plotted as a function of the modulus of the scattering vector $q(|q| = 4\pi \sin(\theta)/\lambda$,

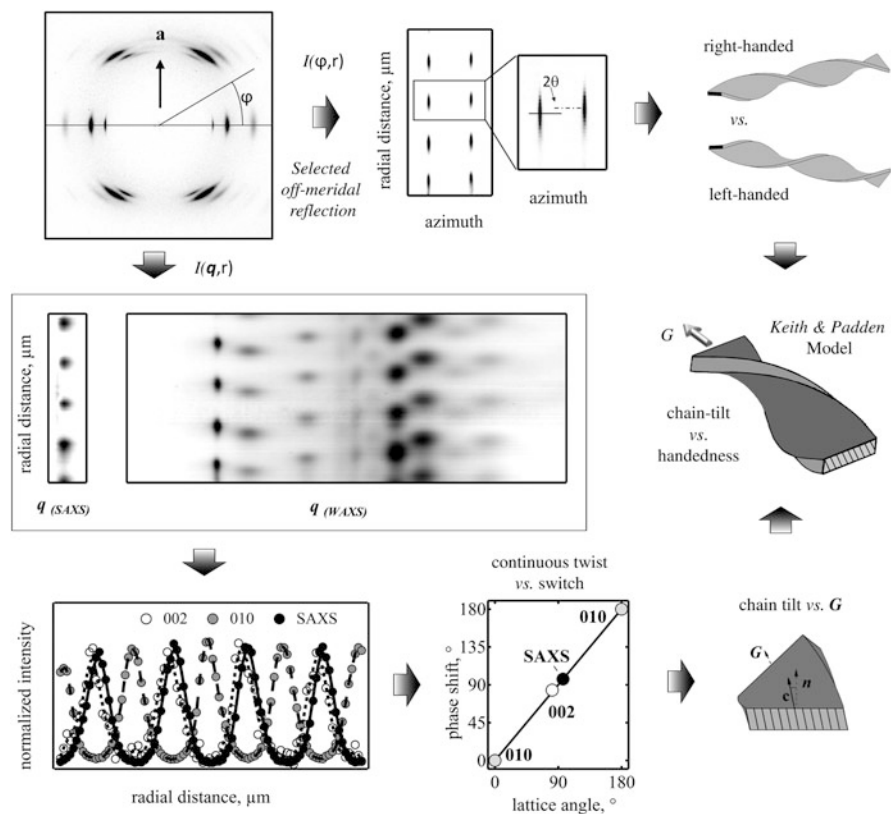


Fig. 8 Methodology of micro- or nanofocus X-ray scattering experiment on a banded polymer spherulite, exemplified for the case of melt-crystallized PTT. *Top left:* Typical 2D diffractogram for a location within a spherulite positioned on a vertical radial line. Chirality of the twisting lamella is determined from the order of appearance of the reflection and its symmetric counterpart (*top center* and *top right*). Reduction of the arrays of 2D diffractograms acquired in the course of a radial scan to the form of the $I(q, r)$ function allows exploration of the twisted growth mode (*middle left* and *bottom left*). Correlations between the chain tilt in the lamella (*bottom center*) and lamella chirality are examined to check the predictions of the KP-model for the chosen polymer (*right*)

where θ is the Bragg angle, λ the wavelength, and r the radial distance from the spherulite center (see Fig. 8, middle, left). Representation of data in the form of $I(q, r)$ makes it possible to rapidly examine whether the different crystallographic reflections and the small-angle intensity appear periodically along the radius. Periodic behavior (visualized as regular “blinking” of the peaks) signifies that radial scanning of the spherulite is equivalent to crystal rotation, during which the crystal enters and exits the reflection conditions for different diffraction peaks. Assuming the twist is regular, the distance between two successive maxima of the same reflection (for simplicity, issues related to peak multiplicity are not considered here) corresponds to a half turn of the crystal. Apart from regularity, it is also instructive to check the twist uniformity (i.e., to determine whether the rate of

angular rotation of the crystal is constant). An alternative to uniform twist is growth with a stepwise lamella twist, for which a change in crystal orientation occurs within a short fraction of the spherulitic band, followed by further growth of the crystal with invariable orientation over a noticeable distance. This analysis can be performed using locations at which the diffraction peaks reach their maximum intensity (Fig. 8, bottom left). It is thus necessary to check whether the observed reflections appear with radial offsets to each other, corresponding to the difference between their respective crystallographic angles derived from the unit cell parameters. Note that the crystallographic angles should be taken in their projection on the plane perpendicular to the crystal growth axis. The match of the two angles (i.e., the angle derived from the radial offset normalized by the width of the band and the angle calculated from the coordinates of the corresponding reciprocal space vector; Fig. 8, bottom center) indicates that the lamellar stacks rotate uniformly about the growth axis.

One of the most important chiral parameters of the twisting lamella crystal is its twist hand (i.e., left or right). Distinction between the lamella helicoids according to their chirality can be readily carried out using the offset between a selected reflection and its symmetric counterpart, as shown in Fig. 8 (top center). The reason why lamella chirality is amenable to X-ray analysis is the pronounced curvature of the Ewald sphere for the wavelength used (cf. Fig. 9). The situation here is at variance with that typically encountered in electron diffraction, where the Ewald spheres are extremely flat. The intensity of a given reflection becomes detectable when the Ewald sphere corresponding to the observation conditions intersects the intensity distribution on the reciprocal-space sphere with a radius equal to the norm

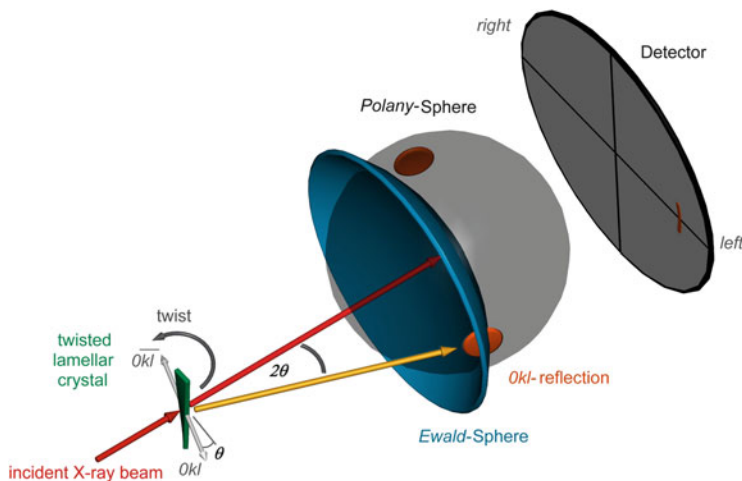


Fig. 9 Method of determination of twisted lamella chirality. The conditions of observation of reflection are created when the Ewald sphere intersects the so-called Polanyi sphere [35]. The sign of the offset between the positions corresponding to observation of a selected reflection and its symmetric counterpart can be readily converted into the chirality of the twisted lamella crystal

of the corresponding \mathbf{q} -vector, the so-called Polanyi sphere [35]. The moments at which intersection by the Ewald sphere of the intensity distributions pertinent to the reflection and its symmetric counterpart do not occur simultaneously during the radial nanofocus scan (cf. Figs. 9 and 8, top center). The sequence of appearance on the detector of the reflection and its counterpart (the radial difference between which equals the scattering angle in terms of the phase offset) allows determination of lamella handedness. It is naturally assumed that one has full information on the correspondence between the acquired detector image and its real orientation in space.

As mentioned in the introductory section, it is crucial to check the main premise of the KP-model, which correlates lamella chirality to the direction of the chain tilt in the crystal (i.e., the angle between the c -axis of the unit cell and the normal to the lamella basal plane). The chain tilt can be assessed from the location of the maximum of the small-angle intensity along the spherulite radius (expressed in degrees), as illustrated in Fig. 8 (bottom center). The position of the SAXS peak on this graph allows determination of the crystallography of the lamella fold plane and, consequently, the angle between the crystalline stem and any other reciprocal space vector of the crystal. The information on lamella chirality and chain tilt enables a conclusion to be drawn about whether the twisted growth occurs according to predictions of the KP-model (cf. Fig. 8, middle right).

3 Results and Discussion

3.1 High-Density Poly(ethylene)

It is appropriate to start with the analysis of banded HDPE, which is undoubtedly the most studied synthetic polymer. It has served as a model system for numerous studies in polymer physics, being considered the archetypal achiral flexible-chain polymer. It is noteworthy that a wealth of structural data on HDPE results from studies carried out on solution-grown single crystals of HDPE. The phenomenon of chain folding was first discovered in these magnificent objects. Structural data pertinent to single crystals are often generously extrapolated to the case of bulk HDPE, which can be problematic. One reason for this is, as Phil Geil states in his famous book on single polymer crystals [36], “The details of the flattening and solvent removal process for solution-grown single PE crystals are crucial for the final structure and can be accompanied by uneven distortion of the lattice whereby each fold domain of the initial markedly non-planar crystals is distorted or tilted individually.” Moreover, even the process of chain folding can be significantly different for polymer crystallization from a dilute solution and from the quiescent polymer melt. On the other hand, the structural information extracted for oriented HDPE fibers cannot simply be transferred to isotropic HDPE because of the structural reorganization processes occurring during drawing.

From the experimental viewpoint, it seems impossible to extract the same amount of microstructural information from studies of isotropic bulk HDPE as obtained for solution-grown crystals. For example, a parameter such as chain tilt with respect to the basal lamella plane cannot be tackled using typical characterization techniques. Therefore, correlations between the direction of chain tilt and lamellar chirality for bulk HDPE, which are the basis of the KP-model, could not be verified until recently. For these reasons, exploration of the banded morphology of HDPE spherulites with nano- or microbeam X-ray scattering is rather tempting.

The present study was conducted on free-standing films of unfractionated linear PE (DuPont Sclair 2901, weight-average molecular mass $M_w = 72,000 \text{ g mol}^{-1}$, number-average molecular mass $M_n = 19,500 \text{ g mol}^{-1}$) melt-crystallized at 105.8°C [26]. The choice of sample was based on its reputed low nucleation density [21], allowing growth of relatively large banded spherulites. The film was processed between cover glass slips to ensure a uniform film thickness of about $20 \mu\text{m}$. After immersion in 1% HF aqueous solution for 2 h, the films were floated off in distilled water.

The left panel of Fig. 10 presents the typical banded spherulite morphology of HDPE, characterized by relatively tight bands only a few microns wide. An averaged 2D WAXS pattern is also shown in Fig. 10. It exhibits oriented diffraction peaks, with the azimuthal position of the 020 peak located on the pattern equator. This means that all patterns were acquired along the horizontal radial line of a spherulite. Note that, although solution-grown single crystals of HDPE exhibit lozenge-shaped or truncated lozenge-shaped crystals with 110 or 200 growth faces [37–39], the crystal growth direction in the bulk occurs along the b -axis. This corresponds to the situation where a pair of adjacent growth faces, (-110) and (110) , advance at comparable rates. Importantly, the pronounced orientation of the patterns makes it possible to consider the local texture of this morphology as being quasi-single crystalline, which simplifies the analysis.

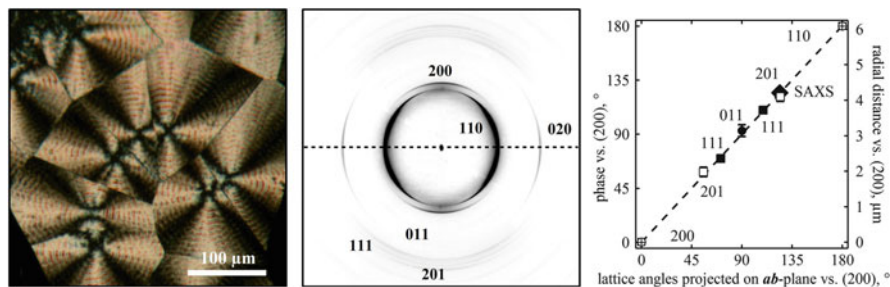


Fig. 10 Results of microfocus X-ray scattering study of the banded spherulite morphology of HDPE. *Left*: Banded spherulites of HDPE formed at 105.8°C . *Middle*: Averaged WAXS pattern obtained during microfocus X-ray scan along the horizontal radial line. *Right*: Correlation between phases of the different reflections of HDPE and lattice angles of the same reciprocal space vectors, measured from their projections on the ab -plane with respect to a reference reflection such as 200. The angular position of the SAXS interference maximum coincides with that of the 201 peak

The torsion of the crystal about the growth axis b is similar to the crystal rotation. As described earlier, the modes of crystal twist can be analyzed by plotting the correlation between the crystallographic angles of the HDPE reflections and their phase shifts. The latter can be calculated from the radial distances at which they reach their maximum intensity after normalization by the helicoid period (or twice the band spacing of the optical micrograph). The crystallographic angles of the HDPE unit cell are the angles between the projections of the corresponding reciprocal space vectors onto the plane perpendicular to the b -direction with respect to any reference vector in this plane (e.g., the 200 reflection; see Fig. 10, right). The studied correlation exhibits a linear behavior and shows that both angles remain similar. This means that crystal rotation about the b -axis is continuous and regular. This conclusion is not as trivial as it may appear. Indeed, in the past, it was suggested that the lamellar twist in PE occurs in a stepwise manner (e.g., in the works of Bassett and Hodge [14, 16]). These authors concluded from microscopy data that the lamellae of PE stayed untwisted over about one-third of the band spacing and afterwards exhibited an abrupt variation in c -axis orientation as a result of a sequence of screw dislocations of consistent sign. It is clear that the X-ray data shown here do not provide support for these findings. In addition, the sequence of appearance of diffraction peaks along the spherulite radius makes it possible to determine the direction of chain tilt in the crystals and its correlation with lamella chirality. As shown in Fig. 11A, the chain tilt deduced from arrays of acquired diffraction patterns is 35° , making the fold plane of the lamellae very close to (201). This value was first suggested for solution-grown single crystals [36]; however, a closer look at the values of the chain tilt shows that the angles depend on the crystallography of the crystal sector [38] and, more generally, can be significantly affected by the conditions of crystal formation and sedimentation on the electron microscope grid. The similar chain tilts observed for crystallization in bulk and for

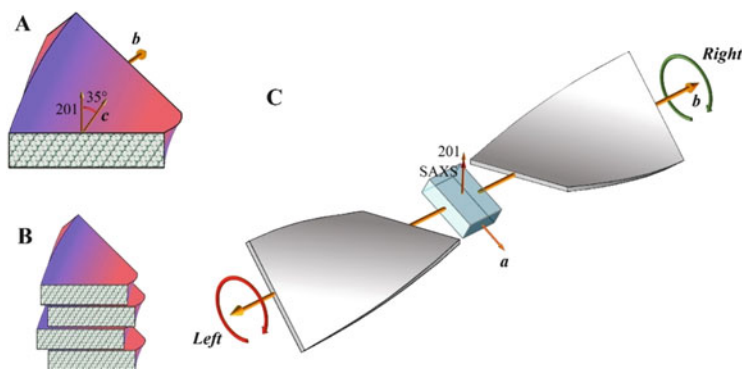


Fig. 11 (A) Correlation between the direction of chain tilt and lamella rotation for the case of HDPE. The lamellar crystal is viewed along the growth direction b . (B) The direction of chain tilt is found to be unique across the whole HDPE lamellar stack; it corresponds to the predictions of the KP-model. (C) The majority of HDPE lamellae contain left- and right-handed parts, forming hybrid left-right helicoids; chirality is inverted in the spherulitic center

solution-grown crystals indicate that the microstructural information on HDPE obtained on single crystals can be adequate for analysis of bulk morphology.

Apart from chain tilt, the microfocus data provides other information for checking the main premise of the KP-model, which states that the lamellar twist occurs in the direction of the chain tilt when one looks along the growth direction. This is indeed what is observed in the microfocus experiments on banded spherulites of HDPE (Fig. 11A). Moreover, the one-to-one correlation between lamella chirality and chain tilt direction signifies that the latter must remain invariable across the entire lamellar stack, as sketched in Fig. 11B. Indeed, a crystal in a stack with an opposite direction of chain tilt would adopt a different chirality, resulting in immediate crashing of this twisting lamella onto its neighbors during growth. Therefore, only crystals with one chain direction can survive in a stack, and this chain direction matches that predicted by Keith and Padden. The fact that, locally, all crystals not only have the same orientation, but also a unique stem direction, makes the polarity of the growth axis common to all of them.

Another conclusion directly following from the KP-model is that each lamella switches its chirality when passing through the spherulite center (cf. Fig. 11C). The HDPE spherulite is thus composed of hybrid left- and right-handed lamella helicoids forming hemispheres of opposite chirality. Overall, the lamellae of HDPE remain achiral. It is very tempting to link the chirality of the radially growing lamellae with the polarity of the growth axis. However, the fact that left- and right-handed helicoids are present shows that crystals can grow in both b and $-b$ directions, which are indistinguishable crystallographically because of the high symmetry of the HDPE unit cell. The division of type-II spherulites into two homochiral fields symmetric about a plane passing through the spherulite center has been previously reported using AFM imaging [40] and a combination of AFM and circular extinction microscopy [41]. It is noteworthy that, in our case, the handedness inversion is not observed for all performed radial scans because the scan can cross not only the well-organized sheaf-like part of the initial immature spherulite, but also the less-ordered spherulitic “eyes” formed during later in-filling lamellar growth [42]. During consideration of the typical lamella helicoids formed by HDPE, it is instructive to also consider other crystal shapes. Figure 12 (left) shows the typical morphology of semicrystalline PPA, as viewed by polarized optical microscopy [30]. Analysis of twisted lamella growth in PPA is discussed next.

3.2 *Poly(propylene adipate)*

PPA was synthesized from dimethyladipate and 1,3-propanediol glycol using a two-stage polymerization procedure described elsewhere [43]. The M_w of the PPA sample was $75,500 \text{ g mol}^{-1}$ with a polydispersity of 2.42. Free-standing films (10–20 μm thick) were prepared by solution casting from chloroform (40 g L^{-1}) onto glass slides previously cleaned by sonication in ethanol. After solvent evaporation,

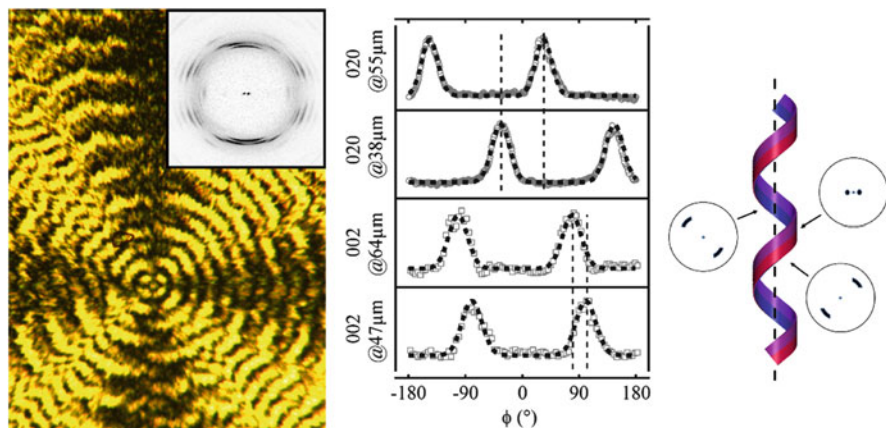


Fig. 12 *Left:* Polarized optical image of a poly(propylene adipate) (PPA) banded spherulite grown from the melt at T_c of 33°C. The *inset* shows an averaged 2D WAXS pattern measured during a vertical microfocus scan along the spherulite radius. *Middle:* Azimuthal intensity profiles of the 002 and 020 reflections measured at different radial positions. *Right:* Flat-on oriented helical ribbon of PPA lamella together with the model microfocus X-ray patterns containing WAXS and SAXS peaks and corresponding to different spatial positions of the beam

the resulting semicrystalline polymer films were melted at 50°C for 3 h, followed by isothermal crystallization at selected temperatures. After completion of crystallization, the films were detached from the glass substrates by floating them off in fluoric acid solutions (1 wt%).

Crystallization from the melt at 33°C results in a spherulitic pattern with well-defined bands. However, closer inspection of the pattern reveals that the morphology exhibits a characteristic zigzag extinction pattern, which was previously modeled by rotation of an uniaxial indicatrix about an axis oblique to the optic axis [44]. The model employed in the simulation of optical properties implies that the crystal shape is helical. It is, however, clear that simulation of the extinction pattern remains qualitative and that the microstructural parameters of such a morphology cannot be easily extracted. Therefore, a microfocus X-ray experiment was needed to determine the details of such a peculiar banded spherulite morphology.

Analysis of radial microfocus scans revealed a very interesting feature: regular azimuthal wagging of reflections such as 002 and 020 (cf. Fig. 12, middle). Such behavior is not typical of lamella helicoids as formed, for example, by HDPE lamellae. The results suggest that a different 3D shape can account for such patterns. A scheme of a flat-on helical lamellar ribbon is given in Fig. 12 (right). The ribbon winds around a virtual cylinder and has an opening angle of about 30°. In this case, each change in ribbon direction during winding can produce the azimuthal wagging of reflections observed in the experiment.

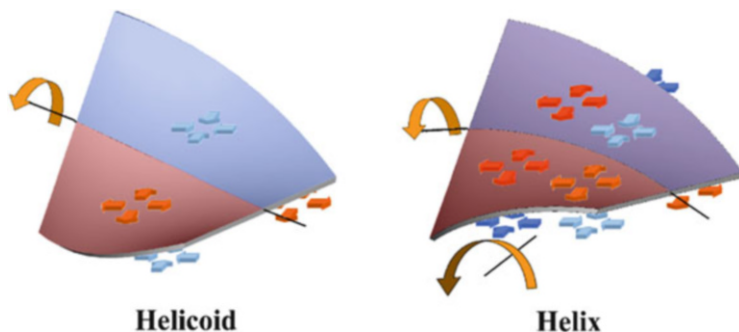


Fig. 13 Unbalanced surface stresses resulting in different 3D crystal shapes such as helicoid (*left*) and helix (*right*). Different tones of *red* and *blue* and different numbers of *arrows* express the variation in absolute values of the positive (*red*) and negative (*blue*) stresses operating at the interface

To envisage possible reasons for such an unusual lamella shape, the main arguments of the KP-model [19] should be recalled. The pattern of surface stresses making a flat lamella twist into the typical helicoidal shape contains two halves with opposite locations of positive and negative surface stresses (cf. Fig. 13, left). These unbalanced stresses on each of the halves induce opposite bending moments and give rise to the overall twist. In the case of a helix (cf. Fig. 13, right), the surface stresses should generate an additional curvature of the ribbon.

To curve the long lamella axis, the surface stresses acting on the two lamella halves have to be unbalanced, not only in terms of their sign but also in terms of their absolute value. This can be achieved, for example, by combining the stress distribution patterns pertinent to the helicoid and scroll (cf. Fig. 14). The implications of the helical crystal shape are in contradiction to the well-established paradigm of spherulitic microstructure, as described in Sect. 1. Indeed, in this case, the growth direction of the crystals is no longer radial. In the other words, the spherulites formed from such crystals are not radially symmetric. Instead, they are tilted away from the radial direction by the corresponding opening helix angle, which in this case equals approximately 30° . Therefore, the banded spherulites of PPA do not exhibit a radially symmetric texture, which is at variance with the classical view of polymer spherulite morphogenesis.

In subsection 3.1 dedicated to the HDPE banded spherulite morphology, it was mentioned that it was not possible to extract a correlation between lamellar chirality and growth axis polarity because of the high symmetry of the HDPE unit cell. Such a correlation could, nevertheless, be very interesting to address. To circumvent this limitation, one can consider banded spherulites formed by polymers of lower crystal symmetry. One of the most studied examples of such low crystal symmetry polymers forming magnificent banded spherulites is PTT, which will be discussed next.

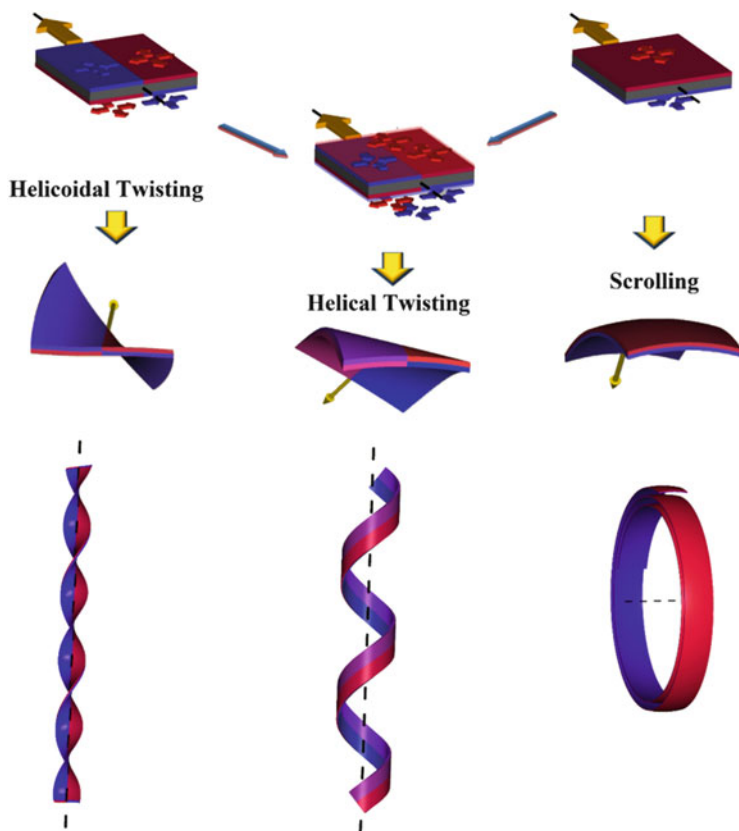
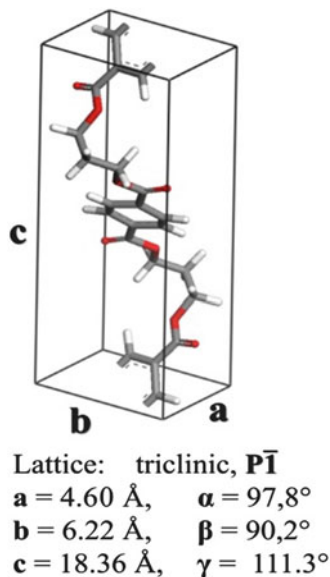


Fig. 14 Surface stress distributions giving rise to different 3D shapes of the twisting lamellae such as helicoid (*left*) and scroll (*right*). Superposition of the stresses pertinent to these two extreme cases results in formation of a flat-on helical ribbon (*middle*)

3.3 Poly(trimethylene terephthalate)

The chemical structure of PTT lies between that of the “even”-numbered polymers poly(ethylene terephthalate) (PET) and poly(butylene terephthalate) (PBT). It was only in 1998 that PTT became commercially available as a result of development of new technology for production of 1,3-propanediol via hydroformylation of ethylene oxide [45]. The interest in PTT is explained by its excellent elastic deformation recovery, which is unmatched by the homologous aryl-polyesters [46]. Selected-area electron diffraction (SAED) data collected by Poulin-Dandurand and co-authors [47] on PTT single crystals formed from dilute solutions showed that the dominating growth axis corresponds to the a -direction [47], similar to what was found for PTT melt crystallization [48]. The molecular model of the PTT unit cell and its structural parameters are given in Fig. 15. According to Cheng and

Fig. 15 Molecular model of the PTT triclinic unit cell with the parameters indicated



co-authors [49], the best estimates for PTT unit cell parameters were given by Hall [50] ($a = 4.600 \text{ \AA}$, $b = 6.220 \text{ \AA}$, $c = 18.360 \text{ \AA}$, $\alpha = 97.8^\circ$, $\beta = 90.2^\circ$, and $\gamma = 111.3^\circ$, resulting in a lattice density of $1,414 \text{ g cm}^{-3}$). The latter is used for analysis of PTT X-ray nanofocus data in this work.

The banded spherulite morphology of PTT was addressed in the past by combination of polarized light microscopy, AFM, and electron microscopy coupled with SAED [48, 51–54]. Correlation of the banded spherulite texture with crystallization temperature was attempted by describing the dependence of band spacing with a power-law function. Chuang and co-authors [53] found that the critical exponent equals 0.5, which can be compared with the well-known critical exponent of the order parameter in the mean-field theory of equilibrium phase transitions [55, 56]. However, not everything is set in the description of the banding behavior of PTT. Indeed, Chuang and co-authors observed that the banded–nonbanded transition (BNB) for PTT occurs at 195°C on the low-temperature side and at about 215°C on the high-temperature side [51]. The results of Chuang and Hong [51, 53] are, however, significantly different from those in other reports on PTT. Wu and Woo [57] reported that the BNB transitions of PTT occur at 150°C and 215°C . By contrast, in the work of Wang and co-authors [48], the temperature window of the banded morphology is reduced to $135\text{--}165^\circ\text{C}$. Therefore, for unknown reasons, the existing literature data on PTT banding is far from consistent.

It is worth noting in passing that, when one examines the banded textures of PTT in crossed polars, the spherulites have a striking colorful appearance. Importantly, the color patterns are observed without addition of any light retardation elements. Such behavior is not typical for polymers forming banded spherulites and is

explained by the high birefringence of PTT, which has been discussed by Yun and co-authors [58, 59] and Chen and co-authors [60].

To clarify the banded spherulite morphology of PTT, we conducted nanofocus X-ray scattering experiments on commercial-grade PTT (Corterra LP 509200, Shell). The M_n is about $17,300 \text{ g mol}^{-1}$ and M_w $35,200 \text{ g mol}^{-1}$. The samples were prepared between cover glass slides, resulting in films approximately $20 \mu\text{m}$ thick, and melt-crystallized isothermally at $130\text{--}205^\circ\text{C}$. A short dwelling time in the melt (e.g., 2 min at 260°C) was used to erase the structural memory before isothermal crystallization. Upon cooling to room temperature, free-standing films were obtained by immersing the films in 1% aqueous solution of HF for 24 h.

The case of a banded spherulite of PTT was used to explain the experimental methodology. Therefore, it is already clear to the reader that the texture of PTT banded spherulites generates highly oriented X-ray patterns. Analysis of the sequence of appearance of diffraction peaks along the spherulite radius confirmed that the lamella twist in PTT is regular and uniform. The phase angle of the SAXS signal with respect to the 010 reflection was 84° , which corresponds to inclination of the ab -plane by about 12° in the positive b -direction with respect to the lamella basal plane. This signifies that the chain tilt is about 4° in this direction, as shown in Fig. 8 (bottom right).

As can be grasped from the schematics of Fig. 8, the established correlations formally satisfy the underlying assumption of the KP-model. However, despite agreement with the KP-model, a chain tilt of 4° does not appear sufficient for generation of the surface stresses required for twisted lamellar growth. Moreover, examination of the PTT morphologies formed at different crystallization temperatures and, in particular, dependence of the spherulite bandwidth on T_c (cf. Fig. 16, left), reveals a very interesting behavior that was not documented before. Instead of a common monotonically increasing trend, which would reflect simple stiffening of the lamella crystals with increasing T_c (cf. dashed line in Fig. 16, left), one observes

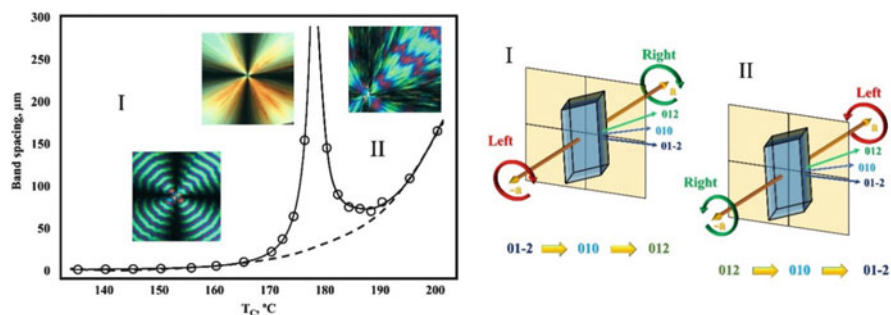


Fig. 16 Left: Band spacing for isothermally crystallized spherulites of PTT as a function of crystallization temperature. In low-temperature *region I*, the band spacing strongly increases, becoming virtually infinite at a “critical” temperature T_{CR} . By contrast, in the high-temperature *region II* the band spacing first decreases and then starts to increase slightly. *Insets* show the spherulitic morphologies formed in temperature *regions I* and *II* and in the proximity of T_{CR} . Right: Order of appearance of diffraction peaks for right- and left-handed helicoids of PTT

a pronounced nonmonotonic dependence where the band spacing strongly increases on the low-temperature side, reaching a virtually infinite value at a “critical” temperature T_{CR} of about 180°C. Above this temperature, the bandwidth first decreases and then starts increasing again, but at a slower pace. It is clear that such behavior cannot be explained, for example, by the model describing banding as a sequence of successive isochiral screw dislocations activated by thermal fluctuations, as initially proposed by Basset and Hodge [14] and further developed by Toda and colleagues [17, 18, 61, 62]. The successive isochiral screw dislocations result in a macroscopic isochiral twist of the lamella crystal, which occurs in the form of the so-called Eshelby twist [63]. However, the mechanics of lamella crystal formation by these mechanisms can only account for a strictly monotonic increase in bandwidth with crystallization temperature and, therefore, are not fully applicable for the banding of PTT.

The unusual banding behavior of PTT certainly deserves special investigation because it could bring new insights into the phenomenon of spherulite banding in general. Also, the example of PTT could help to verify the predictive power of the KP-model for such typical aromatic polyesters, that is, for polymers with structure and properties very different from those of HDPE (for which the KP-model was initially developed). To this end, we performed nanofocus X-ray scanning on PTT spherulites formed below and above T_{CR} . To more easily understand the microstructure of the hybrid left–right helicoids of PTT, the sequences of appearance of diffraction peaks for left-handed and right-handed helicoids are given in Fig. 16 (right). In contrast to HDPE, determination of the growth axis polarity (i.e., distinction between the a and $-a$ growth axes) is possible for the triclinic unit cell of PTT because the equatorial peaks 012 and 01-2 show up at different rotation angles of the crystal. This means that, for the same handedness of the PTT helicoid, the relative appearance order of these peaks allows unambiguous determination of the sign of the growth axis.

Switching the right- to left-handed twist of the PTT helicoid implies inversion of the peak sequence from 01-2 \rightarrow 010 \rightarrow 012 to 012 \rightarrow 010 \rightarrow 01-2, which occurs at the spherulite center. However, detailed examination of the PTT spherulite microstructure formed below and above the critical temperature T_{CR} indicates that the chirality of the lamellae formed at these two temperatures are intrinsically different and cannot be reduced exclusively to the switch in lamella handedness. The schematics given in the right panel of Fig. 16 is valid only for PTT crystallized within temperature region I. At higher crystallization temperatures, the same hand of the lamellar twist no longer corresponds to the same growth axis polarity, as illustrated in Fig. 17. More specifically, the lamellae formed below T_{CR} are characterized by the chiral parameter pairs (R, $-a$) and (L, a), whereas those formed above this temperature have the other possible two-parameter combinations, (R, a) and (L, $-a$).

It is important to mention that the chain tilt is practically independent of the crystallization temperature, being equal to about 4.0° with a standard deviation of less than 2.0° (not shown here). This means that the crystalline stems remains almost vertical in the lamellar crystal at crystallization temperatures. In particular,

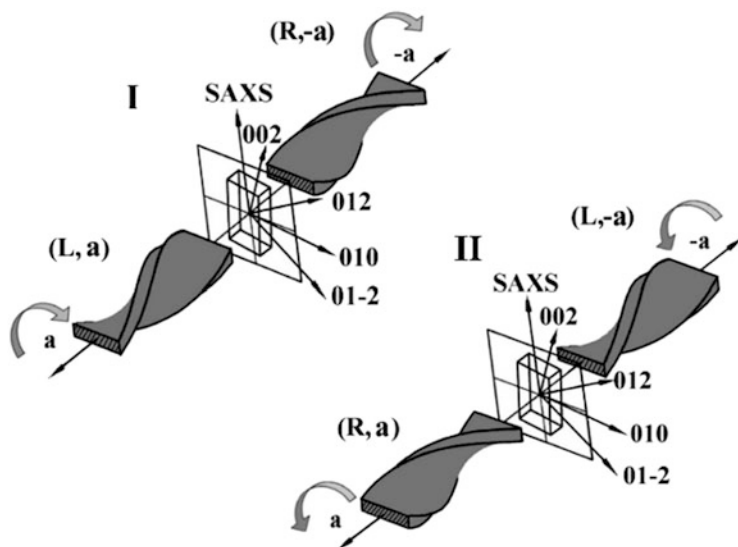


Fig. 17 Lamellar twist of PTT melt-crystallized at 170 (case I) and 190°C (cases II). The pairs of chiral parameters characterizing the state of the twisting lamellae are given by (L/R, $-/+a$). The lamellae formed within temperature regions I and II have different pairs of chiral parameters: (R, $-a$) and (L, a) for region I and (R, a) and (L, $-a$) for region II. See text for more details

the chain tilt does not appreciably change its value across the chirality inversion point T_{CR} . Therefore, upon scrutiny, the premise of the KP-model linking helicoid handedness with chain tilt direction is found to be generally incorrect for PTT. The particular banding behavior of PTT, which exhibits a switch in lamella chirality, results in two opposite situations for correlation of the twist hand with chain tilt. If, even in the low-temperature region, the premise of the KP-model is formally satisfied, this is no longer the case for the high-temperature crystallization region. Therefore, this extended investigation confirms our previous [28] suggestion that a chain tilt of 4° does not appear to be sufficient reason for generation of the surface stresses required for twisted lamellar growth [29]. It is noteworthy that such chirality inversions bear some similarity to the mechanism suggested by Samulski and co-authors for formation of cholesteric liquid crystals [64]. However, despite the fact that, in both cases, the lamella twist is governed by intermolecular interactions, in the case of semicrystalline PTT the system is trapped in a metastable state and would not exhibit any structural evolution without significant perturbation such as an increase in temperature (see further in this section).

To rationalize the observed twisting behavior of PTT crystals, one can consider the chain conformation in crystals containing rigid terephthalic units alternating with flexible propyl moieties. Figure 18 emphasizes the difference between PTT lamella crystals formed at two selected crystallization temperatures of 160°C and 200°C (i.e., in the temperature regions I and II, respectively). The rigid parts of the chain form straight segments, as emphasized by the brown parallelepipeds. The soft

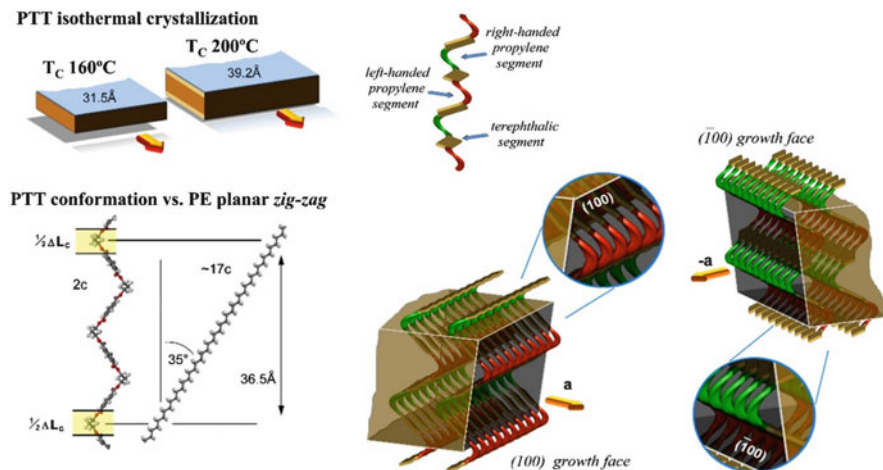


Figure 18 Molecular models of PTT lamellae illustrating switching of chirality at the critical crystallization temperature. *Top left:* PTT lamellae isothermally grown at 160°C and 200°C, i.e., in temperature regions I and II, respectively. *Bottom left:* Comparison of the chain conformations of PTT and HDPE. The difference in thickness of the PTT lamellae formed at the two temperatures is highlighted in yellow. *Right:* PTT crystalline conformation showing rigid terephthalic moieties and flexible propylene segments having left- (green) and right-handed (red) conformations. The two growth planes of PTT have propylene segments of opposite chirality protruding from the surface

segments form alternating right- and left-handed helical sequences (highlighted in red and green, respectively).

The difference in thickness of the crystals of about 8 Å is transposed onto the molecular conformation of PTT in Fig. 18 (bottom right). The sketch depicting the borders of the corresponding lamella crystals assumes that the lamella surface is exclusively composed of flexible segments. It is noteworthy that the unit cell of PTT is large along the c -parameter (ca. 18 Å), especially compared with the typical thickness of PTT lamella (ca. 5 nm) [65, 66]. If one neglects the small overall tilt of the chain stems discussed above, the projection of one soft segment onto the c -axis is estimated to be equal to ca. 24% of the c -parameter, and the hard segment covers the remaining half of the c -parameter (i.e., 26%). This is at variance with the case of PE, shown in Fig. 18 for comparison. Lamellae of HDPE contain several tens of unit cells along the thickness direction. In addition, the size of the HDPE zigzag is much smaller than that of PTT. Therefore, it is understandable that any variation in HDPE lamella thickness with crystallization temperature hardly affects chain conformation at the crystal–amorphous interphase, because even minor roughness of the lamella basal plane completely smears out the configuration of the PE segments protruding from the lamella surface as a result of the small size of the molecular zigzag. In the case of PTT, all variation in lamellar thickness in the range of crystallization temperatures of 160–200°C is encompassed by the length of two flexible segments. It is thus logical to assume that the configuration of PTT

segments protruding from the lamella surface is a key factor in defining lamella twisted growth from the point of view of interfacial stresses. Indeed, it is generally admitted that, for the family of semirigid chain polymers, the crystalline core is intimately linked to the amorphous region by a flux of chains emanating from the crystal surface [67–69]. Accordingly, a reduction in the fraction of folds at the surface of semirigid chain crystals has been shown in computer simulations using the Bragg–Williams mean-field approximation [70, 71]. It is therefore quite probable that the angle at which the outmost segment of the crystalline stem protrudes from the lamella surface is important for the absolute value and sign of the interfacial stresses, similar to the assumption underlying the KP-model. One can clearly see from Fig. 18 that the angle between the protruding segment and the lamella surface significantly changes when the crystallization temperature is changed from 160°C to 200°C, which can account for the particular banding behavior of PTT. It is then expected that the stresses generated at the interface change their sign by passing through the critical crystallization temperature, which results in a strongly nonmonotonic behavior of the bandwidth.

The right-hand panel of Fig. 18 shows the two growth faces of PTT (i.e., the 100 and -100 planes). As mentioned above, the banded spherulites of PTT are predominantly composed of hybrid left- and right-handed helicoids, forming two spherulite hemispheres. The topology of the growing faces in such objects differs from the point of view of chirality: the 100 face contains only right-handed flexible propylene sequences protruding from the surface, whereas the symmetric -100 face is built of left-handed protruding segments. It is clear that, although the topology of the two faces is different, the growth rates of the PTT crystals along the 100 and -100 directions are very similar, which is manifested by the circular symmetry of the spherulites. Inversion of the growth face chirality is reflected by the only symmetry operation of the PTT unit cell (P-1), the central symmetry operation. The latter inverts the chirality of the respective conformations. In the context of lamella chirality inversion across T_{CR} , it is clear that it is not the chirality of the growth face topography that determines lamella chirality, because the same growth face induces formation of lamellae with opposite chiralities for crystallization temperature regions I and II.

As discussed later (cf. section 3.5), the symmetry operations of the unit cell can act on much larger spatial scales and can control the chirality of lamella helicoids. In the case of PTT, the simultaneous existence of left- and right-handed halves of lamella helicoids is in agreement with the central symmetry operation of the unit cell.

To conclude the discussion on the morphology and exceptional banding behavior of PTT, it is noteworthy that in the literature the multiple melting behavior of PTT is sometimes associated with its banded spherulite structure [53, 54]. PTT is also known to exhibit very interesting thermal behavior, characterized by extensive reorganization on heating. It often reveals multiple melting peaks and sometimes even an exothermic recrystallization peak, which is exceptional for aromatic polyesters [72]. In-situ studies of the evolution of the semicrystalline structure of PTT on heating are expected to provide new insights into the mechanisms of twisted

lamellar growth and the physics of the crystallization process in general. In this respect, an in-situ combination of ultrafast nanocalorimetry and high-detection-rate synchrotron microfocus X-ray scattering (the technique being developed by our group [73, 74]) targets the mechanisms of fast reorganization processes, which were previously experimentally inaccessible [75–77]. The possibility of applying very high heating rates ($1,000 \text{ K s}^{-1}$ and higher) in situ and being able to simultaneously acquire X-ray diffraction patterns at kilohertz frequencies makes it possible to obtain deeper understanding of the reorganization processes. Importantly, experiments can be performed repeatedly on the same submicron-sized region of the sample, which was only possible in the past using AFM [78–81].

3.4 Poly(3-hydroxybutyrate)

The discussion on banded polymer morphology presented above was entirely focused on achiral polymers. It was shown that the banded spherulites of such polymers are composed of generally achiral helicoids, which are in fact hybrid left- and right-handed helicoids. On the other hand, it is well documented that chiral polymers form helicoids of only one hand. Examples of structures formed by a chiral polymer, PHB, are given in Fig. 19. It is known that in the crystalline state PHB forms left-handed molecular helices [21, 82] and that chirality of the lamella helicoids is invariably left-handed. Previous comparison of PHB and poly(3-hydroxyvalerate) (PHV), both having the same handedness of the molecular

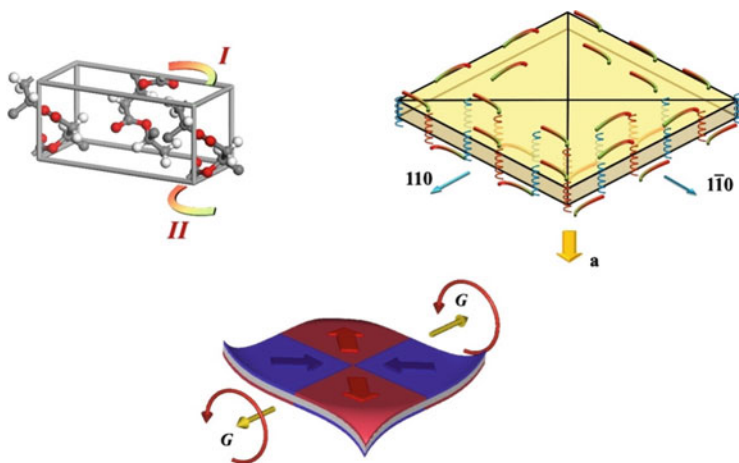


Fig. 19 *Top left:* Molecular model of the unit cell of poly(3-hydroxybutyrate) (PHB). *Top right:* Single crystal of PHB showing distribution of folds having different conformations, which are expected to generate unbalanced stresses on the crystal surface. *Bottom:* Distribution of surface stresses in a single crystal of PHB growing in two opposite directions, creating lamella halves of identical chirality

helices and opposite handedness of the lamella helicoids, indicated that the general correlation between chirality at the molecular and supramolecular levels is not universal [82]. However, it is clear that such conclusions cannot be drawn without careful microstructural analysis of the underlying morphologies. In a later publication [83], it was discovered that PHV is in fact capable of forming both left- and right-handed lamella helicoids, depending on the crystallographic growth direction (i.e., a or b). Although this conclusion is straightforward from the general viewpoint of analytical geometry because the classic helicoid has zero mean curvature, it has an important implication in this particular context that makes the general perspective of correlating chirality at different spatial scales less pessimistic.

Looking at the specific handedness of lamella helicoids formed for a particular polymer, we believe it is important to understand why, for the same crystallographic growth direction, taken both with positive and negative sign, the lamella handedness remains invariable. The unit cell model of PHB given in Fig. 19, containing up- and down-oriented chains, shows the direction of the bonds protruding from the unit cell faces. These are expected to form chain folds with different levels (and/or signs) of interfacial stresses on the lamellar crystal, as shown in the top right panel of Fig. 19. Because the lattice of PHB is chiral (i.e., only symmetry operations preserving chirality are present), the stress pattern generated at opposite tips of the lamella crystal should result in the same handedness of the growing lamella. The surface stresses are sketched in the bottom panel of Fig. 19 for the screw-axis operation present in the unit cell of PHB.

3.5 Correlation of Chiralities at Different Spatial Scales

The ideas about linking chirality at different spatial scales are generalized in Fig. 20. It can be seen that for achiral polymers such as HDPE and PTT, the handedness of the lamella halves symmetric about the spherulite center is always inverted. This fact can be correlated with the symmetry operation of the unit cell, which is central symmetry. Note that the lattice of HDPE is drawn in an unconventional way: the sketch takes into account the chain tilt with respect to the lamella normal, which breaks the high symmetry of the HDPE lattice and results in generation of unbalanced stresses on the lamella surface. Here, instead of the common orthorhombic unit cell, one can imagine a supercell of HDPE that is characterized by monoclinicity in the plane perpendicular to the fast crystal growth direction. Similar to the case of PTT, switching of lamella chirality at the spherulitic center can be accounted for by the central symmetry operation. The situation described for achiral polymers is different for the chiral lattices of PHB and PHV that obviously do not have any chirality-inverting operations. In this case, the two halves of the twisting lamella have identical handedness because the stress distribution patterns on the opposite tips of the growing crystal necessarily have the same chirality. Further studies will be necessary to confirm the proposed relationship between the symmetries of the unit cell and those of lamella helicoids.

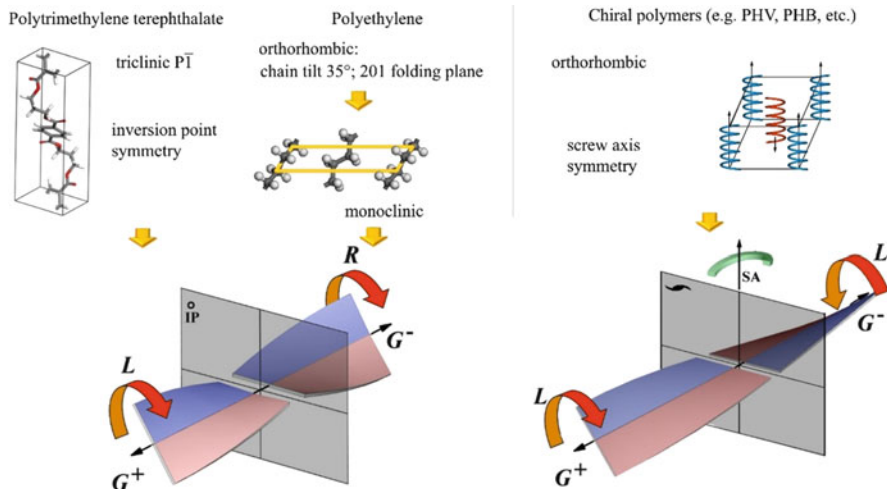


Fig. 20 Correlation of symmetry operations in the unit cell with chirality of twisted lamellae for the case of achiral (HDPE, PTT) and chiral (PHB, PHV) polymers. *Top left*: Molecular models of the unit cells of PTT and HDPE. For HDPE, a supercell is drawn instead of the conventional orthorhombic lattice, which takes into account the chain tilt in the lamella. *Top right*: Molecular conformations in the unit cells of chiral polymers such as PHB and PHV. *Bottom*: Symmetry operations of the unit cell are extrapolated on the correlation linking chirality of the lamella halves, symmetric about the spherulite center. The fact that PHV can form both left- and right-handed helicoids is omitted for the sake of simplicity

4 Conclusions

This paper describes the microstructure of several semicrystalline commodity polymers such as HDPE, PTT, PVDF, and PHB that exhibit banded spherulite morphology. It is noteworthy that the internal structural organization and 3D shape of the constitutive crystalline lamellae in such morphologies have long been a topic of interest in polymer physics. We show the capacity of synchrotron-based nanofocus X-ray scattering for microstructural analysis of such polymer morphologies. In particular, we explain the methodology of X-ray nanobeam experiments and the ways of interpreting the arrays of microdiffractograms acquired along the spherulitic radius. The developed analysis unambiguously shows that in the studied cases the process of crystal twisting occurring during radial outward growth is regular and uniform. Moreover, the proposed analysis makes it possible to obtain insights into such fine structural parameters as chain tilt with respect to the lamellar normal, twisted lamella chirality, and lamella shape. The access to such rich microstructural information makes it possible to better understand twisted growth mechanisms and, for example, to check the premises of the model of Keith and Padden. Importantly, X-ray data provide support for the view of banded spherulite morphology as having single-crystalline character at the local scale. For example,

the direction of chain tilt in the lamellae of poly(ethylene) was found to be invariant across the whole lamellar stack. In addition, in-depth analysis of microdiffraction data gives more general conclusions concerning the chiralities pertinent to different spatial scales and their interrelationship.

Acknowledgements The authors thank the Ministry of Education and Science of the Russian Federation (contract № 14.604.21.0079 (RFMEFI60414X0079) of 30 June 2014. The authors acknowledge Manfred Burghammer from the ID13 beamline of the ESRF for excellent technical support and valuable discussions, and thank Bernard Lotz for donation of the Sclair sample.

References

1. Bassett DC (2003) Polymer spherulites: a modern assessment. *J Macromol Sci Part B Phys* 42:227–256
2. Talbot WHF (1837) On the Optical Phenomena of Certain Crystals. *Philos Trans R Soc London* 127:25
3. Knoll PM, Kelker H (2010) Otto Lehmann: Researcher of the liquid crystals. Books on Demand GmbH, Norderstedt
4. Shtukenberg AG PYO, Gunn E KB (2012) Spherulites. *Chem Rev* 112:1805–1838
5. Keller A (1958) Morphology of crystalline polymers. In: Turnbull D, Doremus RH, Roberts BW (eds) *Growth and perfection of crystals*. Chichester, Wiley Interscience, pp 499–528
6. Keller A (1959) The morphology of crystalline polymers. *Makromol Chem* 34:1–28
7. Fujiwara Y (1960) Superstructure of melt-crystallized polyethylene (1) screwlike orientation of the unit cell in polyethylene spherulites with periodic extinction rings. *J Appl Polym Sci* 4:10–15
8. Seiler DA (1998) *Modern fluoropolymers*, 2nd edn. Wiley, Chichester
9. Lovinger AJ (1981) *Developments in crystalline polymers*. Applied Science, London
10. Gianotti G, Capizzi A, Zamboni V (1973) New aspects of polymorphism in poly(vinylidene fluoride). Relations between morphology and reaction kinetics. *Chim Ind* 55:501
11. Prest Jr WM, Luca DJ (1975) The morphology and thermal response of high-temperature-crystallized poly(vinylidene fluoride). *J Appl Phys* 46:4136–4143
12. Keith HD, Lovinger AJ (1979) Electron diffraction investigation of a high-temperature form of poly(vinylidene fluoride). *Macromolecules* 12:919–924
13. Garcia-Ruiz JM, Melero E, Hyde S (2009) Morphogenesis of self-assembled nanocrystalline materials of barium carbonate and silica. *Science* 323:362–365
14. Bassett DC, Hodge AM (1978) On lamellar organization in certain polyethylene spherulites. *Proc R Soc Lond A* 359:121–132
15. Bassett DC, Hodge AM (1981) On the morphology of melt-crystallized polyethylene. III. Spherulitic organization. *Proc R Soc Lond A* 377:61–71
16. Bassett DC, Hodge AM (1978) On lamellar organization in banded spherulites of polyethylene. *Polymer* 19:469–472
17. Toda A, Arita T, Hikosaka M (2001) Three-dimensional morphology of PVDF single crystals forming banded spherulites. *Polymer* 42:2223–2233
18. Toda A, Keller A (1993) Growth of polyethylene single crystals from the melt: morphology. *Colloid Polym Sci* 271:328–342
19. Keith HD, Padden FJ (1984) Twisting orientation and the role of transient states in polymer crystallization. *Polymer* 25:28–42
20. Keith HD (2001) Banding in spherulites: two recurring topics. *Polymer* 42:9987–9993

21. Cheng SZD, Lotz B (2005) A critical assessment of unbalanced surface stresses as the mechanical origin of twisting and scrolling of polymer crystals. *Polymer* 46:577–610
22. Gazzano M, Focarete ML, Riekel C, Scandola M (2004) Structural study of poly(L-lactic acid) spherulites. *Biomacromolecules* 5:553–558
23. Gazzano M, Focarete ML, Riekel C, Scandola M (2000) Bacterial poly(3-hydroxybutyrate): an optical microscopy and microfocus X-ray diffraction study. *Biomacromolecules* 1:604–608
24. Focarete ML, Gazzano M, Ripamonti A, Riekel C, Scandola M (2001) Structural investigation of poly(3-hydroxybutyrate) spherulites by microfocus X-ray diffraction. *Macromol Chem Phys* 202:1405–1409
25. Kajioaka H, Yoshimoto S, Gosh RC, Taguchi K, Tanaka S, Toda A (2010) Microbeam X-ray diffraction of non-banded polymer spherulites of it-polystyrene and it-poly (butene-1). *Polymer* 51:1837–1844
26. Rosenthal M, Bar G, Burghammer M, Ivanov DA (2011) On the nature of chirality imparted to achiral polymers by the crystallization process. *Angew Chem Int Ed Engl* 123:9043–9047
27. Rosenthal M, Anokhin DV, Luchnikov VA, Davies RJ, Riekel C, Burghammer M, Bar G, Ivanov DA (2010) Microstructure of banded polymer spherulites: studies with micro-focus X-ray diffraction. *IOP Conf Ser: Mater Sci Eng* 14:012014
28. Rosenthal M, Burghammer M, Portale G, Bar G, Samulski ET, Ivanov DA (2012) Exploring the origin of crystalline lamella twist in semi-rigid chain polymers: the model of Keith and Padden revisited. *Macromolecules* 45:7454–7460
29. Rosenthal M, Burghammer M, Bar G, Samulski ET, Ivanov DA (2014) Switching chirality of hybrid left–right crystalline helicoids built of achiral polymer chains: when right to left becomes left to right. *Macromolecules* 47:8295–8304
30. Rosenthal M, Hernandez JJ, Odarchenko YI, Soccio M, Lotti N, Di Cola E, Burghammer M, Ivanov DA (2013) Non-radial growth of helical homopolymer crystals: breaking the paradigm of the polymer spherulite microstructure. *Macromol Rapid Commun* 34:1815–1819
31. Nozue Y, Hirano S, Kurita R, Kawasaki N, Ueno S, Iida A, Nishi T, Amemiya Y (2004) Co-existing handednesses of lamella twisting in one spherulite observed with scanning micro-beam wide-angle X-ray scattering. *Polymer* 45:8299–8302
32. Luchnikov VA, Ivanov DA (2009) Micro-beam X-ray diffraction from twisted lamellar crystals: theory and computer simulation. *J Appl Crystallogr* 42:673–680
33. Luchnikov VA, Ivanov DA (2010) Theory of geometrical broadening of diffraction peaks from twisted lamellar crystals for interpretation of X-ray micro-beam and selected-area electron diffraction experiments. *J Appl Crystallogr* 43:578–586
34. Luchnikov VA, Anokhin DV, Bar G, Cheng SZD, Wang CL, Ivanov DA (2011) Theory of X-ray reflection broadening for textures with double-axis averaging: from semicrystalline polymers exhibiting twisted lamellar growth to discotic liquid crystals. *J Appl Crystallogr* 44:540–544
35. Polanyi M (1921) The X-ray fiber diagram. *Z Phys* 7:149–180
36. Geil PH (1963) *Polymer single crystals*. Interscience (Wiley), New York
37. Magonov SN, Yerina NA, Ungar G, Reneker DH, Ivanov DA (2003) Chain unfolding in single crystals of ultra long alkane C390H782 and polyethylene: an atomic force microscopy study. *Macromolecules* 36:5637–5649
38. Hocquet S, Dosière M, Thierry A, Lotz B, Koch MHJ, Dubreuil N, Ivanov DA (2003) Morphology and melting of truncated single crystals of linear polyethylene. *Macromolecules* 36:8376–8384
39. Dubreuil N, Hocquet S, Dosière M, Ivanov DA (2004) Melting of isochronously decorated single crystal of linear polyethylene, as monitored with atomic force microscopy. *Macromolecules* 37:1–5
40. Toda A, Arita T, Hikosaka M, Hobbs JK, Miles MJ (2003) An atomic force microscopy observation of PVDF banded spherulites. *J Macromol Sci Part B* 42:753–760
41. Gunn E, Sours R, Benedict JB, Kaminsky W, Kahr B (2006) Mesoscale chiroptics of rhythmic precipitates. *J Am Chem Soc* 128:14234–14235

42. Gedde UW (1995) *Polymer physics*. Chapman & Hall, London
43. Soccio M, Lotti N, Finelli L, Gazzano M, Munari A (2007) Aliphatic poly(propylene dicarboxylate)s: effect of chain length on thermal properties and crystallization kinetics. *Polymer* 48:3125–3136
44. Keith HD, Padden FJ Jr (1959) The optical behavior of spherulites in crystalline polymers. Part I Calculation of theoretical extinction patterns in spherulites with twisting crystalline orientation. *J Polym Sci* 39:101–122
45. Chuah HH (2001) Crystallization kinetics of poly(trimethylene terephthalate). *Polym Eng Sci* 41:308–313
46. Ward IM, Wilding MA, Brody H (1976) The mechanical properties and structure of poly(m-methylene terephthalate) fibers. *J Polym Sci Polym Phys Ed* 14:263–274
47. Poulin-Dandurand S, Pérez S, Revol JF, Brisse F (1979) The crystal structure of poly(trimethylene terephthalate) by X-ray and electron diffraction. *Polymer* 20:419–426
48. Wang B, Li CY, Hanzlicek J, Cheng SZD, Geil PH, Grebowicz J, Ho RM (2001) Poly(trimethyleneterephthalate) crystal structure and morphology in different length scales. *Polymer* 42:7171–7180
49. Yang J, Sidoti G, Liu J, Geil PH, Li CY, Cheng SZD (2000) Morphology and crystal structure of CTFMP and bulk polymerized poly(trimethylene terephthalate). *Polymer* 42:7181–7195
50. Hall IH (1984) *Structure of crystalline polymers*. Elsevier, London, p 39
51. Hong PD, Chung WT, Hsu CF (2002) Crystallization kinetics and morphology of poly(trimethylene terephthalate). *Polymer* 43:3335–3354
52. Ho RM, Ke KZ, Chen M (2000) Crystal structure and banded spherulite of poly(trimethylene terephthalate). *Macromolecules* 33:7529–7537
53. Chuang W-T, Hong P-D, Chuah HH (2004) Effects of crystallization behavior on morphological change in poly(trimethylene terephthalate) spherulites. *Polymer* 45:2413–2425
54. Wu PL, Woo EM (2003) Correlation between melting behavior and ringed spherulites in poly(trimethylene terephthalate). *J Polym Sci Part B: Polym Phys* 41:80–93
55. Sornette D (2006) *Critical phenomena in natural science*. Springer, New York
56. Auyang SY (1998) *Foundations of complex system theories*. Cambridge University Press, New York
57. Wu PL, Woo EM (2002) Linear versus nonlinear determinations of equilibrium melting temperatures of poly(trimethylene terephthalate) and miscible blend with poly(ether imide) exhibiting multiple melting peaks. *J Polym Sci Part B: Polym Phys* 40:1571–1581
58. Yun HJ, Kuboyama K, Chiba T, Ougizawa T (2006) Crystallization temperature dependence of interference color and morphology in poly(trimethylene terephthalate) spherulite. *Polymer* 47:4831–4838
59. Yun JH, Kuboyama K, Ougizawa T (2006) High birefringence of poly(trimethylene terephthalate) spherulite. *Polymer* 47:1715–1721
60. Chen YF, Woo EM, Wu PL (2007) Alternating-layered spherulites in thin-film poly(trimethylene terephthalate) by stepwise crystallization schemes. *Mater Lett* 61:4911–4915
61. Toda A, Okamura M, Taguchi K, Hikosaka M, Kajioaka H (2008) Branching and higher order structure in banded polyethylene spherulites. *Macromolecules* 41:2484–2493
62. Toda A, Taguchi K, Kajioaka H (2008) Instability-driven branching of lamellar crystals in polyethylene spherulites. *Macromolecules* 41:7505–7512
63. Eshelby JD (1953) Screw dislocations in thin rods. *J Appl Phys* 24:176–179
64. Duke RW, DuPre DB, Samulski ET (1977) Temperature dependence of orientational order in a polypeptide liquid crystal. *J Chem Phys* 66:2748–2749
65. Ivanov DA, Bar G, Dosière M, Koch MHJ (2008) A novel view on crystallization and melting of semirigid chain polymers: The case of poly(trimethylene terephthalate). *Macromolecules* 41:9224–9231
66. Ivanov DA, Hocquet S, Dosière M, Koch M (2004) Exploring the melting of a semirigid chain polymer with synchrotron time- and temperature-resolved small-angle X-ray scattering. *Eur Phys J E* 13:363–378

67. Ivanov DA, Legras R, Jonas AM (1999) The crystallization of poly(aryl-ether-ether-ketone) (PEEK). Interdependence between the evolution of amorphous and crystalline regions during isothermal cold-crystallization. *Macromolecules* 32:1582–1592
68. Ivanov DA, Jonas AM, Legras R (2000) The crystallization of poly(aryl-ether-ether-ketone) (PEEK). Reorganization processes during gradual reheating of cold-crystallized samples. *Polymer* 41:3719–3727
69. Ivanov D, Pop T, Yoon D, Jonas A (2002) Direct space detection of order-disorder interphases at crystalline-amorphous boundaries in a semicrystalline polymer. *Macromolecules* 35:9813–9818
70. Kumar SK, Yoon DY (1989) Lattice model for interphases in binary semicrystalline/amorphous polymer blends. *Macromolecules* 22:4098–4101
71. Kumar SK, Yoon DY (1991) A lattice model for interphases in binary semicrystalline/amorphous polymer blends. 2. Effects of tight fold energy. *Macromolecules* 24:5414–5420
72. Amalou Z (2006) Contribution à l'étude de la structure semi-cristalline des polymères à chaînes semi-rigides. Thesis. Université Libre de Bruxelles, Brussels, Belgium
73. Rosenthal M, Doblas D, Hernandez JJ, Odarchenko YaI, Burghammer M, Di Cola E, Spitzer D, Antipov AE, Aldoshin LS, Ivanov DA (2014) High-resolution thermal imaging with a combination of nano-focus X-ray diffraction and ultra-fast chip calorimetry. *J Synchrotron Radiat* 21:223–228
74. Riekel C, Di Cola E, Burghammer M, Reynolds M, Rosenthal M, Doblas D, Ivanov DA (2015) Thermal transformations of self-assembled gold glyconanoparticles probed by combined nanocalorimetry and X-ray nanobeam scattering. *Langmuir* 31:529–534
75. Melnikov AP, Rosenthal M, Rodygin AI, Doblas D, Anokhin DV, Burghammer M, Ivanov DA (2016) Re-exploring the double-melting behavior of semirigid-chain polymers with an in-situ combination of synchrotron nano-focus X-ray scattering and nanocalorimetry. *Eur Polym J* 81:598–606. DOI: [10.1016/j.eurpolymj.2015.12.031](https://doi.org/10.1016/j.eurpolymj.2015.12.031)
76. Rosenthal M, Melnikov AP, Rychkov AA, Doblas D, Anokhin DV, Burghammer M, and Ivanov DA (2016) Design of an in-situ setup combining nanocalorimetry and nano- or micro-focus X-ray scattering to address fast structure formation processes. In: Schick C, Mathot V (eds) *Fast scanning calorimetry*. Springer, Switzerland, pp 299–326
77. Melnikov AP, Rosenthal M, Burghammer M, Anokhin DV, Ivanov DA (2016) Study of melting processes in semicrystalline polymers using a combination of ultrafast chip calorimetry and nanofocus synchrotron X-ray diffraction. *Nanotechnol Russ* 11:305–311. doi:[10.1134/S1995078016030113](https://doi.org/10.1134/S1995078016030113)
78. Ivanov DA, Jonas AM (1998) Isothermal growth and reorganization upon heating of a single poly(aryl-ether-ether-ketone) (PEEK) spherulite, as imaged by atomic force microscopy. *Macromolecules* 31:4546–4550
79. Ivanov DA, Nysten B, Jonas AM (1999) Atomic force microscopy imaging of single polymer spherulites during crystallization: application to a semi-crystalline blend. *Polymer* 40:5899–5905
80. Ivanov DA, Amalou Z, Magonov SN (2001) Real-time evolution of the lamellar organization of poly(ethylene terephthalate) during crystallization from the melt: high-temperature atomic force microscopy study. *Macromolecules* 34:8944–8952
81. Basire C, Ivanov DA (2000) Evolution of the lamellar structure during crystallization of a semicrystalline-amorphous polymer blend: time-resolved hot-stage SPM study. *Phys Rev Lett* 85:5587–5590
82. Saracovan J, Keith HD, Manley RSJ, Brown GR (1999) Banding in spherulites of polymers having uncompensated main-chain chirality. *Macromolecules* 32:8918
83. Ye HM, Xu J, Guo BH, Iwata T (2009) Left- or right-handed lamellar twists in poly[(R)-3-hydroxyvalerate] banded spherulite: dependence on growth axis. *Macromolecules* 42:694–701

Real-Time Fast Structuring of Polymers Using Synchrotron WAXD/SAXS Techniques

Giuseppe Portale, Enrico M. Troisi, Gerrit W.M. Peters, and Wim Bras

Abstract In industrial processes, polymer melts are often exposed to a combination of fast cooling rates, high flow fields, and high pressures. The processing conditions have an ultimate impact on the structure that develops during cooling. The final structure at the nano- and microscopic level determines the properties of the final polymer product. Small and wide angle X-ray scattering and diffraction (SAXS/WAXD) are the best techniques for investigating in-situ and real-time fast polymer structuring at a scale ranging from 0.1 to 100 nm. This contribution reviews the main quantities that can be extracted from SAXS and WAXD experiments on semicrystalline polymers and shows the most recent results on real-time investigation of polymer structuring with millisecond time resolution. Examples of structuring during fast cooling, flow in confined geometry, and uniaxial stretching are discussed. Future directions for the use of synchrotron SAXS/WAXD to study fast polymer structuring are also discussed.

Keywords Millisecond time resolution • Polymer crystallization • Processing • SAXS • Shear induced crystallization • WAXS

G. Portale (✉)

Department of Polymer Chemistry, Zernike Institute for Advanced Materials,
University of Groningen, Nijenborgh 4, 9747 AG Groningen, The Netherlands
e-mail: g.portale@rug.nl

E.M. Troisi and G.W.M. Peters

Department of Mechanical Engineering, Materials Technology Institute,
Eindhoven University of Technology, P.O. Box 513, 5600 MB Eindhoven,
The Netherlands

W. Bras

DUBBLE CRG BM26@ESRF, Netherlands Organization for Scientific Research (NWO),
European Synchrotron Radiation Facility, BP 220, 38043 Grenoble Cedex, France

Contents

1	Introduction	128
2	Methods and Scientific Background	130
2.1	WAXD	131
2.2	SAXS	135
2.3	Detectors	144
3	Recent Examples of Fast Polymer Structuring Studied by SAXS/WAXD	145
3.1	Ballistic Cooling of Propene/Ethylene Copolymers: Influence of Co-monomer Content	145
3.2	Structure Development During Flow-Induced Crystallization of iPP: How Short is Short?	148
3.3	Pressure Rise Effect on Flow-Induced Crystallization in Confined Geometries: Slit Flow	152
3.4	Rheo-SAXS/WAXD, In-situ Extensional Rheology of iPP	156
4	New Challenges and Future Developments	160
	References	162

1 Introduction

Polymer materials are widely used in every-day life, with thousands of applications ranging from automotive to textile industries and from food packaging to medicine. The wide range of properties showed by polymers make plastic the most versatile material available nowadays. The final properties of polymeric samples depend on the chemical composition, chain architecture, and thermomechanical history applied during processing.

Polymers, often called macromolecules, are built up from a large number of monomeric units that are linked together by covalent bonds, forming long polymeric chains. Unlike polymer chains in solution, bulk semicrystalline polymers cannot be simply described by the laws of thermodynamic equilibrium. A polymer chain in the melt is usually found in a coiled state. Chains are mutually interpenetrating, forming so-called entanglements. To form a perfect crystal, the interpenetrated coiled polymer chains would have to fully disentangle and stretch, packing together to form extended-chain polymer crystals. This process is not possible in practice under standard conditions as a result of the high entropy barrier and would require a long time to occur. As a result, when a polymer melt is cooled below its melting temperature, the structure that develops at a given temperature is the one with the maximum rate of formation rather than the structure with the lowest free energy. Chains fold several times in and out of the growing crystal to form an alternated amorphous–crystalline layered structure, typical of semicrystalline polymers. The lamellar nature of semicrystalline polymers was originally established in polyethylene single crystals in 1957 [1, 2]. As a result of the folding mechanism, polymer crystallization is directed by kinetics and therefore kinetic aspects have to be taken into account together with the thermodynamic driving forces. Kinetic control over structure formation plays a central role, especially

when polymers are subjected to external forces (shear, pressure, etc.) and to fast cooling rates.

The combination of changes in the physical conditions experienced by polymeric materials during the most common production processes (e.g., injection molding, film blowing, and fiber spinning) are often extreme. The crystallizing polymer melt is subjected to different cooling rates (often above 100°C/s), high pressures, and high flow rates. During injection molding, for example, the polymer is melted in an extruder and subsequently injected into a cold mold where it solidifies and acquires the mold shape. The particular thermomechanical history to which the polymer melt is subjected determines the formation of complex skin-core morphologies, where the formation of mesomorphic, highly oriented/highly crystalline, and isotropic structures occurs simultaneously [3, 4]. Insights into the influence of the different processing parameters on the final polymer structure is of vital importance for both industry and academy because of their impact on the ultimate properties of the product.

Extensive work has been conducted over the last 60 years following the seminal works by Keller [1, 5], and the basic roles describing polymer crystallization in quiescent conditions are known to a large extent today [6–11]. However, polymer crystallization under industrial conditions is still not fully understood because of the non-ideal conditions, which are difficult to reproduce with laboratory equipment. As a result of the fast cooling rates and high flow fields encountered in polymer processing, structure formation usually lasts only a few seconds. It is thus crucial to develop techniques that allow experiments with subsecond time resolution in order to follow polymer structure formation in real-life conditions. Several techniques with second and millisecond time resolution have been developed through the years with the aim of studying structure formation at different length scales. They include light scattering [12, 13], synchrotron Fourier transform infrared (FTIR) and Raman spectroscopy [14, 15], synchrotron small angle X-ray scattering (SAXS), wide angle X-ray diffraction (WAXD) [16–19], and combinations of two or more techniques [18, 20–23]. Of all these techniques, synchrotron SAXS and WAXD are perhaps the best techniques because of the fast sampling rate achievable and the possibility of performing experiments *in situ* with complex sample environments. Moreover, SAXS and WAXD measurements can be simultaneously conducted to gain information from 0.1 to 100 nm at once, allowing study of the structure and morphology of soft matter and, particularly, polymers. This is the reason why all modern synchrotrons offer SAXS/WAXD beamlines [24–28].

This chapter aims to describe recent developments and results in the field of fast polymer crystallization, followed utilizing real-time SAXS/WAXD with millisecond time resolution. A brief overview of the SAXS and WAXS techniques, along with the main quantities measured for semicrystalline polymers using these two techniques, is given in Sect. 2. This is followed by description of a developed apparatus for real-time studies of polymer crystallization, together with some scientific examples. In particular, we discuss ultrafast ballistic cooling of isotactic polypropylene (iPP)-based copolymers (Sect. 3.1); structure development in iPP during short but high flow pulses (Sect. 3.2); the effect of pressure on flow-induced

crystallization of linear low density polyethylene (LLDPE) (Sect. 3.3); and rheo/SAXS/WAXD investigation of iPP crystallization during uniaxial flow (Sect. 3.4). Finally, we discuss challenging experiments that are currently being developed and future directions in the field of fast polymer structure formation using synchrotron-based scattering techniques.

The examples given here are the results of the last 5 years of collaboration between universities, industries, and synchrotron laboratories. The data were obtained using the beamline BM26B at the European Synchrotron Radiation Facility (ESRF) in Grenoble (France) [26], which is strongly involved in the development of new complex sample environments allowing the study of polymer crystallization in real-time and real-life conditions. The reason for using these data is not that other groups have not worked in this field, but mainly because we are more familiar with these data sets and the way they have been collected.

2 Methods and Scientific Background

Semicrystalline polymers crystallize once cooled below their melting temperature. In quiescent conditions, semicrystalline polymers structure themselves in a hierarchical fashion, forming objects called spherulites that are characterized by different length scales ranging from a nanometer to microns (see Fig. 1). Spherulites are clusters of radially arranged crystalline lamellae separated by amorphous material. Spherulites show optical anisotropy. When observed by polarized optical microscopy (POM), spherulites show the typical Maltese cross (Fig. 1a). Analysis of the sign of the birefringence shows that the polymer chains are always oriented perpendicular to the spherulite radius. Radially growing lamellae can, in some polymers, have regular twisting, creating banded spherulites [29–32].

Figure 1b shows a schematic drawing of the hierarchical structure found in a spherulite, together with the typical length scales. It is thus clear that a single characterization technique is not sufficient for investigating the morphology of semicrystalline polymers. Although spherulite size, shape, and density can be

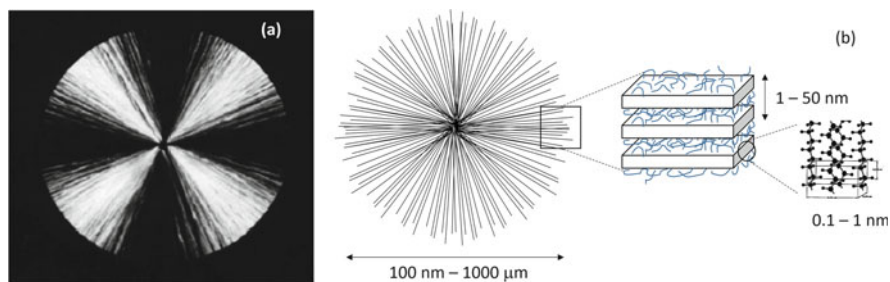
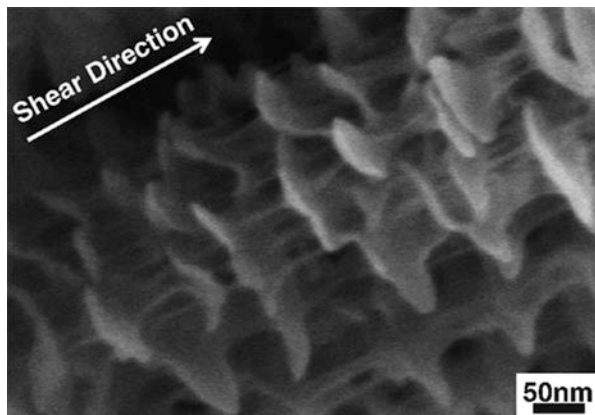


Fig. 1 (a) POM image of a growing polymer spherulite. (b) Hierarchical structure found in a semicrystalline polymer spherulite

Fig. 2 SEM image of a polyethylene shish-kebab structure. Reprint with permission from [35]



measured using POM, the lamellar morphology is better investigated using higher resolution microscopy techniques such as scanning electron microscopy (SEM), transmission electron microscopy (TEM), and atomic force microscopy (AFM).

Polymeric materials are usually processed from the melt. When a polymer melt is cooled below its melting temperature and flow is applied, the longer chains tend to align along the flow direction and are continuously stretched. Anisotropic precursors are formed and develop further, forming crystalline fibrils with nanometer-sized diameter. These fibrils serve as nuclei for further crystallization of lamellae growing perpendicularly to the fibrils. As a result, the crystallization rate is significantly enhanced by flow [33, 34]. Moreover, a drastic change in the morphology occurs and the so-called shish-kebab structure develops (see Fig. 2).

Although spherulite growth can be successfully followed by POM, and lamellar morphology can be studied by AFM and TEM, the development of morphology and chain packing cannot be followed in real time using microscopy techniques. X-ray scattering and diffraction experiments are ideal to follow structure development in the range of 0.1–100 nm. In the following sections, the main characteristics and information that can be extracted from the use of WAXD and SAXS techniques are described.

2.1 WAXD

WAXD is an X-ray diffraction technique that offers the possibility to study structural periodic order with real space repeat distances ranging from interatomic distances to several times the monomeric polymer size, thus enabling determination of the crystalline structure of the studied materials. Polymer chains pack in their crystalline state according to unit cells having typical dimensions falling within the WAXD range. Polyethylene for instance has an orthorhombic unit cell with dimensions $a = 0.742$ nm, $b = 0.495$ nm, and $c = 0.255$ nm [36]. Isotactic polypropylene

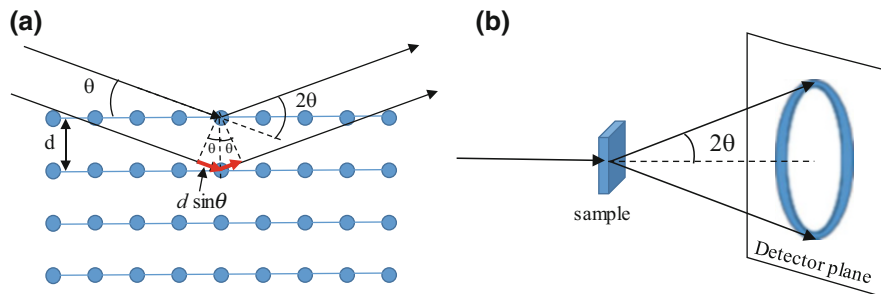


Fig. 3 (a) Scheme of the Bragg diffraction event. An incident plane X-ray wave is scattered from a crystalline lattice in a constructive way. (b) Interception between a diffracting ring with diffraction angle 2θ and the plane of a flat X-ray detector

(iPP) in its most stable α -form shows a monoclinic unit cell with $a = 0.666$ nm, $b = 0.2078$ nm, and $c = 0.6495$ nm [37]. Typically for an isotropically oriented semicrystalline sample with spherulitic morphology (i.e., obtained in quiescent conditions), the WAXD patterns show a certain number of diffraction peaks, whose position and intensity is dictated by the unit cell symmetry and dimensions.

The position of each diffraction peak is related by Bragg's law to the distance between planes containing atoms. The Bragg's formulation considers the diffraction event as originating from the specular reflection of X-ray plane waves by a crystal lattice (see Fig. 3a). Two adjacent X-ray waves are scattered constructively when their path length difference, $2d\sin\theta$, is equal to an integer number of wavelength λ :

$$n\lambda = 2d \sin \theta \quad (1)$$

where n is an integer, d is the interplanar distance, and θ is half of the scattering angle. Bragg's law can also be expressed in terms of the module of the scattering vector q by combining Eq. (1) with Eq. (3).

When a two dimensional (2D) detector is used, WAXD images from spatially isotropic samples show diffraction rings generated by the interception of the diffraction cones and the flat detector plane, as illustrated in Figs. 3b and 4a. Each ring is associated with a lattice plane determined by the three Miller indices hkl . Although a linear detector would render all the required information, in the context of fast experiments, the advantage of using a 2D detector to collect WAXD images is that the exposure time per data frame can be drastically reduced. This is because the signal is simultaneously collected over 360° and can then be integrated, thus improving the statistical quality of the data and allowing fast sampling during the structuring process. Moreover, information about crystal and chain orientation becomes accessible.

A WAXD experiment allows the following information to be obtained: (1) average spacing between diffraction planes, (2) orientation of crystals or grains,

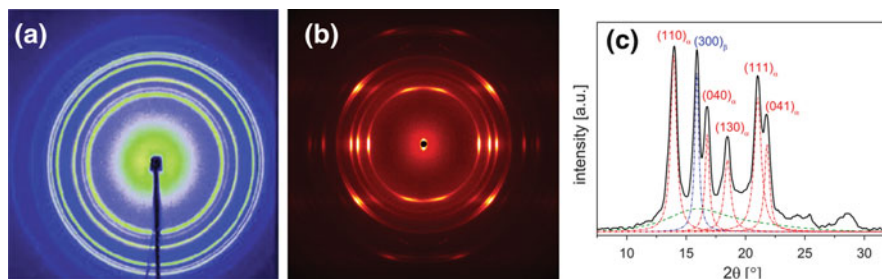


Fig. 4 (a) 2D WAXS image of an isotropic iPP sample in the gamma phase. Image is characterized by diffraction rings, given by the intersection between the scattered cones and a flat 2D detector. (b) 2D WAXS image for an oriented iPP sample. Diffraction signals appear as arcs whose angular spreading depends on the degree of orientation. (c) Procedure for separating the WAXS diffraction peaks from an iPP sample containing α - and β -forms

(3) crystal structure or crystal structures in the case of polymorphic materials, and (4) average size of small crystalline regions.

Figure 4b shows a WAXD image for an oriented iPP sample. Here the diffraction signals are concentrated into diffraction arcs whose orientation is determined by the average orientation of the crystals, and thus of the polymer unit cell, inside the specimen with respect to the incoming beam direction.

When following polymer crystallization in real time, an important parameter is the degree of crystallinity and, for polymorphic materials, the content of the different phases versus temperature and/or time. Because of the semicrystalline nature of polymers, it is impossible to reach 100% crystallinity and the sample always contains a significant portion of amorphous material. The crystallinity can be calculated as the ratio of the area of the diffraction peaks to the total area of the WAXS curve. In practice, deconvolution of the contribution to the scattering pattern of the different crystalline forms and the amorphous material is needed to perform this calculation. Figure 4c illustrates the result of the procedure for separating the multiple diffraction crystalline peaks from the amorphous halo for a typical iPP WAXD pattern. The analyzed sample contains both α - and β -forms of iPP. The WAXD shape of the diffraction peaks can be successfully approximated using Lorentzian or pseudo-Voigt functions. By contrast, the amorphous halo is more difficult to describe by a mathematical function. Although high degree polynomial functions can be used, the best method consists of using the WAXS pattern of a fully amorphous sample. When possible, fully amorphous samples can be obtained by quenching the polymer from its molten state to temperatures well below the glass transition, so that the amorphous halo can be directly measured. Because it is practically impossible to quench iPP to the amorphous state, the WAXD profile from amorphous atactic PP can be successfully used instead, as in the example illustrated in Fig. 4c.

Diffraction peaks are usually broadened by four main factors: (1) instrumental broadening as a result of beam size, macroscopic sample dimensions, and detector pixel size; (2) crystallite size; (3) crystal lattice disorder; and (4) microstrains

[38]. The first factor depends on the experimental configuration used, but the other three parameters are sample dependent. Thus, a proper diffraction peak analysis would give structural information from the line breadth study. Because of the defective nature of polymer crystals, a detailed peak shape analysis is not always possible, especially for low crystallinity and highly defective samples. However, for polymers such as PE, PP, nylons, and polyesters, the diffraction peaks can be quite strong and well defined above the amorphous halo, so that line breadth analysis is possible. Two main parameters can be used for line breadth analysis: the angular width $\Delta\theta$ or the integral breadth $\delta\beta$. The integral breadth is defined as the ratio between the peak area and its intensity. After correction for instrumental broadening (generally small for semicrystalline polymers measured at synchrotrons), study of the integral breadth evolution as a function of the reflection order n can provide information about the factors responsible for the diffraction peak broadening. For example, $\delta\beta$ is determined by the finite crystallite size as:

$$\delta\beta = 1 / \langle D_{hkl} \rangle$$

where $\langle D_{hkl} \rangle$ is the average domain size giving coherent diffraction in the direction perpendicular to the family of planes hkl . Thus, peak broadening as a result of finite crystallite size does not depend on the reflection order n . By contrast, microstrains and paracrystalline disorder are proportional to n and n^2 , respectively.

As discussed above, many industrial processes involve the use of flow and therefore polymer products such as fibers, tapes, and films often show oriented structures. The degree of orientation of the polymeric samples as a function of changing processing conditions is thus an important parameter to be characterized. Analysis of the angular spreading of WAXS signals like those in Fig. 4b allows calculation of the orientation of the crystallographic axes of the crystallites. Crystallite (i.e., lamellar) orientation can be characterized by 2D SAXS analysis, as showed in Sect. 2.2.

The simplest way to deal with structural orientation is to use the orientation order parameter S . The orientation function is, in this case, a simple mathematical equation that can be used to describe the extent of orientation of the chain axis relative to an axis of interest:

$$S = f(\phi) = \left\langle \frac{3 \cos^2 \phi - 1}{2} \right\rangle \quad (2)$$

where ϕ is the angle between the chain axis and the axis of interest. The axis of interest could be the drawing, the shear, or any other external field direction. The orientation function can be used to model the angular dependence of a diffraction peak and has the property to be equal to 1 for perfect alignment, 0 for random alignment, and -0.5 for perpendicular alignment. Because of the industrial relevance of polymer orientation, more detailed and rigorous methods have been developed specifically for semicrystalline polymers [39–43].

2.2 SAXS

SAXS is an X-ray based technique that offers the possibility to measure large distances classically in the range 1–100 nm, although most of the modern synchrotron beamlines allow solving structures up to 400 nm and more. The main experimental difference between a WAXD and a SAXS experiment is the different sample-to-detector distance used. In a simultaneous SAXS/WAXD experimental setup, two detectors are used at the same time and are separated by a large distance. The WAXD detector is usually placed 20–50 cm away and under a significant angle. The SAXS detector is placed 1–8 m away from the sample and is placed at the end of a vacuum tube to eliminate air scattering and absorption.

Analysis of the bulk structure in semicrystalline polymers is generally performed using scattering experiments. Depending on the nature of the system under study and on the characteristic length scale being investigated, X-ray, neutrons, or light photons can be used. In particular, if one is interested in fast phase transformation on a second and subsecond time scale, synchrotron X-ray scattering experiments are the most suitable.

When an X-ray photon of an incoming beam with original intensity I_o and wavelength λ encounters an atom, it can be scattered and the scattering vector \vec{q} is defined as:

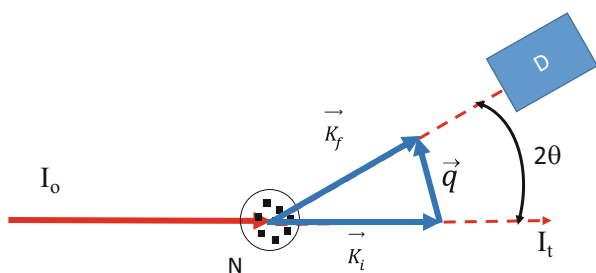
$$\vec{q} = \vec{K}_f - \vec{K}_i$$

where \vec{K}_i and \vec{K}_f are the wave vectors on the incident and scattered plane waves, respectively. In the elastic (Thompson) scattering approximation, $K_f = K_i = 2\pi/\lambda$ and, according to the geometrical description in Fig. 5, the modulus q of the scattering vector depends on the scattering angle θ and is defined as:

$$|\vec{q}| = \frac{4\pi}{\lambda} \sin(\theta) \quad (3)$$

The scattered intensity at the detector can be conveniently expressed in the form of the differential scattering cross-section:

Fig. 5 General setup for a scattering experiment. See text for description of symbols



$$\frac{d\sigma}{d\Omega} = \frac{(\text{number of photons}/s)}{(\text{Incident photons})\Delta\Omega} = \frac{\text{Scattered energy through unit solid angle}}{\text{Incident energy per unit area}}$$

where $\Delta\Omega$ is the portion of the solid angle defined by the detector dimension.

SAXS is now a well-established technique and detailed treatment about SAXS theory can be found in many books [44–47]. We discuss here the basic SAXS equations and the main quantities that can be extracted from a SAXS experiment and are useful in the field of polymer crystallization.

For an ensemble of N particles in an irradiated volume V , and under the two classical assumptions that (1) the system is isotropic and (2) there is no long-range order, the SAXS macroscopic differential scattering cross-section can be written as:

$$I(q) = \frac{d\Sigma}{d\Omega} = \frac{N}{V} \frac{d\sigma}{d\Omega} = NV^2 \Delta\rho^2 P(q)S(q) \quad (4)$$

where $\Delta\rho^2$ is the contrast term (i.e., electron density difference between the scatterers and the surrounding media for X-rays) and $P(q)$ and $S(q)$ are the so-called form and structure factors. $P(q)$ is the intraparticle interference factor related to the shape and size of the scattering particles and $S(q)$ is the interparticle interference factor describing the spatial correlation among neighboring particles. Eq. (4) represents the most general of the SAXS equations.

In the field of polymers, Eq. (4) describes excellently the scattering from polymer colloidal systems obtained from phase separation both in solution and solid state, such as block copolymer micelles in solution or in bulk. If the electron density inside the particles is uniform, the system can be considered as a two-phase ideal system. For dilute systems, where there is no spatial correlation between particles, $S(q)$ is equal to 1 and the scattering cross-section depends only on $P(q)$. For a dilute suspension of N identical spherical particles with radius R , the scattering cross-section has the analytical expression:

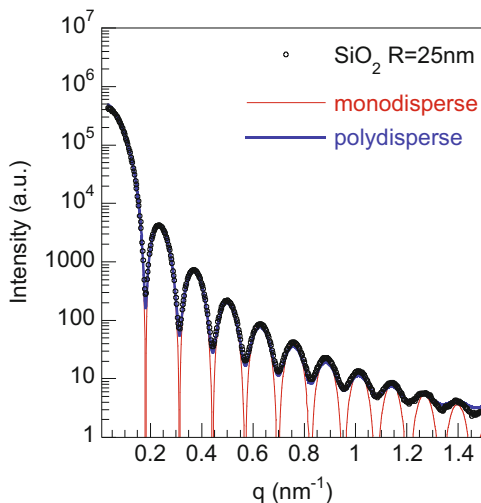
$$\frac{d\Sigma}{d\Omega} = NV^2 \Delta\rho^2 \left[3 \frac{\sin(qR) - qR \cos(qR)}{(qR)^3} \right]^2 \quad (5)$$

In reality, samples always show some polydispersity and Eq. (4), in the case $S(q) = 1$, is modified in order to take into account the size distribution function $D(R)$:

$$\frac{d\Sigma}{d\Omega} = \frac{N}{V} \frac{d\sigma}{d\Omega} = N\Delta\rho^2 \int_{R1}^{R2} V(R)^2 P(q, R) D(R) dR \quad (6)$$

The most used functions to describe the size distribution are the Gaussian, Schultz, and Weibull distribution functions. Figure 6 shows the SAXS curve for a dilute aqueous suspension of silica spheres with radius of 25 nm and low polydispersity, compared with the best fits obtained using Eqs. (5) and (6). The position of the

Fig. 6 SAXS profile of a dilute aqueous suspension of silica spheres of 25 nm radius (R). *Red curve* is the best fit using Eq. (6) for monodisperse spheres. *Blue curve* is the best fit for polydisperse spheres using Eq. (6), where $P(q)$ is given by term between squared brackets in Eq. (5). $R = 24.9 \pm 0.7$ nm is obtained using a polydisperse spherical model



minima and maxima in the SAXS curve are only a function of the particle radius, whereas the shape of the curve is characteristic of the particle shape.

Equation (4) specifies that the SAXS intensity is dependent on the shape of the particles that scatter (the $P(q)$ term) and on their spatial arrangement (the $S(q)$ term). This implies that a model based on the particle shape often has to be used to interpret the SAXS results. However, three main quantities can be derived independently of the nature of the scattering system: the gyration radius, the specific surface, and the invariant.

For dilute systems with limited polydispersity, the SAXS intensity at low angles ($q \rightarrow 0$ low resolution limit) has the shape of a Gaussian function centered at $q=0$ and with the full width at half maximum (FWHM) inversely proportional to the particle dimension. It can be showed that the intensity can be well approximated by a general equation that depends only on the gyration radius R_G of the particles, according to the equation:

$$I(q) = \Phi V_{\text{part}} \exp\left(-\frac{R_G^2 q^2}{3}\right) \quad (7)$$

where Φ is the volume fraction and V_{part} is the volume of the particle. Equation (7) is known as the Guinier equation [44] and is valid in the range $q < 1/R$. The gyration radius can be easily calculated by plotting the logarithm of the SAXS intensity as a function of q^2 . Similarly, cross-sectional radius R_c and thickness radius R_t can be obtained for rod-like and flat-like particles:

$$\text{Rod-like : } I(q) \propto \frac{1}{q} \exp\left(-\frac{R_c^2 q^2}{2}\right) \quad (8)$$

$$\text{Flat-like : } I(q) \propto \frac{1}{q^2} \exp(-R_1^2 q^2) \quad (9)$$

Generally, Guinier analysis is not used when studying semicrystalline polymers because the systems are polydisperse and not dilute. However, Eq. (8) can be used to estimate the shish cross-sectional radius, as discussed later in this section.

Another important quantity that can be extracted from the SAXS curve of any kind of system is the invariant Q [48], given by:

$$Q = \int_0^{+\infty} I(q) q^2 dq = 2\pi\Phi(1 - \Phi)(\rho_2 - \rho_1)^2 \quad (10)$$

where Φ and ρ_1 are the volume fraction and electron density of phase 1, and $(1 - \Phi)$ and ρ_2 are the volume fraction and electron density of phase 2. Equation (10) is rigorously valid only for an isotropic two-phase system. A proper calculation of the invariant is not easy, because the integral extends from 0 to $+\infty$ and careful extrapolation should be performed. However, Eq. (11) can be successfully used to follow the system evolution during the melting or crystallization processes [49] and to estimate the volume fraction of the crystalline material [50] for semicrystalline polymers.

At large scattering angles, the SAXS intensity contains information about the surface of the scattering objects. For large values of q the SAXS intensity of a two-phase system can be described by the Porod law [51]:

$$\lim_{q \rightarrow \infty} \frac{I(q)}{Q} = \frac{1}{q^4} \frac{1}{\pi\Phi(1 - \Phi)} \frac{S}{V} \quad (11)$$

where S and V are the average values for the surface and volume of the scattering objects, respectively.

Equation (11) holds independently of the system under study and is the result of the existence of an interface between the two phases. Deviations from the ideal two-phase system can be taken into account and modified equations for curved or rough interfaces, and for transition regions between the phases, have been obtained [52–54]. Equation (11) and its modified forms have been applied to semicrystalline polymers to study the nature of the amorphous–crystalline phase separation during crystallization and melting and as a function of the polymer chain nature [52, 55].

As discussed above, semicrystalline polymers crystallize using the chain folding/packing mechanism and form lamellar crystals. In quiescent conditions, lamellae cluster together to form spherulites. Inside the spherulites, the lamellae are not perfect: they can be curved, can have limited lateral extension, and might not be perfectly parallel. However, these imperfections are usually in the micrometer range

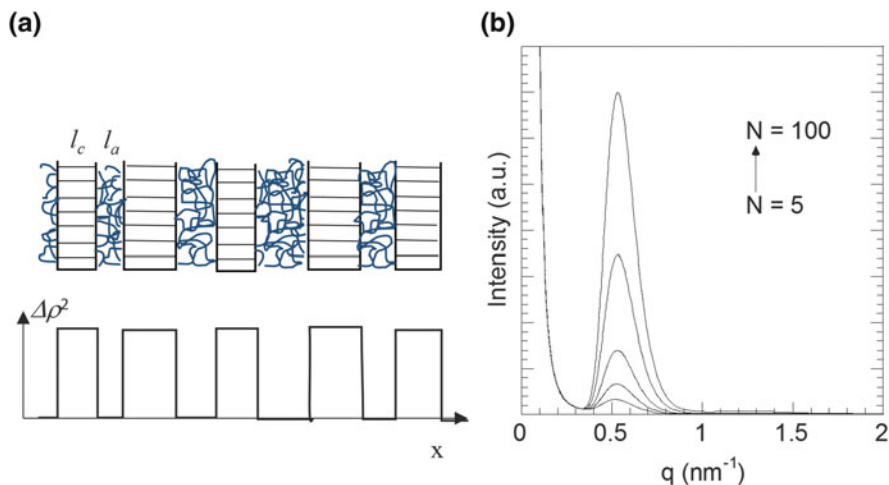


Fig. 7 (a) Electron density profile inside a lamellar stack; x is the direction perpendicular to the lamellar plane. (b) Evolution of the SAXS scattered intensity calculated using Eq. (13) as a function of increasing stack height (N lamellae in a stack); $L_p = 10$ nm, $l_c = 6$ nm

and, from the SAXS point of view, one can consider the crystalline lamellae to be piled up one on top of the other, separated by amorphous chains, forming so-called lamellar stacks. If the lamellar stacks are infinitely large, the lamellae are perfectly parallel and only crystalline and amorphous regions alternate inside the stack, the system is ideal and can be described using the ideal lamellar model.

The SAXS image of an isotropic polymer sample is generally not rich in features and is characterized by a broad scattered ring whose position q^* is related to the average distance between two adjacent crystalline lamellae L_p by Bragg's law, $L_p = 2\pi/q^*$, as derived by combining Eqs. (1) and (3). Despite the broad nature of the signal, SAXS modeling allows one to derive the average values and distributions for the thicknesses of the crystalline and amorphous regions inside the spherulites.

Calculation of the scattered intensity from an ideal lamellar model is simplified by the fact that the electron density varies only in the direction perpendicular to the lamellar plane (see Fig. 7a). Detailed description and calculations of the scattering from an ideal lamellar model are given in the literature [38, 56–58]. For an infinitely high stack, the scattered intensity can be calculated as:

$$I(q) = \frac{(\rho_c - \rho_a)^2}{q^2} \text{Re} \left[\frac{(1 - H_c)(1 - H_a)}{1 - H_c H_a} \right] \quad (12)$$

where ρ_c and ρ_a are the electron densities of the crystalline and amorphous phases, respectively. H_c and H_a are the real part of the Fourier transforms of the distribution functions $D(l_c)$ and $D(l_a)$ for the thickness of the crystalline (l_c) and amorphous (l_a) layers. The long period L_p is given by $L_p = l_c + l_a$.

Several deviations from the ideal model occur in practice and the scattered intensity must be adjusted to take such imperfections into account. The most common deviation is the finite stack size. The scattered intensity for a stack of finite height $L_p N$ with a certain distribution in height is given by Eq. 13 [58, 59]:

$$I(q) = \frac{N(\rho_2 - \rho_1)^2}{q^2} \text{Re} \left[\frac{(1 - H_1) - (1 - H_2)}{1 - H_1 H_2} + \frac{H_2(1 - H_1)^2 \left[1 - \langle (H_1 H_2)^N \rangle \right]}{\langle N \rangle (1 - H_1 H_2)^2} \right] \quad (13)$$

where $\langle N \rangle$ is the average value of N . Subscripts 1 and 2 refer to the layer type, which is assigned to the amorphous and crystalline phases depending on the sample crystallinity and on the basis of complementary information coming from microscopy, calorimetry etc.

Figure 7b shows the calculated SAXS profiles for lamellar stacks of different size.

According to Eq. (13), the SAXS intensity increases with increasing stack height NL_p or the contrast factor. The curve shape is dominated by the thickness distribution functions and structural disorder.

Other kinds of imperfections that can be taken into account are the result of the existence of a transition region between the amorphous and crystalline layers and to distorted (undulated, twisted, splayed, etc.) lamellae [38].

Alternative approaches for extracting structural parameters from the SAXS curves are the correlation function [50, 60, 61] and the chord or interface distribution function [58, 62–64]. These two approaches work in direct space and can highlight structural differences between different samples more easily with respect to the scattered intensity. The normalized one-dimensional correlation function $\gamma_1(x)$ can be extracted from the experimentally measured scattered intensity by a cosine Fourier transform:

$$\gamma_1(x) = \frac{\int_0^\infty I(q) q^2 \cos(qx) dq}{\int_0^\infty I(q) q^2 dq} \quad (14)$$

Importantly, the linear correlation function can also be written as a function of the differences in the electron density of the sample $\gamma_1(x) = \overline{\eta_A \eta_B} / \overline{\eta_A^2}$, where η_i is the difference between the electron density of phase i with respect to the average density of the system, as introduced by Debye in 1957 [65].

Because the integrals in Eq. (14) are defined between 0 and infinity, extrapolation of the experimentally measured intensity to zero angles and infinity (high angles) is necessary. Although the extrapolation to low angles is not critical because of the multiplication for q^2 , extrapolation at large angles is quite important and depends on the model used to describe the structure [55]. Moreover, any kind of

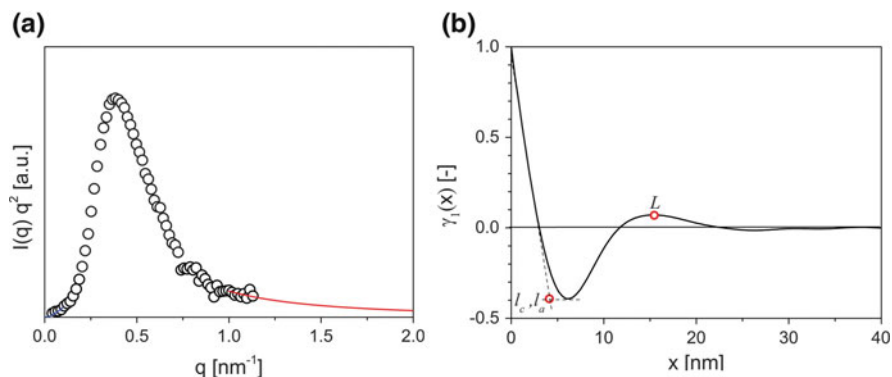


Fig. 8 (a) Lorentz-corrected intensity for a PE sample with small and large angle extrapolated portions. (b) Linear correlation function calculated for the extrapolated intensity. The values for L_p and l_c (or l_a) are highlighted with red circles

background has to be removed carefully from the measured intensity. Extrapolation to $q=0$ can be performed after Lorentz correction is applied using the Debye–Beuche equation [66], $I(q) = B/(1 + C^2q^2)$, where C and B are the interpolation parameters. Extrapolation to large angles ($q \rightarrow \infty$) can be obtained by using the appropriate Porod law, initially fitted to the experimental data in the Porod region. Different expressions have been found to describe the Porod behavior for semi-crystalline polymer systems and can be used to extrapolate the intensity at large q values [55]. Figure 8a shows the extrapolated intensity for a polyethylene sample in its Lorentz-corrected $I(q)q^2$ form. Figure 8b shows the correlation function for a PE sample. The long period L and the thickness of the crystalline and amorphous phases can be extracted directly from $\gamma_1(x)$. The long period is given by the value of the maximum of the first oscillation of $\gamma_1(x)$, whereas the thickness of one of the phases can be extracted from the intercept at the level of the first minimum (i.e., background level) of the extrapolation of the linear part of the correlation function (as indicated in Fig. 8b). The thickness of the other phase is given by $l_2 = L - l_1$.

It has been discussed above how flow can drastically affect the morphology of polymers. The SAXS pattern of an oriented polymeric sample contains more information than the isotropic SAXS diffuse signal from an isotropic sample.

Although the SAXS images from stretched polymer films and fibers usually display typical four-point patterns, oriented structures obtained from flow-induced crystallization process are characterized by equatorial streaks and meridional spots or lobes (see Fig. 9a). Such a pattern is typical for the shish-kebab morphology described in Sect. 2, where shish scattering gives origin to the equatorial streaks and kebab stacks are responsible for the meridional lobes (see Fig. 9b).

Interpretation and modeling of anisotropic SAXS images of oriented polymers is thus essential for obtaining information about fundamental polymer properties. SAXS modeling can in this case provide information not only about the thickness and distribution of crystalline and amorphous regions characteristic of the kebab

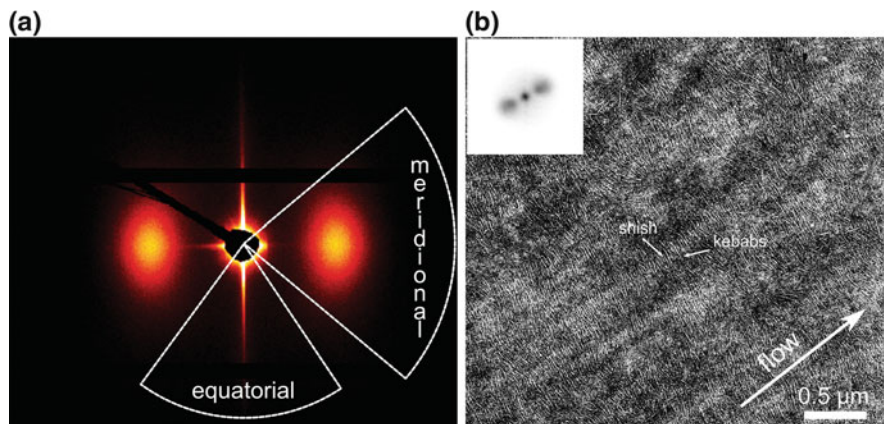


Fig. 9 (a) SAXS pattern for an oriented low density polyethylene fiber produced by uniaxial stretching. (b) TEM image for an oriented LLDPE sample. Elongated bright bundles aligned along the flow direction are the shish. Perpendicular to the shish are the kebabs. *Inset* shows the 2D Fourier transform of the TEM image. Lobes generated by the kebabs characteristic separation are clearly visible

structure, but also the diameter and length of the shish, diameter of the kebabs, and extent of orientation of both shish and kebab. Moreover, the SAXS image can be divided into three main regions: the equatorial region related to the shish, the meridional region related to the kebabs, and the diagonal region related to the isotropic structure, if present.

The shish cross-section radius can be examined by analyzing the integrated equatorial SAXS profiles using the Guinier approximation for rod-like scatterers [67]:

$$I(s) \propto \frac{1}{s} \exp(-2\pi^2 R_C^2 s^2)$$

where R_C represents the radius of gyration of the cross-section and s is the scattering vector, expressed as $2\sin\theta/\lambda$. The shish cross-section radius R_C can be obtained by fitting the linear portion of the $\ln[I(s) s]$ versus s^2 plot in the low s region of the curve, as shown in Fig. 10.

The average values and distributions of thickness, long period, and diameter of kebabs can be obtained using a structural model to fit SAXS data, as proposed by the group of Hsiao, based on the factorization of the scattered intensity in structure and form factors [68, 69]. The model is based on the assumption that shish-kebabs are formed by stacks of perfectly aligned disks having cylindrical symmetry around the shish axis with average diameter D , thickness T , and long-period L , each dimension having a certain distribution that is statistically independent of the others. The scattered intensity in the meridional region can then be expressed as:

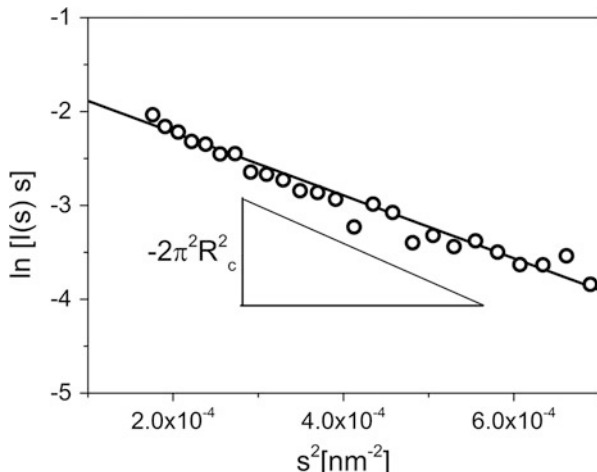


Fig. 10 Typical Guinier plot of the lowest angle part of the SAXS equatorial scattered intensity for an oriented polymer sample with shish-kebab morphology

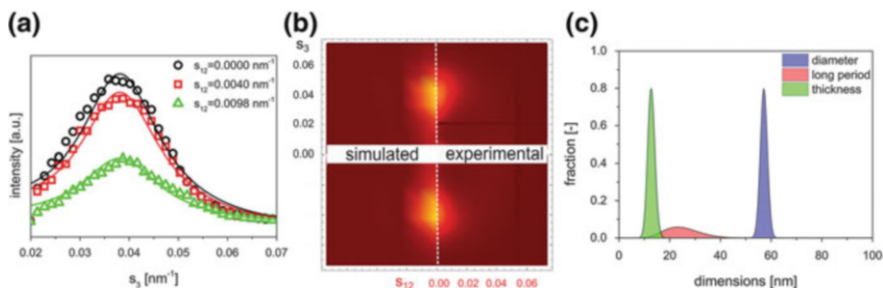


Fig. 11 (a) Experimental intensities profiles (*symbols*) as a function of s_3 extracted at different values of s_{12} and corresponding fitted profiles using the shish-kebab model (*lines*). (b) 2D comparison between simulated (*left*) and experimental (*right*) SAXS patterns. (c) Resulting distribution of diameter, long period, and thickness of the kebabs evaluated using the model

$$I(s_{12}, s_3) s_3^2 = K \left[\left\langle |A(s_{12}, s_3)|^2 \right\rangle_{D,T} - \left| \langle A(s_{12}, s_3) \rangle_{D,T} \right|^2 + \left| \langle A(s_{12}, s_3) \rangle_{D,T} \right|^2 |Z_L(s_3)|^2 \right] \quad (15)$$

where K is a proportionality factor, s_{12} and s_3 are the components of the scattering vector in equatorial and meridional directions, $A(s_{12}, s_3)$ is the form factor of the electron density distribution of a single disk, and $Z_L(s_3)$ is the structure factor along the meridional direction.

Using Γ -distributions to describe the distribution functions of diameter, thickness, and long period, the equation has analytical solutions and can be used to fit a set of three different meridional intensity slices along s_3 at different s_{12} . Examples of the fitting procedure on an experimental pattern of an iPP sample stretched and isothermally crystallized at 145°C and the resulting calculated distributions are shown in Fig. 11.

2.3 Detectors

In fast time-resolved experiments, the position-sensitive X-ray detectors that are used play an important role. Several parameters can be considered in this, including the time framing rate of which the detectors are capable. The minimum time resolution is defined by the minimum length of a single data frame and the time required to store this data frame on a digital storage medium. The latter is not without importance if one realizes that, as a rather extreme example, a piece of X-ray film can be exposed in nanoseconds but requires up to 30 min to process.

Even when using slow time-framing detectors it is still possible to compose a fast time series by repeating the experiment several times and stagger the data collection points [70]. However, it is preferable to utilize a detector that can handle high enough local and overall count rates and can handle time frame rates that are compatible with the time scales over which the samples show structural changes. In these short time frames, the statistical data quality required to obtain the parameters that one wants to use in the data analysis should be sufficient. This means that if one is only interested in the invariant [see previous section and Eq. (11)], which can be obtained using the integrated intensity over all detector pixels, fewer counts per pixel are required than for determination if a diffraction peak is present or for determination of the Porod slope. For peak determination, only a limited number of pixels are available; for determining the Porod slope, one invariable is in the scattering vector regime where the number of scattered photons is low. With only a few events per pixel, the question of whether to use a single photon counting detector or an integrating detector becomes relevant. Single photon counters can be, for instance, gas-filled wire chambers [71, 72], as still widely used in home laboratory setups, or new generation solid-state Si pixel detectors [73]. An alternative is the integrating detector, where every photon is converted into an electronic charge, which is stored in a capacitor and read out at fixed intervals. This means that one can handle very high count rates, but the disadvantage is that the read-out process introduces noise that can seriously impact data quality in the low count rate regime [74]. Also, the capacitor has a limited capacity, which means that the dynamic range (i.e., the difference between the strongest and weakest signals that can be detected during one time frame) is limited. This is rarely a problem for SAXS experiments on polymer samples, but for WAXS and polymer crystallization, where sharp diffraction peaks have to be detected on a weak and changing background, this is problematic. Photon counting devices intrinsically have a lower count rate that they can handle, because every event has to be individually processed. This is the reason that gas-filled wire chambers have fallen out of favor on synchrotron beamlines. However, Si-based pixel detectors have overcome the count rate limitation to a great extent.

An often overlooked parameter is the pixel size of the detector. In principle this does not have to be smaller than the size of the direct beam. Using smaller pixel sizes than the direct beam does not increase the information content of the experiment, but has the disadvantage that the data sets are much larger and therefore take

more time to write to a digital storage medium and are more difficult to handle in the data analysis. The pixel size of the detector, however, is not the only parameter that determines the resolution of a detector. How much information spills over from one pixel into the neighboring pixels, the so-called point spread function, is also of importance. This point spread function is often a function of the local count rate of the detector.

The last issue that should be taken into consideration is the active area of the detector. A larger active area allows collection of a larger scattering vector range, at the expense of an increase in the data set size. For WAXS experiments one cannot increase the size of the detector indiscriminately. If a linear detector is too long, it cannot cut appropriately through the diffraction Ewald sphere [75] unless one uses a curved detector. This means that for certain diffraction peaks an erroneous or even absence of diffraction intensity is registered.

The current state of the art with respect to detectors suitable for fast time-resolved polymer crystallization and processing experiments are pixel hybrid detectors [76]. The development of these detectors is still in progress and, undoubtedly, competing technologies will also be marketed in the coming years.

Besides the technical developments that have taken place and will take place, it is good to realize that most synchrotron radiation beamlines, which are required for the fast time-resolved experiments that are the subject of this chapter, do not have the choice of several detector systems. As a result of financial and experimental constraints only a limited number of detectors are available. With most of these detector systems one can perform fast time-resolved experiments. The important issue is that one first has to define which parameters one would like to obtain from an experiment and then see how the experimental configuration, including detector systems, can be adapted so that these parameters are obtained with sufficient experimental accuracy to be able to make confident statements with respect to the outcome of the experiment.

3 Recent Examples of Fast Polymer Structuring Studied by SAXS/WAXD

3.1 Ballistic Cooling of Propene/Ethylene Copolymers: Influence of Co-monomer Content

Industrial processing involves cooling rates ranging from 10 to 1,000 K/s, which are well above those used in the laboratory with standard calorimetric techniques. Such high cooling rates can be achieved by recently developed fast chip-based calorimetry (flash differential scanning calorimetry), whereby a few nanograms of polymer sample can be cooled linearly down to target temperatures with high cooling rates [77–81]. An alternative effective method consists of cooling down the polymer specimen using ballistic nonlinear conditions. In this case, the molten sample is

allowed to cool down towards a final target temperature at a certain initial nominal cooling rate that is defined by the difference between the initial and final temperature according to Newton's law of cooling:

$$T(t) = T(\infty) + [T(0) - T(\infty)]\exp(-Bt) \quad (16)$$

where $T(0)$ is the initial temperature of the polymer in the molten state, $T(\infty)$ is the target temperature, and B is a time constant for the cooling process, which depends on the overall heat exchange coefficient. The sample temperature decreases exponentially with time if no transformation inside the sample takes place. If the polymer specimen crystallizes during cooling, latent heat is released during the crystallization process and a deviation from the exponential thermal decay curve is detected. This feature can be detected during fast cooling if the temperature inside the sample can be measured with acceptable accuracy, and can be measured with high framing rate. This concept allows the construction of a simple quenching device that can be easily implemented on a synchrotron beamline. A picture of the quenching device and a schematic drawing of the implementation on BM26B are reported in Fig. 12a, b [82].

The ballistic cooling apparatus has been successfully used to study, in real time, polymer crystallization of polyolefins and polyamides in conditions that are comparable with industrial environments [83–87]. The temperature jump is achieved by switching between hot and cold air streams. The instant temperature is collected by reading a thermocouple incorporated inside a 150- μm polymer film. The temperature reading is synchronized with the X-ray SAXS and WAXD data collection software at a 30 frames/s collection rate.

The WAXD profile evolutions as a function of time representative for fast structuring of iPP homopolymer and a propene/ethylene copolymer cooled at two different cooling rates are shown in Fig. 13. During continuous cooling at 30°C/s the iPP homopolymer melt transforms in the α -phase, as evidenced by the

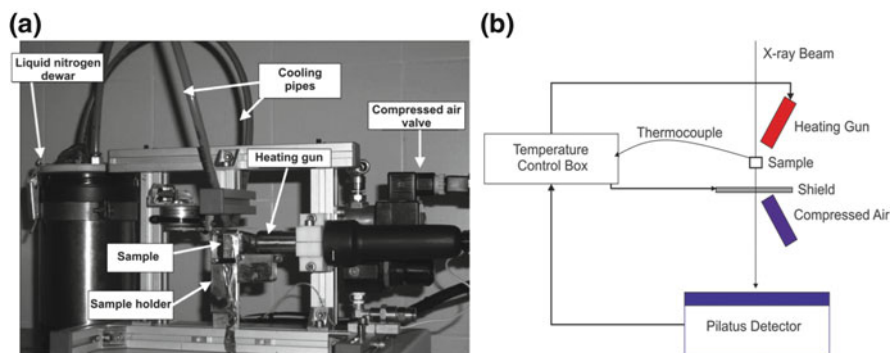


Fig. 12 (a) Photograph of the ballistic cooling device. (b) Implementation of the ballistic device at BM26-DUBBLE. Reproduced with permission from [82]

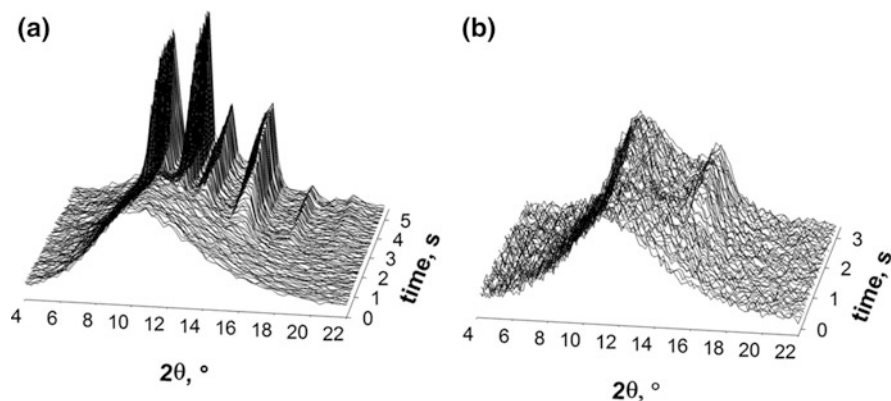


Fig. 13 Real-time WAXD patterns collected during fast cooling. (a) i-PP homopolymer cooled at ca. 30°C/s . (b) Propene/ethylene copolymer with 7.3 mol% of co-monomer cooled at ca. 160°C/s . Reproduced with permission from [84]

diagnostic diffraction peaks typical for the iPP α -form (Fig. 13a). When solidification takes place at high cooling rate, crystalline phase formation is overcome and a disordered phase with characteristics between those of the crystalline and amorphous phases is formed. For instance, the WAXD pattern of a propene/ethylene random copolymer with 7.6% ethylene content cooled at 160°C/s is characterized by two broad reflections centered at 5.9 and 4.1 Å, attributed to the distance between aligned parallel chains and to the helical periodicity, respectively [88] (Fig. 13b). Such a WAXD pattern is typical for the so-called iPP mesophase.

The time/temperature window in which the mesophase occurs is narrow, and only millisecond WAXD analysis conducted with very high framing rate and highly sensitive and efficient detectors can follow the mesophase formation process in real time.

The onset of the structuring process, as well as the instantaneous amount of phases formed upon cooling, can be calculated by the WAXD profiles. An interesting approach for describing the fast structuring during continuous cooling in material science is the use of continuous-cooling-transformation (CCT) diagrams and time-temperature-transformation (TTT) diagrams. Although they were initially developed in metallurgy [89–91], they have recently been used for polymers [83, 92, 93]. If only one phase is formed in the range of the explored cooling rates, the TTT diagram has the shape of a single C. However, for a polymorphic material, one or more C-shaped curves compose the TTT diagram. The characteristic C shape can be understood considering that the time to obtain a given extent of transformation depends on the nucleation time. Thus, the transformation is particularly slow both at high and low temperatures and exhibits a maximum rate in the intermediate range of undercooling. This is reminiscent of the nucleation rate and growth rate curves in polymer crystallization [8, 94, 95].

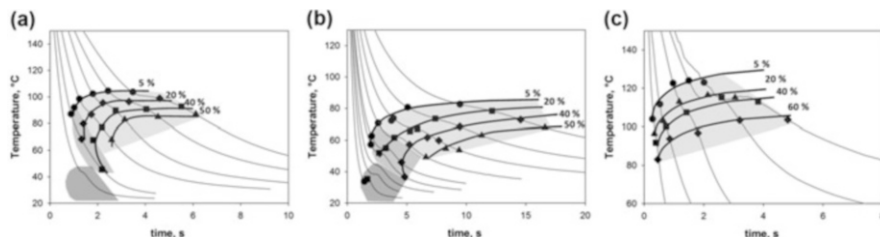


Fig. 14 Continuous-cooling-transformation (CCT) diagrams of (a) i-PP homopolymer, (b) propene/ethylene copolymers with 7.3 mol% co-unit, and (c) i-PP homopolymer containing 0.1% nucleating agent (NA11). Shaded areas indicate the crystallization region of α -phase, mixed structure, and mesophase, from light to dark gray, respectively

CCT diagrams for iPP homopolymer, propene/ethylene random copolymer with 7.3% of co-unit, and iPP homopolymer with nucleation agent are shown in Fig. 14a–c.

The CCT diagrams shows that the monoclinic α -phase is formed at low and intermediate cooling rates for both the homo- and copolymer samples. Mesophase formation occurs when the sample is quenched at high cooling rates (dark grey areas in Fig. 14a, b). Mesophase formation is easier to achieve for the propene/ethylene copolymers. At a given cooling rate, α -phase formation takes place progressively at lower temperatures and longer times when the ethylene co-monomer content is increased. The iso-transformation curves in Fig. 14a, b shift progressively towards the bottom-right part for high co-monomer content with respect to pure homopolymer. Mesophase formation is also influenced by the co-monomer concentration, but to a lesser extent. Thus, mesophase formation occurs at higher cooling rates than for pure iPP homopolymer. However, introduction of nucleating agents such as NA11 strongly increase the nucleation rate of the monoclinic phase and mesophase formation can be completely suppressed [96, 97]. In the presence of this nucleating agent, mesophase formation is suppressed even at the highest cooling rate attainable with the ballistic cooling device.

3.2 Structure Development During Flow-Induced Crystallization of iPP: How Short is Short?

The large effect of flow in the crystallization and morphology of semicrystalline polymers has already been mentioned above. Early studies on flow-induced crystallization focused on structure development in continuous flow fields [98, 99]: formation of crystals during flow causes an increase in melt viscosity, hence giving rise to a self-enhancing mechanism. Consequently, the dynamics of structure development were often too complicated to unambiguously establish the relations between flow field, kinetics, and resulting morphology.

A valuable approach has been proposed by the group of Janeschitz-Kriegl with the “short-term shearing protocol” [100], in which the flow time is short compared with the crystallization time scale. In this way, nucleation and growth processes are separated and the characteristics of flow-induced nuclei can be revealed indirectly by studying the resulting crystallization kinetics and morphology.

In the high flow rate regime, however, this is not always true and structures can also be formed during short-term flow [33, 101]. Structure formation during flow changes the viscosity and influences the crystallization process. The change in viscosity during flow can be directly measured by rheology and the structure formation can be followed in real time using SAXS and WAXD with millisecond time resolution [102].

Flow-induced crystallization experiments using a short-term shearing protocol can be successfully carried out in a slit flow cell operating on a modified multipass rheometer [103]. Shear flow is applied by simultaneously moving the two pistons, between which the polymer melt is confined, at constant velocity and for a given time. This experimental setup permits combination of rheology measurements, via pressure transducers placed near each piston, and allows real-time structural analysis by single crystal diamond windows placed in the middle of the slit, thus enabling in-situ SAXS/WAXD measurements (see Fig. 15)

Figure 16 shows the experimental protocol used to study flow-induced crystallization of iPP. The polymer melt was initially annealed at 220°C for 10 min and subsequently cooled down at the flow temperature of 145°C, taking care to pressurize the sample at 50 bar to avoid shrinkage holes. At this temperature, flow was applied using seven different piston speeds, ranging from 20 to 140 mm/s, using a flow time of 0.25 s for the five slower piston speeds and 0.23 and 0.20 s for piston speeds of 140 and 120 mm/s, because of piston displacement limitations. After shear, the material was crystallized isothermally for 20 min and then cooled down at room temperature for ex-situ characterization. Simultaneous WAXD and SAXS measurements were carried out at the Dutch–Belgian beamline (DUBBLE) at the ESRF in Grenoble (France) using a wavelength of 1.033 Å. Two high-speed noiseless detectors (Pilatus 1M for SAXS and Pilatus 300K for WAXD) were used to record the scattered intensity at high and low angles for 1 s after the start of flow, with an acquisition frequency of 30 Hz.

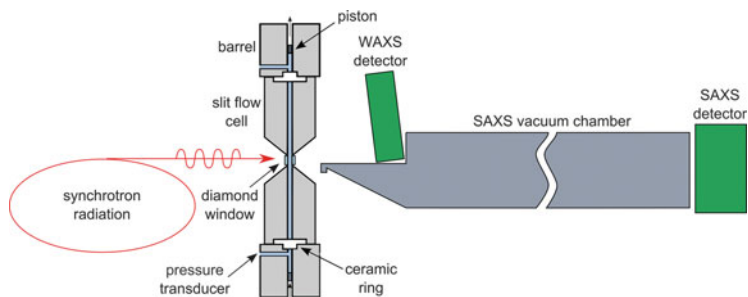
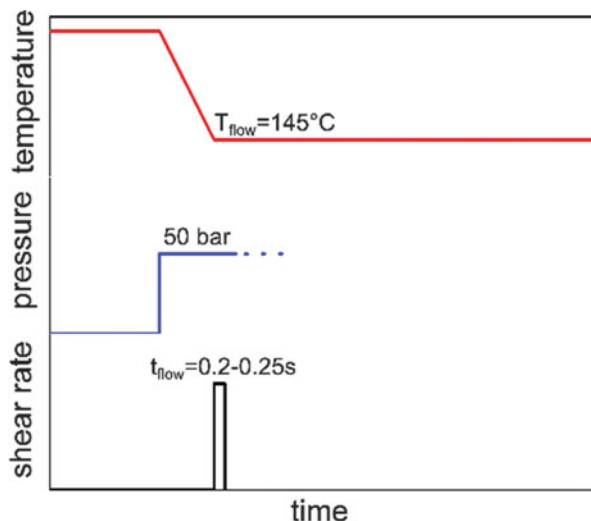


Fig. 15 Multipass rheometer equipped with a slit flow cell combined with SAXS/WAXS

Fig. 16 Experimental protocol adopted for flow-induced crystallization experiments



The apparent wall shear rate is calculated as $\dot{\gamma} = 6Q/WH^2$, where Q is the volumetric flow and W and H are the width and the thickness of the slit, respectively. Because the observation reported in this case study relates to the outermost wall shear layer, the wall shear rates (instead of the average shear rates) are used to characterize the seven different experiments.

The time evolution of the pressure difference measured at the transducers during flow is reported in Fig. 17. Two different regimes can be recognized. The first regime is found for $\dot{\gamma} \leq 160 \text{ s}^{-1}$, where the pressure difference shows a first overshoot followed by a steady-state level. Such behavior is the typical nonlinear rheological response for a polymer melt subjected to start-up shear flow. The second regime is found for $\dot{\gamma} \geq 240 \text{ s}^{-1}$ where, after the first overshoot, the pressure difference increases instead of leveling off. Because the pressure difference scales directly with the wall shear stress and thus with the apparent viscosity, it is evident that, in the latter case, the basic assumption of the “short-term shear protocol” (i.e., no viscosity changes during flow) is not valid.

The viscosity increase is a result of some polymer structuring during the flow, which gives rise to the observed upturn in the pressure difference. However, rheology alone cannot solve the nature of the structure formed during flow. Figure 18 shows SAXS and WAXD images collected during and immediately after flow for $\dot{\gamma} \leq 400 \text{ s}^{-1}$. Equatorial streaks in SAXS and a weak but strongly polarized (110) reflection of the monoclinic iPP α -form in WAXD appear simultaneously 0.23 s after the start of the flow. The increase in viscosity is thus related to the formation of partially crystalline fibrils oriented along the flow direction.

The same behavior is recorded for all shear rates above 400 s^{-1} , whereas equatorial streaks appear after flow for rates of 320 and 240 s^{-1} . In the case of shear rates lower than 240 s^{-1} , no crystalline shish formation is observed within the time observation window of 1 s.

Fig. 17 Evolution of the pressure difference registered at the pistons during flow for the seven flow conditions used. Flow time was 0.25 s for apparent wall shear rates of 80, 160, 240, 320, and 400 s^{-1} ; 0.23 s for 480 s^{-1} ; and 0.2 for 560 s^{-1} . For apparent wall shear rates of 480 and 560 s^{-1} the final part of the curve is extrapolated with a linear function (*dashed line*). Adapted with permission from [102]

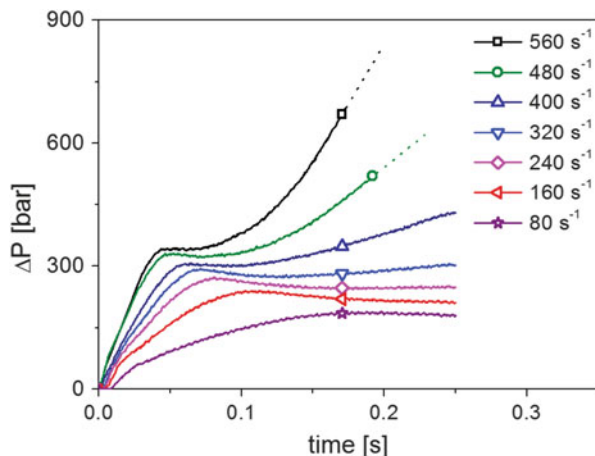
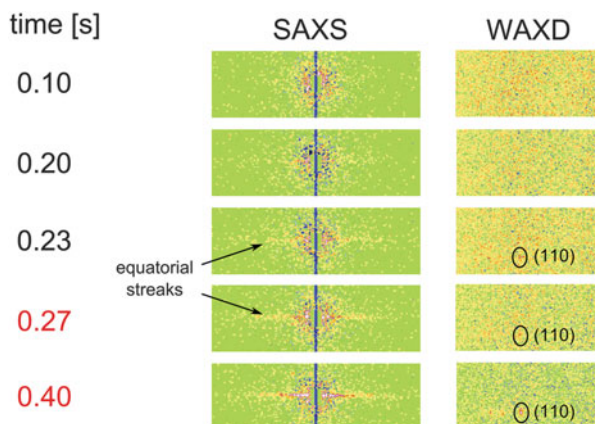


Fig. 18 Representative SAXS (*left*) and WAXD (*right*) patterns for the experiment performed with an apparent wall shear rate of 400 s^{-1} and a flow time of 0.25 s. Patterns acquired after flow are indicated by time in *red*. Flow direction is vertical. Adapted with permission from [102]



Flow strength therefore appears to be the key factor governing the possibility and the time scale of structure formation. Interestingly, there is a clear offset in the onset time of the viscosity upturn and onset of the appearance of SAXS streaks (Fig. 19a). This offset can be the result of two possibilities: (1) the specific precursors for shish influence rheology but are undetectable by the scattering techniques used or (2) shish are formed at another position in the slit flow device, far away from the X-ray observation window.

To investigate the second hypothesis, ex-situ microscopy analysis of the sample sheared at 240 s^{-1} was performed. Cross-sections of the specimen collected at different positions along the slit were microtomed and analyzed using polarized optical microscopy (POM), permitting determination of the thickness of the shear layer. As reported in Fig. 19b, the shear layer is significantly thicker closer to the position of the driving piston, where flow starts. This result strongly suggests that the viscosity upturn could be caused by the formation of structures at an upstream

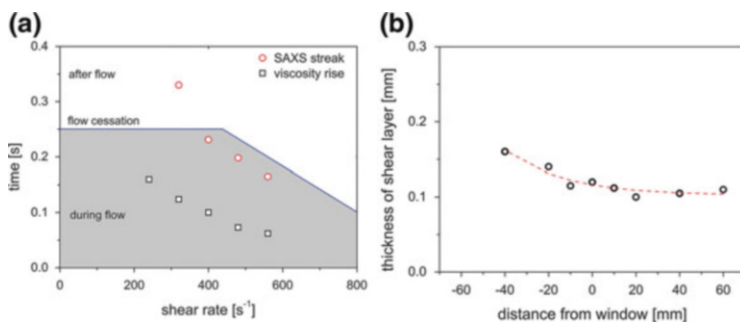


Fig. 19 (a) Onset time for viscosity rise recorded by rheological response (*black squares*) and appearance of SAXS streaks (*red circles*). The *shaded region* represents the flow time for the different shear rates. (b) Thickness of the shear layer as a function of the distance from the X-ray observation window for the experiment performed with an apparent wall shear rate of 240 s^{-1} . The X-ray observation position is at 0, the flow direction is from *left to right*. Adapted with permission from [102]

position before scattering objects are formed in front of the X-ray observation window.

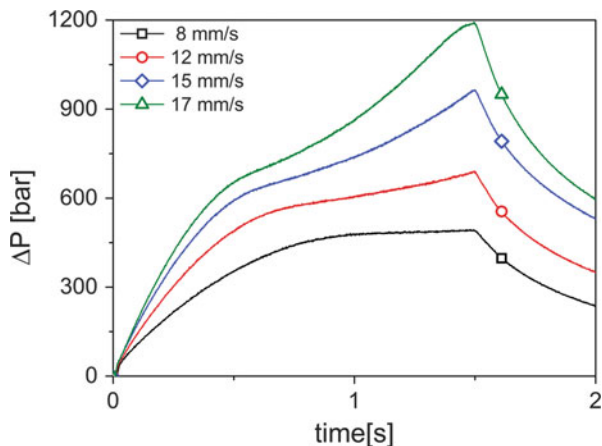
3.3 Pressure Rise Effect on Flow-Induced Crystallization in Confined Geometries: Slit Flow

Structure formation during short-term shear in the regime of high flow stress has a huge effect on the viscosity of a polymer melt. This can cause large increases in pressure and, thus, large changes in thermodynamic properties that, in turn, strongly influence the structure formation process. Consequently, a complex, mutual self-influencing process arises, occurring at rather short times. The effect of the pressure rise on the genesis and development of oriented crystals during the early stages of crystallization in linear low density polyethylene (LLDPE) has recently been shown [104]. LLDPE is one of the most used industrial polymers and is used for plastic bags, wraps, covers, pipes, etc. Moreover, from a scientific point of view LLDPE is an interesting model material because it exhibits slow crystallization kinetics in quiescent conditions and ambient pressure at the chosen temperature (above the nominal melting point), but the undercooling is strongly dependent on pressure.

LLDPE flow-induced crystallization in a slit flow geometry can be studied using the same experimental setup, based on a modified multipass rheometer [103] equipped with diamond windows (as illustrated in Fig. 15).

The pressure drop (ΔP) measured between the two transducers during shear flow of LLDPE (molecular weight 94,000 g/mol, polydispersity index 3.9%, 1.2 mol% butyl branching) is presented in Fig. 20. Generally, the rheology of a polymer melt subjected to start-up shear flow with a constant shear rate should first show an overshoot and, for well-developed flow, approach a steady-state level

Fig. 20 Measured pressure drop between the pressure transducers for the four different piston speeds. Flow time is 1.5 s. Reproduced with permission from [104]



[104]. Clearly, this is not the case: the pressure drop does not show any steady-state level and presents an upturn immediately after the first overshoot for all flow conditions. The viscosity rise is more pronounced and occurs at shorter times with increasing piston speed. This deviation from the ideal rheological behavior of a polymer melt is evidence for structure formation during flow. The viscosity upturn during flow can be explained as shish formation in the proximity of the walls [32]. As a result of the high shear rates close to the walls, nuclei are readily formed. Because polymer chains are continuously sheared during flow, shish grow in length. When the shish density reaches a critical value, the rheology of the material changes and the viscosity increases. The influence of the shish on sample rheology can be seen as a consequence of the hairy nature of the shish, as proposed by Keller [105, 106]: the chain segments sticking out from the shish are highly entangled with the surrounding melt and can thus macroscopically influence the flow field and, consequently, the rheology around the shish.

Structure formation during flow can be efficiently probed using WAXD. The evolution of the area underneath the 110-Bragg reflection, A_{110} , during the first 6 s from the beginning of flow is shown in Fig. 21a for all flow conditions. As expected, crystalline structures are formed during flow and their amount increases with increasing piston speed, perfectly in line with rheological observations. Surprisingly, A_{110} starts to decrease at around 0.3 s after cessation of the shear pulse, suggesting substantial melting of the crystalline structures developed during flow. Evolution of the SAXS scattered intensities (presented in Fig. 21b) clearly shows that the equatorial intensity, related to shish structures, does not show a significant decrease. However, the meridional intensity, related to stacks of lamellae growing perpendicularly on a shish template (kebabs), decreases during the same interval in which the decrease in crystallinity is observed. On the basis of these observations, the decrease in crystallinity is unambiguously attributed to the partial melting of kebabs grown during flow.

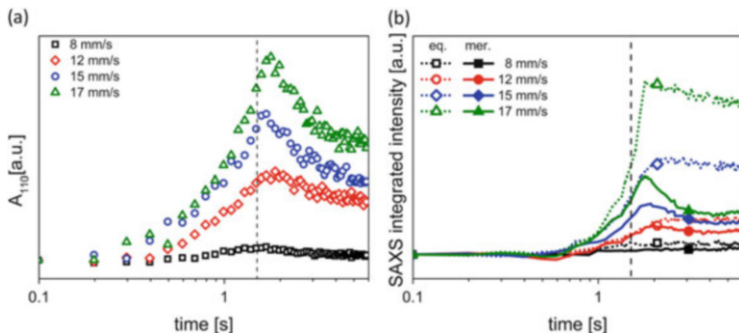


Fig. 21 Time evolution of (a) the area underneath the (110) diffraction peak and (b) SAXS integrated equatorial (*full lines*) and meridional (*dotted lines*) intensities during the first 6 s after start of piston displacement for the four flow conditions. The *vertical dashed line* indicates the end of flow. Reproduced with permission from [104]

Such a partial melting behaviour after flow is rather peculiar and not usually considered in the literature. During flow, the fraction of LLDPE not yet crystallized within the shear layer experiences very high pressures for short times, with consequences for structure formation during flow. The equilibrium melting temperature for this polyethylene grade at ambient pressure is 139°C and it shifts to higher values with increasing pressure according to the Clausius–Clapeyron equation [107]: $T_m^0(P) = T_m^0 + (dT_m^P/dP)\Delta P$, where $(dT_m^P/dP) = 35.2$ K/kbar and $\Delta P = P_{\text{average}} - P_{\text{amb}}$. P_{average} is the average pressure in the middle of the slit (where the X-ray observation window is placed).

Assuming a linear pressure profile along the slit length, the average pressure in the middle can be simply calculated as $P_{\text{average}} = 1/2\Delta P$, with ΔP being the pressure drop measured between the pressure transducers. The time evolution of the undercooling, $\Delta T = T_m^0(P) - T_{\text{exp}}$, is plotted in Fig. 22a together with the A_{110} -Bragg reflection for all flow conditions.

According to classical thermodynamics, the critical stable lamellar thickness, l_c , is also dependent on the undercooling ΔT :

$$l_c = \frac{2\sigma_e T_m^0}{\Delta H_m \Delta T} \quad (17)$$

where σ_e is the surface free energy of a crystal stem, T_m^0 the equilibrium melting temperature, and ΔH_m the heat of fusion.

The pressure change occurring during flow can thus promote the nucleation of shorter stems, leading to crystallization of metastable thinner lamellae, which re-enter the melt when pressure and undercooling decrease and their thermodynamic stability is reduced.

Using the SAXS model for kebab morphology [5] to fit the scattering data according to Eq. (15), the time evolution of the average dimensions of kebabs

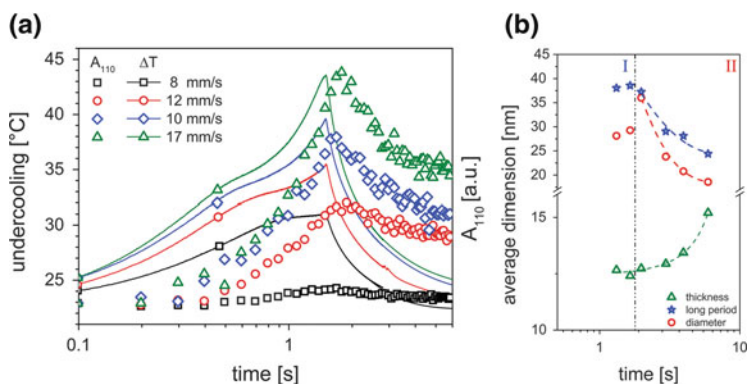


Fig. 22 (a) Time evolution of undercooling evaluated according to the Clausius–Clapeyron equation (*lines*) and of the area underneath the (110) reflection (*symbols*) for all flow conditions. (b) Time evolution of average thickness (*triangles*), long period (*stars*), and diameter (*circles*) of kebabs evaluated using the shish-kebab model for a piston speed of 17 mm/s; *lines* are to guide the eye. The *vertical dashed line* indicates the start of decrease in crystallinity/meridional intensity (region II). Reproduced with permission from [104]

(shown in Fig. 22b) was obtained for the experiment performed with fastest piston speed (17 mm/s). A sharp decrease in kebab diameter and long period is observed when flow stops and pressure relaxes back to equilibrium values, whereas the average thickness increases.

Based on these observations, we propose a mechanism to describe the formation and melting behavior of kebab structures in the presence of combined shear and high pressures (illustrated in Fig. 23). In region I (“pressure quench”), the increase in undercooling as a result of pressure promotes nucleation of thinner lamellae on pre-existing crystals; the nucleation does not happen on shish cores but on pre-existing kebabs. Because the nucleation of thinner lamellae occurs in a random fashion, some kebabs grow faster than others, and this leads to a shish-kebab morphology with different diameters and gradually decreasing thicknesses during the pressure quench. When flow stops and pressure relaxes back to equilibrium values (region II), the thinner lamellae formed in region I lose their thermodynamic stability and relax back to the coiled state. The average diameter and spacing between them decreases, whereas the average thickness increases.

It was shown that, although very short in terms of time, the viscosity rise during flow in confined geometries can have a dominating influence on the crystallization of materials such as polyethylene, which show a strong dependency of the undercooling on pressure. These results show the importance of this phenomenon for understanding and modeling real-life processes such as injection molding, where a combination of flow and pressure is always present.

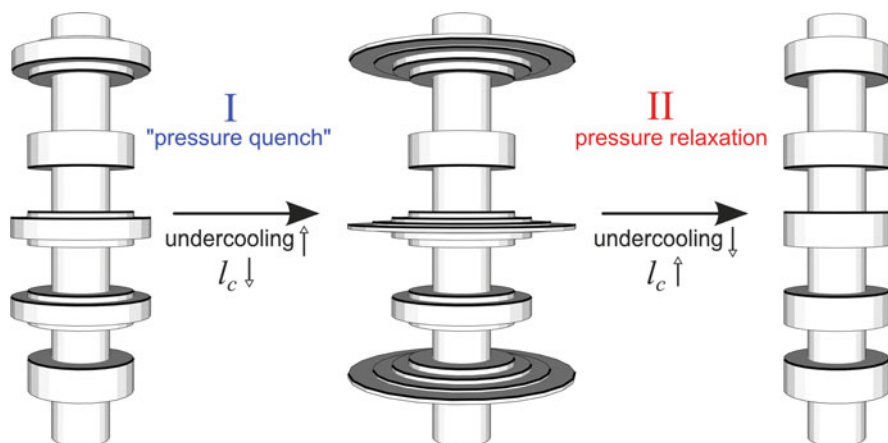


Fig. 23 Kebab crystallization and melting under the influence of sharp pressure changes during and after flow. Reproduced with permission from [104]

3.4 *Rheo-SAXS/WAXD, In-situ Extensional Rheology of iPP*

Common processing operations for semicrystalline polymers, such as fiber spinning, film stretching, and film blowing, involve uniaxial and biaxial deformation of the crystallizing melt. Depending on the applied stress, highly oriented structures can be formed in the machine direction as shish-kebabs, where shish are extended chain crystals and kebabs are lamellae growing perpendicularly from the shish template. This can be advantageous for some polymer products; for instance, shish-kebabs cause a high modulus and high mechanical strength in fibers [108].

The key to understanding the formation of oriented structures in a crystallizing polymer melt subjected to flow is their genesis. Understanding the mechanisms of shish formation is crucial in defining the experimental conditions for controlling flow-induced crystallization and thus for controlling the final properties of polymer products.

Recently, there have been several studies of the crystallization of polymer melts subjected to elongational flow using in-situ X-ray [109, 110]. However, the non-availability of sensitive and efficient high framing rate detectors has limited the full understanding of the mechanisms behind the early stages of crystallization, such as the formation of elongated precursors and their propagation during flow. Moreover, coupling of rheology with X-ray data is essential in understanding the flow-induced crystallization process.

In this case study, we show preliminary results on the possibility of following, in real time, the origin of extended chain crystals (i.e., shish) during elongational flow at relatively high strain rates (up to 25 s^{-1}) and, hence, at very short time scale.

Elongational flow-induced crystallization of iPP can be studied using a Sentmanat extension rheometer (SER) universal testing platform fixture [111] (Fig. 24b) hosted on an Anton Paar MCR 502 rheometer coupled with a specially

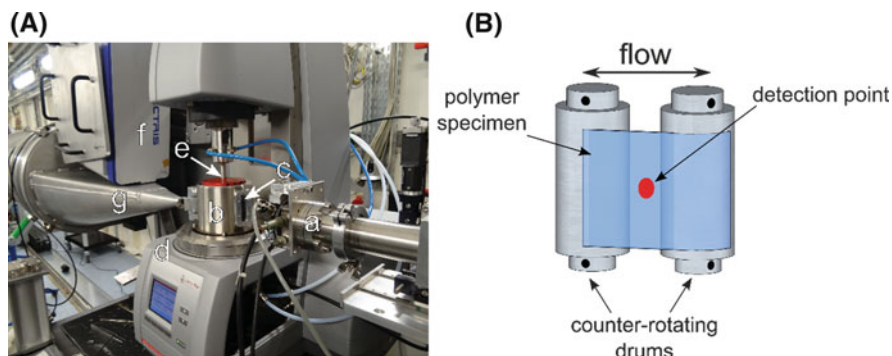


Fig. 24 (a) Rheometer installed at BM26B, ESRF: (a) incoming X-ray beam vacuum pipe, (b) convection oven, (c) X-ray transparent mica window, (d) Anton Paar rheometer, (e) SER shaft, (f) WAXS detector, (g) SAXS vacuum chamber. SAXS detector is at 6 m from the sample, out of the picture. (b) Drawing of the Sentmanat extensional rheometer (SER)

designed X-ray transparent oven, based on a convection temperature control (Fig. 24a). The setup can perform transient uniaxial extensional viscosity measurements and simultaneously record combined SAXS/WAXD data.

The iPP sample is initially kept at 210°C for 5 min to erase all thermomechanical history and subsequently cooled down to the experimental temperature, $T_{\text{ext}} = 135^\circ\text{C}$. After a stabilization time of 5 min at T_{ext} , the maximum achievable Hencky strain (ϵ_{H}) of 3.5 is imposed on the polymer melt using five different Hencky strain rates ($\dot{\epsilon}_{\text{H}}$).

Time-resolved X-ray experiments were carried out at beamline BM26B at ESRF in Grenoble with a wavelength $\lambda = 0.1$ nm, using a Pilatus 1M detector ($981 \times 1,043$ pixels of 172×172 μm placed at a distance of 5.08 m) for the SAXS and a Pilatus 300K detector ($1,472 \times 195$ pixels of 172×172 μm placed at a distance of 0.35 m) for the WAXS. Importantly, the detectors were triggered by an electric TTL pulse at the start of the rotation of the drums. The first 2.8 s from the start of extensional flow were monitored at an acquisition frequency of 30 frames/s. The following 20 min during isothermal crystallization were recorded using a relatively slower acquisition mode (exposure time of 2 s, resulting in a total acquisition time of about 3.5 s).

Equatorial and meridional regions were defined in the 2D SAXS images to quantify the scattering caused by structures extended in the direction of the flow (i.e., shish) and the scattering related to lamellae growing radially (i.e., kebabs), respectively. The spacing between lamellae oriented perpendicularly with respect to flow direction was obtained after Lorentz correction of the scattered meridional intensity and by simple application of Bragg's law, $L_{\text{P}} = \frac{2\pi}{q^*}$, where q^* is the value of the scattering vector corresponding to the maximum in intensity.

Two different iPP crystal polymorphs (α and β) were observed during the performed experiments. The relative amount of the α - and β -phases was obtained from the two most intense reflections: (110) for the α -form and (300) for the β -form. After background and amorphous scattering subtraction, the azimuthal integrations

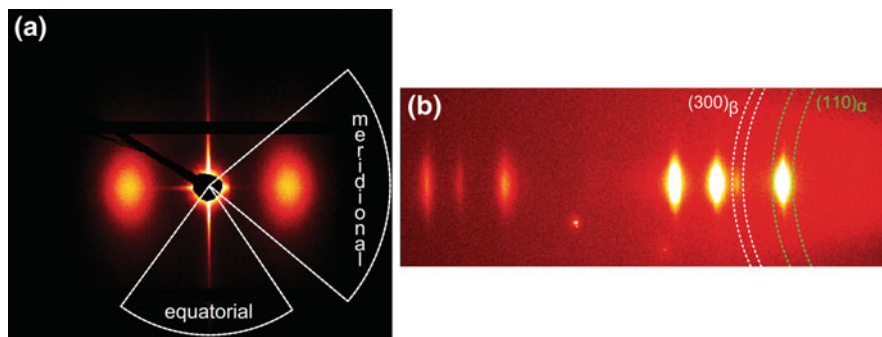


Fig. 25 (a) Anisotropic 2D SAXS image with the definition of meridional and equatorial azimuthal regions. (b) WAXD pattern for a stretched iPP sample showing the presence of both α - and β -forms. Azimuthal regions for the integration of the two characteristic diffraction reflections are shown by the *green and white arcs*, respectively. Elongational flow direction is horizontal

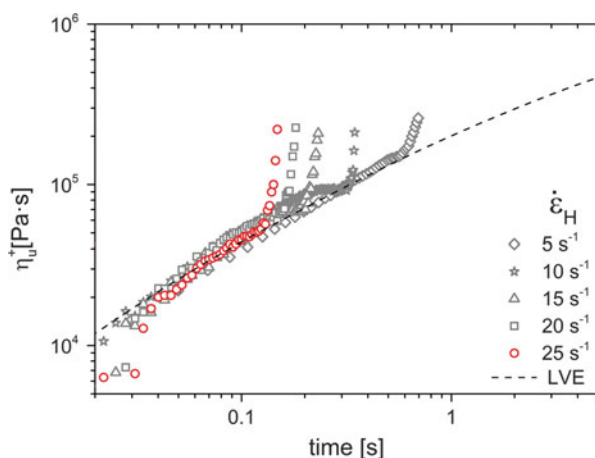


Fig. 26 Transient uniaxial viscosity curves for material studied over a range of Hencky strain rates measured at melt temperatures of 135°C. The *red symbols* represent the experiment discussed in Sect. 3.4. The *dashed line* represents the linear viscoelastic envelope (LVE)

of the two peaks were fitted with a Lorentzian function and the values of the fitting area were used to quantify the time evolution of the two phases. Definitions used in this case study are shown in Fig. 25.

Transient uniaxial elongational viscosities (η_u^+) at strain rates ranging from 5 to 25 s^{-1} are presented in Fig. 26. The dashed line represents the transient elongational viscosity of the linear viscoelastic envelop (LVE) evaluated according to the Trouton ratio, $\eta_u^+(t) = 3\eta_s(t)$, where $\eta_s(t)$ is the transient shear viscosity calculated on the basis of the discrete relaxation spectrum evaluated from the storage and loss moduli data at 180°C. Then, the spectrum was shifted to the experimental temperature using the Arrhenius shift factor a_T , corresponding to the experimental temperature of 135°C.

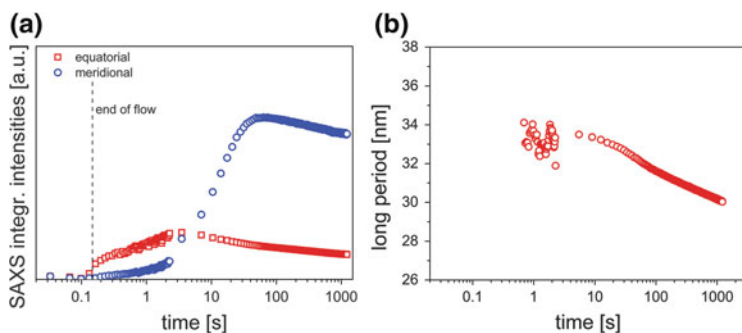


Fig. 27 (a) SAXS integrated equatorial and meridional intensity and (b) long period evolution for the experiment performed at a Hencky strain rate of 25 s^{-1} . The vertical dashed line represents the end of elongational flow

At low deformations, the initial part of the elongational viscosity curves corresponds well to the predicted level at 135°C for all the strain rates used. Subsequently, a clear deviation from linearity is observed. The uniaxial elongational viscosity undergoes a sudden upturn at a Hencky strain of about 3 for all the experiments ($t = 0.12 \text{ s}$), which is a clear indication of crystallization during flow.

Time evolutions of equatorial and meridional intensities for the experiment performed with the highest Hencky strain rate (25 s^{-1}) are presented in Fig. 27a. The equatorial intensity, related to scattering of extended chain crystals aligned along the flow direction, starts to increase at a Hencky strain of about 3 (after 0.12 s), confirming that the deviation from linearity observed in rheology can be related to structure formation during flow.

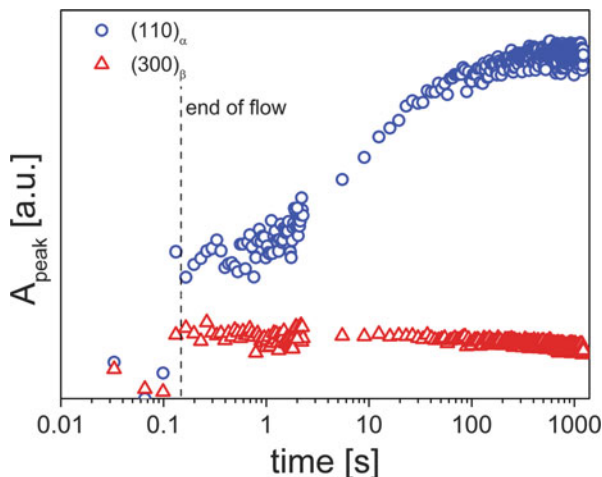
During isothermal crystallization and after flow has been applied, the equatorial intensity continues to increase for about 3 s, indicating the continuous development of shish structures. Simultaneously, meridional intensity shows a slight increase, indicating nucleation of lamellar stacks on the shish cores (i.e., kebabs). Within about 40 s, both the meridional and equatorial intensities reach a maximum value and then show a small decrease during the 20 min time observation window.

The long period evolution is shown in Fig. 27b. During the same time interval, kebabs start interdigitating, which causes a decrease in the average spacing between oriented lamellae and a loss of contrast in the direction perpendicular to flow. This results in the decrease observed in meridional intensity.

The time evolution of the area underneath the $(110)_\alpha$ and $(300)_\beta$ reflections (related to the amount of α -form and β -form crystals, respectively) of the same experiment are shown in Fig. 28. A clear increase in the area underneath the $(110)_\alpha$ reflection is observed after about 0.15 s , indicating, as expected, formation of shish structures consisting of α -form crystals in line with rheological and SAXS observations.

Surprisingly, an increase in the area underneath the $(300)_\beta$ peak is observed during elongational flow. This indicates that β -form crystals form during flow, most probably growing from the already formed shish α -form template. During the

Fig. 28 Time evolution of the area underneath the $(110)_\alpha$ and $(300)_\beta$ reflections for the experiment performed with a Hencky strain of 25 s^{-1} . The vertical dashed line indicates the end of elongational flow



20 min of isothermal crystallization, the area underneath the $(110)_\alpha$ reflection continues to increase until reaching a plateau value, similarly to SAXS meridional intensity evolution, whereas the area related to the $(300)_\beta$ peak stays constant. This indicates that the kebabs are entirely composed of α -form crystals.

4 New Challenges and Future Developments

Despite the perception that polymer crystallization is mostly understood, deep knowledge of the structuring of polymeric materials in real life and industrially relevant conditions is lacking. Pioneering works conducted between the 1980s and 1990s mostly used ex-situ SAXS and WAXD results on polymer specimens processed in well-controlled laboratory conditions. With the advance of synchrotron radiation, in-situ SAXS and WAXD experiments on polymer crystallization in quiescent conditions with second and subsecond time resolution has become possible. In the scientific examples reported here, we have seen how novel experimental tools have been developed in the last few years to study in-situ fast structuring of polymers. Acquisition of structural information during polymer crystallization simultaneously with mechanical, thermal, and rheological data is the challenge that modern laboratories are now facing. In Sect. 3.4 we reported the first successful results of simultaneous real-time rheo-SAXS/WAXD experiments for uniaxial flow with a real rheometer. However, rheological experiments are usually carried out using plate–plate and cone–plate geometries. These geometries are typically employed in the laboratory to study quiescent and shear-induced crystallization in semicrystalline homopolymers, polymer blends, copolymers, and polymer nanocomposites but are difficult to couple with in-situ SAXS/WAXD because of space limitation around the rheometer plates.

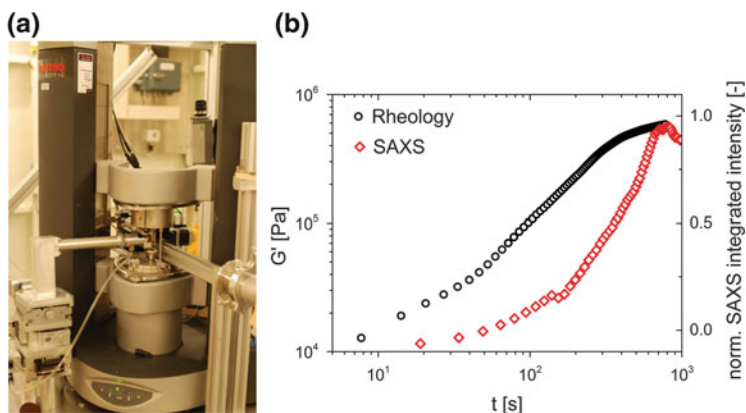


Fig. 29 (a) Vertical beam rheo-SAXS setup installed at BM26B at the ESRF. (b) Preliminary results of polyamide 6 crystallization followed by in-situ rheo-SAXS using a vertically deflected synchrotron beam

An interesting recent approach to the collection of simultaneous rheo-SAXS data makes use of a vertically deflected X-ray beam [112]. This setup has been successfully applied to liquid crystals [113], block copolymers [114], and colloidal systems [115]. This experimental approach will be useful in the future for the study of combined rheology with SAXS/WAXD techniques to verify and develop the structural aspects of several rheological models in the field of polymer science [116, 117]. A preliminary experiment has been performed on BM26B at the ESRF using rheo-SAXS with vertically deflected beam geometry for the isothermal crystallization of polyamide 6 (see Fig. 29a, b). The onset of crystallization and the kinetics of crystal formation can be probed successfully by both rheology and SAXS. Future developments include the possibility of measuring rheology at high torque values and performing WAXD experiments.

A future challenge is the implementation of biaxial flow and stretching devices in X-ray synchrotron beamlines. Biaxial flow is found in many industrial processes such as injection molding, film blowing, blow molding, etc. On-line film blowing of LDPE has already been investigated using 2D WAXS [118]. SAXS experiments during on-line film blowing are in progress.

Another field where development can be expected in the near future is the coupling between X-ray experiments and fast chip calorimetry. In the late 1990s, differential scanning calorimetry (DSC) was successfully coupled with simultaneous SAXS/WAXD, emerging techniques at that time [119–121]. Simultaneous fast chip calorimetry/SAXS/WAXD was then successfully employed for polymeric and nonpolymeric samples [122, 123]. The recent development of fast-operating chip-based calorimeters (flash DSC), now allows study of polymer structure formation at cooling rates comparable to those used in industrial processing. X-ray investigation of polymeric structures produced via flash DSC is usually possible in situ but not in real time [124, 125]. Recently, Baeten et al. developed a sensor

unit that can be decoupled from the electronics and mounted outside the calorimeter [126]. The sensor was successfully coupled with WAXD to follow crystallization of polyethylene and polyamide. Future experiments will follow different polymeric and nonpolymeric systems and the development of a flash DSC/SAXS/WAXD setup will open new opportunities in the field of fast polymer structuring.

An additional overlooked aspect of technique combination is the importance of establishing the connection between X-ray results and the data that can be obtained using more widely available laboratory techniques. This is necessary because synchrotron X-ray beamtime is scarce. The limited amount of synchrotron X-ray data can be extrapolated to the more abundant results of, for instance, Raman, FTIR, UV-vis, rheology, etc., that are commonly used in industrial research environments. For this reason, a number of combined simultaneous experiments are still required.

References

1. Keller A (1957) *Philos Mag* 2:1171
2. Till PH (1957) *J Polym Sci* 24:301
3. Kantz MR, Newman HD, Stigale FH (1972) *J Appl Polym Sci* 16:1249
4. Katti SS, Schultz M (1982) *Polym Eng Sci* 22:1001
5. Lauritzen JI Jr, Hoffman JD (1959) *J Chem Phys* 31:1680
6. Keller A, Machin MJ (1967) *J Macromol Sci Part B Phys* 1:41
7. Norton DR, Keller A (1985) *Polymer* 26:704
8. Armistead K, Goldbeck-Wood G, Keller A (1992) Polymer crystallization theories. In: Armistead KA (ed) *Macromolecules: synthesis, order and advanced properties*, vol 100/1, *Advances in polymer science*. Springer, Berlin, pp 219–312
9. Keller A, Goldbeck-Wood G, Hikosaka M (1993) *Faraday Discuss* 95:109
10. Strobl G (2000) *Eur Phys J E* 3:165
11. Strobl G (2006) *Prog Polym Sci* 31:398
12. Okada T, Saito H, Inoue T (1992) *Macromolecules* 25:1908
13. Lee CH, Saito H, Inoue T (1993) *Macromolecules* 26:6566
14. Matsuba G, Kaji K, Nishida K, Kanaya T, Imai M (1999) *Macromolecules* 32:8932
15. Bulkin BJ, Lewin M, Kim J (1987) *Macromolecules* 20:830
16. Bark M, Zachmann HG, Alamo R, Mandelkern L (1992) *Makromol Chem* 193:2363
17. Bras W, Derbyshire GE, Ryan AJ, Mant GR, Felton A, Lewis RA, Hall CJ, Greaves GN (1993) *Nucl Instrum Methods Phys Res, Sect A* 326:587
18. Wang Z-G, Hsiao BS, Sirota EB, Agarwal P, Srinivas S (2000) *Macromolecules* 33:978
19. Heeley EL, Maidens AV, Olmsted PD, Bras W, Dolbnya IP, Fairclough JPA, Terrill NJ, Ryan AJ (2003) *Macromolecules* 36:3656
20. Pogodina NV, Siddiquee SK, Van Egmond JW, Winter HH (1999) *Macromolecules* 32:1167
21. Sasaki S, Tashiro K, Kobayashi M, Izumi Y, Kobayashi K (1999) *Polymer* 40:7125
22. Bras W, Derbyshire GE, Bogg D, Cooke J, Elwell MJ, Komanschek BU, Naylor S, Ryan AJ (1995) *Science* 267:996
23. Bryant GK, Gleeson HF, Ryan AJ, Fairclough JPA, Bogg D, Goossens JGP, Bras W (1998) *Rev Sci Instrum* 69:2114
24. Urban V, Panine P, Ponchut C, Boesecke P, Narayanan T (2003) *J Appl Crystallogr* 36:809
25. Kellermann G, Vicentin F, Tamura E, Rocha M, Tolentino H, Barbosa A, Craievich A, Torriani I (1997) *J Appl Crystallogr* 30:880

26. Bras W, Dolbnya IP, Detollenaere D, van Tol R, Malfois M, Greaves GN, Ryan AJ, Heeley E (2003) *J Appl Crystallogr* 36:791
27. Hexemer A, Bras W, Glossinger J, Schaible E, Gann E, Kirian R, MacDowell A, Church M, Rude B, Padmore H (2010) *J Phys Conf Ser* 247(1):012007. doi:10.1088/1742-6596/247/1/012007
28. Kirby NM, Mudie ST, Hawley AM, Cookson DJ, Mertens HD, Cowieson N, Samardzic-Boban V (2013) *J Appl Crystallogr* 46:1670
29. Keller A (1959) *J Polym Sci* 39:151
30. Bassett DC, Hodge AM (1978) *Polymer* 19:469
31. Keith HD, Padden FJ (1996) *Macromolecules* 29:7776
32. Roozmond PC, van Drongelen M, Ma Z, Spoelstra AB, Hermida-Merino D, Peters GWM (2015) *Macromol Rapid Commun* 36:385
33. Kumaraswamy G, Issaian AM, Kornfield JA (1999) *Macromolecules* 32:7537
34. Fernandez-Ballester L, Gough T, Meneau F, Bras W, Ania F, Balta-Calleja FJ, Kornfield JA (2008) *J Synchrotron Radiat* 15:185
35. Hsiao BS, Yang L, Somani RH, Avila-Orta CA, Zhu L (2005) *Phys Rev Lett* 94:117802
36. Bunn CW, Holmes DR (1958) *Discuss Faraday Soc* 25:95
37. Natta G, Corradini P (1960) *Il Nuovo Cimento* 1955–1965. 15:40
38. Balta-Calleja FJ, Vonk CG (1989) *X-ray scattering of synthetic polymers*. Elsevier, Amsterdam
39. Hermans JJ, Hermans PH, Vermaas D, Weidinger A (1946) *Recl Trav Chim Pays-Bas* 65:427
40. Wilchinsky ZW (1960) *J Appl Phys* 31:1969
41. Stein RS (1958) *J Polym Sci* 31:327
42. Stein RS (1958) *J Polym Sci* 31:335
43. Norris FH, Stein RS (1958) *J Polym Sci* 27:87
44. Guinier A, Fournet G (1955) *Small angle X-rays*. Wiley, New York
45. Glatter O, Kratky O (1982) *Small angle scattering*. Academic, New York
46. Brumberger H (1994) *Modern aspects of small-angle scattering*. Springer, The Netherlands
47. Zemb T, Lindner P (2002) *Neutrons, X-rays and light: scattering methods applied to soft condensed matter*, North-Holland delta series. Elsevier, Amsterdam
48. G. Porod (1952) *Kolloid Z* 125(1):51 doi:10.1007/BF01519615
49. Ryan AJ, Bras W, Mant GR, Derbyshire GE (1994) *Polymer* 35:4537
50. Goderis B, Reynaers H, Koch MHJ, Mathot VBF (1999) *J Polym Sci B Polym Phys* 37:1715
51. Porod G (1951) *Colloid Polym Sci* 124:83
52. Vonk CG (1973) *J Appl Crystallogr* 6:81
53. Ciccariello S, Goodisman J, Brumberger H (1988) *J Appl Crystallogr* 21:117
54. Ciccariello S (1985) *Acta Crystallogr A* 41:560
55. Koberstein JT, Morra B, Stein RS (1980) *J Appl Crystallogr* 13:34
56. Vonk CG (1978) *J Appl Crystallogr* 11:541
57. Brämer R, Gerdes C, Wenig W (1983) *Colloid Polym Sci* 261:293
58. Ruland W, Smarsly B (2004) *J Appl Crystallogr* 37:575
59. Hosemann R, Bagchi SN (1962) *Direct analysis of diffraction by matter*. North-Holland, Amsterdam
60. Vonk CG, Kortleve G (1967) *Kolloid Z Z Polym* 220:19
61. Strobl GR, Schneider M (1980) *J Polym Sci Polym Phys Ed* 18:1343
62. Ruland W (1977) *Colloid Polym Sci* 255:417
63. Stribeck N, Ruland W (1978) *J Appl Crystallogr* 11:535
64. Stribeck N (2001) *J Appl Crystallogr* 34:496
65. Debye P, Anderson HR Jr, Brumberger H (1957) *J Appl Phys* 28:679
66. Debye P, Bueche AM (1949) *J Appl Phys* 20:518
67. Keum JK, Zuo F, Hsiao BS (2008) *Macromolecules* 41:4766
68. Avila-Orta CA, Burger C, Somani R, Yang L, Marom G, Medellin-Rodriguez FJ, Hsiao BS (2005) *Polymer* 46:8859

69. Keum JK, Burger C, Hsiao BS, Somani R, Yang L, Chu B, Kolb R, Chen H, Lue CT (2005) *Prog Colloid Polym Sci* 130:114
70. Liu J, Pancera S, Boyko V, Shukla A, Narayanan T, Huber K (2010) *Langmuir* 26:17405
71. Worgan JS, Lewis R, Fore NS, Sumner IL, Berry A, Parker B, D'Annunzio F, Martin-Fernandez ML, Towns-Andrews E, Harries JE, MantGR, Diakun GP, Bordas J (1990) *Nucl Instrum Methods Phys Res Sect A* 191:447
72. Lewis R, Worgan JS, Fore NS, d'Annunzio F, Hall C, Parker B (1991) *Nucl Instrum Methods Phys Res, Sect A* 310:70
73. Henrich B, Bergamaschi A, Broennimann C, Dinapoli R, Eikenberry EF, Johnson I, Kobas M, Kraft P, Mozzanica A, Schmitt B (2009) *Nucl Instrum Methods Phys Res, Sect A* 607:247
74. Labiche J-C, Mathon O, Pascarelli S, Newton MA, Ferre GG, Curfs C, Vaughan G, Homs A, Carreiras DF (2007) *Rev Sci Instrum* 78:091301
75. Klug HP, Alexander LE (1974) *X-ray diffraction procedures*, 2nd edn. John Wiley, New York
76. Kraft P, Bergamaschi A, Broennimann C, Dinapoli R, Eikenberry EF, Henrich B, Johnson I, Mozzanica A, Schlepütz CM, Willmott PR et al (2009) *J Synchrotron Radiat* 16:368
77. Mathot V, Pyda M, Pijpers T, Poel GV, Van de Kerkhof E, Van Herwaarden S, Van Herwaarden F, Leenaers A (2011) *Thermochim Acta* 522:36
78. Pijpers TF, Mathot VB, Goderis B, Scherrenberg RL, van der Vegte EW (2002) *Macromolecules* 35:3601
79. Huth H, Minakov AA, Serghei A, Kremer F, Schick C (2007) *Eur Phys J Spec Top* 141:153
80. Zhuravlev E, Schick C (2010) *Thermochim Acta* 505:1
81. Zhuravlev E, Schick C (2010) *Thermochim Acta* 505:14
82. Portale G, Cavallo D, Alfonso GC, Hermida-Merino D, van Drongelen M, Balzano L, Peters GWM, Goossens JGP, Bras W (2013) *J Appl Crystallogr* 46:1681
83. Cavallo D, Azzurri F, Floris R, Alfonso GC, Balzano L, Peters GW (2010) *Macromolecules* 43:2890
84. Cavallo D, Portale G, Balzano L, Azzurri F, Bras W, Peters GW, Alfonso GC (2010) *Macromolecules* 43:10208
85. Cavallo D, Gardella L, Alfonso GC, Portale G, Balzano L, Androsch R (2011) *Colloid Polym Sci* 289:1073
86. Mileva D, Cavallo D, Gardella L, Alfonso GC, Portale G, Balzano L, Androsch R (2011) *Polym Bull* 67:497
87. Mileva D, Androsch R, Cavallo D, Alfonso GC (2012) *Eur Polym J* 48:1082
88. McAllister PB, Carter TJ, Hinde RM (1978) *J Polym Sci Polym Phys Ed* 16:49
89. Grange RA, Kiefer JM (1941) *Trans ASM* 29:85
90. Moniz BJ (1994) *Metallurgy*. American Technical, Homewood
91. Davenport ES, Bain EC (1970) *Metall Mater Trans B* 1:3503
92. Bas C, Grillet AC, Thimon F, Alberola ND (1995) *Eur Polym J* 31:911
93. Maffezzoli A, Kenny JM, Nicolais L (1993) *J Mater Sci* 28:4994
94. Strobl GR, Strobl GR (1997) *The physics of polymers*. Springer, Berlin
95. Muthukumar M (2004) *Adv Chem Phys* 128:1
96. Libster D, Aserin A, Garti N (2007) *Polym Adv Technol* 18:685
97. Gahleitner M, Grein C, Kheirandish S, Wolfschwenger J (2011) *Int Polym Process* 26:2
98. Haas TW, Maxwell B (1969) *Polym Eng Sci* 9:225
99. Wolkowicz MD (1978) *J Polym Sci Polym Symp* 63(1):365–382. doi:[10.1002/polc.5070630129](https://doi.org/10.1002/polc.5070630129)
100. Liedauer S, Eder G, Janeschitz-Kriegl H, Jerschow P, Geymayer W, Ingolic E (1993) *Int Polym Process* 8:236
101. Balzano L, Rastogi S, Peters GW (2009) *Macromolecules* 42:2088
102. Ma Z, Balzano L, van Erp T, Portale G, Peters GW (2013) *Macromolecules* 46:9249
103. Housmans J-W, Balzano L, Santoro D, Peters GWM, Meijer HEH (2009) *Int Polym Process* 24:185

104. Troisi EM, Portale G, Ma Z, van Drongelen M, Hermida-Merino D, Peters GWM (2015) *Macromolecules* 48(8):2551–2560
105. Barham PJ, Keller A (1985) *J Mater Sci* 20:2281
106. Hill MJ, Barham PJ, Keller A (1980) *Colloid Polym Sci* 258:1023
107. Wunderlich B (1980) *Macromolecular physics*. Elsevier, Amsterdam
108. Smith P, Lemstra PJ (1980) *J Mater Sci* 15:505
109. Cui K, Meng L, Tian N, Zhou W, Liu Y, Wang Z, He J, Li L (2012) *Macromolecules* 45:5477
110. Liu D, Tian N, Cui K, Zhou W, Li X, Li L (2013) *Macromolecules* 46:3435
111. Sentmanat ML (2004) *Rheol Acta* 43:657
112. Stellamanns E, Meissner D, Lohmann M, Struth B (2013) *J Phys Conf Ser* 425:202007. doi:[10.1088/1742-6596/425/20/202007](https://doi.org/10.1088/1742-6596/425/20/202007)
113. Struth B, Hyun K, Kats E, Meins T, Walther M, Wilhelm M, Grübel G (2011) *Langmuir* 27:2880
114. Pulamagatta B, Ostas E, Herbst F, Struth B, Binder WH (2012) *Eur Polym J* 48:1127
115. Lettinga MP, Holmqvist P, Ballesta P, Rogers S, Kleshchanok D, Struth B (2012) *Phys Rev Lett* 109:246001
116. Pogodina NV, Lavrenko VP, Srinivas S, Winter HH (2001) *Polymer* 42:9031
117. Housmans J-W, Steenbakkens RJ, Roozmond PC, Peters GW, Meijer HE (2009) *Macromolecules* 42:5728
118. van Drongelen M, Cavallo D, Balzano L, Portale G, Vittorias I, Bras W, Alfonso GC, Peters GW (2014) *Macromol Mater Eng* 299:1494
119. Russell TP, Koberstein JT (1985) *J Polym Sci Polym Phys Ed* 23:1109
120. Koberstein JT, Russell TP (1986) *Macromolecules* 19:714
121. Bras W, Ryan AJ (1998) *Adv Colloid Interface Sci* 75:1
122. Semmler K, Meyer HW, Quinn PJ (2000) *Biochim Biophys Acta Biomembr* 1509:385
123. Turković A, Dubček P, Juračić K, Bernstorff S, Buljan M (2013) *Am J Nanosci Nanotechnol* 1:6
124. van Drongelen M, Meijer-Vissers T, Cavallo D, Portale G, Poel GV, Androsch R (2013) *Thermochim Acta* 563:33
125. Rosenthal M, Doblas D, Hernandez JJ, Odarchenko YI, Burghammer M, Di Cola E, Spitzer D, Antipov AE, Aldoshin LS, Ivanov DA (2014) *J Synchrotron Radiat* 21:223
126. Baeten D, Mathot VB, Pijpers TF, Verkinderen O, Portale G, Van Puyvelde P, Goderis B (2015) *Macromol Rapid Commun* 36(12):1184–1191

Strain-Induced Crystallization in Natural Rubber

Pierre-Antoine Albouy and Paul Sotta

Abstract Rather than an exhaustive review of the numerous reported studies of strain-induced crystallization (SIC) in natural rubber, this chapter discusses some aspects of the physical mechanisms involved that we think are fundamental for understanding crystallization kinetics and processes such as reinforcement. We mainly focus on the rich information that can be retrieved from X-ray diffraction studies. In particular, we show how easily knowledge of the strain state of the amorphous fraction can be obtained quantitatively from X-ray diffraction patterns and how informative that knowledge is. Considering, for instance, the hardening sequence observed during stretching, it is clear that no prediction of the stress level can be made without knowing both the crystalline content and the average elongation of the remaining molten chains. Particular emphasis is put on the strain relaxation effect that accompanies SIC in both static and dynamic conditions. This fundamental effect is described in the theory of SIC developed by Flory, which we present from an innovative perspective to emphasize its deep analogy to the liquid–gas phase transformation. In spite of the fact that Flory’s theory has only been qualitatively verified experimentally and is limited to static and equilibrium conditions, it grasps the essential of the driving mechanisms at play. Some simple experiments are presented within this framework that should enlighten the most fundamental aspects of SIC. The crystallization kinetics underlies most aspects of SIC and is discussed in detail. Tensile impact tests, which allow conceptually simple but very informative experiments, are treated first. We try to show that the time dependence of the crystalline content is tentatively related to the mechanism of

P.-A. Albouy
Laboratoire de Physique des Solides, Univ. Paris-Sud, CNRS, UMR 8502, F-91405,
Orsay Cedex, France

P. Sotta (✉)
Laboratoire Polymères et Matériaux Avancés, CNRS, Solvay, UMR 5268, F-69192,
Saint-Fons Cedex, France
e-mail: paul.sotta-exterieur@solvay.com

strain relaxation in a simple manner. Knowledge of crystallization kinetics is also essential for explaining the hysteretic behavior observed in dynamic conditions. Similarities and/or differences between dynamic and static SIC are discussed.

Keywords Crystallization kinetics, Natural rubber, Strain induced crystallization, Strain relaxation, X ray diffraction

Contents

1	Introduction	168
2	Basics of X-Ray Diffraction for the Study of Strain-Induced Crystallization	169
3	Segmental Orientation in the Amorphous Phase	173
4	Crystalline Morphologies in the Quiescent State and Under Strain	176
5	Theory of Strain-Induced Crystallization	177
6	Isothermal Strain-Induced Crystallization Kinetics in Static Conditions	183
7	Isothermal Strain-Induced Crystallization Kinetics During Mechanical Cycling	189
	7.1 Stretching	195
	7.2 Recovery	199
8	Conclusion	202
	References	203

1 Introduction

Strain-induced crystallization (SIC) in natural rubber (NR) was reported 90 years ago by Katz [1], and one may wonder about the need for another review devoted to this topic. Although the underlying physics was clearly identified by Flory in 1947 [2], many aspects of this fascinating phenomenon remain unclear. Furthermore, the importance of NR as a base material for the elaboration of some essential products explains a never-halting research effort. In particular, there has been a burst in real-time X-ray diffraction experiments during the last 10 years that was made possible by dramatic technical improvements. The reader interested in this field can find an extensive survey in the review by Huneau [3]. An excellent textbook recently published by Toki, which contains a wealth of information about SIC, must also be mentioned [4]. However, our purpose is somewhat different. We do not claim to be exhaustive on the subject. We present our own point of view on some aspects of the physics involved and on how these aspects can potentially help in understanding crystallization kinetics and processes such as reinforcement. This also explains the particular emphasis on X-ray diffraction, which has been extensively used by one of us, with special emphasis on relaxation of the remaining amorphous fraction that accompanies SIC. We believe that this phenomenon is so essential that the term “crystallization-induced strain relaxation” should be used rather than “strain-induced crystallization” to underline its importance.

This chapter is organized as follows: The types of information that can be retrieved from X-ray diffraction data are first described in detail (Sects. 2 and 3). In particular, we show how the strain experienced by the remaining amorphous fraction during crystallization can be evaluated (Sect. 3). In Sect. 4, we describe the differences in crystalline morphology that can be observed in the case of strain-induced crystallization and for crystallization in the quiescent state, also called temperature-induced crystallization (TIC). It is a recognized fact that polymers that crystallize easily under strain generally crystallize only slowly in the quiescent state (the converse is also true). The explanation may lie in the ability of some elastomers to form extended crystals, which is the morphology favored under extension. The theory of SIC developed by Flory is then briefly described in Sect. 5. Its profound analogy with the liquid–gas phase transformation, as implicitly noted by Miyamoto et al. [5], is emphasized. In spite of the fact that Flory’s theory has only been qualitatively verified experimentally, we think it grasps the essentials of the driving mechanisms at play. Some simple experiments are presented within this frame that should enlighten the most fundamental aspects of SIC. The theory developed by Flory deals with thermodynamic equilibrium. However, crystallization kinetics underlies most aspects of SIC. We first discuss tensile impact tests, which allow conceptually simple but very informative experiments. We try to show that the time dependence of the crystalline content can be tentatively related to the mechanism of strain relaxation in a simple manner. Knowledge of crystallization kinetics is also fundamental in explaining the hysteretic behavior observed in dynamic conditions. Similarities and differences between dynamic and static SIC are discussed in Sect. 6. This review is restricted to the simpler case of uniaxial deformation. Other geometries may be of interest for practical applications, but the difficulty of their analysis arises from the higher complexity of the associated strain field; the physics involved remains the same. The interested reader can find examples of the use of X-ray diffraction for the study of SIC under multiaxial stretching in the literature [6–8]. We conclude by discussing the most obscure and puzzling questions that still await explanation.

Before entering the core of the subject, one remark should be made. Many figures presented here are based on personal unpublished data but we do not claim exclusivity. In some cases, this is merely for convenience because their equivalent can be found in the literature. Other figures correspond to new results that we thought necessary to include to illustrate some important points.

2 Basics of X-Ray Diffraction for the Study of Strain-Induced Crystallization

Because X-ray diffraction is the main method used for the present work, some basic principles need to be briefly outlined. Different processes can occur when an atom is hit by an incident X-ray photon. The process of interest for X-ray diffraction

is Thomson scattering, whereby the atom reemits a spherical wavelet of nearly similar wavelength (elastic scattering). Wavelets scattered by atoms located within some coherence volume characteristic of the incident beam (namely its geometry and monochromaticity) present phase relations and can interfere. The conditions for constructive interference essentially depend on the vectors between scatterers and the observation angle with respect to the incidence beam direction. In the case of a crystal where positional order is long range, conditions for constructive interferences are strict and require a precise sample orientation to be observed. The diffracted intensity is then restricted to well-defined directions that correspond to the so-called Bragg reflections. The crystal acts as a three-dimensional grating and each reflection is associated with one of the grating periodicities, d , by the Bragg law $2d \sin \theta = \lambda$, where 2θ is the angular deviation of the diffracted beam and λ the X-ray wavelength (see for instance [9]). In the case of smaller crystallites, the relatively restricted number of atoms makes the conditions for constructive interferences less stringent and reflections are broader. Their angular width is inversely proportional to some specific crystallite dimensions, according to the Scherrer formula [10]. Small crystallites grown in a semicrystalline polymer exhibit a wide range of orientations so that the conditions for observation of diffraction spots in terms of sample orientation are much looser (see for instance [11]).

In the case of an amorphous or liquid material, the order is only short range and conditions for constructive interference are highly relaxed. The scattered intensity is more evenly distributed angularly and maxima are quite broad (so-called amorphous halos). The halos essentially originate from interferences between wavelets emitted by nearest neighbor atoms. Fourier inversion of the intensity gives access to the differential radial distribution function (DRDF). In brief, the DRDF indicates the different distances between correlated atoms and the relative proportion of atoms involved in each distance [12].

The organization of macromolecules in the molten and quiescent state of NR was studied by Simard and Warren as early as 1936 [13]. This issue was revisited in 1978 by Wang and Yeh and we rely on their analysis [14]. In the quiescent state, the diffraction pattern is isotropic and displays a broad and intense maximum followed by weak secondary maxima at higher scattering angles (Fig. 1, left). Analysis of the DRDF (Fig. 1, right) shows that secondary maxima on the diffraction pattern are associated with intrachain first or second neighbor distances, whereas the first intense maximum mainly originates from interferences between wavelets scattered by atoms located on neighboring chains. The three maxima at 0.568, 1.065, and 1.525 nm observed on the DRDF function are approximate first, second, and third harmonics of an interchain correlation distance of ca. 0.53 nm. This distance is tentatively associated with a local orthorhombic arrangement of parallel segments that extends laterally over a distance of ca. 1.5 nm. Such an organization is reminiscent of that observed in the crystalline state (see below). Stretching causes the first intense diffraction maximum to arc about the equator. On the other hand, meridional arching is expected for the halos at higher diffraction angles, but their intensity is too low for proper observation. The way in which the anisotropy of the first halo may be quantitatively related to the strain state of polymeric chains is detailed at the end of this section.

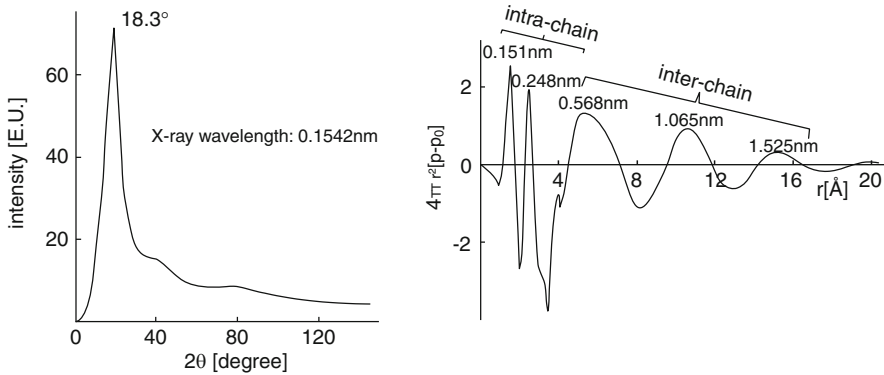


Fig. 1 *Left*: Diffraction by amorphous NR shown by plot of scattering intensity versus diffraction angle; the “amorphous halo” is centered at 18.3° (copper $K\alpha$ radiation). *Right*: Differential radial distribution function; the indicated distances correspond to peak positions (After [15])

The exact structural organization of NR in the crystalline state remains controversial. However, the structure does not depend on whether crystallites are grown in the quiescent state or under strain. We rely on the analysis recently published by Rajkumar et al. [16]. NR crystallizes in the orthorhombic system and the space group is $P2_12_12_1$. Indicative values for the lattice constants are $a = 1.26$ nm, $b = 0.90$ nm, and $c = 0.83$ nm (with c along the chain axis). In the case of crystallites grown during SIC, these parameters not only depend on temperature but also on the magnitude of the applied strain. Reported lattice constants for crystallites grown in the quiescent state are slightly smaller [17]. The orthorhombic assignment has been recently confirmed by Che et al. and very nice simulations of X-ray patterns can be found in publications by this group [17, 18]. The crystalline structure is represented in Fig. 2.

Four molecular chains with two isoprene units within the unit cell run along the \vec{c} -axis. Chains 1 and 3 contain methyl groups pointing upwards and chains 2 and 4, downwards. Rajkumar et al. have observed weak diffuse X-ray scattering between Bragg reflections, which indicates some disorder [16]. Accordingly, a model in which the strict alternation of up and down chains is relaxed has been proposed. The existence of a conformational disorder had been previously suggested as a possible explanation for the unusually low melting entropy of NR [19–21].

A representative X-ray diffraction pattern for an NR sample submitted to uniaxial extension is given in Fig. 3 (left). The corresponding scattering geometry is depicted in Fig. 3 (right). The well-defined and intense spots originate from the crystalline phase and are identified by their hkl indices [3]. The fact that reflections with $l = 0$ (in this case 200 and 120) are concentrated at the equator indicates that the \vec{c} -axis of crystallites (which coincides with the polymer chain axis) is preferentially aligned parallel to the stretching axis. The degree of alignment can be estimated from the half-angular (azimuthal) width of the equatorial reflections $\delta\varphi_{1/2}$

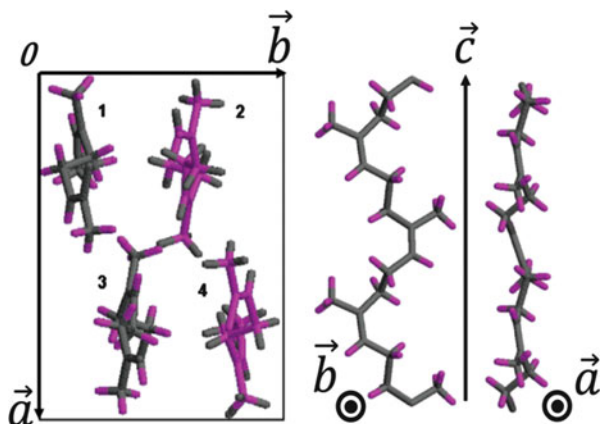


Fig. 2 Polyisoprene chain packing in the crystalline state in the absence of packing disorder [16]. Chains are running along the \vec{c} -axis; methyl groups are pointing upwards in chains 1 and 3, downwards in chains 2 and 4

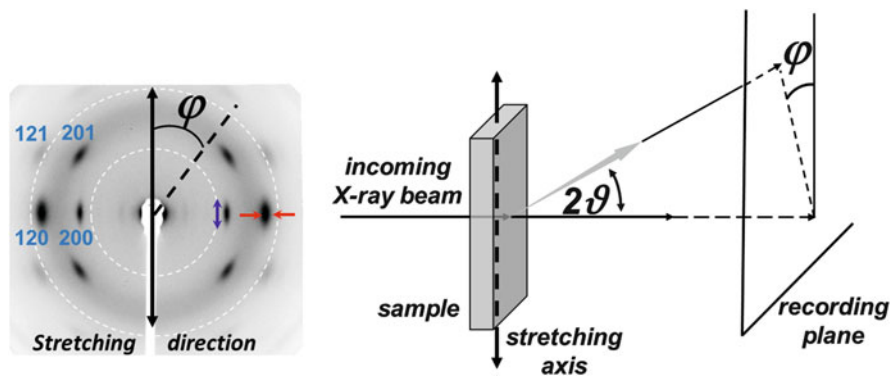


Fig. 3 *Left*: Representative X-ray diffraction pattern for NR specimen partially crystallized under strain. Dotted white circles indicate integration range used, ϑ scattering angle, blue arrow angular width of the equatorial reflections, red arrows reflection radial width. See text for more details. *Right*: The associated scattering geometry

(blue arrow in Fig. 3, left). A high degree of orientation is found even at relatively low extension. For instance, in the case of static crystallization conducted at -25°C , $\delta\varphi_{1/2}$ values ranging from 12° at an elongation $\lambda=2$ to 4° at $\lambda=6$ have been reported by Trabelsi et al. [22]. Another relevant parameter is the reflection radial width (red arrows in Fig. 3, left), which is related to the average crystallite dimension in a given direction by the Scherrer formula, as explained above (see also Fig. 6). Calculation of the percentage of crystalline phase is based on the fact that the wavelet is reemitted by an individual atom independently of whether it is embedded in a crystallite or in the amorphous phase. This means that the respective

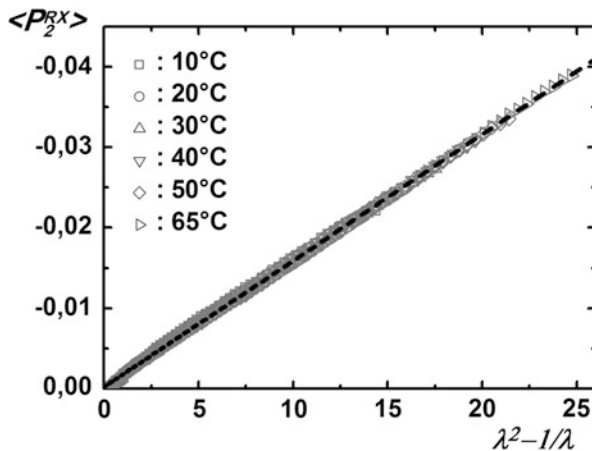
amounts of intensity scattered in the whole space by the crystalline and amorphous phases are indicative of their respective fractions. Based on this, X-ray diffraction is one of the most common (if not the easiest) technique used to determinate percentage crystallinity in semicrystalline polymers [11]. In practical conditions, the integration range is limited and the obtained ratio is not an absolute measurement; for this reason, the term “crystallinity index” is preferred. For instance, the integration range used in our investigations is restricted to the zone delimited by the two dotted white circles shown in Fig. 3 (left) where the most intense crystalline reflections are located. The intense amorphous halo is similarly contained in this zone. Separation of the crystalline and amorphous contributions can be based on the analysis of radial scans, with the disadvantage of smearing-off all the pattern anisotropy [9, 11]. For this reason, angular φ -scans (as depicted in Fig. 3, left) are preferred.

3 Segmental Orientation in the Amorphous Phase

Strain-induced anisotropy of the amorphous scattering in NR is relatively weak compared with the strongly oriented scattering from the crystalline phase (see Fig. 3 left). This fact is often misinterpreted as proof that most chains in the amorphous phase retain a relaxed coil conformation while the minority becomes highly extended, eventually related to crosslink heterogeneity. However, double-quantum proton NMR experiments have indicated without ambiguity that sulfur-vulcanized NR samples generally present a high degree of homogeneity as regarding crosslink density [23]. Data reported in the pioneering work of Mitchell show that the degree of equatorial arching for the amorphous halo is within the magnitude expected from statistical rubber elasticity theory [24].

This point deserves a more quantitative discussion. In the case of uniaxial stretching, the segmental orientation distribution $N(\chi)$ (where χ is the angle between a statistical segment and the stretching direction) displays cylindrical symmetry around the stretching direction. The distribution $N(\chi)$ can be expanded in Legendre polynomials of even order $P_{2n}(\cos \chi)$. In the domain of extensions in which Gaussian approximation applies, the expansion of $N(\chi)$ can be limited to the second order, higher order coefficients being negligible. For the affine junction network model, the statistical theory of hyperelasticity gives $\langle P_2 \rangle = (\lambda^2 - 1/\lambda)/(5N)$, where N is the average number of statistical segments between crosslinks [25]. According to the Curie principle, the associated scattering must have cylindrical symmetry as well. Thus, the circular anisotropy of the amorphous scattering measured at any given diffraction angle can be similarly characterized by a second-order Legendre coefficient. In the particular case of the integration range defined in Fig. 3 (left) we denote this Legendre coefficient $\langle P_2^{\text{RX}} \rangle$. As mentioned above, this coefficient is mainly related to inter- rather than intrachain scattering, and the question of the relation between $\langle P_2 \rangle$ and $\langle P_2^{\text{RX}} \rangle$ arises. It is clear that the average orientations of the carbon-

Fig. 4 Second-order Legendre coefficient $\langle P_2^{\text{RX}} \rangle$ characterizing the anisotropy of the X-ray intensity scattered by the amorphous fraction as a function of $(\lambda^2 - 1/\lambda)$ (sulfur-vulcanized NR sample, $N \approx 46$) [28]

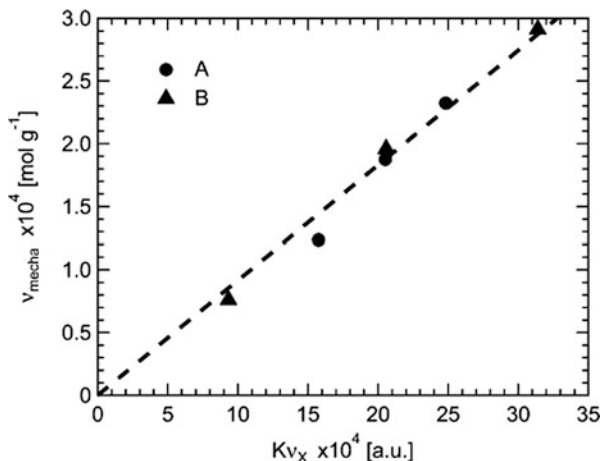


carbon vectors involved in intrachain scattering follow the average chain orientation. Based on early work by Deas [26], the intrachain scattering has been related to $N(\chi)$ in a rigorous way by Mitchell et al. [27]. To the best of our knowledge, no such rigorous demonstration exists for interchain scattering. A quite convincing argument is based on a symmetry argument, related to the above-mentioned local orientation order between neighboring chains: the local environment of a given segment (in terms of atoms or electron density) is expected to have, on average, a uniaxial symmetry around the mean reference segment axis (which is the same as the chain backbone axis). The proportionality then follows from the spherical addition theorem. Consequently, the vectors joining one atom of the reference segment to closer atoms located in surrounding chains are expected to be, on average, perpendicular to the reference segment. Scattering is then stronger perpendicular to the stretching direction and presents equatorial enhancement. Beyond such general speculations, the most prominent evidence for the existence of a linear relation between $\langle P_2 \rangle$ and $\langle P_2^{\text{RX}} \rangle$ is given in Fig. 4, showing that $\langle P_2^{\text{RX}} \rangle \approx K(\lambda^2 - 1/\lambda)$ in absence of crystallization, which indeed is the behavior expected for $\langle P_2 \rangle$ [28]. In the particular case of Fig. 4, the prefactor K is equal to -0.00157 . Based on geometrical considerations, Mitchell estimated $\langle P_2^{\text{RX}} \rangle \approx -0.33 \langle P_2 \rangle$ or equivalently $K \approx -0.33(1/5N)$ [24]. In the present case, $N \approx 46$ and the calculated K value is -0.00143 , which is close to the experimental determination.

A further point that has been recently validated is the linear dependence of the coefficient K on $1/N$ or equivalently on the number of elastic chains per unit volume ν (which is twice the crosslink density for a perfect tetrafunctional network). Vieyres et al. compared crosslink density values evaluated by double-quantum proton NMR, equilibrium swelling, mechanical response, and X-ray diffraction in a series of samples vulcanized with various amounts of sulfur [29]. Figure 5 illustrates the nearly perfect correlation between the values estimated from the mechanical modulus (ν_{mecha}) and the parameter $-K$ (denoted $K\nu_X$ in the graph).

Fig. 5 Crosslink density estimated from the mechanical modulus versus the slope

$-\langle P_2^{RX} \rangle / (\lambda^2 - 1/\lambda)$ for samples vulcanized with different sulfur contents (ranging from 0.5 to 2.5 parts per hundred parts of rubber) [29]



Similar results have been obtained by comparing K with crosslink density values evaluated by NMR and equilibrium swelling. To summarize, the parameter $\langle P_2^{RX} \rangle$ closely follows the behavior expected for a homogeneous elastomer.

A question arises concerning use of the parameter $\langle P_2^{RX} \rangle$ to evaluate the elongation state of the remaining amorphous fraction λ_{Am} once the sample has partially crystallized. Crystallization is expected to reduce the average number of statistical segments per molten chain and thus to affect the initial value of the parameter K . This effect can be tentatively estimated by replacing N by $N(1 - \chi)$, leading to the modified relation $\langle P_2^{RX} \rangle \approx (K/(1 - \chi))(\lambda_{Am}^2 - 1/\lambda_{Am})$. The correction is small for moderate crystalline indices and was not used in our previous publications [28, 30]. Another related, although distinct, effect is that crystallites may act as effective multifunctional crosslinks, which could also affect the elastic constant $1/N$.

A sample thickness of around 1.5 mm is optimal for X-ray diffraction at a wavelength of 0.154 nm. For thicknesses not too far from this value, conventional X-ray generators equipped with a copper anode are sufficient for most studies. All data extracted from our published works were obtained in this way (ca. 10^9 photons/s for beam diameter 1 mm). The exposure time does not exceed 10 s per diffraction frame. Kinetic measurements such as tensile impact tests require the much higher flux provided by synchrotron facilities. In that case, the flux, which is generally delivered on a smaller cross-section, is at least three orders of magnitude higher. This could lead to irradiation-induced crosslinking. However, to the best of our knowledge, this issue has not been addressed.

This section shows that $\langle P_2 \rangle$ can be evaluated quantitatively from the anisotropy of the amorphous halo, with a prefactor that depends only on the nature of the elastomer.

4 Crystalline Morphologies in the Quiescent State and Under Strain

It is a well-established fact that crystallization of NR in the quiescent state (TIC) is always a slow process, even at -25°C where crystallization kinetics is at a maximum [31]. Interestingly, fatty acids that are naturally present in NR appear to have some impact on the crystallization rate for unvulcanized samples [32]. By contrast, apparently instantaneous crystallization is detected at high extension levels, even well above room temperature [4]. This undoubtedly shows that two different crystallization modes are at work, and that they are most probably associated with different crystalline morphologies. In the case of TIC, transmission electron microscopy (TEM) observations of thin films obtained by fractionation of pure gum reveal different crystallization regimes, depending on the temperature or the average molecular weight; however, lamellar growth is observed in all cases [31]. When the samples are stretched, TEM reveals a succession of morphologies from spherulitic in the quiescent state to filamentous at above 300% extension, with filaments oriented along the stretching axis [33]. Although it is widely accepted that this roughly corresponds to a transition from lamellar to extended crystal growth (without folds), the existence of some row-nucleated lamellar growth is still debated. Data obtained by Trabelsi et al. for the average dimensions of crystallites grown under various static elongations also indicate an evolution toward a needle-like morphology at higher strains [22]. Figure 6 shows that the average crystallite dimension along the \vec{c} -axis (i.e., chain axis within crystallites) l_{002} increases from ca. 5 nm at lower extensions ($\lambda = 2$) to 15 nm above $\lambda = 6$. Conversely, the two perpendicular, l_{200} and l_{120} , dimensions (see Fig. 6, right) steadily decrease. Even in the presence of some packing disorder, up and down chains alternate in the crystallites, which imposes some packing restriction. Because the crystallization

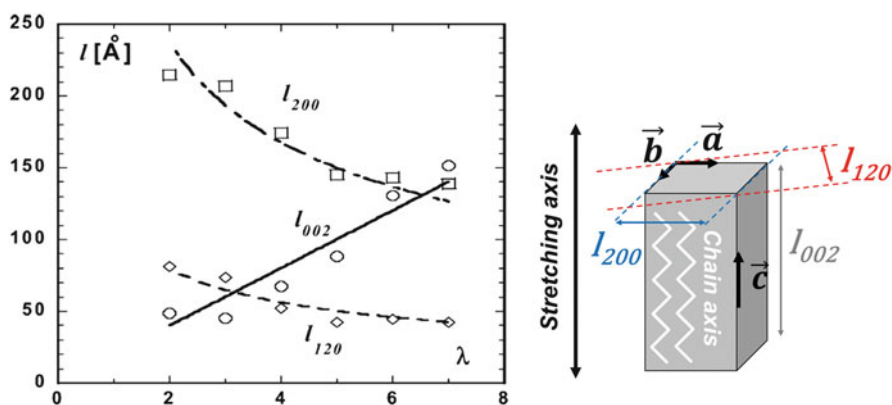


Fig. 6 *Left*: Average crystallite size for crystallites grown in static conditions under various elongations, as determined by the Scherrer formula (crystallization and measuring temperature -25°C). *Right*: Directions associated with the involved dimensions (After [22])

rate increases rapidly with elongation, it is thought that less time is allowed for the chains to pack with the correct alternation sequence, resulting in a decrease in lateral dimensions. For the sake of simplicity, only the formation of extended crystals is considered here.

5 Theory of Strain-Induced Crystallization

Flory’s theory for strain-induced crystallization was published in 1947 [2] and several alternative theories have been proposed since then [34, 35]. Although predictions can be quantitatively different, the physics involved is fundamentally similar. Even though Flory’s theory is restricted to conditions of static equilibrium, to emphasize the underlying physics it is essential to understand out-of-equilibrium and dynamic situations.

In Flory’s theory, the conditions for equilibrium between the amorphous and crystalline fractions within polymer chains are established. What happens at the scale of network chains is considered to be representative of the whole material. As implicitly recognized by Miyamoto et al. [5], this description has deep analogy with the liquid–gas transition of a molecular liquid. Working out this analogy allows recovering Flory’s main conclusions in a very simple way. Flory’s theory essentially relies on the following assumptions for chain conformations (see also Fig. 7, left):

1. Chains within crystallites are perfectly oriented along the stretching axis, and directions perpendicular to the stretching axis are assumed not to be affected by crystallization. The chain axis in crystallites is, on average, close to the stretching direction.

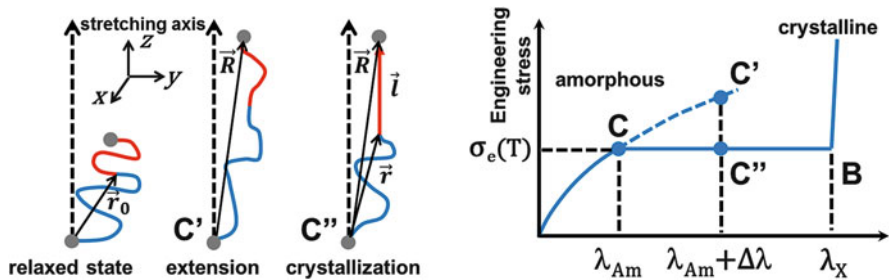


Fig. 7 *Left*: Representation of the crystallization process in Flory’s theory. *Right*: The corresponding Clapeyron diagram for the equilibrium between amorphous and crystalline phases in a NR elastomer. The *blue curve* is an isotherm at temperature T . The value $\sigma_e(T)$ on the plateau is the engineering stress corresponding to amorphous/crystal coexistence at temperature T . Starting from the fully amorphous material (elongation λ_{Am} , point C), increasing the macroscopic elongation to $\lambda = \lambda_{Am} + \Delta\lambda$ (C to C’) induces a fraction of crystalline phase, given by the lever rule, to appear (point C’')

2. Chains are not allowed to re-enter a crystallite by folding. This assumption is in line with the discussion above.
3. Chain elongations are moderate so that Gaussian statistics apply.

The possibility of folding and extension to non-Gaussian statistics has been considered by Gaylord [36]. The reader is referred to this publication for a very clear description of the calculations involved in Flory's theory.

Following the approach of Miyamoto et al. [5], the thermodynamic potential (analogous to the free enthalpy in the case of liquid–gas transition) to consider for describing uniaxial elongation is $\Omega = E - TS - \sigma\lambda$, where E is the internal energy, T the temperature, S the entropy, σ the engineering stress in the traction direction, and λ the elongation. In this way, when describing the phase equilibrium, the intensive variables that must be uniform throughout the system are temperature and engineering stress. This generalized thermodynamic potential can be written as the function $\Omega_N(y, \sigma, T)$ where y is an intensive variable that differentiates the phases (the “order parameter”, analogous to the volume available per molecule in the liquid–gas transition). The subscript N indicates that, for an elastomer, there is a dependence on the chain length N between crosslinks or, equivalently, on the number of elastic chains per unit volume (as already noted, this is twice the crosslink density for a tetrafunctional network) $\nu \approx 1/Na^3$, where a^3 is the volume per monomer (or, more precisely, per statistical segment).

A natural choice for the intensive variable y is the local elongation ratio λ . In the relaxed amorphous state $\lambda = 1$, while the “natural” average length of a chain (along the stretching direction) can be defined by $\langle z^2 \rangle_0^{1/2} = a\sqrt{N/3}$ (a is the segment length). For an elongation λ , the natural average length becomes $\langle z^2 \rangle^{1/2} = a\lambda\sqrt{N/3}$. In the crystalline state (subscript X), the chain is almost fully stretched along the stretching direction, with $\langle z^2 \rangle_X^{1/2} \cong aN$. In terms of chain elongation ratio, this corresponds to a maximum extension ratio $\lambda_{\text{Max}} = \langle z^2 \rangle_X^{1/2} / \langle z^2 \rangle_0^{1/2} = \sqrt{3N}$, which in general is considered large compared with λ .

In a range of T and σ values, $\Omega_N(y, \sigma, T)$ has two minima that define the generalized thermodynamic potentials Ω_X and Ω_{Am} of the crystalline and amorphous phases, respectively. Within this range, for each value of σ , there is a temperature $T_m(\sigma)$ such that $\Omega_X = \Omega_{\text{Am}}$. Equivalently, for a given temperature T , there is a value σ_e such that $\Omega_X = \Omega_{\text{Am}}$. The (σ_e, T) phase diagram can be established from the way in which $T_m(\sigma)$ varies as a function of σ . Then, the locations $y_X(\sigma)$ and $y_{\text{Am}}(\sigma)$ of the minima of $\Omega_N(y, \sigma, T)$ for each value of T give the constitutive equations for each of the phases. The $y(\sigma)$ diagram is the equivalent of the Clapeyron–Clausius diagram in the context of the liquid–gas transition.

Here, an explicit expression for the thermodynamic potential $\Omega_N(y, \sigma, T)$ is not known a priori. The thermodynamic potential (per monomer) for the amorphous phase is given by the rubber elasticity theory:

$$\begin{aligned}\Omega_{\text{Am}} &= \frac{k_{\text{B}}T\nu a^3}{2} (\lambda_{\text{Am}}^2 + 2\lambda_{\text{Am}}^{-1}) - a^3\sigma\lambda_{\text{Am}} = -\frac{k_{\text{B}}T\nu a^3}{2} (\lambda_{\text{Am}}^2 - 4\lambda_{\text{Am}}^{-1}) \\ &= -\frac{k_{\text{B}}T}{2N} (\lambda_{\text{Am}}^2 - 4\lambda_{\text{Am}}^{-1}),\end{aligned}\quad (1)$$

where the relation $\sigma = k_{\text{B}}T\nu(\lambda_{\text{Am}} - \lambda_{\text{Am}}^{-2})$ has been used; λ_{Am} is the elongation in the amorphous phase. The chemical potential of the crystalline phase can be written as $\Omega_{\text{X}} = E_{\text{X}} - a^3\sigma\lambda_{\text{X}}$, where E_{X} is the energy of the crystalline phase per monomer (which may be supposed not to depend significantly on λ , because the elongation modulus of the crystalline phase must be much higher than that of the rubbery phase) and λ_{X} is the chain elongation in the crystalline phase (which is close to λ_{Max}). The entropy of the crystalline phase is neglected.

From the above considerations, $\sigma(\lambda)$ isotherms (Clapeyron diagram) can be established, as schematized in Fig. 7 (right). The different steps considered for the calculation of the thermodynamic changes occurring during SIC are illustrated in Fig. 7 (left).

On the coexistence plateau $\sigma_{\text{c}}(T)$, for a given value of the macroscopic elongation λ , the equilibrium crystalline fraction χ is given by the lever rule:

$$\chi = \frac{\lambda - \lambda_{\text{Am}}}{\lambda_{\text{X}} - \lambda_{\text{Am}}}, \quad (2)$$

Any change in the macroscopic elongation λ of the sample induces a change in the crystalline fraction. In that sense, it can be said that the phase transformation is induced by the variation in stretching ratio or, equivalently, that the driving force for crystallization is overstretching of the amorphous phase. From the simple equation (2), the decrease in stress associated with crystallization (from point C' down to C'' in Fig. 7, right) can be estimated. Equation (2) is rewritten:

$$\lambda_{\text{Am}} = \frac{\lambda - \chi\lambda_{\text{X}}}{1 - \chi}. \quad (3)$$

Approximating $\sigma \cong k_{\text{B}}T\nu\lambda_{\text{Am}}$ and $\lambda_{\text{X}} \cong \lambda_{\text{Max}} \cong \sqrt{3N}$ gives:

$$\sigma \cong \frac{k_{\text{B}}T\nu}{1 - \chi} (\lambda - \chi\sqrt{3N}). \quad (4)$$

This is similar to Flory's formula (within the same level of approximation $1/\lambda^2 \ll \lambda$), with $\lambda_{\text{M}} \cong (3N)^{1/2}$ instead of $(6N/\pi)^{1/2}$ in Flory's original work:

$$\sigma \cong \frac{k_B T v}{1 - \chi} \left(\lambda - \chi \left(\frac{6N}{\pi} \right)^{1/2} \right). \quad (5)$$

The prediction of Flory's theory that has perhaps received most attention is the dependence of equilibrium melting temperature $T_M(\lambda)$ on elongation λ . At equilibrium melting, the chemical potentials Ω_X and Ω_{Am} are equal, which gives the melting temperature directly as a function of the engineering stress σ and melting enthalpy ΔH_M^0 (assumed to be independent of T and λ), according to:

$$T_M(\sigma) = \frac{\Delta H_M^0 + \sigma(\lambda_X - \lambda_{Am})}{S_{Am}(\sigma) - S_X(\sigma)} = \frac{\Delta H_M^0 + \sigma(\lambda_X - \lambda_{Am})}{S_{Am}(\sigma) - S_{Am}(0) + \Delta S_M^0}, \quad (6)$$

$S_{Am}(0) - S_X(\sigma)$ has been identified with the melting entropy ΔS_M^0 in the quiescent state, assuming that the entropy of the crystalline phase $S_X(\sigma)$ is independent of σ . Then, substituting $S_{Am}(\sigma) - S_{Am}(0)$ and σ by their expressions from rubber elasticity theory, Eq. (6) can be rewritten:

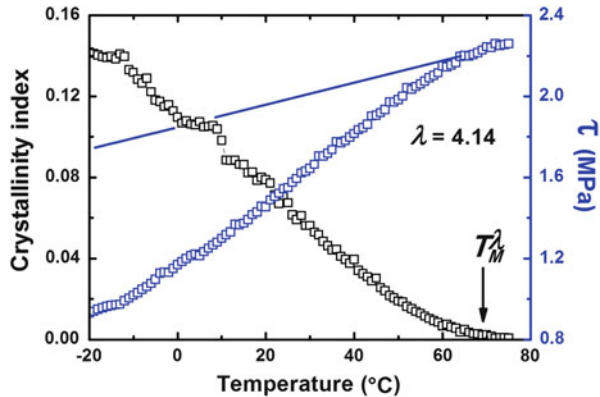
$$\frac{1}{T_M^0} - \frac{1}{T_M(\lambda)} = \frac{R}{N\Delta H_M^0} \left[\lambda\lambda_X - \frac{\lambda^2}{2} + \frac{2}{\lambda} - \frac{\lambda_X}{\lambda^2} - \frac{3}{2} \right], \quad (7)$$

where $T_M^0 = \Delta H_M^0 / \Delta S_M^0$ denotes the melting temperature in the quiescent state and R the gas constant. Considering again that $\lambda_X \cong \lambda_{Max} \cong \sqrt{3N}$, Eq. (7) is similar to the original Flory equation (8) if one restricts to the most significant factors at higher elongation [2]:

$$\frac{1}{T_M^0} - \frac{1}{T_M(\lambda)} = \frac{R}{\Delta H_M^0} \left[\lambda \left(\frac{6}{\pi N} \right)^{1/2} - \frac{1}{N} \left(\frac{\lambda^2}{2} + \frac{1}{\lambda} \right) \right]. \quad (8)$$

Note that Eq. (7) still holds at $\lambda = 1$, which is not the case for Flory's formula. In order to compare the predictions of Flory's theory with experimental data, it is crucial to reach true thermodynamic equilibrium in static conditions. Let us suppose that the equilibrium crystallinity of the sample is χ_{eq} at some temperature T and elongation λ . We show in the next sections that reaching this state by simply isothermally stretching the sample to λ may require quasi-infinite duration. This is simply because the driving force for SIC is overstretching, which decreases as crystallization proceeds as a result of the concomitant relaxation of the amorphous phase. Two protocols have been proposed to circumvent this obstacle. The first method consists in maintaining the elongation λ constant and cooling the sample to well below T , until the crystalline fraction largely exceeds χ_{eq} . Quasi-equilibrium can then be reached after warming the sample back up to T . The second method consists in maintaining the sample at constant temperature T and stretching it to well above λ , until the crystalline fraction exceeds χ_{eq} , followed by relaxation to λ .

Fig. 8 Crystallinity index (grey symbols) and engineering stress (blue symbols) measured during progressive warming of a sulfur-vulcanized sample submitted to static elongation (crystallization temperature ca. -25°C). The blue line represents the engineering stress expected in the absence of SIC (Albouy P-A, unpublished data)



The section on mechanical cycling (Sect. 7) shows that the equilibrium state obtained with the second method is apparently different to that obtained by the static procedure. The first protocol corresponds to the experimental pathway described, for instance, by Luch and Yeh [37]. These authors applied rapid stretching at high temperature to avoid crystallization, followed by cooling to -25°C until no apparent evolution in the retraction force was observed, followed by slow heating. Typical data obtained during progressive warming at constant elongation are shown in Fig. 8. The blue line in Fig. 8 represents the engineering stress expected in the absence of SIC, as extrapolated from values obtained during cooling in the absence of crystallization (with a modulus proportional to temperature, according to rubber elasticity theory). The correlation between crystallization and the decrease in stress is clearly apparent. The smoothing of the crystallinity curve close to melting could be the result of some small sample inhomogeneity.

The first exhaustive experimental test of the predictions of Flory's theory for the evolution of stress, crystalline content, and melting temperature was probably conducted by Arlman and Goppel in 1951 [37]. More recent works can be found in the literature [22, 38–40]. The general conclusion was that a satisfying agreement between experimental data and Flory's formula can be obtained only by giving non-realistic values to either T_M^0 , ΔH_M^0 or N . Another fundamental discrepancy is demonstrated in Fig. 9, in which the melting temperatures for three samples with different numbers of repeating units per chain are plotted as a function of the elongation ratio [40]. All data fall on a common master curve, although Flory's formula predicts different slopes [see Eq. (8)]. This fact was also reported by Trabelsi et al. [22]. However, it is important to stress that the dependence of ΔH_M^0 on the chain length N remains an open question. This dependence could perhaps counterbalance the N dependence of the factor within brackets.

All the experiments presented above were conducted under strain-controlled conditions. By contrast, Miyamoto et al. performed stress-controlled measurements [5]. After being cooled to -50°C , samples were heated at 1 K/min while maintaining a constant predefined nominal stress value, and the necessary changes

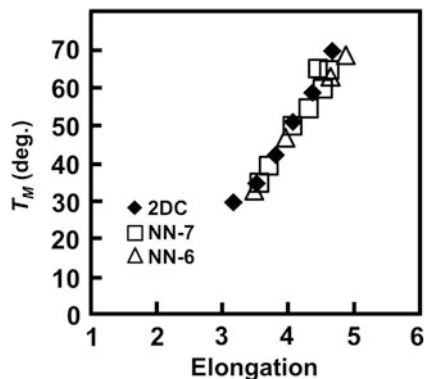


Fig. 9 Relationship between equilibrium melting temperature and elongation for three NR samples with different crosslink densities. *2DC* sample cured with dicumyl peroxide, *NN-7* and *NN6* samples crosslinked by γ -irradiation. Numbers of repeat units per chains: *2DC*, 198; *NN-7*, 140; *NN-6*, 154 (After [40])

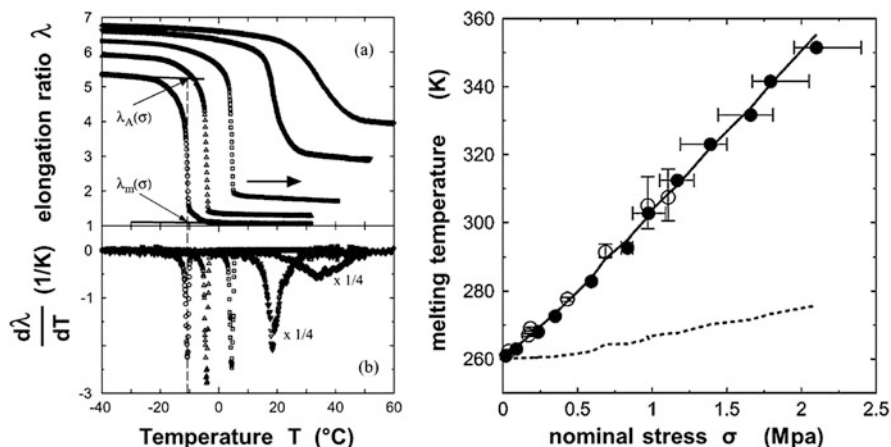


Fig. 10 *Left*: Change in elongation on heating (1 K/min) of a sample submitted to constant nominal stress conditions (*circles* 0.036 MPa, *up triangles* 0.18 MPa, *squares* 0.42 MPa, *down triangles* 0.68 MPa, *diamonds* 1.11 MPa). *Right*: Relation between temperature and nominal stress at melting [5]

in elongation ratio were recorded as a function of temperature. The data acquired in these conditions are reported in Fig. 10 (left).

The data reported in Fig. 10 (left) fully confirm the Flory-type approach presented above. These data emphasize the fact that SIC can be considered as a phase transition, with the elongation ratio playing the role of the order parameter that distinguishes the phases. The curves in Fig. 10 (left) are fully analogous to isobaric curves in the (T,V) diagram for the liquid–gas transition of a pure

substance, with a vertical jump corresponding to the temperature at the coexistence plateau for the given stress value.

Accordingly, the melting temperature can be expressed as a function of the engineering stress, rather than the elongation ratio, as shown in Fig. 10 (right). The graph confirms that Eq. (4) is indeed in good agreement with experimental data. Specifically, it gives the correct slope for the $T_M(\sigma)$ curve.

Note that, in the experiments performed by Miyamoto et al. [5], equilibrium between the amorphous and semicrystalline parts of the material was considered, which is somehow different from the crystal–amorphous local equilibrium described in Eqs. (1)–(6). However, the good semiquantitative agreement between predictions and experimental data shows that the essential physical mechanisms have been correctly captured. In particular, within this framework, relaxation of the amorphous fraction associated with the increase in crystallinity, specific to elastomers, is simply understood as being analogous to the lever rule in liquid–gas coexistence at constant overall volume. A major difference, however, is that for polymers and certainly for elastomers, chain segment diffusion is a limiting kinetic factor that induces extremely long characteristic time scales. These kinetic aspects are discussed in the next section.

6 Isothermal Strain-Induced Crystallization Kinetics in Static Conditions

SIC is a continuous kinetic process that can start at subsecond time scales and extend over weeks. Accessing the shorter time range is a major experimental difficulty. This issue can be tackled in two ways. The first method consists in performing tensile impact tests, in which the samples are brought to a given elongation at very high strain rates. However, the acquisition technique used to monitor crystallinity changes must be fast enough. It requires high beam intensity (synchrotron radiation is mandatory) and efficient detectors with a rapid read-out (typically pixel detectors). Another way to proceed is to periodically repeat the test so that data can be accumulated during a number of successive cycles [41]. This technique has been recently revisited by several authors. Some results are discussed here. The reader is referred to the original papers for further details [30, 42]. The first convincing experiment combining tensile impact tests and time-resolved measurements was probably performed by Mitchell and Meier in 1968 [43]. They used a microthermocouple element embedded into the sample to measure the temperature rise following rapid stretching. One problem was to separate the respective effects of SIC and thermo-elasticity. It is shown in Fig. 11 that SIC onset could be detected about 40 ms after stretching at the maximum investigated elongation ($\lambda \approx 6.5$). It must be clearly understood that this duration is inherently dependent on the sensitivity of the method. It defines a faster time limit and not a real induction time. More recently, some authors have taken advantage of the high

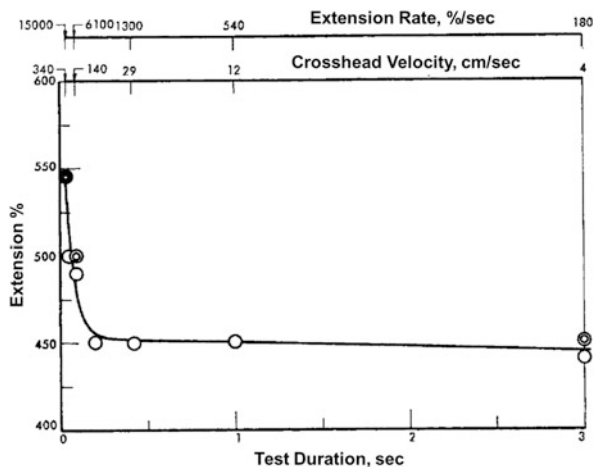


Fig. 11 Thermometric experiment by Mitchell and Meier: the extension for the onset of noticeable crystallization as a function of test duration (sulfur-vulcanized NR sample) [43]

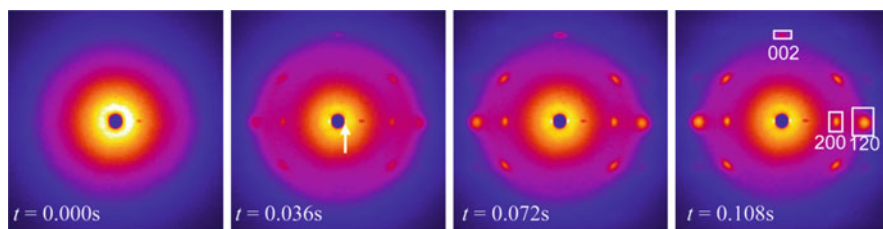


Fig. 12 Evolution of diffraction patterns after reaching final elongation ($\lambda = 7$, sulfur-vulcanized sample, network-chain density 1.95×10^{-4} mol/cm³). Evolution of crystallinity is characterized by the increase in diffracted intensity measured within the areas marked by rectangles. The white arrow in the second pattern from left is of no relevance here [44]

intensity delivered by synchrotron radiation sources and of the development of ultrafast X-ray cameras. Tosaka et al. and Brüning et al. performed tensile impact experiments coupled with rapid X-ray data acquisition. The main results of these two studies are presented here in detail [44, 45].

With the apparatus devised by Tosaka et al., extensional rates up to 1,000 mm/s (corresponding to strain rates up to $\dot{\lambda} = 40$ s⁻¹) can be applied, and frame acquisition duration is 34 ms [44]. For the higher elongation investigated ($\lambda = 7$), the final elongation state is reached within ca. 0.15 s. The first diffraction patterns obtained after reaching final elongation ($\lambda = 7$) are shown in Fig. 12. Surprisingly, the first pattern is completely isotropic, including for the signal of the added stearic acid. This is puzzling because nanoplatelets of stearic acid are thought to readily orient in stretched samples [46]. Appearance of the crystalline phase becomes clear in the second pattern. The evolution of crystallinity is characterized by the increase in diffracted intensity measured within the rectangular areas depicted in the right-hand pattern of Fig. 12.

Fig. 13 Intensity at the locations of most intense reflections (see Fig. 12) as a function of elapsed time (sulfur-vulcanized sample, network-chain density $1.95 \times 10^{-4} \text{ mol/cm}^3$) [44]

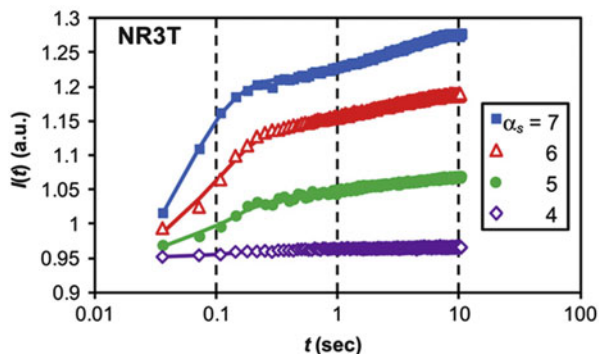
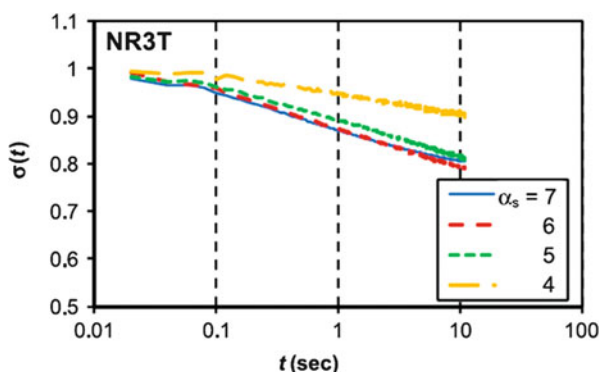


Fig. 14 Stress relaxation after tensile impact tests, concomitant with the increase in crystallinity shown in Fig. 13 [44]



Representative data for the change in crystalline content with elapsed time are given in Fig. 13 for elongations ranging from 4 to 7. The results clearly indicate two distinct crystallization processes with different time constants, τ_f (fast) and τ_s (slow). Accordingly, the data were fitted by an equation of the form $I(t) = I_0 + I_f[1 - e(-t/\tau_f)] + I_s[1 - e(-t/\tau_s)]$. τ_f is in the range 50–200 ms, whereas τ_s is a few seconds. It is interesting to note that the time constants do not show any significant dependence on the strain ratio.

The authors hypothesize that the fast process is associated with the crystallization of highly aligned chains that require only small movements to become included in the crystallites. Segments of less-oriented chains need to diffuse on a longer path and are the origin of the slow process.

The time evolution of the stress was measured concomitantly with crystallinity (see Fig. 14). Even though slow disentanglement processes contribute to stress relaxation, the authors estimate that at least 50% of the stress decrease is the result of crystallization-induced strain relaxation. The fact that the fast initial crystallization process is not accompanied by commensurate stress relaxation has not yet been explained.

Brüning et al. obtained markedly different results in the short time range [45]. Both the acquisition rate (140 frames/s, corresponding to ca. 7 ms per

Fig. 15 Crystallinity versus time for a sulfur-vulcanized NR sample submitted to a quasi-instantaneous 410% strain step [45]

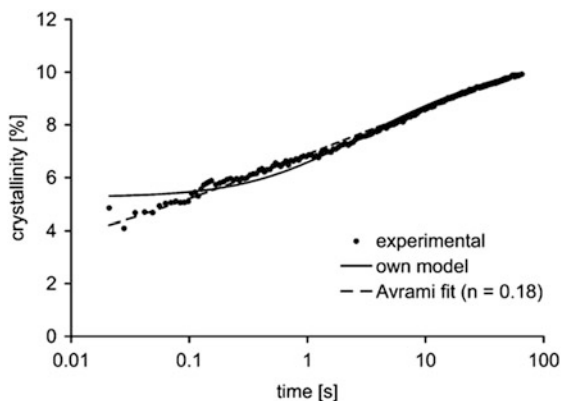
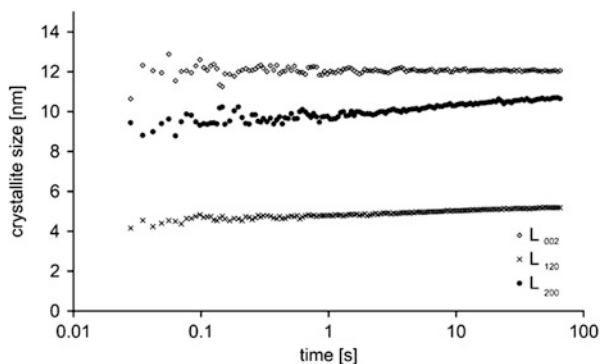


Fig. 16 Time evolution of average crystallite sizes during the same experiments shown in Fig. 15 [45]

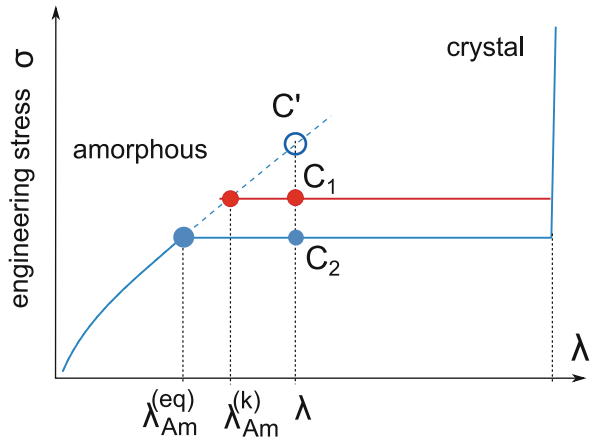


frame) and deformation rate (maximal extension reached within 5–10 ms) were slightly superior to those used by Tosaka et al. Although the apparatus offers the possibility of simultaneous stress measurements, this was not used for tensile impact tests. Figure 15 shows the time evolution of the crystallinity for a sulfur-vulcanized sample step-strained to $\lambda = 5.1$.

The first point to notice is that the crystalline content has already reached a significant value at the time of the first measurement, which corresponds to ca. 20 ms after step completion. This is in contrast to previous results [44], in which no crystallinity was detected in the first frame (ca. 30 ms after step completion). The second point is that a simple logarithmic time dependence is observed for the whole observation duration. This does not formally exclude the existence of a two-step crystallization mechanism, but the time constant τ_s should then be well below the estimates given above. On the other hand, direct extrapolation of the data to the shorter time would give zero crystallinity at about 0.1 ms, which is shorter than the stretching time. Thus, whether one or two characteristic times are present remains an open question.

The time evolution of average crystallite sizes (analogous to those defined in Fig. 6) has also been precisely determined (see Fig. 16). The crystallite size l_{002}

Fig. 17 Blue curve is the theoretical isotherm at a temperature T at thermodynamic equilibrium (same as in Fig. 7). Superscript (eq) stands for equilibrium. As a result of crystallization kinetics, a sample overstretched up to point C' is blocked at point C_1 , with the amorphous phase strained to $\lambda_a^{(k)}$ (superscript (k) stands for kinetic) and the crystallinity effectively given by the lever rule on the red plateau



along the \vec{c} -axis (i.e., chain axis within crystallites) remains constant, whereas the two lateral dimensions l_{120} and l_{200} increase slightly but regularly with a logarithmic time dependence. This indicates that the increase in crystallinity is mainly a result of the growing number of crystallites, and that further growth is limited. As pointed out by the authors, large scale diffusion of molten chains is made impossible by crosslinks and it is not possible to apply Avrami equations, even if modified to take into account the anisotropy of crystal growth [45]. Accordingly, the authors developed a model in which the limiting step is the lateral diffusion necessary for inclusion of a chain section into a crystallite. The crystallization rate accordingly depends on the number of available crystallizable chains, so that $d\chi/dt = (k(\chi_f - \chi))^n$, where χ_f is the crystallinity at final equilibrium and n describes the propensity of amorphous segments to crystallize. An additional parameter is the initial crystallinity caused by nucleation after completion of the strain step. Data could be satisfactorily adjusted using these three parameters. This model has been developed in detail in a recent publication [47]. Note that the impact of thermo-elastic heat release as a result of rapid sample extension was not discussed in either study.

However, and without discussing the pertinence of the models described above, it can be noticed that the strain relaxation process associated with crystallization at fixed overall elongation has not been taken into account in an explicit manner. These kinetic effects can be included in a modified Clapeyron diagram, as illustrated in Fig. 17. A sample overstretched up to point C' follows the path $C'C_2$ during the crystallization process. Point C_1 corresponds to an intermediate crystallization time, with the amorphous phase strained to $\lambda_a^{(k)} > \lambda_a^{(eq)}$ (superscript (k) stands for kinetic) and where the associated crystallinity is effectively given by the lever rule on the plateau shown in red in Fig. 17.

As pointed out above, crystallization is kinetically limited by nucleation, and further crystal growth only plays a minor role. According to standard homogeneous nucleation theory [48], the nucleation barrier (or activation energy) associated with the formation of a stable crystalline nucleus is given by:

$$H = \frac{16\pi}{3} \frac{\gamma^3}{\Delta\Omega_v^2}, \quad (9)$$

where γ is the interface energy (or surface tension) between the crystalline and amorphous phases, and $\Delta\Omega_v$ is the difference in generalized thermodynamic potential per unit volume between the amorphous and crystalline phases at any moment (e.g., at point C₁ in Fig. 17). Strictly speaking, these considerations are for a spherical nucleus of an isotropic nucleated phase. However, the formula in Eq. (9) contains the basic physical ingredients that qualitatively account for the observed behavior. Because nucleation is the essential step, the crystallization rate $d\chi/dt$ should then be proportional to $\exp[-H/k_B T]$. Using Eq. (1), one can write $\Delta\Omega_v \cong k_B T v (\lambda_X - \lambda_{Am}/2) \lambda_{Am}^k \approx k_B T v \lambda_X \lambda_{Am}^k$. Parameter λ_{Am}^k can be linearized as $\lambda_{Am}^k \approx \lambda - \chi(\lambda_X + \lambda)$, based on Eq. (2) for moderate crystallinity, and $\Delta\Omega_v$ decreases linearly with crystallinity. This results in an increase in the nucleation barrier, leading to a slow-down of the crystallization process. For moderate crystalline indices, the barrier H can be similarly linearized as function of the crystalline index and one obtains an approximate equation, $d\chi(t)/dt \propto \exp(-A\chi(t)/k_B T)$. Logarithmic evolution of the crystallinity versus time then naturally follows. In other words, progressive relaxation of the amorphous phase could be the main factor governing the crystallization kinetics.

We close this section with some considerations on the time necessary to reach quasi-equilibrium (close to the state at point C2) after tensile impact tests. For this purpose, some results recently obtained on our laboratory set-up are presented. After rapid stretching to the target elongation (at strain rate 40 s⁻¹), the sample crystallinity was allowed to evolve for ca. 5 h at room temperature. To determine the value of the crystallinity at or close to equilibrium, the sample was cooled to ca. -25°C for 1 h at the end of the test and heated back to room temperature. The crystalline content is then assumed to be close to the equilibrium value. The time to reach close equilibrium is extrapolated, supposing that the logarithmic time dependence remains valid up to equilibrium or near equilibrium. This procedure is illustrated in Fig. 18 and some relevant data are collected in Table 1. It is clear that near-equilibrium becomes out of reach as the stretching ratio become closer to the elongation where no crystallization is possible (in the present case, below $\lambda \approx 2.8$ at 20°C).

Fig. 18 Extrapolation of the time to reach close equilibrium based on a tensile impact test (Albouy P-A, unpublished data)

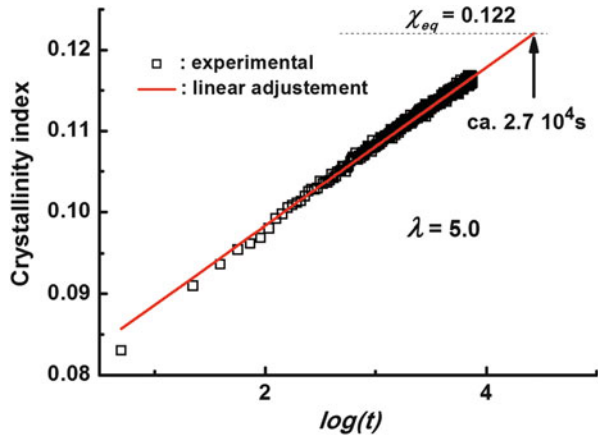


Table 1 Time and crystallinity close to equilibrium for tensile impact tests at different stretching ratios

Stretching ratio	Close-to-equilibrium crystallinity	Close-to-equilibrium time (s)
3.7	0.045	10^{25}
4.1	0.075	10^9
4.6	0.095	10^5
5.0	0.122	2.7×10^4

Calculation procedure is described in Fig. 18 (Albouy P-A, unpublished data)

7 Isothermal Strain-Induced Crystallization Kinetics During Mechanical Cycling

In most applications, elastomeric products undergo some cyclic deformation. Mechanical cycling tests, mostly under uniaxial deformation, are thus widely used for the characterization of base materials. Representative stress–strain curves for an NR sample measured at different maximum strain ratios are displayed in Fig. 19. The large mechanical hysteresis and the stress upturn at higher extension are typical. The origin of both effects, and in particular the stress upturn, has been a long-debated issue. Limited extensibility or SIC can be evoked for the stress upturn because both become manifest in the same strain region. Furthermore, the strain relaxation that accompanies SIC appears adverse to a rapid increase in stress, although Flory proposed that newly formed crystallites could act as physical crosslinks [2]. In his famous text book, Treloar came to the conclusion that the effects of crystallization produced only minor modifications [49]. However, an opposite conclusion has since been established through improvements in investigation techniques. Indeed, both the rapid stress increase and hysteresis are essentially the result of SIC.

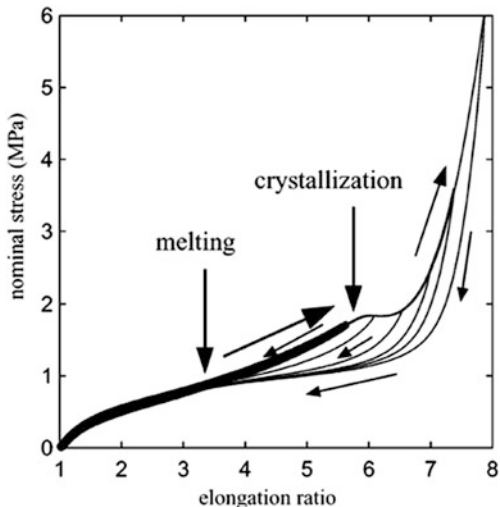


Fig. 19 Maximum strain dependence of stress–strain curves at 29°C at a deformation rate of 0.07 s^{-1} (sulfur-vulcanized sample). *Right-pointing arrows* indicate stretching and *left-pointing arrows* retraction [5]

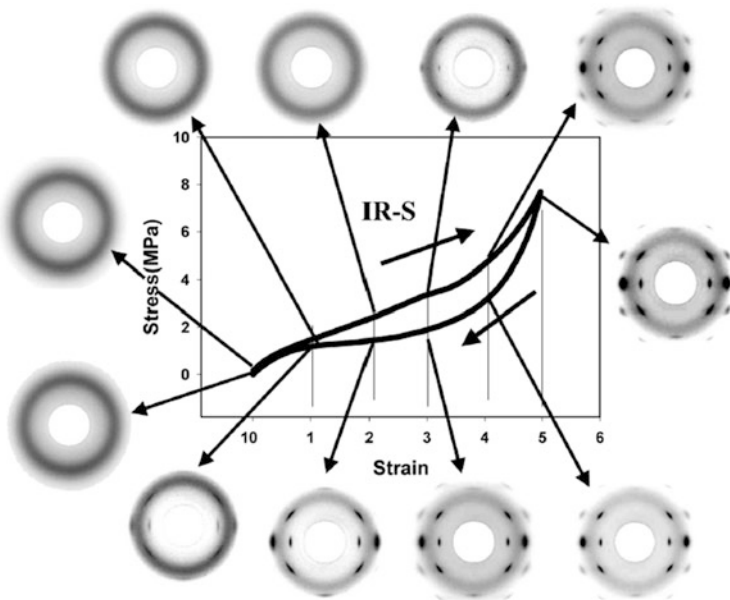


Fig. 20 Stress–strain curve and selected diffraction patterns collected during stretching (*right-pointing arrow*) and retraction (*left-pointing arrow*) of a sulfur-vulcanized synthetic polyisoprene rubber (temperature $T = 0^\circ\text{C}$) [51]

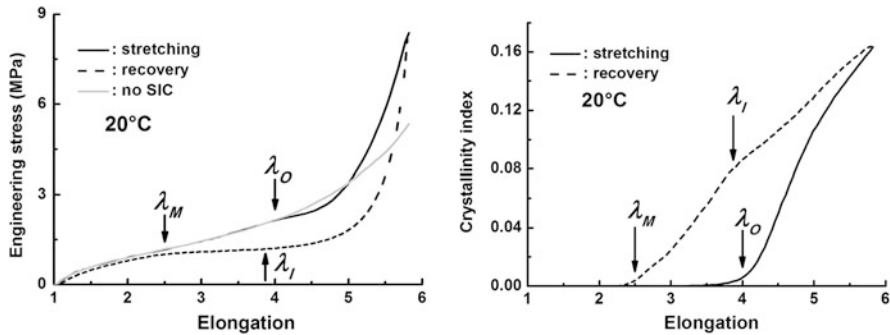


Fig. 21 Stress–strain curve (*left*) and crystallinity–strain curve (*right*) measured simultaneously at a strain rate of 0.003 s^{-1} (sulfur-vulcanized sample) (Adapted from [28])

The link between hysteretic behavior and SIC was definitely established by Toki et al. in 2000 on the basis of time-resolved X-ray diffraction experiments [50]. This relation is well illustrated in Fig. 20, reproduced from a subsequent publication [51].

Based on similar experiments, Trabelsi et al. found that hysteresis is almost exclusively due to crystallization and proposed the empirical relation $H = 0.1 \chi_{\max} J/\text{cm}^3$, where H is the mechanical hysteresis and χ_{\max} the crystallinity reached at maximum extension [22].

In order to clarify this point, simultaneous stress–strain and crystallinity–strain curves are shown in Fig. 21. The stress curve in absence of SIC is extrapolated from measurements at higher stretching speed and temperature (80°C). It is clear that the stress upturn observed in the presence of SIC cannot be related to finite extension effects. Three values of the elongation (λ_0 , λ_1 , and λ_M) correlate with specific features:

1. On stretching: the elongation at crystallization onset λ_0 or more precisely the elongation at which significant crystallization can be detected. λ_0 generally coincides with an inflexion observed on the stress curve (see Fig. 21, left). Note that this inflexion may be hardly visible on highly crosslinked samples. Trabelsi et al. [22], Tosaka et al. [52], and Ikeda et al. [53] found λ_0 to be almost independent of the crosslink density in sulfur-cured NR samples (a clear dependence of λ_0 on crosslink density is found in peroxide crosslinked samples [53], which could be attributed to their higher inhomogeneity [23]). λ_0 depends on the strain rate and this crucial point is discussed below. At a given strain rate, λ_0 increases linearly with temperature (see Fig. 22).
2. On recovery: the elongation λ_1 at which the melting rate increases, which coincides with the onset of a plateau for the retraction force. This specific elongation is only detected if the crystallinity at maximum elongation has reached some characteristic level (see below).
3. On recovery: the elongation λ_M below which the crystalline phase cannot be detected any longer. Both stretching and recovery stress curves become very close below this value. As expected, λ_M increases with temperature (see Fig. 21) and is close to values determined under static conditions [54].

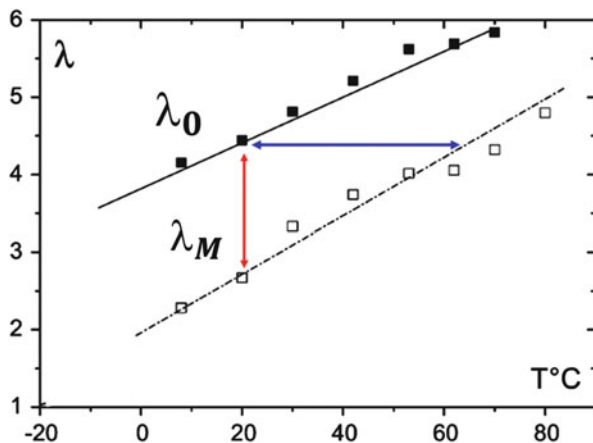


Fig. 22 Temperature dependence of the characteristic elongations λ_0 and λ_M (see Fig. 20) (Adapted from [54])

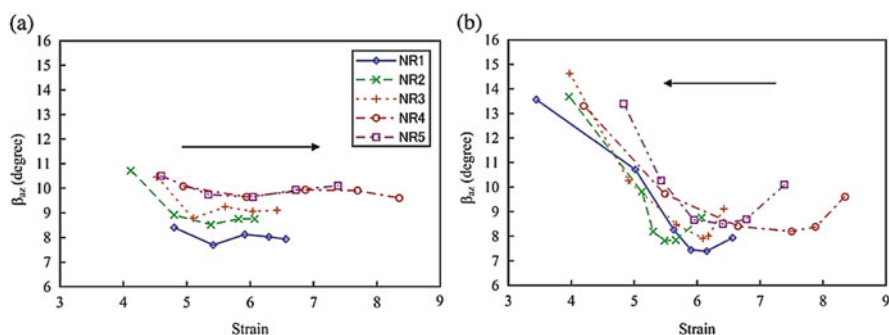


Fig. 23 Variation of the azimuthal half-width of the (200) reflection with strain during stretching (*left*) and recovery (*right*) [55]

All first-order transitions, and in particular crystallization and melting, present hysteresis. There is no delay for melting, whereas crystallization requires some degree of undercooling. This is the basic explanation for stress hysteresis. Conditions for crystallization onset can be viewed in term of undercooling (blue arrow in Fig. 22) or overstraining (red arrow in Fig. 22). Before discussing these points in more depth, other important parameters measured during cycling are presented.

The average disorientation of crystallites with respect to the stretching axis has been characterized by different authors [22, 55, 56]. Representative data obtained by Tosaka et al. are shown in Fig. 23 [55]. The crystallite orientation remains nearly constant during stretching, whereas a slight increase in disorientation is observed during retraction; this latter effect is attributed to the system relaxation.

The same authors have evaluated the small variation in crystal lattice parameters that accompanies stress increase during stretching (see Fig. 24) [55]. The

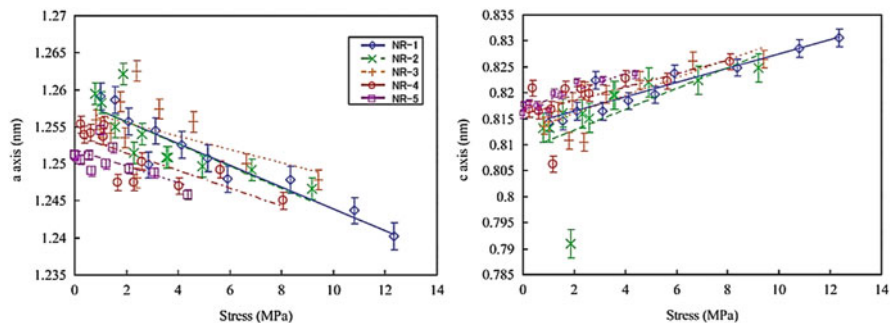


Fig. 24 Deformation of the crystal lattice parameters a (left) and c (right) with nominal stress [55]

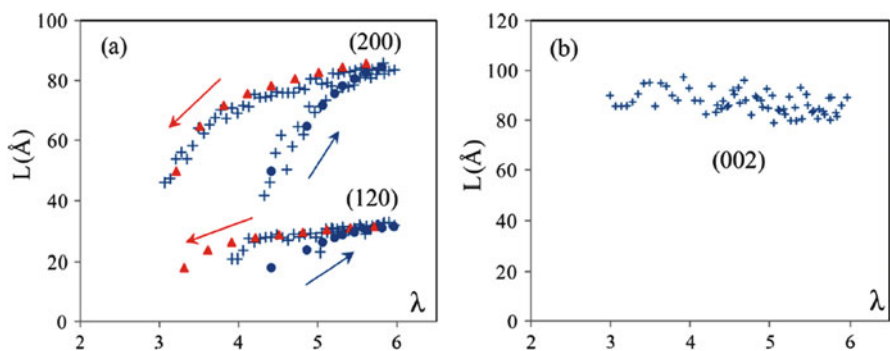
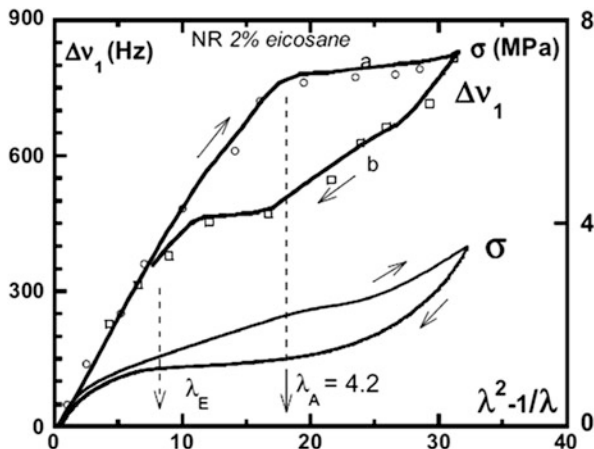


Fig. 25 Crystallite size (plus symbols) along the lateral dimensions l_{200} and l_{120} (left) and along the stretching axis l_{002} (right) versus the stretching ratio (other symbols are not relevant here) [57]

contraction perpendicular to the stretching axis is at the origin of the decrease in parameter a . A similar trend is observed for parameter b . By contrast, the parameter c increases under extension.

Different authors have agreed that the crystallite size along the stretching axis l_{002} remains almost unaltered during cycling (see Fig. 25, right) [22, 55–57]. Trabelsi et al. furthermore reported a decrease in l_{002} with increasing crosslink density [22]. Contradictory results have been obtained concerning the lateral dimensions of crystallites. Tosaka et al. reported a decrease during stretching and constancy during retraction [55]. Candau et al. arrived at the opposite conclusion of an increase with increasing elongation (see Fig. 25, left) [57]. The latter authors claim that such a discrepancy is the result of an improvement in the method of analysis. They attribute the increase in lateral dimensions with increasing elongation to substantial inhomogeneities of the network, such that regions with higher crosslink density crystallize first, yielding crystallites with smaller lateral dimensions. Without judging the opposite results, we insist that, although the existence of strong inhomogeneities in the network is often evoked for sulfur-cured NR, double-quantum NMR indicates that the crosslink density is quite homogeneous in this kind of system [23].

Fig. 26 Comparison of the nominal stress $\sigma(\lambda)$ and quadrupolar splitting $\Delta v_1(\lambda)$ curves during similar deformation cycles (sulfur-vulcanized sample) [61]

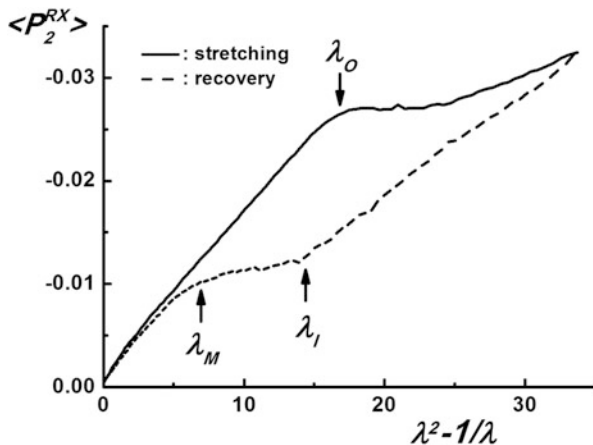


Knowing the strain state of the amorphous fraction in the presence of crystalline phase is fundamental to an understanding of the material properties. Infrared dichroism [58] or optical birefringence [59] have been used for this purpose. However, the difficulty of separating the contributions of each phase is a definite drawback. ^2H -NMR has the advantage of probing only the average extension state of molten chains; more precisely, the so-called quadrupolar splitting of the NMR resonance line of deuterium nuclei is proportional to the segmental orientation parameter $\langle P_2 \rangle$ [60]. To the best of our knowledge, the first ^2H -NMR measurements during cycling were reported by Rault et al. [61]. Deuterated alkanes were added as probe to compensate for the low natural deuterium content of NR. Access to the measuring zone was too constrained to allow for continuous elongation so data were acquired step-by-step. NMR data are compared with a stress curve σ obtained at an equivalent strain rate in Fig. 26.

In the absence of crystallization ($\lambda < \lambda_E$ in Fig. 26), the quadrupolar splitting $\Delta v_1(\lambda)$ depends linearly on $\lambda^2 - 1/\lambda$, as expected from the classical theory of hyperelasticity in the Gaussian regime [60]. A plateau starts at crystallization onset (λ_A in Fig. 26), which indicates that the extension of the amorphous fraction λ_{Am} nearly stops increasing. A steep decrease follows the beginning of recovery, corresponding to rapid strain relaxation. This decrease is followed by another plateau-like region before final melting. It is shown in Fig. 27 that the parameter $\langle P_2^{RX} \rangle$ (see Sect. 3) displays similar behavior, which strengthens its systematic use to evaluate the strain state of the amorphous fraction. Advantages of X-Ray diffraction measurements compared with ^2H -NMR are rapidity of acquisition and the obvious fact that crystallinity index and retraction force are also simultaneously measured.

We now analyze stretching and recovery separately. As correctly emphasized by Candau et al. [60], most studies reported in the literature have been carried out at a relatively low strain rate, typically 0.05 s^{-1} , and this is indeed the case for experiments presented in the next two sections). Some final comments are devoted to the case of high speed cycling.

Fig. 27 Dependence of the parameter $\langle P_2^{RX} \rangle$ on $\lambda^2 - 1/\lambda$ during mechanical cycling [28]



7.1 Stretching

The stretching part of the cycle is inherently dominated by kinetic factors, as are all crystallization processes. This obvious fact is well illustrated by the stress data presented in Fig. 28. The sample was brought to a given elongation, which was subsequently maintained. Immediate and continuous relaxation follows halting of stretching. The stretching section is similar to that in tensile impact tests, with the difference being that the stretching time is significantly longer. It is thus not surprising that a logarithmic dependence is observed at longer observation times, similar to that reported in Sect. 6.

Another consequence of the kinetic aspect of crystallization during stretching is that the elongation at SIC onset (λ_0) increases with the stretching velocity, which can be viewed as an increase in necessary undercooling or overstraining (see Fig. 22). This effect has been recently measured precisely by Candau et al. using three techniques: mechanics (apparition of the stress inflexion, see Fig. 22, left), calorimetry (detection of heat release as a result of crystallization), and X-ray diffraction [62]. In this way, a wide range of strain rates (from $\dot{\lambda} = 6 \times 10^{-5} \text{ s}^{-1}$ to $\dot{\lambda} = 2.8 \times 10^1 \text{ s}^{-1}$) could be investigated (see Fig. 29). In Fig. 29, the induction time is defined as $\lambda_0/\dot{\lambda}$. A quasi-logarithmic time dependence is observed that is similar to the results obtained in tensile impact tests. Such a relatively weak time dependence explains why only small changes in λ_0 as a function of the strain rate are reported for the range of strain rates used in “standard” cycling measurements [61].

We now discuss the segmental relaxation associated with the plateau observed in Figs. 26 and 27. In Sect. 3 the formula $\langle P_2^{RX} \rangle \approx (K/(1 - \chi))(\lambda_{Am}^2 - 1/\lambda_{Am})$ was introduced to relate the experimental $\langle P_2^{RX} \rangle$ to the elongation state of the amorphous fraction λ_{Am} ; recall that SIC induces some chain shortening that is tentatively accounted for by the factor $1 - \chi$. The data presented in Fig. 30 were extracted from the curve reported in Fig. 27. A striking effect is that λ_{Am} remains very close to

Fig. 28 Time variation of the retractive force after drawing the sample at different maximum draw ratios [61]

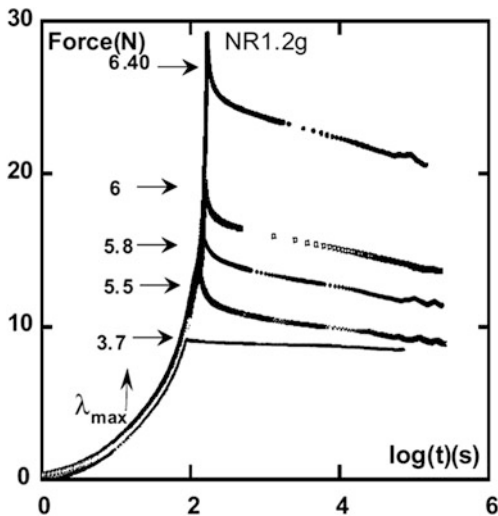
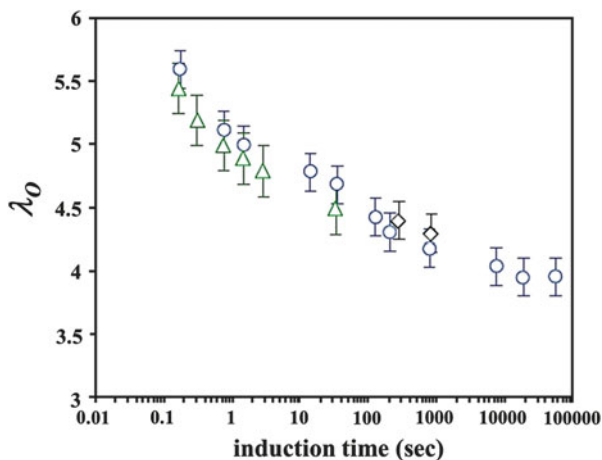


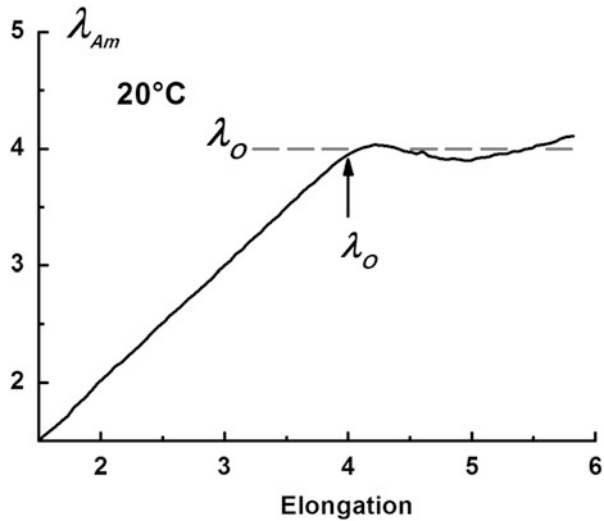
Fig. 29 λ_0 versus time to SIC onset deduced from X-ray diffraction (diamonds), mechanical data (stress inflexion; circles), and temperature variation (triangles) [62]



λ_0 after SIC starts (the slight decrease in λ_{Am} is not reported in reference [28], where no correction was applied to account for chain shortening). We coined this effect the “strain-regulation process” and we think it plays a fundamental role in the various effects linked to SIC during stretching.

This observation is a direct consequence of the phenomenon illustrated in Fig. 17. λ_0 is supposed to be the elongation above which SIC starts, not only at the macroscopic level but also at the microscopic level. At any step of SIC, λ_0 coincides with the elongation denoted $\lambda_{Am}^{(k)}$ in Fig. 17. When a sample is continuously stretched beyond λ_0 , crystallization proceeds as soon as the elongation λ_{Am} locally exceeds λ_0 , resulting in local strain relaxation. This local process almost stops when $\lambda_{Am} \approx \lambda_0$ because the crystallization kinetics becomes too slow at the

Fig. 30 Dependence of the elongation of the amorphous fraction (λ_{Am}) on macroscopic elongation (see also [28])



experimental time scale. Such a “regulation process” actively limits the actual strain experienced by the molten fraction to values close to λ_0 and could thus be an important protective effect of SIC. We now show how this process can explain some experimental observations. It implies first that crystallites are growing in an amorphous matrix whose strain state remains almost unchanged. Under such conditions, neither the orientation nor dimension of the crystallites along the stretching axis are expected to change, which is indeed observed (see Figs. 23 and 25). Second, it has been proposed that, under static conditions, the crystalline content χ and the elongation of the amorphous fraction are related by Eq. (2) $\chi = (\lambda - \lambda_{Am}) / (\lambda_X - \lambda_{Am})$. In the presented dynamic conditions, an excellent agreement with experimental data is reached for an adjusted value of the elongation in the fully crystalline material (as introduced in Sect. 5) $\lambda_X = 14.4$, which compares rather well with the expected value of $\sqrt{3N} = 11.7$ (for $N = 46$): this is illustrated in Fig. 31. In other words, we see that the SIC process during stretching is fundamentally similar to what happens in static conditions. The crystalline content is that necessary to maintain λ_{Am} close to λ_0 . Furthermore, the maximum crystallinity that can be reached during stretching is limited as a result of crosslinks and entanglements. When this limit is reached, the system loses its ability to stabilize the level of strain and failure may occur close to this limit.

We finally address the issue of stress upturn. The relationship between the engineering stress and elongation in the absence of SIC is known (see grey curve in Fig. 21, left) and can be fitted by some polynomial function of the macroscopic elongation λ . The contribution of the remaining amorphous fraction can be roughly estimated by inserting λ_{Am} instead of λ into the adjustment function. As expected, this contribution remains almost constant, as shown in Fig. 32. It thus plays no role in the stress upturn, which means that finite extensibility effects can be discarded.

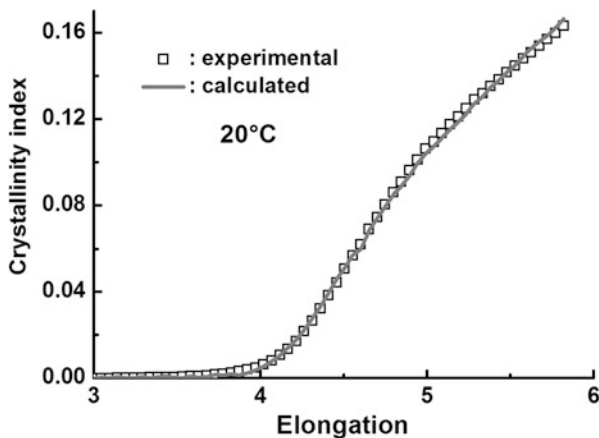


Fig. 31 Comparison of the experimental crystallinity index with values calculated on a relaxation process basis (see text for details) (Albouy P-A, unpublished data)

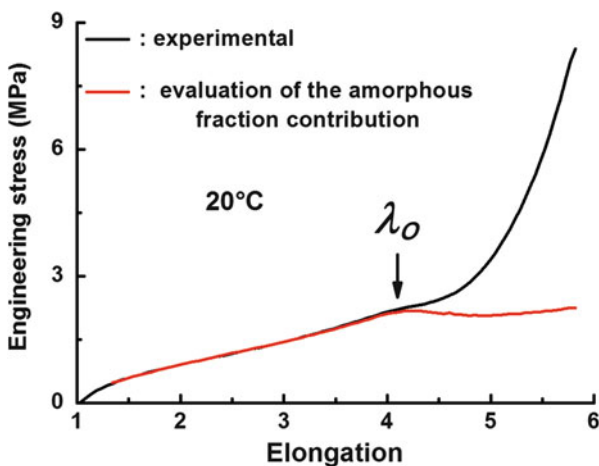


Fig. 32 Comparison of the experimental engineering stress with the estimated contribution of the amorphous fraction (After [28])

Instead, we attribute the upturn solely to the reinforcing effect of crystallites and, in particular, to formation of some degree of crystallite networking [28]. SIC is thus unique because it provides both stiffness and strain relaxation by the same mechanism. Further work is needed to support this idea.

7.2 Recovery

The first point to consider is melting kinetics. Brüning et al. performed step-like unloading tests from 500% elongation down to 0% and it was concluded that melting duration was below 10 ms [45]. This time actually corresponds to the technical limitation of their set-up. It would be interesting to perform similar tests by changing the lower strain value, which has not yet been done to the best of our knowledge. At the strain rates presently considered, it is reasonable to assume that there is no melting retardation (some melting retardation effects have been reported for particular configurations [30]).

During stretching, any measured effect follows a relatively well-defined master curve (see Figs. 19 and 33). Conversely, during retraction, curves obtained for different maximal extensions merge only on some partial sections of the curves (see Fig. 33). Only those common sections can be assumed to correspond to real equilibrium. This is not a trivial point and is discussed next.

We first consider case C in Fig. 33, which corresponds to the lower maximum elongation. The crystallinity still increases after recovery has started. This apparently puzzling fact was previously observed by Toki et al. [50]. It simply means that retraction has started at an elongation such that the given strain rate exceeds the crystallization rate. Curves associated with case C are well separated from the other curves and are clearly out of equilibrium, except close to final melting. The retraction curve associated with case B merges with that of case A at elongations below ca. λ_I and are thus most probably close to equilibrium in this region. Curves associated with A should be compared with data obtained at even higher maximum elongations, which become difficult to obtain because of the very steep stress increase. Two regions can be clearly distinguished: The first region is above λ_I , where both the stress and segmental orientation ($\langle P_2^{RX} \rangle$) decrease most rapidly. It can be supposed that the crystallite network disintegrates in this region. The second region is below λ_I , where a stress plateau is observed, accompanied by a leveling-off of $\langle P_2^{RX} \rangle$. Similar to the plateau observed in the stretching zone above λ_0 , the strain state of the amorphous fraction becomes nearly unchanging. Under some conditions, the stress remains absolutely constant and is accompanied by the

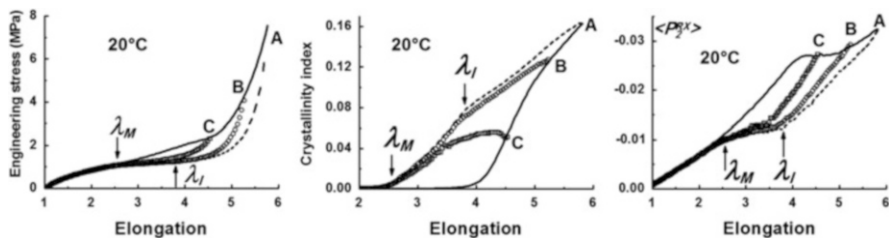
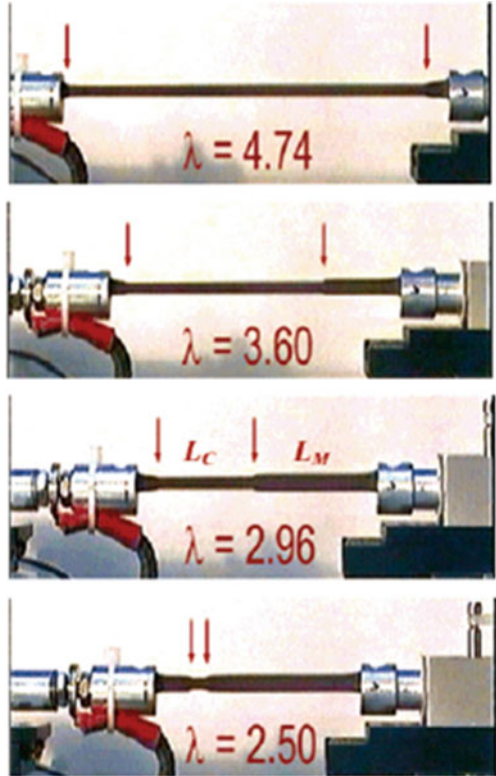


Fig. 33 Recovery part as obtained for different maximal extensions. Engineering stress, crystallinity index and $\langle P_2^{RX} \rangle$ plotted against elongation. *Solid line* stretching; *symbols* recovery for maximal extensions A, B, and C (Albouy P-A, unpublished data)

Fig. 34 The “inverse yielding” effect [22]. The *red arrows* indicate the extent of the semicrystalline phase



macroscopic coexistence of two distinct phases, molten and semicrystalline [22, 54]. This spectacular manifestation of SIC is shown in Fig. 34. We have used the term “inverse yielding” to refer to this appearance of macroscopic necking. The composition of the crystalline phase remains unchanged until it disappears [54]. A similar effect has been reported by Miyamoto et al. and corresponds to the curve in Fig. 9 (left) where the elongation ratio drops most rapidly [5]. Indeed, inverse yielding is associated with a first-order transition where the semicrystalline phase transforms into the molten phase at constant engineering (or nominal) stress, as described in Sect. 5 (the transformation is not reversible upon motion inversion because of kinetic effects). To the best of our knowledge, conditions for the observation of “inverse yielding” have not been the object of systematic studies, but it can be stated that the lower the crosslink density, the higher the temperature where the effect is still present.

In most cases, only partial stress stabilization is observed and the outer appearance of the sample is homogeneous. Similarly, the crystallinity smoothly decreases without exhibiting the abrupt jumps that are characteristic of inverse yielding. It is supposed that only microdomains of molten and semicrystalline zones homogeneously develop throughout the sample. This is different from stretching or static crystallization, which a priori are homogeneous processes. An argument in

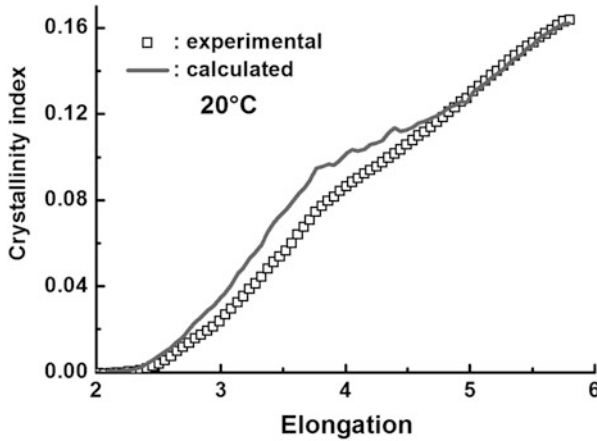


Fig. 35 Comparison of the experimental crystallinity index with values calculated on the basis of an homogeneous relaxation process (see text for details) (Albouy P-A, unpublished data)

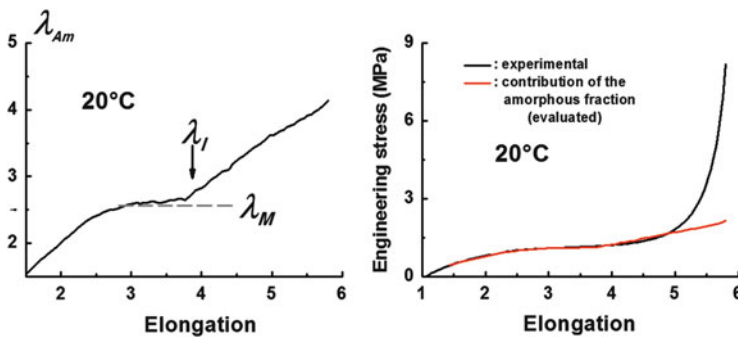


Fig. 36 *Left:* Elongation of the amorphous part. *Right:* Comparison of the experimental engineering stress and the estimated contribution of the amorphous fraction (After [28]).

favor of this essential difference is illustrated in Fig. 35, where experimental crystallinity index values are compared with those obtained from Eq. (2) $\chi = (\lambda - \lambda_{Am}) / (\lambda_X - \lambda_{Am})$ and $\lambda_X = 14.4$ as determined above. A good agreement is obtained in the first part of the recovery curve, but some discrepancy appears and increases as retraction proceeds. Compared with stretching, a smaller crystalline content is needed to reach a similar amorphous strain state. This could be tentatively attributed to some percolation of molten microdomains.

We now turn to the stress behavior. Similarly to the stretching section, elongation of the amorphous part was derived from $\langle P_2^{RX} \rangle$ curves presented in Fig. 33 (see Fig. 36, left). Following the above-detailed procedure, the contribution of the amorphous fraction to stress was evaluated (see Fig. 36, right) [28]. It is clear that below $\lambda \approx 5$ the stress is essentially a result of the retractive force exerted by the molten chain. Disintegration of the crystallite network is thought to take place between the maximum elongation and this latter value.

8 Conclusion

In this chapter, we have presented an overview of the physical mechanisms involved in strain-induced crystallization of natural rubber. We first reviewed the information that can be retrieved from X-ray diffraction patterns, as it can be very helpful, for example, for mechanical engineers. In particular, we have tentatively shown how easily knowledge of the strain state of the amorphous fraction can be retrieved quantitatively from X-ray diffraction patterns and how informative such knowledge can be. We have adopted a progressive approach, focusing first on static or quasi-static conditions (Sect. 6) and moving on to dynamic conditions (Sect. 7).

One of our purposes was to clearly emphasize the fact that, for engineering applications, one has to deal with nonequilibrium states, in particular during mechanical cycling.

Considering for instance the self-reinforcement effect provided by SIC (i.e., the strain-hardening sequence observed during tensile stretching), it is clear that the increase in stress cannot be predicted without knowing both the crystalline content and the average elongation of the remaining molten chains. As stated above, both quantities can be obtained from X-ray diffraction studies. This analysis of X-ray diffraction patterns can be similarly applied to the case of NR samples filled with carbon black or silica, as recently shown by Pérez-Aparicio et al. [63]. In such materials, X-ray diffraction can be used as a selective probe of the mechanical response of the elastomer matrix in nanocomposites. The increased amorphous orientation observed in filled NR samples compared with unfilled reference samples was interpreted as evidence of local strain amplification caused by the filler. This particular contribution to the overall mechanical reinforcement could thus be discriminated from other contributions coming from rigid filler network effects [63]. A strong relaxation effect of the local strain as a result of SIC was also shown in such reinforced materials. Because of the importance of filled materials in the industrial application of NR and other elastomers, this latter effect should certainly be investigated more thoroughly. Local strain relaxation is undoubtedly the effect that controls SIC kinetics, and it should be systematically evaluated during, for example, tensile impact tests. Other strain-crystallizing elastomers include polychloroprene, polyisobutylene, and *cis*-polybutadiene. The existence of a strain regulation mechanism in these materials should be checked and its efficiency correlated with the resistance to failure. In particular, such a mechanism could play a crucial role in the large increase in not only the stress at break, but also the strain at break, generally observed in NR in the presence of SIC.

References

1. Katz JR (1925) Röntgenspektrographische Untersuchungen am gedehnten Kautschuk und ihre mögliche Bedeutung für das Problem der Dehnungseigenschaften dieser Substanz. *Naturwissenschaften* 19:410–416
2. Flory PJ (1947) Thermodynamics of crystallization in high polymers. I Crystallization induced by stretching. *J Chem Phys* 15:397–408
3. Huneau B (2011) Strain-induced crystallization of natural rubber: a review of X-ray diffraction investigations. *Rubber Chem Technol* 84:425–452
4. Toki S (2014) The effect of strain-induced crystallization (SIC) on the physical properties of natural rubber (NR). In: Kohjiya S, Ikeda Y (eds) *Chemistry, manufacture and applications of natural rubber*. WoodHead/Elsevier, Cambridge
5. Miyamoto Y, Yamao H, Sekimoto K (2003) Crystallization and melting of polyisoprene rubber under uniaxial deformation. *Macromolecules* 36:6462–6471
6. Oono R, Miyasaka K, Ishikawa K (1973) Crystallization kinetics of biaxially stretched natural rubber. *J Polym Sci Polym Phys* 11:1477–1488
7. Pannier Y, Proudhon H, Mocuta C, Thiaudière D, Cantournet S (2011) In situ multi-axial loading frame to probe elastomers using X-ray scattering. *J Synchrotron Radiat* 18:907–911
8. Beurrot S, Huneau B, Verron E (2011) Strain-induced crystallization of natural rubber subjected to biaxial loading conditions as revealed by X-ray diffraction. In: Jerrams S, Murphy N (eds) *Constitutive models for rubber VII: Proceedings of the 7th European conference on constitutive models for rubber*, ECCMR, Dublin, Ireland, 20_23 Sept 2011. CRC/Taylor & Francis, Boca Raton, pp 23–28
9. Klug HP, Alexander LE (1959) X-ray diffraction procedures for polycrystalline and amorphous materials. Wiley, New York
10. Langford JI, Wilson JC (1978) Scherrer after sixty years: a survey and some new results in the determination of crystallite size. *J Appl Crystallogr* 11:102–113
11. Kakudo M, Kasai N (1972) X-ray diffraction by polymers. Kodansha Ltd/Elsevier, Tokyo/Amsterdam
12. Wendorff JH (1982) The structure of amorphous polymers. *Polymer* 23:543–557
13. Simard GL, Warren BE (1936) X-ray study of amorphous rubber. *J Am Chem Soc* 58:507–509
14. Wang CS, Yeh GS (1978) DRDF analysis of wide-angle X-ray scattering of natural rubber. *J Macromol Sci Phys B15:107–118*
15. Yeh GSY (1980) Current concepts of morphology of amorphous polymers. *Polym Sci USSR* 21:2686–2703
16. Rajkumar G, Squire JM, Arnott S (2006) A new structure for crystalline natural rubber. *Macromolecules* 39:7004–7014
17. Che J, Burger C, Toki S, Amnuayporn Sri S, Sakdapipanich J, Rong L, Hsiao SB (2013) Crystal and crystallite structure of natural rubber and synthetic *cis*-1,4- polyisoprene by a new two dimensional wide-angle X-ray diffraction simulation method. I. Strain-induced crystallization. *Macromolecules* 46:4520–4528
18. Che J, Burger C, Toki S, Amnuayporn Sri S, Sakdapipanich J, Rong L, Hsiao SB (2013) Crystal and crystallite structure of natural rubber and peroxide vulcanized natural rubber by a two dimensional wide-angle X-ray diffraction simulation method. II. Strain-induced crystallization versus temperature-induced crystallization. *Macromolecules* 46:9712–9721
19. Immirzi A, Tedesco C, Monaco G, Tonelli AE (2005) Crystal structure and melting entropy of natural rubber. *Macromolecules* 38:1223–1231
20. Benedetti E, Corradini P, Pedone C (1975) Conformational isomorphism in crystalline 1,4-*cis*-polyisoprene. *Eur Polym J* 11:585–587
21. De Rosa C, Auriemma F (2014) *Crystals and crystallinity in polymers*. Wiley, Hoboken
22. Trabelsi S, Albouy P-A, Rault J (2003) Crystallization and melting processes in vulcanized stretched natural rubber. *Macromolecules* 36:7624–7639

23. Valentín JL, Psadas P, Fernández-Torres A, Malmierca MA, Gonzáles L, Chassé W, Saalwächter K (2010) Inhomogeneities and chain dynamics in diene rubbers vulcanized with different cure systems. *Macromolecules* 43:4210–4222
24. Mitchell GR (1984) A wide-angle X-ray study of the development of molecular orientation in crosslinked natural rubber. *Polymer* 25:1562–1572
25. Nobbs JH, Bower DI (1978) Orientation averages for drawn rubber networks. *Polymer* 19: 1100–1103
26. Deas HD (1952) The diffraction of X-rays by a random assemblage of molecules having partial alignment. *Acta Crystallogr* 5:542–546
27. Michell GR, Windle AH (1982) Conformational analysis of oriented non-crystalline polymers using wide-angle X-ray scattering. *Colloid Polym Sci* 260:754–761
28. Albouy P-A, Vieyres A, Pérez-Aparicio R, Sanséau O, Sotta P (2014) The impact of strain-induced crystallization on strain during mechanical cycling of cross-linked natural rubber. *Polymer* 55:4022–4031
29. Vieyres A, Pérez-Aparicio R, Albouy P-A, Sanséau O, Saalwächter K, Long DR, Sotta P (2013) Sulfur-cured natural rubber elastomer networks: correlating cross-link density, chain orientation, and mechanical response by combined techniques. *Macromolecules* 46:889–899
30. Albouy P-A, Guillier G, Petermann D, Vieyres A, Sanséau O, Sotta P (2012) A stroboscopic X-ray apparatus for the study of the kinetics of strain-induced crystallization in natural rubber. *Polymer* 53:3313–3324
31. Philips PJ, Vatansver N (1987) Regime transitions in fractions of *cis*-polyisoprene. *Macromolecules* 20:2138–2146
32. Kawahara S, Kakubo T, Sakdapipanich JT, Isono Y, Tanaka Y (2000) Characterization of fatty acids linked to natural rubber – role of linked fatty acids on crystallization of the rubber. *Polymer* 41:7483–7488
33. Andrews EH (1972) The influence of morphology on the mechanical properties of crystalline polymers. *Pure Appl Chem* 31:91–112
34. Yamamoto M, White JL (1971) Theory of deformation and strain-induced crystallization of an elastomeric network polymer. *J Polym Sci Polym Chem* 9:1399–1415
35. Wu WL (1978) A thermodynamic approach to the stress-induced crystallization in cross-linked rubbers. *J Polym Sci Polym Phys* 16:1671–1683
36. Gaylord RJ (1976) A theory of stress-induced crystallization of crosslinked polymeric networks. *J Polym Sci Polym Phys* 14:1827–1837
37. Arlman JJ, Goppel JM (1951) On the degree of crystallinity in natural rubber. *Appl Sci Res* 2: 1–8
38. Luch D, Yeh GSY (1973) Strain-induced crystallization of natural rubber. III. Reexamination of axial-stress changes during oriented crystallization of natural rubber vulcanizates. *J Polym Sci Polym Phys* 11:467–486
39. Gent AN (1954) Crystallization and the relaxation of stress in stretched natural rubber vulcanizates. *Trans Faraday Soc* 50:521–533
40. Poompradub S, Tosaka M, Kojiya S, Ikeda Y, Toki S, Sics I, Hsiao B (2005) Mechanism of strain-induced crystallization in filled and unfilled natural rubber vulcanizates. *J Appl Phys* 97:103529
41. Kawai H (1975) Dynamic X-ray diffraction technique for measuring rheo-optical properties of crystalline polymeric materials. *Rheol Acta* 14:27–47
42. Candau N, Chazeau L, Chenal J-M, Gauthier C, Ferreira J, Munch E, Rochas C (2012) Characteristic time of strain induced crystallization of crosslinked natural rubber. *Polymer* 53:2540–2543
43. Mitchell JC, Meir DJ (1968) Rapid stress-induced crystallization in natural rubber. *J Polym Sci Polym Chem* 6:1689–1703
44. Tosaka M, Senoo K, Sato K, Noda M, Ohta N (2012) Detection of fast and slow crystallization processes in instantaneously-strained samples of *cis*-1,4-polyisoprene. *Polymer* 53:864–872

45. Brüning K, Schneider K, Roth SV, Heinrich G (2012) Kinetics of strain-induced crystallization in natural rubber studied by WAXD: dynamic and impact tensile experiments. *Macromolecules* 45:7914–7919
46. Trabelsi S, Albouy P-A, Rault J (2002) Stress-induced crystallization around a crack tip in natural rubber. *Macromolecules* 35:10054–10061
47. Brüning K, Schneider K, Roth SV, Heinrich G (2015) Kinetics of strain-induced crystallization in natural rubber: a diffusion-controlled rate law. *Polymer* 72:52–58
48. Landau LD, Lifchitz EM (1967) *Statistical physics*. Nauka, Moscow
49. Treloar LRG (1975) *The physics of rubber elasticity*. Clarendon, Oxford, p 124
50. Toki S, Fujimaki T, Okuyama M (2000) Strain-induced crystallization of natural rubber as detected real-time by wide-angle X-ray diffraction technique. *Polymer* 41:5423–5429
51. Toki S, Sics I, Ran S, Liu L, Hsiao BS (2003) Molecular orientation and structural development in vulcanized polyisoprene rubbers during uniaxial deformation by in situ synchrotron X-ray diffraction. *Polymer* 44:6003–6011
52. Tosaka M, Kohjiya S, Murakami S, Poompradub S, Ikeda Y, Toki S, Sics I, Hsiao B (2004) Effect of network-chain length on strain-induced crystallization of NR and IR vulcanizates. *Rubber Chem Technol* 77:711–723
53. Ikeda Y, Yasuda Y, Hijikata K, Tosaka M, Kohjiya S (2008) Comparative study of strain-induced crystallization behavior of peroxide cross-linked and sulfur cross-linked natural rubber. *Macromolecules* 41:5876–5884
54. Albouy P-A, Marchal J, Rault J (2006) Chain orientation in natural rubber, part I: the inverse yielding effect. *Eur Phys J E* 17:247–259
55. Tosaka M, Murakami S, Poompradub S, Kohjiya S, Ikeda Y, Toki S, Sics I, Hsiao B (2004) Orientation and crystallization of natural rubber network as revealed by WAXD using synchrotron radiation. *Macromolecules* 37:3299–3309
56. Chenal J-M, Chazeau L, Guy L, Bomal Y, Gauthier C (2007) Molecular weight between physical entanglements in natural rubber: a critical parameter during strain-induced crystallization. *Polymer* 48:1042–1046
57. Candau N, Laghmach R, Chazeau L, Chenal J-M, Gauthier C, Biben T, Munch E (2014) Strain-induced crystallization of natural rubber and cross-link densities heterogeneities. *Macromolecules* 47:5815–5824
58. Amran B, Bokobza L, Queslel J-P, Monnerie L (1986) Fourier-transform infra-red dichroism study of molecular orientation in synthetic high *cis*-1,4-polyisoprene and in natural rubber. *Polymer* 27:877–882
59. Tosaka M, Kohjiya S, Ikeda Y, Toki S, Hsia B (2010) Molecular orientation and stress relaxation during strain-induced crystallization of vulcanized natural rubber. *Polym J* 42: 474–481
60. Sotta P (1998) Local order and induced orientation in PDMS model networks, studied by ^2H NMR. *Macromolecules* 31:3872–3879
61. Rault J, Marchal J, Judenstein P, Albouy P-A (2006) Chain orientation in natural rubber, part II: ^2H -NMR study. *Eur Phys J E* 21:243–261
62. Candau N, Laghmach R, Chazeau L, Chenal J-M, Gauthier C, Biben T, Munch E (2015) Influence of strain rate and temperature on the onset of strain induced crystallization in natural rubber. *Eur Polym J* 64:244–252
63. Pérez-Aparicio R, Vieyres A, Albouy P-A, Sanséau O, Vanel L, Long DR, Sotta P (2013) Reinforcement in natural rubber elastomer nanocomposites: breakdown of entropic elasticity. *Macromolecules* 46:8964–8972

Non-isothermal Crystallization of Semi-Crystalline Polymers: The Influence of Cooling Rate and Pressure

M. van Drongelen, P.C. Roozmond, and G.W.M. Peters

Abstract During industrial processing, polymer melts are exposed to local high cooling rates, strong deformation rates and high pressures. Nowadays, research in the field of semi-crystalline polymers still strives towards an accurate prediction of the evolution and final appearance of the crystalline morphology in polymer products. After all, the amount, number, phase and orientation of the crystallites act in a combined way and control the final optical and mechanical properties. This chapter discusses recent experimental and model developments concerning the influence of industrially relevant cooling rates and pressures on the non-isothermal crystallization of both an isotactic polypropylene and a linear low-density polyethylene grade. The influence of flow gradients is discussed in Chapter (Roozmond et al., Adv Polym Sci, 2016).

Keywords Crystallization • Kinetics • Modelling • Polypropylene • Polyethylene

Contents

1	Introduction	208
2	Crystallization of Isotactic Polypropylene: Multiple Crystal Phases	209
2.1	Theory	210
2.2	Fast Cooling Experiments	212
2.3	Effect of Pressure	217

M. van Drongelen and G.W.M. Peters (✉)
Department of Mechanical Engineering, Materials Technology Institute, Eindhoven University of Technology, P.O. Box 513, 5600 MB Eindhoven, The Netherlands
e-mail: g.w.m.peters@tue.nl

P.C. Roozmond
DSM Material Science Center, Urmonderbaan 22, 6167 RD Geleen, The Netherlands

3	Crystallization of Linear Low-Density Polyethylene: Multiple Crystal Processes	224
3.1	Thermal Characterization	224
3.2	Small-Angle Light Scattering	228
3.3	Primary Crystallization Model	230
3.4	Secondary Crystallization Model	233
4	Concluding Remarks	237
	References	238

1 Introduction

Thermoplastic polymer products are commonly processed into their final shape using production processes such as injection moulding, film blowing, extrusion or fibre spinning. During these processes, when starting in the melt phase, the polymer is exposed to elevated pressures and/or high deformation rates being simultaneously cooled within tenths of seconds, before it solidifies into the final shape. The crystallization process of the semi-crystalline polymers is strongly affected by these extreme processing conditions, process–properties relationships linking the final properties of a product to the processing history [1, 2]. A full understanding of this mechanism is a prerequisite to tailor the ultimate properties of semi-crystalline plastic products. Moreover, the material functions and/or material parameters in these relations can be linked to molecular properties and, in this way, help to design polymers for specific applications [3, 4]. To achieve the aforementioned, the ongoing development and experimental validation of crystallization modelling tools, relevant to industrial conditions, are a key component [5–8].

Crystallization of synthetic polymers has been extensively studied in recent decades, providing a basic understanding of the rules and kinetics under ideal circumstances [9–15]. The most established physical picture of quiescent crystallization is nucleation and subsequent growth of spherulites; crystalline lamellae grow in three dimensions starting from point-like nuclei. The nucleation density and growth rates have been studied as functions of temperature for a range of materials ([16] and references therein). For some polymers the reported growth rates are comparable for different grades (isotactic polypropylene (iPP)) whereas for others there is a strong dependency on the molecular weight (polyethylene terephthalate (PET)) [16]. The nucleation density is always unique because of residuals and catalysts remaining from the industrial synthesis [13, 17]. To boost crystallization rates or in the case of desired crystal phase morphologies, nucleation agents can be added on purpose. A great contrast may be found between the available agents regarding their efficiency and selectivity [18–20]. Many attempts have been made to model the crystallization process in semi-crystalline polymers as a function of thermal history [21–31], often using experimentally obtained non-isothermal crystallization kinetics. Most models lack the incorporation of the ability to form different crystal phases, i.e. polymorphism behaviour, and/or do not account for relevant processing conditions (the effect of pressure is particularly

often left aside). A counter example is a kinetic model that uses pressure-dependent rate equations for the α -phase and mesomorphic phase in iPP [25, 26]. Unfortunately, the nucleation density and growth rate are indistinguishable in these rate equations and hence the kinetic parameters lose their physical meaning. Most often, a similar kinetic approach is used to describe non-isothermal crystallization of polyethylene-based polymers. Because of their extremely fast crystallization behaviour, the temperature window for isothermal studies is mostly limited to very low levels of undercooling [32]. Hence, the nucleation density and growth rate can only be obtained in a narrow temperature range below the melting temperature, unable to describe crystallization in a broad range of cooling rates [33]. An additional complexity is found for branched polyethylenes, such as linear low-density polyethylene (LLDPE) because of the high levels of secondary crystallization (sometimes up to 50% of the final crystallinity) produced by a continuous insertion or thickening of lamellar features inside spherulites [34]. In the case of LLDPE, the most promising approach is found in extended Avrami-type models to account for secondary crystallization effects [35–37].

Although flow has a pronounced effect on the crystallization kinetics and the resulting morphology, the focus of this chapter is on the characterization of quiescent non-isothermal and isobaric crystallization. The polymers considered in this chapter are iPP, typical for the multiphase crystallization behaviour, and a linear low-density polyethylene (LLDPE), typical for multiple-stage kinetics. Both the experimental characterization for processing relevant conditions and the development of models able to capture this complex behaviour are discussed. The work presented here is largely based on recently published work from our group [38, 39].

2 Crystallization of Isotactic Polypropylene: Multiple Crystal Phases

The temperature-dependent nucleation density and growth rate of iPP are usually measured by optical microscopy in conditions that typically promote the α -phase. However, it is well known that iPP is a polymorphic material, i.e. a polymer that, depending on the conditions, can develop different crystal modifications [40]. Most common is the monoclinic α -phase, a stable crystal form created under moderate conditions. Shear or specific nucleation agents results in formation of hexagonal β -crystallites [41–43]. Furthermore, orthorhombic γ -crystals are formed at elevated pressures or in copolymers [44–48]. The mesomorphic phase, with features intermediate to those of the crystalline and the amorphous states, is obtained when a sample is cooled from the melt at high cooling rates [49, 50]. The nucleation density and spherulitic growth rates of the different polymorphs of iPP homopolymers are, in general, difficult to measure in a single experiment, especially when high cooling rates and/or elevated pressures are required to induce a specific crystal phase. Therefore, crystallization kinetics of the different polymorphs is not well established as a function of temperature and pressure. An increase in pressure

results in an increase of the nucleation density [51] and in the equilibrium melting temperature T_m^0 [27], and thus in a higher undercooling ($\Delta T = T_m^0 - T$), the driving force for crystallization. However, the exact effect of pressure on the growth rate of a given crystal phase is not extensively investigated. For example, it is speculated from modelling and numerical simulations that the growth rate of the α -phase shifts towards higher temperatures with pressure accompanied by a decrease in the maximum growth rate [52]. In contrast, the first results of measurements with an optical high-pressure cell show a increase of this maximum value [53].

2.1 Theory

Polymer crystallization from an iPP melt is dominated by heterogeneous nucleation. Nuclei grow in time, depending on the temperature and pressure, forming spherulites which impinge and stop growing when complete space filling is reached. Therefore, a basic model describing polymer crystallization should contain expressions for the nucleation density and the spherulitic growth rates. In this case, the effect of secondary crystallization is not considered as it does not play a major role. The proposed non-isothermal multiphase crystallization model is based on the Kolmogoroff–Avrami expression [21–23]. Space filling is given by

$$\xi(t) = \frac{\chi(t)}{\chi_\infty} = 1 - \exp(-\varphi_0(t)), \quad (1)$$

where χ and χ_∞ are the crystallized volume fractions at time t and at equilibrium conditions, respectively. The quantity φ_0 represents the sum of the expected crystallized volume of the different phases when impingement is not taken into account, $\varphi_0(t) = \sum \varphi_{0,i}(t)$. Multiple phases can be the α -, β -, γ - or mesophase. However, in this part we restrict ourselves to α -, γ - and the mesophase. Parameter χ_∞ is the maximum value of crystallinity allowed by the external conditions and the thermal and mechanical histories experienced by the sample [54] and is determined per experiment using

$$\chi_\infty = \sum \psi_i \chi_{i,\max}, \quad (2)$$

in which ψ_i is the final crystal fraction acquired by X-ray analyses and $\chi_{i,\max}$ the maximum crystal fraction, both per phase i . For non-isothermal conditions, the crystal volumes $\varphi_{0,i}(t)$ are given by the Schneider rate equations, which provide structure information in terms of the number of spherulites, radius, surface and volume [55] (for clarity we leave out the index i in this set of equations):

$$\dot{\varphi}_3 = 8\pi\dot{N}(\varphi_3 = 8\pi N), \quad (3)$$

$$\dot{\varphi}_2 = G\varphi_3(\varphi_2 = 8\pi R_{\text{tot}}), \quad (4)$$

$$\dot{\varphi}_1 = G\varphi_2(\varphi_1 = S_{\text{tot}}), \quad (5)$$

$$\dot{\varphi}_0 = G\varphi_1(\varphi_0 = V_{\text{tot}}), \quad (6)$$

with nucleation rate \dot{N} and crystal growth rate G . The morphology is described, per phase i , per unit volume by the total volume of spherulites V_{tot} , their total surface S_{tot} , the sum of their radii R_{tot} and the number of nuclei N . We assume that only one nuclei reservoir is available in the melt and each crystal phase has an individual growth rate. Adding specific nucleation agents can create separate nuclei reservoirs. The nucleation density N and the growth rate per phase G_i are functions of the temperature and pressure and given by

$$N(T, p) = N_{\text{ref}} \exp(-c_N(T(t) - T_{N\text{ref}}(p))), \quad (7)$$

$$G_i(T, p) = G_{\text{max},i}(p) \exp(-c_{G,i}(T(t) - T_{G\text{ref},i}(p))^2), \quad (8)$$

where N_{ref} and $G_{\text{max},i}$, are values at the reference temperatures $T_{N\text{ref}}$ and $T_{G\text{ref},i}$, respectively, and c_N and $c_{G,i}$ are constants.

During solidification in a multiphase system, every crystal form i generates a crystal volume fraction $\varphi_{0,i}$ using a share of the available number of nuclei and having its own growth rate. The ratio in which the nuclei are divided between the crystal phases is not accessible experimentally. Therefore, the assumption is made that the allocation of nuclei to a given crystal form scales with the ratio of the individual crystal phase growth rates at the current temperature and pressure. For isobaric conditions, the nucleation rate for a given crystal form is given by

$$\dot{N}_i = g_i \frac{dN}{dT} \dot{T}, \quad (9)$$

with the growth rate fraction, g_i , given by

$$g_i = \frac{G_i}{\sum G_i}. \quad (10)$$

The influence of pressure on the crystallization process is, among the yet to be determined influences on the growth rate parameter $G_{\text{max},i}$, caused by a shift of the reference temperatures in (7) and (8). This shift is given by

$$T_{k,\text{ref},i} = T_{k,\text{ref},i}^0 + \zeta(p - p_0). \quad (11)$$

where ζ is a constant ($\sim 27.5\text{--}30.0^\circ\text{C}/1,000\text{ bar}$ for iPP [56]) and $T_{k,\text{ref},i}^0$ ($k=N,G$) is a reference temperature at atmospheric conditions p_0 . For iPP, the effect of pressure

on the glass transition temperature T_g is not clear, but it is assumed that T_g shifts similar to T_m with ζ [57, 58]. The bell-shaped growth rate function (8) is valid in between T_g and T_m and herein $T_{Gref,i}$ is an intermediate value. Therefore, it is valid to shift the reference temperatures of all individual crystal phase growth rates according to (11). Because T_g and T_m shift equally with pressure, the width of the growth rate function is maintained and thus $c_{G,i}$ is independent of pressure. Similar to the pressure dependence of the growth rate, the effect of pressure on the nucleation density is implemented by shifting the reference temperature T_{Nref} .

With the nucleation density and individual growth rates modified for non-isothermal and isobaric conditions, space filling in a multiphase structure is calculated as a function of time using

$$\dot{\xi}_i = (1 - \xi)\dot{\phi}_{0,i}. \quad (12)$$

For computational purposes, the set of rate equations (3)–(6) are numerically integrated using an explicit Euler scheme to calculate $\phi_{0,i}$.

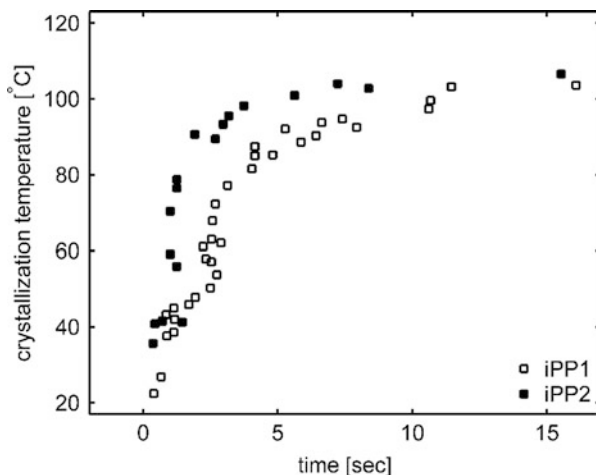
A single set of parameters for the growth rate of each phase and the nucleation density is numerically determined from experimental data. The input consists of the temperature and pressure history and the time-resolved fractions of the different crystalline phases for every experimental data set obtained. The number of free parameters depends on the number of crystal phases concerned. These different experiments are discussed below.

2.2 Fast Cooling Experiments

A quenching device [49, 59] is used to perform multiple cooling experiments on two commercial IPP grades named iPP1 (HD234, Borealis) [60] and iPP2 (HD601, Borealis) [61, 62]. In this device, a film 250–300 μm thick is covered in standard aluminium foil and placed in a vertical holder, after which it is heated to a controlled temperature by a heating gun which blows hot air tangential to the samples surface. Quenching is performed by blowing compressed air at both sides of the sample using two small hoses and, meanwhile, the sample temperature is monitored using an embedded micro thermocouple. Cooling rates are non-constant and are defined by the slope between 195°C and 130°C and are in the range of ca. 10–260°C/s, each experiment being labelled according to the average cooling rate defined. In Fig. 1 the crystallization temperature T_c is plotted against crystallization time in a so-called continuous cooling transformation (CCT) diagram. Two regimes can be distinguished – a range of cooling rates where iPP2 crystallizes at higher temperatures compared to iPP1 (>50°C) and a range where both materials crystallize at similar temperatures (30–50°C).

The first region is referred to as the α -region, where for both materials the applied cooling rates (<100°C/s) result in the formation of a prevailing α -phase.

Fig. 1 Crystallization temperature T_c for two different polypropylenes as a function of time obtained by applying various cooling rates under atmospheric conditions. Cooling start from 220°C at $t = 0$. Reproduced with permission from [38]



The transition to the second region marks the formation of the mesomorphic phase. For this, high cooling rates ($>200^\circ\text{C/s}$) are applied and T_c is reached within less than 1 s. The growth rate for the α -phase (at atmospheric pressure) is reported in the literature and found to be similar for different iPP grades [12, 63]. Non-isothermal crystallization can be described with nucleation and subsequent growth of spherulites, so the difference for the two iPPs in T_c in the α -region is, most probably, caused by a difference in nucleation density. This is supported by the values for nucleation density of these grades as can be found in the literature [17]. The transition temperature between both regions is $\sim 50^\circ\text{C}$. Because, for iPP1, this crystallization temperature is reached with lower cooling rates, it is concluded that the mesomorphic phase is formed more easily for iPP1 compared to iPP2. However, it seems that for both grades the crystallization temperatures coincide on the same CCT curve for the mesomorphic phase region. During quenching from the melt, for these high cooling rates, a large number of nuclei are created. It is assumed that the growth rate for the mesomorphic phase is the same for iPP1 and iPP2.

For both iPPs fast cooling experiments are performed in combination with real-time wide-angle X-ray diffraction (WAXD) pattern collection. X-Ray data are collected from a selected volume at 1 mm from the embedded thermocouple head. By means of a peak decomposition technique [64], the evolution of the different crystal fractions as a function of time and temperature is accessed. Figures 2 and 3 show the development of the α - and mesomorphic phases for four (selected) cooling rates for iPP1 and iPP2, respectively. Crystallization of the α -phase is controlled kinetically and is suppressed for higher cooling rates which also lead to a decrease of T_c . The total crystallinity, which is divided between the α - and mesomorphic phases and determined using (2), is set to 0.6 for the experiments in which only the α -phase develops and at 0.55 for the experiments where both the α - and mesomorphic phases are present.

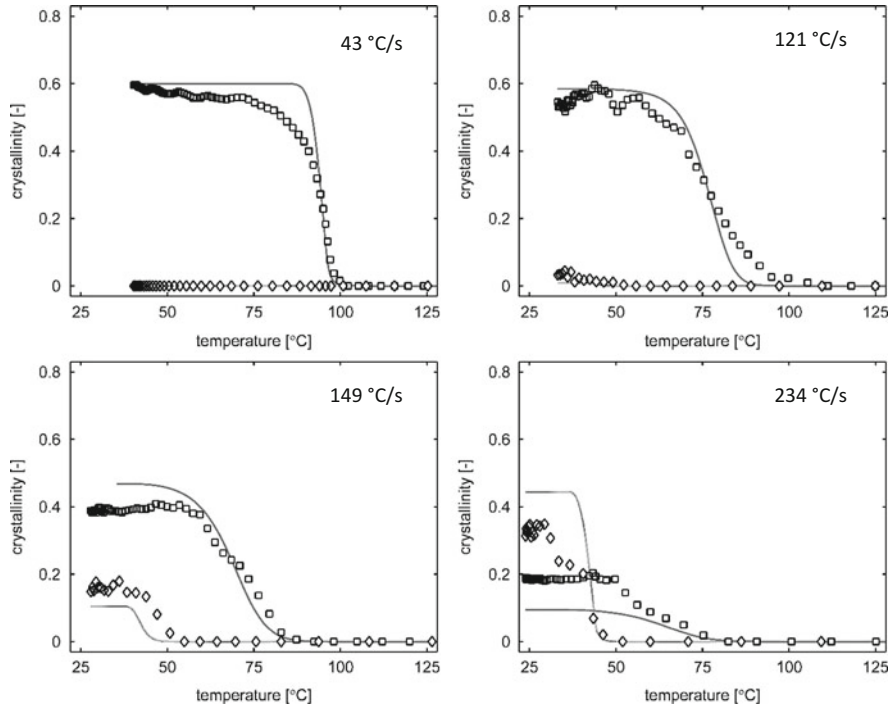


Fig. 2 Measured (*symbols*) and computed (*lines*) crystallinity evolution for α - (*open squares*) and mesomorphic phase (*open diamonds*) for iPP1 at p_0 for multiple cooling rates. Reproduced with permission from [38]

The mesomorphic phase is formed in a lower temperature range in addition to the α -phase and at high cooling rates only. When complete space filling has occurred before this temperature range is reached, as in relatively slow cooling experiments, the crystallized volume consists purely of α -phase. Applying high cooling rates, the crystallizing material reaches a lower temperature region in less time, which gives a lower T_c and initiates competition between the α - and mesomorphic phases until complete solidification takes place.

These results are used to determine the kinetic parameters for the α -phase. The numerical procedure to obtain the optimal parameter values is described elsewhere [38]. The evolution of the α -phase is well captured and, with G_α taken from the literature [51, 63], the parameters describing N are determined for both grades using the cooling rate data where only the α -phase is formed. This leads to an accurate description of the formation of the α -phase for this grade, even for cooling rates of the order of 200°C/s. The optimized parameter values, describing the nucleation density, are given in Table 1. The results are comparable to those reported in the literature [51].

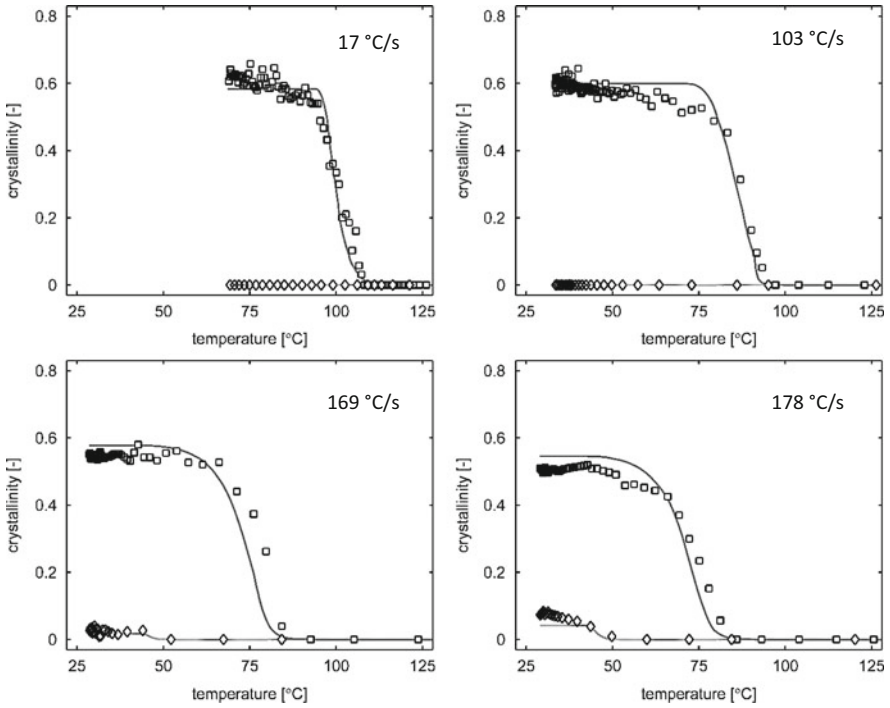


Fig. 3 Measured (*symbols*) and computed (*lines*) crystallinity evolution for α - (*open squares*) and mesomorphic phase (*open diamonds*) for iPP2 at p_0 for multiple cooling rates. Reproduced with permission from [38]

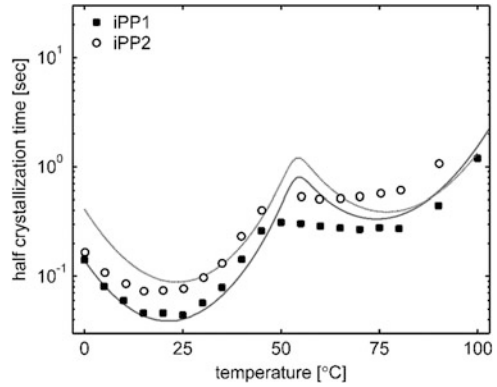
Table 1 Growth rate and nucleation density parameters for iPP1 and iPP2, both at atmospheric pressure

Parameter	iPP1	iPP2	Unit
N_{ref}	2.7×10^{14}	1.2×10^{14}	($1/m^3$)
T_{Nref}	383	383	(K)
c_N	0.181	0.219	(1/K)
$G_{max,\alpha}$	4.5×10^{-6a}	4.5×10^{-6a}	(m/s)
$T_{Gref,\alpha}$	363 ^a	363 ^a	(K)
$c_{G,\alpha}$	2.3×10^{-3a}	2.3×10^{-3a}	($1/K^2$)
$G_{max,m}$	7.4×10^{-7}	7.4×10^{-7}	(m/s)
$T_{Gref,m}$	308	308	(K)
$c_{G,m}$	2.7×10^{-3}	2.7×10^{-3}	($1/K^2$)
$G_{max,\gamma}$		1.04×10^{-6b}	(m/s)
$T_{Gref,\gamma}$		377	(K)
$c_{G,\gamma}$		3.5×10^{-3}	($1/K^2$)

^aParameters taken from the literature [51, 63]

^bAt a pressure of 50 bar

Fig. 4 Half crystallization time $t_{1/2}$ vs temperatures measured by FSC for iPP1 and iPP2 (markers) and model predictions (solid lines). Reproduced with permission from [38]



A certain crystal fraction only increases noticeably in time if nuclei are appointed to this crystal phase and the growth rate of that phase is significant. Because it is proposed that nuclei are divided between the crystal phases according to their respective growth rate ratio g_i (see (10)), it is concluded that the growth rate curve of the mesomorphic phase G_m must be located at a lower temperature range compared to the growth rate of the α -phase. However, the data in Figs. 2 and 3 are insufficient to determine G_m in a substantial temperature range because data on the mesomorphic structure formation is limited between $\sim 30^\circ\text{C}$ and 50°C . Therefore G_m is determined using additional measurements with Fast Scanning Calorimetry (FSC) [65–67]. The overall crystallization rate can be expressed in terms of the crystallization half-time $t_{1/2}$, and is obtained with isothermal crystallization experiments; see Fig. 4. Samples are cooled from the relaxed melt to the desired crystallization temperature at a rate of $2,000^\circ\text{C/s}$, which is fast enough to prevent the onset of crystallization before reaching this temperature. Again, two regimes can be distinguished marked by a transition temperature at $\sim 55^\circ\text{C}$ – a range at high temperatures where the α -phase prevails, followed by a range of mesomorphic formation at low temperatures. Similar experiments were reported by multiple authors [68, 69]. Again, the difference between the two grades is caused by the difference in nucleation density.

Although it has been proposed that the formation of the mesomorphic phase is governed by homogeneous nucleation [69, 70], in this work the mesomorphic structure is considered to be the result of growth from the heterogeneous nuclei. The nucleation density in the low temperature region of mesomorphic growth is very high ($\sim 10^{24}$ at 0°C for iPP2), directly giving a measure for the low crystallization half-time in that region. Function G_m is determined such that the calculated $t_{1/2}$ for the mesomorphic region (0 – 50°C) agrees with the experimental values.

It is found that G_m , which is assumed equal for both grades, is located in a much lower temperature region compared to G_α , which is marked by $T_{\text{ref},m} = 35^\circ\text{C}$. Quantitative agreement is found with values describing mesomorphic growth for a kinetic model [26]. Moreover, the obtained G_m also captures the formation of the

mesomorphic phase in non-isothermal conditions quite well; see Figs. 2 and 3. Moreover, the crystallization half-time in the α -region described by the model is in good agreement with the FDSC experiments (Fig. 4). A complete overview of the parameters is given in Table 1.

For the crystallinity development as displayed for the highest cooling rate in Fig. 2, a discrepancy between the calculated and measured crystal fractions is found. It is stressed that when a mixture of α - and mesomorphic fractions is present, the decomposition technique of the X-ray patterns is difficult to apply because of the superposition of the independent diffractions peaks around the same diffraction angle [64]. This leads to a slight mismatch in the described crystallinity levels for both present phases. Nonetheless, the total crystallinity level obtained is in agreement with the measurements.

2.3 Effect of Pressure

The effect of pressure on the crystallization process has been studied for two different pressure levels (50 and 250 bar) and two (relatively low) cooling rates (0.1°C/s and 2.0°C/s) in combination with in situ X-ray collection for iPP2 only, using a slit flow device [71–73]. Decomposition of the acquired WAXD patterns show that, as a result of the applied pressure, γ -phase is always formed in combination with the α -phase and the corresponding onset temperature of both structure formations is equal. The measured crystallinity development of the α - and γ -phases for these conditions is displayed in Fig. 5. For the higher pressure a larger amount of the γ -fraction is developed which goes with a lowering of the α -phase. The final γ -fraction is noticeably higher for the lower cooling rate. Comparable results considering the formation of the γ -phase were previously reported in literature; γ -phase is obtained at elevated pressures with low cooling rates [74] or isothermal conditions at high pressures [46, 75].

As proposed, the assignment of nuclei to a given crystal phase scales with the ratio of their respective growth rates values, g_i . For low cooling rates, such as 0.1°C/s, the material spends sufficient time in a high temperature range where g_γ is large before complete space filling is reached. For the higher cooling rate (2.0°C/s), the temperature range before complete solidification holds a larger overall g_α and thus more nuclei are appointed to the α -phase. From this it can be concluded that G_γ is located in a higher temperature range compared to G_α . An increase of the final γ -fraction with pressure is again explained by means of the growth rate fraction g_i ; when the applied pressure raises $G_{\max,\gamma}$ with respect to $G_{\max,\alpha}$, more nuclei are appointed to the γ -phase and this increased growth rate also enhances the corresponding crystal fraction. On the basis of experimental observations by Alamo et al. [76], it was concluded that $G_{\max,\gamma}$ is lower than $G_{\max,\alpha}$ because of the unusual packing of the γ -form.

The above considerations help to determine the growth rate functions G_γ relative to G_α . The parameter $T_{G_{\text{ref}},\gamma}$ is found to be higher than $T_{G_{\text{ref}},\alpha}$ and $G_{\max,\gamma}$ lower than

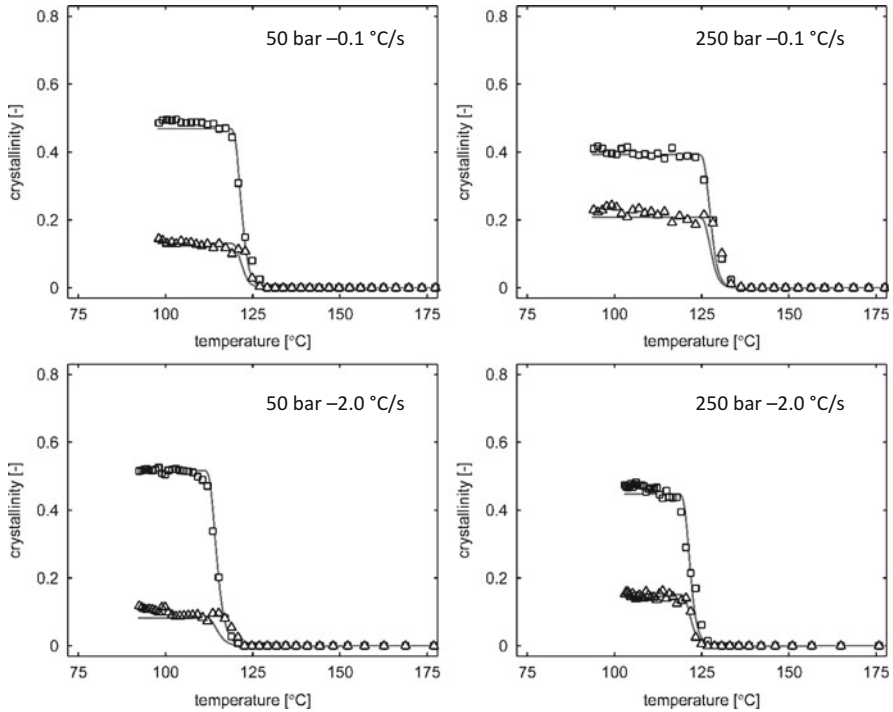


Fig. 5 Measured (*symbols*) and computed (*lines*) crystallinity evolution for α - (*open squares*) and γ -phase (*open triangles*) for iPP using isobaric, non-isothermal experiments for multiple pressures and cooling rates. Reproduced with permission from [38]

$G_{\max,\alpha}$ The parameters $c_{G,\gamma}$ and $c_{G,\alpha}$ are found to be independent of pressure. The effect of pressure is incorporated by shifting the reference temperatures in the expressions for N and G_i according to (11) and by determining $G_{\max,i}$ per pressure. The resulting computed crystal fractions, presented in Fig. 5, show that with the estimated parameter values a very good description of the formation of both phases is obtained. The optimal G_γ gives a good description of the formation of the γ -fraction for all applied conditions. $G_{\max,\gamma}$ is zero at atmospheric pressure because no γ -phase is measured during the fast cooling experiment series; see the previous section. Discussion with respect to the effect of pressure on the individual growth rates is continued in the next section. Results are presented in Fig. 9 together with the results of dilatometry (see next section).

2.3.1 Dilatometry

Dilatometer experiments using a Pirouette dilatometer [77–79] are performed at four different pressures and at three cooling rates for iPP2 only and subsequent structural characterization is carried out by ex situ X-ray analysis. The dilatometer

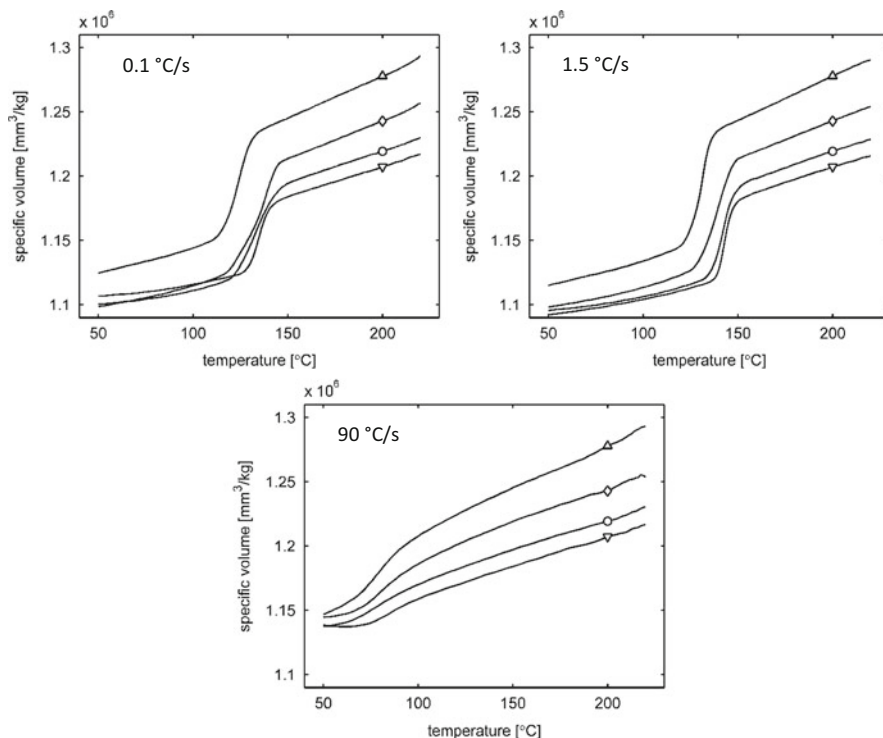


Fig. 6 Influence of pressure and cooling rate on the specific volume of iPP2 measured at 300 (*open triangles*), 600 (*open diamonds*), 900 (*open squares*) and 1,200 bar (*v*). Reproduced with permission from [38]

provides structural information in the form of specific volume, v , as function of temperature at different pressures and cooling rates; see Fig. 6. As is well known, a higher pressure results in a lower specific volume and the transition region, representing the start of crystallization, moves to a higher temperature because of an increase in the equilibrium melting temperature T_m^0 [45].

With increasing cooling rate, the transition region spreads out over a wider temperature range and T_c shifts to a lower temperature, which is in agreement with Fig. 1.

At the lower temperatures, e.g. below 60°C, the measurement data become less accurate and some curves seem to cross each other. At these temperatures the apparatus is unable to measure accurately the shrinkage of the sample, simply because the friction between the (by now fully solidified) sample and the inner components is too high.

A clear correlation between the phase contents and the pressure is observed; see Fig. 7. With increasing cooling rate, the α -phase increases at the cost of the γ -phase and for the highest cooling rate a relatively low fraction of the mesomorphic phase is present whereas no γ -phase is formed. The cooling rate of 90°C/s results in a

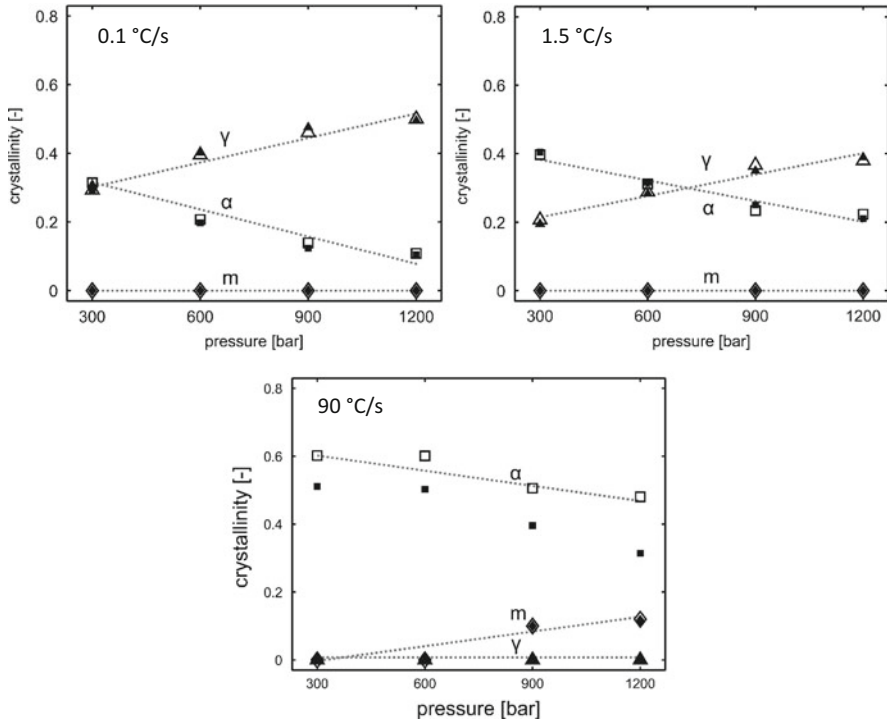


Fig. 7 Final crystallinity fraction for the α - (open squares), γ - (open triangles) and mesomorphic phase (open diamonds) determined by ex situ X-ray decomposition (open symbols) and as predicted by the non-isothermal model (closed symbols). Lines are a guide to the eye. Reproduced with permission from [38]

decrease of the α -phase content and a subsequent increase of the mesomorphic fraction with pressure. Even at the highest pressure this cooling rate is sufficient to prevent any formation of γ -phase.

With an increase in isobaric pressure, the fraction of γ -phase increases at the cost of the α -phase (see also Fig. 5). The highest fraction of the γ -phase is, once more, found for the lowest cooling rate, and this is again explained by the location of G_γ at a higher temperature region compared to G_α . With a large growth rate fraction g_γ at high temperatures, a considerable amount of nuclei grow into spherulites with γ -phase content [80]. The increase of the γ -phase with pressure indicates an increase of $G_{\max,\gamma}$, with respect to $G_{\max,\alpha}$, as g_γ increases with temperature and enhances γ -formation for lower cooling rates.

The recorded thermal and pressure history of the samples serves as input for the non-isothermal model to describe the final multiphase structure. Values for N , G_α , G_γ and G_m are obtained from the previous (fast cooling and slit flow) experiments. The only free parameters allowed are the maximum growth rate levels $G_{\max,i}$ for the different phases, which are determined as a function of the pressure using the complete set of available cooling rates. This enables the complete multiphase

description for the PVT experiments, resulting in an accurate description of the crystal fractions for prescribed processing conditions; see Fig. 7. A discrepancy between model and measurements is observed for the highest cooling rate in Fig. 7 – an underestimation of the α -phase followed by an overestimation of the mesomorphic fraction. Just as in previous experiments, the total crystallinity in equilibrium conditions follows from X-ray analysis (see (2)) and is found to be ~ 0.6 . However, in the model this crystallinity level cannot be achieved by α -phase formation only. Incomplete space filling is reached and, as a result, the remaining space filling is occupied by the mesomorphic phase. For high pressures combined with a high cooling rate, such as 90°C/s , the temperature history is critical for the final crystal structure. Though the temperature of the sample in the dilatometer is calculated from the six temperatures measured with thermocouples placed in the metal housing close to the sample [78] and using a heat balance, we are not sure of the exact temperature, especially at high cooling rates. Therefore, we examine the sensitivity of the results by varying the measured temperature according to

$$T_{\text{corr}}(t) = T_{\text{meas}}(t) + a\frac{t}{t_r}, \quad (13)$$

where T_{corr} is the corrected temperature, T_{meas} the measured temperature (via a heat balance) and t_r the time needed for T_{meas} to reach room temperature initially. With $a=6$ the difference between the measured and corrected temperature is $\sim 2.5^\circ\text{C}$. (Note, this problem does not occur for the fast cooling experiment; here the thermocouple is placed within the sample.) Using this estimated correction, the final crystalline fractions described by the model are now within good agreement of the measurements; see Fig. 8.

It follows from the optimized values for $G_{\text{max},i}$ that, with pressure, the maximum growth rate slightly increases for the α -phase (consistent with pressurized cooling experiment results; see also Fig. 5), increases for the γ -phase and decreases for the mesomorphic phase; see Fig. 9. Because of this, the increase of the γ -fraction and simultaneous decrease of the α -phase can be understood. In this figure, G_m is not included for 300 and 600 bar; for these conditions no mesomorphic content is measured so $G_{\text{max},m}$ could not be determined. In the model, the effect of pressure on the growth rate of a given crystal phase is introduced by a shift of the reference temperature and via the maximum growth rate, which is found to be pressure dependent; see Fig. 9. Pantani et al. [27] proposed an exponential relationship between pressure and the maximum kinetic parameter. Hence, it is proposed that the maximum growth rate depends on pressure according to

$$G_{\text{max},i} = G_{\text{max},i}^0 \exp\left(a_i(p - p_0) + b_i(p - p_0)^2\right) \quad (14)$$

where a_i and b_i are constants and $G_{\text{max},i}^0$ is the reference growth rate at atmospheric pressure p_0 . The constants for each crystal phase are determined with the data presented in Fig. 9 and are given in Table 2. Regarding the mesomorphic phase, a_m

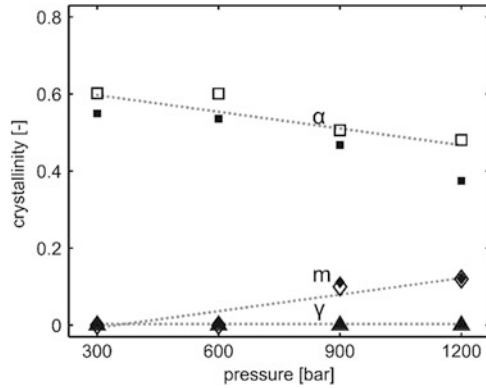


Fig. 8 Final crystallinity fraction for the α - (open squares), γ - (open triangles) and mesomorphic phase (open diamonds) determined by ex situ X-ray decomposition (open symbols) and as predicted by the non-isothermal model (closed symbols) using an uncertainty on the measured temperature in the dilatometer. Lines are a guide to the eye. Reproduced with permission from [38]

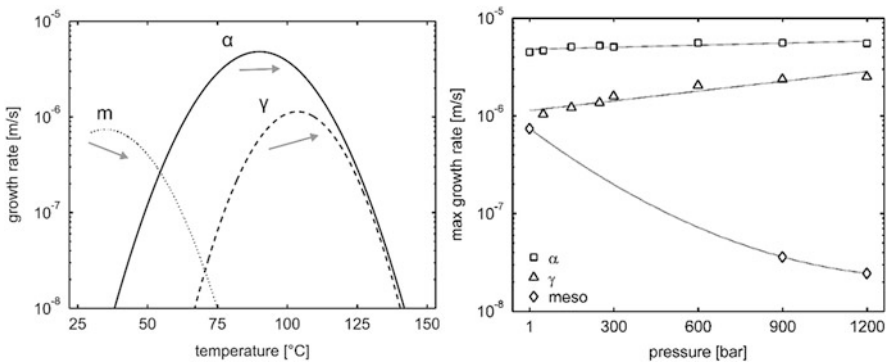


Fig. 9 (left) Growth rate functions for the α - (solid line), γ - (dashed line) and mesomorphic phase (dotted line) as function of temperature. Arrows indicate the effective shift of G_i with pressure (right). Effect of pressure on maximum growth rates $G_{max,i}$, for the α - (open squares), γ - (open triangles) and mesomorphic phase (open diamonds). Lines give the exponential relationship as function of pressure – see (14). Reproduced with permission from [38]

is determined at 4.92×10^{-8} 1/Pa, which is in quantitative agreement with Pantani et al. [27].

Finally, predictions of the crystallinity evolution as a result of various applied processing conditions are made with the complete set of optimized parameters. As illustrated in Fig. 10, the multiphase structure development of iPP2 is satisfactorily predicted using an approach in which the nucleation density and growth rate are functions of temperature and pressure.

Table 2 Constants for each crystal phase for the maximum growth rate as a function of pressure for iPP2 using (14)

Parameter	iPP2	Unit
$G_{max,\alpha}^0$	4.81×10^{-6}	(m/s)
a_α	1.60×10^{-9}	(1/Pa)
b_α	0	(1/Pa ²)
$G_{max,m}^0$	7.40×10^{-7}	(m/s)
a_m	-4.92×10^{-8}	(1/Pa)
b_m	1.73×10^{-16}	(1/Pa ²)
$G_{max,\gamma}^0$	1.13×10^{-16}	(m/s)
a_γ	7.66×10^{-9}	(1/Pa)
b_γ	0	(1/Pa ²)

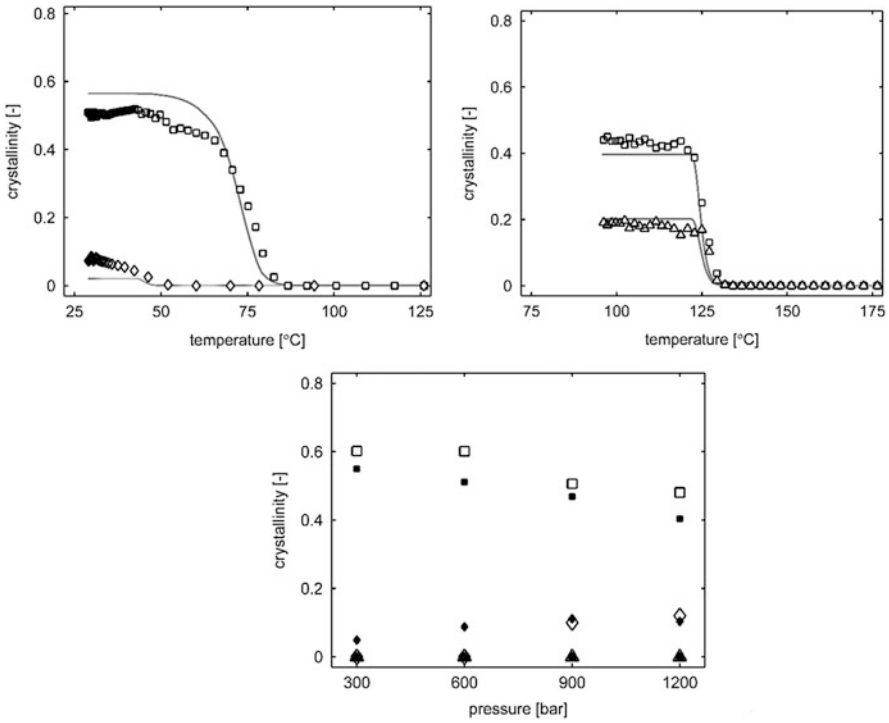


Fig. 10 Measured (open symbols) and computed (lines (top left and top right), closed symbols (bottom)) crystallinity for the α - (open squares), γ - (open triangles) and mesomorphous phase (open diamonds) for (top left) fast cooling at p_0 and 178°C/s , (top right) pressurized cooling at 150 bar and 0.1°C/s and (bottom) dilatometer experiments, each using $G_{max,i}$ determined as a function of pressure by (14). Reproduced with permission from [38]

β -Phase in iPP

The formation of the β -phase in quiescent processing conditions is investigated by the addition of a specific β -nucleation agent to the iPP homopolymer. Fast cooling experiments with in situ WAXD similar to those included in Figs. 2 and 3 were used to determine a temperature-dependent secondary reservoir of nuclei and to optimize the growth rate of β -crystals. This analysis is not included here; for more details the reader is referred to the literature [38].

3 Crystallization of Linear Low-Density Polyethylene: Multiple Crystal Processes

In this section, quiescent crystallization of a metallocene LLDPE (m-LLDPE) grade is discussed, followed by characterization of the complex solidification kinetics using the combined results of thermal (differential scanning calorimetry (DSC) and FSC) and scattering (small angle laser scattering (SALS)) methods. The material investigated is a commercial butyl-branched LLDPE (ExxonMobil). The crystallization model previously discussed for iPP is modified to describe crystallization consisting of multiple processes, i.e. one primary and a two-step secondary process. The influence of flow gradients on this material was also studied but is not described here [39].

3.1 Thermal Characterization

Metallocene-type polymerization provides that m-LLDPE is a substantially linear polymer with a controllable amount of short branches. The intermolecular distribution of these side chain branches is called homogeneous when the distribution of branches between the molecules is narrow, although the sequence length distribution between branches can still be broad. The longer ethylene sequences, having a higher melting point, crystallize faster [81–83] and fold into stacked lamellae that span the spherulite. This is defined as primary crystallization [34]. Quenching the melt at increasing rates smears out this process over a larger temperature range and/or postpones crystallization to lower temperatures because of insufficient time for nucleation and growth [38, 84]. Crystallinity increases further because of secondary crystallization of the shorter sequence length chain sections, even before spherulitic impingement [85], as they form lamellar stacks in the amorphous regions between the primary lamellae inside the spherulites [85, 86].

The influence of comonomer content is reflected by a second peak in the crystallization process commonly observed at low temperatures in DSC [87, 88]. During the lamellar folding process, the length of the side chain

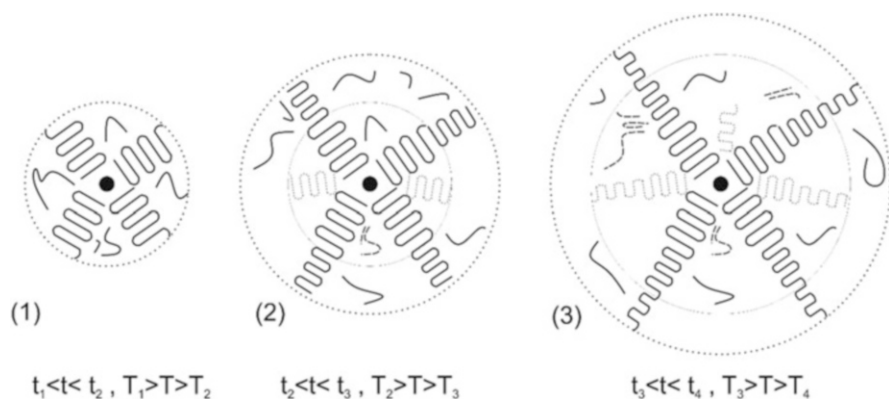
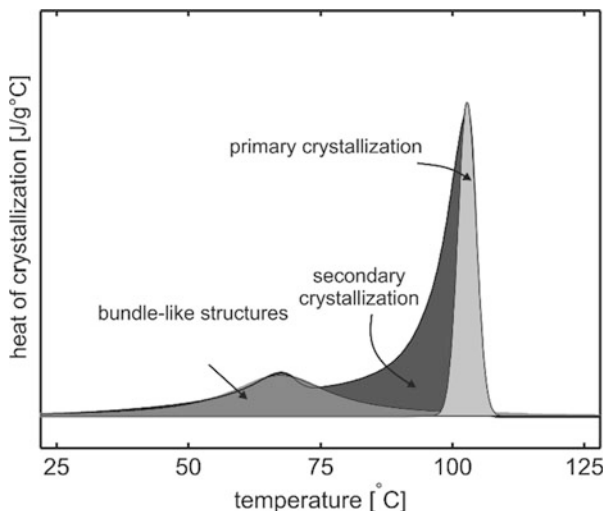


Fig. 11 Schematic time discretized overview of primary and secondary crystallization process during cooling. (1) A nucleated spherulite grows in time as a function of temperature, fast growing primary lamellae are formed from the most linear molecular sequences. (2) Shorter sequence lengths induce secondary lamellar growth in the remaining amorphous regions. Lamellae gradually become thinner with undercooling according to classical theories [93]. (3) Finally, at high undercooling, free chain sections locally order into small bundled structures. Reproduced with permission from [39]

determines whether or not it is excluded from the crystal lattice [89–91]. As the already formed lamellae restrict the topological movement of the remaining sequences, these are unable to take part in the chain folding process. Hence, at high levels of undercooling, a second stage of secondary crystallization yields a granular morphology of small bundled structures or loosely packed ethylene sequences [87, 88, 90, 92]. A simplified, schematic, and time-discretized overview of the primary and two-stage secondary process is given in Fig. 11.

For each DSC and FSC experiment the total baseline subtracted heat capacity, or the excess heat capacity, is composed of the contributions of the crystallization processes, i.e. one primary and two secondary crystallization events. Peak decomposition of the signal is used to determine each process as function of temperature; see Fig. 12. In our approach, the primary process is marked by the symmetric fraction of the sharp peak at high temperatures, and (although this is simplification) is described by a Gaussian function. During cooling, the crystallization rate increases as the remaining crystallisable material decreases, and we assume that this results in a symmetric release of heat as function of temperature. A pronounced exotherm with a peak at $\sim 60^\circ\text{C}$ caused by bundle-like features was best described by using a much broader Lorenzian function. The lamellar insertion process that rapidly follows primary crystallization at slightly higher undercooling and the corresponding heat release provides the peak with a high asymmetry. Depending on the comonomer content, a separate crystallization peak or a distinct shoulder is observable. It is assumed that the heat capacity not included in both peak functions can be fully attributed to the insertion of lamellae (see again Fig. 12), which can be

Fig. 12 Schematic of the peak decomposition process of the measured excess heat capacity. Reproduced with permission from [39]



described with an n -number of Gaussian functions vs temperature, representing multiple lamellar insertion processes with decreasing lamellar thickness [93]. Although it is more common to apply peak decomposition on DSC melting curves, the melting characteristics of this material consist of one clear peak only and do not allow for such a procedure [39, 94]. Good fits of the peak functions to the data were always obtained, as is shown in Fig. 13, where both DSC and FSC measurements are displayed, i.e. for low and high cooling rates, including the determined peak functions.

Regarding conventional DSC experiments, crystallinity was calculated from the integrated peak, which was normalized for sample mass and cooling rate. The (linear) extrapolated heat capacity of the melt was used as a baseline [95]. The transitional enthalpy for polyethylene, $\Delta H(T)$, was taken from the literature [96] and assumed to be a function of temperature only. We do not distinguish between the folding energy of lamellae and bundle-like features. For the FSC sample, the same protocol was applied, with the sample mass determined iteratively at ~ 400 ng by matching the amount of primary crystallinity calculated at the slowest cooling rate with FSC to the value obtained at the highest rate with DSC. It was assumed that, in this range of cooling rates, primary crystallization was not suppressed, i.e. complete space filling is obtained.

When crystallinity is plotted vs temperature, for example for 500°C/s in Fig. 14, it becomes clear that the primary process fully covers the first, steep increase at high temperatures. This rapid process covers a maximum of 15.2% of total crystalline volume, in agreement with values found by Goderis et al. [97]. At this stage, the crystallinity distribution inside the spherulites is presumed to be inhomogeneous (see Fig. 11). Upon further cooling, crystallinity develops more slowly via lamellar insertion, the rather sharp transition point at approximately 50°C corresponding to a bundle-like structure formation.

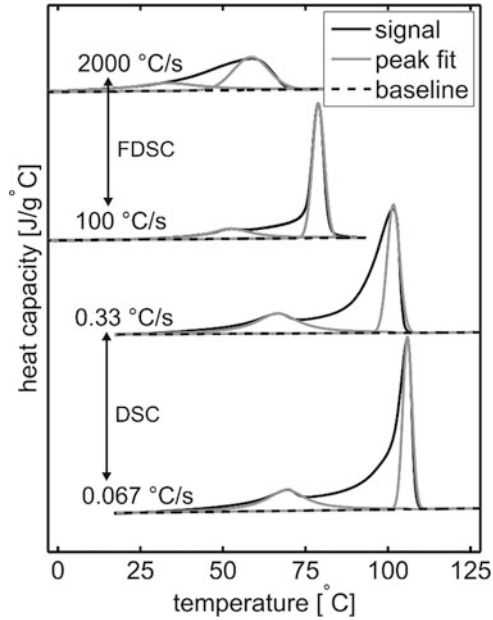


Fig. 13 Summary of the peak fitting process of the excess heat capacity during cooling in the scan rates investigated for DSC and FSC. Reproduced with permission from [39]

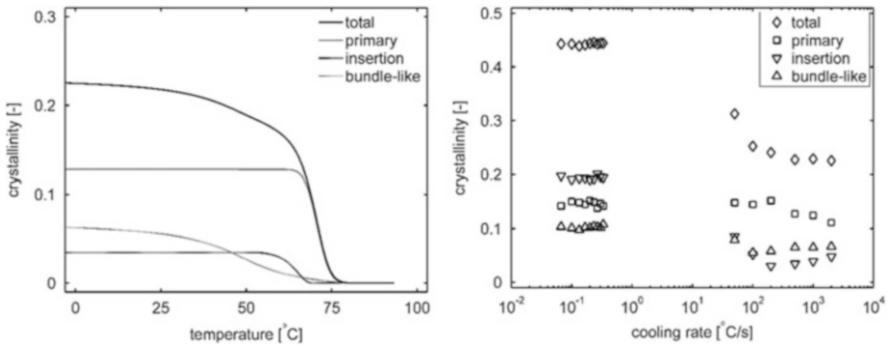


Fig. 14 Deconvoluted crystallinity vs temperature at 500 °C/s (*left*) and final crystallinity fractions for all cooling rates investigated (*right*). Reproduced with permission from [39]

Table 3 Maximum crystallinity content for the primary-, lamellar insertion-, bundle-like fractions and total crystallinity, respectively

χ_{∞}^p	χ_{∞}^l	χ_{∞}^b	χ_{∞}^t	Unit
0.152	0.202	0.103	0.457	(–)

Both techniques used cover together a wide range of cooling rates, albeit with a large gap in between roughly 10^0C/s and 10^1C/s ; see Fig. 14. At low rates a more or less constant crystallinity distribution was observed for primary and both stages of secondary crystallization and for all conditions. In the case of the FSC scan rates, a gradual decrease of the total crystallinity was obtained, mainly caused by a reduced level of lamellar insertion, a process which is slow compared to primary growth. Hence, when the time available for crystallization decreases the average crystallinity in each spherulite reduces. The drop in the total crystallinity is outside the reach of both the DSC and the FSC setups (between 10^0C/s and 10^1C/s). Only at very high cooling rates is a minor decrease of the primary crystallinity noted. For many semi-crystalline polymers it is possible to obtain a fully amorphous material by rapid cooling of the sample from the melt at a critical cooling rate, \dot{T}_{crit} . From the data plotted here, \dot{T}_{crit} could be estimated to be in the order of 10^6C/s .

Good fits of the peak functions to the data were always obtained, as is shown in Fig. 13, where both DSC and FSC measurements are displayed, i.e. for low and high cooling rates, including the determined peak functions.

The maximum crystallinity for each fraction, χ_i , was determined from the same figure (see Table 3) and used in our modelling section later on.

3.2 Small-Angle Light Scattering

Light scattering of semi-crystalline polymers has been studied for an extensive amount of time and is commonly used to extract morphological details from polymers [86, 98–100]. The method was first applied by Debye and Bueche [101], and later on more detailed and complex theories were developed for polarized light scattering of common polymer morphologies such as single spherulites [102–104] and solid films with space-filling architectures [105]. Scattering in H_v mode is dependent on the size and anisotropy of the spherulitic entities. As a result, spherulitic growth can be detected by the transient scattering patterns and quantified from the integrated 2D scattering patterns. When it is assumed that only perfect spherulitic structures are formed, the average radius of the spherulites, R_{av} , can be determined by tracing the scattering vector with maximum intensity, q_{max} , in time using [106]:

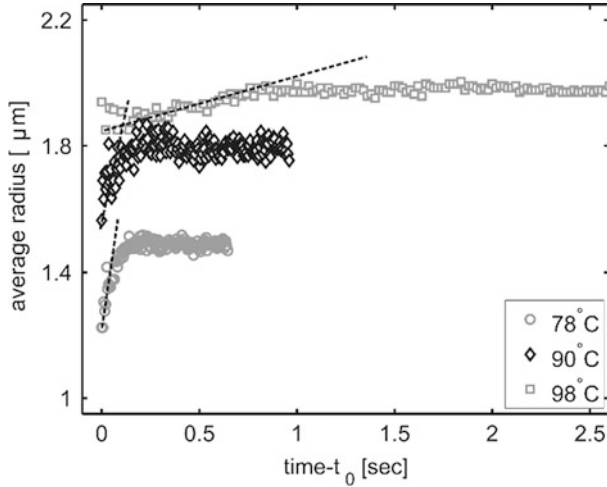


Fig. 15 Average spherulitic radius vs time for three different temperatures measured using SALS. Dashed lines indicate the linear growth rate. Reproduced with permission from [39]

$$R_{av} = \frac{4.09\lambda_0}{4\pi n_m \sin\left(\frac{\theta}{2}\right)} \approx \frac{4.09}{q_{max}}, \tag{15}$$

where λ_0 is the wavelength of light in vacuum, θ the radial scattering angle and n_m the refractive index of the medium. To successfully investigate very fast crystallizing polymers under (approximately) isothermal conditions, the challenge is to reach the desired temperature before any significant amount of crystallization takes place. In this work, a temperature jump stage allows us to study crystallization of m-LLDPE up to high levels of undercooling, although no real-time measure for the actual sample temperature can be provided, such as in the setup of Ding and Sprueill [107, 108]. Reaching real isothermal conditions becomes critical for relatively high undercooling and corrections might be required. We discuss this issue in detail in the next section. The obtained time evolution of radii is displayed for three different temperatures so as not to crowd Fig. 15. These data were selected to provide an overview of the measurements in the temperature range investigated. Data is shifted in time with t_0 , which represents the experimental time at which a clear peak in the scattering pattern was obtained.

Only when a sufficient amount of scattering data is recorded can q_{max} be determined accurately. Consequently, only the final part of linear growth and subsequent impingement is detected. Nevertheless, a first-order function can be fitted to the data to obtain the temperature-dependent spherulitic growth rate, $G(T)$.

The average growth rate is plotted for all experiments in Fig. 16 and shows the characteristic bell-shaped curve as commonly observed for semi-crystalline polymers [16]. An apparent maximum growth rate of approximately 3 $\mu\text{m/s}$ is measured at $\sim 78^\circ\text{C}$. Although the temperature at the maximum growth rate is in agreement

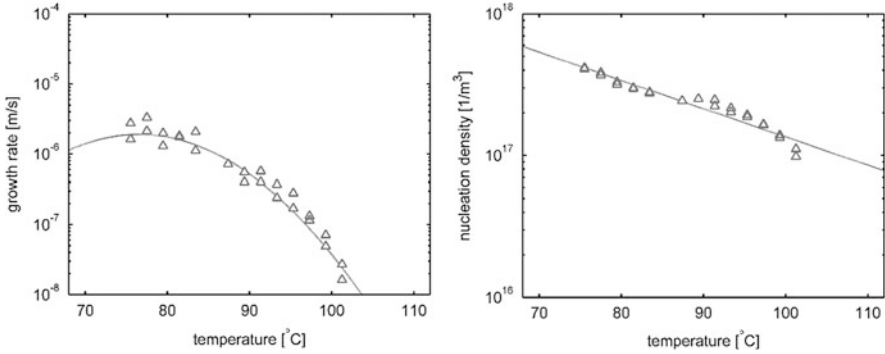


Fig. 16 Spherulitic growth rate (*left*) and nucleation density (*right*) vs temperature measured using SALS. *Dashed lines* indicate the least squares approximation of (7) and (8), respectively. Reproduced with permission from [39]

with earlier findings [108], the growth rate is much lower compared to values for ethylene copolymers reported in the literature [109].

The temperature-dependent heterogeneous nucleation density, $N(T)$, plotted in Fig. 16, was estimated from the final radius measured using [21, 22]

$$\xi = 1 - \exp\left(-\frac{4}{3}\pi R^3 N\right), \quad (16)$$

which, at a space filling of 50%, can be rewritten using the final spherulite radius, R_f :

$$N = \frac{-\ln\left(\frac{1}{2}\right)}{\frac{2}{3}\pi R_f^3}, \quad (17)$$

and shows the usual logarithmic decrease of the number of spherulites with temperature [12]. Temperature-dependent functions for $G(T)$ and $N(T)$ can be obtained via least-square approximation of the measurements using (7) and (8). Good fits are obtained and are included in Fig. 16.

3.3 Primary Crystallization Model

The non-isothermal primary crystallization kinetics are again calculated using the Schneider rate equations [55] (3)–(6) containing the spherulitic crystal growth rate G and nucleation density N as function of temperature (7) and (8). In this case, calculation of the undisturbed volume fraction concerns the growth of primary crystals only, where

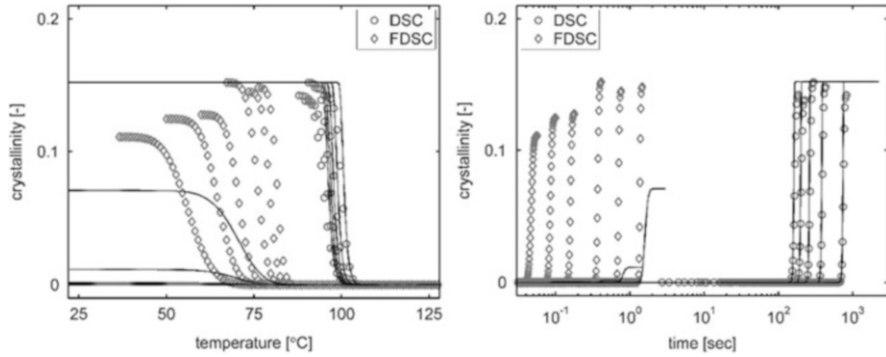


Fig. 17 Primary crystallinity from calorimetry experiments vs temperature (*left*) and time (*right*). *Dashed lines* are the computed values with crystallization kinetics from SALS. Reproduced with permission from [39]

$$\xi_p(t) = \frac{\chi_p(t)}{\chi_\infty^p}. \tag{18}$$

Figure 17 shows the primary crystallinity obtained from calorimetry and the crystallinity calculated from the FSC and DSC temperature profiles and the $G(T)$ and $N(T)$ from SALS measurements by the methodology described above. It immediately becomes clear that only the cooling experiments from DSC are described accordingly. Here, independent of the cooling rates used, crystallization always takes place at approximately 100°C, and thus only the SALS data obtained at low levels of undercooling describe the data well. For the high cooling rates, the calculated crystallization rate is too low and, consequently, the final primary crystallinity level is as well. In the next section we analyse the SALS results in more detail to evaluate the measurement data at higher undercooling.

3.3.1 Temperature Correction Calculations

The design of the jump stage is such that the cooling rate of the support can be considered infinite. The polymer sample, however, does not reach the set temperature instantaneously. For low set temperatures this leads to a discrepancy between the set temperature and the temperature at which crystallization takes place. To account for this, the transient temperature in the sample needs to be determined [110]. Calculations were performed by solving the heat balance on a 1D finite difference grid representing the experimental setup; see Fig. 18.

The heat balance is given by

$$\rho^k c_p^k \frac{\delta T}{\delta t} = \lambda^k \frac{\delta^2 T}{\delta x^2} + \rho^k \chi_\infty \Delta H \dot{\xi}, \tag{19}$$

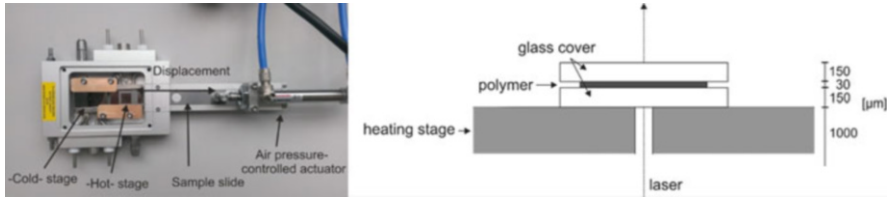


Fig. 18 (left) Temperature jump stage and (right) cross section and dimensions of the sample and the temperature jump stage located in the SALS setup. Reproduced with permission from [39]

Table 4 Parameters for energy balance [111]

	Silver	Glass	Polyethylene	Unit
ρ	10.5	2.5	0.76	(10^3 kg/m^3)
C_p	233	0.5	3,000	(J/kg K)
λ	429	1.05	0.23	(W/mK)

with T the temperature and t time. Further, ρ denotes density, c_p is the heat capacity, and λ is the thermal conductivity. Superscript k denotes the material: silver (heating element), glass (sample cover) or polymer. Values are given in Table 4. The last term in the right-hand side represents the heat release produced by crystallization of the polymer, with $\Delta H(T)$ the heat of fusion [75], χ_∞ the final crystallinity of the material and $\dot{\xi}$ the crystallization rate as given by the Schneider rate equations, including the obtained functions for nucleation density and growth rate. We assume that the maximum reachable crystallinity in this temperature range consists of crystals grown during the primary and lamellar insertion process. From Table 3 we obtain $\chi_\infty = \chi_\infty^p + \chi_\infty^l = 0.35$.

The crystallization temperature is defined as the temperature at which space filling in the centre of the polymer sample reaches 70%, which is similar to the crystallinity level at which the linear growth rate was determined in SALS analyses. In Fig. 19 we present the results of this analysis. Figure 19 (left) shows the calculated crystallization temperature vs the set temperature for the originally measured data. The dashed line shows the case where these would be equal. The corresponding temperature transients in the centre of the polymer sample are presented in Fig. 19 (right). Clearly, the crystallization temperature starts to deviate from the set temperature from 92°C downwards.

If the calculated temperature shift, $\delta T(T)$, is implemented as a correction to the SALS results, only part of the data shifts to higher temperatures, whereas both the growth rate and nucleation density values are maintained. Consequently, the functions determined in (7) and (8) have to be re-evaluated. Because δT is a function of the crystallization rate and thus of the measurement points themselves (see (19)), a different approach is needed to calculate the correct material functions for N and G . From Fig. 19 (left), it becomes clear that δT is not significant for measurements above 90°C ($<1^\circ\text{C}$). Thus, these points can be used in the corrected least-squares approximation of the nucleation density, $N^*(T)$. This number of data points is insufficient to determine a corrected bell-shaped growth rate function, $G^*(T)$.

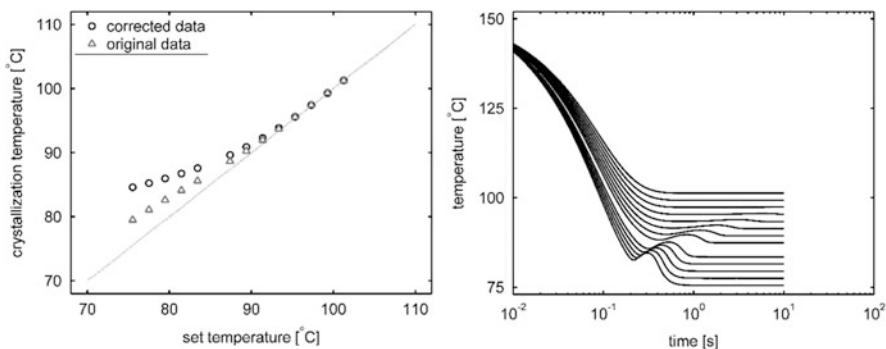


Fig. 19 Results of the heat balance calculations (*left*). The calculated crystallization temperature vs the set stage temperature for measured data and corrected data (see next section) and (*right*) the heat traces in the centre of the polymer sample. Reproduced with permission from [39]

Instead, G^* was obtained by least-square optimization of the calculated primary crystallization fraction from calorimetry, where N^* is included for calculations. As expected, an excellent description of the primary crystallinity content is obtained in a range exceeding five decades in time; see Fig. 20. Parameter values obtained are displayed in Table 5 for both the original and the corrected functions.

When the obtained growth rate function is verified it becomes apparent that, at lower temperatures, e.g. below 90°C, G^* strongly deviates from G and a much higher maximum growth rate value is obtained, ensuring a significant crystallization rate even at low temperatures. The values of G_{\max} and $T_{G_{\text{ref}}}$ show good agreement with the literature [108, 109].

When G^* and N^* are implemented in (19) and, again, δT is calculated, both shifted measurement data for N and G correspond with both G^* and N^* ; see Fig. 21. Data above 90°C still show a negligible δT and overlap the set temperature during the SALS measurements; see also Fig. 19 (left). This confirms the accuracy of our calibration and analysis methods to calculate the growth rate and nucleation density, but simultaneously shows the SALS setup cannot be used for this material below 90°C without additional heat balance calculations. The sample dimensions required do not allow for a micro-thermocouple to be included, for example, between the two glass sample covers, so this is the only method available at the moment.

3.4 Secondary Crystallization Model

The total crystallinity fraction, including the increase of crystallinity produced by secondary crystallization, can be expressed in terms of a convolution integral [35, 37]:

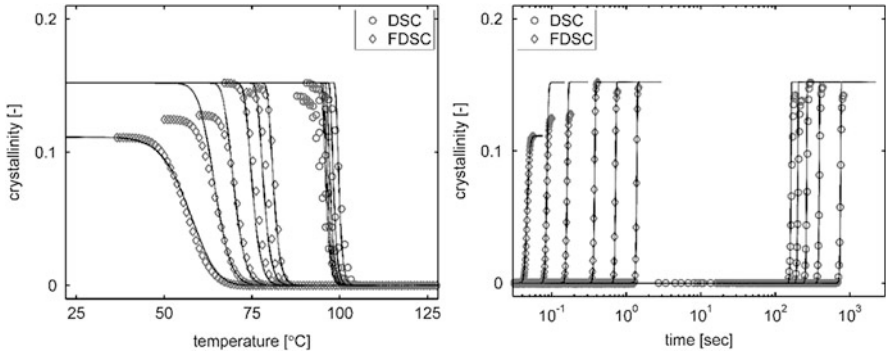


Fig. 20 Primary crystallinity from calorimetry experiments vs temperature (*left*) and time (*right*). *Dashed lines* are computed with temperature corrected functions for nucleation and growth. Reproduced with permission from [39]

Table 5 Parameters for nucleation and growth functions

Parameter	Original	Temperature corrected	Unit
G_{max}	1.90×10^{-6}	5.55×10^{-5}	(m/s)
c_G	7.10×10^{-3}	5.60×10^{-3}	(1/K ²)
T_{Gref}	349.5	336.5	(K)
N_{max}	1.35×10^{17}	1.26×10^{17}	(1/m ³)
c_N	4.60×10^{-2}	7.24×10^{-2}	(1/K)
T_{Nref}	383	383	(K)

^aValues for functions obtained after temperature correction

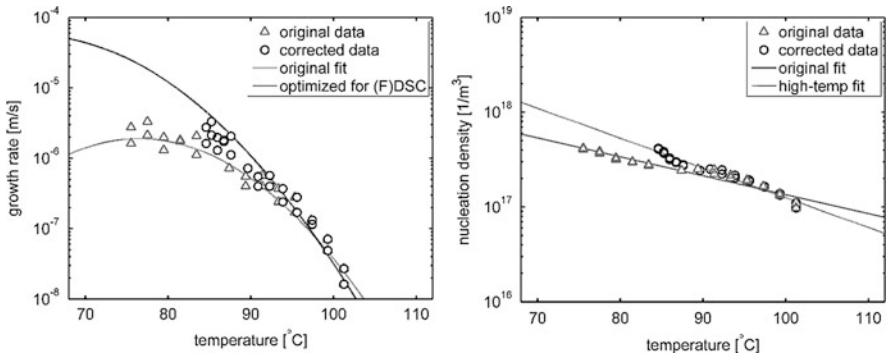


Fig. 21 Original and temperature corrected growth rate (*left*) and nucleation density (*right*) vs temperature. Reproduced with permission from [39]

$$\chi(t) = \int_{\tau=0}^t \dot{\xi}(t-\tau)\chi_{\infty}(t)d\tau, \quad (20)$$

where χ_{∞} is, once more, the maximum value of crystallinity determined by the external conditions experienced by the sample [28]. If each spherulite has an initial (primary) crystallinity equal to χ_{∞}^p , the evolution of the maximum crystallinity during solidification yields

$$\chi_{\infty} = \int_{\tau}^t \dot{\chi}_{\infty}(T(t))dt + \chi_{\infty}^p. \quad (21)$$

Here, the increase of the maximum crystallinity, $\dot{\chi}_{\infty}$, can be expressed as a strong function of the environmental conditions, e.g. temperature, and the current amount of remaining amorphous material using, similar to (12):

$$\dot{\chi}_{\infty}(T(t)) = \sum (1 - \xi_{\infty}^i)^{n_i} K_i(T), \quad (22)$$

where n_i is similar to a diffusion constant which provides a strong dependence on the current amount of amorphous material,

$$\xi_{\infty}^i = \frac{\chi_i(t)}{\chi_{\infty}^i}, \quad (23)$$

where i denotes the multiple secondary crystallization processes and

$$K_i(T) = a_i \exp\left(-b_i \frac{(T - T_{\text{ref},i})^2}{T^2}\right), \quad (24)$$

is introduced as a temperature-dependent rate function with constants a_i , b_i and $T_{\text{ref},i}$. We briefly discuss the context of these constants. The reference temperature, $T_{\text{ref},i}$, corresponds to the temperature of the maximum rate, a_i , of secondary structure formation. The value of b_i governs the width of the function, i.e. determines the temperature range in which secondary morphologies are able to form. Subscripts l and b are used for lamellar insertion and formation of bundle-like structures, respectively. The maximum crystallinity values for each process, χ_{∞}^i , in (23) are obtained from calorimetric analysis and were provided earlier in Table 3.

By employing the convolution integral approach, nucleated spherulites that have grown for a longer period, i.e. those that are formed at higher temperatures, contain a higher amount of secondary crystallinity. The contributions of both the lamellar insertion and bundle-like ordering process were determined vs time and temperature from calorimetry. With the primary process described accurately, parameters for the rate functions can be determined. Typical initial values for this process could be estimated from calorimetry results. The results of applying this model are shown

in Fig. 22. The model is able to describe the multiple crystallization processes rather well, especially for conventional DSC data. Here, the onset of the lamellar insertion process starts during the fast primary space filling process. The inflection point that marks the bundle-like ordering is also captured well. Regarding the FSC experiments, good agreement is obtained in most cases. The final crystallinity level decreases with cooling rate although the final values and secondary processes are not always described accurately.

Parameters for the rate functions are given in Table 6 and both rate functions are displayed in Fig. 23. The reference temperature, $T_{\text{ref},i}$ is lower for the bundle-like process, coherent with calorimetry measurements. Clearly, this process is dominant at low temperatures, i.e. $<60^\circ\text{C}$. The maximum rate, a_i , is found to be orders of magnitude higher for the bundle-like process.

The scaling parameter, n_b in (22), provides the secondary crystallization rate with a strong dependency on the remaining crystallisable amount of amorphous material and, consequently, a_b is relatively large. Both peak functions show a strong decrease at high and low temperatures, in the vicinity of the melting and glass transition temperatures, respectively.

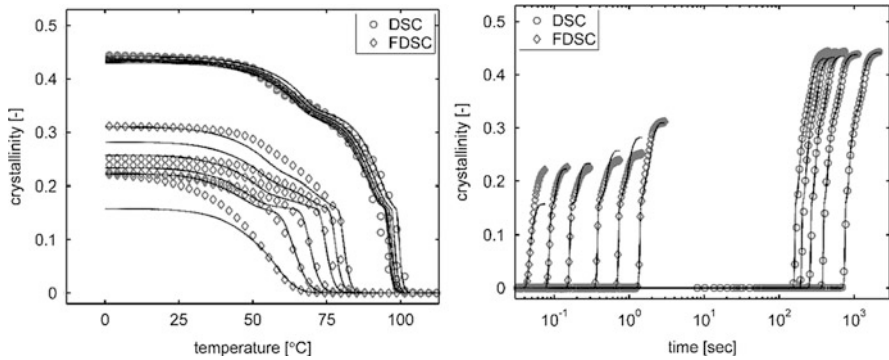
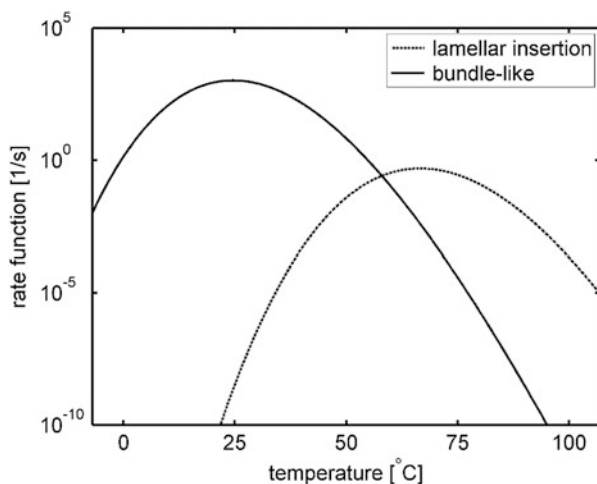


Fig. 22 Total crystallinity from calorimetry experiments vs temperature (*left*) and time (*right*). *Dashed lines* are the computed values with the model for primary and secondary crystallization. Reproduced with permission from [39]

Table 6 Constants for each secondary crystallization process in (22) and (24)

Parameter	K_l	K_b	Unit
a_i	0.485	1.034×10^3	(1/s)
b_i	963.78	817.02	(-)
$T_{\text{ref},i}$	339.6	297.6	(K)
n_i	3.32	8.45	(-)

Fig. 23 Rate function, K_i , of both secondary crystallization processes vs temperature. Reproduced with permission from [39]



4 Concluding Remarks

From the above it is clear that both the evolution of multiphase crystal structure of iPP and the multi-kinetics crystallization of LLDPE can be accurately predicted for conditions relevant for processing, using a model largely based on nucleation and growth of spherulites. In the case of iPP, the development of three different crystal phases was captured as a function of cooling rate and pressure. The kinetics of a fourth phase (the β -phase) can be found in the literature [38]. On the other hand, the description of the complex crystallization process of LLDPE requires, because of the large contribution of secondary formed crystals, two additional rate equations to describe quiescent crystallization over a timespan close to five decades. At the root of both examples lies a relatively simple yet powerful modelling framework based on the Schneider rate equations (calculated unhindered volume) and Avrami approach (real volume). However, the accuracy of the model mainly relies on the quality of the experimental input. Ongoing development of available tools and/or new devices has provided new opportunities for understanding polymer crystallization in conditions relevant to industry. This includes the infrastructure at synchrotron facilities to monitor the on-line formation of crystals under high cooling rates and the development of advanced calorimetric techniques such as fast scanning calorimetry and extended dilatometry. The authors strongly believe that, by performing the right experiments, this modelling framework is applicable to most other semi-crystalline polymer systems, such as random copolymers, high- or low-density polyethylenes or, slightly more complex, polyamides and polylactic acids. Polymer processing seldom occurs without the presence of flow and, therefore, this framework is extended to include the influence of flow in the next chapter [112].

References

1. Schrauwen BAG et al (2004) Structure, deformation, and failure of flow-oriented semicrystalline polymers. *Macromolecules* 37:8618–8633
2. Galeski A (2003) Strength and toughness of crystalline polymer systems. *Prog Polym Sci* 28:1643–1699
3. De Rosa C et al (2004) Structure–property correlations in polypropylene from metallocene catalysts: stereodeficient, regioregular isotactic polypropylene. *J Am Chem Soc* 126:17040–17049
4. De Rosa C, Auriemma F (2006) Structure and physical properties of syndiotactic polypropylene: a highly crystalline thermoplastic elastomer. *Prog Polym Sci* 31:145–237
5. Custódio FJMF, Steenbakkens RJA, Anderson PD, Peters GWM, Meijer HEH (2009) Model development and validation of crystallization behavior in injection molding prototype flows. *Macromol Theory Simul* 18:469–494
6. Roozmond PC, van Drongelen M, Ma Z, Hulsen MA, Peters GWM (2015) Modeling flow-induced crystallization in isotactic polypropylene at high shear rates. *J Rheol N Y* 59:613–642
7. Doufas AK (2014) A microstructural flow-induced crystallization model for film blowing: validation with experimental data. *Rheol Acta* 53:269–293
8. Guo X, Isayev AI, Guo L (1999) Crystallinity and microstructure in injection moldings of isotactic polypropylenes. Part 1: a new approach to modelling and model parameters. *Polym Eng Sci* 39:2096–2114
9. Keller A (1957) A note on single crystals in polymers: evidence for a folded chain configuration. *Philos Mag* 2:1171–1175
10. Mandelkern L (1964) *Crystallization of polymers*. McGraw-Hill, New York
11. Armitstead K, Goldbeck-Wood G (1992) *Polymer crystallization theories*. Springer, Berlin, pp 219–312
12. Varga J, Eder G, Janeschitz-Kriegl H (1997) *Materials science and technology*. In: Meijer HEH (ed) vol 18. Wiley VCH, New York, pp 57–115
13. Strobl G (2006) Crystallization and melting of bulk polymers: new observations, conclusions and a thermodynamic scheme. *Prog Polym Sci* 31:398–442
14. Ziabicki A, Alfonso GC (1994) Memory effects in isothermal crystallization. 1. Theory. *Colloid Polym Sci* 272:1027–1042
15. Alfonso GC, Ziabicki A (1995) Memory effects in isothermal crystallization II. Isotactic polypropylene. *Colloid Polym Sci* 273:317–323
16. Janeschitz-Kriegl H, Eder G, Stadlbauer M, Ratajski E (2005) A thermodynamic frame for the kinetics of polymer crystallization under processing conditions. *Monatshefte fur Chem* 136:1119–1137
17. Housmans J-W, Steenbakkens RJA, Roozmond PC, Peters GWM, Meijer HEH (2009) Saturation of pointlike nuclei and the transition to oriented structures in flow-induced crystallization of isotactic polypropylene. *Macromolecules* 42:5728–5740
18. Menyhard A, Varga J, Molnar G (2006) Comparison of different β -nucleators for isotactic polypropylene, characterisation by DSC and temperature-modulated DSC (TMDSC) measurements. *J Therm Anal Calorim* 83:625–630
19. Menyhard A, Dora G, Horvath Z, Faludi G, Varga J (2012) Kinetics of competitive crystallization of β - and α -modifications in β -nucleated iPP studied by isothermal stepwise crystallization technique. *J Therm Anal Calorim* 108:613–620
20. D’Haese M, Van Puyvelde P, Langouche F (2010) Effect of particles on the flow-induced crystallization of polypropylene at processing speeds. *Macromolecules* 43:2933–2941
21. Avrami M (1939) Kinetics of phase change. I. General theory. *J Chem Phys* 7:1103–1112
22. Avrami M (1940) Kinetics of phase change. II – Transformation-time relations for random distribution of nuclei. *J Chem Phys* 8:212–224

23. Kolmogoroff AN (1937) K statisticheskoi teorii kristallizacii metallov. *Isvest Akad Nauk SSSR Ser Math* 1:335–339
24. Nakamura K, Katayama K, Amano T (1973) Some aspects of nonisothermal crystallization in polymers. II. Consideration of the isokinetic condition. *J Appl Polym Sci* 17:1031–1041
25. La Carrubba V, Brucato V, Piccarolo S (2002) Phenomenological approach to compare the crystallization kinetics of isotactic polypropylene and polyamide-6 under pressure. *J Polym Sci Part B Polym Phys* 40:153–175
26. La Carrubba V, Piccarolo S, Brucato V (2007) Crystallization kinetics of iPP: influence of operating conditions and molecular parameters. *J Appl Polym Sci* 104:1358–1367
27. Pantani R, Coccorullo I, Speranza V, Titomanlio G (2007) Morphology evolution during injection molding: effect of packing pressure. *Polymer* 48:2778–2790
28. Lamberti G (2011) Isotactic polypropylene crystallization: analysis and modeling. *Eur Polym J* 47:1097–1112
29. Derakhshandeh M, Mozaffari G, Doufas AK, Hatzikiriakos SG (2014) Quiescent crystallization of polypropylene: experiments and modeling. *J Polym Sci Part B Polym Phys* 52:1259–1275
30. Menyhárd A, Bredács M, Simon G, Horváth Z (2015) Determination of nucleus density in semicrystalline polymers from nonisothermal crystallization curves. *Macromolecules* 150409160303008. doi:10.1021/acs.macromol.5b00275
31. Boyer SAE, Robinson P, Ganet P, Melis J-P, Haudin J-M (2012) Crystallization of polypropylene at high cooling rates: microscopic and calorimetric studies. *J Appl Polym Sci* 125:4219–4232
32. Patel RM (2012) Crystallization kinetics modeling of high density and linear low density polyethylene resins. *J Appl Polym Sci* 124:1542–1552
33. Tavichai O, Feng L, Kamal MR (2006) Crystalline spherulitic growth kinetics during shear for linear low-density polyethylene. *Polym Eng Sci* 46:1468–1475
34. Zachmann HG, Stuart HA (1960) Schmelz- und Kristallisationserscheinungen bei makromolekularen Substanzen. *Die Makromol Chemie* 41:131–147
35. Hillier IH (1965) Modified {Avrami} equation for the bulk crystallization kinetics spherulitic polymers. *J Polym Sci Part A Polym Chem* 3:3067–3078
36. Perez-Cardenas FC, Del Castillo LF, Vera-Graziano R (1991) Modified Avrami expression for polymer crystallization kinetics. *J Appl Polym Sci* 43:779–782
37. Hinrichs V, Kalinka G, Hinrichsen G (1996) An Avrami-based model for the description of the secondary crystallization of polymers. *J Macromol Sci B* 35:295–302
38. Van Drongelen M, Van Erp TB, Peters GWM (2012) Quantification of non-isothermal, multi-phase crystallization of isotactic polypropylene: the influence of cooling rate and pressure. *Polymer* 53:4758–4769
39. Van Drongelen M, Roozmond PC, Troisi EM, Doufas AK, Peters GWM (2015) Characterization of the primary and secondary crystallization kinetics of a linear low-density polyethylene in quiescent- and flow conditions. *Polymer* 76:254–270
40. Brückner S, Meille SV, Petraccone VP, Pirozzi B (1991) Polymorphism in isotactic polypropylene. *Prog Polym Sci* 16:361–404
41. Lovinger AJ, Chua JO, Gryte CC (1976) An apparatus for in situ microscopy of zone solidifying polymers. *J Phys E* 9:927–929
42. Morrow DR, Newman BA (1968) Crystallization of low-molecular-weight polypropylene fractions. *J Appl Phys* 39:4944–4950
43. Somani RH et al (2001) Structure development during shear flow induced crystallization of iPP: in situ wide-angle X-ray diffraction study. *Macromolecules* 34:5902–5909
44. Mezghani K, Phillips PJ (1997) The γ -phase of high molecular weight isotactic polypropylene. II: the morphology of the γ -form crystallized at 200 MPa. *Polymer* 38:5725–5733
45. Mezghani K, Phillips PJ (1998) The γ -phase of high molecular weight isotactic polypropylene. III: the equilibrium melting point and the phase diagram. *Polymer* 39:3735–3744

46. Angeloz C et al (2000) Crystallization of isotactic polypropylene under high pressure (γ -phase). *Macromolecules* 33:4138–4145
47. Foresta T, Piccarolo S, Goldbeck-Wood G (2001) Competition between α and γ phases in isotactic polypropylene: effects of ethylene content and nucleating agents at different cooling rates. *Polymer* 42:1167–1176
48. Hosier IL, Alamo RG, Estes P, Isasi JR, Mandelkern L (2003) Formation of the α and γ polymorphs in random metallocene-propylene copolymers. Effect of concentration and type of comonomer. *Macromolecules* 36:5623–5636
49. Cavallo D et al (2010) Real-time WAXD detection of mesophase development during quenching of propene/ethylene copolymers. *Macromolecules* 43:10208–10212
50. Androsch R, Di Lorenzo ML, Schick C, Wunderlich B (2010) Mesophases in polyethylene, polypropylene, and poly(1-butene). *Polymer* 51:4639–4662
51. Eder G, Hierzenberger P, Amorim P (2010) Pressure effects on polymer crystal nucleation. In: Workshop on polymer crystallization under conditions relevant to processing, Genova, Italy
52. Ito H (1997) Modelling and numerical simulation of polymer crystallization in injection moulding process. In: PPS Europe meeting, Göteborg, Sweden
53. Boyer SAE, Fournier FEJ, Gandin C-A, Haudin J-M (2014) CRISTAPRESS: an optical cell for structure development in high-pressure crystallization. *Rev Sci Instrum* 85:013906
54. Lamberti G (2011) Flow-induced crystallization during isotactic polypropylene film casting. *Polym Eng Sci* 51:851–861
55. Schneider W, Koppl A, Berger J (1988) Non-isothermal crystallization. System of rate equations. *Int Polym Process* 2:151–154
56. He J, Zoller P (1994) Crystallization of polypropylene, nylon-66 and poly(ethylene terephthalate) at pressures to 200 MPa: kinetics and characterization of products. *J Polym Sci Part B Polym Phys* 32:1049–1067
57. Ito H et al (1995) Simulations of polymer crystallization under high pressure. *Colloid Polym Sci* 273:811–815
58. Gitsas A, Floudas G (2008) Pressure dependence of the glass transition in atactic and isotactic polypropylene. *Macromolecules* 41:9423–9429
59. Cavallo D et al (2010) Continuous cooling curves diagrams of propene/ethylene random copolymers. The role of ethylene counts in mesophase development. *Macromolecules* 43:2890–2896
60. Gahleitner M et al (2005) Propylene-ethylene random copolymers: comonomer effects on crystallinity and application properties. *J Appl Polym Sci* 95:1073–1081
61. Van der Beek MHE, Peters GWM, Meijer HEH (2006) Influence of shear flow on the specific volume and the crystalline morphology of isotactic polypropylene. *Macromolecules* 39:1805–1814
62. Balzano L, Rastogi S, Peters GWM (2008) Flow induced crystallization in isotactic polypropylene – 1,3 : 2,4-bis(3,4-dimethylbenzylidene)sorbitol blends: implications on morphology of shear and phase separation. *Macromolecules* 41:399–408
63. Lamberti G (2004) A direct way to determine iPP density nucleation from DSC isothermal measurements. *Polym Bull* 52:443–449
64. Housmans J-W, Gahleitner M, Peters GWM, Meijer HEH (2009) Structure–property relations in molded, nucleated isotactic polypropylene. *Polymer* 50:2304–2319
65. Mathot V et al (2011) The Flash DSC 1, a power compensation twin-type, chip-based fast scanning calorimeter (FSC): first findings on polymers. *Thermochim Acta* 522:36–45
66. Van Herwaarden S et al (2011) Design, performance and analysis of thermal lag of the UFS1 twin-calorimeter chip for fast scanning calorimetry using the Mettler-Toledo Flash DSC 1. *Thermochim Acta* 522:46–52
67. Iervolino E et al (2011) Temperature calibration and electrical characterization of the differential scanning calorimeter chip UFS1 for the Mettler-Toledo Flash DSC 1. *Thermochim Acta* 522:46–52
68. De Santis F, Adamovsky SA, Titomanlio G, Schick C (2007) Isothermal nanocalorimetry of isotactic polypropylene. *Macromolecules* 40:9026–9031

69. Silvestre C, Cimmino S, Duraccio D, Schick C (2007) Isothermal crystallization of isotactic poly(propylene) studied by superfast calorimetry. *Macromol Rapid Commun* 28:875–881
70. Mileva D, Androsch R, Zhuravlev E, Schick C, Wunderlich B (2012) Homogeneous nucleation and mesophase formation in glassy isotactic polypropylene. *Polymer* 53:277–282
71. Housmans J, Balzano L, Santoro D, Peters G, Meijer H (2009) A design to study flow induced crystallization in a multipass rheometer. *Int Polym Process* 24(2):185–197
72. Balzano L et al (2010) Dynamics of fibrillar precursors of shishes as a function of stress. *J Phys Conf Ser* 14:012005–1/7
73. Ma Z, Balzano L, Portale G, Peters GWM (2013) Short-term flow induced crystallization in isotactic polypropylene: how short is short? *Macromolecules* 46:9249–9258
74. Van der Beek MHE, Peters GWM, Meijer HEH (2005) The influence of cooling rate on the specific volume of isotactic poly(propylene) at elevated pressures. *Macromol Mater Eng* 290:443–455
75. Brückner S, Phillips PJ, Mezghani K, Meille SV (1997) On the crystallization of γ -isotactic polypropylene: a high pressure study. *Macromol Rapid Commun* 18:1–7
76. Alamo RG, Ghosal A, Chatterjee J, Thompson KL (2005) Linear growth rates of random propylene ethylene copolymers. The changeover from γ dominated growth to mixed ($\alpha+\gamma$) polymorphic growth. *Polymer* 46:8774–8789
77. Van der Beek MHE, Peters GWM, Meijer HEH (2005) A dilatometer to measure the influence of cooling rate and melt shearing on specific volume. *Int Polym Process* 20:111–120
78. Forstner R, Peters GWM, Meijer HEH (2009) A novel dilatometer for PVT measurements of polymers at high cooling – and shear rates. *Int Polym Process* 24:114–121
79. Forstner R, Peters GWM, Rendina C, Housmans J-W, Meijer HEH (2009) Volumetric rheology of polymers: the influence of shear flow, cooling rate, and pressure on the specific volume of iPP and P/E random copolymers. *J Therm Anal Calorim* 98:683–691
80. Zhang L, Van Drongelen M, Alfonso GC, Peters GWM (2015) The effect of pressure pulses on isotactic polypropylene crystallization. *Eur Polym J* 71:185–195
81. Bassett DC, Hodge AM (1981) On the morphology of melt-crystallized polyethylene I. Lamellar profiles. *Proc R Soc A Math Phys Eng Sci* 377:25–37
82. Bassett DC, Hodge AM, Olley RH (1981) On the morphology of melt-crystallized polyethylene II. Lamellae and their crystallization conditions. *Proc R Soc A Math Phys Eng Sci* 377:39–60
83. Bassett DC, Hodge AM (1981) On the morphology of melt-crystallized polyethylene. III. Spherulitic organization. *Proc R Soc A Math Phys Eng Sci* 377:61–71
84. Piccarolo S (1992) Morphological changes in isotactic polypropylene as a function of cooling rate. *J Macromol Sci* 31:501–511
85. Kolb R, Wutz C, Stribeck N, Von Krosigk G, Riekkel C (2001) Investigation of secondary crystallization of polymers by means of microbeam X-ray scattering. *Polymer* 42:5257–5266
86. Akpalu Y et al (1999) Structure development during crystallization of homogeneous copolymers of ethene and 1-octene: time resolved synchrotron X-ray and SALS measurements. *Macromolecules* 32:765–770
87. Alizadeh A et al (1999) Influence of structural and topological constraints on the crystallization and melting behavior of polymers. I. Ethylene/1-octene copolymers. *Macromolecules* 32:6221–6235
88. Vanden Eynde S, Mathot VBF, Koch MHJ, Reynaers H (2000) Thermal behaviour and morphology of homogeneous ethylene-1-octene copolymers with high comonomer contents. *Polymer* 41:4889–4900
89. Wilfong DL, Knight GW (1990) Crystallization mechanisms for LLDPE and its fractions. *J Polym Sci Part B Polym Phys* 28:861–870
90. Jokela K et al (2001) Scattering, and wide-angle X-ray scattering on homogeneous and heterogeneous ethylene- α -copolymers. *J Polym Sci Part B Polym Phys* 39:1860–1875
91. Rabiej S (2005) The influence of side branches on the structure of crystalline phase in ethylene-1-alkene copolymers. *Eur Polym J* 41:393–402

92. Tarasova E, Poltina T, Krumme A, Lehtinen A, Viikna A (2009) Study of very low temperature crystallization process in ethylene/alpha-olefin copolymers. *Macromol Symp* 282:175–184
93. Hoffman JD, Miller RL (1997) Kinetic of crystallization from the melt and chain folding in polyethylene fractions revisited: theory and experiment. *Polymer* 38:3151–3212
94. Mamun A, Chen X, Alamo RG (2014) Interplay between a strong memory effect of crystallization and liquid-liquid phase separation in melts of broadly distributed ethylene-1-alkene copolymers. *Macromolecules* 47:7958–7970
95. Mathot VBF, Pijpers MFJ (1983) Heat capacity, enthalpy and crystallinity for a linear polyethylene obtained by (DSC). *J Therm Anal Calorim* 28:349–358
96. Mathot VBF (1984) Temperature dependence of some thermodynamic functions for amorphous and semi-crystalline polymers. *Polymer* 25:579–599
97. Goderis B, Reynaers H, Koch MHJ (2002) Primary and secondary crystallization in a homogeneous ethylene-1-octene copolymer: crystallinity heterogeneity studied by SAXS. *Macromolecules* 35:5840–5853
98. Søndergaard K, Minà P, Piccarolo S (1997) Wide-range cooling characteristics of a selected isotactic polypropylene. *J Macromol Sci Part B Phys* 36:733–747
99. Bernland KM (2010) Nucleating and clarifying polymers. *Polymer*. doi:[10.3929/ethz-a-006371353](https://doi.org/10.3929/ethz-a-006371353)
100. Acierno S, van Puyvelde P (2005) Effect of short chain branching upon the crystallization of model polyamides-11. *Polymer* 46:10331–10338
101. Debye P, Bueche AM (1949) Scattering by an inhomogeneous solid. *J Appl Phys* 20:518–525
102. Stein RS, Rhodes MB (1960) Photographic light scattering by polyethylene films. *J Appl Phys* 31:1873–1884
103. Clough SB, Stein RS, Picot C (1971) Low-angle light-scattering equations for polymer spherulites. *J Polym Sci Part A-2 Polym Phys* 9:1147–1148
104. Samuels RJ (1971) Small-angle light scattering from optically anisotropic spheres and disks. Theory and experimental verification. *J Polym Sci Part A-2 Polym Phys* 9:2165–2246
105. Samuels RJ (1974) Small-angle light scattering and crystallization processes in solid polymers films. *J Polym Sci Polym Phys Ed* 12:1417–1439
106. Haudin JM (1986) Optical properties of polymers. In: Meeten GH, Elsevier Applied Science, Essex
107. Ding Z, Spruiell JE (1996) An experimental method for studying nonisothermal crystallization of polymers at very high cooling rates. *J Polym Sci Part B Polym Phys* 34:2783–2803
108. Patki RP, Philips PJ (2008) Crystallization kinetics of linear polyethylene: the maximum in crystal growth rate-temperature dependence. *Eur Polym J* 44:534–541
109. Wagner J, Philips PJ (2001) The mechanism of crystallization of linear polyethylene, and its copolymers with octene, over a wide range of supercoolings. *Polymer* 42:8999–9013
110. Derakhshandeh M et al (2014) Quiescent and shear-induced crystallization of polypropylenes. *Rheol Acta* 53:519–535
111. Incropera FP, DeWitt DP, Bergman TL, Lavine AS (2007) Introduction to heat transfer. Wiley, New York
112. Roozmond PC, van Drongelen M, Peters GWM (2016) Modeling flow-induced crystallization. *Adv Polym Sci*. doi:[10.1007/12_2016_351](https://doi.org/10.1007/12_2016_351)

Modeling Flow-Induced Crystallization

Peter C. Roozmond, Martin van Drongelen, and Gerrit W.M. Peters

Abstract A numerical model is presented that describes all aspects of flow-induced crystallization of isotactic polypropylene at high shear rates and elevated pressures. It incorporates nonlinear viscoelasticity, including viscosity change as a result of formation of oriented fibrillar crystals (shish), compressibility, and nonisothermal process conditions caused by shear heating and heat release as a result of crystallization. In the first part of this chapter, the model is validated with experimental data obtained in a channel flow geometry. Quantitative agreement between experimental results and the numerical model is observed in terms of pressure drop, apparent crystallinity, parent/daughter ratio, Hermans' orientation, and shear layer thickness. In the second part, the focus is on flow-induced crystallization of isotactic polypropylene at elevated pressures, resulting in multiple crystal phases and morphologies. All parameters but one are fixed a priori from the first part of the chapter. One additional parameter, determining the portion of β -crystal spherulites nucleated by flow, is introduced. By doing so, an accurate description of the fraction of β -phase crystals is obtained. The model accurately captures experimental data for fractions of all crystal phases over a wide range of flow conditions (shear rates from 0 to 200 s^{-1} , pressures from 100 to 1,200 bar, shear temperatures from 130°C to 180°C). Moreover, it is shown that, for high shear rates and pressures, the measured γ -phase fractions can only be matched if γ -crystals can nucleate directly on shish.

P.C. Roozmond

Department of Mechanical Engineering, Eindhoven University of Technology, PO Box 513,
5600 MB Eindhoven, The Netherlands

DSM Ahead Materials Science Center, PO Box 18, 6160 MD Geleen, The Netherlands

M. van Drongelen and G.W.M. Peters (✉)

Department of Mechanical Engineering, Eindhoven University of Technology, PO Box 513,
5600 MB Eindhoven, The Netherlands

e-mail: g.w.m.peters@tue.nl

Keywords Compressibility • Dilatometry • Flow induced crystallization • Lamellar branching • Non-isothermal • Nonlinear viscoelasticity • Polymer Processing • Polymorphism • Polypropylene • Shish-kebab

Contents

1	Introduction	244
1.1	State of the Art	246
1.2	Scope	247
2	Experimental	248
2.1	Material	248
2.2	Extended Dilatometry	249
2.3	Slit Flow	250
3	Formation of Multiple Morphologies at High Shear Rates	252
3.1	Model	253
3.2	Results	264
3.3	Parameter Sensitivity Analysis	267
3.4	Conclusions	273
4	Formation of Multiple Crystal Phases and Morphologies	274
4.1	Crystallization Model	275
4.2	Results	282
5	Conclusions	287
	Appendix: Model Without Increase in α -Growth Rate as a Result of Orientation	288
	References	289

1 Introduction

The phenomenon known as flow-induced crystallization (FIC) has important consequences for production processes that rely on shaping semicrystalline polymers in their molten state (e.g., injection molding, blow molding, and fiber spinning). The reason is that the crystalline structure determines to a great extent the mechanical, optical, and barrier properties [1, 2]. An illustrative example is an injection-molded product of isotactic polypropylene (iPP), which is composed of layers of different microstructures and even different phases (Fig. 1). At the surface, where the material that enters the mold first comes in contact with the cold wall, a skin layer is located consisting of quenched material. In this layer, the material is cooled through the temperature window for crystallization in such a short time that crystallization is suppressed and crystallinity decreases; a mesophase may even form. Toward the center of the product, a shear layer is observed where flow effects dominate, resulting in a highly oriented crystalline structure. A model that can predict the formation of this layer is one of the main topics of this chapter. Further from the wall, we find a fine-grained layer where the effect of flow is limited to an increase in nucleation sites. The final morphology of this layer is still isotropic, but the crystallization kinetics are strongly enhanced. Crystallization in the core of the product is influenced by packing pressure, but largely unaffected by flow.

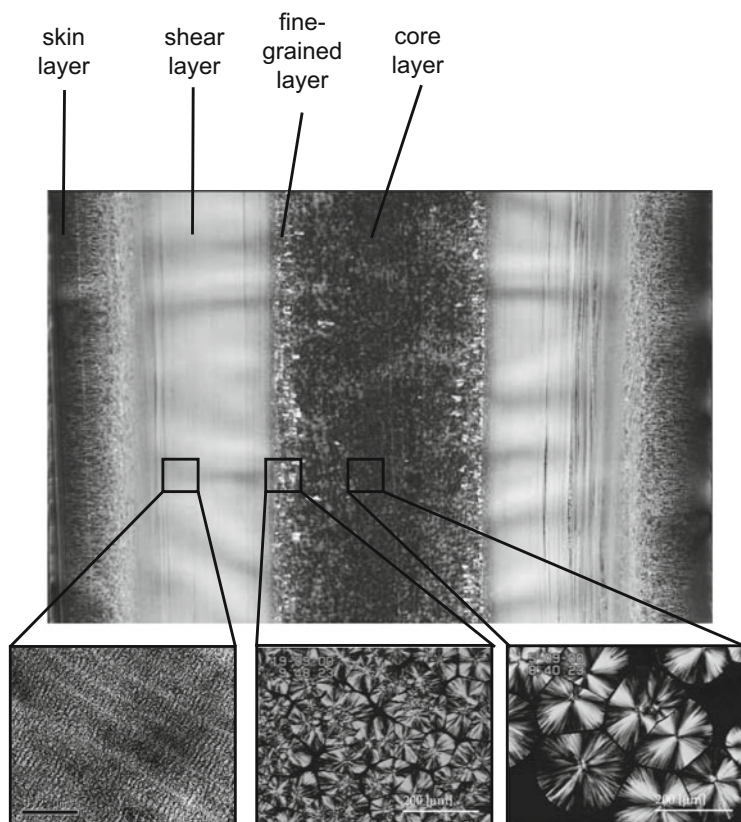
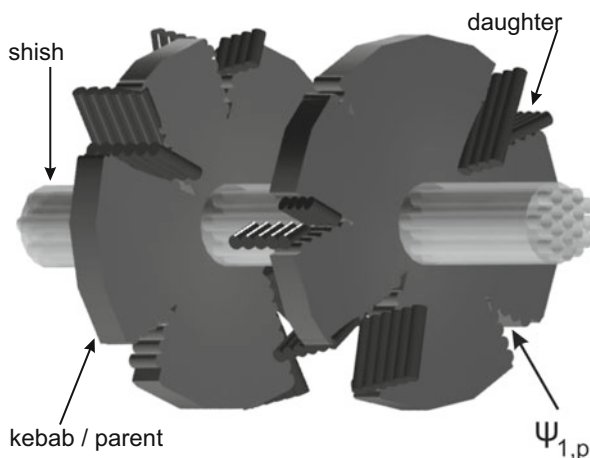


Fig. 1 Layered crystalline structure in an injection-molded product

Taking a closer look at the crystalline morphology in the shear layer, so-called shish-kebabs appear. Shish are fibrillar crystalline structures on which kebabs grow radially outward. These kebabs are also known as parent lamellae, because on their (010) lateral surface another species of lamellae, known as daughters, nucleate [3, 4]. Figure 2 depicts the three morphologies in a schematic way.

As the present work is focused on modeling the formation of multiple crystal morphologies and crystal phases, a concise overview of the various crystal phases that can be formed by iPP is given. Four different crystal phases can be present in stereoregular iPP. Most dominantly present is typically the α -phase [6], formed at atmospheric pressure and low to moderate cooling rate. Crystallization under the influence of moderately strong flow conditions or specific nucleating agents can induce the β -phase [7], whereas crystallization of the γ -phase can be achieved in several ways, such as inclusion of small amounts of 1-olefin co-units [8], introduction of stereo- and regio-irregularities controlled by a metallocene catalyst [9, 10], use of materials of very low molecular weight [11], or crystallization under elevated pressure and high temperature [12, 13]. The latter is especially relevant in the context of the present work. Additionally, the formation of stable crystalline phases

Fig. 2 Depiction of a shish with parent kebab and daughter lamellae. The surface area of a kebab on which both parent and daughter morphology can grow is denoted by $\psi_{1,p}$. Reproduced with permission of the copyright owner [5]



can be suppressed in favor of a mesomorphic phase [14, 15] at high cooling rates (>100 K/s). For completeness, we should also mention the recently discovered δ -phase (in iPP with long branches [16]) and ϵ -phase (in stereodeficient polypropylene [17]).

1.1 State of the Art

Work from the group of Janeschitz-Kriegl and coworkers can be considered as one of the milestones in the field of FIC of polymer melts. They introduced the short-term flow protocol to systematically study FIC [18], wherein a sample is subjected to a well-defined flow field for a short duration compared with the crystallization time; isothermal crystallization is monitored afterward. Because timescales for flow and crystallization are separated, this protocol isolates flow-induced structure formation. Using this protocol, flow-induced point-like nucleation (appearing for low to mild flow rates) has been thoroughly characterized, using a shear cell combined with optical microscopy, for iPP [19–28], isotactic poly(1-butene) [29–31], and poly(lactic acid) [32]. Alternatively, a rheometer can be used to apply flow and monitor subsequent crystallization in terms of rheology [32–38]. Using a model for the crystallinity dependence of rheological properties [39, 40], it is even possible to extract nucleation density from rheological data [25, 35]. The evolution of rheological properties with flow-induced structure formation may also play a complex role when strong flows are concerned; it has been observed that the amount of flow-induced structure saturates at a certain level, presumably as a result of decreasing deformation rate caused by increasing viscosity [41, 42].

For high deformation rates, the effect of flow is no longer limited to an increase in nucleation sites and can cause the appearance of oriented structures. The transition is quite sharp, and the critical flow conditions for the appearance of oriented structures has received attention from a number of authors [18, 35, 43–47].

For such experiments, a shear cell is combined with in-situ X-ray diffraction (XRD) [4, 48–53], birefringence [18, 23, 43], or light scattering [46], or examined ex-situ with microscopy [4]. The critical flow conditions are usually expressed in terms of stress [4, 44], mechanical work [35, 45], or shear rate for a fixed strain [43]. It has been shown in a number of papers that long chains play a catalytic role in the formation of shish-kebabs [23, 41, 47, 49, 54]. However, their concentration in such structures is not high compared with the rest of the material [55].

Another issue is the speed at which flow-induced structures crystallize. The well-known Kolmogorov–Avrami equation [56, 57] accurately captures the crystallization kinetics of spherulites, even when their number density is strongly increased by flow [35, 58]. However, for shish-kebab structures, in-situ XRD has revealed that the Avrami model often fails [49, 59–61].

Regarding the modeling of structure creation, most authors relate FIC to deformation on a continuum level. Most literature focuses on the case of flow-induced (point-like) nucleation. The Janeschitz-Kriegl group found scaling laws for flow-induced nucleation density as a function of mechanical work [62]. Their approach was extended by the Peters group, who coupled flow-induced nucleation rate to backbone stretch [63–66]. Because the chains on the high side of the molecular weight distribution are most likely to be stretched, this effect is dominated by the longest chains in the material [21, 29, 63, 67], that is, in a multimode viscoelastic model by the mode with the highest relaxation time(s). Based on an extension of the Schneider rate equations [68] proposed by Eder and coworkers [18, 69], Zuidema et al. proposed a model that calculates shish density (i.e., the line nucleation density for kebabs) from continuum-level deformation [63]. Their model was validated to capture accurately the shear layer thickness in a number of experiments [63, 66]. Several other authors have adapted an expression for free energy to incorporate deformation and derive nucleation rate [38, 70–76]. Crystallization rate can be calculated using these models, but no information about the final morphology is obtained. Ultimately, most of these models are of a phenomenological nature, which capture limited sets of experimental data quite well but lack predictive capabilities relevant for processing conditions. Because the final (anisotropic) properties are determined by the crystalline morphology, we have chosen to adopt the approach pioneered by the Janeschitz-Kriegl group and validate the modeling with experimental data relevant for the processing conditions. Finally, it should be noticed that some work was performed on models at a molecular level [77–80]. Although insightful, this approach is computationally too expensive for process modeling, which is the ultimate application goal for the type of modeling presented here.

1.2 Scope

The work presented in this chapter is aimed at modeling various aspects of FIC in polymer melts. The goal is to develop a predictive modeling framework that can be used to exploit fully a broad set of experimental data, which are often too complex

to yield quantitative results without an intermediate modeling step. The modeling framework developed describes various aspects of FIC, such as nucleation and growth of isotropic and oriented structures, formation of multiple crystal phases and morphologies, and the enhancement of crystal growth rate as a result of flow-induced molecular orientation. The full modeling framework can be used to research certain aspects of FIC by applying it to model experiments, or parts of the framework can be used as building blocks in a code for modeling real production (shaping) processes. Because flow-induced point-like nucleation has been extensively described in the literature, we focus here on FIC under strong flow conditions, yielding highly oriented crystal structures. We focus on experimental data obtained for iPP, but similar modeling has been successfully used to predict FIC kinetics for linear low density polyethylene (LLDPE) and poly(1-butene) [29, 81] and is now being applied to poly(lactic acid).

This chapter is divided into two parts. The first part (Sects. 2 and 3) focuses on modeling shear layer thickness and crystal orientation in a slit flow geometry, with shear rates relevant for injection molding (up to $1,000 \text{ s}^{-1}$). The second part (Sect. 4) considers conditions in which flow rate and pressure are varied independently, resulting in formation of various crystal phase compositions. The modeling framework to describe both scenarios is the same, but different parts of the framework are highlighted.

2 Experimental

The models presented in this chapter are validated with experimental data from two types of experiments. This section introduces both types.

2.1 Material

The material used in both experiments described below is an iPP homopolymer (Borealis HD601CF, $M_w = 365 \text{ kg mol}^{-1}$, $M_n = 68 \text{ kg mol}^{-1}$), also the material of choice for many other crystallization studies [35, 82]. The material contains no nucleating additives. The model used in this work calculates nucleation rate and longitudinal shish growth rate from backbone stretch on a continuum level. The former is calculated from stretch of a mode representative of the longest chains in the material and the latter from stretch of an average mode. The extended pom-pom (XPP) model [83] is used to calculate the backbone stretch, with parameters for the XPP model as given in Sect. 3. Full rheological characterization of the material and parametrization of the XPP model are presented in the literature [35, 84].

2.2 Extended Dilatometry

The experiments were performed in the Pirouette apparatus [67, 82, 85]. This extended dilatometer can be used to monitor specific volume of a material at a range of temperatures and pressures. It possesses the added ability to subject the material to shear flow in a Couette cell.

The experimental protocol is as follows: starting from the molten state, $T_m = 230^\circ\text{C}$, the material is cooled at $\sim 1^\circ\text{C/s}$ to room temperature under isobaric conditions at four different pressures ($p = 100, 500, 900, 1,200$ bar). During cooling, a shear pulse is applied with fixed duration of 1 s and varying shear rate of $\dot{\gamma} = 0, 3, 10, 30, 100, 180\text{ s}^{-1}$ at undercooling of 30°C or 60°C . The undercooling is the difference between the temperature at which the shear pulse is applied and the melting temperature, taking into account the variation in melting temperature with pressure according the Clapeyron equation [86] (Eq. 34). The melting temperature at atmospheric pressure is taken as 197°C . All experimental conditions are summarized in Table 1. The specific volume of the material is monitored and the experimental crystallization temperature defined as shown in Fig. 3. Van Erp et al. [67] determined that this point corresponds to a space filling of $\sim 10\%$.

Table 1 Overview of all experimental conditions

Pressure (bar)	Undercooling	Shear temperature	Shear rates
	$\Delta T_{\dot{\gamma}}$ ($^\circ\text{C}$)	$T_{\dot{\gamma}}$ ($^\circ\text{C}$)	$\dot{\gamma}$ (s^{-1})
100	30	167	0, 10, 30, 100, 180
500	30	179	0, 10, 30, 100, 180
900	30	190	0, 10, 30, 100, 180
1,200	30	201	0, 10, 30, 100, 180
100	60	137	0, 3, 10, 30, 100, 180
500	60	149	0, 3, 10, 30, 100, 180
900	60	161	0, 3, 10, 30, 100, 180
1,200	60	170	0, 3, 10, 30, 100, 180

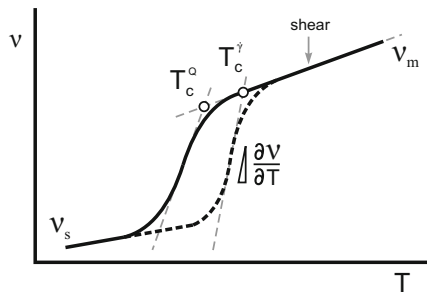


Fig. 3 Experimental protocol: *Solid line* indicates crystallization under quiescent conditions and the *dashed line* crystallization after a shear pulse. Reproduced with permission of the copyright owner [87]

The effect of flow on the crystallization kinetics is expressed by the dimensionless transition temperature Θ ,

$$\Theta = \frac{T_c^{\dot{\gamma}}}{T_c^Q}, \quad (1)$$

with T_c^Q being the crystallization temperature under quiescent conditions and $T_c^{\dot{\gamma}}$ the crystallization temperature after shear. Hence, $\Theta = 1$ if shear has no effect and increases with shear rate.

Ex-situ wide-angle X-ray diffraction (WAXD) single-shot experiments were performed on the solidified samples at the Dutch–Belgian (DUBBLE) beamline BM26 [88] of the European Synchrotron Radiation Facility (Grenoble, France) using a high-resolution Pilatus 1M detector and a wavelength of $\lambda = 1.033 \text{ \AA}$. Two-dimensional (2D) images were acquired and corrected for spatial distortion and for scattering of the empty sample cell [82]. Volume fractions of α -, β -, and γ -phases were obtained from WAXD images, as described by van Erp et al. [82].

2.3 Slit Flow

Flow was applied in a confined slit flow geometry within a modified multipass rheometer by moving two pistons, between which the material was confined, in the same direction. This setup allows simultaneous probing of rheology, via pressure transducers positioned near both pistons, and of structure development through diamond windows in the slit placed halfway between both pistons. Part of the experimental data used for validation purposes has already been presented elsewhere [61]. The reader is referred to this paper for a full description of the experimental setup. Samples remained molten at 220°C for 10 min to erase thermomechanical history. Next, the samples were cooled to a temperature of 145°C and subjected to flow at different piston speeds for different flow durations (see Table 2). The material near the pistons was kept above the melting temperature to guarantee proper functioning of the pressure transducers.

Table 2 Experimental conditions in the multipass rheometer

Piston speed [mm/s]	Flow duration [s]	$\dot{\gamma}_w$ [s^{-1}]	σ_w [MPa]
60	0.25	370	0.121
80	0.25	500	0.135
100	0.11–0.20–0.23–0.25	635	0.147
120	0.11–0.17–0.20–0.23	769	0.157
140	0.20	904	0.166

Wall shear rate $\dot{\gamma}_w$ and wall shear stress σ_w were calculated at steady state using a Carreau–Yasuda model for the shear rate dependence of the viscosity

Morphological and structural developments were evaluated during flow and during subsequent isothermal crystallization using WAXD. During and immediately after flow, 2D patterns were recorded at a frequency of 30 Hz for a total time of 2 s using a Pilatus 300 K detector. Subsequent isothermal crystallization was monitored in a higher azimuthal range ($>90^\circ$) using a Frelon detector with an acquisition time of 2.66 s per frame and a total duration of 22 min.

Crystallinity evolution was calculated from the radially integrated patterns as the ratio between the scattered intensity by crystals and the total scatter intensity. The separate crystallization kinetics of the kebab lamellae and the branching lamellae (known as daughters [89]) was determined from the Frelon detector signal. For the data collected with the Pilatus, the area of the reflection is given by the area underneath the (isotropic) baseline-subtracted scattering pattern. Regarding the patterns acquired with the Frelon detector, azimuthal scans of the (110) reflection were fitted by Lorentzian peaks, which were integrated to obtain the area of the peaks. Proper geometric corrections were applied [90]. Examples of procedures for both detectors are given in Fig. 4.

It is important to note that the crystallinity obtained in this way is an apparent crystallinity because it is an average over the slit thickness. Because the shear rate is maximal at the wall of the channel and zero in the center, crystallinity progresses faster at the walls than at the center.

Herman's orientation factor [91, 92] was applied to quantify the average level of molecular orientation in the sample thickness direction and at the location of the diamond window. The orientation factor is denoted by f_H , which is defined as

$$f_H = \frac{3\langle \cos^2\phi \rangle - 1}{2}, \quad (2)$$

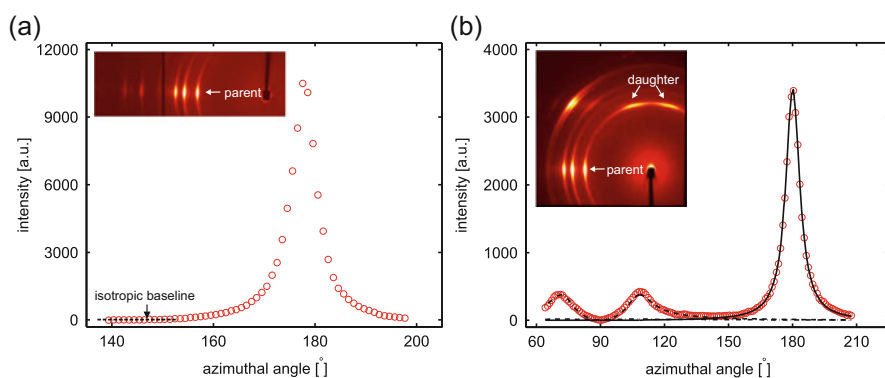


Fig. 4 Azimuthal scans of the (110) diffraction of WAXD patterns (*insets*) obtained with (a) Pilatus detector and (b) Frelon detector. Flow direction is vertical. Reproduced with permission of the copyright owner [5]

where ϕ is the angle between the crystallographic axis and a reference axis (in this case the flow direction) and $\langle \cos^2 \phi \rangle$ is the average value of the cosine squared of this angle given by

$$\langle \cos^2 \phi \rangle = \frac{\int_0^{\pi/2} I(\phi) \cos^2 \phi \sin \phi d\phi}{\int_0^{\pi/2} I(\phi) \sin \phi d\phi} \quad (3)$$

The orientation factor f_H is zero for a fully random orientation and 1.0 or -0.5 for a sample fully oriented parallel or perpendicular to the machine direction, respectively. Orientation functions for the b - and c -axes, f_b and f_c , were extracted from the baseline-subtracted (110) and (040) reflections taken from the Frelon recorded 2D WAXD patterns. Because only low levels of γ - and β crystals were detected, it is assumed that all reflected intensity originated from monoclinic α -crystals.

Defining the angles ϵ and σ between the b - and c -axes and the flow direction, and assuming rotational symmetry of all oriented structures, the orientation functions were obtained according to Eq. 2, with:

$$\langle \cos^2 \epsilon \rangle = \langle \cos^2 \phi_{040} \rangle \quad (4)$$

$$\langle \cos^2 \sigma \rangle = 1 - 0.901 \cdot \langle \cos^2 \phi_{040} \rangle - 1.099 \cdot \langle \cos^2 \phi_{110} \rangle \quad (5)$$

where $\langle \cos^2 \sigma \rangle$ was calculated using Wilchinsky's method [93].

3 Formation of Multiple Morphologies at High Shear Rates

A number of models have been developed in attempts to capture the formation of shish-kebabs and the resulting shear layer. Liedauer et al. coupled the parameter $\dot{\gamma}^4 t_s^2$, with shear rate $\dot{\gamma}$ and flow time t_s , to the density of shish [18], see also [69]. Their approach was used as a starting point for the Eindhoven group, who linked nucleation rate to deformation of the high molecular weight mode on a continuum level [21, 29, 63] and subsequent shish growth (after overcoming a critical flow criterion) to deformation of a mode corresponding to the average molecular weight [63, 64, 66]. This approach was validated in terms of shear layer thickness in both channel flow and capillary rheometer. The model was also validated as accurate in terms of crystallization kinetics in extended dilatometry experiments [67].

Recent experiments using piston-driven channel flow have revealed a strong coupling between structure formation and rheology [61, 94]. As a result of this self-regulating effect, the density of shish within the shear layer is, for strong enough flows, independent of flow conditions. The only affected parameter is the shear layer thickness.

We present a model that includes all important physical mechanisms to explain these observations. The creation rate of flow-induced nuclei is governed by stretch in the high molecular weight tail, as in previous work from the Eindhoven group. The shish growth mechanism is based on the “streamers” concept proposed by the Kornfield group [41], and shish growth rate is taken to be directly proportional to shear rate. The effects of compressibility, nonlinear viscoelasticity, nonisothermal conditions caused by shear heating, and heat release as a result of crystallization are significant and, therefore, all taken into account. It is hypothesized that shish influence the rheology in their surroundings on a scale that is much larger than their radius. The model has been extensively validated by channel flow experiments in terms of pressure drop, crystallinity, and shear layer thickness.

We attempted to extend the well-validated phenomenological model for point-like nucleation to creation of oriented structures and the accompanying viscosity increase to investigate the physics that are at play. Some of the open questions that we have tried to answer are:

- Is there a critical flow criterion that needs to be surpassed before shish appear?
- What determines shish propagation speeds?
- At what stage in the FIC process do shish noticeably start altering the viscosity of the polymer melt?
- What governs Hermans’ orientation factor, which can be related to mechanical properties [1]?

3.1 Model

The model presented in this section is solved numerically in two dimensions with an in-house finite element method (FEM) code. The material confined between the two pistons is tracked using a moving mesh. The left boundary corresponds to the driving piston (see Fig. 5). The right boundary corresponds to the material boundary near the co-moving piston. The other nodes move accordingly with a linear dependence. The arbitrary Lagrangian Eulerian (ALE) formulation [95] is employed to take the moving mesh into account. Because compressibility plays a significant role and, therefore, the motion of the left and right material boundary is different during flow start-up, there is stretching and compression of the mesh in the flow direction. The governing equations are solved sequentially per time step with semi-implicit Euler time stepping and semi-implicit formulation of the stress in the momentum balance [96]. A number of stabilization techniques were employed: discrete elastic-viscoelastic stress split (DEVSS) [97, 98], streamline-upwind Petrov–Galerkin (SUPG) [99], and log-conformation representation (LCR) [100].

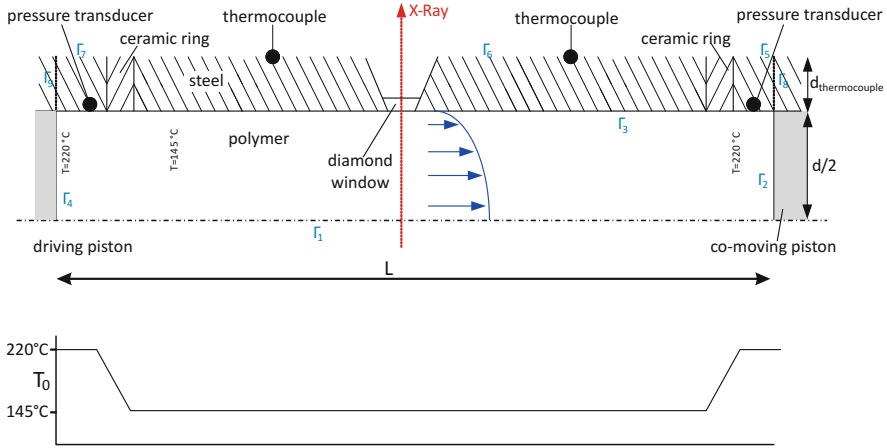


Fig. 5 Geometry of the multipass rheometer. The *graph* below indicates the initial conditions for temperature. Reproduced with permission of the copyright owner [5]

3.1.1 Geometry

Figure 5 schematically shows the domain for which the governing equations are solved, corresponding to half of the slit in which the experiments were conducted. The thickness of the slit in the velocity gradient direction is $d = 1.5$ mm and the length between the two pistons $L \approx 185$ mm. The polymer melt (area enclosed by Γ_1 and Γ_4) is confined between two pistons (area $\Gamma_1 - \Gamma_2 - \Gamma_3 - \Gamma_4$). By simultaneously moving the pistons in the same direction, the material is subjected to a Poiseuille flow. Near both pistons, pressure transducers are embedded in the steel of the barrels. The distance between the two pressure transducers is 160 mm. To avoid structure formation influencing the pressure measurements, the barrels are kept at 220°C. The barrels and the measurement geometry (kept at 145°C) are separated by ceramic rings. Thermocouples are embedded in the steel at a distance of 0.5 mm from the wall of the flow geometry. The information from these thermocouples is used for the boundary condition regarding temperature: $T = 220^\circ\text{C}$ on $\Gamma_7 - \Gamma_9 - \Gamma_4$ and $\Gamma_2 - \Gamma_8 - \Gamma_5$, and $T = 145^\circ\text{C}$ on Γ_6 .

3.1.2 Momentum Balance

The momentum balance is given by

$$\rho(p) \frac{D\mathbf{u}}{Dt} = -\nabla p + \nabla \cdot \boldsymbol{\tau} + \nabla \cdot (2\eta_s \mathbf{D}), \tag{6}$$

where \mathbf{u} is velocity and ρ is the density of the material, which depends on the pressure p according to Eq. 10. The material derivative $\frac{D\mathbf{u}}{Dt} = \left(\frac{\partial \mathbf{u}}{\partial t} + \mathbf{u} \cdot \nabla \mathbf{u} \right)$.

A viscous component with viscosity $\eta_s = 10^{-2}$ Pa s is added for numerical reasons. The deformation rate tensor is denoted by \mathbf{D} . The extra stress is given by

$$\boldsymbol{\tau} = \sum_i G_i (\mathbf{c}_i - \mathbf{1}), \quad (7)$$

where c_i is the conformation tensor of mode i , calculated with the XPP viscoelastic model [101] (see Sect. 3.1.3).

Boundary and Initial Conditions

The fluid is at rest at the start of the simulation ($t = 0$):

- $\mathbf{u} = \mathbf{0}$ for all \mathbf{x}

On the driving piston, the velocity is prescribed:

- $u_x = v_{\text{piston}}$, on Γ_1
- $u_y = 0$, on Γ_1

On the centerline we have:

- $\frac{\partial \mathbf{u}}{\partial y} = 0$, on Γ_2

and on the wall:

- $\mathbf{u} = \mathbf{0}$, on Γ_4

On the wall near the pistons, a small slip velocity is applied in the x -direction to avoid singularities at points where the pistons and the wall meet. The velocity at the wall is equal to the piston speed at the pistons and falls linearly to zero in 4 mm. At the co-moving piston, we define a zero force constraint:

- $\mathbf{F} = \mathbf{0}$, on Γ_3

Hence, the material does not stick to the co-moving piston (which would result in pressure less than 0). Instead, the material at this end of the channel has a straight, free surface. The velocity of this free surface becomes an extra unknown, which in steady state is equal to the velocity of the driving piston but increases to this steady state with a time scale governed by compressibility effects.

3.1.3 Viscoelastic Fluid Model

The rheological behavior of the material is modeled using the multimode XPP model. This model was originally developed for branched polymer melts, but was later found to also accurately describe the behavior of linear polydisperse melts [83, 101]. The conformation tensor is given by

$$\overset{\nabla}{\mathbf{c}}_i + 2 \frac{\exp \left[v_i \left(\sqrt{\text{tr } \mathbf{c}_i / 3} - 1 \right) \right]}{\lambda_{s,i}} \left(1 - \frac{3}{\text{tr } \mathbf{c}_i} \right) \mathbf{c}_i + \frac{1}{\lambda_{b,i}} \left(\frac{3\mathbf{c}_i}{\text{tr } \mathbf{c}_i} - \mathbf{I} \right) = \mathbf{0}. \quad (8)$$

Here, $\overset{\nabla}{\mathbf{c}}_i$ denotes the upper convected derivative of the conformation tensor of mode i , $\lambda_{b,i}$ denotes the relaxation time for backbone tube orientation of mode i , $\lambda_{s,i}$ denotes backbone stretch relaxation time of mode i , and the parameter v_i depends on the number of arms of the molecule q_i following $v_i = 0.1/q_i$ [83]. The Giesekus α -parameter is set to 0. The backbone stretch, used in the crystallization model to calculate nucleation density, is given by

$$\Lambda_i = \sqrt{(\text{tr } \mathbf{c}_i / 3)}. \quad (9)$$

The linear viscoelastic spectrum of the iPP used in this study, obtained from small angle oscillatory shear (SAOS) measurements, is given in Table 3 ($i = 2-7$). The stretch relaxation times (needed to calculate backbone stretch in the XPP model) are somewhat difficult to determine, as this material hardly shows strain hardening in the range of strain rates that can be probed by the usual experimental techniques [21, 84]. The relation $\lambda_{s,i} \approx \lambda_{b,i}/4$ has been observed for several other polydisperse linear polymer melts [83]. Therefore, we took $\lambda_{s,i} \approx \lambda_{b,i}/4$ and $q = 1$ for all modes, except for the mode with the longest relaxation time. For the latter, the parameters were obtained from a fit to uniaxial extensional viscosity data [84]. There is some ambiguity in the way these relaxation times are determined. However, the approach is phenomenological and some uncertainty is permitted because of the scaling parameters that link structure formation to these rheological variables. All relevant rheological parameters for the average and long modes are given in Table 3. To capture steady-state pressure drop values it was necessary to add an additional mode with low relaxation time (mode 1 in Table 3), the viscosity of which was chosen such that steady-state pressure drop values for the lowest piston speeds were in acceptable agreement with experimental values. This is justified because SAOS does not probe the material at shear rates in excess of $1,000 \text{ s}^{-1}$, even with the use of time-temperature superposition. Pressure dependence of relaxation times was not implemented. Although this effect is appreciable at relevant pressures (200 bar gives a 1.38-fold increase in relaxation times [67]),

Table 3 Linear viscoelastic spectrum at $T_{\text{ref}} = 220^\circ\text{C}$

Mode	Viscosity η_0 , i [Pa s]	Backbone tube relaxation time $\lambda_{b,i}$ [s]	Backbone stretch relaxation time $\lambda_{s,i}$ [s]	Number of arms q_i [-]
1	20.0	5×10^{-5}	2×10^{-5}	1
2	131	0.0014	3.5×10^{-4}	1
3	303	0.011	2.7×10^{-3}	1
4	480	0.060	1.5×10^{-2}	1
5	377	0.29	7.3×10^{-2}	1
6	183	1.67	0.42	1
7	46.0	11.5	2.21	12

start-up behavior is not affected because it is dominated by compressibility effects. The only significant effect would be a vertical shift in pressure drop. Hence, to obtain good agreement with experimental results, the viscosity of the shortest mode would be lower, but the overall results would not be affected. Relaxation times shift with temperature according to an Arrhenius relation, with activation energy $E_a = 40$ kJ/mol.

3.1.4 Compressibility

The compressibility of the material is taken into account by considering the polymer melt to be like an elastic solid in volume,

$$p = p_0 - K \ln J. \quad (10)$$

Here, p is pressure, p_0 initial pressure, K the compression modulus, and the Jacobian $J = \det \mathbf{F}$ with \mathbf{F} being the deformation gradient tensor between the initial (reference) configuration Ω_0 and the current configuration Ω . The Jacobian J is a measure of the change in volume. For iPP, the compressibility modulus $K = 10^9$ Pa [102, 103].

3.1.5 Heat Balance

The crystallization process, both in terms of structure formation and crystal growth, is strongly dependent on temperature. To calculate the temperature distribution, the heat balance is solved,

$$\rho_k c_{p,k} \frac{DT}{Dt} = \lambda_k \nabla^2 T + \rho_k \chi_\infty \Delta H \dot{\xi} + \boldsymbol{\sigma} : \mathbf{D}, \quad (11)$$

where subscript k denotes polymer or steel. Values of parameters are given in Table 4. The first term on the right-hand side represents heat conduction, the second

Table 4 Material parameters for the heat balance

Parameter	Symbol	Value [unit]	Reference
Density (polymer)	ρ_p	800 [kg/m ³]	[66]
Heat capacity (polymer)	$c_{p,p}$	3,157 [J/kg K]	[66]
Heat conduction coefficient (polymer)	λ_p	0.11 [W/m K]	[66]
Final crystallinity	χ_∞	65 [%]	[52]
Heat of crystallization	ΔH	207 [J/g]	[66]
Density (steel)	ρ_s	8,000 [kg/m ³]	[104]
Heat capacity (steel)	$c_{p,s}$	670 [J/kg K]	[104]
Heat conduction coefficient (steel)	λ_s	80 [W/m K]	[104]

term latent heat release as a result of crystallization (Eq. 28), and the third term shear heating, with stress calculated from the XPP model (Eq. 8). We do not take into account the changes in specific heat, thermal diffusivity, and density with temperature or during the phase transition from the molten to crystalline phase. Because most of the heat is generated by shear heating during flow, we expect these effects to be minor while all the polymer is in the molten phase. Moreover, the anisotropy of thermal diffusivity, which can be significantly increased in the direction of flow [105], is not accounted for. Because the thermal gradient in flow direction in our experiments is generally quite small and the thermal diffusivity perpendicular to flow direction is affected much less [105], we trust this is a reasonable approximation.

Boundary and Initial Conditions

The initial conditions for temperature are shown in Fig. 5. In both barrels, the temperature is 220°C with a gradient over the ceramic rings. In the flow geometry, the temperature is 145°C. For boundary conditions, we prescribe the temperature of the barrel on both pistons:

- $T = 220^\circ\text{C}$ on $\Gamma_4 - \Gamma_9$ and on $\Gamma_2 - \Gamma_8$

On the centerline, we have:

- $\frac{\partial T}{\partial y} = 0$, on Γ_2

On the horizontal line coinciding with the thermocouples in the metal part, we prescribe:

- $T = 220^\circ\text{C}$ on Γ_5, Γ_7
- $T = 145^\circ\text{C}$ on Γ_6
- The temperature varies linearly from 220°C to 145°C on the ceramic rings

3.1.6 Structure Formation

Extensive research during the past decade into the phenomenon of FIC has indicated that flow-enhanced point-like nucleation is dominated by the chains at the high end of the molecular weight distribution [21, 29, 106]. Following earlier experiences by Steenbakkers and Peters [21], Roozmond and Peters [29], Custódio et al. [66], and van Erp et al. [82], the creation rate of point-like nuclei is coupled in a phenomenological way to the momentary stretch in the high molecular weight tail of the material (corresponding to the mode having the longest relaxation time; mode 7 in Table 3) on a continuum level,

$$\frac{DN_f}{Dt} = g_n(T, p) \exp(\mu_n (\Lambda_{\text{hmw}}^2 - 1)). \tag{12}$$

Here, Λ_{hmw} is the backbone stretch calculated using the XPP constitutive model [83] and μ_n and g_n are scaling parameters, the latter of which depends on temperature and pressure following

$$g_n(T, p) = g_{n,\text{ref}} 10^{c_{n,T}(T-T_{\text{ref}}) + c_{n,p}(p-p_{\text{ref}})} \tag{13}$$

All parameters in the above equations are given in Table 5. Characterization of this model is discussed in Sect. 3.2.1.

The growth mechanism in our model (see Fig. 6) is based on the “streamers” concept proposed by the Kornfield group [41]. Shish propagate in lengthwise direction by the addition of chain segments with length ξ_{seg} . In a crude sense, the flow attaches these segments as crystals to the tip of the shish. Because deformation rates in the channel are high (possibly even more so in the surroundings of a shish [107]), we can assume that the material deforms affinely. We can then express the lengthwise propagation speed of a shish as

$$v_{\text{prop}} = \dot{\gamma} \xi_{\text{seg}}. \tag{14}$$

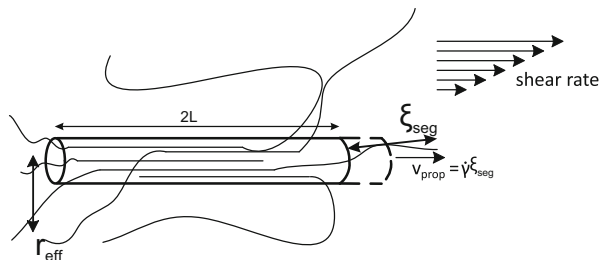
In our model, all nucleation sites grow in lengthwise direction with this mechanism. Therefore, the total line nucleation density for kebabs (i.e., the specific shish length) is given by

$$\frac{DL_{\text{tot}}}{Dt} = 2N_f \dot{\gamma} \xi_{\text{seg}}. \tag{15}$$

Table 5 Parameters for the flow-induced nucleation model at reference temperature of 166°C and reference pressure of 100 bar

Parameter	Value [unit]
$g_{n,\text{ref}}$	$10^{12} \text{ [m}^{-3} \text{ s}^{-1}\text{]}$
$c_{n,T}$	$-0.016 \text{ [}^\circ\text{C}^{-1}\text{]}$
$c_{n,p}$	$7.58 \times 10^{-4} \text{ [bar}^{-1}\text{]}$
μ_N	0.03 [-]

Fig. 6 Depiction of segment addition to a shish. Reproduced with permission of the copyright owner [5]



Note that there is no critical flow condition for the formation of shish, as was used in previous versions of FIC modeling [63]. However, for weak to mild flow conditions, no shish creation is observed because both nucleation rate \dot{N}_f and propagation rate \dot{L} are low for such flow conditions. There is no explicit dependence on molecular weight in the growth rate of shish; this comes in via the nucleation rate, which is coupled to backbone stretch in the high molecular weight tail.

It has been observed that shish strongly influence the rheology of the melt before the crystalline volume fraction reaches considerable proportions [94]. Chains protruding from the shish into the melt, so-called “hairs” [108, 109], were hypothesized to influence the rheology on a macroscopic scale. This is implemented in an empirical way. The dynamic viscosity as a function of space filling is accurately described by the simple equation [39, 110]

$$\log_{10} \left(\frac{|\eta^*|(\xi, \omega)}{|\eta^*|(\xi = 0, \omega)} \right) = \log_{10}(\mu(\omega))\xi, \quad (16)$$

where

$$\mu(\omega) = \frac{|\eta^*|(\xi = 1, \omega)}{|\eta^*|(\xi = 0, \omega)} \quad (17)$$

is the frequency-dependent ratio between the dynamic viscosity of the solidified and molten materials. Obviously, there are a number of limitations to this approach that restrict its suitability for the current conditions. First, the materials described in the literature [39, 110] crystallized in quiescent conditions, yielding spherulites,¹ whereas under the experimental conditions used here the material crystallizes in highly oriented, more elongated structures. Second, the approach was validated only for small angle oscillatory shear, whereas in this case the material is flowing with $\dot{\gamma} \approx 1000 \text{ s}^{-1}$. Therefore, the relevant material properties are not only the linear viscoelastic properties, but also the nonlinear viscoelasticity. We also expect shear-thinning behavior to be affected by this more solid-like phase [111]. Unfortunately, at the moment we are unable to formulate a more detailed model for these complex structures. The most straightforward way of implementing the proposed effect, requiring the least number of adjustable parameters, is to adjust the viscosity of the material via the modulus. Therefore, following Pogodina et al. [58], we express the moduli of the material as

$$G_i = G_{0,i} 10^{\log_{10}(\mu)^{v_{\text{eff}}}}. \quad (18)$$

¹The influence of spherulite growth on rheology has already extensively been modeled and tested [25, 39, 40].

Here, $G_{0,i}$ is the modulus of mode i in the molten state as given in Table 3, μ is the ratio between moduli of crystal and melt, typically for iPP $\mu = 10^4$ [35]. Finally, v_{eff} is the effective space filling of shish-kebabs, taking into account their hairy nature, given by

$$v_{\text{eff}} = 1 - \exp(-\pi L_{\text{tot}} r_{\text{eff}}^2). \quad (19)$$

Here, r_{eff} is the effective radius of a shish. Because of the number of uncertainties in this approach, we treat r_{eff} as an adjustable parameter. A priori, we expect r_{eff} to be about 35 nm, because shish have a typical radius of 10 nm and the average radius of gyration of this material is estimated to be 23.5 nm [112].

3.1.7 Crystallization Kinetics

As a result of the speed at which crystallization progresses under the conditions of interest, the heat released during crystallization cannot diffuse fast enough to keep the sample at constant temperature. Therefore, the temperature dependence of the crystal growth rate needs to be accounted for. The growth rate in quiescent conditions can be calculated with [113]

$$G_{\text{q}} = G_{\text{ref}} \exp(-c_G (T - T_{\text{ref}})^2), \quad (20)$$

where G_{q} is the crystal growth rate in quiescent conditions, and G_{ref} and c_G are parameters given in Table 6. The reference temperature T_{ref} depends on pressure according to the Clapeyron equation,

$$T_{\text{ref}}(p) = T_{\text{ref}}^0 + \zeta(p - p_0). \quad (21)$$

Pressure p is measured in bar, with the reference pressure p_0 being 1 bar. The pressure dependence of the melting temperature ζ is 27.5°C/kbar [86]. The reference temperature T_{ref}^0 is given at $p = 1$ bar in Table 6.

Additionally, as proposed by Roozmond et al. [89], the growth of kebabs is promoted during the flow pulse and relaxation afterward because chains are oriented in the c -axis direction of their unit cells [49, 59]. We account for this in the following way: during flow, the growth rate of parents is increased by a factor μ_{flow} .

Table 6 Material parameters for the crystallization kinetics [113]

Quantity	Symbol	Value [unit]
Maximum crystal growth rate	G_{ref}	4.5 [$\mu\text{m/s}$]
Growth rate temperature dependence	c_G	0.0023 [1/K]
Reference temperature	T_{ref}^0	363 [K]

After flow, this effect relaxes because chains relax toward their equilibrium conformation with a time scale λ_G . The growth rate of parent lamellae G_p is given by

$$G_p(t, T) = G_q(T)[1 + \mu_{\text{flow}} \exp(-t/\lambda_G)], \quad (22)$$

where μ_{flow} is the additional growth rate due to flow, λ_G is the relevant time scale for relaxation of this effect, and t is the time since cessation of flow. In the present experiments, we use the same values as found in Roozmond et al. [89], $\mu_{\text{flow}} = 4$ and $\lambda_G = 9$ s.

The chain orientation and stretch in the flow direction make crystallization in the daughter morphology less preferable. However, because growth of daughter crystals only becomes noticeable when the chains have relaxed to their equilibrium conformations, we take the growth rate for this species as always being equal to the quiescent growth rate. For isotropic spherulites, we also take the growth rate to be equal to the value in quiescent conditions,

$$G_d(T) = G_{\text{sph}}(T) = G_q(T). \quad (23)$$

To calculate crystalline volume fraction from the nucleation density, specific shish length, and crystal growth rate, two sets of coupled differential equations are used. The first set, also known as the Schneider rate equations [23, 68], describes the evolution of the number density, radius density, area density, and undisturbed volume fraction for spherulites from the measured temperature- and pressure-dependent nucleation density and crystal growth rate. These equations read:

$$\begin{aligned} \frac{D\phi_3}{Dt} &= 8\pi\dot{N} & (\phi_3 = 8\pi N), \\ \frac{D\phi_2}{Dt} &= G_{\text{sph}}\phi_3 & (\phi_2 = R_{\text{tot}}), \\ \frac{D\phi_1}{Dt} &= G_{\text{sph}}\phi_2 & (\phi_1 = S_{\text{tot}}), \\ \frac{D\phi_0}{Dt} &= G_{\text{sph}}\phi_1 & (\phi_0 = V_{\text{tot}}), \end{aligned} \quad (24)$$

where G_{sph} is the crystal growth rate as determined from Eq. 20. The flow-induced nucleation rate $\frac{DN_f}{Dt}$ is given by Eq. 12. For the kebabs growing on shish (parents) we have:

$$\begin{aligned} \frac{D\psi_{2,p}}{Dt} &= 4\pi\dot{L}_{\text{tot}}, \\ \frac{D\psi_{1,p}}{Dt} &= G_p\psi_{2,p}, \\ \frac{D\psi_{0,p}}{Dt} &= G_p f_p \psi_{1,p}. \end{aligned} \quad (25)$$

Here, L_{tot} denotes the specific shish length given by Eq. 15, G_p is the crystal growth rate of parent species, and $\psi_{2,p}$, $\psi_{1,p}$, and $\psi_{0,p}$ are measures for the shish length per unit volume, the surface area of kebabs, and undisturbed volume of kebabs, respectively. The volume fraction of the shish is neglected because it is very small compared with the total volume of shish-kebabs; the radius of a shish is about 10 nm [108], whereas the radius of a shish-kebab grows to about 100 nm (cf. Roozmond et al. [94], Seki et al. [114]).

Following the model proposed by Roozmond et al. [89], daughter lamellae nucleate on the surface of the parents,

$$\frac{D\psi_{0,d}}{Dt} = G_d f_d \psi_{1,p}, \quad (26)$$

where $\psi_{0,d}$ is the undisturbed volume fraction of daughters. The surface area of parent crystals, $\psi_{1,p}$, is obtained from Eq. 25. This area acts as the nucleation site for both parents and daughters, and is allocated to either parent or daughter morphology based on their momentary growth rates [113]:

$$\begin{aligned} f_p &= \frac{G_p}{G_p + G_d} \\ f_d &= \frac{G_d}{G_p + G_d} = 1 - f_p. \end{aligned} \quad (27)$$

Here too it is important that the crystallization of parent crystals is promoted during flow; when the crystal growth rate of parents is increased with respect to the quiescent value, more surface of the kebabs is assigned to nucleate parent crystals.

To correct for impingement, we use the Kolmogorov–Avrami equation [56],

$$\xi = 1 - \exp(-\phi_0 - \psi_{0,p} - \psi_{0,d}), \quad (28)$$

where ξ is the crystalline volume fraction or space filling. From Eq. 28, it follows that the respective crystallization rates of spherulites, parents, and daughters are given by

$$\begin{aligned} \dot{\xi}_{\text{sph}} &= (1 - \xi)\dot{\phi}_0 \\ \dot{\xi}_p &= (1 - \xi)\dot{\psi}_{0,p} \\ \dot{\xi}_d &= (1 - \xi)\dot{\psi}_{0,d}. \end{aligned} \quad (29)$$

When crystallization is complete, the total space filling $\xi = \xi_{\text{sph}} + \xi_p + \xi_d = 1$. By looking at the individual contributions from the different morphologies, we can quantify the final crystalline structure in terms of morphological composition.

3.2 Results

3.2.1 Parameter Characterization for Point-Like Nucleation

Parameters for the FIC model were characterized using the experimental data from extended dilatometry, as described in Sect. 2.2. Van Erp et al. determined the critical shear rate for appearance of oriented crystalline structures using SAXS [67, 82]. Generally, the morphology was isotropic for shear rates up to 100 and 30 s^{-1} for undercoolings of 30°C and 60°C , respectively. In this section we use only the experiments that yielded exclusively isotropic structures to find the parameters for our flow-induced nucleation model. This model calculates nucleation rate from the backbone stretch of a high molecular weight mode:

$$\dot{N}_f = g_n(T, p) \exp(\mu_n (\Lambda_{\text{hmw}}^2 - 1)) \quad (30)$$

where the pressure and temperature dependence of g_n is given by Eq. 13. Hence, we need to determine four parameters to fully characterize flow-induced nucleation: μ_n , $g_{n,\text{ref}}$, $c_{n,T}$, and $c_{n,p}$. To achieve this, the fitting is performed in three steps:

1. μ_n and $g_{n,\text{ref}}$ are determined from experiments with $\Delta T_{\dot{\gamma}} = 30^\circ\text{C}$ and $p = 100$ bar
2. $c_{n,T}$ is determined from experiments with $\Delta T_{\dot{\gamma}} = 60^\circ\text{C}$ and $p = 100$ bar
3. $c_{n,p}$ is determined from experiments with $\Delta T_{\dot{\gamma}} = 30, 60^\circ\text{C}$ and $p = 500, 900, \text{ and } 1,200$ bar

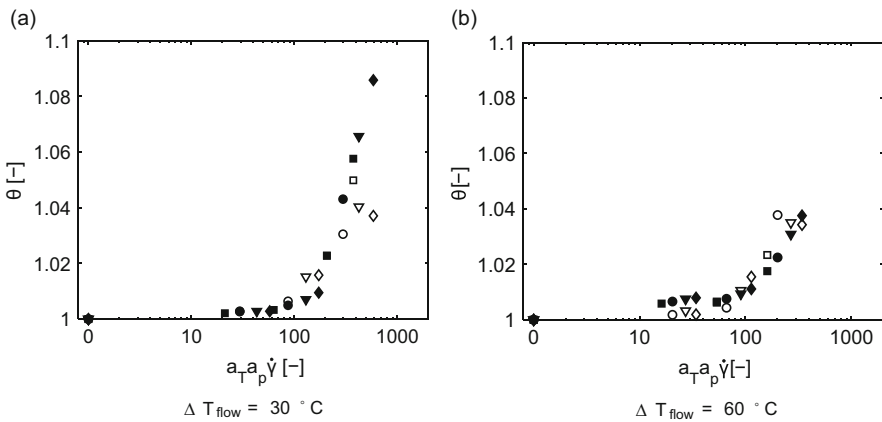


Fig. 7 Dimensionless crystallization temperature versus shear rate corrected for temperature and pressure for (a) undercooling of 30°C (e.g., $T_{\text{shear}} = 167^\circ\text{C}$ at 100 bar) and (b) undercooling of 60°C (e.g., $T_{\text{shear}} = 137^\circ\text{C}$ at 100 bar). *Open symbols* show measurements, *closed symbols* show calculations. Reproduced with permission of the copyright owner [5]

The resulting parameters are given in Table 5. Calculations using these parameters are compared with experimental data in Fig. 7. The experimental data and calculations show good agreement, indicating that, for these conditions, the presented model gives an accurate representation of flow-induced nucleation.

3.2.2 Compressibility Effects

It is important to realize that, in such extreme conditions, compressibility of the polymer melt plays an important role in start-up behavior. This is illustrated in Fig. 8, where simulations and experiments are compared, with the only difference being that in the results depicted in the left-hand figure the material is incompressible, and compressibility is switched on for the results shown in the right-hand figure. Clearly, the dominant time scale for flow start-up is the compressibility, as was also observed by, for example, Hatzikiriakos and Dealy [115]. The upturn in the measured pressure drop for higher flow rates is caused by structure formation, which was turned off in these simulations.

3.2.3 Interplay Between Structure Formation and Rheology

Figure 9 demonstrates in detail the evolution of several quantities during flow with a piston speed of 100 mm/s for 0.20 s. The flow start-up behavior is demonstrated most clearly in the columns showing velocity and pressure. The temperature (not shown in the metal part) clearly shows strong shear heating effects and increases by as much as 5°C.

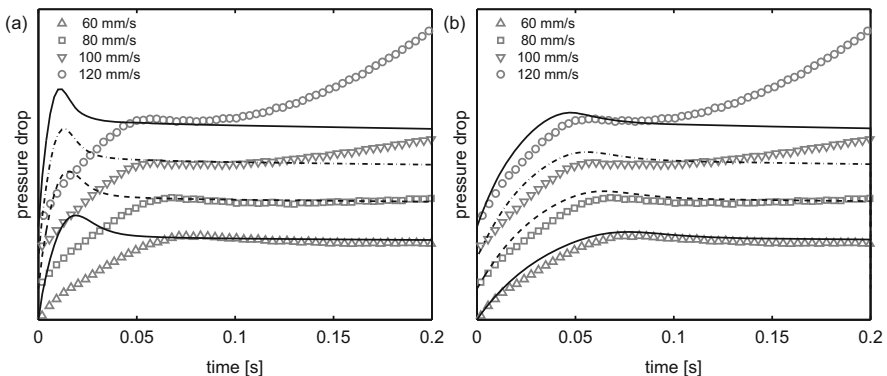


Fig. 8 Time evolution of pressure drop over the slit. *Symbols* show measurements, *lines* show simulations for the iPP used in this study, which is taken to be (a) incompressible or (b) compressible. Signals are shifted in vertical direction for clarity. Reproduced with permission of the copyright owner [5]

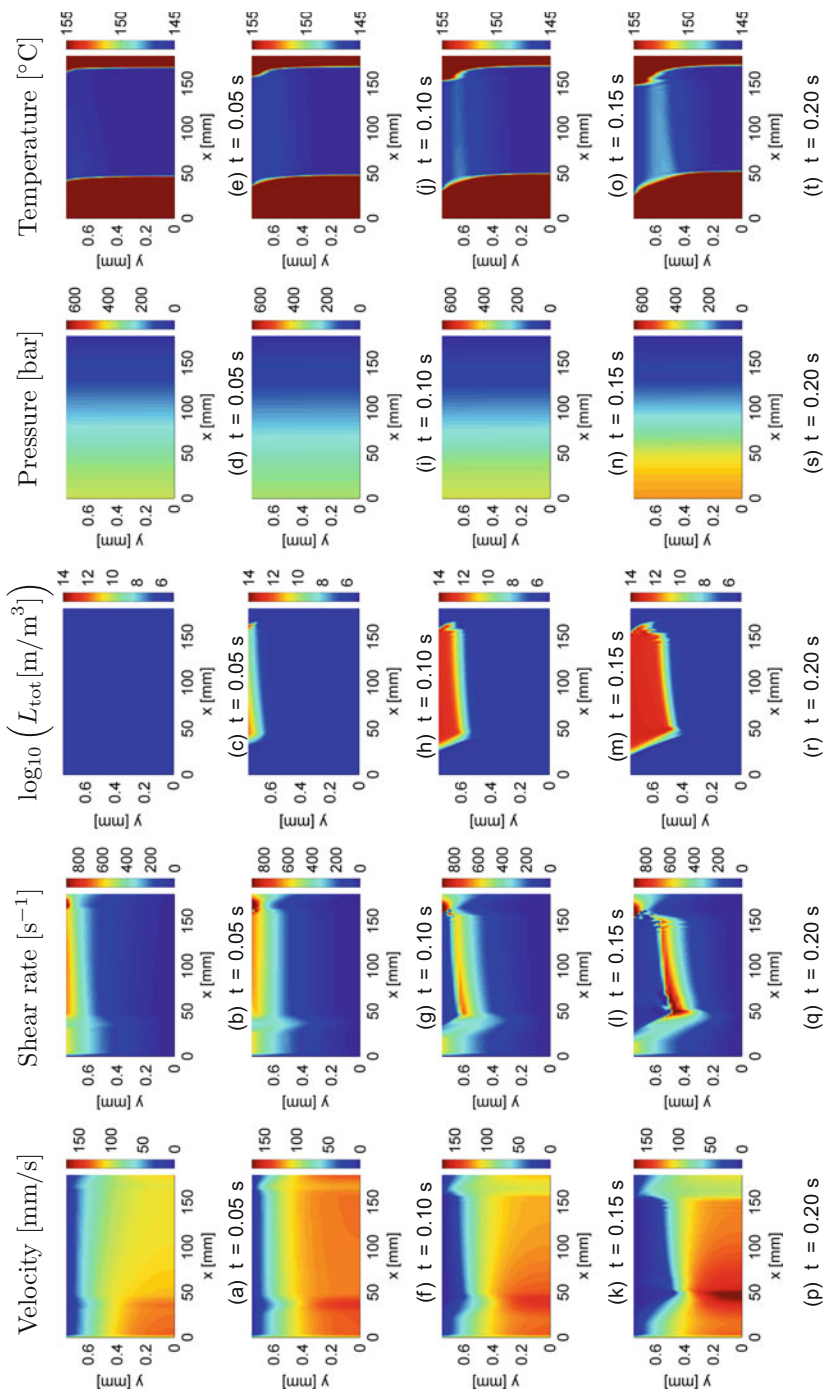


Fig. 9 From *left to right*: velocity, shear rate, specific shish length, pressure, and temperature during flow at 100 mm/s. Time increases from *top to bottom*. The *center line* is located at $y = 0$ mm, the wall is at $y = 0.75$ mm. Flow direction is from *left to right*. The driving piston is at $x = 0$ mm and the co-moving piston is at $x \approx 185$ mm. Parameters are $r_{eff} = 50$ nm and $\xi_{seg} = 5$ nm. Note that to improve readability, the y -scale has been magnified more than the x -scale

The specific shish length is also presented in Fig. 9 (middle column). From 0.10 s, a significant part of the channel is filled with a large amount of shish (inter-shish distance of roughly 100 nm). As a result, the viscosity of the material in this region is increased, giving rise to a lower velocity, higher overall pressure drop, and a high shear rate region where shish formation takes place and that propagates from the wall toward the center.

3.3 Parameter Sensitivity Analysis

Figure 10 presents simulation results for a flow condition of 100 mm/s for 0.20 s, with varying segment length ξ_{seg} . The radius at which shish influence the rheology r_{eff} was kept constant at 50 nm. The segment length has only a minor influence on the results. Notably, the specific shish length within the shear layer is hardly

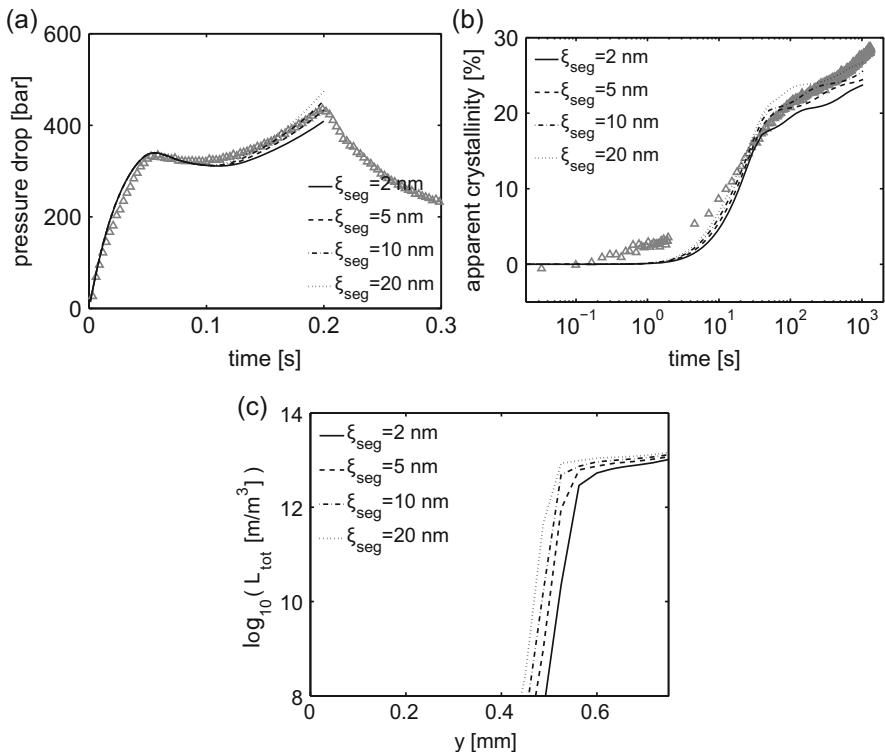


Fig. 10 (a) Pressure drop, (b) apparent crystallinity, and (c) shish length density at the window, for varying ξ_{seg} . The radius at which shish affect the rheology is kept constant at $r_{eff} = 50$ nm. Symbols show experimental data, lines show results from simulations. Reproduced with permission of the copyright owner [5]

affected by the segment length. The main effect of varying ξ_{seg} is an increase in shear layer thickness; because shish grow at higher speeds, the modulus increases faster, causing faster propagation of the shear layer.

The specific shish length within the shear layer and the crystallization kinetics are dominated by the effective radius of shish. This is demonstrated in Fig. 11, where the radius at which shish affect rheology r_{eff} was varied. For low r_{eff} , shish only start affecting rheology at a high density, resulting in a small shear layer with high nucleation density and fast crystallization kinetics. The apparent crystallinity, however, is quite low because the shear layer is thin. For high r_{eff} , the modulus of the melt is already increased significantly for shish that are spaced far apart (i.e., low L_{tot}), causing fast propagation of the shear layer front but low total shish density within the layer.

From Figs. 10 and 11, we conclude that good agreement with experiments is obtained for the parameter set $\xi_{\text{seg}} = 5$ nm and $r_{\text{eff}} = 50$ nm. The segment length, being of the order of nanometers, attains a sensible magnitude. The same goes for the radius at which shish influence the velocity, being of the order of the radius of

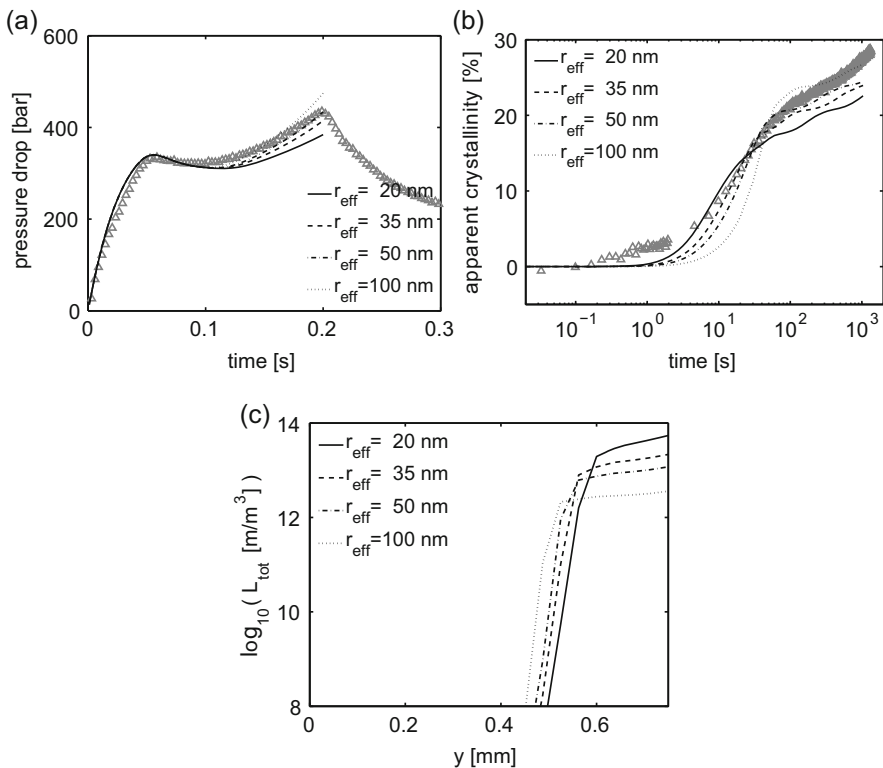


Fig. 11 (a) Pressure drop, (b) apparent crystallinity, and (c) shish length density at the window, for varying r_{eff} . The segment length is kept constant at $\xi_{\text{seg}} = 5$ nm. Symbols show experimental data, lines show results from simulations. Reproduced with permission of the copyright owner [5]

gyration (shish radius of 10 nm plus the average radius of gyration of 23.5 nm for this material [112] gives 33.5 nm).

However, it must be noted that no conclusions should be made concerning the exact values of these parameters; the model is a very crude representation of what might be the actual physics taking place. The flow field around a shish is probably strongly distorted [107], so the macroscopic shear rate might be increased. Moreover, the approach for calculation of the effect of shish on rheology (Eq. 18) does not take into account the influence of shish on the nonlinear viscoelastic properties. Most probably, shish not only increase the modulus, but also significantly decrease shear thinning behavior (similar to glass fibers, cf. Moigne et al. [111]). Therefore, the relation used might underpredict the effect that shish have on viscosity at these high shear rates. A more detailed model for the effect of shish-like structures on nonlinear viscoelastic properties, possibly based on numerical calculations, is highly desirable. A possible direction for such a model has been proposed by Steenbakkers and Peters [39].

3.3.1 Validation with Experimental Results

The results described in the previous section show that good agreement with experiments at a flow condition of 100 mm/s for 0.2 s are obtained for the two adjustable parameters $r_{\text{eff}} = 50$ nm and $\xi_{\text{seg}} = 5$ nm. Using this parameter set, we performed simulations for additional flow conditions. Comparison between experiments and simulations are presented in Fig. 12. Simulations capture the experimental data quite accurately, both in terms of pressure drop (Fig. 12a) and apparent crystallinity (Fig. 12b). Note that for the fastest piston speed (140 mm/s), we only show the calculated pressure drop up to 0.165 s. The reason for this is explained in Sect. 3.3.2. One clear discrepancy concerns the crystallization during flow; our

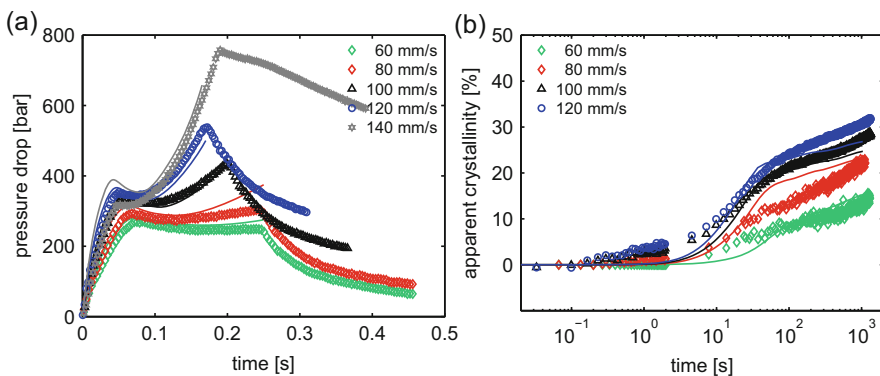


Fig. 12 Comparison between experiments (*symbols*) and simulations (*lines*) for five flow conditions: 60, 80, 100, 120, and 140 mm/s. Flow times are 0.25, 0.25, 0.2, 0.17, and 0.20 s, respectively. (a) Pressure drop, (b) apparent crystallinity. Reproduced with permission of the copyright owner [5]

simulations clearly underpredict the early evolution of crystallinity, indicating that the initial growth of shish-kebabs is much faster than in our model. A possible explanation is that chains protruding from the shish into the melt have an enhanced crystallization rate, an effect that is not accounted for in the current model.

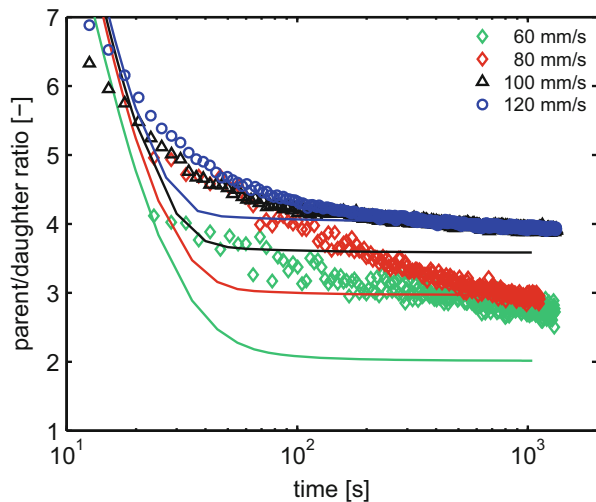
Figure 13 depicts evolution of the parent/daughter ratio. Although the trend of increasing parent/daughter ratio with flow strength is captured well by our simulations, the exact values are generally underpredicted. This discrepancy might also be resolved by a higher crystallization rate during flow. Because the growth of parent crystals is favorable over growth of daughter crystals during and shortly after flow, an increased crystallization rate would lead to an increased parent/daughter ratio.

Ultimately, this work is aimed at connecting processing conditions to final properties. Schrauwen et al. [1] showed that yield stress is related to orientation of the crystalline phase, expressed in the Hermans' orientation factor of the c -axis of the unit cell, f_c . From our calculations, we can extract the Hermans' orientation factor from the volume fractions of parent and daughter crystals. Kebabs (parents) have their c -axis oriented parallel to flow direction (i.e., $f_c = 1$), whereas daughter lamellae are oriented at an angle of approximately 80° with respect to flow direction ($f_c = -0.45$). The Hermans' orientation factor in an oriented crystalline piece of material is therefore given by

$$f_c = \frac{1 \cdot \xi_p - 0.45 \xi_d}{\xi_p + \xi_d}, \quad (31)$$

with ξ_p and ξ_d being the volume fractions of parents and daughters, respectively. The X-ray beam traverses across the thickness direction in the present experiments; therefore, we should calculate the average Hermans' orientation factor over the thickness of the slit at the location of the beam,

Fig. 13 Parent/daughter ratios from experiments (*symbols*) and simulations (*lines*). Reproduced with permission of the copyright owner [5]



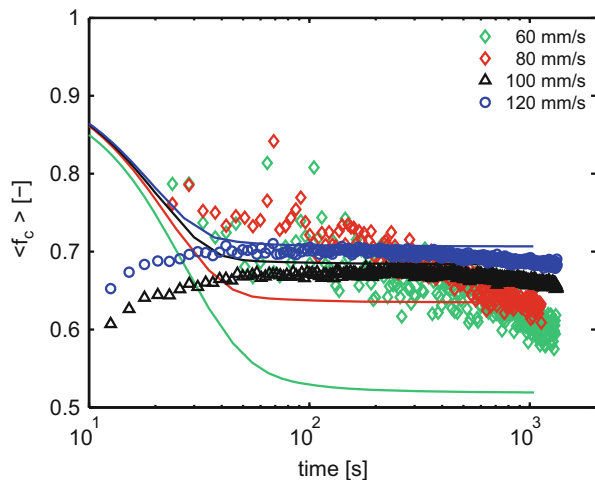
$$\langle f_c \rangle = \frac{1}{d} \int_0^d f_c \, dy, \tag{32}$$

where d is the thickness of the slit. Experimental and calculated values for the average Hermans' orientation factor of the c -axis $\langle f_c \rangle$ are presented in Fig. 14. The final value is captured quite well by our calculations for all flow conditions. An interesting direction for future work would be to investigate whether the calculated Hermans' orientation factor is a good predictor of mechanical properties.

3.3.2 Shear Layer Thickness and Flow Instabilities

Figure 15 shows polarized optical microscopy (POM) pictures of the sample in the slit at nine positions along the flow direction for piston speeds of 60 mm/s (Fig. 15a) and 140 mm/s (Fig. 15b). The shear layer is distinctly visible in the POM images. The specific shish length from simulations is shown next to the POM images, where the color scale ranges from an intershish distance of 1 mm (blue) to 50 nm (red). For the piston speed of 60 mm/s, shear layer thickness is captured accurately. For the piston speed of 140 mm/s, however, we are unable to reproduce experimental results. As the thickness of the shear layer increases and the channel effectively becomes narrower, the calculated velocity starts showing oscillations in the x -direction, as a result of which the numerical model no longer converges. The morphology shown in Fig. 15 is the morphology at 0.165 s. Shortly after this moment the flow becomes unstable. The exact time at which these oscillations start occurring depends on the mesh size; with a finer mesh these oscillations start at earlier times. Also, the POM images for this piston speed do not reveal the shear layers with straight edges that can be found for the lower piston speed. Such instabilities have also been reported in other studies [42, 66]. These are indications

Fig. 14 Average Hermans' orientation factor of the c -axis from experiments (symbols) and simulations (lines). Reproduced with permission of the copyright owner [5]



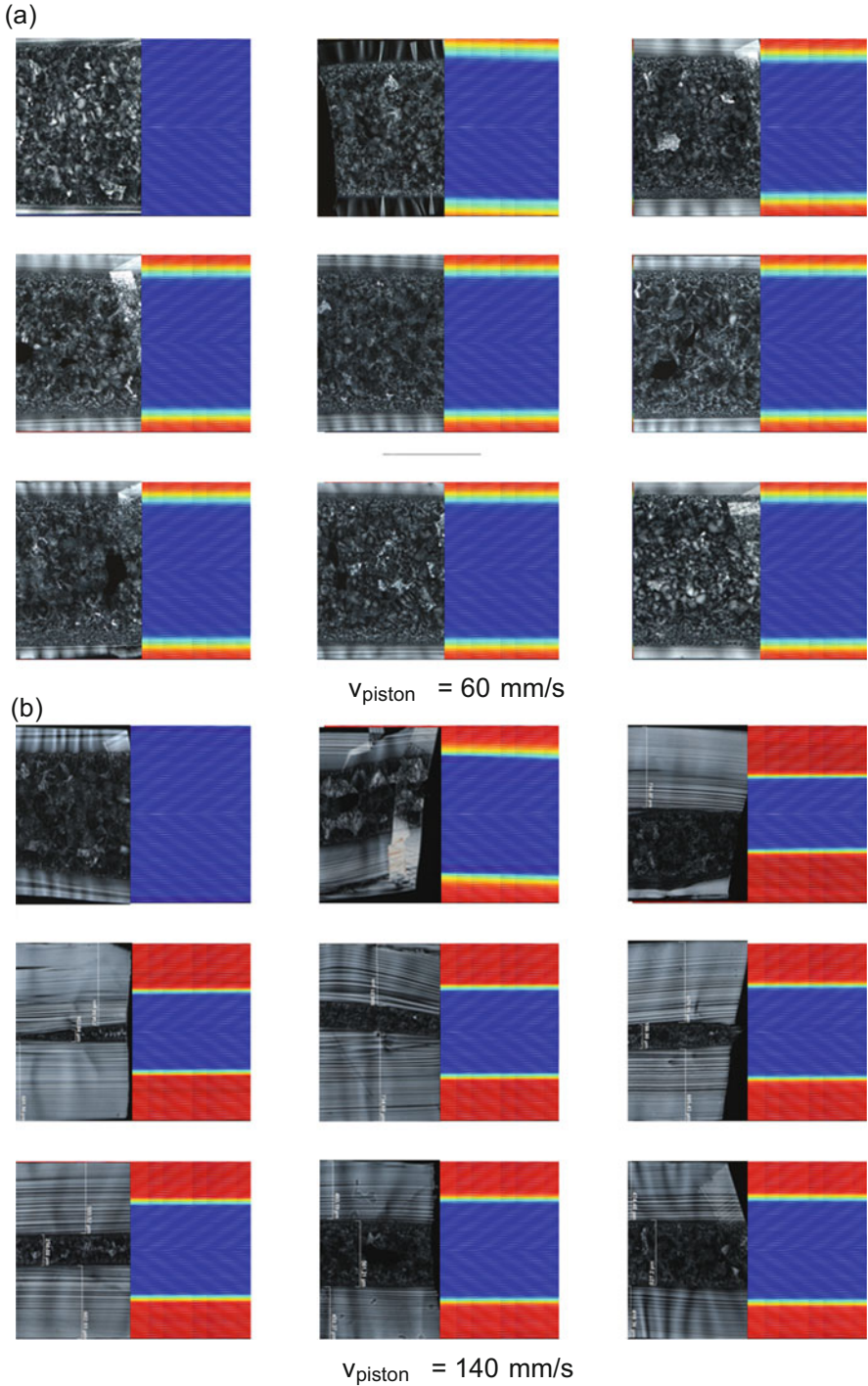


Fig. 15 Polarized optical microscopy images side-by-side with specific shish length from simulations, where *blue* depicts 10^5 m/m^3 and *red* 10^{14} m/m^3 , corresponding to an inter-shish distance

that the oscillations are not a numerical artifact, but that the flow might become unstable under these conditions.

Because the simulations stop converging at some time during the flow pulse, we cannot quantitatively compare the shear layer thickness or crystallization kinetics for this flow condition. However, the variation in layer thickness with position along the flow direction is reproduced quite well. Near both pistons, the shear layer is thin as a result of high temperature. Between pistons there is a negative gradient in shear layer thickness versus distance along the flow direction caused by pressure and start-up effects. Moreover, the pressure drop (Fig. 12a) is reproduced very well up to the time when oscillations start to occur.

3.4 Conclusions

We have presented a detailed model for FIC at high shear rates. The model calculates nucleation rate from the backbone stretch of the mode with the highest relaxation time. Growth of nuclei in the flow direction is directly related to local shear rate. Crucially, the model describes a strong effect of shish on the macroscopic viscosity, even at low crystalline volume fractions.

The model was implemented in a numerical code that solves for flow field, constitutive behavior, temperature, and crystallization kinetics in two dimensions. In this way, the model was validated with experiments at high shear rates. It was found that the model captures the necessary physics (with only two adjustable parameters) to accurately describe experimental results in terms of morphology (i.e., shear layer thickness), crystallization kinetics, and rheology during structure formation. Simulations were also performed for milder flow conditions. It was found that, qualitatively, the model predicts the different types of morphology that have been described in the literature.

Coming back to the questions that were posed in the “Introduction,” the following conclusions can be stated:

- Crystalline morphologies created in both in low and high shear rate regimes can be modeled without posing a critical flow criterion for the formation of shish.
- For these high shear rates, for which a fine molecular deformation occurs, the propagation speed of shish can be linked directly to shear rate and is in the order of micrometers per second.



Fig. 15 (continued) range of 1 mm to 50 nm. **(a)** Results for piston speed of 60 mm/s and flow time 0.25 s. **(b)** Results for piston speed of 140 mm/s and flow time 0.165 s. The nine different *subfigures* correspond to different positions along the flow direction in the slit: from *top left* to *bottom right*: 13, 32, 53, 60, 73, 82, 90, 113, and 130 mm from the driving piston (see Fig. 5). Reproduced with permission of the copyright owner [5]

- Shish significantly affect the melt viscosity at very low levels of space filling (about 1%), indicating that noncrystalline material (possibly in the form of chains tethered to shish) plays a crucial role.
- The Hermans' orientation factor is a result of different crystal orientations (parent and daughter lamellae) growing on shish.

A recommended improvement for the current model is a more accurate description of the influence of dispersed elongated structures on viscoelastic properties at high flow rates. Furthermore, the proposed (very straightforward) relation between shear rate and shish propagation velocity needs to be more thoroughly validated, for example, at different temperatures and pressures, using different materials, and with more complex flow fields.

4 Formation of Multiple Crystal Phases and Morphologies

The model presented in the section, which deals with the two issues of validation and multiple phase/multiple morphologies, combines two phenomenological approaches to FIC of iPP that have been validated in previous works: nonisothermal crystallization leading to varying compositions of crystal phases (α , β , γ , meso) [113] and flow-induced structure formation leading to various crystalline morphologies (spherulite, shish-kebab with parent and daughter crystals) (see Sec. 3 of this chapter and [5, 116]). Aside from the obvious goal of validating the approach of combining these models, this research is aimed at investigating two phenomenon specific to FIC of iPP:

1. Flow-induced β -phase formation. In quiescent conditions that only appear if a specific nucleating agent is present, small fractions of β -phase can be formed in relatively mild flow conditions [82]. In the present model, this is captured by assigning a fixed portion of flow-induced nuclei to the β -phase. In this research, we investigate the size of the fraction of flow-induced nuclei that form β -crystallites.
2. Nucleation of γ -phase on shish. It has recently been observed that under strong flow conditions at high pressure ($\dot{\gamma} \leq 100 \text{ s}^{-1}$), which is relevant to, for example, the injection molding process, γ -crystals can have a strong preferential orientation of 40° with respect to flow direction [117]. However, it is not clear whether γ -crystals only nucleate on kebabs formed by α -crystals, or if they can also nucleate directly on shish. The present model allows us to investigate the effects of both possibilities on the phase composition and to compare the results with experimental findings [82].

4.1 Crystallization Model

The starting concept of the model presented in this paper was presented by van Drongelen et al. [113]. For each crystal phase, the Schneider rate equations [68, 69] are solved to calculate the crystallization kinetics. To do so, only temperature-dependent nucleation density and growth rate are required. The growth rates of the α -, β -, and γ -polymorphs were determined by van Drongelen [113]. The kinetics of formation of the mesomorphic phase were also determined, but are not used in this paper because the experiments did not show any of this phase as a result of the relatively low cooling rate. Nuclei can be spawned by cooling or by the application of flow. Upon creation, fractions of nuclei are allocated to one of the three crystal phases on the basis of their momentary growth rates. Each nucleus grows until impingement at the crystal growth rate of their respective crystal phases, which depends on the momentary temperature and pressure. This is the mechanism that determines the final fractions of α -, β -, and γ -phases in the material. The addition with respect to the work by van Drongelen and coworkers is that, whereas they only considered quiescent conditions (i.e., the only source of nucleation is thermally activated heterogeneous nuclei, and only spherulite growth occurs), we have added flow-induced nucleation and growth of shish-kebab structures including lamellar branching (i.e., a parent and daughter structure).

Because we want to present a description of the multiple phase/multiple morphology mode that is as complete as possible, some parts of earlier sections are repeated here.

4.1.1 Crystal Growth Rate

The crystal growth rate of each of the crystal phases is one of the most important determining factors in this modeling framework. Not only does it determine the rate at which space filling of each crystal phases takes place, it also governs the allocation to different crystal phases of nuclei that are created by either cooling or the application of flow. In this work, we use a simple but effective description for the growth rate of each crystal phase, which, like the well-known Hoffman–Lauritzen theory [118], yields a bell-shaped curve for growth rate versus temperature,

$$G_i(T) = G_{\max,i} \exp\left(-c_{G,i}(T - T_{G,\text{ref},i})^2\right). \quad (33)$$

Here, G is the crystal growth rate, T temperature, G_{\max} the crystal growth rate at reference temperature $T_{\text{ref},G}$, and c_G a parameter governing the temperature dependence of the growth rate. Because applying pressure increases undercooling, the reference temperature is adjusted with pressure according to the Clapeyron equation [86],

$$T_{G,\text{ref},i} = T_{G,\text{ref},i,0} + \zeta(p - p_0) \quad (34)$$

with $\zeta = 27.5^\circ\text{C/kbar}$ and the reference pressure $p_0 = 1$ bar. Additionally, pressure has an influence on the maximum growth rate,

$$G_{\text{max},i} = G_{\text{max},0,i} \exp(\alpha_i(p - p_0)). \quad (35)$$

Subscript i denotes the possible different crystal phases. All parameters in the above equations are given in the literature [113] and summarized in Table 7.

Effect of Orientation on Growth Rate

Crystal growth rate can be enhanced by orientation of chains in the flow direction [22, 89]. Therefore, in the case of shish-kebab crystallization, the growth rate of α -phase kebabs is increased. This is accounted for by increasing the α -crystal growth rate by a factor during flow, relaxing to the quiescent value with a relaxation time similar to an average rheological relaxation time [119]. In mathematical terms,

$$G_{\alpha,p}(T, t) = G_{\alpha}(T) \left(1 + \mu_{\text{flow}} e^{-t/\lambda_G} \right), \quad (36)$$

where $G_{\alpha,p}$ is the growth rate of α -phase kebabs and $\mu_{\text{flow}} = 4$ and $\lambda_G = 9$ s are empirical parameters determined by Roozmond et al. [89]. The effect is active from the start of flow and starts relaxing from the cessation of flow, denoted by t .

In the current formulation of orientation-induced growth rate increase, there is no dependence of the growth rate on the molecular orientation and/or stretch; it attains the same value irrespective of flow strength. This choice is obviously flawed. The crystal growth rate should be some function of molecular orientation/stretch, which depends on the magnitude of the shear rate and, during stress growth, on shear time. However, this would introduce complexity in the form of additional fitting parameters that, at the moment, cannot be determined independently. The crystal growth rate of the γ -phase and α -daughters, denoted in this paper by G_{γ} and $G_{\alpha,d}$, respectively, are not affected by flow, as the c -axis of chains in these crystals

Table 7 Parameters for quiescent nucleation and crystal growth rate

Nucleation density			
N_{ref} (m^{-3})	2.2×10^{15}		
$T_{N,\text{ref}}$ ($^\circ\text{C}$)	110		
c_N ($^\circ\text{C}^{-1}$)	0.211		
Crystal growth rate			
	α -phase	β -phase	γ -phase
$G_{\text{max},0}$ ($\mu\text{m/s}$)	4.8	7.1	1.1
$T_{G,\text{ref}}$ ($^\circ\text{C}$)	90	107	104
c_G ($10^{-3}^\circ\text{C}^{-1}$)	2.3	6.6	3.5
α (bar^{-1})	0	0	7.7×10^{-4}

is not in the direction of flow. Moreover, crystallization of these species typically occurs only after the flow-induced orientation has relaxed.²

4.1.2 Crystallization Kinetics

Quiescent Nucleation Density

The heterogeneous nucleation density as a function of temperature is calculated using

$$N_q(T) = N_{\text{ref}} \exp(-c_N(T - T_{N,\text{ref}})), \tag{37}$$

where the reference temperature is shifted in the same way as in Eq. 34. Parameter values are given in the literature [113] (see also Table 7). The nucleation density versus temperature at reference pressure of 1 bar is shown in Fig. 16b. During cooling, the nucleation rate is therefore given by

$$\dot{N}_q = \dot{T} \frac{dN_q}{dT} \tag{38}$$

Flow-Induced Point-Like Nucleation

Extensive research in the past decade into the phenomenon of FIC has indicated that flow-enhanced point-like nucleation is dominated by the chains on the high end of the molecular weight distribution [21, 29, 106]. Similar to the approach taken in

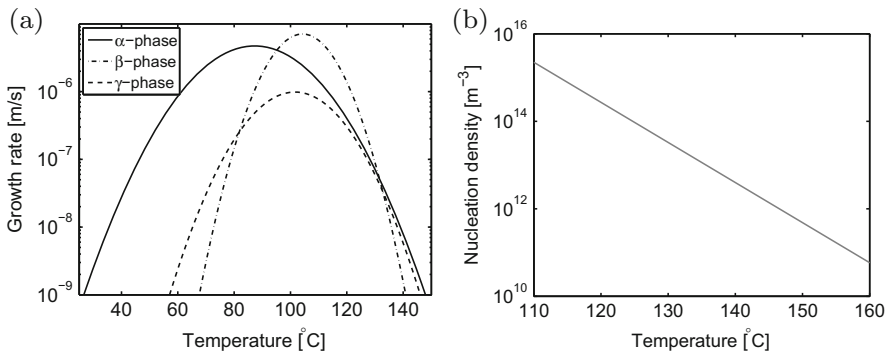


Fig. 16 (a) Crystal growth rate versus temperature for different crystal phases at a reference pressure of 1 bar. (b) Quiescent nucleation density of the iPP used in this work. Reproduced with permission of the copyright owner [87]

²For these phases orientation might decrease crystal growth rate; however, there is no experimental evidence for this effect.

earlier work from our group [21, 29, 66, 82], the creation rate of point-like nuclei is coupled in a phenomenological way to the momentary stretch in the high molecular weight tail of the material on a continuum level,

$$\dot{N}_f = g_n(T, p) \exp(\mu_n (\Lambda_{\text{hmw}}^2 - 1)). \quad (39)$$

Here, Λ_{hmw} is the backbone stretch calculated using the XPP constitutive model [83], and μ_n and g_n are scaling parameters, the latter of which depends on temperature and pressure following

$$g_n(T, p) = g_{n, \text{ref}} 10^{c_{n,T}(T-T_{\text{ref}}) + c_{n,p}(p-p_{\text{ref}})} \quad (40)$$

All parameters in the above equations are given in Table 5. Further details on the calculation of backbone stretch and characterization of this model have been presented by Roozmond et al. [5].

An extended version of the Schneider rate equations is used to calculate crystallization kinetics. For spherulites, we have:

$$\begin{aligned} \dot{\phi}_{3,i} &= 8\pi \dot{N}_i \quad (\phi_3 = 8\pi N), \\ \dot{\phi}_{2,i} &= G_i \phi_{3,i} \quad (\phi_2 = 8\pi R_{\text{tot}}), \\ \dot{\phi}_{1,i} &= G_i \phi_{2,i} \quad (\phi_1 = S_{\text{tot}}), \\ \dot{\phi}_{0,i} &= G_i \phi_{1,i} \quad (\phi_0 = V_{\text{tot}}), \end{aligned} \quad (41)$$

where subscript i denotes different crystal phases. G_i is the crystal growth rate as determined from Eq. 33. The nucleation density for each phase is allocated from the total reservoir of nuclei,

$$\dot{N}_i = f_{i,f} \dot{N}_f + f_{i,q} \dot{T} \frac{dN_q}{dT}, \quad (42)$$

with \dot{N}_f and $\frac{dN_q}{dT}$ from Eqs. 38 and 39, respectively. f_i denotes the factor by which the nucleation density is divided between the crystal modifications. This is carried out in the same way as described previously [113], using their momentary growth rates. The basic idea behind this approach is that, in iPP, a nucleation site can become a crystallite composed of either α -phase or γ -phase. The chance that a nucleation site becomes a crystal of α -phase or γ -phase depends on how favorable the growth of the respective phases is at the momentary temperature and pressure. It is assumed that this is reflected by the growth rates of the phases.

The β -phase is a different story, as it can only be nucleated by specific nucleating agents or flow. Therefore, a different approach must be chosen for calculation of its nucleation density. In quiescent conditions, the number of β -nuclei is simply set to zero. In the case that β -nucleating agents are added, this can be accounted for by ascribing an amount of nuclei to the β -phase that is unrelated to the nucleation

density of α -phase and γ -phase [113]. The quiescent nucleation densities for the three phases now follow from:

$$\begin{aligned} f_{\alpha,q} &= \frac{G_\alpha}{G_\alpha + G_\gamma} \\ f_{\beta,q} &= 0 \\ f_{\gamma,q} &= \frac{G_\gamma}{G_\alpha + G_\gamma}. \end{aligned} \quad (43)$$

With application of flow, a small amount of β -phase is formed. Because the growth rate of the β -modification is much higher than that of the other two phases (see Fig. 16a), it can be demonstrated that only a small number of β -nuclei are needed to yield considerable β -space filling. Here, we take the simplest approach possible and assign a fixed fraction of flow-induced nuclei to the β -phase. The corresponding parameter value is determined later on in this paper see Sec. 4.2.2. The remaining nuclei are assigned to α - and γ -phases as above:

$$\begin{aligned} f_{\alpha,f} &= (1 - f_{\beta,f}) \frac{G_\alpha}{G_\alpha + G_\gamma} \\ f_{\beta,f} &= f_{\beta,f} \\ f_{\gamma,f} &= (1 - f_{\beta,f}) \frac{G_\gamma}{G_\alpha + G_\gamma}. \end{aligned} \quad (44)$$

Shish-Kebab Nucleation

The shish growth mechanism in our model (see Fig. 6) is based on the “streamers” concept proposed by the Kornfield group [41]. Shish propagate in the lengthwise direction by the addition of chain segments of length ξ_{seg} . The length per unit volume of shish, denoted by L , is assumed to be constant after cessation of flow. In a crude sense, the flow attaches these segments as crystals to the tip of the shish. Because deformation rates for the experiments are high (possibly even higher in the surroundings of shish [107]), we can assume that the material deforms affinely. We can then express the lengthwise propagation speed of shish as

$$\dot{L} = \dot{\gamma} \xi_{\text{seg}}. \quad (45)$$

In our model, all nucleation sites grow in the lengthwise direction with this mechanism. Therefore, the total line nucleation density for kebabs (i.e., the specific shish length) is given by

$$\dot{L}_{\text{tot}} = 2N_f \dot{\gamma} \xi_{\text{seg}}. \quad (46)$$

Note that we do not apply a critical flow condition for the formation of shish as was done in previous work [63, 67]. In those papers, the critical flow condition was invoked to obtain a set of equations that could describe flow-induced nucleation in both low and high shear rate regimes. In the current formulation this is not necessary. For weak to mild flow conditions, no shish creation is observed because nucleation rate \dot{N}_f as well as propagation rate \dot{L} are low for such flow conditions. There is no explicit dependence on molecular weight in the growth rate of shish; this comes in via the nucleation rate, which is coupled to backbone stretch in the high molecular weight tail.

Shish-Kebab Crystallization Kinetics

Janeschitz-Kriegl and coworkers adapted the Schneider rate equations for crystallization of shish-kebab structures [18]. Based on their work, we derived a mathematical model to capture the crystallization kinetics of parent and daughter crystals in polypropylene composed solely of the α -phase [89] (see also Sec. 3 of this chapter). We extend this model to also incorporate crystals of the γ -phase growing on shish-kebabs. In most cases, the γ -phase is only observed as daughter lamellae. However, van Erp et al. [117] recently observed in WAXD a highly oriented pattern, possibly indicating that this crystal phase can also grow in the parent morphology. Therefore, we consider two cases in the present paper, one where γ -crystals only grow in the daughter morphology, and one where γ -crystals can also form parent crystals, that is, nucleate directly on shish to create kebabs consisting purely of γ -phase (i.e., only α -phase kebab forms).

The Schneider rate equations for shish-kebabs are presented below. For the growth of kebabs on shish, in the case that the γ -phase does not form kebabs:

$$\begin{aligned} \dot{\psi}_{1,\alpha} &= 4\pi G_\alpha L_{\text{tot}} \\ \dot{\psi}_{1,\gamma} &= 0. \end{aligned} \quad (47)$$

In the case that the γ -phase can form kebabs, using again growth rate weighing:

$$\begin{aligned} \dot{\psi}_{1,\alpha} &= 4\pi G_\alpha L_{\text{tot}} \frac{G_\alpha}{G_\alpha + G_\gamma} \\ \dot{\psi}_{1,\gamma} &= 4\pi G_\gamma L_{\text{tot}} \frac{G_\alpha}{G_\alpha + G_\gamma} \end{aligned} \quad (48)$$

Here, ψ_1 denotes the surface area per unit volume of crystals growing on kebabs and the different growth rates G_i are as given by Eq. 36.

On shish, three different crystal morphologies can nucleate: α -parents (with c -axis oriented in the flow direction), α -daughters (with c -axis at an angle of 80° to the

flow direction), and γ -daughters (with c -axis at an angle of 40° with respect to the α -phase on which they nucleate). Therefore, only α -parents have increased growth rate as a result of orientation. The growth rates of the other two morphologies are always equal to the growth rate of the respective phases in quiescent conditions. It is assumed that only the γ -phase grows on γ -kebabs. In mathematical terms, this becomes:

$$\begin{aligned}
 \dot{\psi}_{0,\alpha,p} &= G_{\alpha,p} \psi_{1,\alpha} \frac{G_{\alpha,p}}{G_{\alpha,p} + G_{\alpha,d} + G_\gamma} \\
 \dot{\psi}_{0,\alpha,d} &= G_{\alpha,d} \psi_{1,\alpha} \frac{G_{\alpha,d}}{G_{\alpha,p} + G_{\alpha,d} + G_\gamma} \\
 \dot{\psi}_{0,\gamma,p} &= G_\gamma \psi_{1,\alpha} \frac{G_\gamma}{G_{\alpha,p} + G_{\alpha,d} + G_\gamma} \\
 \dot{\psi}_{0,\gamma,d} &= \frac{G_\gamma \psi_{1,\gamma}}{G_\gamma \psi_{1,\gamma}}
 \end{aligned} \tag{49}$$

where $\psi_{1,i}$ is given by either Eqs. 47 or 48, depending on whether γ -parent growth is on or off. Subscripts p and d denote whether the volume is, respectively, in parent crystals or daughter crystals.

Impingement

To correct for impingement, we use the Kolmogorov–Avrami equation [56]:

$$\xi_{\text{tot}} = 1 - \exp\left(-\sum_i \phi_{0,i} + \psi_{0,i}\right). \tag{50}$$

Here, ξ_{tot} is the total space filling, which reaches 1 when the crystallization process is complete. From this, it follows that the space filling of each individual crystal phase is given by

$$\dot{\xi}_i = (1 - \xi_{\text{tot}})(\dot{\phi}_{0,i} + \dot{\psi}_{0,i}). \tag{51}$$

The crystallization temperature in our calculations is defined as the temperature when ξ_{tot} reaches 10%, as in the experiments (see Fig. 3). For all conditions in this paper, the cooling rate is sufficiently low to allow the material to fully crystallize; hence, $\xi_{\text{tot}} = 1$ at the end of each experiment. The volume fractions of the respective phases, which are compared with experimental data from WAXD, are given by $\xi_i / \xi_{\text{tot}} = \xi_i$.

4.2 Results

In this section, we compare calculations for the volume fraction of different phases found in different polymorphs with experimental data obtained from WAXD. As stated in the “Introduction,” the presented model contains two elements that have not been explored previously. First, we explore the creation of β -nuclei and β -growth in the regime of flow conditions where the number of nucleation sites is increased, but the final morphology is still more or less isotropic. Second, the model allows us to investigate the possibility of forming kebabs consisting purely of γ -phase, next to purely α -phase kebabs, under conditions of high shear rate and high pressure. It is important to note here that all other facets of FIC resulting in multiple phases and different polymorphs (e.g., formation of α - and γ -crystals under mild shear conditions and the formation of shish-kebabs) were taken from previous work [5, 113]. Hence, the mathematical framework and necessary parameters are fixed a priori.

4.2.1 Experimental and Modeling Results

The experimental details and conditions are described in Sect. 2. Figure 17 shows all results, experimental and numerical, in terms of the fractions of the different crystal phases. To elucidate the β -nuclei and β -growth and the γ -phase kebab issues, subsets of these data are used in the following sections.

4.2.2 Point-Like Nucleation: Flow-Induced β -Phase

At atmospheric pressure, the growth rate of β -phase exceeds that of the other polymorphs of iPP in the range 95–130°C (see Fig. 16). Therefore, one could expect the strongest contribution of β -phase in experiments where the crystallization temperature lies in this range, corresponding to an undercooling of 65–110°C. However, the lowest observed crystallization temperature T_c is about 120°C, with a corresponding undercooling of 75°C. A lower T_c is not reached because, for the cooling rate applied, space filling is complete at that temperature, even for quiescent conditions and the lowest applied pressure (100 bar). Therefore, we expect (and indeed find) no β -nuclei under these conditions. Upon application of flow, however, the crystallization temperature increases and the material crystallizes at such an undercooling that the growth rate of β -phase exceeds that of the α - and γ -phases.

This is demonstrated in Fig. 18a, where we have plotted the experimentally found volume fraction of β -phase against undercooling (i.e., taking into account the effect of pressure; see Eqs. 34 and 40). Figure 18b–d shows corresponding calculations with varying fractions of flow-induced nuclei assigned to the β -phase (f_β in Eq. 44). The best agreement with experiments is observed for $f_\beta = 2 \times 10^{-3}$,

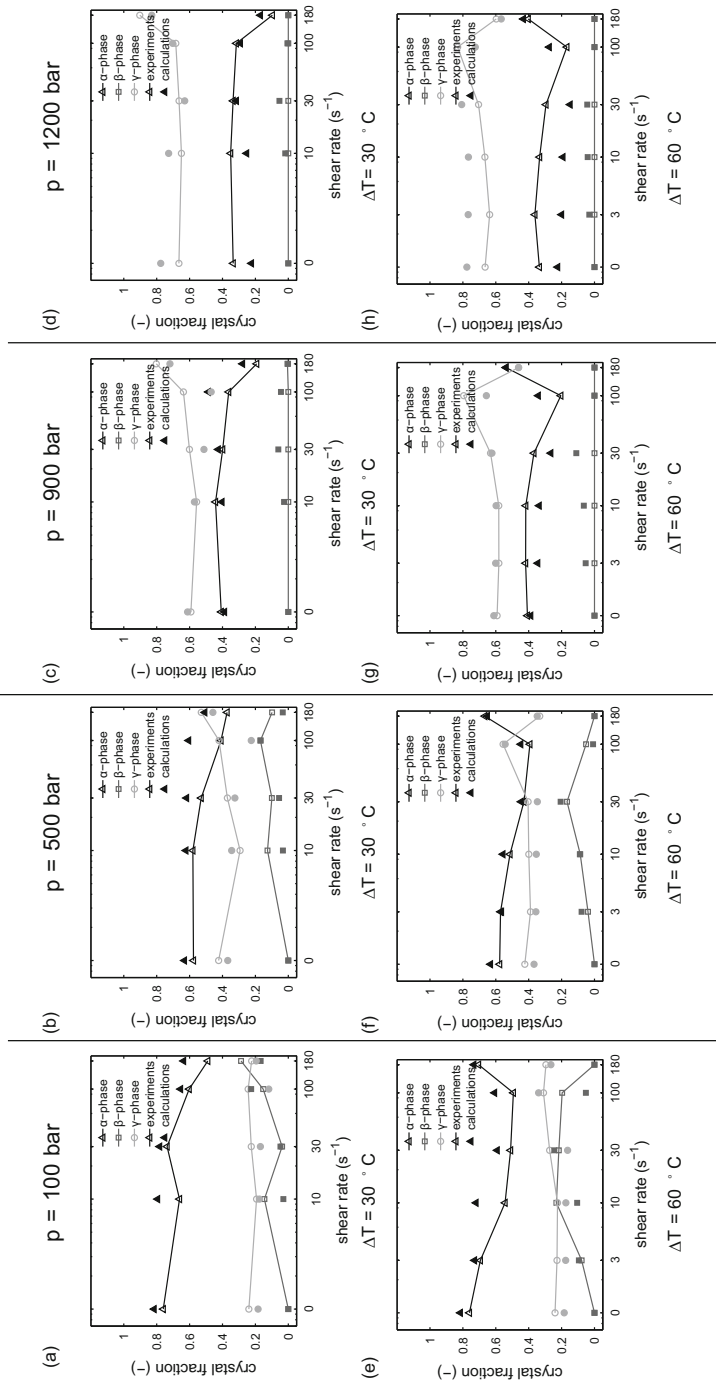


Fig. 17 Fraction of crystal phases as a function of shear rate for all pressures (columns) and undercoolings (rows). Connected symbols show experiments, symbols show calculations

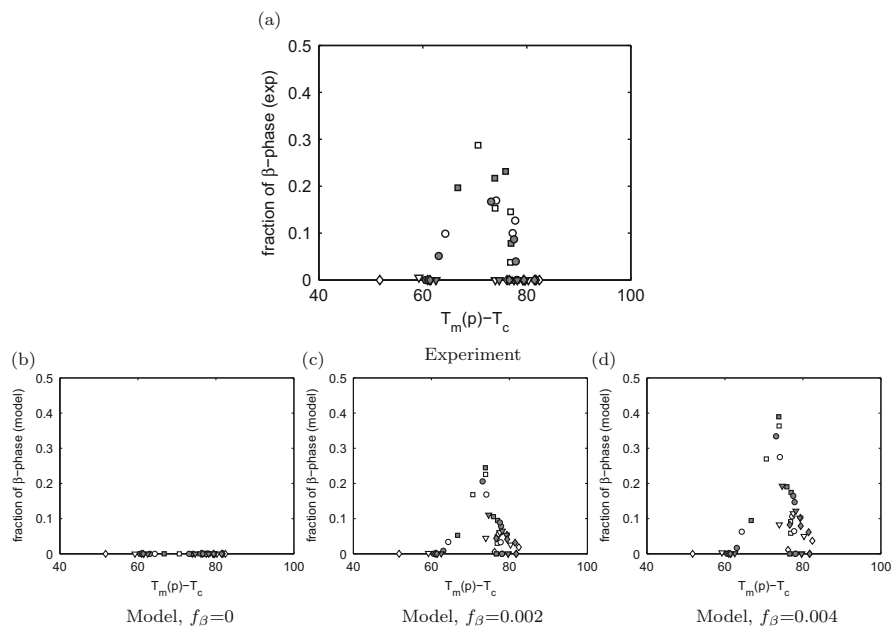


Fig. 18 Final volume fraction of the β -polymorph as a function of undercooling at the point of crystallization. (a) Shows experimental results, and (b–d) show calculations with varying amounts of flow-induced nuclei assigned to the β -phase. *Unfilled symbols* indicate that shear pulse was applied at an undercooling of 30°C; *filled symbols* indicate undercooling of 60°C. *Different symbols* indicate different pressures. Reproduced with permission of the copyright owner [87]

meaning that 0.2% of all flow-induced nuclei become β -spherulites. Again, the reason that such a low number gives a significant volume fraction of β -phase is that the growth rate of this phase in the relevant temperature region far exceeds the growth rates of the other polymorphs of iPP (see Fig. 16a).

4.2.3 Oriented Regime: Can γ -Phase Grow in Kebabs?

As already demonstrated by van Erp et al. [82], the polymorphic crystallization of iPP correlates strongly with the crystallization temperature, which is a result of thermodynamic and flow conditions. The qualitative effect of flow during cooling can therefore easily be estimated. By increasing the strength of flow (and hence the number of flow-induced nuclei), the crystallization temperature is increased and, therefore, more γ -phase is generally formed at the expense of α -phase, with a narrow temperature range where flow also generates the β -phase (see Sec. 4.2.2). This is clearly visible when the volume fractions of the α - and γ -phases are plotted against the crystallization temperature for all experiments (Fig. 19, top row).

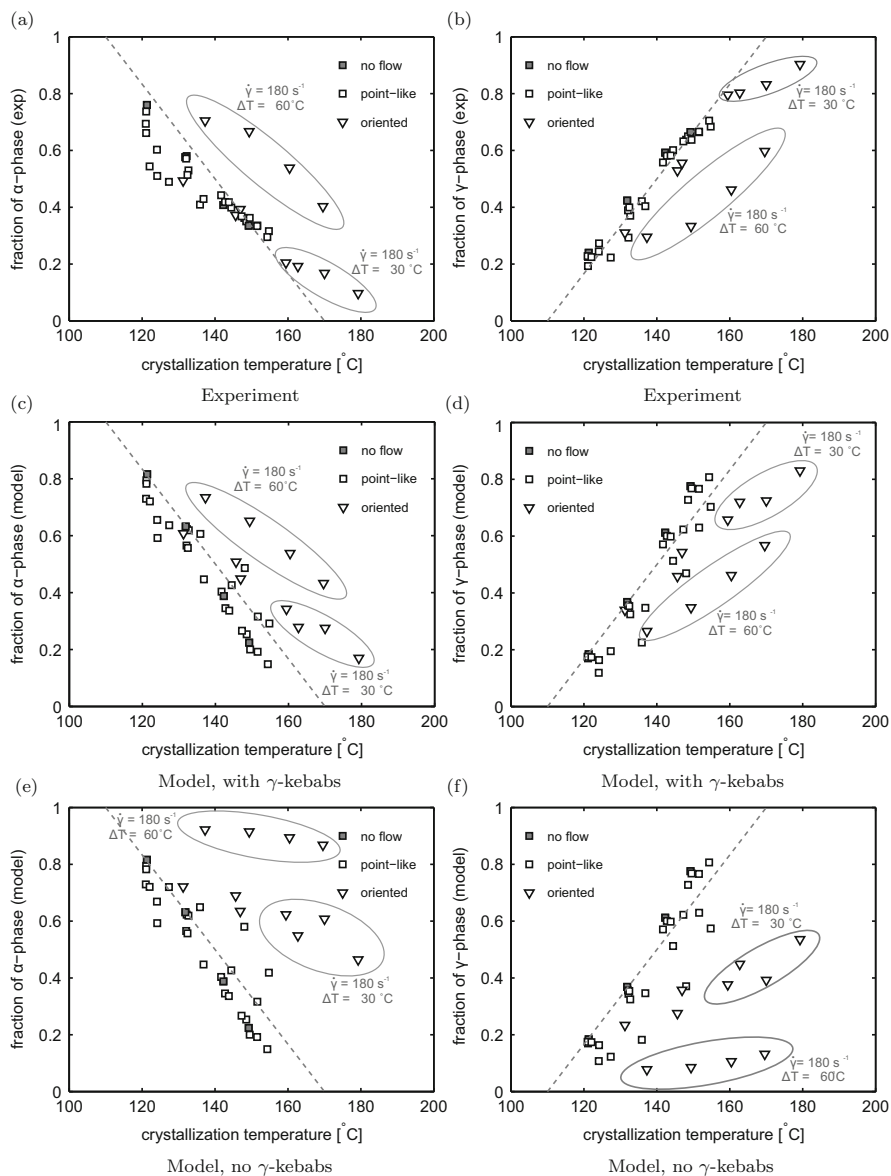


Fig. 19 Volume fractions of different polymorphs (*columns*) as a function of crystallization temperature. *Top row* shows experimental results, *middle row* shows calculations with γ -kebabs, and *bottom row* shows calculations with no γ -kebabs. *Different symbols* indicate varying degrees of orientation as measured by WAXD [82]. The *dashed lines* are added as a guide for the eye. Reproduced with permission of the copyright owner [87]

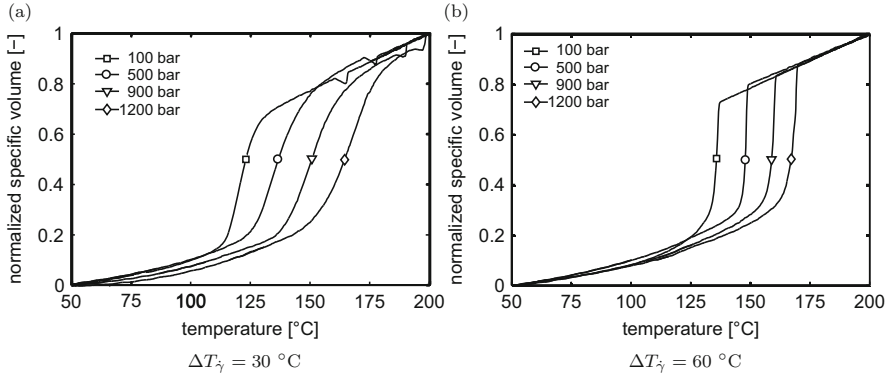


Fig. 20 Normalized specific volume as a function of temperature for experiments with shear rate of 180 s^{-1} for all pressures and undercooling of (a) 30°C and (b) 60°C . Reproduced with permission of the copyright owner [87]

The simple reason for the observed trends is that, at low temperatures, the growth rate of α -phase is clearly higher than that of γ -phase, whereas at higher temperatures the difference in growth rate between the two phases becomes smaller (see Fig. 16). The creation of β -phase is also observed in the lower range of crystallization temperatures, where there is a dip in the α -phase fraction. Additionally, with increasing pressure the crystallization temperature shifts to even higher values because the growth rate of γ -phase is strongly increased by the effect of pressure (Eq. 35).

However, the eight experiments for the highest shear rate ($\dot{\gamma} = 180 \text{ s}^{-1}$, $p = 100, 500, 900, 1,200 \text{ bar}$, T -shear undercooling of 30°C and 60°C) clearly deviate from the trend line (indicated in Fig. 19). In all of these cases, the amount of α -phase formed is higher than expected by comparison with data points where no orientation was observed (i.e., point-like crystallization). For these experiments, the normalized specific volume versus temperature is shown in Fig. 20. Here, we observe that crystallization is reached rather rapidly after the flow pulse (within 20 s).³ Because of this, the effect of orientation on α -growth rate (Eq. 36) becomes dominant. This is highlighted in the Appendix, where this effect was turned off in our model and all points collapse more or less on the same line.

These experiments are very sensitive to the nucleation of γ -phase on kebabs. The middle and bottom row in Fig. 19 show model calculations corresponding to the experimental data set shown in the top row. The middle row shows that the γ -phase can also grow directly on the shish as kebabs. The bottom row shows the results when this possibility is turned off in the model, as described in Sec. 4.1.2. Good

³For shear undercooling of 30°C , the shear pulse is visible as a temporary dip in the specific volume. For shear undercooling of 60°C , crystallization occurs during the shear pulse and therefore the dip is not visible.

agreement is observed with experimental data for the case that the γ -phase can nucleate directly on shish (middle row). On the other hand, if growth of γ -kebabs is turned off, the α -phase consumes an even larger portion of volume because of its increased growth rate as a result of orientation (Eq. 36), causing a strong overestimation of the volume fraction of α -phase. From these results, it can therefore be concluded that our modeling approach indicates that γ -phase must be able to nucleate directly on shish.

5 Conclusions

A modeling framework was presented to describe flow-induced crystallization of iPP at elevated pressures in multiple crystal phases and morphologies. The framework was constructed by combining two models developed in previous work [5, 113]. All parameters in these models were fixed in the aforementioned papers. In the present work, only one additional parameter was introduced, determining the portion of nuclei created by flow that form β -crystals.

Model calculations show good agreement with experimental data for crystal volume fractions of all phases over a very wide range of flow-conditions, with shear rates varying from 0 to 200 s^{-1} , pressures from 100 to 1,200 bar, and shear temperatures from 130°C to 180°C such that, for a given pressure, undercoolings of 30°C or 60°C were obtained when shear was applied. Moreover, the model provides a tool for investigating open questions regarding crystallization of iPP.

First, we have shown that the experimentally obtained volume fractions of β -phase can be explained by assigning a seemingly low number of 0.2% of all flow-induced spherulites to the β -phase. Because of the high growth rate of β -phase compared with the α - and γ -phases, even such a low number of nuclei is enough to explain volume fractions of β -phase up to 20%. Moreover, the model also captures the range of pressure-dependent undercooling at which the β -phase forms very well. Second, the model was derived for two possible growth mechanisms of γ -phase on highly oriented flow-induced crystallites (shish): one where γ -crystals can only form on α -kebabs in the form of daughter lamellae, and one where γ -crystals can also nucleate directly on shish and form kebabs, next to γ -phase daughters on the kebab. Good agreement with experimental data was only observed for the form of the model where γ -crystals can nucleate directly on shish, indicating that under appropriate conditions (high pressure, high shear rate), a considerable fraction of the kebabs can consist of γ -phase.

For further validation of the presented model, as well as linking flow-induced crystal structure to final properties (mechanical and optical), it would be desirable to analyze the morphology of the experimental samples in more detail. Crystallite dimensions (e.g., from TEM) and lamellar thickness (from SAXS) are thought to

play a determining role in mechanical properties. The former can be obtained directly from the Schneider rate equations and the latter can be estimated via the crystallization temperature. A successful example of such an approach (i.e., coupling structure formation to final mechanical properties via predicted lamellar thickness distributions) has been published [120].

Furthermore, the presented approach for modeling crystallization of the β -phase implies that under mild flow conditions there would be a small number of β -crystals that fill a large fraction of the volume. Therefore, these crystals should have a much larger radius than those composed of α -phase or γ -phase. This prediction could be checked, for example, using optical microscopy.

Appendix: Model Without Increase in α -Growth Rate as a Result of Orientation

Figure 21 shows calculations for the volume fractions of α - and γ -phases for the case that the γ -phase can nucleate directly on shish to form kebabs, with no increase in α -growth rate during and shortly after flow as a result of orientation (i.e., $G_{\text{flow}} = 0$ in Eq. 36). It is observed that the eight data points highlighted in Sect. 4.2.3 now all collapse on the, approximately, linear relation between crystal volume fraction and crystallization temperature. This is an indication that the deviation from this trend is caused by the α -phase having an increased growth rate as a result of orientation caused by flow.

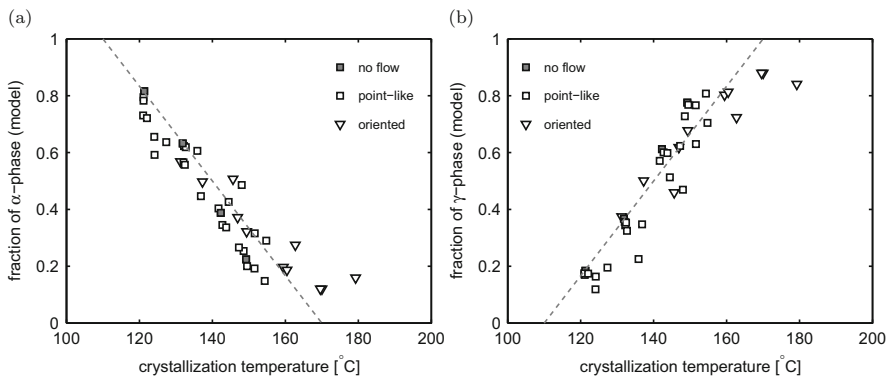


Fig. 21 Volume fractions of (a) α -polymorphs and (b) γ -polymorphs as a function of crystallization temperature. In these calculations, the increase in α -growth rate as a result of orientation has been turned off (see Eq. 36). *Different symbols* indicate varying degrees of orientation as measured by WAXD [82]. Reproduced with permission of the copyright owner [87]

References

1. Schrauwen BAG, van Breemen LCA, Spoelstra AB, Govaert LE, Peters GWM, Meijer HEH (2004) Structure, deformation, and failure of flow-oriented semicrystalline polymers. *Macromolecules* 37:8618–8633
2. Bernland K, Tervoort T, Smith P (2010) Phase behavior and optical- and mechanical properties of the binary system isotactic polypropylene and the nucleating/clarifying agent 1,2,3-trideoxy-4,6:5,7-bis-*O*-[(4-propylphenyl) methylene]-nonitol. *Polymer* 50:2460–2464
3. Ma Z, Balzano L, Peters GWM (2012) Pressure quench of flow-induced crystallization precursors. *Macromolecules* 45:4216–4224
4. Fernandez-Ballester L, Thurmand DW, Kornfield JA (2009) Real-time depth sectioning: Isolating the effect of stress on structure development in pressure-driven flow. *J Rheol* 53:1229–1254
5. Roozmond PC, van Drongelen M, Ma Z, Hulsen MA, Peters GWM (2015) Modeling flow-induced crystallization in isotactic polypropylene at high shear rates. *J Rheol* 59:613–642
6. Natta G, Corradini P (1960) Structure and properties of isotactic polypropylene. *Nuovo Cimento Ser 10* 15:40–51
7. Lotz B, Kopp S, Dorset D (1994) An original crystal-structure of polymers with ternary helices. *Comptes Rendus de l'Academie des Sciences Serie II* 319:187–192
8. Turner-Jones A (1971) Development of the γ -crystal form in random copolymers of propylene and their analysis by DSC and X-ray methods. *Polymer* 12(8):487–508
9. Alamo RG, Kim M-H, Galante MJ, Isasi JR, Mandelkern L (1999) Structural and kinetic factors governing the formation of the γ polymorph of isotactic polypropylene. *Macromolecules* 32(12):4050–4064
10. Auriemma F, De Rosa C (2002) Crystallization of metallocene-made isotactic polypropylene: Disordered modifications intermediate between the α and γ forms. *Macromolecules* 35(24):9057–9068
11. Lotz B, Graff S, Straupe C, Wittmann JC (1991) Single crystals of γ phase isotactic polypropylene: combined diffraction and morphological support for a structure with non-parallel chains. *Polymer* 32(16):2092–2910
12. Bruckner S, Meille SV (1989) Non-parallel chains in crystalline gamma-isotactic polypropylene. *Nature* 340:455–457
13. Mezghani K, Phillips PJ (1997) The gamma-phase of high molecular weight isotactic polypropylene. II: The morphology of gamma-form crystallized at 200 MPa. *Polymer* 38:5725–5733
14. Natta G, Pino P, Corradini P, Danusso F, Mantica E, Mazzanti G, Moraglio G (1960) Crystalline high polymers of alpha-olefins. *J Am Chem Soc* 77:1708–170
15. Wunderlich B, Grebowicz J (1984) Thermotropic mesophases and mesophase transitions of linear, flexible macromolecules. *Adv Polym Sci* 60:1–59
16. De Rosa C, Auriemma F, Di Girolamo R, Romano L, De Luca MR (2010) A new mesophase of isotactic polypropylene in copolymers of propylene with long branched comonomers. *Macromolecules* 43:8559–8569
17. Lotz B (2014) A new ϵ crystal modification found in stereodeficient isotactic polypropylene. *Macromolecules* 47:7612–7624
18. Liedauer S, Eder G, Janeschitz-Kriegl H, Jerschow P, Geymayer W, Ingolic E (1993) On the kinetics of shear-induced crystallization in polypropylene. *Int Polym Process* 8(3):236–244
19. Lamberti G (2014) Flow induced crystallisation of polymers. *Chem Soc Rev* 43:2240–2252
20. Janeschitz-Kriegl H, Ratajski E, Stadlbauer M (2003) Flow as an effective promoter of nucleation in polymer melts: a quantitative evaluation. *Rheol Acta* 42:355–364
21. Steenbakkens RJA, Peters GWM (2011) A stretch-based model for flow-enhanced nucleation of polymer melts. *J Rheol* 55(2):401–433
22. Pantani R, Coccorullo I, Volpe V, Titomanlio G (2010) Shear-induced nucleation and growth in isotactic polypropylene. *Macromolecules* 43:9030–9038

23. Jerschow P, Janeschitz-Kriegl H (1997) The role of long molecules and nucleating agents in shear induced crystallization of isotactic polypropylenes. *Int Polym Process* 12:72–77
24. Pogodina NV, Lavrenko VP, Srinivas S, Winter HH (2001) Rheology and structure of isotactic polypropylene near the gel point: quiescent and shear-induced crystallization. *Polymer* 42:9031–9043
25. Ma Z, Steenbakkens RJA, Giboz J, Peters GWM (2011) Using rheometry to determine nucleation density in a colored system containing a nucleating agent. *Rheol Acta* 50:909–915
26. Karger-Kocsis J, Csikai I (1987) Skin-core morphology and failure of injection-molded specimens of impact-modified polypropylene blends. *Polym Eng Sci* 27:241–253
27. Fujiyama M (1995) Higher order structure of injection-molded polypropylene. In: Karger-Kocsis J (ed) *Polypropylene: structure, blends and composites*, vol 1. Chapman & Hall, London, pp 167–204
28. Varga J, Mudra I, Ehrenstein GW (1998) Morphology and properties of beta-nucleated injection molded isotactic polypropylene. *ANTEC Proc* 3:3492–3496
29. Roozmond PC, Peters GWM (2013) Flow-enhanced nucleation of poly(1-butene): model application to short-term and continuous shear and extensional flow. *J Rheol* 57:1633–1653
30. Ottonello P (2003) Flow-induced crystal nucleation in polymeric systems. Master's thesis, University of Genova, Italy
31. Baert J (2009) Flow-induced crystallization of poly-1-butene. PhD thesis, Katholieke Universiteit Leuven, Belgium
32. Fang H, Zhang Y, Bai J, Wang Z (2013) Shear-induced nucleation and morphological evolution for bimodal long chain branched polylactide. *Macromolecules* 46:6555–6565
33. Carrot C, Guillet J, Boutahar K (1993) Rheological behavior of a semi-crystalline polymer during isothermal crystallization. *Rheol Acta* 32:566–574
34. Vleeshouwers S, Meijer HEH (1996) A rheological study of shear induced crystallization. *Rheol Acta* 35:391–399
35. Housmans JW, Steenbakkens RJA, Roozmond PC, Peters GWM, Meijer HEH (2009) Saturation of pointlike nuclei and the transition to oriented structures in flow-induced crystallization of isotactic polypropylene. *Macromolecules* 42:5728–5740
36. Hadinata C, Gabriel C, Ruellman M, Laun HM (2005) Comparison of shear-induced crystallization behavior of PB-1 samples with different molecular weight distribution. *J Rheol* 49(1):327–349
37. Hadinata C, Boos D, Gabriel C, Wassner E, Ruellmann M, Kao N, Laun M (2007) Elongation-induced crystallization of a high molecular weight isotactic polybutene-1 melt compared to shear-induced crystallization. *J Rheol* 51(2):195–215
38. Acierno S, Coppola S, Grizzuti N (2008) Effects of molecular weight distribution on the flow-enhanced crystallization of poly(1-butene). *J Rheol* 52(2):551–566
39. Steenbakkens RJA, Peters GWM (2008) Suspension-based rheological modeling of crystallizing polymer melts. *Rheol Acta* 47(5–6):643–665
40. Roozmond PC, Janssens V, van Puyvelde P, Peters GWM (2012) Suspension-like hardening behavior of HDPE and time-hardening superposition. *Rheol Acta* 51:97–109
41. Fernandez-Ballester L, Thurman DW, Zhou W, Kornfield JA (2012) Effect of long chains on the threshold stresses for flow-induced crystallization in iPP: shish kebabs vs sausages. *Macromolecules* 45:6557–6570
42. Kornfield JA, Kumaraswamy G, Issaian AM (2002) Recent advances in understanding flow effects on polymer crystallization. *Ind Eng Chem Res* 41:6383–6392
43. Baert J, van Puyvelde P, Langouche F (2006) Flow-induced crystallization of PB-1: from the low shear rate region up to processing rates. *Macromolecules* 39:9215–9222
44. Kumaraswamy G, Issaian AM, Kornfield JA (1999) Shear-enhanced crystallization in isotactic polypropylene. 1. Correspondence between in situ rheo-optics and ex situ structure determination. *Macromolecules* 32:7537–7547

45. Mykhaylyk OO, Chambom P, Graham RS, Fairclough JPA, Olmsted PD, Ryan AJ (2008) The specific work of flow as a criterion for orientation in polymer crystallization. *Macromolecules* 41:1901–1904
46. Mykhaylyk OO, Chambom P, Impradice C, Fairclough JPA, Terrill NJ, Ryan AJ (2010) Control of structural morphology in shear-induced crystallization of polymers. *Macromolecules* 43:2389–2405
47. Okura M, Mykhaylyk OO, Ryan AJ (2013) Effect of matrix polymer on flow-induced nucleation in polymer blends. *Phys Rev Lett* 110:087801
48. Kumaraswamy G, Verma RK, Issaian AM, Wang P, Kornfield JA, Yeh F, Hsiao BS, Olley RH (2000) Shear-enhanced crystallization in isotactic polypropylene Part 2. Analysis of the formation of the oriented “skin”. *Polymer* 41:8931–8940
49. Kumaraswamy G, Verma RK, Kornfield JA, Yeh F, Hsiao BS (2004) Shear-enhanced crystallization in isotactic polypropylene: in-situ synchrotron SAXS and WAXD. *Macromolecules* 37:9005–9017
50. Somani RH, Hsiao BS, Nogales A, Sics I, Balta-Calleja FJ, Ezquerro TA (2000) Structure development during shear flow-induced crystallization of i-PP: in-situ small-angle X-ray scattering study. *Macromolecules* 33:9385–9394
51. Somani RH, Yang L, Hsiao BS, Agarwal PK, Fruitwala HA, Tsou AH (2002) Shear-induced precursor structures in isotactic polypropylene melt by in-situ Rheo-SAXS and Rheo-WAXD studies. *Macromolecules* 35:9096–9104
52. Somani RH, Yang L, Zhu L, Hsiao BS (2005) Flow-induced shish-kebab precursor structures in entangled polymer melts. *Polymer* 46:8587–8623
53. Hsiao BS, Yang L, Somani R, Avila-Orta CA, Zhu L (2005) Unexpected shish-kebab structure in a sheared polyethylene melt. *Phys Rev Lett* 94:117802
54. Somani RH, Yang L, Hsiao BS (2006) Effects of high molecular weight species on shear-induced orientation and crystallization of isotactic polypropylene. *Polymer* 47:5657–5668
55. Kimata S, Sakurai T, Nozue Y, Kasahara T, Yamaguchi N, Karino T, Shibayama M, Kornfield JA (2007) Molecular basis of the shish-kebab morphology in polymer crystallization. *Science* 316:1014–1017
56. Avrami M (1939) Kinetics of phase change. I: General theory. *J Chem Phys* 7(12):1103–1112
57. Avrami M (1940) Kinetics of phase change. II: Transformation-time relations for random distribution of nuclei. *J Chem Phys* 8(2):212–224
58. Pogodina NV, Winter HH, Srinivas S (1999) Strain effects on physical gelation of crystallizing isotactic polypropylene. *J Polym Sci B Polym Phys* 37:3512–3519
59. Balzano L, Ma Z, Cavallo D, van Erp TB, Fernandez-Ballester L, Peters GWM (2016) Molecular aspects of the formation of shish-kebab in isotactic polypropylene. *Macromolecules* 49:3799–3809
60. Cui K, Meng L, Tian N, Zhou W, Liu Y, Wang Z, He J, Li L (2012) Self-acceleration of nucleation and formation of shish in extension-induced crystallization with strain beyond fracture. *Macromolecules* 45:5477–5486
61. Ma Z, Balzano L, van Erp T, Portale G, Peters GWM (2013) Short-term flow induced crystallization in isotactic polypropylene: how short is short? *Macromolecules* 46:9249–9258
62. Janeschitz-Kriegl H, Ratajski E (2005) Kinetics of polymer crystallization under processing conditions: transformation of dormant nuclei by the action of flow. *Polymer* 46:3856–3870
63. Zuidema H, Peters GWM, Meijer HEH (2001) Development and validation of a recoverable strain-based model for flow-induced crystallization of polymers. *Macromol Theory Simul* 10:447–460
64. Swartjes FHM, Peters GWM, Rastogi S (2003) Stress induced crystallization in elongational flow. *Int Polym Process* 18:53–66
65. Hwang WR, Peters GWM, Hulslen MA, Meijer HEH (2006) Modeling of flow-induced crystallization of particle-filled polymers. *Macromolecules* 39:8389–8398

66. Custódio F, Steenbakkers RJA, Anderson PD, Peters GWM, Meijer HEH (2009) Model development and validation of crystallization behavior in injection molding prototype flows. *Macromol Theory Simul* 18(9):469–494
67. van Erp TB, Roozmond PC, Peters GWM (2013) Flow-enhanced crystallization kinetics of iPP during cooling at elevated pressure: characterization, validation, and development. *Macromol Theory Simul* 22:309–318
68. Schneider W, Köppl A, Berger J (1988) Non-isothermal crystallization of polymers. System of rate equations. *Int Polym Process* 2(3–4):151–154.
69. Eder G, Janeschitz-Kriegl H (1997) Structure development during processing: crystallization. In: Meijer HEH (ed) *Processing of polymers*, volume 18 of materials science and technology: a comprehensive treatment. Wiley-VCH, Weinheim, pp 269–342
70. Coppola S, Grizzuti N (2001) Microrheological modeling of flow-induced crystallization. *Macromolecules* 34:5030–5036
71. Ziabicki A, Alfonso GC (1994) Memory effects in isothermal crystallization. I. Theory. *Colloid Polym Sci* 27:1027–1042
72. Ziabicki A, Alfonso GC (2002) A simple model of flow-induced crystallization memory. *Macromol Symp* 185:211–231
73. Lamberti G (2011) Flow-induced crystallization during isotactic polypropylene film casting. *Polym Eng Sci* 51:851–61
74. Doufas AK, Dairanieh IS, McHugh AJ (1999) A continuum model for flow-induced crystallization of polymer melts. *J Rheol* 43:85–109
75. Doufas AK, McHugh AJ (2001) Simulation of melt spinning including flow-induced crystallization. Part III. Quantitative comparisons with PET spinline data. *J Rheol* 45:403–420
76. Doufas AK, Rice L, Thurston W (2011) Shear and extensional rheology of polypropylene melts: experimental and modeling studies. *J Rheol* 55:95–126
77. Baig C, Edwards BJ (2010) Atomistic simulation of flow-induced crystallization at constant temperature. *Eur Phys Lett* 89:36003
78. Graham RS, Olmsted PD (2009) Coarse-grained simulations of flow-induced nucleation in semicrystalline polymers. *Phys Rev Lett* 103(11):115702
79. Graham RS, Olmsted PD (2010) Kinetic Monte-Carlo simulations of flow-induced nucleation in polymer melts. *Faraday Discuss* 144:1–22
80. Muthukumar M (2005) Modeling polymer crystallization. *Adv Polym Sci* 191:241–274
81. van Drongelen M, Roozmond PC, Troisi EM, Doufas AK, Peters GWM (2015) Characterization of the primary and secondary crystallization kinetics of a linear low-density polyethylene in quiescent- and flow-conditions. *Polymer* 76:254–270
82. van Erp TB, Balzano L, Spoelstra AB, Govaert LE, Peters GWM (2013) Quantification of non-isothermal, multi-phase crystallization of isotactic polypropylene: the influence of shear and pressure. *Polymer (United Kingdom)* 53:5896–5908
83. Verbeeten WMH, Peters GWM, Baaijens FPT (2001) Differential constitutive equations for polymer melts: the extended pom-pom model. *J Rheol* 45(4):823–843
84. Roozmond PC, Steenbakkers RJA, Peters GWM (2011) A model for flow-enhanced nucleation based on fibrillar dormant precursors. *Macromol Theory Simul* 20(2):93–109
85. Housmans JW, Balzano L, Santoro D, Peters GWM, Meijer HEH (2009) A design to study flow induced crystallization in a multipass rheometer. *Int Polym Process* 24(2):185–197
86. He J, Zoller P (1994) Crystallization of polypropylene, nylon-66 and poly(ethylene Terephthalate) at pressures to 200 MPa: kinetics and characterization of products. *J Polym Sci B Polym Phys* 32:1049–1087
87. Roozmond PC, van Erp TB, Peters GWM (2016) Flow-induced crystallization of isotactic polypropylene: modeling formation of multiple crystal phases and morphologies. *Polymer* 89:69–80
88. Portale G, Cavallo D, Alfonso GC, Hermida-Merino D, van Drongelen M, Balzano L, Peters GWM, Bras W (2013) Polymer crystallization studies under processing-relevant conditions at the SAXS/WAXS DUBBLE beamline at the ESRF. *J Appl Crystallogr* 46:1681–1689

89. Roozmond PC, Ma Z, Cui K, Li L, Peters GWM (2014) Multimorphological crystallization of shish-kebab structures in isotactic polypropylene: quantitative modeling of parent–daughter crystallization kinetics. *Macromolecules* 47:5152–5162
90. Dean DM, Rebenfeld L, Register RA, Hisao BS (1998) Matrix molecular orientation in fiber-reinforced polypropylene composites. *J Mater Sci* 33:4797–4812
91. Hermans JJ, Vermaas D, Hermans PH, Weidinger A (1946) Quantitative evaluation of orientation in cellulose fibres from the X-ray fibre diagram. *Recueil des Travaux Chimiques des Pays-Bas* 65:427–447
92. Stein RS, Norris FH (1958) The X-ray diffraction, birefringence, and infrared dichroism of stretched polyethylene. *J Polym Sci* 21:381–396
93. Wilchinsky ZW (1960) Measurement of orientation in polypropylene film. *J Appl Phys* 31:1969–1972
94. Roozmond PC, van Drongelen M, Ma Z, Spoelstra AB, Hermida-Merino D, Peters GWM (2015) Self-regulation in flow-induced structure formation of isotactic polypropylene. *Macromol Rapid Commun* 36:385–390
95. Hirt CW, Amsden AA, Cook JL (1974) An arbitrary Lagrangian-Eulerian computing method for all flow speeds. *J Comput Phys* 14:227–253
96. D’Avino G, Hulsen MA (2010) Decoupled second-order transient schemes for the flow of viscoelastic fluids without a viscous solvent contribution. *J Non-Newtonian Fluid Mech* 165:1602–1612
97. Guenette R, Fortin M (1995) A new mixed finite element method for computing viscoelastic flows. *J Non-Newtonian Fluid Mech* 60:27–52
98. Bogaerds ACB, Grillet AM, Peters GWM, Baaijens FPT (2002) Stability analysis of polymer shear flows using the eXtended Pom-Pom constitutive equations. *J Non-Newtonian Fluid Mech* 108:187–208
99. Brooks AN, Hughes TJR (1982) Streamline upwind/Petrov-Galerkin formulations for convection dominated flows with particular emphasis on the incompressible Navier-Stokes equations. *Comput Methods Appl Mech Eng* 33:199–259
100. Hulsen MA, Fattal R, Kupferman R (2005) Flow of viscoelastic fluids past a cylinder at high Weissenberg number: stabilized simulations using matrix logarithms. *J Non-Newtonian Fluid Mech* 127:27–39
101. Verbeeten WMH, Peters GWM, Baaijens FPT (2004) Numerical simulations of the planar contraction flow for a polyethylene melt using the XPP model. *J Non-Newtonian Fluid Mech* 117(2-3):73–84
102. Zoller P (1979) Pressure-volume-temperature relationships of solid and molten polypropylene and poly(butene-1). *J Appl Polym Sci* 23:1057–1061
103. van der Beek MHE (2005) Specific volume of polymers: influence of the thermomechanical history. PhD thesis, Eindhoven University of Technology, Netherlands
104. Incropera FP, DeWitt DP, Bergman TL, Lavine AS (2007) Introduction to heat transfer. Wiley, Hoboken
105. Venerus DC, Schieber JD, Iddir H, Guzman JD, Broerman AW (1999) Relaxation of anisotropic thermal diffusivity in a polymer melt following step shear strain. *Phys Rev Lett* 82:366–369
106. van Meerveld J, Peters GWM, Huetter M (2004) Towards a rheological classification of flow induced crystallization experiments of polymer melts. *Rheol Acta* 44:119–134
107. Hwang WR, Hulsen MA, Meijer HEH (2004) Direct simulations of particle suspensions in a viscoelastic fluid in sliding bi-periodic frames. *J Non-Newtonian Fluid Mech* 121:15–33
108. Keller A, Kolnaar HWH (1997) Flow-induced orientation and structure formation. In: Meijer HEM (ed) Processing of polymers, volume 18 of materials science and technology: a comprehensive treatment. Wiley-VCH, Weinheim, pp 189–268
109. Hill MJ, Keller A (1981) “Hairdressing” shish-kebabs by melting. *Colloid Polym Sci* 259:335–341

110. Roozmond PC (2014) Flow-induced crystallization of polymers: modeling morphology and kinetics. PhD thesis, Eindhoven University of Technology, Netherlands. Available at <http://alexandria.tue.nl/extra2/773182.pdf>
111. Le Moigne N, van den Oever M, Budtova T (2013) Dynamic and capillary shear rheology of natural fiber-reinforced composites. *Polym Eng Sci* 53:2582–2593
112. Ballard DGH, Cheshire P, Longman GW, Schelten J (1978) Small-angle neutron scattering studies of isotropic polypropylene. *Polymer* 19:379–385
113. van Drongelen M, van Erp TB, Peters GWM (2012) Quantification of non-isothermal, multi-phase crystallization of isotactic polypropylene: the influence of cooling rate and pressure. *Polymer* 53:4758–4769
114. Seki M, Thurman DW, Oberhauser JP, Kornfield JA (2002) Shear-mediated crystallization of isotactic polypropylene: the role of long chain-long chain overlap. *Macromolecules* 35:2583–2594
115. Hatzikiriakos S, Dealy JM (1994) Start-up pressure transients in a capillary rheometer. *Polym Eng Sci* 34:493–499
116. Roozmond PC, van Drongelen M, Verbelen L, Van Puyvelde P, Peters GWM (2014) Flow-induced crystallization studied in the RheoDSC device: quantifying the importance of edge effects. *Rheologica Acta*. 54(1):1–8
117. van Erp TB, Balzano L, Peters GWM (2012) Oriented gamma phase in isotactic polypropylene homopolymer. *ACS Macro Lett* 1:618–622
118. Hoffman JD, Guttman CM, DiMarzio EA (1979) On the problem of crystallization of polymers from the melt with chain folding. *Faraday Discuss Chem Soc* 68:177–197
119. Schoonen JFM, Swartjes FHM, Peters GWM, Baaijens FPT, Meijer HEH (1998) A 3D numerical/experimental study on a stagnation flow of a polyisobutylene solution. *J Non-Newtonian Fluid Mech* 79:529–562
120. Caelers HJM, Govaert LE, Peters GWM (2016) The prediction of mechanical performance of isotactic polypropylene on the basis of processing conditions. *Polymer* 86:116–128

Index

A

Acid-functionalized POSS (APOSS), 195
Acyclic diene metathesis polymerization (ADMET), 135, 139, 151, 165
Addition copolymerization, 3, 4
Amphiphiles, 38
 giant, 186, 190, 198, 209
Annealing, 25–32, 118, 160, 188, 206, 220, 268
 domain, 119, 220

B

Bicontinuous double gyroids (DG), 199
Body-centered cubic packed spheres (BCC), 199

C

Calorimetry, 10, 54, 108, 140, 216, 259, 269
Carbon nanotubes (CNTs), 246
Cavitation, 47–50
Chain-growth parameters, 8
Chemical modifications, 2
C₆₀-oligofluorene (OF), 192
Component segregation, 1, 3
Condensation copolymerization, 4
Confinement, 231
Crystal morphology, 23, 35, 95, 257, 272
Crystal nucleation, 38, 216, 257
 heterogenous, 258
 homogenous, 257
Crystalline memory, 222
Crystallization, 1, 93
 analysis fractionation (CRYSTAF), 38
 chain topology, 93

 dilute solutions, 99
 fractionated, 229
 isothermal, 150
 macromolecular segregation, 33
 melt state, 102, 258
 monomer segregation, 3, 13
 monomer-sequence segregation, 3, 25
 rate, 215
Crystallographic slip process, 45, 78
Cyclic polymers, crystallization, 93
Cyclodextrins, 225

D

Dendrimers, 185
 amphiphilic, 194
Differential scanning calorimetry (DSC), 10, 54, 108, 140, 216, 259, 269
Diffusion, 93
Direct ¹³C-NMR peak method (DPM), 8
Dislocation model, 45

E

Electrostatic self-assembly and covalent fixation (ESA-CF), 96
Enthalpy relaxation, 268
Entropic factors, 93
Equilibrium melting temperature, 93
Ethylene–1-alkene, 14, 30
Ethylene–1-butene, 15, 29, 244
Ethylene copolymers, crystallization, 133, 135
Ethylene propylene diene monomer (EPDM) rubber, 9

F

- Fast scanning chip calorimetry (FSC), 259
- Fluorinated polyhedral oligomeric silsesquioxane (FPOSS), 201
- Fullerene, 185, 191

G

- Geometric isomers, 2
- Giant molecules, 183
- Gibbs–Thomson relation, 159
- Glassy amorphous phase, 268

H

- Halogens, precision substitution, 139
- Heterogeneous copolymers, 1, 9, 12
- Hexagonally packed cylinders (Hex), 199
- High density polyethylene (HDPE), 2, 4, 37, 38
- High impact polypropylene (HIPP), 2
- Hoffman–Lauritzen (HL) approach, 107, 111, 242, 259
- Homogeneous copolymers, 1, 9, 12
- Hydrogenated polybutadienes (HPBDs), 12, 32
- Hydroxyl-functionalized POSS (DPOSS), 199

I

- Isobutyl-functionalized POSS (BPOSS), 195

J

- Janus molecules, molecular nanoparticle (MNP)-based, 194

L

- Lamellae (Lam), 26, 37, 46, 63, 68, 76, 83, 102, 139, 147, 199, 237, 263, 280
- Lauritzen–Hoffman theory (LH), 107, 111, 242, 259
- Linear low density polyethylene (LLDPE), 2–5, 17, 23, 35, 227–229
- Linear polymers, 5, 93, 101, 113, 119, 140
- Low density polyethylene (LDPE), 2, 4

M

- Macromolecular segregation, crystallization, 33
- Markov modeling, 4
- Melt, crystallization, 258
 - memory, 215, 222

- supercooling, 257
- Melting domain, 218
- Melting–recrystallization, 47
- Mesophase, polymorphism, 272
- Methylene sequence length method (MSLM), 9
- Micronecking, 47–50
- Molecular nanoparticles, 183, 185
- Molecular weight, 244
- Monomer segregation, crystallization, 3, 13
- Monomer-sequence segregation, 3, 25

N

- Nanoatoms, 183
- Nanoparticles, molecular, 183
- Non-isothermal differential scanning calorimetry (DSC), 108
- Nucleation, agents, 245
 - density, 257, 263
 - efficiency (NE), 245
 - rate, 257
 - spherulitic structures, 102

P

- Pendant group interactions, 162
- Phenyl-C61-butyric acid methyl ester (PCBM), 192
- Polyamide 6 (PA 6), 261
- Polyamide 11 (PA 11), 261
- Polyamide 66 (PA 66), 261
- Polybutadiene-*b*-poly(ethylene oxide), 244
- Polybutadiene, hydrogenated (HPBD) 12, 31, 32
- Poly(butylene succinate) (PBS), 221
- Poly(butylene terephthalate) (PBT), 261
- Poly(*ε*-caprolactone) (PCL), 95, 225, 261
- Poly(*ε*-caprolactone)-*b*-poly(propylene adipate), 243
- Poly(ether ester), 243
- Poly(ethylene-*alt*-propylene) (PEP), 234
- Poly(ethylene azelate), 244
- Poly(ethylene glycol), 243
- Poly(ethylene naphthalate), 243
- Polyethylenes, 4, 102, 133
 - precision alkyl-branched, 157
- Poly(ethylene terephthalate) (PET), 243, 263
- Polyhedral oligomeric silsesquioxane (POSS), 185, 193
- Poly(L-lactic acid) (PLLA), 225, 244, 274
- Polymer brushes, 194
- Poly(methyl methacrylate) (PMMA), 3
- Polymorphism, 45, 150, 239

- Polyolefins, 2, 134, 165
Polyoxometalate (POM), 185
Poly(oxyethylene) (POE), 106
Poly(propylene azelate), 244
Polypropylene, isotactic (iPP), 45
Poly(propylene sebacate), 244
Poly(propylene suberate), 243
Poly(propylene terephthalate), 244
Polystyrene-*b*-poly(ethylene oxide) (PS-*b*-PEO), 201
Poly(tetrahydrofuran) (PTHF), 99, 102
Poly(trimethylene terephthalate), 244
Porphyrin, 191
PPDX-*b*-PCL, 241
Precision branching, 133
Precision copolymers, 133
Precision substitution, 133, 139
Propylene-(1-alkenes), 17, 261, 263
Propylene-(1-butene) (iPPBu), 45, 53, 61–84
Propylene-(ethylene) (iPPEt), 53, 61
Propylene-(1-hexene) (iPPHe), 45, 53
Propylene-(1-octadecene) (iPPOc), 45, 53
Propylene-(1-pentene) (iPPPe), 45, 53
Proteins, 94, 184, 189
PS-*b*-PB-*b*-PCL, 234
- R**
Random copolymers, 6, 35, 45
Ring-closure reactions, 95
Ring-expansion polymerization, 95
Ring-opening metathesis polymerization (ROMP), 135, 163–167, 172
Ring polymers, 94, 122
- S**
Screw dislocations, 47
Self-nucleation, 118–120, 215
Shear flow, 223
Sindiotactic poly(propylene) (sPP), 244
Small angle X-ray scattering (SAXS), 58, 66, 102, 113, 117, 148, 199, 205, 271
- Spherulites, 21, 46, 49, 103–105, 221, 280
 growth rate, 106, 278
Standard crystallization temperature, 217
Statistical copolymers, crystallization, 1
Step crystallization method (SC), 28
Stereoisomers, 2, 14
Successive self-nucleation and annealing (SSA), 28, 120
Supercooling, melt, 257, 261
Supramolecular crystals, 183, 187
Surfactants, giant, 186, 198, 208
- T**
Tacticity, 133, 165–167, 184
Tammann's nuclei development method, 257, 261, 274
Tetraalkylammonium hydroxide (TBAOH), 195
Tetrahedra, giant, 203
Thin films, giant molecules, 206
- U**
Ultra-high molecular weight polyethylene (UHMWPE), 4
- V**
Very low density polyethylene (VLDPE), 2, 36, 37
- X**
X-ray diffraction patterns (WAXS), 58, 82, 99, 221, 239
- Y**
Yield behavior, 45, 52, 73–80